UNIVERSIDADE FEDERAL DO PARÁ
INSTITUTO DE GEOCIÊNCIAS
PROGRAMA DE PÓS-GRADUAÇÃO EM GEOLOGIA E GEOQUÍMICA

TESE DE DOUTORADO Nº 139

GEOLOGIA E METALOGÊNESE DO OURO DO GREENSTONE BELT DA SERRA DAS PIPOCAS, MACIÇO DE TROIA, PROVÍNCIA BORBOREMA, NE–BRASIL

Tese apresentada por:

FELIPE GRANDJEAN DA COSTA
Orientador: Prof. Dr. Evandro Luiz Klein (CPRM)

BELÉM
2018

Dados Internacionais de Catalogação na Publicação (CIP)
Sistema de Bibliotecas da Universidade Federal do Pará
Gerada automaticamente pelo módulo Ficat, mediante os dados fornecidos pelo(a) autor(a)

C837g Costa, Felipe Grandjean
Geologia e metalogênese do ouro do greenstone belt da Serra das Pipocas, Maciço de Troia, Província Borborema, NE-Brasil / Felipe Grandjean Costa. — 2018
xii, 226 f. : il. color

Tese (Doutorado) - Programa de Pós-graduação em Geologia e Geoquímica (PPGG), Instituto de Geociências, Universidade Federal do Pará, Belém, 2018.
Orientação: Prof. Dr. Evandro Luiz Klein

1. Geocronologia. 2. Greenstone Belt. 3. Paleoproterozoico. 4. Ouro Orogênico. 5. Província Borborema. I. Klein, Evandro Luiz, *orient.* II. Título

CDD 553

Universidade Federal do Pará
Instituto de Geociências
Programa de Pós-Graduação em Geologia e Geoquímica

GEOLOGIA E METALOGÊNESE DO OURO DO GREENSTONE BELT DA SERRA DAS PIPOCAS, MACIÇO DE TROIA, PROVÍNCIA BORBOREMA, NE–BRASIL

TESE APRESENTADA POR:

FELIPE GRANDJEAN DA COSTA

Como requisito parcial à obtenção do Grau de Doutor em Ciências na Área de GEOLOGIA

Data de Aprovação: 13 / 12 / 2018

Banca Examinadora:

Prof. Dr. Evandro Luiz Klein
Orientador – CPRM

Prof.ª Dr.ª Lydia Maria Lobato
Membro – UFMG

Prof. Dr. Roberto Perez Xavier
Membro –UNICAMP

Prof. Dr. Paulo Sérgio de S. Gorayeb
Membro – UFPA

Prof. Dr. Raimundo Netuno N. Villas
Membro – UFPA

Para Helena e Isabela

Papai ama vocês

AGRADECIMENTOS

Primeiramente agradeço a Deus, que emana toda sua energia cósmica do reino das possibilidades. Nada é por acaso neste "mundo", tudo é quântico. Pense positivo.

Agradeço ao meu empregador Serviço Geológico do Brasil, conhecido também como Companhia de Pesquisa de Recursos Minerais (CPRM), pelo suporte financeiro e incentivo (liberação) para esta pesquisa. Agradeço ao Antônio Maurilio (enquanto coordenador executivo em Fortaleza), por todo apoio na tramitação burocrática deste doutorado, a Joseneusa pelo apoio na Câmara Técnico–Científica da CPRM e ao Prof. Dr. Roberto Ventura, que enquanto diretor do Departamento de Geologia e Recursos Minerais da CPRM deliberou autorização para este doutorado. Agradeço também aqueles que me acompanham dia a dia na residência de Fortaleza e/ou me acompanharam durante memoráveis trabalhos de campo no sertão do Ceará, incluindo meus amigos(as) geólogos(as) Tércyo Pinéo, Bruno Calado, Edney Palheta, Caê Ganade, João Naleto, Iramaia Braga e Wanessa Souza (laboratório).

Agradeço ao meu orientador Evandro Luiz Klein que articulou tudo (*sequência tipo greenstone + mineralização aurífera + amostras de testemunho = doutorado*) e me fez o convite para desenvolvimento desta Tese, e embora nossa comunicação tenha sido geralmente por email, devido à distância geográfica (orientador em Brasília, eu em Fortaleza), ele sempre se mostrou amigo e profissional em todas as correspondências, sempre finalizando com palavras de incentivo (*ex. "go ahead"*). Valeu Evandro, *many thanks!!!*

Em 2016 tive o prazer de morar na capital paraense, Belém, para obtenção dos créditos (aulas) necessários e utilização de laboratórios. Na CPRM de Belém agradeço todo apoio de Lúcia Travassos (enquanto GEREMI), Marcelo Vasquez (MEV), Rosalva (laboratório) e Cesinha (que me cedeu um canto da sala). Na UFPA, agradeço ao apoio dos professores do PARA–ISO Jean M. Lafon, Candido Moura e Marco A. Galarza. Ao Prof. Régis Munhoz pelas proveitosas discussões nas aulas de inclusões fluidas e mineralizações em granitos, e aos meus colegas de pós–graduação Rafael Corrêa–Lima, Marcos Teódulo (Paraíba) e João Milhomen pela agradável companhia e "algumas cervejas". Agradeço também ao apoio técnico de Gisele Marques (MEV), Joelma Lobo (lâminas) e Cleida (da secretaria da PPGG).

Agradeço ao Conselho Nacional de Desenvolvimento Científico e Tecnológico (CNPq) pela bolsa (203250/2017–6) de doutorado sanduíche no exterior, na Universidade de Cape Town (UCT), África do Sul. Agradeço a orientação do Prof. Dr. Chris Harris durante (jan–jul de 2018) a obtenção de isótopos estáveis no laboratório da UCT, e também todo o apoio e amizade de Sherissa Roopnarain, geóloga e técnica do laboratório.

Agradeço a Jaguar Mining Inc. pela disponibilização dos testemunhos de sondagem, pois sem estas amostras, grande parte deste trabalho não seria exequível.

Agradeço aos membros da banca, professora Lydia Lobato (UFMG) e professores Roberto Xavier (UNICAMP), Paulo Gorayeb (UFPA) e Netuno Villas (UFPA) por aceitarem fazer parte do processo de avaliação desta Tese.

Eu como um bom Campineiro, criado nos arredores da Cidade Universitária, no Bairro do Guará, não posso deixar de agradecer aos meus amigos e professores da UNICAMP, Ticiano (Tirci), Elson Paiva (Elsão), Roberto Xavier (Robertinho) e meu grande amigo de graduação Prof. Wagner Amaral (Lobinho), por todo apoio e incentivo desde os primórdios de minha formação geoacadêmica. Neste contexto, agradeço também a todos aqueles que participaram e ajudaram de alguma maneira nesta minha missão geológica pelo mundo, seja na graduação (UNICAMP), no mestrado (UNICAMP), na CPRM e no doutorado (UFPA). Obrigado a todos! Niguem faz nada sozinho.

Agradeço a minha esposa Tatiana e minhas filhas Helena (9 anos) e Isabela (7 anos), por todo amor e apoio em casa, e por toda paciência durante nossas andanças por Belém (2016) e África do Sul (2018). Valeu!! Papai já vai sair do computador.

Por fim, agradeço aos meus pais Vivaldo Fernando da Costa e Dorthe Grandjean da Costa, por tudo, sempre. Amo vocês.

RESUMO

O Maciço de Troia representa um dos principais domínios de embasamento arqueano/paleoproterozoico da Província Borborema, NE–Brasil, compondo–se principalmente de terrenos granito–*greenstone* riacianos e gnaisses TTGs de idades neoarqueanas. Os g*reenstone belts* paleoproterozoicos do Maciço de Troia compartilham idades, características litoestratigráficas e mineralização aurífera, com aspectos similares de outros *greenstone belts* riacianos dos crátons adjacentes. Uma idade U–Pb em zircão de 2185 ± 4 Ma foi obtida para metatonalito pré–colisional (tonalitos Mirador) com afinidade geoquímica semelhante à adakitos. Para plutons potássicos colisionais (Suíte Bananeira) obteve–se as idades U–Pb em zircão de 2079 ± 4 Ma para um quartzo monzonito deformado e 2068 ± 5 Ma para um granito equigranular menos deformado. Ambos são cálcio–alcalinos de alto–K, derivados da fusão parcial de fonte crustal. As idades modelo Hf em zircão de todos os granitoides variam entre 2800 e 2535 Ma, evidenciando que componentes de crosta arqueana contribuíram para a gênese do magmatismo. No entanto, zircões herdados com c. 2.3 Ga mostraram valores de $\varepsilon_{Hf}(t)$ de c. +4,9, indicando que crosta paleoproterozoica menos radiogênica (juvenil) também participou como fonte de magma. A mineralização de ouro no *greenstone belt* da Serra das Pipocas está associada a zona de cisalhamento, e a principal área mineralizada (o depósito de Pedra Branca) se estabeleceu no limite estratigráfico da unidade metavulcânica máfica e metassedimentar da sequência *greenstone*. O estágio principal da mineralização aurífera é encontrado em associação com veios de quartzo, alteração cálcio–silicática (diopsídio, feldspato potássico, anfibólio, titanita, biotita, pirita, albita, magnetita ± carbonatos) e abitização (albititos). Ouro livre comumente se precipita em estreita associação espacial com magnetita e teluretos de ouro e prata. Duas assembleias de inclusões fluidas foram identificadas em veios de quartzo associados à alteração cálcio–silicática. A assembleia 1 é caracterizada por trilhas pseudo–secundárias que mostram a coexistência de três tipos de inclusões fluidas (aquosas, aquo–carbônicas e carbônicas), sugerindo formação durante a separação de fases (imiscibilidade de fluidos). A intersecção das isócoras médias para inclusões aquosas e carbônicas coexistentes sugere condições de PT de 495°C e 2.83 kbar (10.5 km de profundidade), semelhante a condições de PT de depósitos de ouro orogênico hipozonal. A assembleia 2 é representada por inclusões fluidas secundárias, aquosas e de baixa temperatura (Th < 200°C), provavelmente não relacionadas à mineralização aurífera. Os valores de $\delta^{18}O$, δD e $\delta^{13}C$ dos minerais hidrotermais (quartzo, calcita, biotita, hornblenda e magnetita) evidenciam valores de $\delta^{18}O$ do fluido variando de +8,3 a +11,0 ‰ (n=59), δD do fluido de -98 a -32‰ (n=24) e valores de $\delta^{13}C$ de calcita de -6,35 a -9,40 ‰ (n=3). A

geotermometria por isótopos de oxigênio em pares de quartzo–magnetita forneceu temperaturas de 467 a 526°C (n=7, média de 503°C), que provavelmente, representa a temperatura de deposição de ouro. A associação de ouro com magnetita e teluretos sugere um fluido formador de minério proveniente de magmas oxidados, semelhante àqueles interpretados como "depósitos de ouro orogênico relacionado a intrusões oxidadas", comumente descrito em outros *greenstone belts* pré–cambrianos (ex., Abitibi e Eastern Goldfields). Quatro eventos de deformação (Dn, Dn+1, Dn+2 e Dn+3) são reconhecidos no *greenstone belt* da Serra das Pipocas. O evento Dn é responsável pela foliação Sn, paralela ao acamamento (So) da pilha metavulcanossedimentar. O evento Dn+1 é caracterizado pela foliação Sn+1, de mergulho principal para SE, sendo plano-axial a uma série de dobras assimétricas que evidenciam transporte tectônico para NW. O evento Dn+2 representa a fase de deformação transcorrente e o evento Dn+3 é caracterizado por deformação dúctil–rúptil. O estágio principal da mineralização de ouro é encontrado em veios de quartzo deformados, associados à alteração de alta temperatura (cálcio–silicática e albitização), no entanto, ocorrência de ouro (± Te, Ag) em estruturas Dn+3 (dúctil-rúptil) também foi observada. Uma idade U–Pb em titanita de 2029 ± 28 Ma foi obtida para a alteração de cálcio–silicática (e mineralização de ouro). No entanto, a forte perda de Pb dos grãos de titanita define uma idade de 574 ± 7 Ma no intercepto inferior da linha discórdia, evidenciando metamorfismo neoproterozoico. A idade U–Pb em zircão de 575 ± 3 Ma para diques sin–tectônicos à deformação Dn+3, sugere que a deformação progressiva (Dn+1, Dn+2 e Dn+3) é provavelmente de idade Neoproterozoica, com tensor de compressão máxima (σ1) na direção WNW–ESE. No entanto, em escala local, registros de deformação paleoproterozoica (Dn) ainda estão preservados. Como modelo genético para o depósito de ouro de Pedra Branca, é sugerido aqui, uma mineralização de ouro orogênico controlada por dois estágios de exumação tectônica; (1) mineralização de ouro orogênico hipozonal ocorreu em c. 2029 Ma, após pico do metamorfismo de alto grau e durante primeira exumação tectônica da sequência *greenstone*, e, posteriormente, em c. 575 Ma, (2) mineralização aurífera tardia (remobilização?) ocorreu em nível crustal mais raso, durante o segundo estágio de exumação tectônica, associado à orogênese Brasiliana/Pan–Africana.

Palavras–chave: Geocronologia. *Greenstone Belt*. Paleoproterozoico. Ouro Orogênico. Província Borborema.

ABSTRACT

At the Archean–Paleoproterozoic Troia Massif, in Borborema Province, NE–Brazil, two major Paleoproterozoic greenstone belts are recognized (Algodões and Serra das Pipocas). These share similar ages and lithostratigraphic characteristics with other 2.2–2.1 Ga greenstone belts of the surrounding cratonic domains (e.g. Guiana shield and São Luis–West Africa craton), and also host gold mineralization. In this thesis, a U–Pb zircon age of 2185 Ma was obtained for a pre–collisional metatonalite (Mirador tonalites) with geochemical affinity similar to adakites–like rocks. For syn– to post–collisional potassic plutons (Bananeira suite) we obtained U–Pb zircon ages of 2079 Ma for a deformed quartz monzonite and of 2068 Ma for the less–deformed equigranular granite. These granitoids of the Bananeira suite are both of high–K calc–alkaline affinity, and probably derived from partial melting of crustal sources. Zircon Hf crustal model ages of all granitoids range between 2800 and 2535 Ma, indicating that Archean crustal components contributed to their magma genesis. However, two analyzed c. 2.3 Ga old inherited zircon grains showing $\varepsilon_{Hf}(t)$ values of c. +4.9, indicate that crustal reworking of less–radiogenic Paleoproterozoic sources also participated. Gold mineralization in the Serra das Pipocas greenstone belt is associated with a regional NE-trending shear zone. The mineralized areas (the Pedra Branca gold deposit) are located near–parallel to the stratigraphy, siting on shear zones, between metavolcanic and metasedimentary unit boundaries. The main stage of gold mineralization is found in association with quartz veins, high–temperature calc–silicate alteration (diopside, K–feldspar, amphibole, titanite, biotite, pyrite, albite, magnetite ± carbonates) and albitization. Free–milling gold commonly precipitates in close association with magnetite and gold/silver tellurides. Two fluid inclusion assemblages were identified in mineralized quartz veins. Assemblage 1 is characterized by pseudo–secondary trails that show the coexistence of CO_2–rich and low salinity (0 to 8 wt% NaCl equiv.) CO_2–H_2O–NaCl and H_2O–NaCl inclusions, suggesting formation during phase separation (fluid immiscibility). The mean isochores intersection of CO_2–rich and H_2O–NaCl inclusions of assemblage 1 suggests PT conditions of 495 °C and 2.83 kbar (c. 10.5 km depth), akin to hypozonal orogenic gold deposits. Assemblage 2 is represented by late secondary low–temperature (Th<200°C) H_2O–NaCl inclusions, probably unrelated to gold mineralization. The $\delta^{18}O$, δD and $\delta^{13}C$ values of hydrothermal minerals (quartz, calcite, biotite, hornblende and magnetite) define fluid $\delta^{18}O$ values ranging from +8.3 to +11.0‰ (n=59), fluid δD from -98 to -32‰ (n=24) and $\delta^{13}C$ values of calcite from -6.35 to -9.40‰ (n=3). Oxygen isotope thermometry for quartz–magnetite pairs gave temperatures from 467 to 526°C (n=7, average 503°C), which probably represents the temperature of gold deposition.

The association of gold with magnetite and tellurides strongly suggests an ore–forming fluid sourced by oxidized magmas, similar to those interpreted as ‘orogenic oxidized intrusion–related gold deposits’ in other Precambrian greenstone belts (e.g. Abitibi and Eastern Goldfields). Four deformation events (Dn, Dn+1, Dn+2 and Dn+3) are recognized in the Serra das Pipocas greenstone belt. The Dn event is responsible for the early Sn foliation, parallel to bedding (So) of the greenstone pile. The Dn+1 event is characterized by a pervasive, southeasterly–dipping Sn+1 foliation that is axial–planar to a number of asymmetric, tight to isoclinal and recumbent folds. The Dn+2 event represents a transcurrent deformation phase and the late Dn+3 event is characterized by ductile–brittle deformation. The main stage of gold mineralization is found as deformed quartz veins and associated high–temperature alteration, but some lower temperature gold (±Te, Ag) occurrence along the late stage brittle structures (Dn+3 event) is also observed. The U–Pb titanite age of 2029 ± 28 Ma for the high–temperature calc–silicate alteration (and gold mineralization) is presented here. However, the strong Pb loss of titanite grains defines a 574 ± 7 Ma lower intercept age, evidencing that early gold mineralization were broadly affected by Neoproterozoic deformational events and metamorphism (Brasiliano/Pan–African orogeny). The U–Pb zircon age of 575 ± 3 Ma for syn–tectonic diques bracketed the age of late Dn+3 deformation event. Then, the progressive deformation recorded (Dn+1, Dn+2 and Dn+3) is probably of Neoproterozoic age, with the maximum compressive stress (σ1) in the WNW–ESE direction. However, at local scale, Paleoproterozoic deformation records (Dn) still preserved. The genetic model for the Pedra Branca gold deposit is suggested here by a two–stage exhumation–drive gold mineralization; represented by a (1) early oxidized hypozonal orogenic gold mineralization (main stage) that occurred at c. 2029 Ma, shortly after the high–grade Paleoproterozoic metamorphism and first exhumation processes of the greenstone pile, and later on, at c. 580 Ma, a (2) late gold mineralization (remobilization?) occurred at shallow levels (second exhumation process) associated to late Neoproterozoic Brasiliano/Pan–African orogeny.

Keywords: Geochronology. Greenstone Belt. Paleoproterozoic. Orogenic Gold. Borborema Province.

SUMÁRIO

1. INTRODUÇÃO

1.1. APRESENTAÇÃO

Terrenos granito–*greenstone* arqueanos e paleoproterozoicos apresentam uma grande importância econômica quando o foco da pesquisa é o elemento ouro (Au) (ex. Dubé & Mercier–Langevin, 2015, Foster, 1993; Frimmel, 2008, 2018, Goldfarb *et al.* 2017). Essa íntima relação entre ouro e *greenstone belts* levou na década de 80 à profusão do termo *greenstone–hosted gold deposits*, incluindo modelos singenéticos de mineralização (ex. Hutchinson 1987). No entanto, atualmente, o termo *greenstone–hosted* é enquadrado dentro do modelo genético de **ouro orogênico**, não se restringindo a *greenstone belts* e com origem epigenética claramente demostrada (Goldfarb *et al.* 2005, Groves *et al.* 1998).

Nos domínios cratônicos, em configuração continental pré–mesozoica entre Brasil e África, *greenstone belts* riacianos (2.3–2.0 Ga) são comumente encontrados (**Fig. 1.1**), incluindo os terrenos granito–*greenstone* Transamazônicos/Eburneanos do Cráton Oeste Africano (Block *et al.* 2016, Feybesse *et al.* 2006, Liégeois *et al*. 1991, Petersson *et al*. 2016, 2017) e de sua contraparte Brasileira (Klein & Moura, 2008), assim como terrenos correlatos do Escudo das Guianas (Cráton Amazônico) (Delor *et al.* 2003, McReath & Faraco, 2006, Rosa–Costa *et al.* 2006, Vanderhaeghe *et al.* 1998) e do Cráton do São Francisco (Costa *et al*. 2011, Oliveira *et al.* 2011, Silva *et al.* 2001) (**Fig. 1.1**). Adicionalmente, muitas destas sequências hospedam uma série de depósitos auríferos importantes, geralmente interpretados como do tipo ouro orogênico e associados ao estágio final da orogênese Transamazônica/Eburneana (c. 2.0 Ga) (Béziat *et al*. 2008, Daoust *et al*. 2011, Hammond *et al*. 2011, Klein, 2014, Klein *et al*. 2014, 2015, McReath & Faraco, 2006, Mello *et al*. 2006, Mignot *et al*. 2017, Silva *et al*. 2001, Voicu *et al*. 2001). No entanto, nas margens cratônicas, parte destes *greenstone belts* paleoproterozoicos e depósitos de ouro associados foram retrabalhados pela orogênese Brasiliana/Pan–africana (620–580 Ma) (ex., Maciço de Goiás, Jost *et al*. 2010 e Cinturão Gurupi, Klein *et al*. 2005, 2006) (**Fig. 1.1**).

A Província Borborema, no extremo nordeste do continente sul–americano, é considerada um cinturão móvel neoproterozoico associado à orogênese Brasiliana/Pan–africana (c. 650–535 Ma) (Almeida *et al*. 1981, Brito Neves *et al*. 2000) (**Fig. 1.1**). Esta província compreende vastos domínios de rochas paleoproterozoicas, que representam, pelo menos em parte, margens cratônicas retrabalhadas dos crátons São Luís–Oeste Africano e/ou São Francisco–Congo (Costa *et al*. 2015, Dantas *et al*. 2004, 2013, Fetter *et al*. 2000, Ganade *et al*. 2017, Hollanda *et al*. 2011, Neves, 2015, Souza *et al*. 2016). Neste contexto, o Maciço

de Troia, representa um dos principais núcleos de embasamento arqueano/paleoproterozoico na Província Borborema, sendo composto principalmente por gnaisses TTG de idades neoarqueanas e terrenos granito–*greenstone* de idade paleoproterozoica (Arthaud *et al*. 2008, Costa *et al*. 2015, Fetter, 1999, Fetter *et al*. 2000, Ganade *et al*. 2017, Martins *et al*. 2009, Pessoa *et al*. 1986, Sousa, 2016) (**Fig. 1.1**).

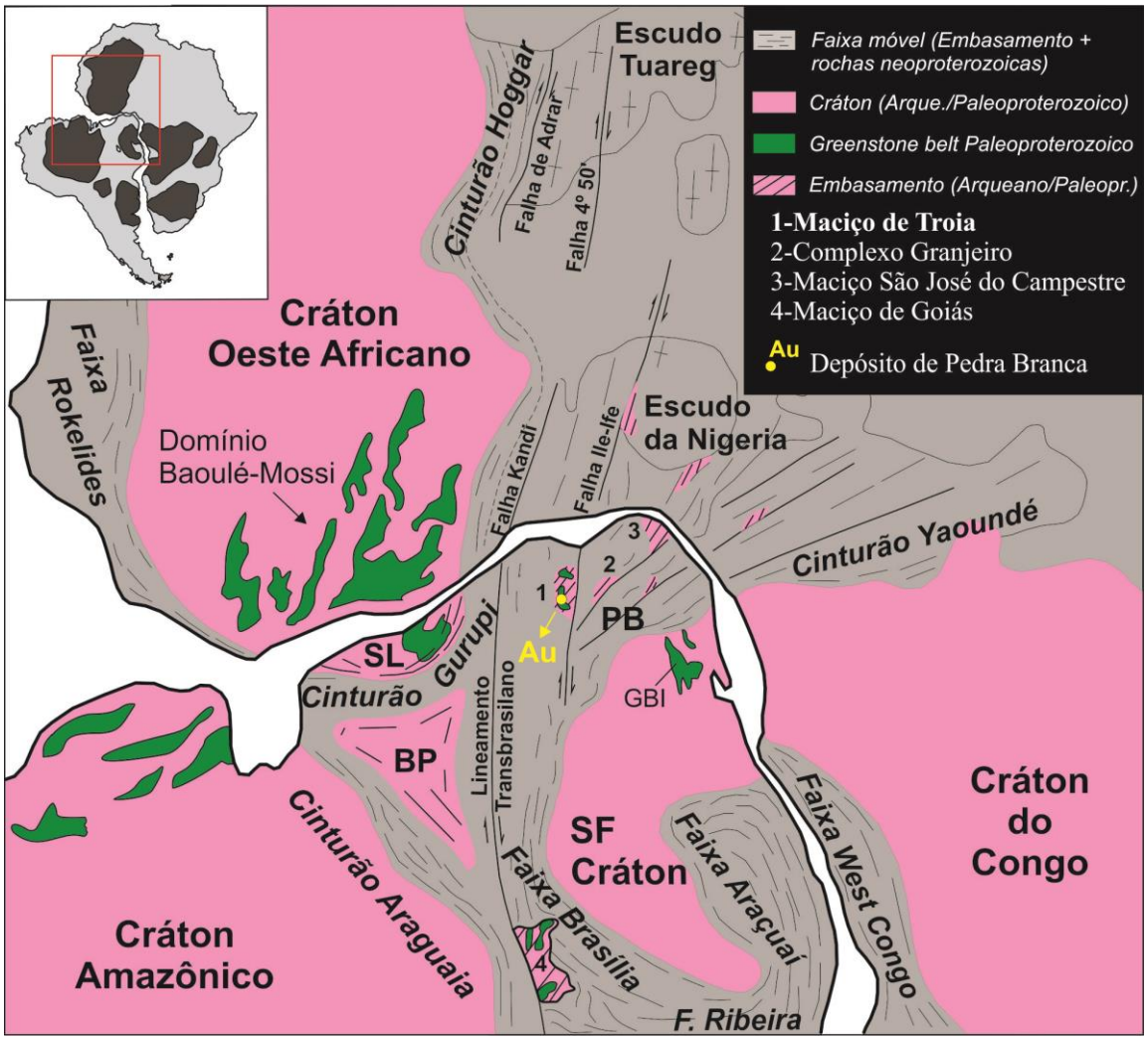

Fig. 1.1. Reconstrução pré–mesozoica da porção N/NE da América do Sul e W/NW da África, mostrando os principais domínios cratônicos, terrenos granito–greenstone paleoproterozoicos e faixas móveis (neoproterozoicas) brasilianas/pan–africanas (modificado de Trompette, 1994) (Figura fora de escala). PB= Província Borborema, SF= São Francisco, BP= Bloco Parnaíba, SL= São Luis e GBI= Greenstone belt do Rio Itapicuru.

Recentemente, no Maciço de Troia, mineralizações de ouro (depósito de Pedra Branca) foram identificadas pela empresa Jaguar Mining no *greenstone belt* da Serra das Pipocas, (Lopez, 2012) (*Pedra Branca project* – www.jaguarmining.com) (**Fig. 1.1**). Geograficamente, o depósito de Pedra Branca localiza–se na região central do Estado do

Ceará, a cerca de 270 km da capital Fortaleza (**Fig. 1.2**). As mineralizações de ouro ocorrem associadas a zonas de cisalhamento regionais de direção NE–SW, cortando sequências de rochas metavulcanossedimentares metamorfizadas em fácies anfibolito (*greenstone belt* da Serra das Pipocas). A mineralização ocorre em veios de quartzo e zonas de alteração hidrotermal associada, medindo centenas de metros ao longo da direção, com 1 a 5 metros de espessura e teor de 2 g/t até 7 g/t ouro (Lopez, 2012). No entanto, nenhuma estimativa de reserva foi ainda publicada para este depósito.

Dentro do contexto apresentado acima, esta Tese de doutorado apresenta estudos acerca da evolução geodinâmica do *greenstone belt* da Serra das Pipocas e metalogênese do ouro nesta sequência (depósito de ouro de Pedra Branca). A área de estudo foi investigada do ponto de vista geocronológico, geoquímico e isotópico e os resultados obtidos foram apresentados na forma de artigos científicos, discutindo alguns temas frequentemente abordados na literatura internacional como: (i) *greenstone belts* paleoproterozoicos e orógenos acrescionários, (ii) depósitos de ouro orogênico hipozonal e fonte de fluidos hidrotermais, (iii) margens de crátons retrabalhadas e depósitos de ouro orogênico e (iv) depósitos de ouro orogênico controlados por exumação tectônica.

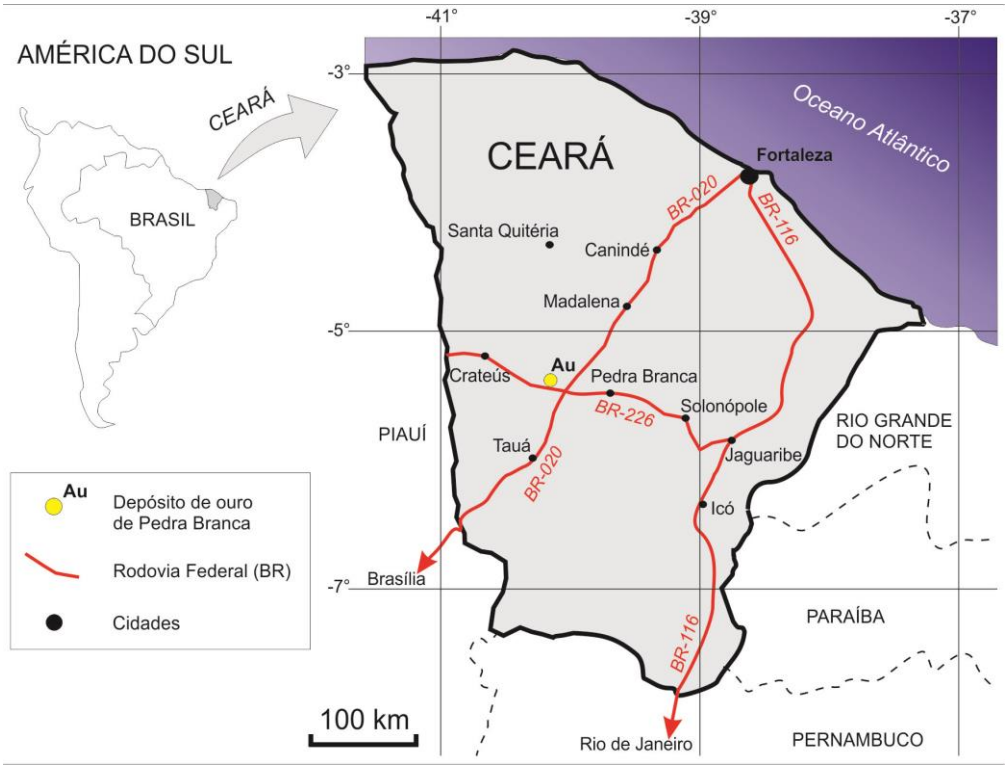

Fig. 1.2. Localização geográfica do depósito de Pedra Branca no Estado do Ceará e as principais rodovias de acesso a partir da capital Fortaleza.

1.2. ESTRUTURA DA TESE

Esta Tese de doutorado é composta de três artigos científicos, em conformidade com o atual regimento do Programa de Pós–Graduação em Geologia e Geoquímica (PPGG) da Universidade Federal do Pará (UFPA). A introdução da Tese (*capítulo 1*) é composta pelos itens; *1.1. Apresentação, 1.2. Estrutura da Tese, 1.3. Problemáticas abordadas e justificativas de Tese, 1.4. Objetivos, 1.5. Materiais e métodos* e *1.6. Geologia regional*.

O corpo principal da Tese constitui–se de um artigo publicado e de outros dois em processo de submissão/revisão. Os artigos apresentam distintas temáticas, conforme descritos abaixo;

No *capítulo 2*, o artigo **"*Geochemistry and U–Pb–Hf zircon data for plutonic rocks of the Troia Massif, Borborema Province, NE Brazil: Evidence for reworking of Archean and juvenile Paleoproterozoic crust during Rhyacian accretionary and collisional tectonics*"**, apresenta uma discussão com dados de U–Pb (SHRIMP e LA–ICPMS) em zircão, isótopos de Hf e litogeoquímica dos granitoides paleoproterozoicos do Maciço de Troia. Este artigo já se encontra publicado no periódico internacional *Precambrian Research*.

No *capítulo 3*, o artigo "***Fluid inclusion and stable isotope (O, H, C) constraints on the genesis of the Pedra Branca gold deposit, Troia Massif, Borborema Province, NE Brazil: A hypozonal orogenic gold mineralization sourced by magmatic–hydrothermal fluid***", apresenta dados de petrografia, inclusões fluidas e isótopos estáveis aplicados no depósito de ouro de Pedra Branca, focando na discussão da fonte de fluidos e condições de PT da mineralização. Este artigo foi submetido ao periódico internacional *Ore Geology Reviews*.

No *capítulo 4*, o artigo **"*Structural control and age of gold mineralization in the Troia Massif, Borborema Province, NE Brazil: A Paleoproterozoic (~2029 ma) hypozonal orogenic gold deposit overprinted by the late Neoproterozoic Brasiliano/Pan–African orogeny*"**, apresenta dados U–Pb em zircão e titanita para discussão sobre a(s) idade(s) da mineralização aurífera, assim como seu controle estrutural e idade da deformação. Este artigo foi submetido ao periódico internacional *Journal of South American Earth Sciences*.

Por fim, o ultimo capítulo (*Capítulo 5 – Conclusões*) constitui–se em um capítulo integrador com uma conclusão unificada ao conteúdo exposto nos três artigos, de modo a apresentar os principais resultados despendidos e futuras lacunas a serem preenchidas.

1.3. PROBLEMÁTICAS ABORDADAS E JUSTIFICATIVAS DE TESE

1.3.1. *Greenstone belts* paleoproterozoicos, granitoides e orógenos acrescionários

Orógenos acrescionários parecem ter sido ativos em grande parte da história da Terra (Cawood *et al*. 2006, 2009), e, segundo Furnes *et al*. (2015), cerca de 85% dos *greenstone belts* precambrianos são interpretados como registro de ofiolitos associados a subducção (*subduction–related ophiolites*). Por exemplo, em *greenstone belts* paleoproterozoicos, processos de crescimento crustal e retrabalhamento ao longo de orógenos acrescionários são, de longe, os modelos mais aceitos para evolução tectônica destes terrenos (ex. Costa *et al*. 2011, 2015, Feybesse *et al*. 2006, Ganne *et al*. 2011, Hanski *et al*. 2016, Hanski & Huhma, 2005, Korja *et al*. 2006, Lahtinen *et al*. 2016, Oliveira *et al*. 2011, Rosa–Costa *et al*. 2006, Silva *et al*. 2001).

Entre os registros de *greenstone belts* paleoproterozicos, diversos trabalhos acerca da evolução geodinâmica são frequentemente publicados para os *greenstone belts* Birimianos e/ou Transamazônicos (2.2–2.0 Ga) do Cráton São Luís–Oeste Africano (Block *et al*. 2016, Feybesse *et al*. 2006, Klein *et al*. 2008, 2012, Liégeois *et al*. 1991, Petersson *et al*. 2016, 2017, 2018) e terrenos correlacionados do Escudo das Guianas (Cráton Amazônico) (Barreto *et al*. 2013, Delor *et al*. 2003, McReath & Faraco, 2006, Rosa–Costa *et al*. 2006, Vanderhaeghe *et al*. 1998) e do norte do Cráton São Francisco (Costa *et al*. 2011, Oliveira *et al*. 2011, Silva *et al*. 2001) (**Fig. 1.1**). Muitos desses terrenos são interpretados como sequências de arco juvenil que evoluíram durante tectônica acrescionária em 2.2–2.1 Ga, seguida de colisão continental e metamorfismo regional em cerca de 2.0 Ga (Block *et al*. 2016, Costa *et al*. 2011, Delor *et al*. 2003, Eglinger *et al*. 2017, Feybesse *et al*. 2006, Klein *et al*. 2008, 2012, Liégeois *et al*. 1991, McReath & Faraco, 2006, Oliveira *et al*. 2011, Parra–Ávila *et al*. 2016, 2017, 2018, Petersson *et al*. 2016, 2017, 2018, Rosa–Costa *et al*. 2006, Vanderhaeghe *et al*. 1998).

Em grande parte dos trabalhos citados acima, as interpretações geodinâmicas são discutidas com base em litogeoquímica, geocronologia pelo método U–Pb em zircão e isótopos de Nd e/ou Hf em granitoides. Por exemplo, isótopos combinados de U–Pb–Hf em zircão foram recentemente relatados em *greenstone belts* do Cráton Oeste Africano, trazendo novas interpretações para a evolução crustal destes terrenos (Block *et al*. 2016, Eglinger *et al*. 2017, Parra–Ávila *et al*. 2016, 2017, Petersson *et al*. 2016, 2017). Segundo Petersson *et al*. (2017), isótopos de Hf obtidos em zircões de granitóides com idades entre 2.22 e 2.13 Ga do domínio Baoulé–Mossi (**Fig. 1.1**), indicam que componentes de crosta arqueana estiveram

envolvidos na gênese destas rochas, provavelmente por meio da subducção de sedimentos continentais em ambiente de arco.

Os *greenstone belts*, em geral, são intrinsicamente associados a granitoides, que representam uma porção inerente da evolução destes terrenos (ex. Laurent *et al*. 2014, Thurston, 2015). Neste sentido, em *greenstone belts* Transamazônicos/Birimianos, o estudo da granitogênese apresenta um alto poder interpretativo sobre a gênese destes domínios granito–*greenstone*, sendo, portanto, frequentemente reportado na literatura (ex. Baratoux *et al*. 2011, Barrueto, 2002, Costa *et al*. 2011, 2015, Eglinger *et al*. 2017, Feybesse *et al*. 2006, Gasquet *et al*. 2003, Klein *et al*. 2008). Geralmente, em *greenstone belts* Transamazônicos/Birimianos, a acresção de arcos intra–oceânicos (crosta juvenil) em margens continentais é uma interpretação muito frequente para a evolução plutônica ao longo desses terrenos (ex. Baratoux *et al*. 2011, Costa *et al*. 2011, Feybesse *et al*. 2006, Klein *et al*. 2008, Oliveira *et al*. 2011). Por exemplo, na região de Gana, no Cráton Oeste Africano, o desenvolvimento de tonalitos (tipo TTG/adakito) de arco intra–oceânicos em torno de 2.25 e 2.17 Ga foi seguido por intrusões de diversos plutons monzoníticos (derivados do manto) durante a acresção destes arcos em torno de 2.15–2.17 Ga, antes do registro final de colisão continental em torno de 2.0 Ga (Feybesse *et al*. 2006). Em outro exemplo, em sequência metavulcanossedimentar paleoproterozoica do Cráton São Luís, Klein et al. (2008) sugerem que o caráter juvenil e a assinatura geoquímica da Suíte Tromaí de ~2168–2147 Ma, refletem um plutonismo intra–oceânico que evoluiu durante o estágio principal do orógeno acrescionário riaciano, antecedendo o estágio de colisão continental e diversas intrusões de granitoides potássicos entre 2076 e 2056 Ma. Similarmente, no norte do Cráton São Francisco, os *greenstone belts* do Rio Itapicuru e Rio Capim têm sido interpretados como arcos intra–oceânicos que colidiram com margens continentais durante a orogênese do Riaciano (Barrueto, 2002 Costa *et al*. 2011, Oliveira *et al*. 2011). No *greenstone belt* do Rio Itapicuru, granitoides com idades de ~2163–2127 Ma apresentam assinatura juvenil por isótopos de Nd e geoquímica similar a de rochas throndjemítica, sendo, portanto, interpretados como magmatismo de arco intra–oceânico (Barrueto, 2002, Costa *et al*. 2011, Oliveira *et al*. 2011). No entanto, em torno de 2110–2100 Ma uma grande mudança na composição dos granitoides ocorreu no *greenstone bet* do Rio Itapicuru, registrado por plutons derivados do manto (ex. sienitos, adakitos de baixa–sílica, granitoides shoshoníticos), provavelmente em resposta a uma colisão do tipo arco–continente, que precedeu a colisão continental e metamorfismo regional em torno de 2.0 Ga (Costa *et al*. 2011, Oliveira *et al*. 2011). Nesta conjuntura, fica evidente que as manifestações plutônicas em *greenstone belts*

representam um elemento chave para interpretação geodinâmica destes terrenos. Nesta Tese, adentra-se nesta discussão (1º artigo) para a área de estudo, com base em dados de campo, litogeoquímicos e U–Pb–Hf em zircão dos granitoides associados ao *greenstone belt* paleoproterozoico da Serra das Pipocas, no Maciço de Troia.

1.3.2. Depósito de ouro orogênico hipozonal e fonte de fluidos hidrotermais

Uma profunda discussão existe na literatura sobre a fonte do ouro e de fluidos hidrotermais associados a depósitos de ouro do tipo orogênico, e, em geral, pesquisadores se dividem em duas principais vertentes de interpretação; (1) fonte metamórfica–hidrotermal (ex. Goldfarb & Groves, 2015, Kerrich & Fyfe, 1981, Large *et al*. 2012, Phillips & Powell, 2009, 2010, Pitcairn *et al*. 2006, Tomkins & Grundy, 2009, Tomkins, 2010, 2013) ou (2) fonte magmática–hidrotermal (ex. Beakhouse 2011, Bucci *et al*. 2002, Doublier *et al*. 2014, Duuring *et al*. 2007, Kendrick *et al*. 2011, Spence–Jones *et al*. 2018, Treloar *et al*. 2014, Xue *et al*. 2013, Zhang *et al*. 2017). Fluidos de origem metamórfica são geralmente assim interpretados por derivarem do metamorfismo de rochas supracrustais, como metavulcânicas máficas (ex. Bierlein & Pisarevsky, 2008, Elmer *et al*. 2006, Phillips & Powell, 2010) e turbiditos e folhelhos negros ricos em pirita diagenética (Large *et al*. 2012; Pitcairn *et al*. 2015). A maior parte dos fluidos metamórficos é liberada quando a rocha atinge temperaturas em torno de 500–550 °C (metamorfismo de fácies anfibolito), e muito pouco fluido é liberado acima de 550 °C (Tomkins 2010, 2013). Isso é condizente com a maior parte dos depósitos de ouro orogênico, pois estes geralmente se encontram associados a rochas de fácies xisto–verde e anfibolito baixo (Groves *et al*. 1998). No entanto, para os depósitos de ouro orogênico hipozonal (c. 12–20 km de profundidade), os fluidos não podem ser facilmente explicados por devolatização de rochas supracrustais, e, portanto, alguns autores (Phillips & Powell, 2010, Tomkins & Grundy, 2009) contestam o modelo elaborado por Groves (1993) de continuidade crustal (*the crustal continuum model*) (**Fig. 1.3**).

Para depósitos de ouro orogênico de alta temperatura (hipozonal), a fonte de fluidos (e ouro) é comumente associada a processos magmático–hidrotermais, sendo granitoides sin– a tardi–colisionais, de composição félsica/intermediára, a principal fonte de fluidos e ouro da mineralização (ex. Bucci *et al*. 2002, Doublier *et al*. 2014, Duuring *et al*. 2007, Mueller 1992). Geralmente, para depósitos de ouro orogênico associado a granitoides, interpretações na fonte de fluidos são baseadas em dados isotópicos (estáveis e radiogênicos) e de inclusões fluidas, além da associação no tempo e espaço entre as mineralizações e granitoides (ex. Bucci *et al*. 2002; Doublier *et al*. 2014, Duuring *et al*. 2007, Salier *et al*. 2005; Zhang *et al*.

2017). Dentro do contexto de fluidos magmático–hidrotermais, alguns autores remetem também à contribuição de fluidos derivados do manto, quando associados a magmas máficos e ultramáficos contemporâneos à mineralização (ex. Griffin *et al*. 2013, Hronsky *et al*. 2012, Mao *et al*. 2008, Rock *et al*. 1989, Vielreicher *et al*. 2010). Fluidos derivados de outros processos, como o de granulitização da base da crosta e desidratação de crosta oceânica subductada também são reportados na literatura (ex. Fu *et al*. 2014, Groves & Santosh, 2016, Pope *et al*. 2011).

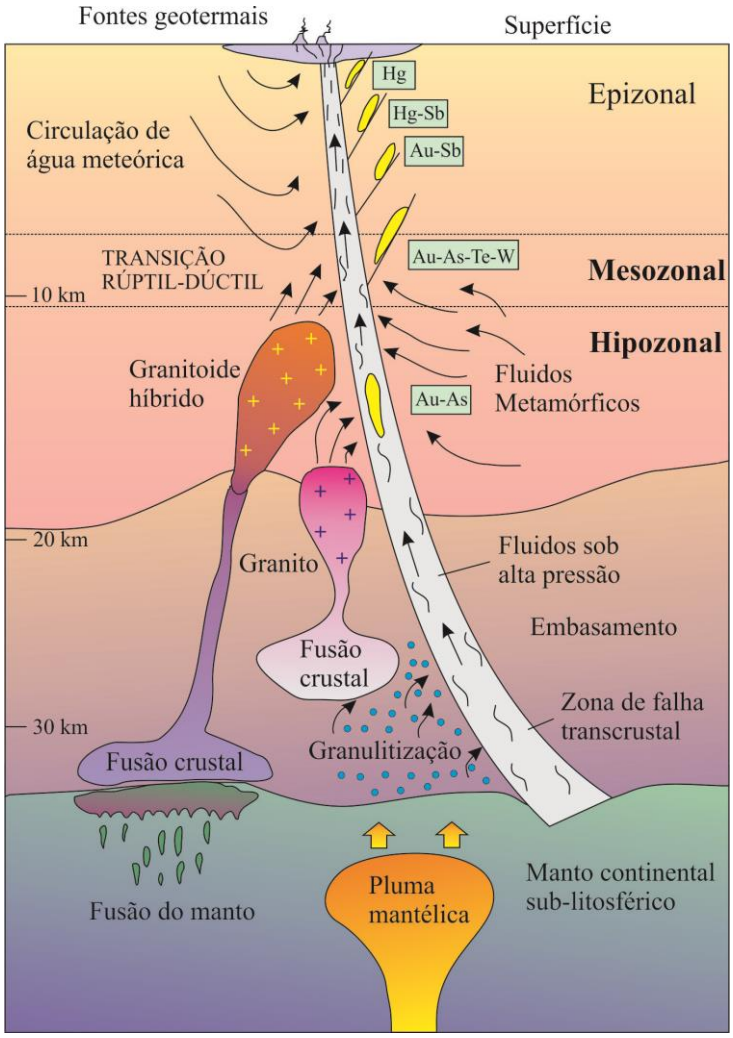

Fig. 1.3. Vários modelos propostos para a fonte de ouro e fluidos em depósito de ouro tipo orogênico, incluindo: circulação de água meteórica, exsolução de fluidos magmático–hidrotermal de diferentes tipos de granitoides, fluidos metamórficos de crosta média e/ou da granulitização da base da crosta. Figura do modelo de crustal continuum extraído de Groves & Santosh (2016).

Nesta Tese, o depósito de ouro estudado, encontra–se hospedado em sequência granito–*greenstone* de fácies anfibolito, e, portanto, este depósito, apresenta–se como uma

boa oportunidade para se adentrar na discussão apresentada acima, referente às prováveis fontes dos fluidos em depósitos de ouro associados à *greenstone belts* de fácies anfibolito.

1.3.3. Margens de crátons retrabalhadas e depósitos de ouro orogênico

As margens retrabalhadas dos crátons são cada vez mais reconhecidas como regiões–chave para mineralizações auríferas, onde a reativação de antigos "sistemas minerais" pode ocorrer repetidamente, gerando sucessivos eventos mineralizadores em níveis economicamente viáveis (Gazley *et al*. 2011, Hronsky *et al*. 2012). Processos tectônicos ao longo das margens de crátons (ex. subducção, colisão, acresção) podem transferir ouro (Au) por fluidos e/ou magmatismo diretamente do manto para crosta, e/ou entre domínios crustais, desempenhando papéis importantes para o fornecimento (*endowment*) em concentrações econômicas deste elemento (Bierlein *et al*. 2006, Groves *et al*. 2018, Groves & Santosh, 2015, Hronsky *et al*. 2012, Li & Santosh, 2017, Tassara *et al*. 2017).

Depósitos de ouro hospedados por sequências metavulcanossedimentares do tipo *greenstone belt* são geralmente encontrados nos domínios cratônicos de idades arqueana e paleoproterozoica, no entanto, também tem sido descrito em margens cratônicas retrabalhadas por orogêneses mais novas (ex. Duclaux *et al*. 2012, Fortes *et al*. 1997, Gazley *et al*. 2011, 2016, Jost *et al*. 2010, Larionova *et al*. 2013, Martins *et al*. 2016, McMillan, 1996, Molnár *et al*. 2016, Morelli *et al*. 2010, Perring & McNaughton, 1990, Queiroz *et al*. 2000; Vielreicher *et al*. 2002, Zhang *et al*. 2018). No entanto, em alguns casos, a presença de mineralizações mais antigas no *greenstone belt* hospedeiro não é reconhecida, mas somente associada a novos eventos de fluxo de fluido imprimidos pela nova orogênese (Carpenter *et al*. 2005, Davies *et al*. 2010, Zhang *et al*. 2014). Em outros casos, os sistemas auríferos orogênicos em margens cratônicas retrabalhadas não estão associados à *greenstone belts*, mas hospedados em gnaisses de alto grau metamórfico e outras rochas do embasamento (Blenkinsop & Doyle, 2014, Doyle *et al*. 2015, Fielding *et al*. 2017, 2018, Kirkland *et al*. 2015, Lawley *et al*., 2014, 2015). Entre estes exemplos, alguns depósitos fogem dos modelos clássicos para ouro orogênico, pelo fato da mineralização ser muito mais jovem do que as rochas encaixantes, como no caso do depósito de ouro de Tropicana, na Australia (Blenkinsop & Doyle, 2014, Doyle *et al*. 2015, Kirkland *et al*. 2015). Segundo Kirkland *et al*. (2015), o depósito de Tropicana se hospeda em gnaisses de alto grau metamórfico (granulitos) com idade neoarqueana (c. 2.7 Ga), no entanto, a mineralização data em torno de 2100 Ma, associada aos estágios iniciais da orogênese Albany–Fraser na borda sudeste do Cráton do Yilgarn. Este exemplo apresenta também similiaridade com os depósitos de ouro orogênico da gigante

província de Jiaodong, no Cráton Norte da China, que contêm depósitos de c. 120 Ma hospedados em crosta pré–cambriana que foi metamorfizada mais de dois bilhões de anos (2.0 Ga) antes da mineralização de ouro (ex. Goldfarb & Santosh, 2014, Groves & Santosh, 2015).

Para o caso de mineralização de ouro orogênico hospedada em *greentone belt* que foi retrabalhado por um novo ciclo orogênico, um dos exemplos mais estudado é encontrado no Marymia *Inlier*, que representa parte da margem do Cráton do Yilgarn retrabalhada pela orogênese Capricorn (1.8–1.7 Ga) (Duclaux *et al*. 2012, McMillan, 1996, Gazley 2011, Gazley *et al*. 2016, Vielreicher *et al*. 2002). No Marymia *Inlier*, que representa um núcleo de embasamento arqueano circundado de rochas proterozoicas, a mineralização de ouro orogênico (depósito Plutonic mine – 10,5 Moz) é hospedada por *greenstone belt* neoarqueano de fácies anfibolito (*Plutonic Well greenstone belt*), estratigraficamente e geoquimicamente semelhante a sequências *greenstone* no Cráton do Yilgarn (Eastern Goldfields Superterrane) (Duclaux *et al*. 2012, McMillan, 1996, Gazley 2011, Gazley *et al*. 2016, Vielreicher *et al*. 2002). Neste cenário, múltiplos eventos de mineralização de ouro ocorreram no Marymia *Inlier*, com mineralização de ouro datada em 2.65 Ga, mas também ocorrendo em c. 1.8–1.7 Ga (remobilizada) durante deformação e metamorfismo associado à orogênese Capricorn (1.8–1.7 Ga) (Duclaux *et al*. 2012, McMillan, 1996, Gazley 2011, Gazley *et al*. 2016, Vielreicher *et al*. 2002).

Similarmente, em faixas móveis brasilianas/pan–africanas (**Fig. 1.1**), uma característica comum entre os núcleos e/ou margens de embasamento é o registro de intensa deformação e metamorfismo neoproterozoico nas rochas, o que dificulta o reconhecimento da história arqueana e/ou paleoproterozoica nestes domínios (ex. Cordeiro *et al*. 2014, Cordeiro & Oliveira, 2017, Cutts *et al*. 2018, Duarte *et al*. 2004, Giustina *et al*. 2009, Heilbron *et al*. 2010, Klein *et al*. 2012, Noce *et al*. 2007, Silva *et al*. 2016, Valladares *et al*. 2017), assim como, o entendimento genético de depósitos auríferos associados (ex. Fortes *et al*. 1997, 2003, Jost *et al*. 2010, Klein *et al*. 2005, 2006, Queiroz *et al*. 2000). Por exemplo, na Faixa Brasília, terrenos granito–*greenstone* do Maciço de Goiás hospedam importantes depósito auríferos (ex. Mina–III no *greenstone belt* de Crixás) que geralmente são descritos como depósitos policíclicos, contendo mineralização tanto de idade paleoproterozoica (c. 2.0 Ga) como neoproterozoica (620–550 Ma) (e.g. Fortes *et al*. 1997, 2003, Jost *et al*., 2010, Queiroz *et al*. 2000).

Neste contexto, a mineralização aurífera do depósito de Pedra Branca, representa um exemplo similar àqueles descritos acima, ocorrendo em margens cratônicas retrabalhadas, onde a mineralização de ouro orogênico foi afetada por orogêneses mais novas.

1.3.4. Depósitos de ouro orogênico controlados por exumação tectônica

Muitos depósitos de ouro orogênico mostram a mesma sequência de colocação de veios mineralizados, desde a formação em níveis mais profundos (dúcteis), geralmente deformados (ex. veios sin–cisalhamento), até a colocação em níveis mais rasos, preenchendo fraturas de fases tectônicas tardias (ex. Amponsah *et al*. 2016, Augustin *et al*. 2017, Fourgerouse *et al*. 2017, Mignot *et al*. 2017, Molnár *et al*. 2018, Perrouty *et al*. 2016). Por exemplo, de acordo com Perrouty *et al*. (2016), no depósito de ouro de Wassa, sudeste de Gana, na África, o primeiro estágio de mineralização tem uma idade de 2164 ± 22 Ma (Re–Os em pirita) e é caracterizado por veios de quartzo deformados, com pirita e ouro também deformados, enquanto que um estágio tardio da mineralização ocorre no final da Orogenia Eburneana (2.1–2.0 Ga), com veios de quartzo–carbonato preenchendo fraturas e falhas, ouro visível e piritas euédricas (sem deformação). Portanto, é sugestivo que neste caso, e em casos similares, a mineralização aurífera na forma de veios acompanha a evolução metamórfica e termobarométrica do terreno durante processo de exumação tectônica, desde níveis crustais profundos até níveis mais rasos.

Em outro exemplo, idades e dados geotermobarométricos do metamorfismo e da mineralização de ouro orogênico no depósito de Damang, em Gana, indicam que a mineralização ocorreu entre 2030 e 1980 Ma, após o pico de metamorfismo regional em 2005 ± 26 Ma, e acompanhando o período de exumação e descompressão do terreno (White et al., 2013; 2014; 2015). Segundo White *et al*. (2015), os fluidos mineralizantes do depósito de Damang foram gerados por devolatização de rochas metamórficas durante processo descompressão, associado a exumação tectônica do terreno.

Dentro do modelo metamórfico para geração de fluidos associados a depósitos de ouro orogênico, a formação de fluidos hidrotermais por descompressão do terreno (durante exumação tectônica) não é comumente mencionada, mas conforme mencionado por White *et al*. (2015), o processo de devolatização (formação de fluidos) controlado por exumação (*Exhumation–drive devolatization)* também é uma alternativa para a gênese de depósitos de ouro orogênico, e não deve ser negligenciado. Durante a exumação tectônica de terrenos metamórficos, devido à forte dependência da pressão na solubilidade de soluções aquosas, a descompressão rápida e quase isotérmica é também uma maneira eficiente de devolatização das rochas metamórficas (Staude *et al*. 2009, Vry *et al*. 2010, Wannamaker, 2010) (**Fig. 1.4**).

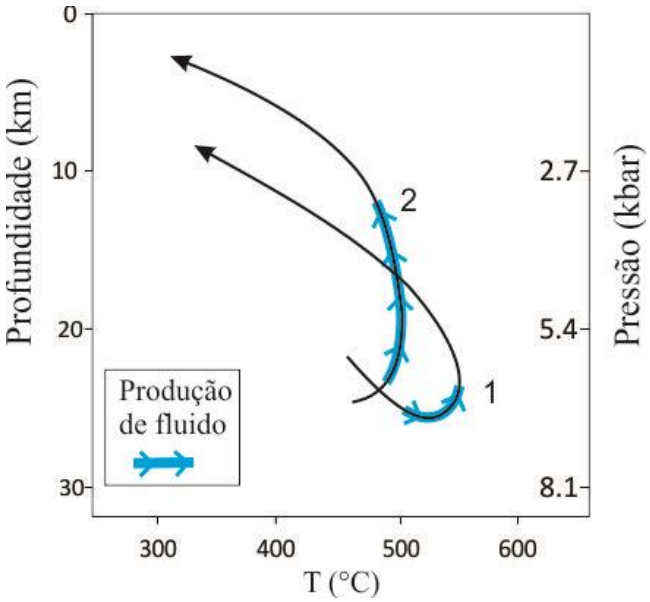

Fig. 1.4. Modelos teóricos de geração de fluidos metamórficos (Wannamaker, 2010); (1) Modelo teórico tradicional (metamorfismo progressivo) com devolatização das rochas metamórficas durante a passagem da transição de fácies xisto–verde para fácies anfibolito em ca. 500ºC, e (2) Modelo teórico de produção de fluidos metamórficos por descompressão (exumação do terreno) pós–pico metamórfico.

Segundo Vry *et al*. (2010), maior parte da geração de fluidos associada a evolução das rochas metamórficas em zonas de colisão ocorre por descompressão, durante o processo de exumação tectônica do terreno. A essência deste modelo é que as rochas metamórficas (com minerais hidratados) se tornam instáveis pela diminuição rápida da pressão, dada por exumação tectônica (ex. transporte por nappes), que pode ocorrer a uma temperatura quase constante (isotérmica) (Vry *et al*. 2010; Wannamaker, 2010) (**Fig. 1.4**). Em muitos depósitos de ouro orogênico, o fato de que geralmente ocorrem sin– à pós–pico do metamórfico regional (Goldfarb *et al*. 2005), sugere que estes já se encontrem em uma trajetória PT de exumação do terreno (descompressão e retro–metamorfismo) (White *et al*. 2013, 2014, 2015) (**Fig. 1.4**). Portanto, a descompressão por exumação tectônica, fornece um modelo alternativo para a introdução de fluido hidrotermal pós–pico metamórfico em um sistema de mineralização de ouro orogênico (Craw *et al*. 2010, Goodwin *et al*. 2017, Mcfarlane, 2018, White *et al*. 2014, 2015).

Esta relação entre exumação tectônica e mineralização aurífera é comumente abordada no estudo de depósitos de ouro orogênico hipozonal, onde geralmente, as assembleias hidrotermais relacionadas ao ouro e minerais metamórficos das rochas hospedeiras seguem o mesmo caminho PT retrógrado (Kolb *et al*. 2015). Isso sugere que a mineralização de ouro orogênico hipozonal é parte integrante da evolução do terreno durante sua exumação, sin– a pós–pico do metamorfismo regional (ex. Blenkinsop *et al*. 2004, Dziggel *et al*. 2010, Kolb *et*

al. 2015, Otto *et al*. 2007). Por exemplo, as rochas hospedeiras da mineralização de ouro orogênico hipozonal do depósito de Renco, no sul do Zimbábue, experimentaram variações de PT, de 830ºC e 8 kbar, para um estágio tardio de retro–metamorfismo associado à mineralização de ouro em 600ºC e 4 kbar (Kolb *et al*. 2000, Kolb & Meyer, 2002). A mineralização neste caso está associada a minerais hidrotermais de alta temperatura, como granada, biotita, feldspato–K, quartzo e anfibólio, em equilíbrio às condições regionais de retro–metamorfismo de fácies anfibolito (Kolb *et al*. 2000, Kolb & Meyer, 2002). Em outro exemplo, no depósito de ouro orogênico hipozonal de New Consort, no greenstone belt de Barberton, na África do Sul, as rochas hospedeiras foram submetidas à exumação do terreno ocasionando variação de 700ºC e 5 kbar para c. 550ºC e 3 kbar (Dziggel *et al*. 2006). A mineralização de ouro na mina de New Consort, ocorreu em equilíbrio com as condições regionais tardias do retro–metamorfismo de fácies anfibolito (550ºC e 3 kbar), apresentando assembleia de alteração hidrotermal composta de granada, diopsídio, hornblenda, feldspato potássico, quartzo, calcita e biotita (Dziggel *et al*. 2010, Otto *et al*. 2007). Segundo Dziggel *et al*. (2010), no depósito de ouro de New Consort, a mineralização de ouro orogênico hipozonal ocorreu pós–pico metamórfico regional, contemporânea a exumação tectônica do terreno. Neste contexto, as características petrográficas e estruturais apresentadas para o depósito de ouro de Pedra Branca são indicativas de descompressão tectônica, sugerindo provável contemporaneidade entre a mineralização aurífera e a exumação tectônica regional. Uma discussão sobre esta possibilidade é apresentada no 3º artigo desta tese.

1.4. OBJETIVOS

Com o reconhecimento de mineralização aurífera no Maciço de Troia, dentro de um contexto de *greenstone belts* paleoproterozoicos, margens cratônicas retrabalhadas e depósitos de ouro orogênico provavelmente hipozonais, configurou–se um quadro oportuno para o desenvolvimento desta Tese, tanto no âmbito da evolução crustal, quanto para metalogênese do ouro.

O estudo metalogenético em terrenos poli–deformados (ex. embasamento retrabalhado) deve estar muito bem amarrado à evolução geológica regional, sendo de extrema importância: (i) um bom mapa geológico da área, (ii) estabelecer idades (U–Pb e Lu–Hf) e litogeoquímica dos principais corpos ígneos da área, (iii) estabelecer idades precisas para evento(s) de metamorfismo regional e (iv) reconhecer as principais características estruturais da área. Portanto, dentre deste contexto, os objetivos específicos desta Tese podem–se listar os seguintes:

1– Investigação litogeoquímica e geocronológica dos principais corpos plutônicos da área, de modo a definir idades, ambiente(s) tectônico(s) de formação e fonte(s) (crustal e/ou mantélico) envolvidas na geração de magma;

2– Discutir a evolução tectônica do *greenstone belt* da Serra das Pipocas e correlacionar com domínios similares, a fim de integrar uma discussão geodinâmica regional;

3– Caracterização mineralógica do minério e da alteração hidrotermal no depósito de ouro de Pedra Branca;

4– Determinar as condições de PT do sistema mineralizador;

5– Discutir sobre as possíveis fontes de fluidos (e ouro);

6– Definir a(s) idade(s) do minério e em quais as estruturas preferencialmente ocorreu a deposição;

7– Propor um modelo genético para a mineralização aurífera;

1.5. MATERIAIS E MÉTODOS

1.5.1. Trabalho de campo

Duas etapas de campo foram realizadas durante o ano de 2015. O intuito principal das etapas de campo foi cartografia do *greenstone belt* da Serra das Pipocas, atualizando assim o mapa geológico e relações estratigráficas da área. Foi realizado um total de 65 pontos de campo na primeira etapa (14 dias em Maio de 2015) e 51 pontos na segunda etapa (18 dias em outubro de 2015). Além dos parâmetros de campo (descrição das rochas e estruturas), foram coletadas 50 amostras de granitoides da área, assim como amostras para geocronologia. Adicionalmente, foi realizada uma visita (três dias) ao galpão de testemunhos da empresa Jaguar mining, para uma descrição (*in locu*) e coleta de amostras.

1.5.2. Integração e interpretação de dados

Com apoio das informações coletadas em campo, foram feitas interpretações de imagens aerogeofísicas e de sensores remotos, principalmente no âmbito da geologia estrutural, sendo de extrema importância no entendimento da mineralização aurífera da área. Os dados aerogeofísicos utilizados para interpretação estrutural são provenientes do Projeto Novo Oriente e do Projeto Norte do Ceará, contratados pelo Serviço Geológico do Brasil (CPRM). Para os referidos projetos, o processamento dos dados aerogeofísicos foi realizado

pela equipe de geofísica da CPRM com o software Oasis Montaj 7.2.1 da GEOSOFT. Para mais informações sobre esta metodologia utilizada, vide o 3º artigo desta Tese.

1.5.3. Litogeoquímica

A preparação e as análises das amostras foram realizadas pela empresa SGS Geossol Laboratórios Ltda. Foram analisados os óxidos de elementos maiores (SiO_2, TiO_2, $Al2O_3$, Fe_2O_3, MgO, CaO, MnO, Na_2O, K_2O, P_2O_5), com abertura por fusão com metaborato de lítio e determinação por Fluorescência de Raios–X (FRX). Elementos menores e Terras Raras (Ba, Be, Co, Cs, Ga, Hf, Nb, Rb, Sn, Sr, Ta, Th, U, V, W, Zr, Y, La, Ce, Pr,Nd, Sm, Eu, Gd, Tb, Dy, Ho, Er, Tm,Yb, Lu) foram determinados por ICP–MS (Induced Coupled Plasma Mass Spectrometry) após abertura por fusão com metaborato de lítio. O tratamento dos dados foi realizado no programa Geochemical Data Toolkit (GCDkit) (Janoušek *et al*. 2006). Para mais detalhes sobre a metodologia e padrões analíticos da SGS Geossol Ltda, vide o 1º artigo desta Tese.

1.5.4. Petrografia (Microscópio convencional e MEV)

Descrições petrográficas foram realizadas principalmente acerca dos corpos graníticos investigados na litogeoquímica e testemunhos de sondagem. A descrição mesoscópica em testemunho de sondagem da mineralizações de ouro e em rochas encaixantes foi realizada visando sempre relacionar com as informações de campo (rochas e estruturas). Para descrição petrográfica das amostras foi utilizado microscópio petrográfico convencional e refinamento das observações com imagens de elétrons retro–espalhados (BSE – *back scattered electrons*) e análises EDS (*Energy Dispersive x–ray Spectrometer*) em microscópio eletrônico de varredura (MEV) da CPRM–Belém. Imagens dos grãos de zircão por catodoluminescência (CL) das analises SHRIMP foram feitas pelo laboratório CPGeo da USP, no entanto outras imagens por CL e de elétrons retro–espalhados foram feitas pelo doutorando no MEV da CRPM–Belém e da UFPA.

1.5.5. Inclusões fluidas

Para o estudo microtermométrico de inclusões fluidas em veios de quartzo mineralizados, foram preparadas secções espessas duplamente polidas (<0,3 mm de espessura) na Universidade Federal do Pará (UFPA). As medições microtermométricas foram realizadas na CPRM de Belém, que está equipado com platina de aquecimento e resfriamento Linkan THMSG 600. A calibração é realizada utilizando padrões sintéticos fornecidos pelo

fabricante. A aquisição dos dados foi feita seguindo procedimentos descritos na literatura (Roedder 1984, Shepherd *et al*. 1985, Wilkinson 2001).

1.5.6. Isótopos radiogênicos (U–Pb e Lu–Hf)

As análises U–Pb em zircões de duas amostras de granitoides foram realizadas no Centro de Pesquisas Geocronológicas da Universidade de São Paulo (CPGeo/USP), no equipamento *Sensitive High Resolution Ion Microprobe* IIe (SHRIMP–IIe). No laboratório do Departamento de Geologia da Universidade Federal de Ouro Preto (DEGEO–UFOP), uma amostra (granitoide) foi analisada por U–Pb em zircão e uma amostra por U–Pb em titanita (mineralização), ambas por *Laser Ablation Induced Coupled Plasma Mass Spectrometry* (LA–ICP–MS). Procedimentos analíticos utilizados para análises U–Pb em zircão por SHRIMP–IIe da USP são descritos por Sato *et al*. (2014) (zircão padrão = Temora 2). Para U–Pb em zircão por LA–ICP–MS na UFOP, os procedimentos são os mesmos descritos em Farina *et al*. (2015) (zircão padrão= GJ–1 e Plesovice). Para as análises U–Pb em titanita na UFOP, os procedimentos são os mesmos utilizados para zircões, mas utilizando–se dos padrões naturais de titanitas; Khan (520 Ma) e BLR (1050 Ma). Os resultados isotópicos de Lu–Hf em zircão (duas amostras) foram obtidos no Laboratório de Geologia Isotópica PARA–ISSO, na Universidade Federal do Pará (UFPA), Belém–Brasil. O procedimento de análise de Hf (Milhomem Neto *et al*. 2015) foi desenvolvido usando um *multicoletor Neptune Thermo Finnigan* ICP–MS acoplado uma microssonda a laser Nd:YAG 213 nm modelo LSX–213 G2 da marca CETAC. A sequência de análises de Lu–Hf empregada intercalou três grãos da amostra com um do padrão GJ–1, no qual a razão $^{176}Hf/^{177}Hf$ é conhecida com precisão. Em todos os laboratórios, o doutorando esteve presente e participou da aquisição dos dados. A separação dos minerais (zircões e titanitas) e preparação do *mount* foi realizada pelo doutorando em laboratórios da CPRM e UFPA.

1.5.7. Isótopos estáveis (O, H, C)

Os dados de isótopos estáveis de oxigênio (n= 64), hidrogênio (n= 28) e carbono (n= 5) apresentados neste estudo foram produzidos na Universidade da do Cabo Cidade (UCT), na África do Sul. As análises foram realizadas durante estágio de Doutorado Sanduíche no Exterior (SWE) aprovado pelo CNPq pelo período de seis meses. A preparação das amostras e a extração dos isótopos foram realizadas no Laboratório de Isótopos Estáveis do Departamento de Ciências Geológicas, e as razões isotópicas foram medidas *off–line* usando um espectrômetro de massas Finnigan Delta XP no modo de dupla entrada, hospedado no

Departamento de Arqueologia da UCT. Para isótopos de oxigênio, ambos os métodos convencionais e de fluoração a laser foram usados. As amostras foram analisadas pelo método a laser, conforme descrito por Harris & Vogeli (2010). O padrão interno MONGT (*Monastery garnet*, $\delta^{18}O$ = +5,55‰) foi analisado para calibrar os dados para a escala SMOW (*Standard Mean Ocean Water*), e as duplicatas deram concordância dentro de 0,2 por mil. Os isótopos de hidrogênio foram extraídos (linha convencional) de 100 mg de anfibólio e 50 mg de biotita e moscovita, utilizando o método de Vennemann & O'Neil (1993) com redução por "*Low–blank Indiana Zinc*" (Schimmelmann & DeNiro, 1993). Isótopos de hidrogênio também foram medidos em amostras (~3,5 g) de veios de quartzo, por decrepitação térmica (> 800°C) das inclusões fluidas. Isótopos de carbono e oxigênio em carbonatos foram medidos segundo método de McCrea (1950), e carbono em grafita segundo Kramer *et al*. (2013).

1.6. CONTEXTO GEOLÓGICO REGIONAL

1.6.1. Província Borborema

A Província Borborema foi definida por Almeida *et al*. (1981) compreende uma área de aproximadamente 450.000 km^2 do nordeste brasileiro, com uma complexa região de domínios tectono–estratigráficos, estruturados durante o Neoproterozoico. Esta província obteve sua configuração final a partir da convergência dos crátons Amazônico, São Luis–Oeste Africano e São Francisco–Congo, por volta de 620–600 Ma, na intitulada colagem brasiliana/pan–africana, durante aglutinação do Supercontinente Gondwana (Brito Neves *et al*. 2000, Brito Neves & Cordani, 1991, Trompette 1994) (**Fig. 1.5A**).

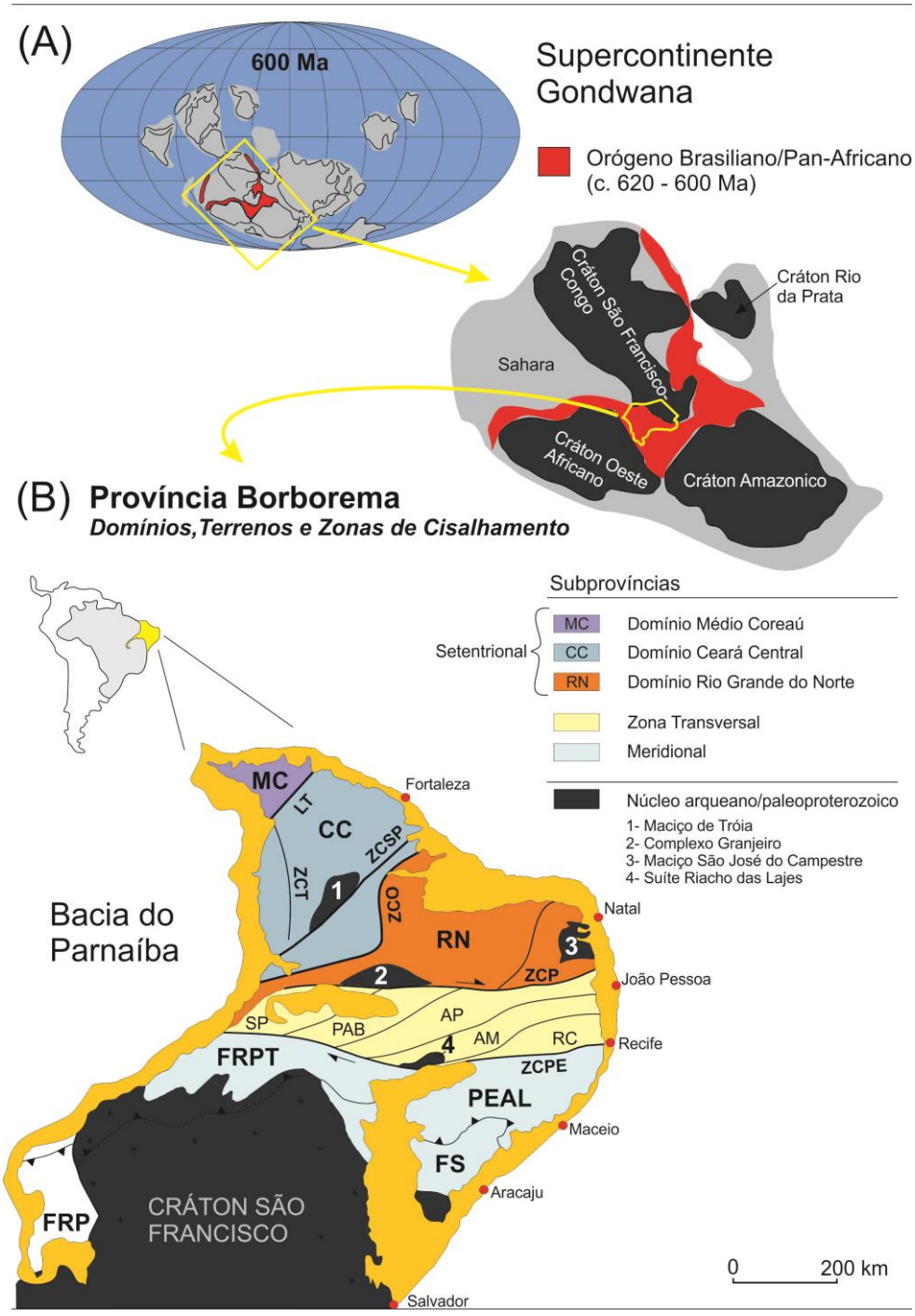

Fig. 1.5. (A) Configuração paleogeográfica do Supercontinente Gondwana em c. 600 Ma (modificado de Li et al., 2008). (B) Província Borborema com localização dos principais domínios, terrenos e zonas de cisalhamento. Zonas de cisalhamento são LT= Lineamento Transbrasiliano, ZCT= Zona de cisalhamento Tauá, ZCSP= Zona de cisalhamento Senador Pompeu, ZCO, Zona de cisalhamento Orós, ZCP= Zona de cisalhamento Patos, ZCPE= Zona de cisalhamento Pernambuco. FRP= Faixa Rio Preto, FRPT= Faixa Riacho do Pontal, FS= Faixa Sergipana, Domínio Pernambuco–Alagoas. Subdivisão da porção Setentrional em RN= Domínio Rio Grande do Norte, CC= Domínio Ceará Central e MC= Domínio Médio Coreaú é segundo Arthaud et al. (1998). A subdivisão de terrenos da Zona Transversal segundo Santos et al (2000) em RC= Rio Capibaribe, AM= Alto Moxotó, AP= Alto Pajeú, PAB= Piancó–Alto Brígida e SP= São Pedro

A Província Borborema é representa em grande parte por rochas paleoproterozoicas e localmente núcleos arqueanos, ambos fortemente retrabalhados pela orogênese Brasiliana/Pan–Africana em c. 620–600 Ma (Ancelmi, 2016, Dantas *et al*. 2004, 2013, Fetter, 1999, Freimann, 2014, Ganade *et al*. 2017, Hollanda *et al*. 2015, Santos *et al*. 2017, Souza *et al*. 2016). Sua principal característica estrutural é a extensa rede de zona de cisalhamento transcorrente com direção principal NE–SW e E–W, geralmente associada à intrusão de vários granitóides sin–tectônicos em c. 580 Ma (Nogueira, 2004, Vauchez *et al*. 1995) (**Fig. 1.5B** e **1.6A**). Os domínios de rochas metassedimentares neoproterozoicas, como as unidades do Grupo Ceará (ou Complexo Ceará) e Grupo Seridó ao norte desta província, ou das faixas Riacho do Pontal, Sergipana e Rio Preto ao sul, em geral, representam sequências tipo QPC (quartzo–pelito–carbonato) deformadas, com continuidade espacial na contraparte africana (Arthaud *et al*. 2008, 2015, Oliveira *et al*. 2006, Oliveira *et al*. 2010, Santos *et al*. 2008; Van Schmus *et al*. 2008) (**Fig. 1.5B** e **1.6A**).

1.6.2. Profusão de “domínios” e “terrenos”

O emaranhado de zonas de cisalhamento é uma característica marcante da Província Borborema e comumente são interpretadas como limites de “terrenos”, separando “domínios” tectônicos distintos (Arthaud *et al*. 1998, Brito Neves *et al*. 2000, Caxito *et al.* 2014, Correa *et al*. 2016, Fetter 1999, Oliveira & Medeiros, 2018, Trompette 1994, Santos 1996, Santos *et al*. 2000, Santos *et al*. 2010) (**Fig. 1.5B**). Com base nas características geológicas, assinaturas crustais de Nd e diferenças de idades U–Pb, Trompette (1994) dividiu a Província Borborema em três grandes subprovíncias: (i) Setentrional, (ii) Transversal e (iii) Meridional (**Fig. 1.5B**). No entanto, cada uma dessas subprovíncias, posteriormente, foi subdividida, por autores diversos, em “domínios” crustais menores (Arthaud *et al*. 1998, Brito Neves *et al*. 2000, Cavalcante 1999, Delgado *et al*. 2003, Fetter 1999, Oliveira 2008, Oliveira & Medeiros, 2018, Padilha *et al*. 2017, Santos *et al*. 2000) (**Fig. 1.5B**).

A Subprovíncia Setentrional, localizada ao norte da zona de cisalhamento Patos, pode ser dividida em três principais domínios segundo alguns autores (ex. Arthaud *et al*. 1998, Fetter 1999); (i) Domínio Médio Coreaú, (ii) Domínio Ceará Central e (iii) Domínio Rio Grande do Norte (**Fig. 1.5B**). No entanto, o limite entre estes os domínios é contrastante segundo diferentes autores (Arthaud *et al*. 1998, Brito Neves *et al*. 2000, Cavalcante, 1999, Delgado *et al*. 2003, Fetter 1999, Fetter *et al*. 2000, Oliveira, 2008, Oliveira & Medeiros, 2018, Padilha *et al*. 2017). Por exemplo, enquanto alguns autores limitam a porção sul do Domínio Ceará Central pela zona de cisalhamento Senador Pompeu (Brito Neves *et al*. 2000,

Fetter *et al*. 2000, Oliveira 2008, Oliveira & Medeiros, 2018, Padilha *et al*. 2017), outros autores referem–se à zona de cisalhamento Orós (Arthaud *et al*. 1998), Porto Alegre (Campelo 1999, Jardim de Sá *et al*. 1997) e Jaguaribe (Santos *et al*. 2000) como o limite sul.

Recentemente, com base em magnetometria e gravimetria, Oliveira & Medeiros (2018) sugerem a inserção do subdomínio Jaguaribe, entre os domínios Ceará Central e Rio Grande do Norte. O domínio Jaguaribe (ou Jaguaribeano) também já foi sugerido por outros autores (Cavalcante 1999, Santos *et al*. 2000). Na última década algumas transectas de geofísica foram realizadas com o método magnetotelúrico (Padilha *et al*. 2013, 2016, 2017, Santos *et al*. 2014) e refração dados sísmicos (Lima *et al*. 2015), que acrescentaram importantes contribuições para subdivisão de "domínios" e "terrenos" na Província Borborema.

Segundo Padilha *et al*. (2017), dados magnetotelúricos coletados ao longo do domínio Setentrional da Província Borborema revelaram que os limites desses blocos são compatíveis com anomalias de alta condutividade na crosta e manto, interpretado como zonas de sutura e correlacionado com o ciclo orogênico Brasiliano/Pan–Africano. O modelo de terrenos acrescionários, herdado do orógeno cordilherano Norte–americano (Coney *et al*. 1980, 1989), foi inicialmente aplicado na Província Borborema por Santos (1996), e posteriormente, amplamente utilizado por diversos autores, especialmente na Zona Transversal (Caxito *et al*. 2014, Correa *et al*. 2016, Brito Neves *et al*. 2000, Kozuch 2003, Santos 1996, Santos *et al*. 2010, 2018). Em favor deste modelo, os autores comumente citam registros de associações de rochas correspondentes a arcos magmáticos, como o arco de Santa Quitéria no Domínio Ceará Central (Fetter *et al*. 2003, Ganade *et al*. 2014), assim como rochas eclogíticas (Beurlen *et al*. 1992, Santos *et al*. 2015). No entanto, grande parte do magmatismo plutônico do Complexo Tamboril–Santa Quitéria, pós–data ou é contemporâneo à idade do metamorfismo de alta pressão (eclogitos) na área (c. 640–620 Ma), e, portanto, para alguns autores, não representa um arco magmático (Costa *et al*. 2010, 2013).

Em aposição ao modelo de terrenos, segundo Neves (2003, 2015), as estruturas de escala regional são apenas reativações de zonas de cisalhamento antigas, sendo que a falta de evidências para um amplo oceano neoproterozoico (zonas de sutura) na Província Borborema, sugere que o metamorfismo, magmatismo e a deformação neoproterozoica em toda esta província representam o produto de um orógeno intracontinental. Segundo Neves (2015), na Província Borborema, a principal época de geração de crosta juvenil e acresção de terrenos (ex. arcos insulares) ocorreram durante a orogênese Transamazônica/Eburneana e formação do Supercontinente Columbia (ou Atlântica) em c. 2.0 Ga, enquanto que o registro do evento

orogênico Brasiliano/Pan–Africano (c. 620–600 Ma) é caracterizado nesta província somente por retrabalhamento de crosta pré–existente.

1.6.3. Embasamento arqueano/paleoproterozoico

Os registros de crosta arqueana no domínio norte (Setentrional) da Província Borborema correspondem a: (i) rochas de 2.8–2.7 Ga do Maciço de Troia (Fetter 1999, Ganade *et al*. 2017, Silva *et al*. 2002), (ii) 3.2–2.5 Ga do Complexo Granjeiro (Ancelmi 2016, Freimann 2014, Hollanda *et al*. 2015, Silva *et al*. 1997) e (iii) 3.4–2.7 Ga do Maciço de São José do Campestre (Dantas *et al*. 2004, 2013, Souza *et al*. 2016) (**Fig. 1.6A**). Mais recentemente, rochas arqueanas também foram identificadas na Província Central da Borborema (Zona Transversal (2.6 Ga – Suíte Riacho das Lages) (Santos *et al*. 2017) (**Fig. 1.6A**). Circundando estes núcleos arqueanos, grande parte do embasamento da Província Borborema é de idade Riaciana (2.3–2.0 Ga) (**Fig. 1.6A**), incluindo granitoides, gnaisses, migmatitos e sequências metavulcanossedimentares (Costa *et al*. 2015, Dantas *et al*. 2004, Fetter *et al*. 2000, Hollanda *et al*. 2011, Souza *et al*. 2007, 2016).

1.6.4. O Maciço de Troia

As rochas do embasamento arqueano/paleoproterozoico no Domínio Ceará Central foram originalmente denominadas de "Maciço de Troia" por Brito Neves (1975). Posteriormente, os gnaisses TTG do Maciço de Troia foram mapeados como Complexo Cruzeta segundo Oliveira & Cavalcante (1993) (**Fig. 1.6B**). As idades U–Pb (TIMS) obtidas em zircão por Fetter (1999) para gnaisses TTG do Complexo Cruzeta confirmaram idades neoarqueanas de 2.8–2.7 Ga para estas rochas. O limite sudeste deste domínio arqueano é nitidamente definido pela zona de cisalhamento de Senador Pompeu (**Fig. 1.6B**), enquanto os limites norte e oeste foram inferidos principalmente com base em dados geocronológicos e gamaespectrometria aérea (Pinéo & Costa, 2013).

Segundo Fetter (1999), o Maciço de Troia pode ser dividido em dois blocos crustais distintos: (i) Pedra Branca e (ii) Bloco Mombaça, ambos com idades U–Pb (TIMS) em zircão de 2.8–2.7 Ga idades, mas diferindo em sua assinatura isotópica Sm–Nd. O Bloco Mombaça tem valores de εNd(t) variando de -0,79 a +2,73, e o Bloco Pedra Branca apresenta valores ligeiramente radiogênicos (juvenil) (entre −0,02 e +2,48) (Fetter 1999).

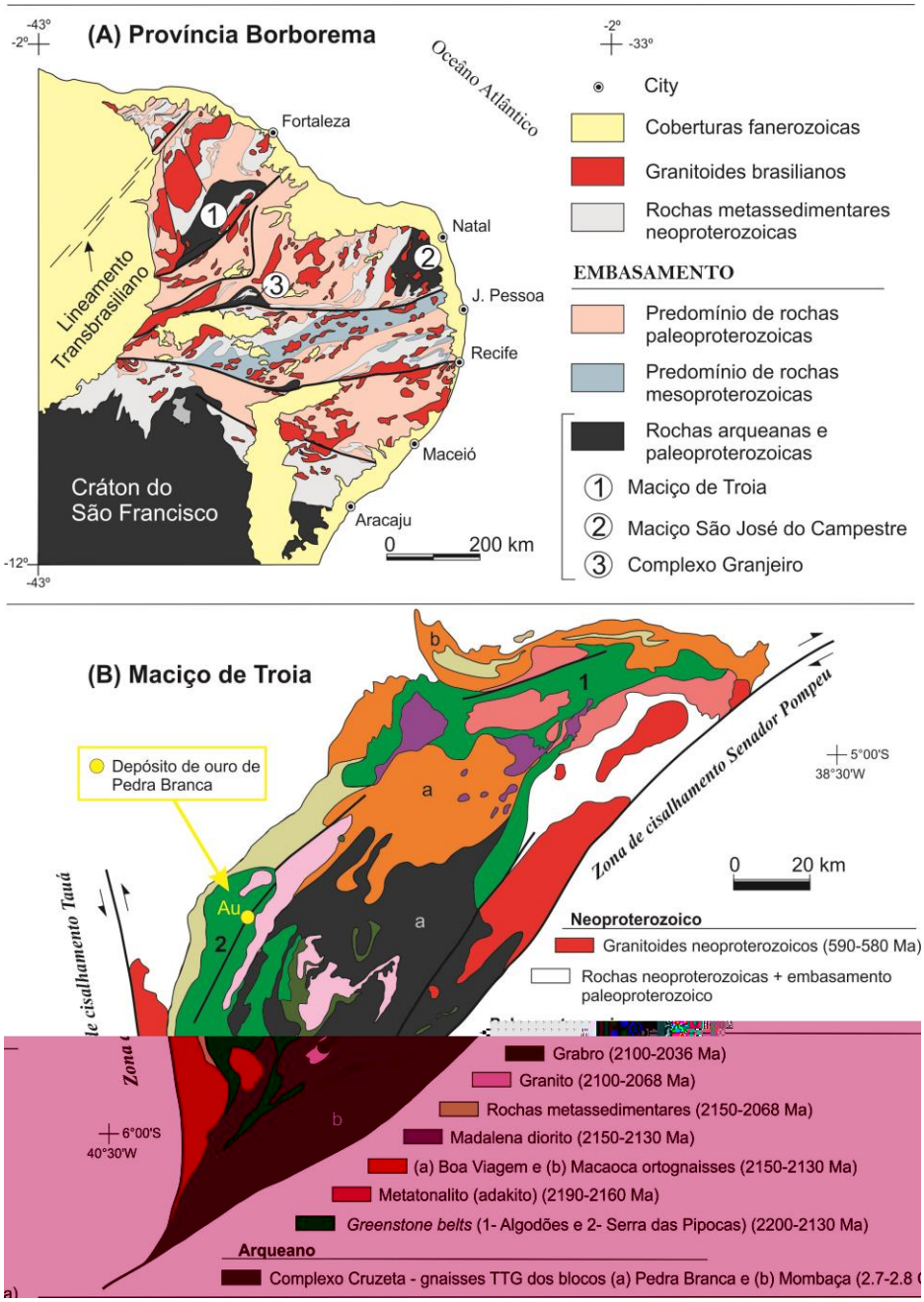

Fig. 1.6. (A) Mapa geológico simplificado da Província Borborema (modificado de Oliveira & Medeiros, 2018) (Localização na Fig. 1.1). (B) Mapa geológico simplificado do Maciço de Troia (modificado de Costa *et al*. 2015).

Segundo Ganade *et al*. (2017), novo dados geocronológicos do SHRIMP U–Pb demonstram que o Bloco Mombaça (2793 ± 6 Ma) é mais antigo que os gnaisses TTG do Bloco Pedra Branca (2698 ± 8 Ma), como também sugerido por Fetter (1999). No entanto, no mapa simplificado do Maciço de Troia, todas as rochas neoarqueanas estão representadas pelo Complexo Cruzeta (**Fig. 1.6B**). Estas rochas arqueanas são principalmente ortognaisses TTG e migmatitos. Os migmatitos são compostos principalmente de metatexitos estomáticos,

derivados de ortognaisses de composição granodiorítica (unidade de Mombaça), e composições tonalítico a diorítico (unidade de Pedra Branca) (Ganade *et al*. 2017).

Embora as idades obtidas para o Maciço de Troia evidenciam rochas predominantemente neoarqueanas, uma idade U–Pb (SHRIMP) de 3270 ± 5 Ma (Paleoarqueano) foi determinada por Silva *et al*. (2002) para uma metatonalito do Complexo Cruzeta. Esta idade fornece evidências que a colocação dos TTGs neoarqueanos do Maciço de Troia ocorreu sobre crosta preexistente com idades semelhantes às relatadas no Maciço José do Campestre (Dantas *et al*. 2004, 2013, Souza *et al*. 2016) e Complexo Granjeiro (Ancelmi 2016, Freimann 2014, Hollanda *et al*. 2015, Silva *et al*. 1997).

Granitoides paleoproterozoicos ocorrem intrusivos em rochas arqueanas do Complexo Cruzeta e *greenstone belts* paleoproterozoico do Maciço de Troia (**Fig. 1.6B**). Por exemplo, o Complexo de Boa Viagem é representado por ortognaisses tonalíticos a granodioríticos com U–Pb (SHRIMP) idades de zircão de 2150 ± 29 Ma e 2124 ± 35 Ma, e podem provavelmente representa um plutonismo de arco continental na porção norte o Complexo Cruzeta (Silva *et al*. 2014) (**Fig. 1.6B**). O Complexo São José da Macaoca, definido por Torres *et al*. (2007) ao norte do Maciço de Troia, também representa uma grande porção de ortognaisses tonalíticos para granodioríticos com idades U–Pb (TIMS) em zircão de 2139 ± 12 Ma (Castro 2004) e 2130 ± 3 Ma (Fetter 1999) (**Fig. 1.6B**). De acordo com Costa *et al*. (2015), estes ortognaisses (Macaoca) têm assinatura geoquímica similar a adakitos de baixa sílica (magmas relacionados ao manto), e provavelmente associado a acresção de arco insular (*greenstone belt* Algodões) a margem norte do Maciço de Troia.

1.6.5. *Greenstone belts* paleoproterozoicos do Maciço de Troia

No Maciço de Troia, duas sequências metavulcanossedimentar foram reconhecidas como terrenos tipo granito–*greenstone*, denominados de *greenstone belt* de Algodões ao norte (Costa *et al*. 2015, Martins *et al*. 2009) e *greenstone belt* da Serra das Pipocas ao sul (Costa *et al*. 2014a, 2015, Pessoa & Archanjo, 1984, Pessoa *et al*. 1986, Sousa, 2016) (**Fig. 1.6B**).

1.6.5.1. O greenstone belt Algodões

A sequência metavulcanossedimentar de Algodões ocorre na porção norte do Maciço de Troia (**Fig. 1.6B**). Esta sequência compreende principalmente anfibolitos derivados de metabasaltos, paragnaisses, metagrauvacas, metarcóseos, metapelitos, quartzitos, metandesitos, metaconglomerados e rochas de cálcio–silicáticas (Costa 2013, Martins 2000, Martins *et al*. 2009). Os anfibolitos foram datados em 2236 ± 55 Ma (isócrona de rocha total

Sm–Nd; quatro amostras) (Martins *et al*. 2009) e apresentam características geoquímicas similares a platôs oceânicos e/ou basaltos de retro–arco (Martins *et al*. 2009, Verma & Oliveira, 2014). As condições metamórficas para a sequência Algodões variam entre fácies xisto–verde alto e anfibolito (Costa 2013, Martins 2000). Estruturalmente, o *greenstone belt* Algodões mostra lineamentos regional de direção nordeste, e foliação mergulhando para SE (Costa 2013, Martins, 2000). Uma idade U–Pb (LA–ICPMS) em zircão de 2046 ± 12 Ma obtida por Gomes (2013) para leucossoma de um ortognaisse migmatítico (Macaoca) ao norte do *greenstone belt* Algodões mostra que o metamorfismo regional de idade paleoproterozoica preservado na área. Com base nas idades Pb–Pb em zircão, isótopos Sm–Nd e geoquímica de rocha total, os metatonalitos Cipó (2190–2160 Ma), intrusivos neste *greenstone belt*, representam rochas plutônicas que provavelmente evoluíram em um arco intra–oceânico, devido sua assinatura juvenil de Nd (idades do modelo TDM = 2.24–2.29 Ga e valores de εNd (t) = + 0,29 até +1.9) (Martins *et al*. 2009). Para essas rochas plutônicas (tonalitos Cipó), Costa *et al*. (2015) relataram idades de U–Pb (LA-ICPMS) em zircão de 2189 ± 14 Ma e 2180 ± 15 Ma, e também sugerem um ambiente pré–colisional para esses tonalitos.

1.6.5.2. O greenstone belt da Serra das Pipocas

Um dos primeiros mapeamentos estrutural e litológico na sequência metavulcanossedimentar da região central de Troia foi apresentado por Pessoa & Archanjo (1984). De acordo com estes autores, a tectônica de empurrão é responsável pelos caráter alóctone das sequências metavulcanossedimentares e rochas metaplutônicas máficas–ultramáficas relacionadas, sobrepondo-se tectonicamente ao embasamento gnáissico-migmatítico do Maciço de Troia. Em trabalho adicional, dados geocronológicos de Rb–Sr e K–Ar evidenciam que o Maciço de Troia exibe um caráter policíclico, com rochas arqueanas e paleoproterozóicas apresentando rejuvenescimento isotópico no sistema Rb–Sr e K–Ar durante o evento orogênico neoproterozóico (Brasiliano/Pan–Africano) (Pessoa *et al*. 1986). Esses autores também sugerem que a tectônica de empurrão no Maciço de Troia é de idade paleoproterozóico. No entanto, devido à falta de resultados isotópicos confiáveis na época, Pessoa *et al*. (1986) interpretou para as sequências supracrustais da região da Serra das Pipocas como uma greenstone belts de idade arqueana, associada a assembleia de gnaisses e migmatitos arqueanos do maciço de Troia. No entanto, mais tarde, Fetter (1999) apresentou idade U-Pb (TIMS) em zircão de 2151 ± 9 Ma para metadacitos próxima à região da Serra das Pipocas, sugerindo idade paleoproterozóica para granito–*greenstone* o greenstone belt da Serra das Pipocas.

O *greenstone belt* da Serra das Pipocas, na porção centro–oeste do Maciço de Troia (**Fig. 1.6B**), é composto de metabasaltos (anfibolitos), rochas metavulcânicas félsicas à intermediárias, rochas metassedimentares, meta*cherts*, mármores, intrusões tonalíticas (tipo TTG), rochas metaplutônicas máficas–ultramáficas, serpentinitos e leucogranitos associados (Cavalcante *et al*. 2003, Costa *et al*. 2014a, Pessoa & Archanjo, 1984, Pessoa *et al.* 1986, Sousa 2016). Segundo Pessoa e Archanjo (1984), metabasaltos com estruturas semelhantes a *pillows* foi identificado nesta área. A geoquímica de rochas metavulcânicas máficas mostra uma transição toleiítica para afinidade cálcio–alcalina com assinatura relacionada ao arco, sugerindo um cenário tectônico tipo retro–arco para este vulcanismo (Sousa 2016). Idades U–Pb em zircões detríticos em metagrauvacas da sequência Serra das Pipocas apresentam uma população de idade mais jovem ao redor 2200 Ma e mais velhos com idades de 3096 ± 53 Ma, 3074 ± 55 Ma, 2608 ± 54 e 2546 ± 55 Ma, o que indica um mistura de fontes arqueanas e riacianas, e uma idade máxima de deposição em c. 2.2 Ga (Costa *et al*. 2014a). A presença de zircões arqueanos sugere um ambiente continental (ou proximidade continental) para evolução tectônica do *greenstone belt* da Serra das Pipocas (Costa *et al*. 2014a). As rochas metaplutônicas máficas e ultramáficas são mais abundantes na região central Região de Troia (**Fig. 1.6B**), e são interpretados principalmente como complexos ígneos acamadados, bem conhecido por causa da mineralização em platina e paládio nos metacromititos (Angeli *et al*. 2009, Barrueto & Hunt, 2010, Pessoa & Archanjo, 1984). Recentemente, uma idade U–Pb (SHRIMP) em zircão de 2036 ± 28 Ma foi obtida para uma amostra de metacromitito (Costa *et al*. 2014b).

2. (1º ARTIGO): GEOCHEMISTRY AND U–Pb–Hf ZIRCON DATA FOR PLUTONIC ROCKS OF THE TROIA MASSIF, BORBOREMA PROVINCE, NE BRAZIL: EVIDENCE FOR REWORKING OF ARCHEAN AND JUVENILE PALEOPROTEROZOIC CRUST DURING RHYACIAN ACCRETIONARY AND COLLISIONAL TECTONICS (Artigo aceito – *Precambrian Research*)

Artigo aceito na revista **Precambrian Research**
https://doi.org/10.1016/j.precamres.2018.04.008

Costa et al. (2018). Precambrian Research, 311, 167–194.

Submetido em 20 junho de 2017; Revisado em 14 de março de 2018; Aceito em 10 de abril de 2018; Publicado online 21 de april de 2018

Geochemistry and U–Pb–Hf zircon data for plutonic rocks of the Troia Massif, Borborema Province, NE Brazil: Evidence for reworking of Archean and juvenile Paleoproterozoic crust during Rhyacian accretionary and collisional tectonics

Felipe Grandjean da Costa[a,b,c], Evandro L. Klein[b,c,d], Jean M. Lafon[c,e], João M. Milhomem Neto[c], Marco A. Galarza[c,e], Joseneusa B. Rodrigues[d], João L. C. Naleto[a], Rafael G. Corrêa Lima[b,c]

a – Geological Survey of Brazil, Fortaleza–CE, Brazil

b – GPGE – Grupo de Pesquisas em Geologia Econômica, Federal University of Pará, Belém–PA, Brazil

c – PPGG – Programa de Pós–Graduação em Geologia e Geoquímica, Federal University of Pará, Belém–PA, Brazil

d – Geological Survey of Brazil, Brasília–DF, Brazil

e – Isotope Geology Laboratory (Pará–iso), Institute of Geosciences, Federal University of Pará, Belém–PA, Brazil

Abstract

Rhyacian (c. 2.30 to 2.05 Ga) subduction–accretion and collisional processes are thought to represent an important event of crustal growth and reworking, often reported in the so–called Tranzamazonian/Eburnean granite–greenstone terranes of N/NE Brazil and West African craton. In this work, we present whole–rock geochemistry and U–Pb–Hf zircon ages for Rhyacian plutonic rocks that intrude Paleoproterozoic granite–greenstone terranes and Archean basement rocks of the Troia Massif, Borborema Province, NE Brazil. U–Pb SHRIMP zircon age of 2185 ± 4 Ma was obtained for a metatonalite sample (Mirador metatonalites). The metatonalites show geochemical affinity similar to those of adakites–like rocks, with all "classic" (slab–derived) adakitic signature (e.g. high Sr/Y, La/Yb and low HREE), but more akin to those evolved from partial melting of the metasomatized mantle wedge, followed by fractional crystallization. Zircon Hf crustal model ages of the metatonalite sample range between 2800 and 2660 Ma, evidencing that Archean crustal components contributed to its magma genesis, probably via subduction of continental–derived sediments to the mantle wedge. For potassic plutons of the Troia Massif (Bananeira suite) we obtained U–Pb SHRIMP zircon age of 2079 ± 4 Ma for a deformed quartz–monzonite with geochemical affinities similar to those derived from low–pressure partial melting of a K–rich mafic protolith. For less–deformed equigranular granites, we obtained a U–Pb LA–ICPMS zircon age of 2068 ± 5 Ma. They are high–K calc–alkaline and slightly peraluminous granites that probably derived from low–pressure partial melting of tonalitic crustal sources (metatonalites) and/or metagraywackes. Zircon Hf crustal model ages of a granite sample range from 2713 to 2535 Ma, evidencing Archean crustal contribution to magma genesis. However, two analyzed c. 2307 Ma inherited zircon grains show $\varepsilon_{Hf}(t)$ values of c. +4.87, indicating that crustal reworking of less–radiogenic Paleoproterozoic sources also participated in its genesis. Regional correlations of our results with the Paleoproterozoic record of the Troia Massif, Borborema Province and surrounding cratonic domains, suggest that the studied plutons are related to the c. 2.2 to 2.0 Ga Transamazonian/Eburnean orogenic cycle. The c. 2185 Ma metatonalites are associated to pre–collisional setting, while the c. 2079–2068 Ma quartz monzonites and granites evolved during collisional setting.

Keywords: Accretionary, Paleoproterozoic, Borborema Province, Troia Massif

2.1. Introduction

The fate of accretionary orogens is generally ending up in a major craton–scale continental collision (Coney, 1987; Condie, 2007; Cawood et al., 2009). As ocean basins close, accretionary orogens are active on one or both continental margins, and final closure is often marked by a continent–continent collision producing a collisional orogeny (Cawood et al., 2009). Indeed, accretionary orogens constitute major sites of continental growth, with successive accretion of oceanic terranes to active continental margins, including island arcs, back–arcs, dismembered ophiolites and oceanic plateaus (Cawood et al., 2009). However, paradoxically, it is also along accretionary orogens, that recycling of crustal components into the mantle may sometimes outweigh juvenile crust formation (e.g. Scholl and von Huene, 2009; Stern and Scholl, 2010). The crustal recycling at accretionary margins occurs where the subducting oceanic slab carries sediments into the mantle and tectonically erodes crustal material from the overriding plate (Scholl and von Huene, 2009; Stern, 2011; Nebel et al., 2011; Spencer et al., 2015). So far, mixing of juvenile arc magmas with subducted continental material has been a common interpretation to discuss geochemical and isotopic variation of subduction–related magmatism in recent (Carpentier et al., 2009; Nebel et al., 2011; Tapster et al., 2014; Shao et al., 2015) and ancient intra–oceanic arcs (Kuzmichev et al., 2005; Kemp et al., 2009; Safonova et al., 2017). For example, according to Nebel et al. (2011), in the Sunda–Banda arc, a modern intra–oceanic arc that is partially colliding with the Australian continental plate, the Hf isotopic composition of zircons from arc magmas show progressively less–radiogenic values toward proximity with the continent, suggesting involvement of subducted continental material to arc magmatism. Nebel et al. (2011) also suggest that similar process could have started very early in Earth's crustal evolution, as sediment recycling in a subduction setting can further account for Hf variations in the Hadean zircon record.

Accretionary orogens appear to have been active throughout much of Earth history (Cawood et al. 2006; 2009) and many Precambrian terranes have been interpreted as a product of subduction–accretion processes (Cawood et al., 2006; Whitmeyer and Karlstrom, 2007; Oliveira et al., 2011; Furnes et al., 2015; Cawood et al., 2016; Chatterjee et al., 2016). According to Furnes et al. (2015), c. 85% of the Precambrian greenstone sequences can be classified as subduction–related ophiolites, generated in back–arc to fore–arc tectonic environments. In Paleoproterozoic times, one of the well–accepted example of crustal growth and reworking along subduction–accretion processes is the c. 2.2–2.0 Ga Birimian/Transamazonian granite–greenstone terranes of São Luís–West African craton (Liégeois et al., 1991; Feybesse et al. 2006; Klein et al., 2008; 2012; Block et al., 2016;

Petersson et al., 2016; 2017) and correlated terranes of the Guyana Shield (Amazon craton) (Vanderhaeghe et al., 1998; Delor et al., 2003; Rosa–Costa et al., 2006; McReath and Faraco, 2006) and northern São Francisco craton (Silva et al., 2001; Costa et al., 2011; Oliveira et al., 2011) (**Fig. 2.1A**). Many of these terranes are interpreted as juvenile arc sequences that evolved during c. 2.2–2.1 Ga accretionary tectonics to late c. 2.1–2.0 Ga continental collision and regional metamorphism (Liégeois et al., 1991; Vanderhaeghe et al., 1998; Delor et al., 2003; Feybesse et al. 2006; McReath and Faraco, 2006; Costa et al., 2011; Oliveira et al., 2011), and most of these interpretations are based on field geology, whole–rock geochemistry, U–Pb zircon ages and Nd isotopic data. However, more recently, combined U–Pb–Hf isotopes in zircon have been reported from Birimian terranes of the São Luís–West African craton, which brought new insights for the crustal evolution on this large Paleoproterozoic granite–greenstone domain (Block et al. 2016; Parra–Avila et al., 2016; 2017; Petersson et al., 2016; 2017; Eglinger et al., 2017). For instance, according to Petersson et al. (2017), zircon Hf isotopes from Birimian granitoids of the Baoulé–Mossi domain (West African craton) (**Fig. 2.1A**), indicate that Archean components were involved in the genesis of many c. 2.22–2.13 Ga Birimian arc–related granitoids, probably by subduction of continental–derived sediments.

The Borborema Province, northeast Brazil (**Fig. 2.1A**), is a Neoproterozoic mobile belt associated to the Pan–African/Brasiliano orogeny (c. 650-535 Ma) (Brito Neves et al., 2000), and much of its geology comprises vast domains of Paleoproterozoic basement rocks, which represent, at least in part, reworked cratonic margins of the São Luís–West African and/or São Francisco cratons (Fetter et al., 2000; Dantas et al., 2004, 2013; Hollanda et al., 2011; Neves et al., 2015; Souza et al., 2016). In the northern Borborema Province, basement rocks are mostly of Paleoproterozoic ages (c. 2.2 to 2.1 Ga) (Fetter et al., 2000; Souza et al., 2007; Hollanda et al., 2011; Martins et al., 2009; Costa et al., 2015; Souza et al., 2016), but Archean crustal domains (c. 2.7 to 3.3 Ga) have also been locally identified (Silva et al., 1997; Fetter, 1999; Dantas et al., 2004, 2013; Ganade et al., 2017) (**Fig. 2.1A**). This mosaic of preserved Paleoproterozoic terranes and Archean fragments is thought to represent the final record of a major Rhyacian accretionary orogeny (Fetter et al., 2000; Arthaud et al., 2008; Neves, 2015; Costa et al., 2015; Souza et al., 2016). For example, in the Troia Massif, northern Borborema Province (**Fig. 2.1A**), Paleoproterozoic metavolcano–sedimentary sequences are tectonically juxtaposed to Archean TTG gneisses (**Fig. 2.1B**) and have been interpreted as the record of intra–oceanic arcs, back–arcs and/or oceanic plateaus, accreted to an Archean paleocontinental margin (Martins et al., 2009; Costa et al., 2015). In this paper,

we present field geology, combined U–Pb–Hf isotopes in zircon and whole–rock geochemistry for Rhyacian plutonic rocks that intrude both Paleoproterozoic metavolcano–sedimentary sequences and Archean gneisses of the Troia Massif (**Fig. 2.1A** and **B**). The results are discussed in order to understand the petrogenesis of these granitoids, and the possible sources of magmatism and tectonic settings. Regional correlation with Paleoproterozoic evolution of Borborema Province, Nigeria shield and Birimian terranes of West African craton is also envisaged.

2.2. Regional geology

2.2.1. The northern Borborema Province and its basement inliers

The Borborema Province represents a c. 650–535 Ma Neoproterozoic mobile belt located between the São Luís–West African and São Francisco–Congo cratons (**Fig. 2.1A**), earning its structural framework during the Pan–African/Brasiliano orogenic cycle, related to the formation of the West–Gondwana supercontinent (Almeida et al., 1981). The Borborema Province is commonly subdivided into the Northern, Central and Southern subprovinces (Brito Neves et al., 2000; Neves, 2003; Van Schmus et al., 2011) (**Fig. 2.1A**). Its main structural feature is the extensive transcurrent shear zone network, usually associated with intrusion of several c. 580 Ma–old syn–tectonic granites (Vauchez et al., 1995; Nogueira, 2004). Based on U–Pb zircon ages and Nd isotopes, the northern Borborema Province, limited to the south by the Patos lineament, has been divided into three main crustal blocks: Médio Coreaú, Ceará Central, and Rio Grande do Norte (Fetter et al., 2000) (**Fig. 2.1A**). The Médio Coreaú and Ceará Central domains are limited by the Sobral–Pedro II shear zone (or Transbrasiliano Lineament) and the limit between the Ceará Central and Rio Grande do Norte domains is marked to the east by the Senador Pompeu shear zone (Brito Neves et al., 2000; Fetter et al., 2000; Padilha et al., 2017). According to Padilha et al. (2017), magnetotelluric data collected along the northern Borborema Province revealed that the limits of these blocks are compatible with high conductivity anomalies in the crust and upper mantle, interpreted as suture zones and correlated to the Neoproterozoic collage. However, according to Neves (2003; 2015), these regional–scale structures are mostly reactivations of older Paleoproterozoic shear zones, and the lack of evidence for vast Neoproterozoic oceans suggests that the Neoproterozoic metamorphism and deformation in the whole Borborema Province may be the product of an intra–continental orogeny.

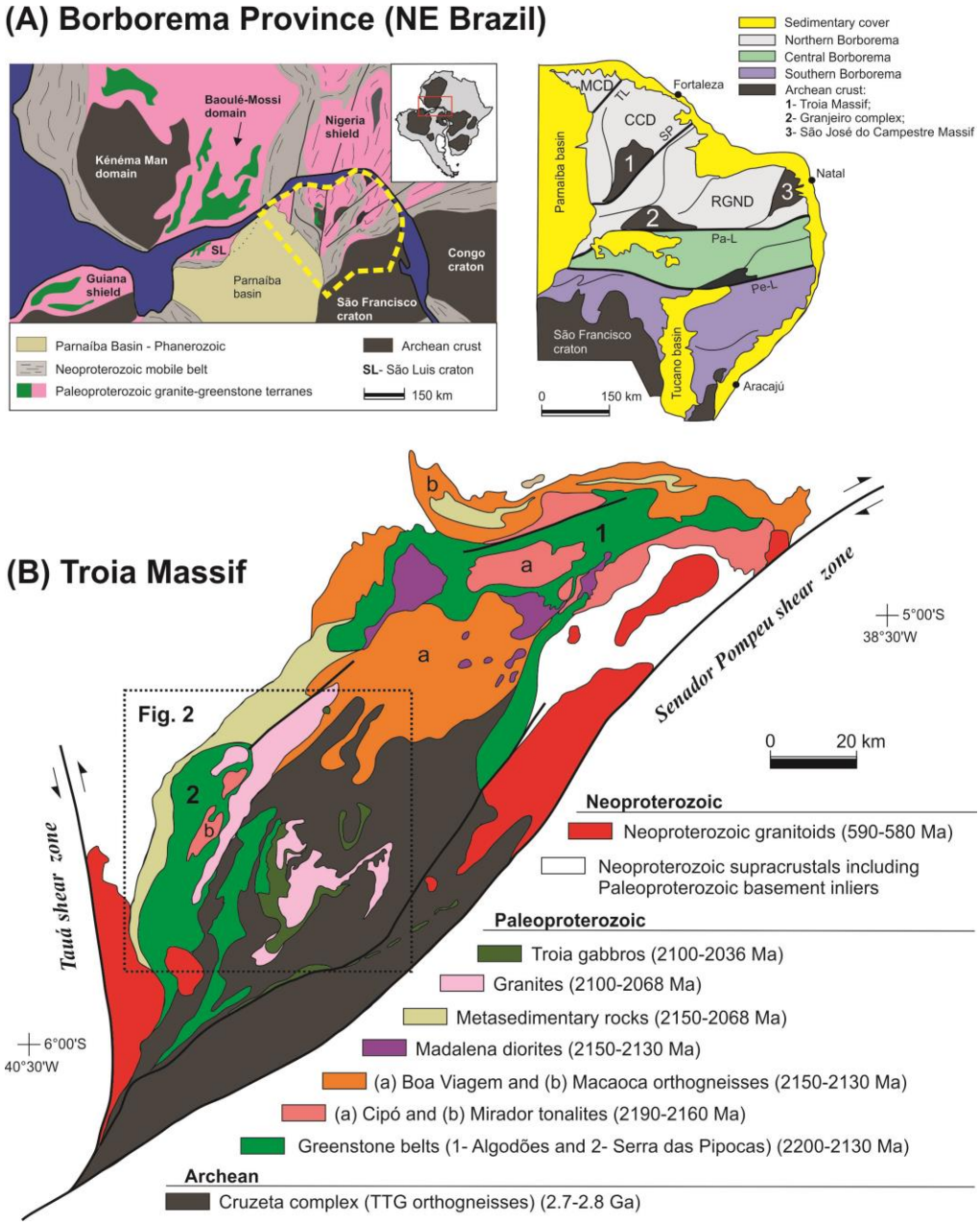

Fig. 2.1. *Simplified geological framework of the Borborema province and Troia massif: (A) Yellow dashed line locates Borborema Province in the pre–drift reconstruction of South America and Africa (modified from Arthaud et al., 2008); and (at right) schematic map of the Borborema Province with three major subdivisions delimited by the Patos (Pa–L) and the Pernambuco Lineaments (Pe–L). Tectonic domains are according to Fetter et al. (2000); MCD= Médio Coreaú Domain, CCD= Ceará Central Domain and RGND= Rio Grande do Norte Domain, and shear zones are SP= Senador Pompeu shear zone and TL= Transbrasiliano lineament (or Sobral–Pedro II shear zone). (B) Simplified geological map of the Troia Massif (Modified from Costa et al., 2015).*

Archean crustal records have been identified in northern Borborema Province, corresponding to: (1) Neoarchean (c. 2.8–2.7 Ga) TTG gneisses of Troia Massif in the Ceará Central Domain (Fetter, 1999; Silva et al., 2002; Ganade et al., 2017); (2) the c. 3.2 to 2.5Ga Granjeiro complex (Silva et al., 1997; Freimann, 2014; Hollanda et al., 2015); and (3) the c.

3.4 to 2.7 Ga São José do Campestre Massif, cropping out in the northeastern portion of the Rio Grande do Norte Domain (Dantas et al., 2004, 2013; Souza et al., 2016). More recently, Archean rocks have also been identified in the Central Borborema Province (**Fig. 2.1A**) (c. 2.6 Ga Riacho das Lages suite) (Santos et al., 2017). Mostly, these Archean fragments are enveloped by Rhyacian granite–gneissic domains and associated metavolcano–sedimentary sequences (Fetter et al., 2000; Dantas et al., 2004; Souza et al., 2007; Hollanda et al., 2011; Costa et al., 2015; Souza et al., 2016). For more details of the northern Borborema Province geology and its correlation with the African counterpart, see Arthaud et al. (2008) and Santos et al. (2008).

2.2.2. The Troia Massif and its Paleoproterozoic granite–greenstone terranes

The Archean–Paleoproterozoic basement rocks in the Ceará Central Domain were originally named Troia Massif by Brito Neves (1975), and as Cruzeta complex by Oliveira and Cavalcante (1993) (**Fig. 2.1B**). U–Pb TIMS zircon ages obtained by Fetter (1999) confirmed its c. 2.8–2.7Ga Archean age. The southeastern limit of this Archean domain is sharply defined by the Senador Pompeu shear zone (**Fig. 2.1B**), whereas the northern and western limits are less clear, and have been inferred on the basis of geochronological data and airborne gamma–spectrometry (Pinéo and Costa, 2013). According to Fetter (1999), the Troia Massif can be divided into two distinct crustal blocks: (i) Pedra Branca and (ii) Mombaça block, both with Neoarchean 2.8–2.7 Ga U–Pb TIMS zircon ages, but differing in their Sm–Nd isotopic signature. The Mombaça block has $\varepsilon_{Nd}(t)$ values ranging from -0.79 to +2.73, and the Pedra Branca block yielded slightly more radiogenic values (juvenile) (-0.02 to +2.48) (Fetter, 1999). According to Ganade et al. (2017), new SHRIMP U–Pb geochronological data demonstrate that the Mombaça block (2793 ± 6 Ma) is older than the grey gneisses of the Pedra Branca block (2698 ± 8 Ma), as also suggested by Fetter (1999). However, in the simplified regional–scale map of the Troia Massif (**Fig. 2.1B**), all the Neoarchean rocks of the Troia Massif are represented by the Cruzeta complex (**Fig. 2.1B**). These Archean rocks are mostly TTG orthogneisses and migmatites. The migmatites are mainly composed of stromatic metatexites with main protolith represented by biotite gneiss of granodioritic composition (Mombaça unit), and tonalitic to dioritic compositions (Pedra Branca unit) (Ganade et al., 2017). The U–Pb (SHRIMP) age of 3270 ± 5 Ma was determined by Silva et al. (2002) for a metatonalite of the Cruzeta complex. This age provides evidence that the emplacement of the Mombaça and Pedra Branca TTGs occurred over pre–existing crust with ages similar to those reported in the São José do Campestre Massif (Dantas et al., 2004, 2013; Souza et al., 2016).

Paleoproterozoic granitoids of the Troia Massif occurs intrusive into both Archean rocks of the Cruzeta complex and Paleoproterozoic greenstone belts (**Fig. 2.1B**). For example, the Boa Viagem complex are represented by tonalitic to granodioritic orthogneisses with U–Pb (SHRIMP) zircon ages of 2150 ± 29 Ma and 2124 ± 35 Ma, and may probably represent continental arc plutonism at the northern portion of the Cruzeta complex (Silva et al., 2014) (**Fig. 2.1B**). The São José da Macaoca complex, defined by Torres et al. (2007) to the north of the Troia Massif, also represents a large portion of tonalitic to granodioritic orthogneisses with similar U–Pb TIMS zircon ages of 2139 ± 12 Ma (Castro, 2004) and 2130 ± 3 Ma (Fetter, 1999) (**Fig. 2.1B**). According to Costa et al. (2015), the c. 2139–2130 Ma Macaoca orthogneisses have low–silica adakitic signature (mantle–related magmas), and were probably associated to the accretion of the Algodões greenstone terrane to the north margin of the Troia Massif. In this massif, two major metavolcano–sedimentary sequences have been recognized as Paleoproterozoic greenstone belts, named Algodões greenstone belt to the north (Martins et al., 2009; Costa et al., 2015), and Troia greenstone belt (or Serra das Pipocas greenstone belt) to the south (Pessoa and Archanjo, 1984; Pessoa et al., 1986; Costa et al., 2014a, 2015; Sousa, 2016) (**Fig. 2.1B**).

2.2.3. The Algodões metavolcano–sedimentary sequence

The Algodões metavolcano–sedimentary sequence occurs at the northern portion of the Troia Massif (**Fig. 2.1B**). This sequence comprises mainly amphibolites derived from metabasalts, fine–grained leucocratic paragneisses, metagreywackes, meta–arkoses, rare metapelites, quartzites, meta–andesites, meta–conglomerates, and calc–silicate rocks (Martins, 2000; Martins et al., 2009; Costa, 2013). The Algodões amphibolites were dated at 2236 ± 55 Ma (whole–rock Sm–Nd isochron; four samples) (Martins et al., 2009) and share geochemical features akin to oceanic plateau and/or back–arc basalts (Martins et al., 2009; Verma and Oliveira, 2014). They record upper greenschist to lower amphibolite metamorphic conditions and lacks migmatization (Martins, 2000; Costa, 2013). Structurally, the Algodões sequence shows penetrative regional northeastward trending foliation dipping to SE (Martins, 2000; Costa, 2013). A LA–ICPMS U–Pb zircon age of 2046 ± 12 Ma obtained by Gomes (2013) for the leucosome of a migmatitic (Macaoca) orthogneiss found close to the Algodões sequence shows that regional metamorphism is probably of Paleoproterozoic age. Based on Pb–Pb zircon ages, Sm–Nd isotopes and whole–rock geochemistry, the c. 2190 to 2160 Ma Cipó tonalites, that intrude the Algodões metavolcano–sedimentary sequence, are thought to represent TTG–like (trondhjemite or high–silica adakite) plutonic rocks that probably evolved

in an intra–oceanic arc, to account for their juvenile Nd signature (TDM model ages = 2.24 to 2.29 Ga and $\varepsilon_{Nd}(t)$ values = +0.29 to +1.9) (Martins et al. 2009). For these plutonic rocks (Cipó tonalites), Costa et al. (2015) reported LA–ICPMS U–Pb zircon ages of 2189 ± 14 Ma and 2180 ± 15 Ma, and also suggested a pre–collisional (arc–related) setting to these tonalites.

2.2.4. The Serra das Pipocas greenstone belt

The first structural and lithological mapping in the central–west part of the Troia Massif was presented by Pessoa and Archanjo (1984). According to these authors, thrust tectonic is responsible for the allochthonous character of the metavolcano–sedimentary sequences and related mafic–ultramafic metaplutonic rocks, overlying the gneiss–migmatitic basement of the Troia Massif. Additional work, with Rb–Sr and K–Ar geochronological data, evidenced that the Troia Massif exhibits a polycyclic character, with Archean and Paleoproterozoic rocks, mostly presenting K–Ar and Rb–Sr isotopic rejuvenating during the Neoproterozoic (Brasiliano) orogenic event (Pessoa et al., 1986). These authors also suggested that the thrust tectonic in the Troia Massif is Paleoproterozoic in age. However, because of the lack of reliable isotopic results for the supracrustal sequences of the Serra das Pipocas region, Pessoa et al. (1986) interpreted it as an Archean greenstone sequence, piecing the assemblage of Archean gneisses and migmatites of the Troia Massif. Later on, Fetter (1999) provided 2151 ± 9 Ma U–Pb zircon age for a metadacite layer close to the Serra das Pipocas region, suggesting a minimum depositional (Paleoproterozoic) age for the Serra das Pipocas granite–greenstone sequence, but the metamafic–ultramafic plutons and associated greenstone belts of the central portion of the massif were still interpreted as of Archean age. However, new U–Pb (in situ) zircon ages in metasedimentary and intrusive rocks confirmed the Paleoproterozoic (Rhyacian c. 2.2–2.0 Ga) age for the Serra das Pipocas metavolcano–sedimentary sequence and related metamafic–ultramafic rocks in the Troia Massif (Costa et al., 2014a, 2014b; Sousa, 2016) (**Fig. 2.2**).

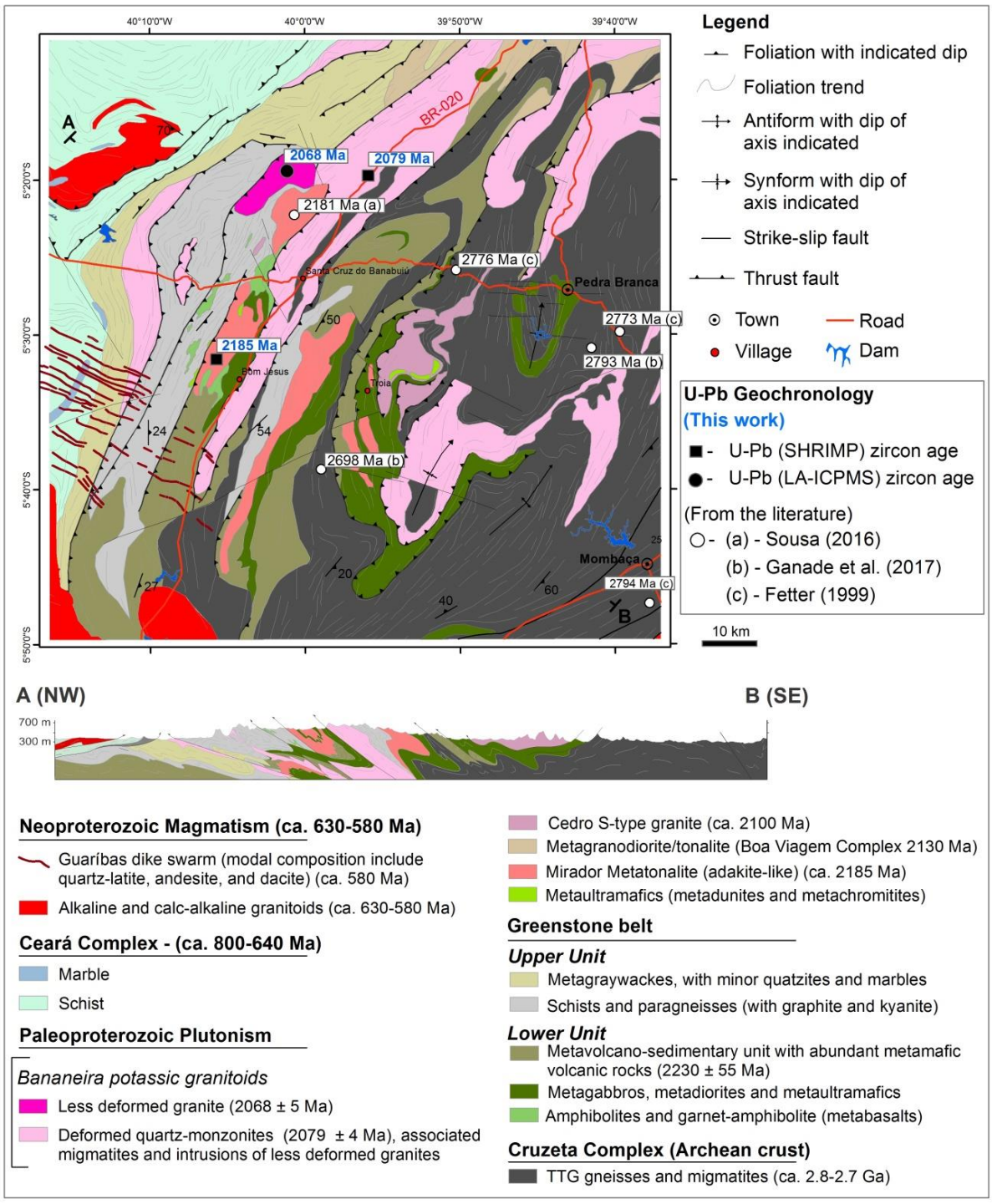

Fig. 2.2. *Geological map of the study area with location for U–Pb zircon ages of this and previous studies. Respective error for U-Pb data on the map can be seen in* ***Table 2.5****.*

The Serra das Pipocas greenstone belt (or Troia metavolcano–sedimentary sequence), in the central–west portion of the Troia Massif (**Fig. 2.1B** and **2.2**) is composed of metabasalts (amphibolites), felsic to intermediate metavolcanic rocks, metasedimentary rocks, metacherts, marbles, serpentinites, and associated S–type leucogranite (i.e., Cedro suite), tonalitic (TTG–like) intrusions and mafic–ultramafic metaplutonic rocks (Pessoa and Archanjo, 1984; Pessoa

et al., 1986; Cavalcante et al., 2003; Costa et al., 2014a; Sousa, 2016). According to Pessoa and Archanjo (1984), metabasalt with pillow–like structures was locally identified. Geochemistry of mafic metavolcanic rocks shows transitional tholeiitic to calc–alkaline affinity and arc–related signature, suggesting an arc/back–arc tectonic setting to this volcanism (Sousa, 2016). U–Pb detrital zircon dating of a metagreywacke of the metavolcano–sedimentary sequence yielded a younger age population around 2200 Ma and older ($^{207}Pb/^{206}Pb$) ages of 3096 ± 53 Ma, 3074 ± 55 Ma, 2608 ± 54 and 2546 ± 55 Ma, which indicates a mixture of Archean and Rhyacian sources and a maximum depositional age of c. 2.2 Ga (Costa et al., 2014a). The presence of Archean detrital zircon grains suggests an ensialic (or continental proximity) setting for part of this granite–greenstone terrane (Costa et al., 2014a). The mafic and ultramafic metaplutonic rocks are more abundant in the central Troia region (**Fig. 2.1B**), and are mainly interpreted as fragmented layered bodies, well–known because of the platinum and palladium mineralization in metachromitites (Pessoa and Archanjo, 1984; Angeli et al., 2009; Barrueto and Hunt, 2010). A Sm–Nd isochron of c. 2060 Ma was obtained for this mafic–ultramafic magmatism (Liégeois, unpublished data; cited by Fetter, 1999), recently attested by a U–Pb (SHRIMP) zircon age of 2036 ± 28 Ma obtained for a PGE–bearing metachromitite sample (Costa et al., 2014b).

2.3. Plutonic rocks: field geology and petrography

The plutonic rocks investigated in this work consist of metatonalites (Mirador Tonalite) intruded into the Paleoproterozoic Serra das Pipocas metavolcano–sedimentary succession, and potassic granitoids of the Bananeira suite, which intruded both Archean TTG gneisses and Paleoproterozoic greenstone sequences (**Fig. 2.2**). All these plutons are generally foliated and locally have gneissic banding, due to deformation under amphibolite facies metamorphism during the Transamazonian (2.2 to 2.0 Ga) and/or Brasiliano (650–535 Ma) orogenies. The dominant structures observed in outcrop are east-dipping foliation (30 to 55°) with associated low-rake stretching lineation plunging 20–35° to NE (**Fig. 2.2**). Many local– and regional–scale fold axis also plunge 20–35° toward NE (**Fig. 2.2**). The NE-SW trending foliations, and the NE–directed lineations and fold axis in these rocks are in structural concordance with the dextral strike–slip Neoproterozoic Senador Pompeu shear zone (**Fig. 2.1B**). However, in this study, the occurrence of less–deformed granites crosscutting strongly deformed quartz–monzonites, both with Paleoproterozoic ages evidence that the c. 2.2 to 2.1 Ga deformation is also preserved in this area.

2.3.1. Mirador tonalites

The Mirador tonalites have intrusive contact with amphibolites and metasedimentary rocks of the Serra das Pipocas greenstone belt, and do not occur in the surrounding basement rocks (**Fig. 2.2**). Additionally, the intrusions are restricted to the basal unit of the greenstone sequences, spatially associated to gabbros and amphibolites (**Fig. 2.2**). The tonalites are generally gray, have medium–grained equigranular texture, and are generally foliated (**Fig. 2.3A**). They are predominantly tonalitic to granodioritic in composition (**Fig. 2.4A**), being composed of plagioclase (An_{48-30}) (20–30%), alkali feldspar (15–10%), quartz (19–29%), biotite (15–20%) and hornblende (15–20%). Plagioclase is euhedral to anhedral and partly altered to sericite and carbonate. Alkali feldspar is generally perthitic and locally albitized at the rims. Hornblende occurs as prismatic grains and is locally replaced by biotite. Quartz grains are anhedral, show undulatory extinction and rarely subgrain boundary. Accessory minerals include titanite, apatite, epidote, zircon and allanite. Zircon grains occur generally associated and/or included in biotite and hornblende. Mafic magmatic enclaves are locally found (**Fig. 2.3B**).

2.3.2. Granites and quartz–monzonites of the Bananeira suite

The Bananeira suite was originally reported by Oliveira and Cavalcante (1993) for granites, potassic orthogneisses and associated migmatites mapped in the central region of the Troia Massif (**Fig. 2.1B** and **2.2**). A large (c. 100 km) NE–SW elongated domain of this igneous–migmatitic association occurs as a regional sheet–like intrusion between Archean basement rocks and Paleoproterozoic greenstone belts (**Fig. 2.2**). In this igneous–migmatitic association, two main types of plutonic rocks can be distinguished: (i) quartz–monzonites and (ii) granites (**Fig. 2.4A**). Quartz–monzonites have medium– to coarse–grained texture, and hornblende as the main mafic mineral (**Fig. 2.3C**). They are mainly composed of plagioclase (An_{38-32}) (andesine) (15–23%), alkali feldspar (13–20%), quartz (5–10%), hornblende (10–20%) and biotite (5–10%). They commonly show porphyritic textures, with feldspar phenocrysts (plagioclase and/or perthitic alkali feldspar). Quartz grains show undulatory extinction and subgrain boundary. Common accessory phases include titanite, apatite, epidote, zircon and allanite. Locally, amphibolite enclaves are found in the quartz–monzonites (**Fig. 2.3D**), but mafic magmatic enclaves are rarely seen, lacking evidence for magma mixing/mingling. These porphyritic quartz–monzonites are usually strongly foliated (**Fig. 2.3C** and **D**) and locally cross–cutt by fine–grained less–deformed granitic dikes (**Fig. 2.3E**).

Fig. 2.3. *Field aspects of the plutonic rocks: (A) Mirador tonalite with medium–grained equigranular texture and mafic enclave. (B) Mirador tonalite with mafic magmatic enclaves, evidencing magma mingling process. (C) Steeply dipping foliation in dark–gray porphyritic quartz–monzonite of the Bananeira suite. (D) Mafic (amphibolite) enclave in quartz–monzonite. (E) Fine–grained granitic dike cross–cutting dark–gray quartz–monzonite gneiss. (F) Weakly deformed, medium–grained equigranular pinkish granite.*

The less–deformed granite occurs as individual semi–circular intrusion at the north of the Serra das Pipocas metavolcano–sedimentary sequence (**Fig. 2.2**). This granite is weakly deformed, with reddish pink to pinkish gray color, and fine– to medium–grained equigranular

textures (**Fig. 2.3F**). It has monzogranitic to syenogranitic composition, with alkali feldspar (29–35%), quartz (15–30%), plagioclase (An_{12-08}) (albite–oligoclase) (15–20%) and biotite (5–10%) as essential minerals. Quartz grains show slightly undulatory extinction and no subgrain boundary. Accessory phases are mainly titanite, allanite, apatite and zircon. Magnetite is also common accessory mineral in the less–deformed granite samples, generally associated to titanite and allanite.

2.4. Material and methods

2.4.1. Whole–rock geochemistry

Major and trace element analyses of whole–rock were carried out respectively by X–ray fluorescence (XRF) and inductively coupled mass spectrometry (ICPMS) at the SGS GEOSOL laboratory in Vespasiano, Minas Gerais (Brazil), according to its pre–established XRF79C and IMS95A analytical method. For major element analyses, the rock powder (2 grams per sample) was dried in an oven and weighed after cooling in a jar containing lithium tetraborate flux. The sample was then transferred to a platinum crucible and homogenized. After homogenization lithium iodide was added before fusion in an automatic machine and analysis by XRF. For trace element analyses, the rock powder (10 grams per sample) was weighed and then fused in a graphite crucible by adding lithium metaborate. After fusion the melt was transferred to a beaker containing a solution of nitric acid and tartaric acid in equal volumes before homogenization and total dissolution under agitation, and analysis of the solutions by ICP–MS. The analytical accuracy was monitored using the geological standard materials TILL–03 and GRE–03 for trace elements on ICPMS, and SG–142 and AMIS0321 for major elements on XRF. Analytical precision for major elements is better than 5% and better than 10% for trace elements. Analyses of blank material yielded values typically below the detection limits. Results are presented in **Table 2.1**. The geochemical analyses were plotted using the GCDkit software (Janousek et al., 2006).

Table 2.1: Whole–rock geochemical data

	FC-19	FC-53	FC-99	FC-96	FC-281	FC-52	FC-274-A	FC-279-C	FC-91-A	FC-93	FC-280-A	FC-288	FC-287	FC-92	FC-14	FC 14-B
							Mirador tonalites									
Major elements (wt%)																
SiO2	64.1	64.4	65.0	65.1	65.4	65.5	65.9	66.1	66.2	66.5	67.0	67.5	67.6	68.0	68.1	68.6
TiO2	0.38	0.44	0.52	0.37	0.40	0.53	0.47	0.44	0.43	0.33	0.41	0.38	0.36	0.33	0.32	0.34
Al2O3	16.3	15.4	16.1	15.5	16.1	15.9	16.0	15.6	15.8	15.5	16.1	16.6	16.5	15.5	15.6	16.4
Fe2O3	3.88	4.11	4.59	3.59	4.10	4.61	4.80	4.41	3.95	3.26	4.05	4.13	3.87	3.17	3.06	3.52
MnO	0.06	0.06	0.09	0.06	0.07	0.09	0.08	0.08	0.07	0.06	0.07	0.08	0.08	0.06	0.05	0.06
MgO	1.53	2.05	2.33	1.92	1.93	2.54	1.72	2.38	2.28	1.83	2.05	1.49	1.32	1.78	1.33	1.17
CaO	4.15	3.94	4.50	3.99	3.77	4.28	3.75	4.04	3.76	3.09	3.65	3.77	3.46	3.43	2.88	3.28
Na2O	5.11	4.52	4.54	5.01	5.08	4.73	4.35	4.54	4.98	4.74	5.01	4.90	4.98	4.89	5.11	4.98
K2O	1.86	2.16	2.09	1.80	1.87	2.17	2.18	1.93	2.35	2.44	1.95	2.22	2.13	2.53	2.48	2.45
P2O5	0.12	0.19	0.25	0.17	0.17	0.30	0.17	0.22	0.22	0.17	0.18	0.12	0.12	0.14	0.10	0.11
LOI	0.56	1.14	0.71	0.80	0.47	0.60	0.93	0.83	1.03	0.85	0.59	0.63	0.57	1.20	0.60	0.59
Total	98.1	98.4	100.7	98.3	99.4	101.2	100.4	100.6	101.1	98.8	101.1	101.8	101.0	101.0	99.6	101.5
Rb	46.6	53.7	95.1	45.7	66.9	53.2	58.0	50.8	46.8	61.7	40.1	46.8	53.2	82.3	57.0	65.5
Sr	1148	963	1260	1447	1423	1028	893	1437	1281	1247	1425	980	1021	1041	915	1068
Ba	964	1294	1743	1879	1532	1469	1220	1714	1781	1870	1751	881	766	1854	1036	950
Ni	17.0	29.0	30.0	29.0	42.0	36.0	19.0	42.0	32.0	27.0	42.0	29.0	26.0	28.0	13.0	24.0
Co	9.70	12.70	12.20	10.40	11.00	14.70	10.40	13.60	11.50	9.30	10.80	8.70	7.80	9.20	7.60	7.00
Nb	4.97	5.26	8.07	4.38	8.55	5.24	4.93	4.04	5.53	4.65	2.94	4.28	6.04	4.64	6.28	3.49
Zr	122	159	178	190	118	137	129	98.7	222	116	101	111	125	108	118	117
Hf	2.58	3.29	4.52	4.37	2.94	2.45	3.31	3.71	5.31	2.58	3.15	2.83	3.23	2.50	2.67	3.30
Y	14.46	11.58	15.00	11.52	10.67	13.09	12.22	11.24	12.24	9.12	10.08	12.07	15.08	9.14	12.75	12.08
Th	1.50	5.20	7.10	2.20	2.30	3.00	4.10	8.30	4.20	4.00	5.40	2.60	3.60	2.60	2.30	3.20
U	0.50	0.95	0.67	0.76	0.85	1.25	1.18	0.79	0.94	1.30	0.57	0.52	0.67	1.08	0.56	1.66
Cs	0.74	2.03	17.57	2.90	9.39	4.20	4.76	2.16	1.61	1.65	2.11	0.94	1.22	7.75	0.94	1.22
Rare earth elements (ppm)																
La	21.6	26.1	32.6	28.9	20.3	29.4	16.6	30.7	25.5	25.8	22.1	12.9	14.8	21.6	15.6	14.4
Ce	32.8	53.1	67.6	52.5	49.5	60.5	42.6	65.0	57.5	48.0	49.5	30.5	34.5	44.4	34.5	33.8
Pr	4.32	5.96	8.26	6.73	6.11	7.37	5.22	7.66	7.19	5.80	6.17	3.63	4.27	5.41	3.90	4.21
Nd	17.2	20.5	29.9	24.8	24.1	25.8	20.0	29.3	26.4	20.6	24.4	14.6	17.2	20.0	15.6	16.8
Sm	3.20	3.40	5.60	4.20	4.30	4.40	3.70	5.10	5.20	3.70	4.30	2.90	3.60	3.40	2.90	3.20
Eu	0.89	0.84	1.28	1.04	1.24	0.98	1.03	1.41	1.20	0.94	1.22	0.79	0.94	0.90	0.70	0.89
Gd	2.92	2.40	3.93	3.08	3.25	3.08	2.92	3.85	3.56	2.59	3.23	2.56	3.13	2.49	2.47	2.88
Tb	0.42	0.31	0.49	0.37	0.40	0.37	0.41	0.49	0.42	0.27	0.40	0.39	0.45	0.32	0.37	0.40
Dy	2.46	1.78	2.75	2.01	2.07	1.98	2.29	2.30	2.34	1.67	1.92	2.21	2.66	1.68	2.17	2.24
Ho	0.50	0.34	0.45	0.38	0.38	0.38	0.45	0.44	0.41	0.28	0.35	0.44	0.53	0.31	0.43	0.45
Er	1.39	0.92	1.39	1.05	1.08	1.02	1.27	1.22	1.17	0.87	0.97	1.34	1.61	0.86	1.19	1.29
Tm	0.20	0.14	0.19	0.15	0.15	0.16	0.22	0.18	0.18	0.14	0.13	0.18	0.23	0.11	0.18	0.19
Yb	1.40	0.90	1.20	0.90	1.00	1.00	1.30	1.10	1.10	0.80	0.90	1.20	1.60	0.80	1.20	1.30
Lu	0.18	0.13	0.19	0.15	0.14	0.13	0.19	0.16	0.17	0.12	0.13	0.18	0.23	0.11	0.17	0.19

Table 2.1_continued

	FC-77	FC-197	FC-75	FC-279-A	FC-250	FC-62	FC-69-A	FC-65	FC-64	FC-66-A	FC-66-E	FC-240	FC-257	FC-278	FC-277
		Mirador tonalites					Quartz-monzonites (Bananeira suite)						Granites (Bananeira suite)		
Major elements (wt%)															
SiO2	68.6	68.7	70.1	70.4	62.8	63.0	63.2	64.1	64.2	64.6	64.6	71.5	72.0	72.0	72.5
TiO2	0.31	0.33	0.26	0.31	0.70	0.62	0.72	0.67	0.62	0.68	0.69	0.52	0.18	0.31	0.34
Al2O3	16.0	15.3	15.5	14.9	16.8	16.0	17.3	16.6	16.6	17.0	16.8	14.6	14.3	14.4	14.2
Fe2O3	3.23	3.37	2.89	3.11	5.24	4.50	4.75	4.59	4.37	4.76	4.97	3.92	2.22	2.81	3.03
MnO	0.05	0.07	0.05	0.06	0.08	0.06	0.06	0.07	0.06	0.07	0.07	0.07	0.03	0.06	0.05
MgO	1.29	1.57	1.03	1.23	1.98	1.80	1.92	1.77	1.67	1.82	1.68	0.65	0.51	0.50	0.49
CaO	3.20	2.77	3.05	2.44	3.55	3.38	3.13	3.54	3.26	3.65	3.44	1.98	1.25	1.59	1.57
Na2O	4.90	4.71	4.67	4.50	3.97	3.92	4.71	4.17	3.95	4.26	4.04	3.67	3.36	3.64	3.60
K2O	2.48	2.77	2.77	2.70	4.36	4.55	4.08	4.62	4.63	4.14	4.27	4.39	5.21	4.72	4.55
P2O5	0.11	0.13	0.10	0.13	0.31	0.29	0.31	0.29	0.29	0.31	0.29	0.14	0.08	0.14	0.15
LOI	0.69	0.42	0.66	0.40	0.63	0.45	0.75	0.60	0.79	0.45	0.30	0.17	0.49	0.30	0.20
Total	100.9	100.1	101.1	100.2	100.4	98.6	100.9	101.0	100.4	101.7	101.2	101.6	99.6	100.5	100.7
Rb	48.5	122.3	52.5	61.4	126.8	185.9	163.8	179.4	137.9	131.5	124.1	99.7	117.4	141.7	129.9
Sr	1016	980	849	943	713	698	712	692	700	753	728	423	392	547	495
Ba	1105	1476	982	1334	1300	1146	1097	1132	1239	1235	1236	2229	1740	1628	1801
Ni	14.0	33.0	9.0	28.0	28.0	13.0	10.0	11.0	10.0	15.0	22.0	16.0	15.0	13.0	14.0
Co	7.10	8.30	5.60	7.30	12.10	11.70	10.80	11.70	10.90	12.50	11.10	4.90	3.60	3.90	3.40
Nb	4.67	4.01	4.73	3.37	7.73	12.63	13.18	11.73	11.58	12.61	12.22	17.26	1.09	12.46	9.63
Zr	144	102	94.4	91.2	338	389	317	387	338	436	313	435	219	214	251
Hf	3.97	2.67	2.28	2.43	8.44	7.80	9.46	7.76	6.47	8.65	8.00	11.45	6.38	5.84	6.67
Y	11.77	15.82	10.35	8.83	21.03	19.84	17.34	19.90	18.46	21.56	21.87	41.74	20.39	37.72	19.91
Th	3.00	4.20	1.80	5.30	8.00	12.10	18.20	11.00	11.60	9.50	9.00	25.60	25.70	22.20	21.50
U	0.44	2.27	0.38	0.96	0.80	1.85	1.48	1.67	1.30	1.37	1.03	3.45	1.35	5.56	3.64
Cs	0.80	7.58	0.85	3.61	1.51	4.10	2.97	3.19	1.94	2.24	1.61	1.57	0.87	1.69	1.99
Rare earth elements (ppm)															
La	14.1	29.3	15.8	24.8	49.9	38.1	53.2	46.9	44.7	44.9	49.6	178.5	175.7	138.1	126.8
Ce	25.1	46.8	22.6	46.9	104.5	91.8	105.6	95.9	95.0	95.4	106.8	340.1	171.6	237.7	255.0
Pr	3.26	6.43	2.92	5.80	11.98	9.37	11.81	10.44	10.16	10.87	12.54	40.29	28.99	31.93	29.46
Nd	12.7	24.6	11.2	21.8	44.3	32.1	40.2	34.7	33.9	37.4	46.3	145.3	94.9	116.5	104.2
Sm	2.70	4.20	2.10	3.60	7.40	5.60	6.60	5.70	5.60	6.30	8.00	22.00	12.90	18.10	15.10
Eu	0.69	1.11	0.56	1.00	1.55	1.07	1.37	1.20	1.10	1.18	1.74	2.86	1.94	2.86	2.40
Gd	2.25	3.74	1.94	2.84	6.09	3.99	4.58	4.19	3.82	4.38	6.27	15.40	9.40	12.73	9.88
Tb	0.34	0.47	0.27	0.35	0.78	0.54	0.60	0.56	0.51	0.61	0.85	1.90	1.02	1.50	1.09
Dy	2.00	2.49	1.56	1.76	4.29	3.04	3.38	3.17	2.92	3.43	4.37	8.80	4.15	7.07	4.65
Ho	0.41	0.52	0.33	0.32	0.77	0.58	0.60	0.57	0.56	0.65	0.80	1.51	0.66	1.21	0.75
Er	1.17	1.44	1.00	0.88	2.20	1.66	1.72	1.70	1.53	1.84	2.37	4.01	1.55	3.36	1.90
Tm	0.17	0.19	0.15	0.14	0.30	0.25	0.26	0.23	0.24	0.25	0.35	0.51	0.20	0.47	0.25
Yb	1.20	1.10	1.00	0.90	2.00	1.70	1.60	1.70	1.50	1.70	2.20	3.20	1.10	2.90	1.70
Lu	0.18	0.16	0.15	0.14	0.27	0.23	0.24	0.25	0.22	0.24	0.31	0.42	0.15	0.42	0.26

2.4.2. In situ zircon U–Pb geochronology

Zircons were separated using conventional techniques (jaw crusher, disk grinder, Frantz isodynamic magnetic separator and hand picking under the binocular loupe). Prior to isotopic analytical work, zircon grains were characterized by cathodoluminescence (CL) and back–scattered (BSE) electron imaging using a scanning electron microscope. For samples FC–17 and FC–66A, CL images were obtained in a Quanta 250 FEG electron microscope at the Geochronological Research Center in São Paulo University, Brazil, and for the sample FC–278, CL and BSE images were acquired using a Zeiss Evo LS–15 electron microscope at the Geological Survey of Brazil, in Belém, Brazil.

Zircon U–Pb isotope analyses for samples FC–17 (Mirador tonalite) and FC–66A (Bananeira quartz–monzonite) were obtained by secondary ion mass spectrometry (SIMS) with the SHRIMP IIe microprobe (Sensitive High Resolution Ion Microprobe) at the Geochronological Research Centre (CPGeo) at the São Paulo University (USP), Brazil. The data have been reduced in similar way to that described by Williams (1998) and Sato et al. (2008). Uncertainties given for individual U–Pb analyses are at the 1σ level. For the age calculations, corrections for common Pb were made using the measured ^{204}Pb and the relevant common Pb compositions from the Stacey and Kramers (1975) model. Concordia plots, regressions and any weighted mean age calculations were carried out using Isoplot/Ex 3.0 (Ludwig, 2003). U–Pb geochronological results are presented in **Table 2.2**. For detail in methods employed for SHRIMP–IIe U–Pb zircon analysis and data processing at the CPGeo–USP, see Sato et al. (2008; 2014).

For sample FC–278 (Bananeira granite), zircon U–Pb isotope analyses were undertaken at the Department de Geology, Federal University of Ouro Preto (UFOP), Brazil. The U–Pb isotopic data were acquired by using a multi–collector (MC)–ICP–MS Thermo–Scientific Neptune Plus system coupled to a Photon–Machines 193 (λ = 193nm) ArF Excimer laser ablation system. Argon was used as sample gas and Helium as carrier gas. The initial spot size was performed with 20 µm, although a smaller spot size (15 µm) was adopted to reduce the signal, because of the high U and Pb content in the analyzed zircons. The raw data were corrected for background signal, and laser induced elemental fractional and instrumental mass discrimination were corrected by the reference zircon (GJ–1) (Jackson et al., 2004). The common Pb correction was based on the Pb composition model of Stacey and Kramers (1975). To evaluate the accuracy and precision of the laser–ablation results, the Plešovice zircon (337±1 Ma; Sláma et al. 2008) was analyzed. The LA–ICP–MS data were reduced using the software Glitter (Van Achterberghet al., 2001) with ages calculated and plotted on

Concordia diagrams using the IsoplotEx 4 program (Ludwig, 2003). The results of the LA–ICP–MS analyses are presented in the **Table 2.3**, with uncertainties on ages at 2σ. The methods employed for analysis and data processing are referred to Santos (2015).

Table 2.2: U-Pb SHRIMP zircon data

Mirador tonalite (sample FC-17)															
(*Spot*)	% ^{206}Pb_c	U (ppm)	Th (ppm)	^{232}Th/^{238}U	^{206}Pb*(ppm)	^{206}Pb/^{238}U	± 1σ	^{207}Pb/^{206}Pb	± 1σ	%disc.	^{207}Pb/^{235}U	%err	^{206}Pb/^{238}U	%err	err corr.
1.1	0.16	83	25	0.31	29	2175	31	2184	11	0	7.56	1.8	0.40	1.7	0.930
11.1	0.05	164	58	0.37	58	2218	33	2185	8	-1	7.74	1.8	0.41	1.7	0.969
2.1	0.01	119	33	0.28	41	2161	32	2193	10	2	7.54	1.8	0.40	1.7	0.950
3.1	0.08	154	59	0.39	53	2177	29	2190	9	1	7.59	1.6	0.40	1.6	0.955
3.2	0.13	124	27	0.23	43	2176	31	2200	9	1	7.63	1.8	0.40	1.7	0.953
4.1	0.01	196	88	0.46	68	2185	30	2184	7	0	7.59	1.7	0.40	1.6	0.971
5.1	0.02	186	53	0.30	65	2195	29	2182	7	-1	7.63	1.6	0.41	1.6	0.965
7.1	0.09	146	28	0.20	50	2155	29	2174	9	1	7.43	1.7	0.40	1.6	0.950
10.1	0.47	112	34	0.31	35	1976	27	2163	16	9	6.67	1.9	0.36	1.6	0.862
12.1	0.10	136	47	0.35	43	2018	25	2196	10	9	6.97	1.6	0.37	1.4	0.934
12.1	0.10	136	47	0.35	43	2018	25	2196	10	9	6.97	1.6	0.37	1.4	0.934
13.1	0.35	120	35	0.30	40	2100	26	2197	14	5	7.30	1.7	0.39	1.5	0.879
13.1	0.35	120	35	0.30	40	2100	26	2197	14	5	7.30	1.7	0.39	1.5	0.879
14.1	0.05	171	81	0.49	55	2068	25	2171	9	5	7.07	1.5	0.38	1.4	0.939
14.1	0.05	171	81	0.49	55	2068	25	2171	9	5	7.07	1.5	0.38	1.4	0.939
6.1	0.14	169	71	0.43	51	1936	26	2132	9	10	6.40	1.7	0.35	1.6	0.948
9.1	0.12	140	39	0.29	46	2075	28	2183	10	5	7.15	1.7	0.38	1.6	0.944
Quartz-monzonite (sample FC-66A)															
4.3	0.02	237	144	0.62	80	2131	15	2097	8	-2	7.02	0.9	0.39	0.8	0.888
5.2	0.02	137	54	0.41	45	2105	15	2110	8	0	6.97	1.0	0.39	0.9	0.876
2.1	0.05	303	122	0.42	99	2071	14	2076	7	0	6.71	0.9	0.38	0.8	0.894
3.1	0.17	308	120	0.40	100	2072	19	2077	7	0	6.71	1.2	0.38	1.1	0.929
6.1	0.09	258	137	0.55	84	2074	14	2086	7	1	6.76	0.9	0.38	0.8	0.907
2.2	0.11	214	85	0.41	69	2057	14	2084	9	1	6.68	0.9	0.38	0.8	0.856
5.1	0.11	158	67	0.44	52	2074	15	2102	10	1	6.82	1.0	0.38	0.9	0.838
4.2	0.06	263	118	0.46	83	2026	14	2090	6	3	6.59	0.9	0.37	0.8	0.909
1.1	0.24	196	100	0.53	62	2027	14	2094	10	3	6.61	1.0	0.37	0.8	0.813
4.1	0.19	163	84	0.53	52	2011	18	2109	15	5	6.60	1.4	0.37	1.0	0.768
3.2	0.43	195	114	0.60	60	1954	14	2079	15	6	6.28	1.2	0.35	0.8	0.709
7.2	0.31	311	202	0.67	88	1834	12	2057	10	12	5.76	0.9	0.33	0.8	0.814

Errors for isotopic ratios are quoted at 1σ level, Pb_c and Pb indicate common and radiogenic portions, respectively.*

%disc. = percent discordance for the given ^{207}Pb/^{206}Pb age.

2.4.3. In situ zircon Lu–Hf isotopes

Lu–Hf isotopic results on zircon were obtained at the Isotope Geology Laboratory (PARA–ISO) in the Federal University of Pará (UFPA), Belém–Brazil. The procedure of Hf analysis (Milhomem Neto et al., 2016) was developed using a Neptune Thermo Finnigan multi–collector (MC)–ICP–MS coupled with a Nd:YAG 213 nm LSX–213 G2 CETAC laser microprobe. The laser spot used was 50 μm in diameter with an ablation time of 60 seconds, repetition rate of 10 Hz, and He used as the carrier gas. Mass bias corrections of Lu–Hf isotopic ratios were done applying the variations of GJ–1 standard. The raw data were processed in Microsoft Excel worksheets to calculate the ^{176}Hf/^{177}Hf and ^{176}Lu/^{177}Hf ratios, the Hf model–age and ƐHf parameter for each analyzed point. Results are presented in **Table 2.4**. εHf has been calculated using current CHUR values of ^{176}Hf/^{177}Hf = 0.282785 and ^{176}Lu/^{177}Hf = 0.0336 from Bouvier et al. (2008). ^{176}Lu/^{177}Hf = 0.0388 e ^{176}Hf/^{177}Hf = 0.28325 were used for depleted mantle (Andersen et al., 2009). ^{176}Lu/^{177}Hf = 0.015 were used as the

average value for continental crust to calculated the two–stage crustal Hf model age (Griffin et al., 2002, 2004; Belousova et al., 2009, 2010).

Table 2.3: U-Pb LA-ICPMS zircon data

Granite (Bananeira suite) (sample FC-278)																			
(*spot*)	U (ppm)	Th (ppm)	Th/U	Pb (ppm)	$\%^{206}Pb\_c$	$^{206}Pb/^{238}U$	±2σ (%)	$^{207}Pb/^{235}U$	±2σ (%)	$^{207}Pb/^{206}Pb$	±2σ (%)	rho	$^{206}Pb/^{238}U$	±2σ (Ma)	$^{207}Pb/^{235}U$	±2σ (Ma)	$^{207}Pb/^{206}Pb$	±2σ (Ma)	conc. (%)
zircons for c. 2307 Ma																			
39	45	18	0.41	22	0.56	0.419	0.88	8.15	1.10	0.141	0.66	0.801	2254	17	2248	10	2242	11	101
37	267	14	0.05	48	2.12	0.188	4.53	2.15	5.06	0.083	2.25	0.896	1109	46	1165	36	1269	44	87
49	304	72	0.24	163	0.0	0.507	1.52	11.65	1.79	0.167	0.94	0.850	2643	33	2577	17	2526	16	105
50	203	17	0.08	91	0.0	0.439	0.90	8.91	0.99	0.147	0.42	0.904	2344	18	2329	9	2316	7	101
42	44	18	0.41	22	0.0	0.438	0.64	8.88	0.89	0.147	0.62	0.717	2340	13	2326	8	2314	11	101
40	108	38	0.36	54	0.0	0.437	1.74	8.84	1.79	0.147	0.44	0.969	2336	34	2321	16	2309	8	101
51	179	156	0.88	98	0.0	0.436	1.30	8.83	1.37	0.147	0.44	0.947	2334	25	2320	13	2308	8	101
53	258	86	0.33	65	1.12	0.219	5.73	4.41	5.88	0.146	1.29	0.975	1277	67	1714	50	2298	22	56
54	359	33	0.09	160	0.0	0.440	2.95	8.80	3.10	0.145	0.94	0.952	2349	58	2318	29	2291	16	103
52	480	417	0.87	88	0.0	0.177	2.73	3.41	2.80	0.139	0.64	0.974	1052	27	1506	22	2220	11	47
41	224	52	0.23	60	0.0	0.262	4.54	3.90	4.59	0.108	0.70	0.988	1502	61	1613	38	1761	13	85
45	260	53	0.20	41	0.0	0.153	2.56	2.16	2.72	0.102	0.93	0.940	919	22	1168	19	1665	17	55
zircon for the c. 2068 Ma																			
61	320	115	0.36	134	0.18	0.380	3.65	6.76	3.68	0.129	0.47	0.992	2074	65	2080	33	2086	8	99
62	270	183	0.68	47	0.0	0.110	15.75	1.94	15.78	0.128	1.07	0.998	671	101	1096	112	2077	19	32
74	154	63	0.41	22	1.86	0.089	10.81	1.58	10.88	0.128	1.21	0.994	552	57	962	70	2073	21	27
75	107	76	0.71	52	0.92	0.395	0.63	6.97	0.97	0.128	0.74	0.645	2145	11	2107	9	2071	13	104
64	250	159	0.64	104	2.98	0.350	4.07	6.17	4.48	0.128	1.86	0.910	1934	68	2000	40	2070	33	93
63	401	114	0.29	161	1.63	0.375	2.42	6.61	2.65	0.128	1.08	0.913	2053	43	2061	24	2068	19	99
66	275	110	0.40	58	0.45	0.169	6.26	2.97	6.31	0.128	0.75	0.993	1005	59	1400	49	2068	13	49
69	316	246	0.78	129	0.0	0.321	1.82	5.65	1.87	0.128	0.43	0.974	1793	29	1923	16	2066	8	87
65	383	231	0.60	152	0.44	0.330	5.51	5.80	5.54	0.127	0.56	0.995	1839	89	1946	49	2063	10	89
36	98	122	1.25	49	1.81	0.366	2.08	6.43	2.37	0.127	1.15	0.875	2011	36	2036	21	2061	20	98
71	771	79	0.10	122	0.0	0.152	3.01	2.66	3.04	0.127	0.44	0.989	912	26	1317	23	2055	8	44
68	729	131	0.18	35	0.0	0.034	13.96	0.59	13.99	0.127	0.92	0.998	214	30	472	54	2054	16	10
44	145	44	0.31	59	0.65	0.374	5.39	6.58	5.43	0.127	0.64	0.993	2050	95	2057	49	2064	11	99
46	192	13	0.07	74	0.0	0.382	4.63	6.69	4.71	0.127	0.84	0.984	2085	83	2071	42	2057	15	101
70	941	292	0.31	128	0.34	0.115	6.97	2.00	7.00	0.126	0.61	0.996	704	47	1117	49	2042	11	34
72	247	25	0.10	12	0.0	0.043	27.03	0.74	27.11	0.126	2.10	0.997	271	72	565	125	2038	37	13
43	177	62	0.35	75	1.11	0.382	4.07	6.76	4.22	0.128	1.09	0.966	2087	73	2081	38	2075	19	101
73	639	70	0.11	122	0.0	0.187	7.13	3.22	7.22	0.125	1.10	0.988	1104	73	1463	58	2032	19	54
38	71	11	0.15	28	0.0	0.369	1.34	6.44	1.61	0.127	0.89	0.832	2025	23	2038	14	2051	16	99
47	339	52	0.15	65	0.0	0.186	4.17	3.17	4.22	0.124	0.65	0.988	1100	42	1450	33	2009	12	55
48	423	23	0.05	60	0.0	0.143	5.62	2.40	5.67	0.122	0.75	0.991	860	45	1242	41	1985	13	43
67	177	147	0.83	22	0.0	0.117	4.79	1.94	5.32	0.120	2.31	0.901	715	33	1094	36	1953	41	37

Errors for isotopic ratios are quoted at 2σ level, and Pb_c indicates common lead.

Table 2.4: LA-MC-ICPMS Lu-Hf isotope data of zircon

spot	$^{176}Hf/^{177}Hf_{sample}$	2σ	$^{176}Lu/^{177}Hf_{sample}$	2σ	$t_{(U-Pb)}$ (Ma)	$\varepsilon_{Hf(0)}$	$\varepsilon_{Hf(t)}$	T_{DM} crustal (Ma)
Mirador tonalite								
03 FC-17 1.1	0.281411	0.000060	0.000508	0.000019	2185	-48.59	**0.14**	**2733**
04 FC-17 3.1	0.281446	0.000051	0.000706	0.000030	2185	-47.35	**1.09**	**2673**
05 FC-17 3.2	0.281420	0.000082	0.001195	0.000039	2185	-48.27	**-0.56**	**2776**
06 FC-17 5.1	0.281434	0.000062	0.000704	0.000022	2185	-47.77	**0.66**	**2700**
07 FC-17 4.1	0.281393	0.000094	0.000630	0.000030	2185	-49.22	**-0.68**	**2784**
08 FC-17 2.1	0.281447	0.000070	0.000608	0.000017	2185	-47.32	**1.27**	**2662**
09 FC-17 6.1	0.281403	0.000092	0.000786	0.000021	2185	-48.87	**-0.56**	**2776**
10 FC-17 10.1	0.281434	0.000078	0.000658	0.000008	2185	-47.77	**0.73**	**2695**
11 FC-17 11.1	0.281412	0.000084	0.000802	0.000012	2185	-48.55	**-0.26**	**2758**
12 FC-17 13.1	0.281404	0.000088	0.000464	0.000019	2185	-48.84	**-0.05**	**2744**
13 FC-17 9.1	0.281399	0.000095	0.000946	0.000037	2185	-49.01	**-0.94**	**2800**
14 FC-17 12.1	0.281449	0.000075	0.000641	0.000046	2185	-47.24	**1.29**	**2660**
Bananeira granite								
17 FC-278 40	0.281507	0.000063	0.001449	0.000105	2307	-45.19	**4.87**	**2530**
18 FC-278 42	0.281476	0.000069	0.000753	0.000071	2307	-46.29	**4.86**	**2530**
19 FC-278 44	0.281483	0.000062	0.000525	0.000028	2069	-46.04	**0.02**	**2650**
20 FC-278 46	0.281489	0.000069	0.001022	0.000082	2069	-45.83	**-0.46**	**2680**
21 FC-278 35	0.281506	0.000085	0.000613	0.000032	2069	-45.22	**0.72**	**2606**
22 FC-278 61	0.281485	0.000061	0.000500	0.000042	2069	-45.97	**0.13**	**2643**
23 FC-278 76	0.281537	0.000052	0.000594	0.000054	2069	-44.13	**1.85**	**2536**
24 FC-278 77	0.281525	0.000068	0.000624	0.000064	2069	-44.54	**1.39**	**2564**
25 FC-278 78	0.281525	0.000083	0.000610	0.000029	2069	-44.54	**1.41**	**2563**
26 FC-278 79	0.281483	0.000074	0.001242	0.000046	2069	-46.04	**-0.98**	**2713**
27 FC-278 58	0.281494	0.000062	0.000501	0.000012	2069	-45.67	**0.43**	**2624**
28 FC-278 68	0.281486	0.000071	0.000892	0.000052	2069	-45.94	**-0.38**	**2675**

For calculation: λ = 1.867x10^{-11} years^{-1} (Söderlund et al., 2004); $^{176}Lu/^{177}Hf$ = 0.0336 and $^{176}Hf/^{177}Hf$ = 0.282785 for present day value of CHUR (Bouvier et al., 2008); 176Lu/177Hf = 0.0388 and 176Hf/177Hf = 0.28325 for the depleted mantle (DM) (Andersen et al., 2009); Two stage crustal model age in million years (Ma) using the measured $^{176}Hf/^{177}Hf$, and 176Lu/177Hf and the respective age, and $^{176}Lu/^{177}Hf$ = 0.015 for the average continental crust (Griffin et al., 2002, 2004; Belousova et al., 2009, 2010).

2.5. Results

2.5.1. Whole–rock geochemistry

In the K_2O+Na_2O vs. SiO_2 (wt.%) diagram, with the chemical classification according to Cox et al. (1979), samples of the Bananeira plutons are mainly classified as syeno–diorites and granites, and the Mirador suite plots as granodiorite to granite (**Fig. 2.4B**). This is quite compatible to our petrographic (modal) observations, but some of the Mirador tonalites, because of their high Na_2O (4.35 to 5.13 wt.%) and SiO_2 (64.1–70.4 wt.%) contents (**Table 2.1**), they are confused with granites in chemical classification (**Fig. 2.4A** and **B**). The Mirador tonalites and Bananeira granites plot as subalkaline magmatic series, according to the limits of Irvine and Baragar (1971), while the Bananeira quartz–monzonites are slightly alkaline (**Fig. 2.4C**). However, in reference to the limits of Kuno (1966), the quartz–monzonites plot within the field of alkaline rocks and the Bananeira granite samples are slightly alkaline (**Fig. 2.4C**). In the Na_2O+K_2O-CaO vs. SiO_2 diagram from Frost et al. (2001), Mirador tonalites follow the trend for calc-alkalic rocks, the quartz–monzonites are alkali–calcic and the Bananeira granites are calc–alkalic to alkali–calcic (**Fig. 2.4C**). In relation to the aluminum saturation index, the samples of the granites are slightly peraluminous (A/CNK = 1.01 to 1.07) (**Fig. 2.4D**), and their normative corundum range from 0.55 to 1.05 %. The Mirador tonalites and the quartz–monzonites are metaluminous (A/CNK < 1.0) (**Fig. 2.4D**) (normative diopside less than 2.4 %). In the SiO_2 vs. K_2O diagram with classification fields of magmatic series according to Peccerillo and Taylor (1976), the granites are similar to those of high–K calc–alkaline series, the quartz–monzonites plot in the shoshonitic field, and the Mirador tonalites are within the field of medium–K calc–alkaline rocks (**Fig. 2.4E**).

In general, all samples show negative correlation of SiO_2 with Al_2O_3, TiO_2, MgO, CaO, FeOt, Ni and P_2O_5 (**Fig. 2.5**), and positive correlation with K_2O (**Fig. 2.4A**). The Mirador tonalites present high Na_2O (4.35 to 5.13 wt.%) and Sr (849 to 1447 ppm) contents, which are much higher than the Bananeira granitoids (**Fig. 2.5**) (**Table 2.1**). The granites are the most evolved rocks, with SiO_2 values approximately between 68 and 75 wt.% and MgO between 0.5 and 0.9 wt.% (**Fig. 2.5**) (**Table 2.1**). Quartz–monzonites have the lower SiO_2 (62.4 – 64.6 wt.%) and higher Al_2O_3 contents (16 – 17 wt.%) compared to the tonalites and granites (**Fig. 2.5**) (**Table 2.1**).

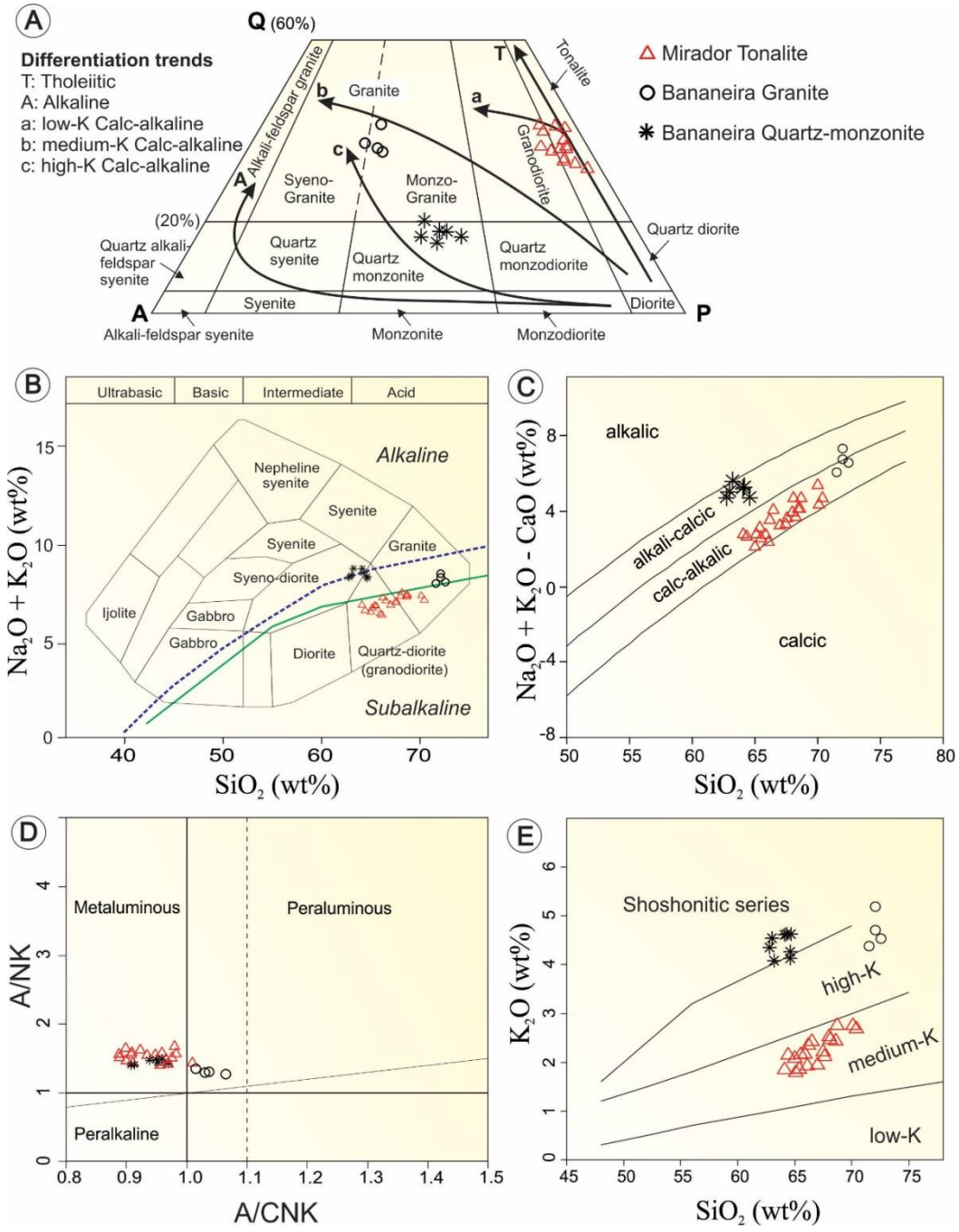

Fig. 2.4. *Petrographic and geochemical composition of the Mirador and Bananeira granitoids. (A) Modal composition of plutonic rocks from the investigated area reported in the Quartz–Alkali feldspar–Plagioclase (QAP) triangle (Streckeisen, 1976). The arrows correspond to differentiation trends after Lameyre and Bowden (1982). (B) K_2O+Na_2O vs. SiO_2 (wt.%) diagram with limits for Alkaline (above) and Subalkaline (below) magmatic series according to Kuno (1966) (continuous green line) and Irvine and Baragar (1971) (blue dashed line). Fields for rock classification are from Cox et al. (1979). (C) Na_2O+K_2O-CaO vs. SiO_2 (wt.%) diagram from Frost et al. (2001). (D) Plot of molar A/CNK ($Al_2O_3/(CaO + Na_2O + K_2O)$) vs. A/NK ($Al_2O_3/(Na_2O + K_2O)$) from Shand (1943) (see Manier and Piccoli, 1989) to discriminate metaluminous, peraluminous and peralkaline compositions. (E) SiO_2 vs. K_2O diagram with the fields of high potassium (high–K), medium potassium (medium–K) and low potassium (low–K) calc–alkaline series according to Peccerillo and Taylor (1976).*

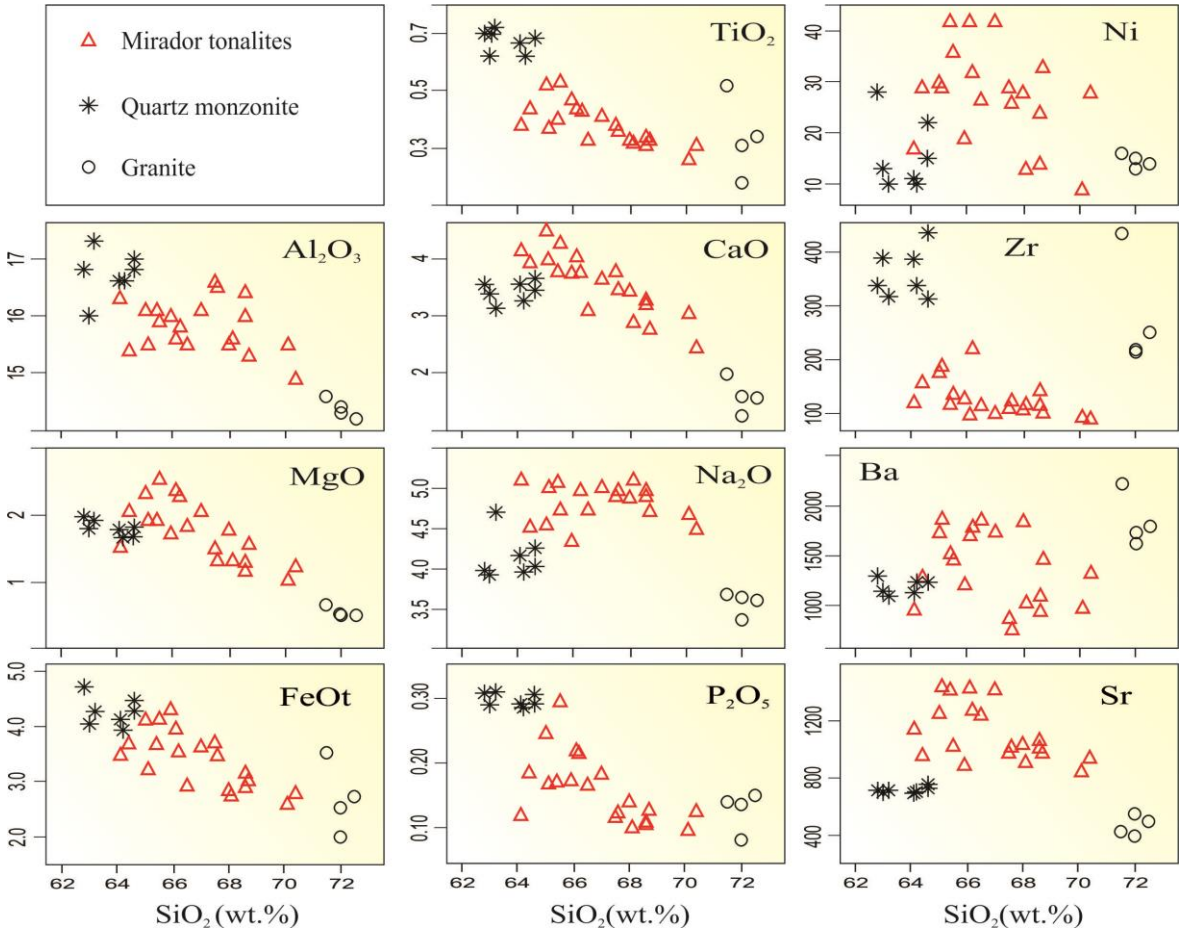

Fig. 2.5. *Binary diagrams using SiO_2 as differentation index for oxides (in wt. %) and trace elements (in ppm).*

The primitive mantle–normalized (Sun and McDonough, 1989) trace–elements plots are characterized by depletion in some of high–field strength elements (HFSE), such as Ti, P and Nb, and enrichment in large ion lithophiles elements (LILE), such as Rb (**Fig. 2.6A**). The Mirador tonalites have high Sr contents (849–1447 ppm) with a well–marked positive Sr anomaly (**Fig. 2.6A**) (**Table 2.1**). In the chondrite normalized diagram with Boynton (1984) values, all plutonic rocks exhibit enrichment in light rare earth element (LREE) relative to heavy rare earth element (HREE) (**Fig. 2.6B**). The La values are 40–100 times the chrondrite for the tonalite, 100–200 for the quartz monzonite and 300–600 for the granites (**Fig. 2.6B**). The granites show pronounced Eu negative anomaly (Eu/Eu* = 0.5 to 0.6), and are the richest in LREE (**Fig. 2.6B**). The quartz–monzonites also show negative Eu anomaly (Eu/Eu* = 0.7 to 0.9), but with less REE fractionated patterns, showing lower $(La/Yb)_N$ ratio ($[La/Yb]_N$ = 16 to 24) than the granites ($[La/Yb]_N$ = 34 to 114) (**Fig. 2.6B**). The Mirador tonalites show slight negative to positive Eu anomalies, with Eu/Eu* values ranging from 0.8 to 1.2, and exhibit moderate to high fractionation of LREE compared to HREE ($[La/Yb]_N$ = 6–45) (**Fig. 2.6B**).

These patterns of the Mirador tonalites are very similar to the average values for Archean TTG and high–silica adakites (HSA) compiled from Martin et al. (2005), while the Bananeira quartz monzonites are more akin to the average values of modern granitoids from Martin (1994) and to the field of late Archean crustal–derived granites (Arsikere–Banavara plutons in the Dhawar craton) from Jayananda et al. (2006) (**Fig. 2.6B).**

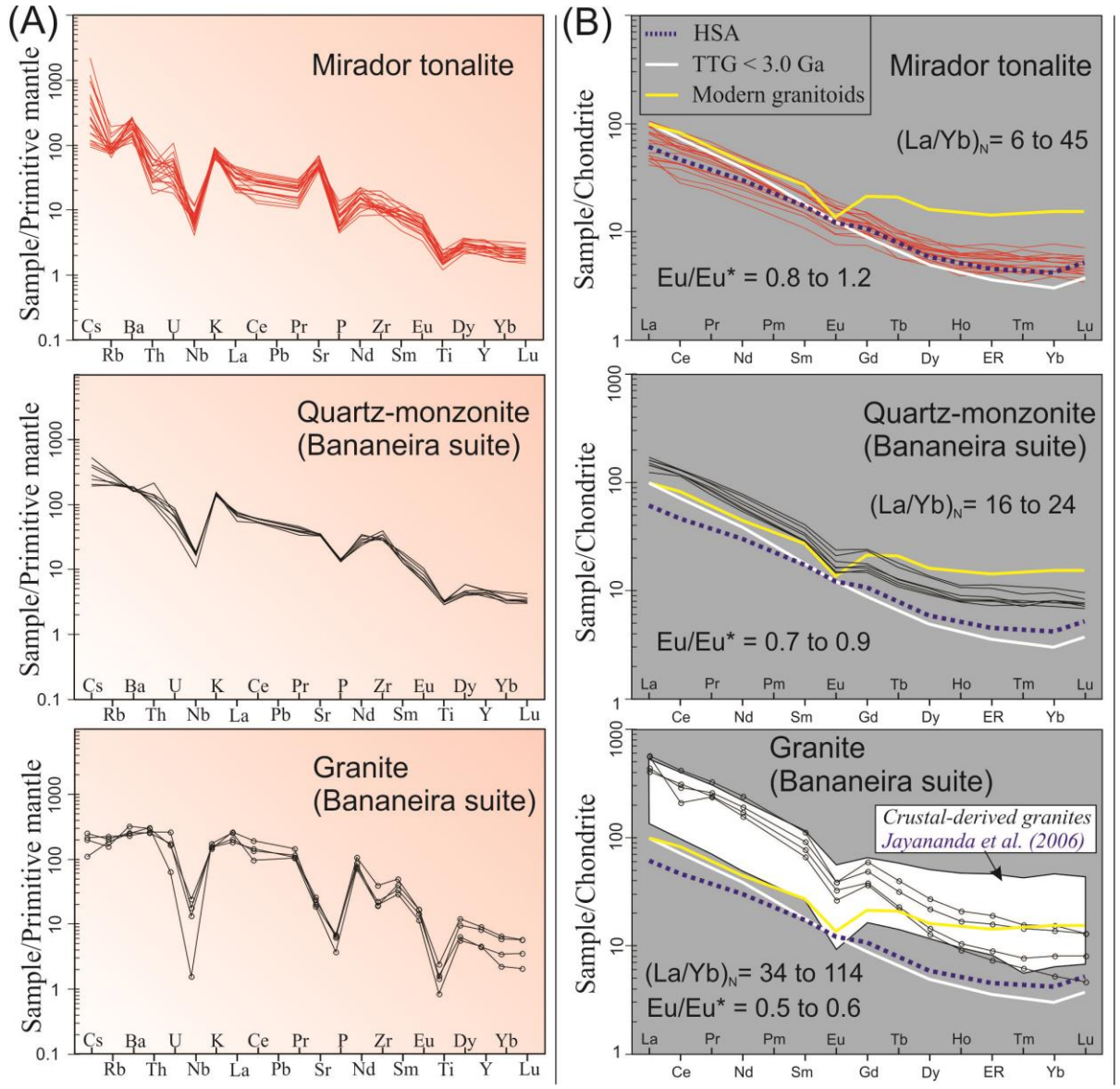

Fig. 2.6. *Trace and rare rarth elements diagrams for the Mirador and Bananeira granitoids. (A) Primitive mantle normalized trace element diagrams (to the right) and (B) Chondrite–normalized REE patterns (to the left). The Primitive mantle values are from Sun and McDonough (1989) and chondrite values from Boynton (1984). Average values for Archean TTG and high-silica adakite (HSA) according to Martin et al. (2005), and modern granitoids according to Martin (1994).*

2.5.2. U–Pb zircon ages

The results of SHRIMP and LA–ICPMS U–Pb zircon analysis are on **Tables 2.2** and **2.3**, respectively, and samples location in **Fig. 2.2**.

2.5.2.1. Mirador tonalite

The zircons analyzed by SHRIMP for sample FC–17 (tonalite) are generally euhedral, elongated, with a length of around 250 μm and width of c. 100 μm (**Fig. 2.7A**). Well–defined oscillatory (igneous) zoning observed in cathodoluminescence (CL) images, and low–luminescence cores are identified in the CL images for some of the analyzed zircons (**Fig. 2.7A**). Analyzed zircons have U contents of 83–196 ppm, Th of 25–88 ppm and Th/U ratios from 0.29 to 0.49 (**Table 2.2**). From a total of 18 analyzed grains, most analyses yielded discordant ages that plot on or scatter along a Discordia line with upper intercept age of 2192 ± 11 Ma, with Mean Square Weighted Deviation (MSWD) equal to 2. (**Fig. 2.8A**) (**Table 2.2**). Eight grains with concordance between 101 and 99% yielded a Concordia age of 2185 ± 4 Ma (MSWD = 0.34) (Probability of fit = 0.56) (**Fig. 2.8A**) (**Table 2.2**). The two ages (upper intercept and Concordant ages) overlap within the limits of analytical error and both can be interpreted as the age of the pluton crystallization. We prefer to use the Concordia age of 2185 ± 4 Ma because of the lower analytical error and lower MSWD. Additionally, a $^{207}Pb/^{206}Pb$ age of 2263 ± 10 Ma was obtained for a slightly discordant (conc. = 94%) zircon (spot 8.1), which is interpreted as an inherited age (**Fig. 2.8A**) (**Table 2.2**).

2.5.2.2. Bananeira potassic granitoids

Quartz–monzonite: For sample FC–66–A, the zircons analyzed by SHRIMP are euhedral to sub–rounded, measuring c. 60 to 80 μm length, and c. 50 μm width (**Fig. 2.7B**). Oscillatory (igneous) zoning is observed for the analyzed grains, and some low–luminescence zircon cores are reveled in CL images (**Fig. 2.7B**). Analyzed zircons have U contents of 137–311 ppm, Th of 54–202 ppm and Th/U ratios from 0.40 to 0.67 (**Table 2.2**). For a total of 12 analyzed grains, the upper intercept in the Concordia diagram yielded an age of 2092 ± 12 Ma (MSWD = 1.8) (**Fig. 2.8B**) (**Table 2.2**). However, six grains with concordance between 100 and 99% yielded a Concordia age of 2079 ± 4 Ma (MSWD = 2.9) (Probability = 0.086) (**Fig. 2.8B**) (**Table 2.2**). All analyzed domains reveal Th/U ratios >0.1 (**Table 2.2**). The upper intercept and Concordia ages overlap within the limits of analytical error and both can be interpreted as the crystallization age of the quartz–monzonite.

Granite: The zircons analyzed by LA–ICPMS for sample FC–278 have euhedral to sub–rounded shapes, lengths between 250 and 100 μm, width between 70 to 150 μm, and commonly igneous oscillatory zoning observed in CL images (**Fig. 2.7C**). High–luminescence cores were found in some zircons, and these are generally involved by later magmatic zircon overgrowth (**Fig. 2.7D** and **E**), suggesting inheritance. CL and back–scattered electron (BSE) images show that these high–luminescence cores have sub–rounded edges, and the rims overgrowth show well–marked (igneous) oscillatory zoning (**Fig. 2.7D** and **E**). For the analyzed zircons, two distinct isotopic/age populations were identified. An age of 2068 ± 5 Ma (MWSD = 2.0) is defined by the upper intercept of 22 analyzed grains, and another age of 2307 ± 14 Ma (MSWD = 5.1) is defined by the upper intercept of 12 grains (**Fig. 2.8C**). For the c. 2068 Ma zircon population, analyzed grains have U contents of 71–941 ppm, Th of 11–292 ppm and Th/U ratios from 0.05 to 1.25 (**Table 2.2**). The age of 2068 ± 5 Ma is interpreted here as the age of granite crystallization, and the age of 2307 ± 14 Ma is interpreted as the age of an inherited zircon population (**Fig. 2.8C**). For the c. 2307 Ma zircon population, analyzed grains have U contents of 44–480 ppm, Th of 14–417 ppm and Th/U ratios from 0.05 to 0.88 (**Table 2.2**). An older values of 2562 ± 16 Ma ($^{207}Pb/^{206}Pb$ age) (spot 49), slightly discordant (concordance = 105%), was obtained for an inherited zircon core (**Fig. 2.7E**) (**Table 2.3**). For this zircon, the strongly discordant $^{207}Pb/^{206}Pb$ apparent age of magmatic overgrowth is 1985 ± 13 Ma (conc. = 43%) (spot 48) (**Fig. 2.7E**) (**Table 2.3**).

2.5.3. Hf isotopes in zircon

Zircons from two samples (FC–17 – Mirador tonalite and FC–278 – Bananeira potassic granitoids) were analyzed for Lu–Hf isotopes on domains with the same or similar internal structure as to those analyzed for U–Pb dating (**Fig. 2.7**). Zircons from sample FC–66A were not analyzed for Hf isotopes because of the small zircon sizes compared to the 50 μm size of the laser spot. In this study, all the Hf isotopic measurements were done on zircons with more than 95% of concordance on U–Pb ages. Initial $^{176}Hf/^{177}Hf$ ratios and $\varepsilon_{Hf}(t)$ values were calculated for respective U–Pb ages of the granitoids, using t= 2185 Ma for sample FC–17, and t= 2086 Ma for sample FC–278. The two–stage Hf crustal model ages were calculated for the analyzed sample. The results are listed in **Table 2.4**.

Mirador tonalite: Twelve representative zircons of sample FC–17 were analyzed. The results show variable $\varepsilon_{Hf}(t)$ values ranging from -0.94 to +1.29 and Hf crustal model ages from 2660 to 2800 Ma with an average age of ~2.7 Ga (**Table 2.4**) (**Fig. 2.8D**). Half of zircon population shows positive $\varepsilon_{Hf}(t)$ values from +0.14 to +1.29 and Hf model ages from 2660 to

2733 Ma. Whereas, the other half has negative $\varepsilon_{Hf}(t)$ values from -0.94 to -0.05 and Hf model ages from 2774 to 2800 Ma (**Table 2.4**) (**Fig. 2.8D**). For one zircon grain with core–rim relationships, the analytical results (spot 3.2 and 3.1) show that the rim has slightly different Hf isotope composition from the core (**Fig. 2.7A**). The rim has positive $\varepsilon_{Hf}(t)$ value of +1.09 and Hf model age of 2673 Ma. In contrast, the inherited core shows negative $\varepsilon_{Hf}(t)$ value of -0.56, and older Hf model ages of 2776 Ma (**Fig. 2.7A**) (**Table 2.4**). However, for others analyzed magmatic rims, $\varepsilon_{Hf}(t)$ revealed slight negative values (**Fig. 2.7A**).

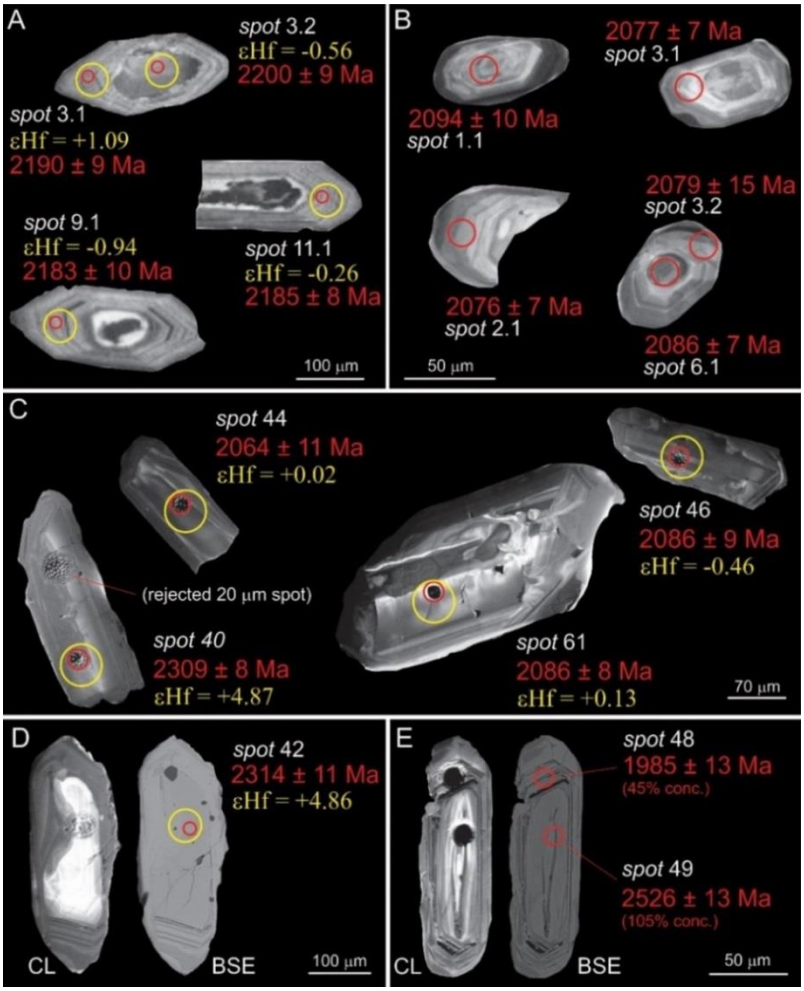

Fig. 2.7. *Zircon cathodoluminescence (CL) and back–scattered electron (BSE) images of representative zircon grains. Ellipses indicate spot locations, small red for U–Pb and large yellow for Lu–Hf. Spot numbers are the same analytical ID for U–Pb and Lu–Hf data tables. Age presented correspond to* $^{207}Pb/^{206}Pb$ *ages. (A) CL images from sample FC–17 (Mirador tonalite); (B) CL images from sample FC–66A (quartz–monzonite); (C) CL images from sample FC–278 (granite); (D) BSE and CL images of a c. 2314 Ma inherited zircon core, from sample FC–278 (granite); (E) BSE and CL images of a c. 2526 Ma inherited zircon core with c. 1985 Ma magmatic overgrowth, from sample FC–278 (granite). Zircons of Fig. D and E show high–luminescence cores with sub–rounded edges, and rims overgrowth with well–marked (igneous) oscillatory zoning.*

Bananeira granite: Hafnium isotopic analyses of representative zircons from sample FC–278 (syenogranite) were obtained in ten grains of the c. 2086 Ma U–Pb crystallization age of the granite, and in two grains of the associated c. 2307 Ma inherited zircon population. The results show that zircons with c. 2086 Ma crystallization age of the granite have only slightly variable $\varepsilon_{Hf}(t)$ values ranging from -0.46 to +1.85 and Hf crustal model ages ranging from 2536 to 2713 Ma (**Table 2.4**) (**Fig. 2.8D**). Two analyzed zircons of the ~2307 Ma inherited population show superchrondritic $\varepsilon_{Hf}(t)$ values of +4.86 and +4.87, and the same Hf crustal model age of 2530 Ma, respectively (**Table 2.4**) (**Fig. 2.7C** and **D**).

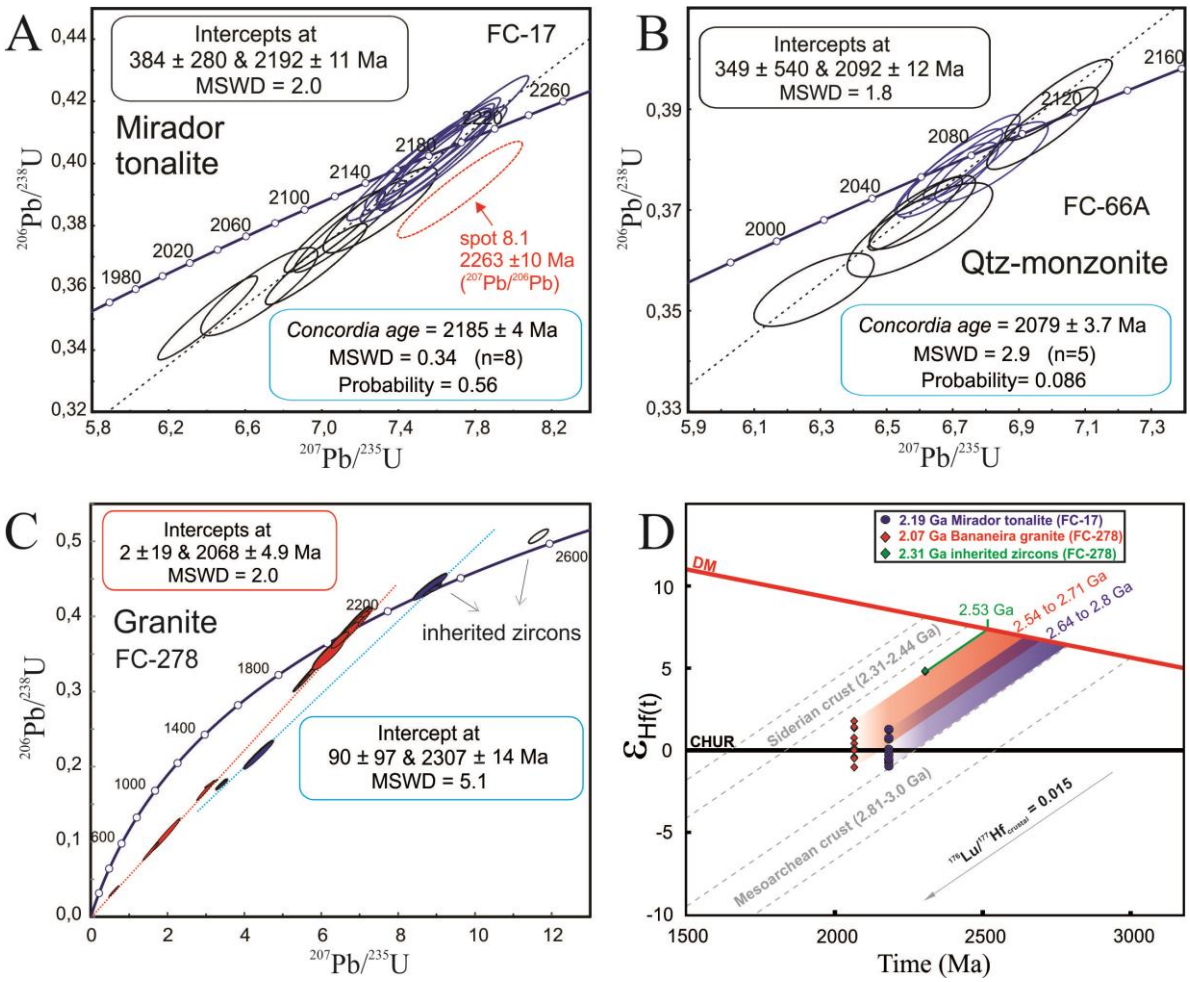

Fig. 2.8. *(A) Concordia diagram with SHRIMP zircon spot data and ages for sample FC–17 (Mirador tonalite). Red ellipse represents discordant inherited zircon. (B) Concordia diagram with SHRIMP zircon spot data and ages for sample FC–66A (quartz–monzonite). (C) Concordia diagram with LA–ICPMS zircon spot data for sample FC–278 (Granite). Discordia lines and ellipses are red for granite age, and blue for inherited zircon population. (For all diagrams, data-point error ellipses are 2σ). (D) εHf(t) vs. crystallization ages, with the results for samples FC–17 (Mirador tonalite) and FC–278 (granite). The range for Siderian and Mesoarchean crustal components of the Troia Massif are based on the Nd model ages presented in* ***Table 2.5****.*

2.6. Discussion

2.6.1. Petrogenesis of the Mirador tonalites

General geochemical data of the Mirador tonalites indicate that they are classified as subalkaline rocks (**Fig. 2.4C**) with similar trend to those of medium–K calc–alkaline series (**Fig. 2.4E**). The Mirador tonalites have average K_2O/Na_2O = 0.47 and Al_2O_3 = 15.8 wt.%, high SiO_2 (64.1–70.4 wt.%) and Sr (849–1447 ppm) contents, and low MgO (2.54–1.03 wt.%), Y (8.83–15.08 ppm) and HREE contents, with no significant Eu anomaly (Eu/Eu* = 0.8 to 1.2) (**Table 2.1**) (**Fig. 2.6B**). All these features are similar to the composition of Archean TTG and high–silica adakites (Barker and Arth, 1976; Martin, 1994; Martin et al., 2005).

The primitive mantle–normalized trace–element plot of the Mirador tonalites shows marked negative anomalies of some high field strength elements (HFSE) such as Nb, P and Ti (**Fig. 2.6A**). Such elemental pattern may be explained by mineral phases like rutile, titanite, alanite, apatite, hornblende, garnet, etc., which are present as residual and/or fractionating phases (Tatsumi et al., 1986; Saunders et al., 1991). The negative anomalies of Nb, Ta, P and Ti are generally considered as typical features of magmas generated in subduction zones (Pearce, 1982; Wilson, 1989), and also, common pattern of Archean TTG and adakites (Martin, 1999; Martin et al., 2005; Moyen, 2011; Moyen and Martin, 2012).

Trondhjemites, which are part of the TTG (Tonalite–Trondhjemite–Granodiorite) suites, were originally defined in Archean terrains, and are characterized as Na–rich tonalites ($K_2O/Na_2O < 0.5$) (Barker and Arth, 1976). Trondhjemites are mainly composed by quartz + sodic plagioclase + biotite ± amphibole, and interpreted as product of partial melting of metabasic rocks under garnet amphibolite to eclogite facies (Barker and Arth, 1976; Martin, 1994). The lack of both negative Eu and Sr anomalies associated with the low HREE content of TTG suites are commonly interpreted as reflecting the presence of garnet and amphibole as well as the lack of plagioclase, either as residual or fractionating phases (e.g. Moyen and Martin, 2012). Therefore, this high–pressure origin (e.g. residual garnet) has become implicit in the term Archean TTGs, which also show secular changes on their pressure–dependent trace elements (Martin and Moyen, 2002). This trace element signature of Archean TTG is very similar to high–silica adakites, but differs drastically from modern granitoids, which have both higher HREE contents and negative Eu anomalie (**Fig. 2.6B**). The Adakite term was originally used to recent subduction–related rocks with composition similar to that of Archean trondhjemites (Kay, 1978; Drummond and Defant, 1990). Most magmas in recent

subduction zones are interpreted to come from the mantle when hydrous fluids are released from dehydration of the subducted oceanic crust, and initiate partial melting of the mantle wedge (e.g. Gill, 1981; Tatsumi et al., 1986). However, Defant and Drummond (1990) recognized that when young oceanic crust (less than 25 millions years old) is subducted, adakites are typically produced in the arc. Once young oceanic crust is subducted, it is "warmer" (closer to the mid–ocean ridge where it formed) than usual subduction, and thus, enables its partial melting (Drummond and Defant, 1990; Peacock et al., 1994; Martin et al., 1999). However, other models have been proposed to explain the adakitic signature, such as partial melting of the mafic lower crust by underplated basalts (Petford and Atherton, 1996; Petford and Gallagher, 2001; Chung et al., 2003) and deep fractionation of hydrous basalt magma (Macpherson et al., 2006; Davidson et al., 2007; Zellmer et al., 2012; Ribeiro et al., 2016). For this latter hypothesis, authors generally refer to "adakite-like" magmatism, and there is also a common discussion on its implication to ore deposits (Richards and Kerrich, 2007; Chiaradia et al., 2012; Chiaradia, 2015; Rabbia et al., 2017). According to Martin et al. (2005), adakites can be divided into two groups: high–silica adakites, with SiO_2 > 64 wt.%, and low–silica adakites, with SiO_2 between 50 and 60 wt.%. The high–silica adakites are interpreted as the product of melting of subducted oceanic crust (low–K tholeiites transformed into garnet–amphibolite and eclogite), in which the melt interacts with peridotites during its ascent through the mantle wedge (Rapp et al., 1999; Martin et al., 2005). The Mg, Cr and Ni contents in the high–silica adakites are higher than those found in tonalitic liquids generated in experimental melts of metabasalts (e.g. Rapp et al., 1991), and therefore, this enrichment is attributed to interaction of the magma (slab melt) with the peridotitic mantle wedge (Martin et al., 2005). The low–silica adakites are thought to represent partial melting of a peridotitic mantle that was previously metasomatized (slab–modified mantle) by adakitic melts, therefore, MgO, Cr and Ni contents are higher in low–silica adakites than in the crust–derived high–silica adakites (Martin et al., 2005). Similarly, the inferred slab–modified mantle source for the low–silica adakites is also an interpretation to those of the high–Mg andesites (e.g. Tatsumi & Ishizaka 1982) and sanukitoid suites (Stern et al., 1991; Smithies and Champion, 1999; Halla et al., 2009).

In the SiO_2 vs. K_2O/Na_2O diagram, most samples of the Mirador tonalites plot within or close to the trondhjemite field, based on classification from Barker and Arth (1976), where trondhjemitic rocks are silica–rich tonalites (SiO_2 > 65 wt.%) with low K_2O/Na_2O ratios (<0.5) (**Fig. 2.9A**). However, some samples of the Mirador tonalites have lower silica content and higher K_2O/Na_2O ratio than typical TTG rocks (**Fig. 2.9A**).

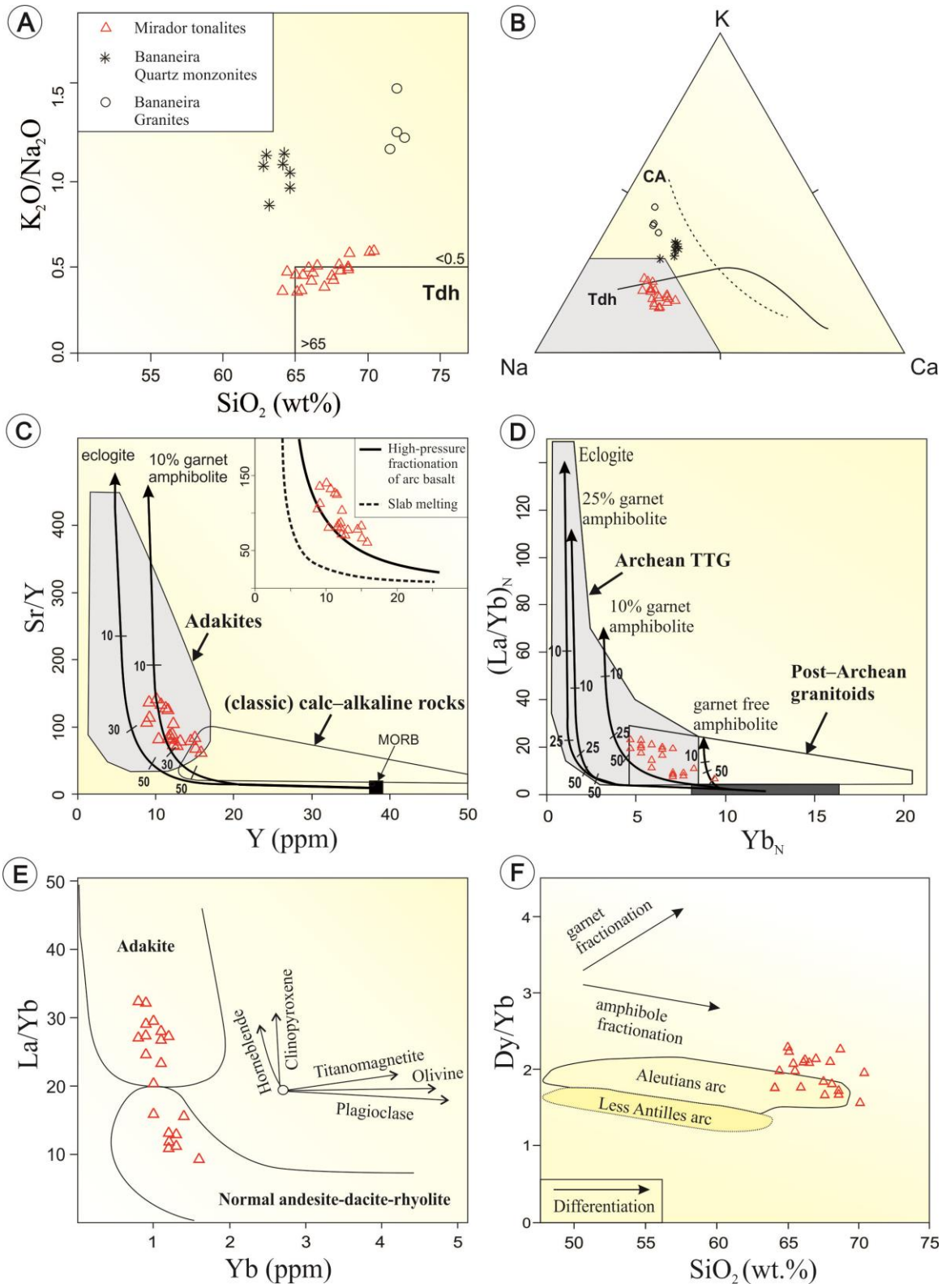

Fig. 2.9. *Discriminant diagrams for TTG and adakitic rocks. (A) K_2O/Na_2O vs. SiO_2 diagram with field for trondhjemites (Tdh) according to classification of Barker and Arth (1976). (B) Cationic Na–K–Ca diagram showing the differentiation trends of calc–alkaline (CA) series from Nockolds and Allen (1953) and trondhjemitic series (Tdh) from Barker and Arth (1976), and the trondhjemite field (Tdh) after Martin (1994). (C) Sr/Y vs. Y plot from Drummond and*

Defant (1990), with the fields for adakites and classic calc–alkaline rocks according to Martin et al. (2005). Basalt partial melting curves leaving either 10% garnet amphibolite or eclogite restite assemblage are from Drummond and Defant (1990). Average MORB value is from Gill (1981). Trend of high-pressure fractionation of arc basalt and slab melt are from McMacpherson et al., (2006). (D) Yb_N vs. $(La/Yb)_N$ diagram proposed by Drummond and Defant (1990) for the distinction between TTG and Post-Archean granitoids. Partial melting curves after Drummond and Defant (1990). For amphibolite and 10% garnet amphibolite restite curves MORB source with $Yb_N = 10$ and $(La/Yb)_N = 1$ is assumed, and the other two partial melting curves (eclogite and 20% hornblende eclogite) assume a MORB source with $Yb_N = 12$ and $(La/Yb)_N = 1$. Percent partial melt values are listed on each of the model curves. (E) La/Yb vs. Yb (ppm) diagram from Castillo et al. (1999), showing fields for adakite and island–arc andesite–dacite–rhyolite lavas. Differentiation paths resulting from fractionation of various minerals are shown schematically (after Castillo et al., 1999). (F) Dy/Yb vs. SiO_2 diagram showing fractionation trends of amphibole and garnet, and the compositional trend for magmatism of the Aleutians and Less Antilles arcs (after Davidson et al., 2007).

In the ternary Na–K–Ca diagram, the Mirador samples plot within the trondhjemite field (Tdh), attesting for their high sodium contents (**Fig. 2.9B**). However, the general trondhjemitic trend from (Barker and Arth, 1976) is not observed for the Mirador tonalites, as they evolve towards the potassium apex, evidencing a typical (potassic) calc-alkaline trend from Nockolds and Allen (1953) (**Fig. 2.9B**). The potassium enrichement instead of sodium for the most evolved samples of the Mirador tonalites is also observed in the SiO_2 vs. K_2O/Na_2O diagram (positive correlation) (**Fig. 2.9A**). According to Moyen and Martin (2012), an important feature of both adakite and TTG is that their K/Na ratio remains low throughout differentiation, and does not correlate with differentiation indicators such as SiO_2. On the contrary, whenever fractionation of amphibole or garnet is suspected (Macpherson et al., 2006; Richards and Kerrich, 2007; Ribeiro et al., 2016) or experimentally observed (Alonso–Perez et al., 2009), the melts invariably become more potassic in the course of differentiation.

In the Sr/Y vs. Y and chondrite–normalized Yb_N vs. $(La/Yb)_N$ diagrams, the fields of adakite (or Archean TTG) and the classic calc–alkaline rocks (or post–Archean granitoids) are clearly distinct (**Fig. 2.9C** and **D**). The field of classic (potassic) calc–alkaline rocks is also referred as calc–alkaline basalt–andesite–dacite–rhyolite (BADR) suites, commonly interpreted as a magmatic series that evolved by assimilation and fractional crystallization (AFC) processes of arc basalts (Drummond and Defant, 1990; Martin, 1994). For post–Archean granitoids (potassic calc–alkaline rocks) the low geothermal gradients along Benioff

planes (as today) supports the partial melting of the mantle wedge metasomatized by fluids released by the dehydration of the subducted lithosphere (Drummond and Defant, 1990; Martin, 1994). However, high geothermal gradients along Benioff planes (assumed to be the common Archean situation) would support the partial melting of the subducted lithosphere at comparatively shallower depths, generating TTG–like (high–silica Adakites) (Martin, 1986; Drummond and Defant, 1990; Martin, 1994). The Mirador tonalites plot largely within the field of adakites in the Sr vs. Y diagram (**Fig. 2.9C**). In this diagram, they follow the trend of partial melting consistent with a 10% garnet amphibolite source (**Fig. 2.9C**). However, they also follow the trend that illustrates fractional crystallization of a high–pressure mineral assemblage (e.g. garnet and amphibole) from basaltic melt (**Fig. 2.9C**). According to Macpherson et al. (2006), adakitic melts from typical arc magma may be produced by fractionation of a garnet–bearing assemblage in arc basalts, as basaltic magma stalled within the mantle, either at the base of the arc lithosphere or at some rheological boundary in the shallow mantle wedge.

In the chondrite–normalized Yb_N vs. $(La/Yb)_N$ the Mirador tonalites plot whithin the field of Archean TTG, with similar trend of the 10% garnet–amphibolite melting curve, but also, plot entirely within the field of post–Archean granitoids, that represent metasomatized mantle–derived magmatism, followed by fractional crystallization (**Fig. 2.9D**). In the Yb (ppm) vs. La/Yb diagram with the fields for adakite and normal andesite–dacite–rhyolite according to Castillo et al. (1999), the Mirador tonalites plot across both classification fields, suggesting the differentiation trend related to hornblende and/or clinopyroxene fractionation (**Fig. 2.9E**). According to Castillo et al. (1999), adakite–like andesites and dacites in Camiguin Island, southern Philippine arc, show similar pattern (crossing fields) in the La/Yb vs. Yb (ppm) diagram, which are interpreted as combined crystal fractionation of primarily hornblende and clinopyroxene from a more primitive arc–basalt member. Fractionation of amphibole, clinopyroxene and/or garnet can reduce Y and Yb from the melt, then increase the Sr/Y and La/Yb ratios (Castillo et al., 1999), while plagioclase fractionation would reduce Sr, Sr/Y and Eu/Eu* (e.g. Martin et al., 2005). Both amphibole and garnet in fractional crystallization process would significantly affect the REE patterns of evolved melts (e.g. Rollinson, 1993). Amphibole preferentially incorporates middle–REEs (e.g. Dy) over heavy REEs (e.g. Yb), while garnet preferentially incorporates heavy–REEs (e.g. Rollinson, 1993). As a result, garnet fractionation will increase Dy/Yb, whereas amphibole fractionation will decrease Dy/Yb (Castillo et al., 1999; Davidson et al., 2007; Moyen, 2009). Our data show a slightly decrease in Dy/Yb with increasing SiO_2, also suggesting amphibole, rather than

garnet fractionation (**Fig. 2.9F**). In this diagram, the Mirador tonalites plot at the end of typical island arc differentiation trends (Aleutians and Less Antilles arcs), interpreted as amphibole (hydrous) fractionation rather than garnet (high-pressure) fractionation (Davidson et al., 2007). However, whole–rock geochemical analysis for less differentiated members of the Mirador tonalites are lacking (e.g. mafic magmatic enclaves, **Fig. 2.3B**), which could probably better delineate the amphibole fractionation trend in the Dy/Yb vs. SiO_2 diagram (**Fig. 2.9E**). In addition, our REE data in the chondrite–normalized diagram define slightly U-shaped trends, which suggest amphibole fractionation (Dy < Yb) rather than garnet (Dy > Yb) (**Fig. 2.6B**). Amphibole fractionation is consistent with lower-crustal depths and high H_2O concentrations in the melt–conditions considered to typify those of magma petrogenesis at subduction zones (Castillo et al., 1999; Davidson et al., 2007).

We suggest, that the Mirador tonalites were probably generated by similar processes as interpreted to those of "adakite–like" rocks (e.g. Castillo et al., 1999; Davidson et al., 2007; Richards and Kerrich, 2007; Rooney et al., 2010; Kolb et al., 2012; Oh et al., 2016; Ribeiro et al., 2017), which may ascribed their adakitic signature by fractionation of amphibole during its magmatic evolution, rather than any connection with partial melting of garnet-amphibolite sources. Therefore, the Mirador tonalites are akin to those of mantle–related magmatism from subduction zones (**Fig. 2.9E** and **F**). However, primary magmas derived directly from partial melting of mantle (e.g., low–silica adakites or high–Mg andesites) are believed to be basaltic, having high Mg-number (470), Ni (4400 ppm) and Cr (41000 ppm) with SiO_2 < 55 wt % (e.g., Martin et al., 2005). This is not the case of the Mirador tonalites. Therefore, we suggest that a basic magma, once formed by melting of the enriched mantle, and evolves by fractional crystallization (e.g. amphibole) at mantle depth or during ascent to the lower continental. In addition, the $\varepsilon_{Hf}(t)$ values ranging from -0.94 to +1.29 for the Mirador tonalites, suggest partial melting of a heterogeneous source, representing crustal reworking of both juvenile and less–radiogenic continental material, probably reflecting a enriched mantle source and/or crustal contamination (**Fig. 2.8D**) (**Table 2.4**).

2.6.2. Crustal sources of the K–rich Bananeira granitoids

2.6.2.1. Quartz–monzonites

Quartz–monzonites of the Bananeira suite show weak alkaline character (**Fig. 2.4C**) and are classified as shoshonitic rocks (**Fig. 2.4E**), indicated by the high Na_2O+K_2O (8.3 – 8.8

wt.%) and K_2O (4.1 – 4.6 wt.%) contents. The quartz–monzonites are slightly metaluminous (A/CNK = 0.9 – 1.0) (**Fig. 2.4D**), they contain normative diopside (0.2 – 0.5 %), no normative corundum, show relatively low SiO_2 (62.8 – 64.6 wt%) and high Fe_2O_3+MgO (6.0 – 7.2 wt%) contents. These preclude partial melting of intermediate crustal source, which would generate peraluminous melt (A/CNK > 1.0), with high SiO_2 (70 – 75 wt.%) and low Fe_2O_3+MgO (< 2 wt.%) (e.g. Patiño Douce, 1999; Watkins et al., 2007). Many authors suggest a hybrid source for quartz–monzonites, with magmas originating from partial melting of subcontinental lithospheric mantle (SCLM) and mafic lower continental crust (e.g. Barbarin, 2005; Şahin, 2008; Liu et al., 2013). However, distinctly from typical hybrid–granitoids, no mafic magmatic enclaves are found in the Bananeira quartz–monzonites, suggesting no interaction (mingling/mixing) with mantle–derived magmas, reflecting on their little whole–rock silica variation (**Fig. 2.5**) (**Table 2.1**). Mafic (amphibolite) enclaves are frequently found in the quartz–monzonites (**Fig. 2.3D**), so, partial melting of amphibolites may be a possible source candidate. However, the quartz–monzonites are characterized by high K_2O/Na_2O ratios (0.9 – 1.2), which is a feature clearly different from those found in adakites or TTG (K_2O/Na_2O < 0.5), which are interpreted as partial melting of mafic crustal rocks (**Fig. 2.9A**) (e.g. Barker and Arth, 1976; Martin, 1994). Therefore, a distinct K–rich mafic crustal source, rather than tholeiitic (low–K) metamafic rocks must be invoked for the genesis of the quartz–monzonites. According to Sisson et al. (2005), experimental melting of medium– to high–K basaltic rocks at 7 kbar and 825–950 °C produce felsic to intermediate "magmatic" liquids similar to high–K calc–alkaline and shoshonitic rocks, with Na_2O, K_2O and SiO_2 contents similar to those of the Bananeira quartz–monzonites. Similarly, in post–collisional settings, felsic to intermediate shoshonitic rocks are proposed to be the products of partial melting of underplated K–rich mafic rocks (e.g. Liégeois et al., 1998; Pe–Piper et al., 2009; Ferreira et al., 2015). The Bananeira quartz–monzonites have lower Sr/Y ratio (33 – 41) and Sr (691 – 753 ppm) contents than adakites or adakite–like rocks. As we already discussed for the Mirador tonalites, variation in Sr, Y and Yb contents is generally associated to the presence or absence of residual (or fractionation) phases, such as plagioclase (for Sr), amphibole and/or garnet (for Y and Yb). Recently, based on experimental data, Qian and Hermann (2013) showed that magmas with high Sr and Eu contents can be produced by melting of K-rich mafic lower continental crust at 800–950 °C and 10–12.5 kbar (~30–40 km), but otherwise, for melting of the same mafic lower continental crust at higher temperature (1000 °C) and lower pressure 10 kbar (~30 km), the obtained melts have obvious Sr and Eu depletions, as plagioclase remains in the residue. In this way, the relatively low Sr content (692 – 753 ppm) and pronounced Eu

negative anomaly of the Bananeira quartz–monzonites (**Fig. 2.6A** and **B**) suggest melting within the plagioclase stability field. The Bananeira quartz–monzonites have high Yb (1.5 – 2.2 ppm) and Y (17.3 – 21.9 ppm), relatively high HREE contents to chondrites values (10 times chrondrite) and flat HREE patterns (**Fig. 2.6**), suggesting little or no garnet as a residual phase (e.g. Qian and Hermann, 2013). So far, in this work, we suggest that the Bananeira quartz–monzonites probably derived by melting of K–rich metamafic crust, under high heat (~1000 °C) and relatively low pressure (~10 kbar) conditions (with plagioclase stable), similar as proposed to many high–K calc–alkaline to shoshonitic magmatism in post–collisional setting (e.g. Liégeois et al., 1998; Pe–Piper et al., 2009; Ferreira et al., 2015).

2.6.2.2. Granites

The granites of the Bananeira suite show whole–rock high SiO_2 (71.5 to 72.5 wt.%) and K_2O (4.39 to 5.21 wt.%), and low Fe_2O_3t + MgO (2.73 – 4.57 wt.%) contents (**Table 2.1**), typical of granites *sensu stricto*, and consistent with their derivation from more evolved crustal rocks. Experimental melting of tonalite and/or metagraywacke generate peraluminous melt (A/CNK > 1.0) with high SiO_2 (70 – 75 wt.%) and K_2O (2 – 6 wt.%), and low Fe_2O_3+MgO (< 5 wt.%) contents (e.g. Patiño Douce, 1999; Watkins et al., 2007). The Bananeira granites have slightly peraluminous affinity (A/CNK ~ 1.01 – 1.07) (**Fig. 2.4D**) and high K_2O/Na_2O ratios (1.20 – 1.55) (**Fig. 2.9A**), which is compatible with melting of intermediate crustal source (e.g. metatonalite and/or metagraywacke) (e.g. Patiño Douce and Beard, 1995; Patiño Douce, 1999; Laurent et al., 2013). The pronounced negative Eu anomaly is consistent with plagioclase–rich residue, implicating on relatively low pressure partial melting of the source rock (**Fig. 2.6**). Fractional crystallization of plagioclase + apatie + titanite might have also lowered the negative Eu anomaly, and deplete the Sr (140 – 637 ppm) contents of the Bananeira granite (**Fig. 2.6**). In the chondrite–normalized REE diagram, samples of the Bananeira granites show strongly fractionated pattern, with $(La/Yb)_N$ ranging from 34 to 114 (**Fig. 2.6B**). Two samples of the granites show strongly depletion on HREE, with Yb and Lu values as low as TTG rocks, while two other samples have less–depleted HREE values (**Fig. 2.6B**). This variable HREE contents is consistent with their derivation from a heterogeneous source and/or variable fractionation (e.g. garnet and/or amphibole). This variable HREE patterns could also be related to presence of inherited zircons in some samples (less–depleted ones), as zircon concentrate HREEs. In addition, inherited zircons in the Bananeira granite were recognized on U–Pb isotopic analysis (**Fig. 2.8C**). However, frequently in the literature, the chondrite–normalized REE diagram for high–K granites show

variable total REE and highly variable HREE contents, commonly interpreted by partial melting of a heterogeneous crustal source (tonalitic ± mafic crust ± metasedimentary rocks) (e.g. Shang et al., 2010; Jayananda et al., 2006; Huang et al., 2012; Laurent et al., 2014; Manya and Maboko, 2016; Tulibonywa et al., 2017). For example, according to Jayananda et al. (2006), the heterogeneous chemical compositions of c. 2.6 Ga potassic granites from Dharwar craton, in India, indicate involvement of various crustal sources and also significantly different depths of partial melting. Similarly, Shang et al. (2010) suggest that variations from flat to steeper HREE patterns of late Archean (c. 2.7 Ga) high–K granites of the Congo craton, in Africa, could be due to variations on garnet-rich and garnet–free residues (heterogeneous source). Garnet is often absent in dehydration melting experiments conducted at less than 8 kbar (e.g. Rushmer, 1991; Rapp et al., 1991). However, during experimental melting of metagraywackes at low oxygen fugacity, garnet can stabilized in the residue at lower pressures (down to approximately 5 kbar) (e.g. Patiño Douce and Beard, 1995; Patiño Douce, 1999). In this view, we suggest that the Bananeira granites probably derived from low–pressure (plagioclase stable) (± garnet) crustal source of intermediate composition, such as a TTG gneisses and/or metagraywackes, similar as interpreted to many Precambrian high–K calc–alkaline granites, commonly associated to collisional setting (e.g. Liégeois et al., 1998; Shang et al., 2010; Laurent et al., 2014; Manya and Maboko, 2016; Tulibonywa et al., 2017).

2.6.3. Tectonic interpretation and *regional* correlation

2.6.3.1. Mirador tonalites: Implications for crustal growth and reworking during subduction

The c. 2185 Ma Mirador tonalites show Hf crustal model ages of 2.80 to 2.66 Ga (**Table 2.4**). This indicates that the Mirador tonalites incorporated Archean crustal components during their genesis. The $\varepsilon_{Hf}(t)$ values ranging of -0.94 to +1.29 suggest partial melting of a heterogeneous source and probably represent crustal reworking of both juvenile and unradiogenic continental material, agreeing with their sub– and superchondritic $\varepsilon_{Hf}(t)$ values (**Fig. 2.8D**) (**Table 2.4**). Thus, partial melting of a Paleoproterozoic juvenile mafic crust and/or depleted mantle wedge in arc setting, without any continental contaminant, may not account for the Archean Hf model ages of the Mirador Tonalites (**Table 2.4**). We suggest that partial melting of mantle source metasomatized with Archean–derived subducted sediments could be a plausible hypothesis. From literature information, mixing of juvenile arc

magmas with subducted continental material has been a common interpretation to discuss variation on trace element and isotope geochemistry of intra–oceanic arc rocks, as reported for modern (e.g. Carpentier et al., 2009; Nebel et al., 2011; Tapster et al., 2014; Shao et al., 2015) and ancient intra–oceanic arcs (e.g. Kuzmichev et al., 2005; Kemp et al., 2009; Safonova et al., 2017). Nebel et al. (2011) also suggest that similar process could have started very early in Earth's crustal evolution, as sediment recycling in a subduction setting can further account for Hf variations in the Hadean zircon record.

The metasomatized mantle wedge source has been proposed as the source for the widespread Rhyacian plutonic rocks (Caicó complex) surrounding the Archean domains of northern Borborema Province (**Fig. 2.10**) (Souza et al., 2007; Souza et al., 2016). According to Hollanda et al. (2011), U–Pb SHRIMP zircon ages and whole–rock Nd isotopes for plutonic rocks of the Caicó complex, show evidence that magmatism occurred mainly at 2.25 to 2.17 Ga, with Nd model ages varying from 2.45 to 2.81 Ga. This indicates that plutonic rocks of the Caicó complex represent juvenile magmatism with different degree of interaction with an older, probably Neoarchean continental material (Hollanda et al., 2011). According to Souza et al. (2007, 2016) most of these Rhyacian plutonic rocks of the Caicó complex, probably evolved by fractional crystallization from basic arc magma, derived from partial melting of a metasomatized mantle. These authors also proposed that this magmatism evolved in subduction zone setting, to account for both negative anomalies in high field strength elements (HFSE) and LILE enrichment, as weel with slightly negative or positive epsilon Nd(t). The mixed Hf isotope signature of crustal and juvenile material preserved in the magmatic zircons of the Mirador tonalites supports the interpretation that these plutons probably formed in an intra–oceanic arc in the vicinity of Archean continental crust, or in a continental arc setting.

The U–Pb SHRIMP zircon age of 2185 ± 4 Ma of the Mirador tonalites is within the range of 2190–2160 Ma reported for the Cipó tonalites of the Algodões granite–greenstone terrane, north of the Troia Massif (Martins et al., 2009; Costa et al., 2015) (**Fig. 2.1B**) (**Table 2.5**). The epsilon Nd(t) (+2.24 and +2.29 Ga) of the Cipó tonalites (**Table 2.5**), together with their high–silica adakitic affinity, suggest that these plutons derived from partial melting of a juvenile mafic source (oceanic slab?), probably in a 2190–2160 Ma intra–oceanic subduction zone, far away from Archean continental crust contamination (Martins et al., 2009; Costa et al., 2015). In contrast, the 2185 Ma Mirador tonalites show Hf crustal model ages from 2.66 to 2.80 Ga (**Table 2.4**), being much older than the Paleoproterozoic Nd model ages of the Cipó tonalites (**Table 2.5**). However, Nd TDM model ages may vary considerably, depending

on which are the assumed initial values for the depleted mantle, which may be those of DePaolo (1981) or Goldstein et al. (1984). Model ages calculated using the Goldstein et al. (1984) model are typically c. 200 m.y. older than those calculated with the DePaolo (1981) model (see Liégeois and Stern (2010) for further discussion). In addition, comparison between Hf (zircon) and Nd (whole–rock) TDM model ages must be carefully interpreted, as Lu-Hf isotopic system is apparently much more sensitive to track crustal contamination in igneous rocks than Sm-Nd isotopes (e.g. Stern et al., 2010; Milhomen Neto et al., 2016). Nevertheless, the "true" adakitic signature of the Cipó tonalites (Costa et al., 2015), distinct from the mantle–related (adakite–like) Mirador tonalites, evidence contrasting sources for these early c. 2190–2160 Ma tonalitic plutonism at the Troia Massif (**Fig. 2.1B**). This interpretation implies in crustal growth by melting of the juvenile subducted oceanic crust to generated "true" adakitic plutons (Cipó tonalites, Costa et al., 2015). For the Mirador tonalites, their possible connection with mantle–related magmatism also implies in crustal growth, but the participation of subducted continental sediments to explain their mixed Hf signature implies in crustal reworking (or recycling). This is fully compatible with a subduction zone setting, which is also a very effective place for crustal recycling, rather than solely juvenile crustal growth (e.g. Scholl and von Huene, 2009; Stern and Scholl, 2010; Stern, 2011).

2.6.3.2. Bananeira potassic plutons: Implication for crustal reworking during collision

Magmatic zircons from the 2086 Ma Bananeira granite yielded in situ zircon Hf crustal model ages between 2536 to 2713 Ma, and $\varepsilon_{Hf}(t)$ values ranging from -0.46 to +1.85, suggesting crystallization from a heterogeneous magma, derived from mixing of juvenile crust and less–radiogenic continental components. The presence of inherited 2.31 Ga juvenile and Archean zircons supports this idea (**Fig. 2.7C** and **D**). Two analyzed zircons of the ~2307 Ma inherited zircon population yielded superchrondritic $\varepsilon_{Hf}(t)$ values of +4.86 and +4.87, and Hf crustal model age of 2530 Ma, evidencing that less–radiogenic 2.31 Ga Siderian crustal component contributed to genesis of the Bananeira granite. These granites are partially intrusive into metasedimentary rocks of the Serra das Pipocas greenstone belt (**Fig. 2.2**), and their slightly peraluminous composition suggests derivation from, or major assimilation of greenstone belt sediments. According to Costa et al. (2014a), detrital zircon grains for metagraywacke sample of the Serra das Pipocas metavolcano–sedimentary sequence, yielded an expressive population aged around 2200 Ma and older zircon grains with $^{207}Pb/^{206}Pb$ ages of 3096 Ma, 3074 Ma, 2600 and 2500 Ma, which indicates a mixture of Archean and Paleoproterozoic sources, and a maximum depositional age of c. 2.20 Ga. However, c. 2.31

Ga detrital zircon grains were not found in this previous work of Costa et al. (2014a), and therefore, melting of an unexposed 2.31 Ga crust, together with Neoarchean 2.7–2.8 Ga TTG rocks of the Troia Massif, could be a better source candidate. The Nd model age for the Neoarchean TTG gneisses of the Troia Massif varies from 3.04 to 2.69 Ga (**Table 2.5**), which is older than the Hf model age of the c. 2086 Ma Bananeira granites (2.54 – 2.71 Ga) (**Table 2.4**), supporting the mixing evidence of Archean TTG and less–radiogenic 2.31 Ga crustal sources. Melting of a heterogeneous crustal source is also compatible with the geochemical signature of the Bananeira plutons, which suggests relatively high temperature and low pressure partial melting of a tonalitic crust and associated K–rich mafic rocks for the genesis of granites and quartz–monzonites, respectively. The ages of 2079 and 2068 Ma clearly relate this potassic magmatic event to the late tectonic evolution of the Rhyacian granite–greenstone terranes of the Troia Massif (**Table 2.5**).

These potassic granitoids have also similar ages to the c. 2100 Ma Boa Viagem mafic–ultramafic intrusion (Almeida, 2014), the 2100–2070 Ma S–type granitoids (Pessoa et al., 1986; Garcia et al., 2014), the c. 2046 Ma leucosome age from migmatites (Gomes, 2013) and the c. 2036 Ma PGE–bearing chromitites of the Troia Massif (Costa et al., 2014b) (**Table 2.5**). The evidence for high–grade metamorphism and the contemporaneity of crustal–derived (e.g. Bananeira granitoids and S–type plutons) and mantle–derived magmas (**Table 2.5**), are typical of collisional setting (e.g. Liégeois et al., 1998; Bonin, 2004). Mantle– and crust–derived magmatism in syn– to post–collisional setting is generally attributed to slab breakoff (Liégeois and Black, 1987; Davies and von Blanckenburg, 1995; Atherton and Ghani, 2002) or large scale continental lithospheric delamination (e.g. Kay and Mahlburg Kay, 1993; Rey et al., 2001; Liégeois et al., 2003, 2013). For both of these geodynamic processes, asthenosphere upwelling (induced by lithospheric processes) is thought to be an important mechanism for heat transfer to continental crust, resulting in partial melting of lower and middle crustal sources, to generate collisional, usually K–rich, magmatism (e.g. Liégeois, 1998; Atherton and Ghani, 2002).

Table 2.5: Geochronological and Nd isotopic data for the Troia Massif.

	Complex / unit	Rock type	Analytical technique	Age (Ma)	Nd isotopes		Refer.
					TDM (Ga)	$\varepsilon_{Nd(t)}$	
	ARCHEAN RECORD						
Basement rocks	Cruzeta complex	Metatonalite	(U-Pb SHRIMP in zircon)	3270 ± 5			Silva et al. (2002)
	Cruzeta complex	Metatonalite	(U-Pb isotopic dilution in zircon)	2857 ± 42	3.04	-0.3	Fetter (1999)
	Cruzeta complex	Metatonalite	(U-Pb isotopic dilution in zircon)	2794 ± 77	2.96	+0.2	Fetter (1999)
	Cruzeta complex	Metatonalite	(U-Pb SHRIMP in zircon)	2793 ± 6.3			Ganade et al. (2017)
	Cruzeta complex	Metarhyolite	(U-Pb isotopic dilution in zircon)	2776 ± 65	2.81	+2.1	Fetter (1999)
	Cruzeta complex	Metatonalite	(U-Pb isotopic dilution in zircon)	2773 ± 60	2.92	-0.2	Fetter (1999)
	Cruzeta complex	Metatonalite	(U-Pb SHRIMP in zircon)	2698 ± 8			Ganade et al. (2017)
	Cruzeta complex	Metatonalite	(U-Pb isotopic dilution in zircon)	2675 ± 64	2.69	+2.5	Fetter (1999)
	PALEOPROTEROZOIC RECORD						
Accretionary event (pre–collisional)	Algodões unit	Amphibolite (metabasalt)	(Sm-Nd whole rock isochron)	2236 ± 55	2.26	+2.9	Martins et al. (2009)
	Cipó tonalites	Metatonalite	(U-Pb LA-ICPMS in zircon)	2190 ± 6			Costa et al. (2015)
	Mirador tonalites	Metatonalite/granodiorite	(U-Pb SHRIMP in zircon)	2185 ± 4			***This work***
	Mirador tonalites	Metatonalite/granodiorite	(U-Pb LA-ICPMS in zircon)	2181 ± 4			Sousa, (2016)
	Cipó tonalites	Metatonalite	(U-Pb LA-ICPMS in zircon)	2180 ± 15			Costa et al. (2015)
	Cipó tonalites	Metatonalite	(Pb-Pb evaporation in zircon)	2172 ± 7	2.29	+0.9	Martins et al. (2009)
	Cipó tonalites	Metatonalite	(Pb-Pb evaporation in zircon)	2160 ± 9	2.24	+1.9	Martins et al. (2009)
	Madalena orthogneiss	Metaquartz diorite	(U-Pb isotopic dilution in zircon)	2156 ± 8	2.30	+1.5	Castro (2004)
	Cruzeta complex	Felsic metavolcanic	(U-Pb isotopic dilution in zircon)	2151 ± 9	2.22	+2.5	Fetter (1999)
	Serra da Palha ortho.	Granitic orthogneiss	(U-Pb LA-ICPMS in zircon)	2150 ± 16			Costa et al. (2015)
	Boa Viagem complex	Bt-Hb-Orthogneiss	(U-Pb SHRIMP in zircon)	2150 ± 29	2.38	-0.3	Silva et al. (2014)
	Madalena orthogneiss	Bt-Hb-Orthogneiss	(U-Pb isotopic dilution in zircon)	2142 ± 20			Castro (2004)
	Algodões unit	Metaquartz diorite	(U-Pb isotopic dilution in zircon)	2140 ± 6	2.27	+1.9	Fetter (1999)
	Madalena orthogneiss	Metatonalite	(Pb-Pb evaporation in zircon)	2140 ± 6	2.23	+1.9	Martins et al. (2009)
	Macaoca orthogneiss	Bt-Hb-Orthogneiss	(U-Pb isotopic dilution in zircon)	2139 ± 12	2.37	+0.6	Castro (2004)
	Boa Viagem complex	Bt-Hb-Orthogneiss	(U-Pb SHRIMP in zircon)	2124 ± 35	2.35	-0.2	Silva et al. (2014)
	Algodões unit	Metarhyolite	(U-Pb SHRIMP in zircon)	2130 ± 17	2.23	+2.3	Castro (2004)
	Macaoca orthogneiss	Metatonalite	(U-Pb isotopic dilution in zircon)	2130 ± 3	2.44	-0.6	Fetter (1999)
	Madalena orthogneiss	Metaquartz diorite	(U-Pb isotopic dilution in zircon)	2130 ± 3	2.23	+1.9	Martins et al. (2009)
Collisional event	Boa Viagem mafic	Metagabbro	(U-Pb LA-ICPMS in zircon)	2103 ± 3			Almeida (2014)
	Bananeira suite	Qtz-monzonite	(U-Pb SHRIMP in zircon)	2079 ± 4			***This work***
	Canindé unit (?)	Leucogranite	(U-Pb LA-ICPMS in zircon)	2070 ± 19			Garcia et al. (2014)
	Bananeira suite	Granite	(U-Pb LA-ICPMS in zircon)	2068 ± 5			***This work***
	Macaoca orthogneiss	Leucosome	(U-Pb LA-ICPMS in zircon)	2046 ± 12			Gomes (2013)
	Troia mafic/ultramafics	Chromitite	(U-Pb SHRIMP in zircon)	2036 ± 28			Costa et al. (2014b)

Bt = biotite, Hb = hornblende, Qtz = quartz, SHRIMP = Sensitive High Resolution Ion Microprobe, LA-ICMS = Laser Ablation Inductively Coupled Plasma Mass Spectrometry
Error for the ages are 1 σ for the SHRIMP technique and 2 σ for the others.

2.6.3.3. On the source of the c. 2.31 Ga less–radiogenic zircons

In this work, an inherited zircon population with an age of 2307 ± 14 Ma (12 grains) was found in the Bananeira granite (**Fig. 2.8C**). The Hf isotopes for two concordant zircons of this inherited population show superchrondritic $\varepsilon_{Hf}(t)$ values of +4.86 and +4.87, and the same Hf crustal model age of 2530 Ma (**Table 2.4**) (**Fig. 2.8D**). This suggests that these 2.31 Ga less–radiogenic zircons may be derived from an igneous rock that was extracted from depleted mantle at c. 2.53 Ga. However, mixing of juvenile Siderian and unradiogenic Archean sources (or less–depleted mantle) is also a plausible hypothesis for the genesis of these zircons. In the Médio Coreaú domain (MCD), northwest of the Borborema Province (**Fig. 2.10**), Siderian TTG gneisses, with U–Pb (TIMS) zircon ages of 2.35 to 2.30 Ga, and Nd model ages between 2.61 Ga and 2.38 were reported by Santos et al. (2009) (**Fig. 2.10**). These Nd isotopes from the Siderian TTG gneisses of the MCD suggest that both Paleoproterozoic

and Archean sources contributed to their genesis. Juvenile orthogneisses with similar Siderian ages were also identified in the Rio Grande do Norte Domain (Dantas et al., 2008). Additionally, more recently, U–Pb (LA–ICPMS) zircon ages of 2356 ± 12 Ma for a biotite–gneiss and 2367 ± 12 Ma for amphibolite were reported at the northeast margin of the Archean Granjeiro complex (Freimann, 2014) (**Fig. 2.10**). Therefore, records of this Siderian crust are becoming more frequent, with advancing geochronological studies in northern Borborema Province. According to Santos et al. (2009), the 2.35 to 2.30 Ga TTG gneisses of the MCD correspond to an early stage of juvenile crust generation, probably in intra–oceanic arcs, prior to the subsequent widespread 2.22 to 2.10 Ga magmatic record in the São Luís–West African craton and northern Borborema Province. In the Birimian terranes, Gasquet et al. (2003) recorded an age of 2312 ± 17 Ma for xenocrystic zircons in a 2170 ± 19 Ma tonalite from the Dabakala area, southeastern of the Baoulé–Mossi domain (**Fig. 2.10**). These xenocrystic zircons have been suggested to represent an early phase of crustal growth in the Birimian terranes (Gasquet et al., 2003). The early crustal growth event around 2.35 to 2.30 Ga has also been identified in other Paleoproterozoic domains of the Brazilian territory, such as the Bacaja domain (southwest Amazon craton) (Vasquez et al., 2008; Macambira et al., 2009) and the northern (Cruz et al., 2016) and southern São Francisco craton (Teixeira et al., 2015).

2.6.3.4. Reworking of Archean crust and Paleoproterozoic juvenile crustal growth in the northern Borborema Province

Archean crust in the northern Borborema Province is represented by the (1) Troia Massif, (2) Granjeiro complex and (3) São José do Campestre Massif (SJCM) (**Fig. 2.10**) (Fetter, 1999; Dantas et al., 2004, 2013; Matteini and Dantas, 2011; Silva et al., 2002; Souza et al., 2016). These basement inliers consist mainly of gneisses and migmatites, and their geochronological data evidence a long history of crustal growth and reworking throughout the Archean Eon, with U–Pb zircon ages concentrating at 3.45, 3.25–3.18, 3.06, 2.85–2.77, 2.68 and 2.55 Ga (Fetter, 1999; Dantas et al., 2004; Matteini and Dantas, 2011; Silva et al., 2002; Dantas et al., 2013; Freimann, 2014; Hollanda et al., 2015; Souza et al., 2016; Ganade et al., 2017). The SJCM (**Fig. 2.10**) contains one of the oldest preserved crust (3412 ± 8 Ma) in the South American Platform (Dantas et al., 2004, 2013). Hf isotopes in zircon from the 3.45 Ga and 3.06 Ga gneissic–migmatitic rocks yielded model ages between 3.49 and 3.90 Ga, evidencing that a polycyclic crustal evolution started in the Paleoarchean at 3.45 Ga with generation of juvenile crust and reworking of older Eoarchean crust (3.90 Ga) (Matteini and

Dantas, 2011). For the Paleoproterozoic record in the SJCM, according to Matteini et al. (2010), zircon cores from a migmatite sample yielded U–Pb LA–ICPMS age of c. 2.05 Ga and Hf model ages from 2.5 to 2.8 Ga. This characterized Paleoproterozoic magmatic protoliths formed by partial melting of an older Archean juvenile crust generated at 2.5–2.8 Ga or, alternatively, may represent Rhyacian juvenile magmas generated at 2.05 Ga, contaminated by older (Archean) crustal material (Matteini et al., 2010).

As already mentioned, abundant Paleoproterozoic plutonic rocks surrounding the Archean SJCM and the Granjeiro complex are known as the Caicó complex (in the Rio Grande do Norte Domain – RGND) (Souza et al., 2007, 2016; Hollanda et al., 2011) (**Fig. 2.10**). According to Souza et al. (2016), these rocks cover about 50% of the northern Borborema Province (**Fig. 2.10**). Their geochemistry indicates potassic calc-alkaline differentiation trends, akin to I– and M–type magmas, and show negative anomalies for Ta, Nb, Ti and P (Souza et al., 2007). Depleted and metasomatized mantle in a subduction zone setting are interpreted to be the main sources of the Caicó magmatism (Souza et al., 2007, 2016). U–Pb ages for this magmatism indicate largely generation of plutonic rocks at 2.24–2.22 Ga and at 2.11 Ga (Souza et al., 2007; Hollanda et al., 2011; Souza et al., 2016).

According to Fetter et al. (2000), based on U–Pb (TIMS) zircon ages and Nd isotopes for Paleoproterozoic basement rocks of the northern Borborema Province, three major crustal domains were delimited as follow: (i) the 2.22 to 2.15 Ga Rio Grande do Norte domain (RGND) (Caicó complex) with abundant negative epsilon Nd values; (ii) the 2.15 to 2.10 Ga Ceará Central domain (CCD) (or Troia Massif) with both positive and negative epsilon Nd values; and (iii) the c. 2.3 Ga juvenile Medio Coreaú domain (MCD) (**Fig. 2.10**). The juxtaposition of contrasting juvenile and reworked Paleoproterozoic terranes in northern Borborema Province occurs at several scales within the CCD and RGND (Fetter et al., 2000). This complex crustal framework, envisaged as an anastomosed mosaic of terranes that differ in their ages and isotopic nature, is typical of accretionary continental margins (e.g. Coney, 1987; Condie, 2007; Cawood et al., 2009). A common feature for accretionary margins is the presence of several accreted terranes, whose nature generally represents intra–oceanic arc records, back–arc sequences. Additionally, a typical exotic terrane in the context of this Rhyacian accretionary orogeny, is represented by the MCD, whose basement rocks consist mainly of 2.35 to 2.30 Ga juvenile crust (Fetter et al., 2000; Santos et al., 2008), contrasting with the nearby Rhyacian (2.22 to 2.06 Ga) domains (CCD and RGND) of both juvenile and reworked nature (**Fig. 2.10**).

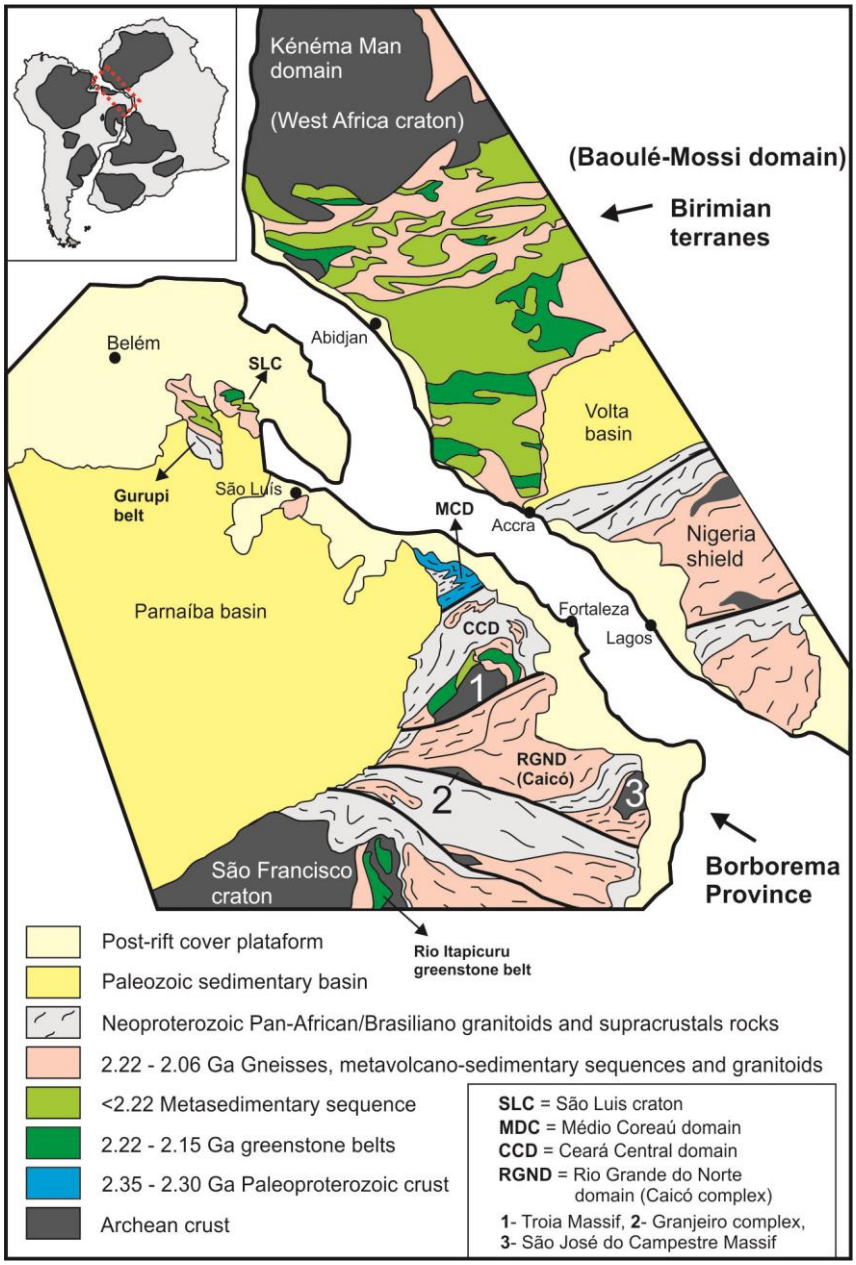

Fig. 2.10. *Pre–drift reconstruction of West–Africa and NE–Brazil, modified from Klein and Moura (2008). Representation of Archean and Paleoproterozoic terranes are not to scale.*

However, Archean domains unlike to represent accreted terranes and were probably dissected by shear zones from larger continental blocks during collision ("metacratonization", see Liégeois et al. 2013). This accretionary–collisional event, that culminated with the amalgamation of diverse juvenile and reworked Paleoproterozoic terranes along with large Archean continental blocks, is thought to represent records of the Eburnean/Transamazonian orogeny (2.2–2.0 Ga), even assuming later rework and terrane displacement during the 650–535 Ma Pan–African/Brasiliano orogenic cycle (Fetter et al., 2000; Dantas et al., 2004; Santos et al., 2009; Hollanda et al., 2011; Souza et al., 2016).

2.6.3.5. Correlation with Nigeria shield and Birimian terranes

The similarities between Paleoproterozoic terranes of the northern Borborema Province and those of the Nigeria shield and São Luís–West African craton have already been discussed by several authors (Caby, 1998; Fetter et al., 2000; Dada et al., 2008; Arthaud et al., 2008; Santos et al., 2008). The pre–drift reconstruction between Brazil and Africa continents, clearly evidence the close spatial relationship of the northern Borborema Province with the Nigeria shield and the Birimian terranes of the West African craton (**Fig. 2.10**).

Archean and Paleoproterozoic rocks have been reported for the basement complex of the Nigeria shield (Bruguier et al., 1994; Dada, 1998; Kroner et al., 2001; Okonkwo and Ganev, 2012, 2015), which is directly linked to the basement rocks of the northern Borborema Province (**Fig. 2.10**). Radiometric ages in the Nigerian basement cluster around 3.5, 3.1−3.0, 2.7−2.5 and 2.1−1.8 Ga, evidencing that the Archean/Early Proterozoic boundary was the major crust-forming period in the Nigeria shield (Dada, 1998; Kroner et al., 2001). One of the oldest rock of West–Africa come from a migmatitic orthogneiss of granodioritic composition from northern Nigeria, which yielded a SHRIMP zircon age of 3571 ± 3 Ma (Kroner et al., 2001). For Paleoproterozoic rocks of the Nigerian basement complex, Okonkwo and Ganev (2015) recently reported LA-ICP-MS zircon ages for granodioritic orthogneisses of 2236 ± 29 Ma, 2228 ± 32 Ma and 2179 ± 28 Ma. Geochemical analysis show that these orthogneisses are calc-alkaline, magnesian, metaluminous and have the characteristics of granitoids emplaced in magmatic arcs (Okonkwo and Ganev, 2015). These are very similar ages and geochemical characteristics of the nearby c. 2.22 Ga Caicó orthogneisses, in the Rio Grande do Norte domain (Souza et al., 2007, 2016), and the c. 2185 Ma Mirador tonalites (this study) (**Fig. 2.10**).

The Birimian terranes of the São Luís–West African craton (**Fig. 2.10**), are generally considered to represent a widespread event of juvenile crustal growth between c. 2.22 to 2.06 Ga (Abouchami et al., 1990; Liégeois et al., 1991; Hirdes et al., 1996; Doumbia et al., 1998; Hirdes and Davis, 2002; Gasquet et al., 2003; Feybesse et al. 2006; Klein et al., 2008, 2012; de Kock et al., 2011; Baratoux et al., 2011; Tapsoba et al., 2013; Block et al., 2016; Parra–Avila et al., 2016, 2017). Based on Sm–Nd isotopes coupled with the U–Pb zircon ages (Liégeois et al., 1991; Doumbia et al., 1998; Feybesse et al. 2006; Baratoux et al., 2011; Tapsoba et al., 2013), and more recently by Hf isotopes in zircon (Block et al., 2016), most of the Birimian terranes has been reported as juvenile crust, evolved far away from any Archean components. According to Block et al. (2016), Hf isotopes in zircon for c. 2.21 to 2.13 Ga granitoids in Birimian granite–greenstone terranes show superchondritic $\varepsilon_{Hf}(t)$ values from +1

to +6, and Hf model ages from 2.35 to 2.61 Ga, indicating that the they derived from the reworking of juvenile crustal components. However, according to Parra–Avila et al. (2016), combined U–Pb–Hf isotope data for >1000 detrital zircons from drainages of the western Baoulé–Mossi domain yielded Paleoproterozoic U–Pb ages between 2.40 and 2.07 Ga, and Hf model ages of 2.8 to 2.1 Ga, indicating some contribution from Archean aged components. More recently, Petersson et al. (2017) obtained zircon U–Pb and Lu–Hf isotope data from Birimian granitoids, showing mostly subchondritic $\varepsilon_{Hf}(t)$ values, indicating that reworking of Archean crust are recorded in almost all their analyzed 2220–2130 Ma zircon grains. This evidence that reworking of Archean crust also occurred at the Baoulé–Mossi domain, at least in the southeastern part (Petersson et al., 2016, 2017). Because of this finding, Petersson et al. (2017) argue in favor of a subduction system in the vicinity of one, or possible in between two Archean cratons. This subduction hypothesis (Petersson et al., 2016, 2017) finds support when it is recognized that large portions of the Paleoproterozoic terrains of northern Borborema Province occur in the proximity of Archean crust (**Fig. 2.10**), and incorporated significant older crustal material in their genesis (Fetter et al., 2000; Souza et al., 2007; Hollanda et al., 2011; Souza et al., 2016; this work). The progressively enrichment in continental components (e.g. less–radiogenic Nd and Hf isotopes) toward east and southeast of the Baoulé–Mossi domain (Petersson et al., 2016, 2017) and Borborema Province (Fetter et al., 2000; Hollanda et al., 2011; this work), probably reflects the proximity of the arc system to an Archean continental margin (**Fig. 2.10**).

Finally, at the end of the Transamazonian/Eburnean orogeny, at 2.10 to 2.06 Ga, several peraluminous and potassic plutons intruded the Birimian terranes of São Luís–West African craton and correlated terranes of the São Francisco–Congo and Amazonian cratons, showing temporal association to regional peak metamorphism (Feybesse et al., 2006; Lerouge et al., 2006; McReath and Faraco, 2006; Mello et al., 2006; de Kock et al., 2011; Klein et al., 2012; Eglinger et al., 2017). These late Rhyacian peraluminous and potassic granitoids represent collisional magmatism, in response to final amalgamation of Archean continental blocks and Paleoproterozoic juvenile terranes (Feybesse et al., 2006; de Kock et al., 2011; Oliveira et al., 2011; Klein et al., 2012, 2014; Block et al., 2016; Eglinger et al., 2017; Wane et al., 2018). For example, Eglinger et al. (2017) reported that mafic and felsic potassic plutons were emplaced in Guinea, in vicinity to the Archean Kénéma–Man domain (KMD) (**Fig. 2.10**), between 2.10 and 2.08 Ga. According to these authors, contemporaneous partial melting of the different mantle and crustal domains perhaps happened in response to lithospheric delamination following the collision of the juvenile Paleoproterozoic Baoulé–

Mossi domain with the Archean KMD (**Fig. 2.10**). These potassic plutons show both juvenile and reworked signatures from Hf isotopes in zircon, interpreted as collisional reworking of juvenile Birimian arc–related crust and Archean–derived components of the KMD (Eglinger et al., 2017). This is very similar to our interpretation on the 2.08 and 2.06 Ga potassic plutons studied in this work (Bananeira granitoids), suggesting that similar collisional processes in the vincinity of Archean continental blocks occurred at both sides of the Baoulé–Mossi domain (**Fig. 2.10**).

2.7. Conclusion

Based on field relationships, U–Pb geochronology, Hf isotopes, geochemical characteristics and regional correlations, the plutonic rocks studied in this work can be divided into two groups: (i) early pre–collisional 2185 Ma Mirador tonalites; and (ii) collisional 2079–2086 Ma granites and quartz monzonites of the Bananeira suite. We summarize below the main conclusions.

(1) The Mirador tonalites are intrusive only into lower stratigraphic levels of the Serra das Pipocas greenstone belt, evidencing that they have intrinsic association with the greenstone evolution. U–Pb SHRIMP zircon age of 2185 ± 4 Ma for these plutons evidences their early evolution in the Rhyacian record of the Troia Massif. Their geochemical signatures suggest evolution by fractional crystallization of mainly amphibole from arc–related mantle–derived magmatism. The zircon Hf crustal model ages for these plutons range between 2660 and 2800 Ma, evidencing that Archean crustal components contributed to the magma genesis, possibly via subduction of continental sediments. However, plutonic rocks of similar ages in the Troia Massif (e.g. Cipó tonalites) present younger whole–rock Nd model ages, suggesting that many of the previously tectonic interpretations provided by Nd isotopes must be reassessed by zircon Hf model ages.

(2) The Bananeira granitoids are intrusive both in Paleoproterozoic greenstone sequences and Archean basement rocks of the Troia Massif. These plutons are mainly represented by deformed quartz–monzonites and less–deformed granites. For the quartz–monzonites we have obtained a SHRIMP U–Pb zircon age of 2079 ± 4 Ma, and their geochemical signatures suggest partial melting of a K–rich mafic rock, at relatively low pressures. The less–deformed granites yielded LA–ICPMS U–Pb zircon age of 2068 ± 5 Ma, and an expressive inherited zircon population of 2307 ± 14 Ma. The high–K and slightly peraluminous geochemical signature of these granites suggests partial melting of tonalitic crustal sources (e.g. TTG gneisses and/or metagraywackes), at relatively low pressures. The zircon Hf crustal model

ages for these granites range from 2536 to 2713 Ma in the crystallization–related zircons, evidencing Archean crustal contribution. However, two analyzed zircon grains of the 2307 Ma inherited zircon population show $\varepsilon_{Hf}(t)$ values of +4.8, and Hf crustal model ages of 2.5 Ga. This indicates that the less–deformed granites represent crustal reworking of both Archean and less–radiogenic Paleoproterozoic sources during collisional processes.

(3) Correlations of our results with the Paleoproterozoic record in basement rocks of the northern Borborema Province (NE Brazil), Nigeria shield and Birimian terranes of the São Luís–West African craton, suggest that the plutonic rocks studied in this work are related to the 2.2 to 2.0 Ga Transamazonian/Eburnean subduction–collision orogenic event. The regional configuration and U–Pb, Hf and Nd isotopic patterns of the Paleoproterozoic basement rocks of the Borborema Province, evidence that they mostly developed in the vincinity of Archean continental blocks.

Acknowledgments

This paper is a contribution of Geological Survey of Brazil (CPRM) through the Troia–Pedra Branca project, which was funded by the Brazilian federal government. This is also a contribution to the Conselho Nacional de Desenvolvimento Científico e Tecnológico (CNPq) project (306798/2016–6) "Evolução crustal, modelos geodinâmicos e metalogênese: exemplos do Maciço de Troia (CE) e do Cinturão Gurupi (PA–MA)". ELK and JML thank CNPq for research grants (306798/2016-6 and 307199/2015-0, respectively). The authors acknowledge the contributions of JP Liégeois and an anonymous reviewer, which greatly improved the manuscript. We thank Prof. G. Zhao and Prof. Wilson Teixeira for editorial handling.

References

Abouchami, W., Boher, M., Michard, A., Albarede, F., 1990. A major 2.1 Ga event of mafic magmatism in West Africa; an early stage of crustal accretion. J. Geophys. Res. B Solid Earth Planets, 95, 605–617.

Almeida, F.F.M., Hasui, Y., Brito Neves, B.B., Fuck, R.A., 1981. Brazilian structural provinces: an introduction. Earth–Sciences Reviews, 17, 1–21.

Almeida, R.S., 2014. Geologia, geoquímica e geocronologia da suíte intrusiva máfica–ultramáfica de Boa Viagem, Ceará, Brasil. Master Dissertation, Federal University of Ceará (UFC), 103 p.

Alonso-Perez, R., Müntener, O., Ulmer, P., 2009. Igneous garnet and amphibole fractionation in the roots of island arcs: experimental constraints on andesitic liquids. Contribution to Mineral. Petrol., 157, 541–558.

Andersen, T., Andersson, U.B., Graham, S., Åberg, G., Simonsen, S.L., 2009. Granitic magmatism by melting of juvenile continental crust: new constraints on the source of Paleoproterozoic granitoids in Fennoscandia from Hf isotopes in zircon. Journal of the Geological Society, 166, 233–248.

Angeli, N., Bevenutti, C.F., Antunes, L.A., Campos, M.C., Mamani, R., 2009. Cromititos do Complexo de Pedra Branca: química mineral e platinóides associados, Ceará, Brasil. In: Simpósio de Geologia do Nordeste, Fortaleza, 23, cd rom.

Arthaud, M.H., Caby, R., Fuck, R.A., Dantas, E.L., Parente, C.V., 2008. Geology of the northern Borborema Province, NE Brazil and its correlation with Nigeria, NW Africa. In: Pankhurst, R.J., Trouw, R.A.J., Brito Neves, B.B., de Wit, M.J. (Eds.), West Gondwana: Pre–Cenozoic Correlations Across the South Atlantic Region, vol. 294. Geological Society of London, pp. 49–67. Special Publications.

Atherton, M.P., Ghani, A.A., 2002. Slab breakoff: a model for Caledonian, late granite syn–collisional magmatism in the orthotectonic (metamorphic) zone of Scotland and Donegal, Ireland. Lithos 62, 65–85.

Baratoux, L., Metelka, V., Naba, S., Jessell, W.M., Gregoire, M., Ganne, J., 2011. Juvenile paleoproterozoic crust evolution during the Eburnean orogeny (2.2–2.0 Ga), western Burkina Faso. Precambrian Res., 191, 18–45.

Barbarin, B., 2005. Mafic magmatic enclaves and mafic rocks associated with some granitoids of the central Sierra Nevada batholith, California: nature, origin, and relations with the hosts. Lithos, 80, 155–177.

Barker, F., Arth, J.G., 1976. Generation of Trondhjemitic–Tonalitic liquids and Archaean bimodal Trondhjemite–basalt suites. Geology 4, 596–600.

Barrueto, H.R., Hunt, W., 2010. Main features of the Pt–Pd chromitite–type ore deposit, Troia Unit, Cruzeta Complex, Northeast Brazil: Insights provided by microscopic and chemical approaches. In: 11th International Platinum Symposium, Sudbury, Canada.

Belousova, E.A., Kostitsyn, Y.A., Griffin, W.L., Begg, G.C., O'Reilly, S.Y., Pearson, N.J., 2010. The growth of the continental crust: Constraints from zircon Hf–isotope data. Lithos, 119, 457–466.

Belousova, E.A., Reid, A.J., Griffin, W.L., O'Reilly, S.Y., 2009. Rejuvenation vs. recycling of Archean crust in the Gawler Craton, South Australia. Evidence from U–Pb and Hf isotopes in detrital zircon. Lithos, 113, 570–582.

Block, S., Baratoux, L., Zeh, A., Laurent, O., Bruguier, O., Jessell, M., Ailleres, L., Sagna, R., Parra–Avila, L.A., Bosch, D., 2016. Paleoproterozoic juvenile crust formation and stabilisation in the south–eastern West African Craton (Ghana); New insights from U–Pb–Hf zircon data and geochemistry. Precambrian Research, 287, 1–30.

Bonin, B., 2004. Do coeval mafic and felsic magmas in post–collisional to within–plate regimes necessarily imply two contrasting, mantle and crustal, sources? A review. Lithos, 78 (1–2), 1–24.

Bouvier, A., Vervoort, J.D., Patchett, P.J., 2008. The Lu–Hf and Sm–Nd isotopic composition of CHUR: Constraints from unequilibrated chondrites and implications for the bulk composition of terrestrial planets. Earth and Planetary Science Letters, 273, 48–57.

Boynton, W.V., 1984. Geochemistry of rare earth elements: meteorite studies. In: Henderson, P. (Ed.), Rare Earth Element Geochemistry. Elsevier, pp. 63–114.

Brito Neves, B.B., 1975. Regionalização geotectônica do Pré–Cambriano Nordestino. PhD Thesis. Universidade de São Paulo, São Paulo–SP, p. 198.

Brito Neves, B.B., Santos, E.J., Van Schmus, W.R., 2000. Tectonic history of the Borborema province, in: Cordani, U.G., Milani, E.J., Thomaz Filho, A., Campos, D.A., (Eds.). Tectonic Evolution of South America, 31° International Geological Congress, Rio de Janeiro (2000), pp. 151–182.

Bruguier, O., Dada, S., Lancelot, J.R., 1994. Early Archaean component (> 3.5 Ga) within a 3.05 Ga orthogneiss from northern Nigeria: U-Pb zircon evidence. Earth Planetary Science Letters, 125, 89–103.

Caby, R. 1989. Precambrian terranes of Benin-Nigeria and northeast Brazil and the Late Proterozoic south Atlantic fit. Geological Society of America, Special paper, 230, 145 – 158.

Carpentier, M., Chauvel, C., Maury, R.C., Mattielli, N., 2009. The “zircon effect” as recorded by the chemical and Hf isotopic compositions of Lesser Antilles forearc sediments. Earth and Planetary Science Letters, 287, 86–99.

Castillo, P.R., Janney, P.E., Solidum, R., 1999. Petrology and geochemistry of Camiguin Island, southern Philippines: insights into the source of adakite and other lavas in a complex arc tectonic setting. Contributions to Mineralogy and Petrology 134, 33–51.

Castro, N.A., 2004. Evolução Geológica Proterozóica da Região entre Madalena e Taperuaba, Domínio Tectônico Ceará Central (Província Borborema). PhD Thesis. Universidade de São Paulo, São Paulo–SP, p. 221.

Cavalcante, J.C., Vasconcelos, A.M., Medeiros, M.F., Paiva, I.P., Gomes, F.E.M., Cavalcante, S.N., Cavalcante, J.E., Melo, A.C.R., Duarte Neto, V.C., Benevides, H.C., (2003). Mapa Geológico do Estado do Ceará. Escale 1:500.000. Serviço Geológico do Brasil, Fortaleza. CPRM.

Cawood, P.A., Kroner, A., Collins, W.J., Kusky, T.M., Mooney, W.D., Windley, B.F., 2009. Accretionary orogens through earth history. Geological Society London Special Publications, 318, 1–36.

Cawood, P.A., kroner, A., Pisarevsky, S., 2006. Precambrian plate tectonics: Criteria and evidence. GSA Today, 16, 4–11.

Cawood, P.A., Strachan, R.A., Pisarevsky, S.A., Gladkochub, D.P., Murphy, J.B., 2016. Linking collisional and accretionary orogens during Rodinia assembly and breakup: Implications for models of supercontinent cycles. Earth and Planetary Science Letters, 449, 118–126.

Chatterjee, C., Vadlamani, R., Kaptan, O.P., 2016. Paleoproterozoic Cordilleran–style accretion along the south eastern margin of the eastern Dharwar craton: Evidence from the Vinjamuru arc terrane of the Krishna orogen, India. Lithos, 263, 122–142.

Chiaradia, M., 2015. Crustal thickness control on Sr/Y signatures of recent arc magmas: An Earth scale perspective: Scientific Reports, 5, 8115.

Chiaradia, M., Ulianov, A., Kouzmanov, K., Beate, B., 2012. Why large porphyry Cu deposits like high Sr/Y magmas? Scientific Reports, 2, 685.

Chung, S.L., Liu, D., Ji, J., Chu, M.F., Lee, H.Y., Wen, D.J., Lee, T.Y., Qian, Q., Zhang, Q., 2003. Adakites from continental collision zones: melting of thickened lower crust beneath southern Tibet. Geology 31, 1021–1024.

Condie, K.C., 2007. Accretionary orogens in space and time. Geol. Soc. Am. Mem., 200, 145–158.

Coney, P. J., Circum–Pacific tectonogenesis in the North American Cordillera, in Circum–Pacific Orogenic Belts and Evolution of the Pacific Ocean Basin, Geodyn. Ser., vol. 18, edited by J. W. H. Monger, and J. Francheteau, pp. 59–69, AGU, Washington, D. C., 1987.

Costa, F.G., 2013. Geologia e Recursos Minerais da Folha Quixadá (SB–24–V–B–VI). Escala: 1:100.000. Programa Levantamentos Geologicos Basicos do Brasil. Serviço Geológico do Brasil, Fortaleza. CPRM.

Costa, F.G., Oliveira, E.P., McNaughton, N., 2011. The Fazenda Gavião granodiorite and associated potassic plutons as evidence for Palaeoproterozoic arc–continent collision in the Rio Itapicuru greenstone belt, Brazil. J. South Am. Earth Sci., 32 (2), 127–141.

Costa, F.G., Palheta, E.S.M., Rodrigues, J.B., Gomes, I.P., Vasconcelos, A.M., 2015. Geochemistry and U–Pb zircon ages of plutonic rocks from the Algodões granite–greenstone terrane, Troia Massif, northern Borborema Province, Brazil: Implications for Paleoproterozoic subduction–accretion processes. Journal of South American Earth Sciences, 59, 45–68.

Costa, F.G., Rodrigues, J.B., Cavalcanti, J.A.D., Palheta, E.S.M., Vasconcelos, A.M., 2014a. U–Pb LA–ICPMS ages of detrital zircons from the Paleoproterozoic Algodões and Serra das Pipocas greenstone–like sequences, Ceará Central Domain. In: 9th South American Symposium on Isotope Geology, São Paulo, Brazil, p. 110.

Costa, F.G., Rodrigues, J.B., Naleto, J.L.C., Vasconcelos, A.M., Barrueto, H.R., 2014b. 2036 Ma SHRIMP U–Pb zircon age for PGE–bearing chromitites of the Troia mafic–ultramafic complex, Ceará Central Domain. In: 9th South American Symposium on Isotope Geology, São Paulo, Brazil, p. 164.

Cox, K.G., Bell, J.D., Pankhurst, R.J., 1979. The Interpretation of Igneous Rocks. George Allen & Unwin, London.

Cruz, S.C.P., Barbosa, J.S.F., Pinto, M.S., Peucat, J.J., Paquette, J.L., Souza, J.S., Martins, V.S., Chemale, F., Carneiro, M.A., 2016. The Siderian–Orosirian magmatism in the Gavião Paleoplate, Brazil: U–Pb geochronology, geochemistry and tectonic implications. Journal of South American Earth Sciences, 69, 43–79.

Dada, S.S., 1998. Crust-forming ages and Proterozoic crustal evolution in Nigeria: a reappraisal of current interpretations. Precambrian Research, 87, 65–74.

Dada, S.S., 2008. Proterozoic evolution of the Nigeria–Borborema province. Geological Society of London Special Publication, 294, 121-136.

Dantas, E.L., Negrão, M.M., Buhn, B., 2008. 2.3 Ga continental crust generation in the Rio Grande do Norte terrane, NE Brazil. VI South American Symposium on Isotope Geology, San Carlos de Bariloche, Argentina, p. 40 (CD–ROM), Abstracts.

Dantas, E.L., Van Schmus, W.R., Hackspacher, P.C., Fetter, A.H., Brito Neves, B.B., Cordani, U., Nutman, A.P., Williams, I.S., 2004. The 3.4–3.5 São José de Campestre massif, NE Brazil: remnants of the oldest crust in South America. Precambrian Res. 130, 113–137.

Davidson, J., Turner, S., Handley, H., Macpherson, C., Dosseto, A., 2007. Amphibole 'sponge' in arc crust? Geology, 35, 787–790.

Davis, J.H., von Blanckenburg, F., 1995. Slab breakoff: A model of lithosphere detachment and its test in the magmatism and deformation of collisional orogens. Earth and Planetary Science Letters, 129 (1–4), 85–102.

de Kock, G.S., Armstrong, R.A., Siegfried, H.P., Thomas, E., 2011. Geochronology of the Birim Supergroup of the West African craton in the Wa–Bolé region of central–west Ghana: implications for the stratigraphic framework. J. Afr. Earth Sci. 59, 1–40.

Delor, C., Lahondère, D., Egal, E., Lafon, J.M., Cocherie, A., Guerrot, C., Rossi, P., Trufert, C., Theveniaut, H., Phillips, D., Avelar, V.G., 2003. Transamazonian crustal growth and reworking as revealed by the 1:500,000-scale geological map of French Guiana (2nd edition). Geologie de la France, 2-3-4, 5-57.

Doumbia, S., Pouclet, A., Kouamelan, A., Peucat, J.J., Vidal, M., Delor, C., 1998. Petrogenesis of juvenile–type Birimian (Paleoproterozoic) granitoids in Central Côte–d'Ivoire, West Africa: geochemistry and geochronology. Precambrian Res. 87, 33–63.

Drummond, M.S., Defant, M.J., 1990. A model for trondhjemite–tonalite–dacite genesis and crustal growth by slab melting: archean to modern comparison. J. Geophys. Res. 95, 21503–21521.

Eglinger, A., Thébaud, N., Zeh, A., Davis, J., Miller, J., Parra–Avila, L.A., Loucks, R., McCuaig, C., Belousova, E., 2017. New insights into the crustal growth of the Paleoproterozoic margin of the Archean Kéména–Man domain, West African craton (Guinea): Implications for gold mineral system. Precambrian Research, 292, 258–289.

Ferreira, V.P., Sial, A.N., Pimentel, M.M., Armstrong, R., Guimarães, I.P., Silva Filho, A.F., Lima, M.M.C., Silva, T.R., 2015. Reworked old crust–derived shoshonitic magma: The Guarany pluton, Northeastern Brazil. Lithos, 232, 150–161.

Fetter, A.H., 1999. U/Pb and Sm/Nd Geocronological Constraints on the Crustal Framework and Geologic History of Ceará State, NW Borborema Province, NE Brazil: Implications for the Assembly of Gondwana. PhD Thesis. Departament of Geology, Kansas University, Lawrence, p. 164.

Fetter, A.H., Van Schmus, W.R., Santos, T.J.S., Nogueira Neto, J.A., Arthaud, M.H., 2000. U–Pb and Sm–Nd geochronological constraints on the crustal evolution and basement architecture of Ceará State, NW Borborema Province, NE Brazil: implications for the existence of the Paleoproterozoic Supercontinent "Atlantica". Revista Brasileira de Geociências, 30 (1), 102–106.

Feybesse, J.L., Billa, M., Guerrot, C., Duguey, J.L.L., Milesi, J.P., Bouchot, V., 2006. The Palaeoproterozoic Ghanaian province: geodynamic model and ore controls, including regional stress modeling. Precambrian Research, 149, 149–196.

Freimann, M.A., 2014. Geocronologia e Petrotrama de quartzo milonitos do duplex transcorrente de Lavras da Mangabeira. Master Dissertation, Universidade de São Paulo, São Paulo–SP, 84 p.

Frost, B.R., Barnes, C.G., Collins, W.J., Arculu, R.J., Ellis, D.J., Frost, C.D., 2001. A geochemical classification for granitic rocks. J. Petrol. 42, 2033–2048.

Furnes, H., Dilek, Y., Wit, M., 2015. Precambrian greenstone sequences represent different ophiolite types. Gondwana Research, 27 (2), 649–685.

Ganade, C.E., Basei, M.A.S., Grandjean, F.C., Armstrong, R., Brito, R.S., 2017. Contrasting Archaean (2.85–2.68 Ga) TTGs from the Troia Massif (NE-Brazil) and their geodynamic implications for flat to steep subduction transition. Precambrian Research, 297, 1–18.

Garcia, M.G.M., Santos, T.J.S., Amaral, W.S., 2014. Provenance and tectonic setting of neoproterozoic supracrustal rocks from the Ceara Central Domain, Borborema Province (NE Brazil): constraints from geochemistry and detrital zircon ages. Int. Geol. Rev. 56 (4), 1–20.

Gasquet, D., Barbey, P., Adou, M., Paquette, J.L., 2003. Structure Sr–Nd isotope geochemistry and zircon U–Pb geochronology of the granitoids of the Dabakala area (Cote d'Ivoire): evidence for a 2.3 Ga crustal growth event in the Palaeoproterozoic of West Africa? Precambrian Res. 127, 329–354.

Gill, J.B., 1981. Orogenic Andesites and Plate Tectonics. Springer-Verlag, New York, 390 p.

Goldfarb, R., Andre–Meyer, A.S., Jowitt, S., Mudd, G.M., 2017. West Africa: The World's Premier Paleoproterozoic Gold Province. Economic Geology, 112 (1), 123–143.

Gomes, E.N., 2013. Protominérios e minérios de manganês de Juá–CE. Master Dissertation, Universidade Federal do Ceará (UFC), Ceará–CE, p. 102.

Griffin, W.L., Belousova, E.A., Shee, S.R., Pearson, N.J., O'Reilly, S.Y., 2004. Archean crustal evolution in the northern Yilgarn Craton: U–Pb and Hf–isotope evidence from detrital zircons. Precambrian Research, 131 (3–4), 231–282.

Griffin, W.L., Wang, X., Jackson, S.E., Pearson, N.J., O'Reilly, S.Y., Zhou, X. 2002. Zircon chemistry and magma genesis, SE China: in–situ analysis of Hf isotopes, Pingtan and Tonglu igneous complexes. Lithos, 61, 237–269.

Halla, J., can Hunen, J., Heilmo, E., Hottla, P., 2009. Geochemical and numerical constraints on Neoarchean plate tectonics. Precambrian Research, 175, 155–162.

Hirdes, W., Davis, D.W., 2002. U–Pb geochronology of paleoproterozoic rocks in the southern part of the Kedougou–Kenieba Inlier, Senegal, West Africa: evidence for diachronous accretionary development of the Eburnean province. Precambrian Research. 118, 83–99.

Hirdes, W., Davis, D.W., Ludtke, G., Konan, G., 1996. Two generations of Birimian (Paleoproterozoic) volcanic belts in northeastern Cote d'Ivoire (West Africa): consequences for the Birimian controversy. Precambrian Research, 80, 173–191.

Hollanda, M.H.B.M., Archanjo, C.J., Bautista, J.R., Souza, L.C., 2015. Detrital zircon ages and Nd isotope compositions of the Seridó andLavras da Mangabeira basins (Borborema Province, NE Brazil): Evidence for exhumation and recycling associated with a major shift in sedimentary provenance. Precambrian Research, 258, 186–207.

Hollanda, M.H.B.M., Archanjo, C.J., Souza, L.C., Dunyi, L., Armstrong, R., 2011. Long–lived Paleoproterozoic granitic magmatism in the Seridó–Jaguaribe domain, Borborema Province – NE Brazil. J. South Am. Earth Sci. 32 (4), 287–300.

Huang, Q.H., Li, X.H., Li, Z.X., Li, W.X., 2013. Intraplate crustal remelting as the genesis of Jurassic high–K granites in the coastal region of the Guangdong Province, SE China. Journal of Asian Earth Sciences 74, 280–302

Irvine, T.N., Baragar, W.R.A., 1971. A guide to the chemical classification of the common volcanic rocks. Can. J. Earth Sci. 8, 523–548.

Jackson, S.E., Pearson, N. J., Griffin, W.L., Belousova, E. A., 2004. The application of laser ablation–inductively coupled plasma–mass spectrometry to in situ U–Pb zircon geochronology. Chemical Geology 211, 47–69.

Janousek, V., Farrow, G., Erban, V., 2006. Interpretation of whole–rock geochemical data in igneous geochemistry: Introducing Geochemical Data Toolkit (GCDkit). J. Petrol. 47, 1255–1259.

Jayananda, M. Chardon, D., Peucat, J.J., Capdevila, R., 2006. 2.61 Ga potassic granites and crustal reworking in the western Dharwar craton, southern India: Tectonic, geochronologic and geochemical constraints. Precambrian Research, 150, 1–26.

Kay, R.W., 1978. Aleutian magnesian andesites: melts from subducted Pacific ocean crust. Journal of Volc. Geotherm. Res. 4, 117–132.

Kay, R.W., Mahlburg Kay, S., 1993. Delamination and delamination magmatism. Tectonophysics, 219, 177–189.

Kemp, A.I.S., Hawkesworth, C.J., W.J. Collins, W.J., Gray, C.M., Blevin, P.L., 2009. Isotopic evidence for rapid continental growth in an extensional accretionary orogen: The Tasmanides, eastern Australia. Earth and Planetary Science Letters, 284, 455–466.

Klein, E.L., 2014. Ore fluids of orogenic gold deposits of the Gurupi Belt, Brazil: a review of the physico–chemical properties, sources, and mechanisms of Au transport and deposition. In:

Garofalo, P. S., Ridley, J. R. (eds). Gold–Transporting Hydrothermal Fluids in the Earth's Crust. Geological Society, London, Special Publications, 402, 121–145.

Klein, E.L., Luzardo, R., Moura, C.A.V., Armstrong, R., 2008. Geochemistry and zircon geochronology of paleoproterozoic granitoids: further evidence on the magmatic and rustal evolution of the São Luís cratonic fragment, Brazil. Precambrian Research, 165, 221–242.

Klein, E.L., Moura, C.A.V., 2008. São Luís craton and Gurupi belt (Brazil): possible links with the West African craton and surrounding Pan–African belts. In: Pankhurst, R.J., Trouw, R.A.J., Brito Neves, B.B., de Wit, M.J. (Eds.), West Gondwana: Pre–Cenozoic Correlations across the South Atlantic Region. Geological Society, London, Special Publications, 294, pp. 137–151.

Klein, E.L., Rodrigues, J.B., Lopes, E.C.S., Soledade, G.L., 2012. Diversity of Rhyacian granitoids in the basement of the Neoproterozoic–Early Cambrian Gurupi Belt, northern Brazil: geochemistry, U–Pb zircon geochronology, and Nd isotope constraints on the Paleoproterozoic magmatic and crustal evolution. Precambrian Research, 220-221, 192–216.

Kolb, M., Quadt, A.V., Peytcheva, I., Heinrich, C.A., Fowler, S.J., Cvetkovic, V., 2013. Adakite-like and normal arc magmas: distinct fractionation paths in the East Serbian segment of the Balkan–Carpathian arc. Journal of Petrology 54, 421–451.

Kroner, A., Ekwueme, B.N., Pidgeon, R.T., 2001. The Oldest Rocks in West Africa: SHRIMP Zircon Age for Early Archean Migmatitic Orthogneiss at Kaduna, Northern Nigeria. The Journal of Geology, 109, 399–406.

Kuno, H., 1966. Lateral variation of basaltic magma types across continental margins and island arcs. Bulletin of Volcanology, 29, 195–222.

Kuzmichev, A., Kroner, A., Hegner, E., Dunyi, L., Yusheng, W., 2005. The Shishkhid ophiolite, northern Mongolia: A key to the reconstruction of a Neoproterozoic island–arc system in central Asia. Precambrian Research, 138, 125–150.

Laurent, O., Martin, H., Moyen, J.F., Doucelance, R., 2014. The diversity and evolution of late–Archean granitoids: Evidence for the onset of "modern–style" plate tectonics between 3.0 and 2.5 Ga. Lithos, 205, 208–235.

Lerouge C., Cocherie A., Toteu S.F., Penaye J., Milési J.–P., Tchameni R., Nsifa, E.N.C., Fanning, M., Deloule, E., 2006. Shrimp U–Pb zircon age evidence for Paleoproterozoic sedimentation and 2.05 Ga syntectonic plutonism in the Nyong Group, South–Western Cameroon: consequences for the Eburnean–Transamazonian belt of NE Brazil and Central Africa. Journal of African Earth Sciences, 44, 127–413.

Liégeois, J.P., Abdelsalam, M.G., Ennih, N., Ouabadi, A., 2013. Metacraton: Nature, genesis and behavior. Gondwana Research, 23, 220–237.

Liégeois, J.P., Black, R., 1987. Alkaline magmatism subsequent to collision in the Pan-African belt of the Adrar des Iforas (Mali). Geological Society, London, Special Publications, 30 (1), 381–401.

Liégeois, J.P., Claessens, W., Camara, D., Klerkx, J., 1991. Short-lived Eburnean orogeny in southern Mali. Geology, tectonics, U–Pb and Rb–Sr geochronology. Precambrian Research, 50, 111–136.

Liégeois, J.P., Latouche, L., Boughrara, M., Navez, J., Guiraud, M., 2003. The LATEA metacraton (Central Hoggar, Tuareg shield, Algeria): behaviour of an old passive margin during the Pan-African orogeny. Journal of African Earth Sciences 37, 161–190.

Liégeois, J.P., Navez, J., Hertogen, J., Black, R., 1998. Contrasting origin of post–collisional high–K calc–alkaline and shoshonitic versus alkaline and peralkaline granitoids. The use of sliding normalization. Lithos, 45, 1–28.

Liégeois, J.P., Stern, R.J., 2010, Sr-Nd isotopes and geochemistry of granite-gneiss complexes from the Meatiq and Hafafit domes, Eastern Desert, Egypt: No evidence for pre-Neoproterozoic crust: Journal of African Earth Sciences, 57, 31–40.

Liu, L., Qiu, J.S., Li, Z., 2013. Origin of mafic microgranular enclaves (MMEs) and their host quartz monzonites from the Muchen pluton in Zhejiang Province, Southeast China: Implications for magma mixing and crust–mantle interaction. Lithos, 160–161, 145–163.

Lloyd, F.E., Arima, M., Edgar, A.D., 1985. Partial melting of a phlogopite–clinopyroxenite nodule from south–west Uganda: an experimental study bearing on the origin of highly potassic continental rift volcanics. Contributions to Mineralogy and Petrology 91, 321–329.

Ludwig, K.R., 2003. Isoplot/Ex Version 3. 00: A Geochronological Toolkit for Microsof–tExcel. Berkeley Geochronology Center, Berkeley, CA.

Macambira, M.J.B., Vasquez, M.L., Silva, D.C.C., Galarza, M.A., Barros, C.E.M., Camelo, J.F., 2009. Crustal growth of the central–eastern Paleoproterozoic domain, SW Amazonian craton: Juvenile accretion vs. reworking. J. South Am. Earth Sci., 27, 235–246.

Maniar, P.D., Piccoli, P.M., 1989. Tectonic discriminations of granitoids. Geol. Soc. Amer. Bull. 101, 635–643.

Manya, S., Maboko, M.A.H., 2016. Generation of Palaeoproterozoic tonalites and associated high–K granites in southwestern Tanzania by partial melting of underplated mafic crust in an intracontinental setting: Constraints from geochemical and isotopic data. Lithos, 260, 120–133.

Martin, H., 1986. Effect of steeper Archean geothermal gradient on geochemistry of subduction-zone magmas. Geology, 14 (9), 753–756.

Martin, H., 1994. The Archean grey gneiss and the genesis of continental crust. In: Condie, K.C. (ed.) The Archean Crustal Evolution, Amsterdam: Elsevier, pp. 205-259.

Martin, H., 1999. The adakitic magmas: modern analogues of Archaean granitoids. Lithos 46 (3), 411–429.

Martin, H., Moyen, J.F., 2002. Secular changes in TTG composition: comparison with modern adakites. Geology, 30 (4), 319–322.

Martin, H., Smithies, R.H., Rapp, R., Moyen, J.–F., Champion, D., 2005. An overview of adakite, TTG and sanukitoid: relationships and some implications for crustal evolution. Lithos 79, 1–24.

Martins, G., 2000. Litogeoquímica e Controles Geocronológicos da Suíte Metamórfica Algodões–Choró. Phd Thesis. Universidade Estadual de Campinas, Campinas–SP, p. 220.

Martins, G., Oliveira, E.P., Lafon, J.M., 2009. The Algodões amphibolite–tonalite gneiss sequence, Borborema Province, NE Brazil: geochemical and geochronological evidence for Paleoproterozoic accretion of oceanic plateu/back–arc basalts and adakitic plutons. Gondwana Res. 15, 71–85.

Matteini, M., Dantas, E.L., 2011. Evidences of polyciclic evolution of the cratonic area of Borborema Province using U–Pb and Lu–Hf isotopes in zircon. In: Schmitt, R.S.; Trow, R., Carvalho, I.S.; Collins, A. (eds.). Gondwana 14, Abstracts, Universidade Federal do Rio de Janeiro, p.40.

Matteini, M., Dantas, E.L., Pimentel, M.M., Buhn, B., 2010. Combined U–Pb and Lu–Hf isotope analyses by laser ablation MC–ICP–MS: methodology and applications. Anais da Academia Brasileira de Ciências, 82 (2), 479–491.

McMacpherson, C.G., Dreher, S.T., Thirlwall, M.F., 2006. Adakites without slab melting: high pressure differentiation of island arc magma, Mindanao, the Philippines. Earth and Planetary Science Letters, 243, 581–593.

McReath, I., Faraco, M.T.L., 2006. Paleoproterozoic greenstone–granite belts in Northern Brazil and the former Guyana Shield – west African Craton province. Geol. USP Série Científica 5 (2), 49–63.

Mello, E.F., Xavier, R.P., McNaughton, N.J., Hagemann, S.G., Fletcher, I., Snee, L., 2006. Age constraints on felsic intrusions, metamorphism and gold mineralization in the Palaeoproterozoic Rio Itapicuru greenstone belt, NE Bahia State, Brazil. Miner. Deposita 40, 849–866.

Milhomem Neto, J.M., Lafon, J.M., Galarza, M.A. 2016. First LA–MC–ICP–MS Lu–Hf zircon results for a Rhyacian granitoid and Mesoarchean orthogneiss of the Southeastern Guyana Shield, north of Brazil. 10th South American Symposium on Isotope Geology (SSAGI), 2016, Puerto Vallarta. v. 10.

Moyen, J.F., 2009. High Sr/Y and La/Yb ratios: The meaning of the "adakitic signature". Litohs, 112, 556–574.

Moyen, J.F., 2011. The composite Archaean grey gneisses: Petrological significance, and evidence for a non–unique tectonic setting for Archaean crustal growth. Lithos, 123 (1), 21–36.

Moyen, J.F., Martin, H., 2012. Forty years of TTG research. Lithos 148, 312–336.

Nebel, O., Vroon, P.Z., van Westrenen, W., Iizuka, T., Davies, G.R., 2011. The effect of sediment recycling in subduction zones on the Hf isotope character of new arc crust, Banda arc, Indonesia. Earth and Planetary Science Letters, 303, 240–250.

Neves, S.P., 2003. Proterozoic history of the Borborema province (NE Brazil): Correlations with neighboring cratons and Pan–African belts and implications for the evolution of western Gondwana. Tectonics, 22 (4), p. 1031.

Neves, S.P., 2015. Constraints from zircon geochronology on the tectonic evolution of the Borborema Province (NE Brazil): Widespread intracontinental Neoproterozoic reworking of a Paleoproterozoic accretionary orogeny. Journal of South American Earth Sciences, 58, 150–164.

Nogueira, J.F., 2004. Estrutura, geocronologia e alojamento dos batólitos de Quixadá, Quixeramobim e Senador Pompeu e Ceará Central. PhD Thesis. Universidade Estadual Paulista (UNESP), Rio Claro–SP, p. 123.

Nockolds, S. R., Allen, R., 1953. The geochemistry of some igneous rock series: Geochim. et Cosmochim. Acta, 4, 105-142.

Oh, J.I., Choi, S.H., Yi, K., 2016. Origin of adakite-like plutons in southern Korea. Lithos, 262, 620–635.

Oliveira, E.P., Souza, Z.S., McNaughton, N., Lafon, J.M., Costa, F.G., Figueiredo, A.M., 2011. The Rio Capim volcanic–plutonic–sedimentary belt, São Francisco Craton, Brazil: geological, geochemical and isotopic evidence for oceanic arc accretion during Palaeoproterozoic continental collision. Gondwana Research, 19 (3), 735–750.

Oliveira, J.F., Cavalcante, J.C., 1993. Folha Mombaça. Folha SB–24–V–D–V. Escala: 1:100.000. Geologia e Metalogênese. In: Programa Levantamentos Geológicos Básicos do Brasil. Fortaleza: Serviço Geológico do Brasil, CPRM.

Padilha, A.L., Vitorello, I., Pádua, M.B., Fuck, R., 2017. Cryptic signatures of Neoproterozoic accretionary events in northeast Brazil imaged by magnetotellurics: Implications for the assembly of West Gondwana. Tectonophysics, 699, 164–177.

Parra–Avila, L.A., Belousova, E., Fiorentini, M.L., Baratoux, L., Davis, J., Miller, J., McCuaig, T.C., 2016. Crustal evolution of the Paleoproterozoic Birimian terranes of the Baoulé–Mossi domain, southern West African Craton: U–Pb and Hf–isotope studies of detrital zircons. Precambrian Research, 274, 25–60.

Parra–Avila, L.A., Kemp, A.I.S., Fiorentini, M.L., Belousova, E., Baratoux, L., Block, S., Jessell, M., Bruguier, O., Begg, G.C., Miller, J., Davis, J., McCuaig, T.C., 2017. The geochronological evolution of the Paleoproterozoic Baoulé-Mossi domain of the Southern West African Craton. Precambrian Research, 300, 1–27.

Patiño Douce, A.E., 1999. What do experiments tell us about the relative contributions of crust and mantle to the origin of granitic magmas? Geological Society London Special Publications, 168 (1), 55–75.

Patiño Douce, A.E., Beard, J.S., 1995. Dehydration–melting of biotite gneiss and quartz amphibolite from 3 to 16 kbar. J. Petrol. 36, 707–738.

Peacock, S.M., Rushmer, T., Thompson, A.B., 1994. Partial melting of subducting oceanic crust. Earth Planet. Sci. Lett. 121, 227–244.

Pearce, J.A., 1982.Trace element characteristics of lavas from destructive plate boundaries. In: Thorpe, R.S. (ed) Andesites: Orogenic Andesitesand RelatedRocks. Chichester: JohnWiley, pp.525–548.

Peccerillo, A., Taylor, S.R., 1976. Geochemistry of Eocene calc–alkaline volcanic rocks from the Kastamonu area, northern Turkey. Contrib. Mineral. Petrol. 58, 63–81.

Pe–Piper, G., Piper, D.J.W., Koukouvelas, I., Dolansky, L.M., Kokkalas, S., 2009. Postorogenic shoshonitic rocks and their origin by melting underplated basalts: the Miocene of Limnos, Greece. Geological Society of America Bulletin, 121, 39–54.

Pessoa, R.R., Archanjo, C.J., 1984. Tectônica de empurrões na região de Troia–CE. In: Congresso Brasileiro de Geologia, 33, Rio de Janeiro: SGB, pp. 1721–1728.

Pessoa, R.R., Brito Neves, B.B., Kawashita, K., Pessoa, D.R., Fuck, R.A., 1986. Contribuição ao estudo de evolução geocronológica do Maciço de Troia–CE. In: 12 Simpósio de Geologia do Nordeste, João Pessoa, pp. 1721–1728.

Petersson, A., Scherstén, A., Gerdes, A., 2017. Extensive reworking of Archaean crust within the Birimian terrane in Ghana as revealed by combined zircon U–Pb and Lu–Hf isotopes. Geoscience Frontier, (in press).

Petersson, A., Scherstén, A., Kemp, A.I.S., Kristinsdóttir, B., Kalvig, P., Anum, S., 2016. Zircon U–Pb–Hf evidence for subduction related crustal growth and reworking of Archaean crust within

the Palaeoproterozoic Birimian terrane, West African Craton, SE Ghana. Precambrian Research, 275, 286–309.

Petford, N., Atherton, M., 1996. Na-rich partial melts from newly underplated basaltic crust: The Cordillera Blanca Batholith, Peru. Journal of Petrology, 37, 1491–1521.

Petford, N., Gallagher, K., 2001. Partial melting of mafic (amphibolitic) lower crust by periodic influx of basaltic magma. Earth and Planetary Science Letters, 193, 493–499.

Pinéo, T.R.G., Costa, F.G., 2013. Dados aerogamaespectrométricos aplicados na delimitação do Complexo Cruzeta (Maciço arqueano de Troia), Domínio Ceará Central da Província Borborema. In: 13th International Congress of the Brazilian Geophysical Society, Rio de Janeiro, Brazil, p. 5.

Qian, Q., Hermann, J., 2013. Partial melting of lower crust at 10–15 kbar: constraints on adakite and TTG formation. Contributions to Mineralogy and Petrology 165, 1195–1224.

Rabbia, O.M., Correa, K.J., Hernándes, L.B., Ulrich, T., 2017. "Normal" to adakite-like arc magmatism associated with the El Abra porphyry copper deposit, Central Andes, Northern Chile. International Journal of Earth Sciences, 106 (8), 2687–2711.

Rapp, R.P., Shimizu, N., Norman, M.D., Applegate, G.S., 1999. Reaction between slab-derived melts and peridotite in the mantle wedge: experimental constraints at 3.8 GPa. Chemical Geology, 160, 335– 356.

Rapp, R.P., Watson, E.B., Miller, C.F., 1991. Partial melting of amphibolite/eclogite and the origin of Archean trondhjemites and tonalites. Precambrian Research, 51 (1–4), 1–25.

Rey, P., Vanderhaeghe, O., Teyssier, C., 2001. Gravitational collapse of the continental crust: definition, regimes and modes. Tectonophysics 342, 435–449.

Ribeiro, J.M., Maury, R.C., Grégoire, M., 2016. Are Adakites Slab Melts or High-pressure Fractionated Mantle Melts? Journal of Petrology, 57 (5), 839–862.

Richards, J.P., Kerrich, R., 2007. Adakite-like rocks: their diverse origins and questionable role in metallogenesis. Economic Geology, 102, 537–576.

Rollinson, H.R., 1993. Using Geochemical Data: Evaluation, Presentation, Interpretation. Longman House, Harlow, 352 p.

Rooney, T.O., Franceschi, P., Hall, C.M., 2010. Water-saturated magmas in the Panama Canal region: a precursor to adakite-like magma generation? Contributions to Mineralogy and Petrology.

Rosa–Costa, L.T., Lafon, J.M., Delor, C., 2006. Zircon geochronology and Sm–Nd isotopic study: further constraints for the Archean and Paleoproterozoic geodynamical evolution of the southeastern Guiana Shield, north of Amazonian Craton, Brazil. Gondwana Research, 10 (3–4), 277–300.

Rubatto, D., Gebauer, D., 2000. Use of cathodoluminescence for U–Pb zircon dating by ion microprobe: some examples from the Western Alps. In: Pagel, M., Barbin, V., Blanc, P., Ohnenstetter, D. (Eds.), Cathodoluminescence in Geosciences. Springer, Berlin, pp. 373–400.

Rushmer, T., 1991. Partial melting of two amphibolites: contrasting experimental results under fluid absent conditions. Contributions toMineralogy and Petrology 107, 41–59.

Safonova, I., Kotlyyarov, A., Krivonogov, S., Xiao, W., 2017. Intra–oceanic arcs of the Paleo–Asian Ocean. Gondwana Research, (in press).

Şahin, S.Y., 2005. Geochemistry of mafic microgranular enclaves in the Tamdere Quartz Monzonite, south of Dereli/Giresun, Eastern Pontides, Turkey. Chemie der Erde – Geochemistry, 68 (1), 81–92.

Santos, M.M., 2015. Desenvolvimento de padrões de zircão para geocronologia U–Pb e análises isotópicas de Hf por Laser Abaltion ICP–MS. Dissertação de Mestrado, Universidade Federal de Ouro Preto, 115 p.

Santos, T.J.S., Fetter, A.H., Nogueira Neto, J.A., 2008. Comparison between the northwestern Borborema Province, NE Brazil, and the southwestern Pharusian Dahomey Belt, SW Central Africa. In: Pankhurst, R.J., Trouw, R.A.J., Brito Neves, B.B., de Wit, M.J. (Eds.), West Gondwana: Pre–Cenozoic Correlations across the South Atlantic Region, vol. 294. Geological Society of London, pp. 101–119. Special Publications.

Santos, T.J.S., Fetter, A.H., Van Schmus, W.R., Hackspacher, P.C., 2009. Evidence for 2.35 to 2.30 Ga Juvenile Crustal Growth in the Northwest Borborema Province, NE Brazil, vol. 323. Geological Society, London, pp. 271–281. Special Publications.

Santos, L.C.M.L., Dantas, E.L., Cawood, P.A., Santos, E.J., Fuck, R.A., 2017. Neoarchean crustal growth and Paleoproterozoic reworking in the Borborema Province, NE Brazil: Insights from geochemical and isotopic data of TTG and metagranitic rocks of the Alto Moxotó Terrane. Journal of South American Earth Science, 79, 342–363.

Sato, K., Basei, M.A.S., Siga, O.J., 2008. New techniques applied to U–Pb method at CPGeo – Igc/USP: advances in chemical digestion, mass spectrometry (TIMS) and examples of application integrated with SHRIMP. Geologia USP Série Científica, 8, 77–99.

Sato, K., Tassinari, C.C.G., Basei, M A.S., Siga Júnior, O., Onoe, A.T., Souza, M.D., 2014. Sensitive High Resolution Ion Microprobe (SHRIMP IIe/MC) of the Institute of Geosciences of the University of São Paulo, Brazil: analytical method and first results. Geologia USP Série Científica, 14, 3–18.

Saunders, A.D., Norry, M.J., Tarney, J., 1991. Fluid influence on the compositions of subduction zone magmas. Philosophical Transactions of the Royal Society of London, 335, 377–392.

Scholl, D.W., von Huene, R., 2009. Implications of estimated magmatic additions and recycling losses at the subduction zones of accretionary and collisional orogens. Geological Society London Special Publications, 318, 105–125.

Shao, W.Y., Chung, S.L., Chen, W.S., Lee, H.Y., Xie, L.W., 2015. Old continental zircons from a young oceanic arc, eastern Taiwan: Implications for Luzon subduction initiation and Asian accretionary orogeny. Geology, 43 (6), 479–482.

Silva, L.C., Armstrong, R., Pimentel, M.M., Scandolara, J., Ramgrab, G., Wildner, W., Angelim, L.A.A., Vasconcelos, A.M., Rizzoto, G., Quadros, M.L.E.S., Sander, A., Rosa, A.L.Z., 2002. Reavaliação da evolução geológica em terrenos Pré–Cambrianos brasileiros com base em novos dados U–Pb SHRIMP, Parte III: Província Borborema, Mantiqueira Meridional e Rio Negro–Juruena. Rev. Bras. Geociências 32, 529–544.

Silva, L.C., Costa, F.G., Armstrong, R., McNaugthon, N.J., 2014. U–Pb (SHRIMP) zircon dating and Nd isotopes at basement inliers from northern Borborema Province, Ceará State, NE Brazil: evidences for the Archean and Paleoproterozoic crustal evolution. In: 9th South American Symposium on Isotope Geology, São Paulo, Brazil, p. 175.

Silva, L.C., MacNaughton, N.J., Vasconcelos, A.M., Gomes, J.R.C., Fletcher, I.R., 1997. U–Pb SHRIMP ages in southern State of Ceará, Borborema Province, NE Brazil: Archean TTG accretion and Proterozoic crustal reworking. In: Second International Symposium on Granites and Associated Mineralizations, Salvador, p. 280.

Silva, M.G., Coelho, C.E.S., Teixeira, J.B.G., Alves da Silva, F.C., Silva, R.A., Souza, J.A.B., 2001. The Rio Itapicuru greenstone belt, Bahia, Brazil: geologic evolution and review of gold mineralization. Miner. Deposita, 36, 345–357.

Sisson, T.W., Ratajeski, K., Hankins, W.B., Glazner, A.F., 2005. Voluminous granitic magmas from common basaltic sources. Contrib Mineral Petrol., 148, 635–661.

Sláma, J., Košler, J., Condon, D.J., Crowley, J.L., Gerdes, A., Hanchar, J.M., Horstwood, M.S.A., Morris, G.A., Nasdala, L., Norberg, N., Schaltegger, U., Schoene, B., Tubrett, M.N., Whitehouse, M.J., 2008. Plešovice zircon – a new natural reference material for U–Pb and Hf isotopic microanalysis. Chemical Geology, 249, 1–35.

Smithies, R.H., Champion, D.C., 1999. High-Mg diorite from the Archean Pilbara Craton; anorogenic magmas derived from a subduction–modified mantle. Geological Survey of Western Australia, Annual Review, 1998–1999, 45–59.

Sousa, H.P., 2016. Caracterização das unidades máfica–ultramáficas e potencial metalogenético da sequência metavulcanossedimentar Serra das Pipocas (Ceará): um provável greenstone belt. Master Dissertation, Universidade Federal do Ceará, Ceará–CE, 203 p.

Souza, Z.S., Martin, H., Peucat, J.J., Jardim de Sá, E.F., Macedo, M.H.F., 2007. Calc–alkaline magmatism at the Archean–Proterozoic transition: the Caicó complex basement (NE Brazil). J. Petrol. 48, 2149–2185.

Souza, Z.S., Kalsbeek, F., Deng, X.D., Frei, R., Kokfelt, T.F., Dantas, E.L., Li, J.W., Pimentel, M.M., Galindo, A.C., 2016. Generation of continental crust in the northern part of the Borborema Province, northeastern Brazil, from Archaean to Neoproterozoic. Journal of South American Earth Sciences, 68, 68–96.

Spencer, C.J., Cawood, P.A., Hawkesworth, C.J., Prave, A.R., Roberts, N.M., Horstwood, M.S., Whitehouse, M.J., 2015. Generation and preservation of continental crust in the Grenville Orogeny. Geoscience Frontiers, 6, 357–372.

Stacey, J.S., Kramers, J.D., 1975. Approximation of Terrestrial Lead Isotope Evolution by a 2–stage Model. Earth and Planetary Science Letters, 26 (2), 207–221.

Stern, R.J., Ali, K.A., Liégeois, J.P., Johnson, P.R., Kozdroj, W., Kattan, F.H., 2010. Distribution and significance of pre-Neoproterozoic zircons in juvenile Neoproterozoic igneous rocks of the Arabian-Nubian shield. American Journal of Science, 310, 791–811.

Stern, C.R., 2011. Subduction erosion: rates, mechanisms, and its role in arc magmatism and the evolution of the continental crust and mantle. Gondwana Research, 20, 284–308.

Stern, R.A., Hanson, G.N., Shirey, S.B., 1989. Petrogenesis of mantle-derived, LILE-enriched Archean monzodiorites and trachyandesites (sanukitoids) in southwestern Superior Province. Canadian Journal of Earth Sciences, 26, 1688–1712.

Stern, R.J., Scholl, D.W., 2010. Yin and Yang of continental crust creation and destruction by plate tectonic processes. International Geology Review, 52, 1–31.

Streckeisen, A.L., 1976. To each plutonic rock its proper name. Earth-Science Reviews, 12, 1–33.

Sun, S.S., Mcdonough, W.F., 1989. Chemical and isotopic systematics of oceanic basalts: implications for mantle composition and processes. In: Saunders, A.D., Norry, M.J. (Eds.), Magmatism in Ocean Basins, vol. 42. Geol. Soc. London Spec, pp. 315–345.

Tapsoba, B., Lo, C.H., Jahn, B.M., Chung, S.L., Wenmenga, U., Iizuka, Y., 2013. Chemical and Sr–Nd isotopic compositions and zircon U–Pb ages of the Birimian granitoids from NE Burkina Faso, West African Craton: Implications on the geodynamic setting and crustal evolution. Precambrian Res., 224, 364–396.

Tapster, S., Roberts, N.M.W., Petterson, M.G., Saunders, A.D., Naden, J., 2014. From continent to intra–oceanic arc: Zircon xenocrysts record the crustal evolution of the Solomon island arc. Geology, 42 (12), 1087–1090.

Tatsumi, Y., Hamilton, D.L., Nesbitt, R.W., 1986. Chemical characteristics of fluid phase released from a subducted lithosphere and origin of arc magmas: evidence from high-pressure experiments and natural rocks. Journal of Volcanology and Geothermal Research, 29, 293–309.

Tatsumi, Y., Ishizaka, K., 1982. Origin of high-magnesian andesites in the Setouchi volcanic belt, southwest Japan, I. Petrographical and chemical characteristics. Earth and Planetary Science Letters, 60 (2), 293–304.

Teixeira, W., Ávila, C.A., Dussin, I.A., Corrêa Neto, A.V., Bongiolo, E.M., 2015. A juvenile accretion episode (2.35–2.32 Ga) in the Mineiro belt and its role to the Minas accretionary orogeny: Zircon U–Pb–Hf and geochemical evidences. Precambrian Research, 256, 148–169.

Torres, P.F.M., Cavalcante, J.C., Palheta, E.S.M., Vasconcelos, A.M., Oliveira, F.V., 2007. Folha Quixadá. Folha SB–24–V–B, Escala 1:250.000. Geologia e Metalogênese. In: Programa Levantamentos Geológicos Básicos do Brasil. Fortaleza: Serviço Geológico do Brasil. CPRM.

Tulibonywa, T., Manya, S., Torssander, P., Maboko, M.A.H., 2017. Geochemistry of the Palaeoproterozoic volcanic and associated potassic granitic rocks of the Ngualla area of the Ubendian Belt, SW Tanzania. Journal of African Earth Sciences, 129, 291–306.

Van Achterbergh, E., Ryan, C.G., Jackson, S.E., Griffin, W., 2001. Data reduction soft–ware for LA–ICP–MS. In: Sylvester, P. (Ed.), Laser Ablation ICPMS in the EarthScience, 29. Mineralogical Association of Canada, pp. 239–243.

Van Schmus, W.R., Kozuch, M., Brito Neves, B.B., 2011. Precambrian history of the Zona Transversal of the Borborema Province, NE Brazil: Insights from Sm–Nd and U–Pb geochronology. Journal of South American Earth Sciences, 31, 227–252.

Vanderhaeghe, O., Ledru, P., Thiéblemont, D., Egal, E., Cocherie, A., Tegyey, M., Milési, J.P., 1998. Contrasting mechanism of crustal growth: geodynamic evolution of the Paleoproterozoic granite–greenstone belts of French Guiana. Precambrian Research, 92 (2), 165–193.

Vasquez, M.L., Macambira, M.J.B. Armstrong, R.A., 2008. Zircon geochronology of granitoids from the western Bacajá domain, southeastern Amazonian craton, Brazil: Neoarchean to Orosirian evolution. Precambrian Research, 161(3–4), 279–302.

Vauchez, A., Neves, S.P., Caby, R., Corsini, M.E.S., Arthaud, M.H., Amaro, V., 1995. The Borborema shear zone system, NE Brazil. J. South Am. Earth Sci. 8, 247–266.

Verma, S.K., Oliveira, E.P., 2014. Tectonic setting of basic igneous and metaigneous rocks of Borborema Province, Brazil using multi–dimensional geochemical discrimination diagrams. J. South Am. Earth Sci., 58, 309–317.

Wane, O., Liégeois, J.P., Thébaud, Miller, J., Metelka, V., Jessell, M. (2018). The onset of the Eburnean collision with the Kenema-Man craton evidenced by plutonic and volcanosedimentary rock record of the Masssigui region, southern Mali. Precambrian Research, 305, 444–478.

Watkins, J.M., Clemens, J.D., Treloar, P.J., 2007. Archean TTGs as sources of younger granitic magmas: melting of sodic metatonalites at c. 0.6–1.2 GPa. Contributions to Mineralogy and Petrology, 154, 91–110.

Whitmeyer, S.J., Karstrom, K.E., 2007. Tectonic model for the Proterozoic growth of North America. Geosphere, 3 (4), 220–259.

Williams, I., 1998. U–Th–Pb geochronology by ion microprobe. In: McKibben, M.A., Shanks, III W.C., Ridley, W.I., (eds.). Applications of microanalytical techniques to understanding mineralizing processes. Society of Economic Geologists. Short course, 7, 1–35.

Wilson, M., 1989. Igneous Petrogenesis. A Global Tectonic Approach. Academic–Division of Unwin Hyman Ltd., Landon, 466 p.

Zellmer, G.F., Iizuka, Y., Miyoshi, M., Tamura, Y., Tatsumi Y., 2012. Lower crustal H_2O controls on the formation of adakitic melts. Geology, 40, 487–490.

Zhao, J.H., Zhou, M.F., 2008. Neoproterozoic adakitic plutons in the northern margin of the Yangtze Block, China: Partial melting of a thickened lower crust and implications for secular crustal evolution. Lithos 104, 231–248.

3. (2º ARTIGO): FLUID INCLUSION AND STABLE ISOTOPE (O, H, C) CONSTRAINTS ON THE GENESIS OF THE PEDRA BRANCA GOLD DEPOSIT, TROIA MASSIF, BORBOREMA PROVINCE, NE BRAZIL: A HYPOZONAL OROGENIC GOLD MINERALIZATION SOURCED BY MAGMATIC–HYDROTHERMAL FLUID (Artigo submetido – *Ore Geology Reviews*)

Artigo submetido para revista **Ore Geology Reviews**

Submetido em 19 de outubro de 2018

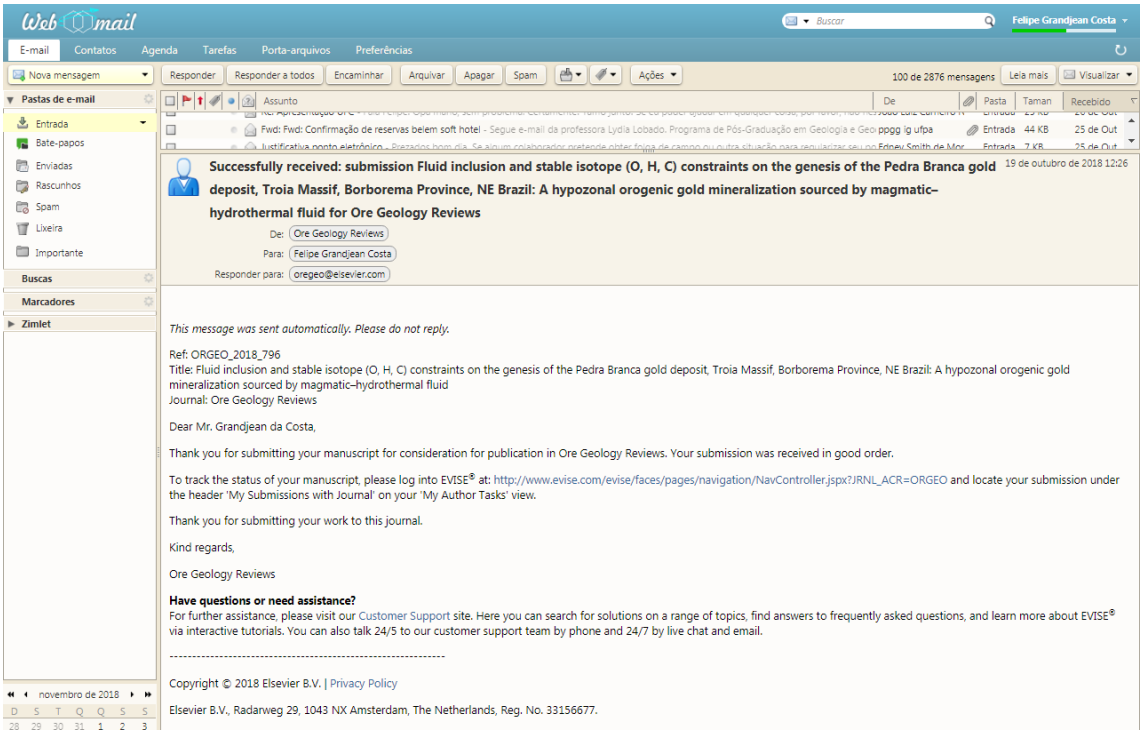

Fluid inclusion and stable isotope (O, H, C) constraints on the genesis of the Pedra Branca gold deposit, Troia Massif, Borborema Province, NE Brazil: A hypozonal orogenic gold mineralization sourced by magmatic–hydrothermal fluid

Felipe Grandjean da Costa[a,b,c], Evandro Luiz Klein[d,b,c], Chris Harris[e], Sherissa Roopnarain[e]

[a] *Geological Survey of Brazil, Fortaleza, CE, Brazil*
[b] *GPGE – Grupo de Pesquisas em Geologia Econômica, Federal University of Pará, Belém, PA, Brazil*
[c] *PPGG – Programa de Pós-Graduação em Geologia e Geoquímica, Federal University of Pará, Belém, PA, Brazil*
[d] *Geological Survey of Brazil, Brasília, DF, Brazil*
[e] *Department of Geological Sciences, University of Cape Town, Rondebosch, South Africa*

Abstract

At the Archean–Paleoproterozoic Troia Massif, NE Brazil, two major Paleoproterozoic greenstone belts are recognized (Algodões and Serra das Pipocas). These share similar lithostratigraphic characteristics with other 2.2–2.1 Ga greenstone belts of the surrounding cratonic domains (e.g. Guiana shield and West Africa craton). Gold mineralization in the Serra das Pipocas greenstone belt is associated with a regional NE–trending shear zone. In the mineralized area (the Pedra Branca gold deposit) the main gold mineralization is found in association with quartz veins, calc–silicate alteration (e.g. diopside, K–feldspar, amphibole, titanite, biotite, pyrite, albite, magnetite ± carbonates) and abitization. Pyrrhotite is commonly found as inclusions in pyrite, and late magnetite substitutes pyrite, suggesting progressive oxidation of the ore–forming fluid. Free–milling gold commonly precipitates at the late stages of alteration, in close association with magnetite and tellurides. The main tellurides found are hessite, altaite, sylvanite, calaverite and tellurobismuthite. Two fluid inclusion assemblages were identified from mineralized quartz veins. Assemblage 1 is characterized by pseudo–secondary trails that show the coexistence of CO_2–rich and low salinity (0 to 8 wt% NaCl equiv.) CO_2–H_2O–NaCl and H_2O–NaCl inclusions, suggesting formation during phase separation (fluid immiscibility). Assemblage 2 is represented by late secondary low–temperature (Th<200°C) H_2O–NaCl inclusions, probably unrelated to gold mineralization. The $\delta^{18}O$, δD and $\delta^{13}C$ values of hydrothermal minerals (quartz, calcite, biotite, hornblende and magnetite) and fluid inclusions are compatible with a magmatic–hydrothermal ore–forming fluid that underwent fluid–rock interaction with the greenstone pile. The calculated fluid $\delta^{18}O$ values range from +8.3 to +11.0‰ (n=59), fluid δD from -98 to -32‰ (n=24) and $\delta^{13}C$ values of calcite from -6.35 to -9.40‰ (n=3). Oxygen isotope thermometry for quartz–magnetite pairs gave temperatures from 467 to 526°C (n=7, average 503°C). This probably represents the temperature of gold deposition, because gold is generally associated to magnetite in the ore mineral assemblage. The possible range of PT conditions for gold mineralization from 467 °C and 1.93 kbar (7 km) to 526 °C and 3.48 kbar (13 km) was obtained from the intersection of isochores with the temperature range from the quartz–magnetite isotopic geothermometer. This PT range is akin to hypozonal orogenic gold deposits. The association of gold with magnetite and tellurides strongly suggests an ore–forming fluid sourced by oxidized magmas, similar to those interpreted as 'orogenic oxidized intrusion–related gold deposits' in other Precambrian greenstone belts (e.g. Abitibi and Eastern Goldfields).

Key words: OXIDIZED, HYPOZONAL, OROGENIC, GOLD

3.1. Introduction

A deep discussion exists in the literature over the source of gold and hydrothermal fluids associated with orogenic gold deposits. Most researchers are divided between two hypotheses; (1) a metamorphic–hydrothermal source (e.g. Kerrich and Fyfe, 1981; Pitcairn et al., 2006; Tomkins and Grundy, 2009; Phillips and Powell, 2010; Tomkins, 2010; Large et al., 2012; Tomkins, 2013, Goldfarb and Groves, 2015) or (2) a magmatic–hydrothermal source (e.g. Bucci et al., 2002; Duuring et al., 2007; Kendrick et al., 2011; Beakhouse, 2011; Xue et al., 2013; Doublier et al., 2014; Treloar et al., 2015; Zhang et al., 2017; Spence–Jones et al., 2018). Fluids of metamorphic origin are generally interpreted as being derived from the metamorphism of supracrustal rocks, such as mafic metavolcanic rocks (e.g. Elmer et al., 2006; Bierlein and Pisarevsky, 2008; Phillips & Powell, 2010), and turbidites and black shales rich in diagenetic pyrite (Large et al., 2012; Pitcairn et al., 2015). Most metamorphic fluids are released before the rock reaches temperatures of around 500–550°C (amphibolite facies metamorphism), and very little fluid is released above 550°C (Tomkins, 2010; 2013). This is consistent with most orogenic gold deposits, as these are generally associated with greenschist to lower–amphibolite metamorphic facies (Groves et al., 1998), so the source of fluid may be inferred as progressive metamorphic devolatilization that occurred some kilometers below the deposit site (Phillips & Powell, 2010). However, for hypozonal orogenic gold deposits (12 to 20 km deep), the fluids cannot be easily explained by devolatization during metamorphism and, as a result, some authors disagree with the crustal continuum model elaborated by Groves (1993) (Tomkins & Grundy, 2009; Phillips & Powell, 2009). For high–temperature (hypozonal) orogenic gold deposits, the source of fluids (and gold) is commonly associated with magmatic–hydrothermal processes, and syn– to late–collisional granitoids are generally interpreted as the main sources of fluids and gold (e.g. Mueller, 1992; Bucci et al., 2002; Duuring et al., 2007; Doublier et al., 2014). Generally, for orogenic gold deposits associated with granitoids, the source of fluids is constrained by isotopic (stable and radiogenic) data and fluid inclusions, as well as the close space/time association between mineralizations and granitoids (e.g. Bucci et al., 2002; Salier et al., 2005; Duuring et al., 2007; Doublier et al., 2014; Zhang et al., 2017). Within the context of magmatic–hydrothermal fluids, some authors also refer to the contribution of mantle–derived fluids when associated with mafic and ultramafic magmas contemporaneous with gold mineralization (e.g. Rock et al., 1989; Mao et al., 2008; Vielreicher et al., 2010; Hronsky et al., 2012; Griffin et al., 2013). Fluids derived from other processes, such as granulitization of the lower crust, dehydration of subducted oceanic crust and devolatilization of the metasomatized lithospheric mantle are also reported

in the literature (e.g. Pope et al., 2011; Fu et al., 2014; Groves and Santosh, 2016; Zhao et al., 2018).

The Troia Massif, in northeastern Brazil, represents one of the main Archean-Paleoproterozoic nuclei in the northern portion of the Borborema Province and hosts gold mineralization (Pedra Branca deposit) in granite-greenstone terrain of Paleoproterozoic age (Costa et al., 2015; 2016; 2018) (**Fig. 3.1A** and **B**). A study of whole–rock geochemistry and U–Pb–Hf isotopes for Paleoproterozoic plutonic rocks intrusive in the Serra das Pipocas greenstone belt (Costa et al., 2018), infers crustal growth (subduction-accretion) and reworking (collision) processes similar to many others c. 2.2–2.0 Ga Birimian/Transamazonian granite-greenstone terranes of São Luís-West African craton (Liégeois et al., 1991; Feybesse et al. 2006; Klein et al., 2008, 2012; Block et al., 2016; Petersson et al., 2016, 2017) and correlated terranes of the Guyana shield (Amazon craton) (Vanderhaeghe et al., 1998; Delor et al., 2003; Rosa-Costa et al., 2006; McReath and Faraco, 2006; Hoffmann et al., 2018) and northern São Francisco craton (Silva et al., 2001; Costa et al., 2011; Oliveira et al., 2011).

The principal aspects of gold mineralization in the Paleoproterozoic Serra das Pipocas greenstone belt are similar to those in the proposed classification of Groves et al. (1998) for orogenic gold deposits, which involves quartz veins, shear zones, regional association with terrane boundaries, and late age (2029 ± 28 Ma U-Pb age in titanite) of gold mineralization in the geotectonic context of the country rocks (2200–2068 Ma) (Costa et al., 2016; 2018; submitted). The hydrothermal assemblage of the Pedra Branca gold deposit is generally composed of diopside – amphibole – biotite – titanite – pyrite – magnetite – quartz ± carbonate, typical of high-temperature (hypozonal) alteration. Therefore, being a potential example of high–temperature hypozonal orogenic gold mineralization, the source of fluids is, as aforementioned, more likely to be related with magmatic–hydrothermal processes. In this article, we present field geology, petrography of ore–related minerals, fluid inclusion and stable isotope (O, H, C) data, with the aim of discussing the genetic model for the Pedra Branca gold deposit, emphasizing the possible source(s) of fluid(s) of the mineralization (e.g., whether magmatic and/or metamorphic in origin).

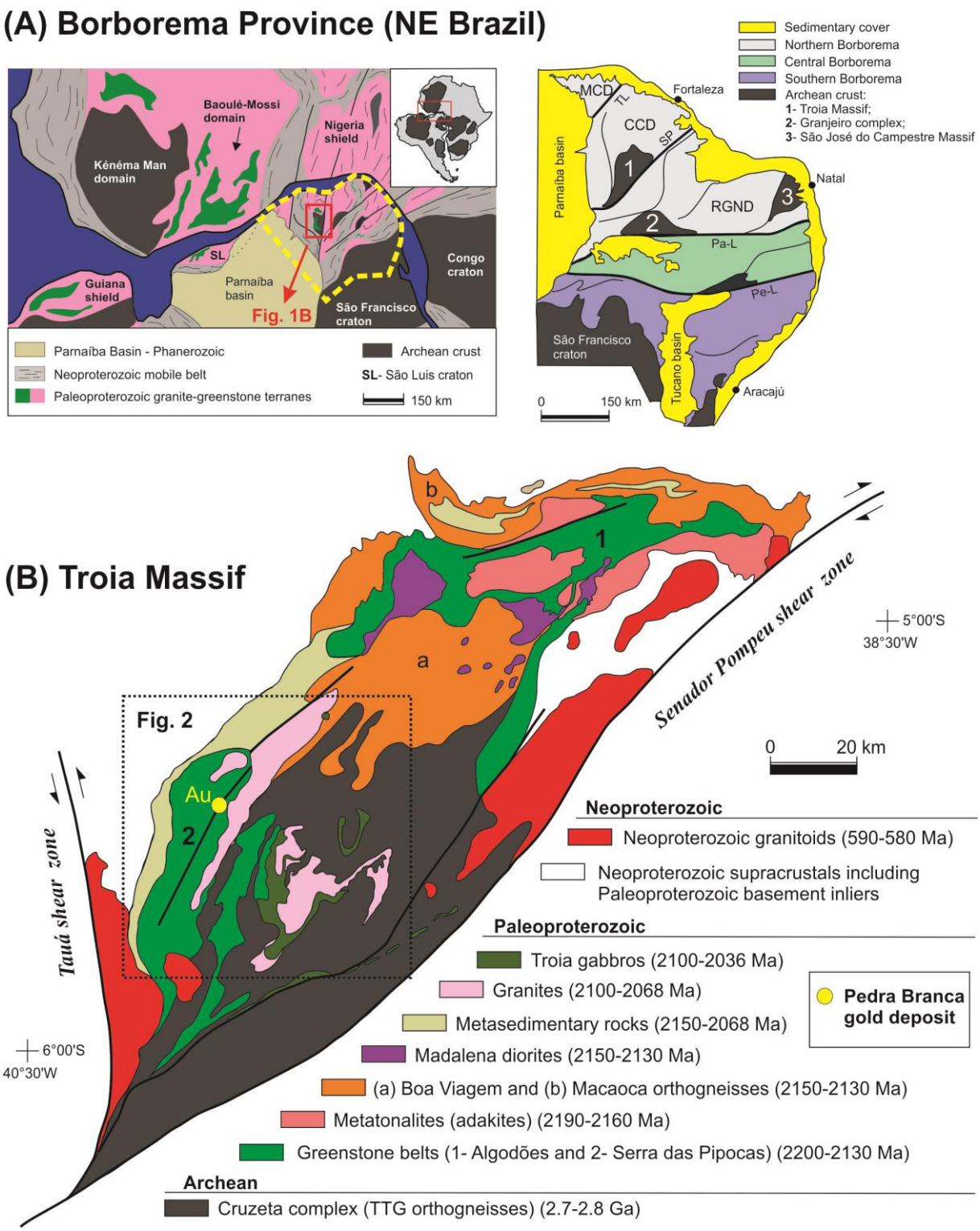

Fig. 3.1. *Simplified geological framework of the Borborema Province and Troia Massif: (A) Yellow dashed line locates Borborema Province in the pre–drift reconstruction of South America and Africa (modified from Arthaud et al., 2008); and (at right) schematic map of the Borborema Province with three major subdivisions delimited by the Patos (Pa–L) and the Pernambuco Lineaments (Pe–L). Tectonic domains are according to Fetter et al. (2000); MCD= Médio Coreaú Domain, CCD= Ceará Central Domain and RGND= Rio Grande do Norte Domain, and shear zones are SP= Senador Pompeu shear zone and TL= Transbrasiliano lineament (or Sobral–Pedro II shear zone). (B) Simplified geological map of the Troia Massif (Modified from Costa et al., 2015).*

3.2. Regional geology

3.2.1. Borborema Province and its basement nuclei

The Borborema Province represents part of a large continental collision between the São Luis–West African and São Francisco–Congo cratons, around 600 Ma, associated with the Pan–African/Brasiliano orogenic cycle (Almeida et al., 1981). This tectonic unit of the West Gondwana supercontinent (**Fig. 3.1A**) has, as its main structural feature, an extensive network of transcurrent shear zones with associated Neoproterozoic magmatism (e.g., Vauchez et al., 1995; Nogueira, 2004). For the northern Domain of the Borborema Province, limited to the south by the Patos shear zone (**Fig. 3.1A**), the basement rocks are mostly of paleoproterozoic ages (e.g., Fetter et al., 2000; Hollanda et al., 2011), and locally, with Archean crustal domains (Silva et al., 1997; Fetter, 1999; Dantas et al., 2004; Freimann, 2014; Ganade et al., 2017). The latter are mainly represented by the Granjeiro Complex, São José do Campestre Massif and the Troia Massif (**Fig. 3.2A**).

3.2.2. The Serra das Pipocas greenstone belt

The first structural and lithological mapping in the central–west part of the Troia Massif was presented by Pessoa and Archanjo (1984). According to these authors, a thrust tectonics is responsible for the allochthonous character of the metavolcano–sedimentary sequences and related mafic–ultramafic metaplutonic rocks, overlying the gneiss–migmatitic basement of the Troia Massif. Additional work, with Rb–Sr and K–Ar geochronological data, evidenced that the Troia Massif exhibits a polycyclic character, with Archean and Paleoproterozoic rocks, mostly presenting K–Ar and Rb–Sr isotopic rejuvenation during the Neoproterozoic (Brasiliano) orogenic event (Pessoa et al., 1986). However, even with the record of Neoproterozoic (Brasiliano) isotopic disturbance, these authors suggested that the thrust tectonic in the Troia Massif is Paleoproterozoic in age.

The Serra das Pipocas greenstone belt (or Troia metavolcano–sedimentary sequence), in the central–west portion of the Troia Massif (**Fig. 3.1B** and **3.2**) is composed of metabasalts (amphibolites), felsic to intermediate metavolcanic rocks, metasedimentary rocks, metacherts, marbles, serpentinites, and associated S–type leucogranite, tonalitic (Adakite–like) intrusions and mafic–ultramafic metaplutonic rocks (Pessoa and Archanjo, 1984; Pessoa et al., 1986; Cavalcante et al., 2003; Costa et al., 2014a; Sousa, 2016; Costa et al., 2018). According to Pessoa and Archanjo (1984), metabasalt with pillow–like structures was locally identified.

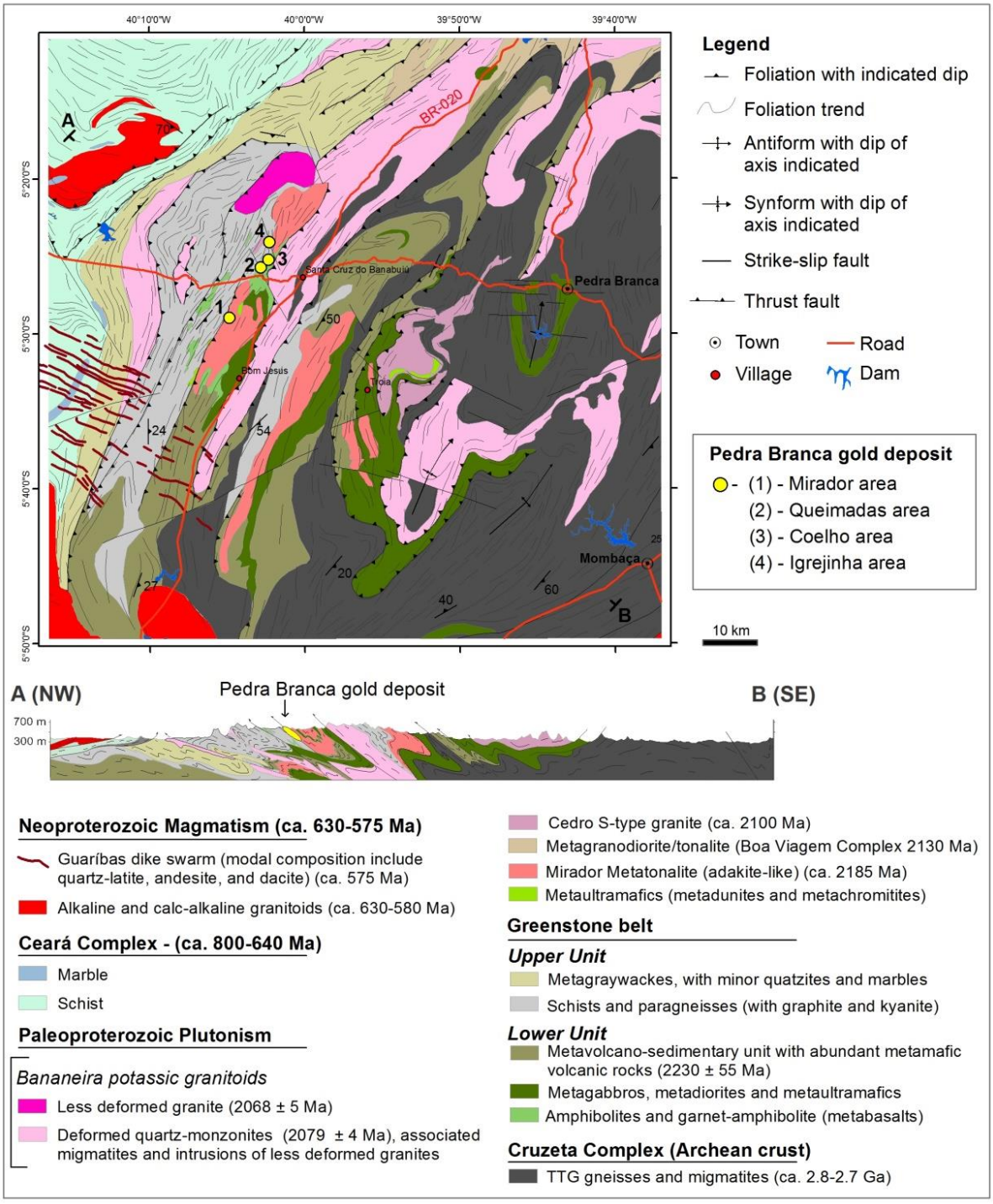

Fig. 3.2*. Geological map of the area showing the principal mineralized areas of the Pedra Branca gold deposit (modified from Costa et al., 2018).*

The mafic metavolcanic rocks shows transitional tholeiitic to calc–alkaline affinity and arc–related geochemical signatures, suggesting an arc/back–arc tectonic setting to this volcanism (Sousa, 2016). U–Pb (in situ) zircon ages in metasedimentary and intrusive rocks confirmed the Paleoproterozoic (Rhyacian c. 2.2–2.0 Ga) age for the Serra das Pipocas metavolcano–sedimentary sequence and related metamafic–ultramafic rocks in the Troia

Massif (Costa et al., 2014a, 2014b; Sousa, 2016). U–Pb detrital zircon dating of a metagreywacke of the metavolcano–sedimentary sequence yielded a younger age population around 2200 Ma and older ($^{207}Pb/^{206}Pb$) ages of 3096 ± 53 Ma, 3074 ± 55 Ma, 2608 ± 54 and 2546 ± 55 Ma, which indicates a mixture of Archean and Rhyacian sources and a maximum depositional age of c. 2.2 Ga (Costa et al., 2014a). The presence of Archean detrital zircon grains suggests an ensialic (or continental proximity) setting for part of this granite–greenstone terrane (Costa et al., 2014a). The mafic and ultramafic metaplutonic rocks are more abundant in the central Troia region (**Fig. 3.1B**), and are mainly interpreted as fragmented layered bodies, well–known because of the platinum and palladium mineralization in metachromitites (Pessoa and Archanjo, 1984; Angeli et al., 2009; Barrueto and Hunt, 2010). A Sm–Nd isochron of c. 2060 Ma was obtained for this mafic–ultramafic magmatism (Liégeois, unpublished data; cited by Fetter, 1999), recently attested by a U–Pb (SHRIMP) zircon age of 2036 ± 28 Ma obtained for a PGE–bearing metachromitite sample (Costa et al., 2014b).

Based on the U–Pb ages (SHRIMP and LA–ICPMS) in zircon and litogeochemical data for the felsic and intermediate metaplutonic rocks, two main plutonic events can be recognized at the Serra das Pipocas granite–greenstone terrain; (1) (2190–2180 Ma) Tonalitic magmatism (Mirador suite) with geochemical affinity similar to those of adakite–like rocks, being exclusively intrusive in the metavolcano–sedimentary sequence, and (2) (2090–2060 Ma) K–rich plutonism (Bananeira suite) represented by deformed quartz monzonites, and less deformed granites (Costa et al., 2018) (**Fig. 3.2**). All these plutons are generally foliated and locally have gneissic banding, due to deformation under lower– to mid–amphibolite facies metamorphism during the Transamazonian (2.2 to 2.0 Ga) and/or Brasiliano (650–535 Ma) orogenies (Costa et al., 2018). In the Serra das Pipocas greenstone belt, deformation and metamorphism occurred under lower– to mid–amphibolite facies metamorphism, but no partial melting has been observed (e.g. Pessoa and Archanjo, 1984; Pessoa et al., 1986; Sousa, 2016). The Archean basement gneisses and migmatites of the Troia Massif show generally more complex poly–deformational patterns than the greenstone sequence, but the dominant structures observed in both greenstone belt and basement rocks are east–dipping foliation (30 to 55°) with associated low–rake stretching lineation plunging 20–35° to NE (**Fig. 3.2**). Many local– and regional–scale fold axis also plunge 20–35° toward NE (**Fig. 3.2**). The NE-SW trending foliations, and the NE–directed lineations and fold axis in these rocks are in structural concordance with the dextral strike–slip Neoproterozoic Senador Pompeu shear zone, suggesting Brasiliano age deformation (**Fig. 3.1B**). However, according to Costa et al.

(2018), the occurrence of less–deformed 2068 Ma granites crosscutting strongly deformed 2079 Ma quartz–monzonites, evidence that Paleoproterozoic deformation is also preserved in this area.

3.3. Pedra Branca gold deposit

Recently, gold mineralization was identified in the Serra das Pipocas greenstone belt, in the western region of the Troia Massif (**Fig. 3.1B** and **3.2**). Gold mineralization occurs associated with NE–SW regional shear zones, crosscutting metavolcano–sedimentary rocks at amphibolite facies conditions. The mineralization occurs in quartz veins associated with zones of hydrothermal alteration, measuring hundreds of meters along the strike, with 1 to 5 meters of thickness, containing ~1 g/t up to 7 g/t of gold (Lopez, 2012). However, no economic report has been released yet for the Pedra Branca gold deposit. The main mineralized areas worked by private companies are referred to as Mirador, Queimadas, Coelho and Igrejinha (**Fig. 3.2**) (Lopez, 2012). Recent works on the genesis of the Pedra Branca gold deposit, suggest that this is an epigenetic gold mineralization, associated to quartz veins and high–temperature hydrothermal alteration in the host rocks (Costa et al., 2016; submitted). According to Costa et al. (submitted), the U–Pb titanite age of 2029 ± 28 Ma places it late in the crustal evolution of the c. 2.2 to 2.1 Ga of the Serra das Pipocas greenstone belt.

3.3.1. Host rocks and structure

The main host rocks of the gold mineralization are metatonalites (Mirador area), amphibolites (Coelho area), intermediate metavolcanic/subvolcanic rocks and metasedimentary rocks (Queimadas and Igrejinha areas) (Lopez, 2012; Costa et al., 2016). According to the current cartography of the area, it is suggested that stratigraphic layers in the Serra das Pipocas greenstone belt are locally overturned by tectonics (**Fig. 3.2** – cross section). In this context, gold mineralization is structurally controlled by shear zones and preferentially sited between contrasting layers of the sequence, occurring near–parallel to the boundary of the lower unit (metavolcanic mafic/intermediate metavolcanic rocks) with the upper unit (predominantly metasedimentary rocks, which includes layers of graphitic–schists) (**Fig. 3.2**). At regional–scale, gold mineralization in the Serra das Pipocas greenstone belt is part of a large fault system, probably of a trans–crustal character, representing the tectonic boundary between the Archean (Cruzeta Complex) and the Paleoproterozoic granite–greenstone terrane (**Fig. 3.1** and **3.2**). This tectonic boundary probably played an important role in gold mineralization of the study area, representing a deep (trans–crustal) first–order

structure, in which large amounts of fluids and magmas may have circulated (**Fig. 3.1** and **3.2**). Syn– to late–tectonic potassic plutons intruded along this shear zone and are mainly represented by the granitoids of the Bananeira suite (**Fig. 3.1** and **3.2**).

3.3.2. Hydrothermal alteration and gold mineralization

Hydrothermal alterations associated to gold mineralization in the Pedra Branca deposit are generally associated to quartz veins and may be classified by two main types: calc–silicate alteration and albitization (**Fig. 3.3A**). Albitization occurs mainly in the intermediate metavolcanic/subvolcanic rocks and associated intrusions (metatonalites), and the calc–silicate alteration occurs mainly in association with quartz veins, as hydrothermal halos (1 to 3 cm) (**Fig. 3.3A**), and generally occur near the contact of the intermediate metavolcanic/subvolcanic rocks with the metasedimentary sequence.

3.3.2.1. Calc–silicate alteration

The calc–silicate hydrothermal alteration at the metasedimentary and/or intermediate metavolcanic/subvolcanic rocks occurs in association with quartz veins containing typical "skarn–type" minerals, being visible in outcrop and drill core samples (**Fig. 3.3A, B** and **C**). These, mainly include diopside, K–feldspar, amphiboles (hornblende and/or uralite), titanite, quartz, pyrite, carbonate and magnetite (**Fig. 3.3C, D** and **E**). In this assemblage, diopside is generally replaced by hornblende (**Fig. 3.3D**). Magnetite usually occurs at the rims of the pyrite crystals, suggesting that it is a late oxidized phase relative to pyrite (**Fig. 3.3E** and **F**). In the calc–silicate hydrothermal assemblage, close to magnetite crystals, gold is commonly in spatial association with tellurides, such as silver and silver/gold (± molybdenum) tellurides (hessite = Ag_2Te; sylvanite = $(Ag, Au)Te_2$) (**Fig. 3.3F**).

Free–milling gold is also found at grain boundaries of hydrothermal biotite and hornblende in some quartz–carbonate samples (e.g. Mirador area) (**Fig. 3.4A, B** and **C**). In this, gold shows no association with magnetite (**Fig. 3.4B** and **C**), suggesting precipitation during a less–oxidized stage. Investigation with a Scanning Electron Microscope (SEM) via Energy Dispersive x–ray Spectrometry (EDS), shows that many of these free–milling gold particles present c. 5% of silver, characterizing them as electrum particles (natural gold and silver alloy) (**Fig. 3.4D**). In addition, free–milling gold particles also occur in contact with chalcopyrite and some telluride minerals, such as calaverite ($AuTe_2$), sylvanite ($(Ag, Au)Te_2$) and altaite (PbTe) (**Fig. 3.4E**). This suggests that for both the Queimadas and Mirador areas, gold mineralization associated to calc–silicate alteration occurred under similar

physicochemical conditions, characterized by gold–silver alloy mineralization together with tellurides.

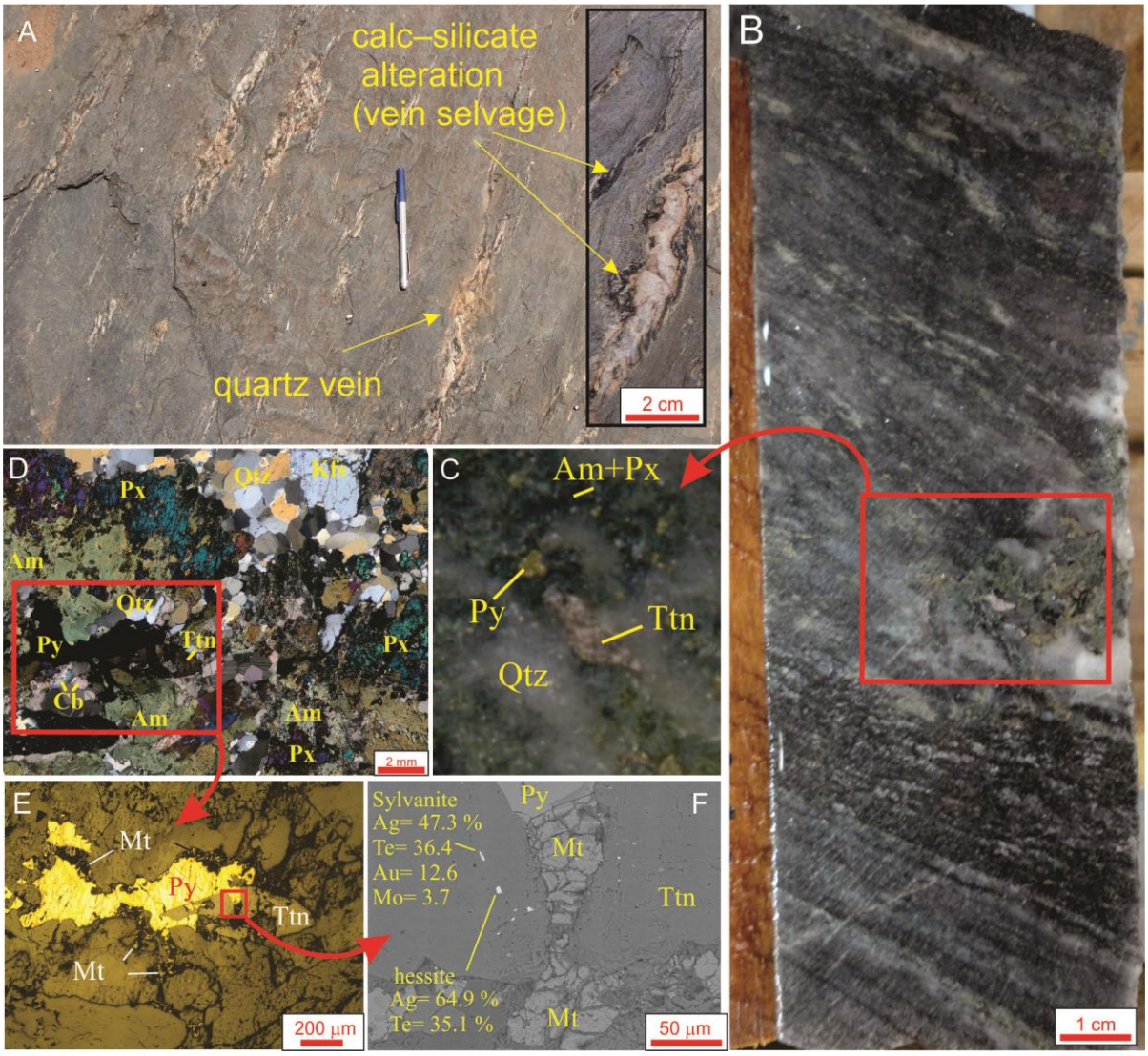

Fig. 3.3*. Queimadas area. (A), Quartz veins hosted by albitized mafic/intermediate metavolcanic/subvolcanic rock, and detail for quartz vein with associated calc–silicate alteration halo (vein selvage). Pencil is pointing to the north. (B) Drill core sample (Fi–12) showing albitized host rock with a "pocket" of hydrothermal calc–silicate minerals associated with quartz vein. (C) Detail of the calc–silicate alteration containing titanite (Ttn), amphiboles (Am), pyroxenes (Px), pyrite (Py) and quartz (Qtz). (D) Photomicrographic image on transmitted light (crossed nicols) showing arrangement of the main minerals of the hydrothermal assembly. (E) Photomicrographic image on reflected light showing intergrowth between pyrite (Py), magnetite (Mt) and titanite. (F) Back–scattered electron (BSE) image and Energy Dispersive x–ray Spectrometry (EDS) analyses by Scanning Electron Microscope (SEM) in gold/silver and silver telluride (sylvanite and hessite) inclusions in titanite, in spatial association with the magnetite.*

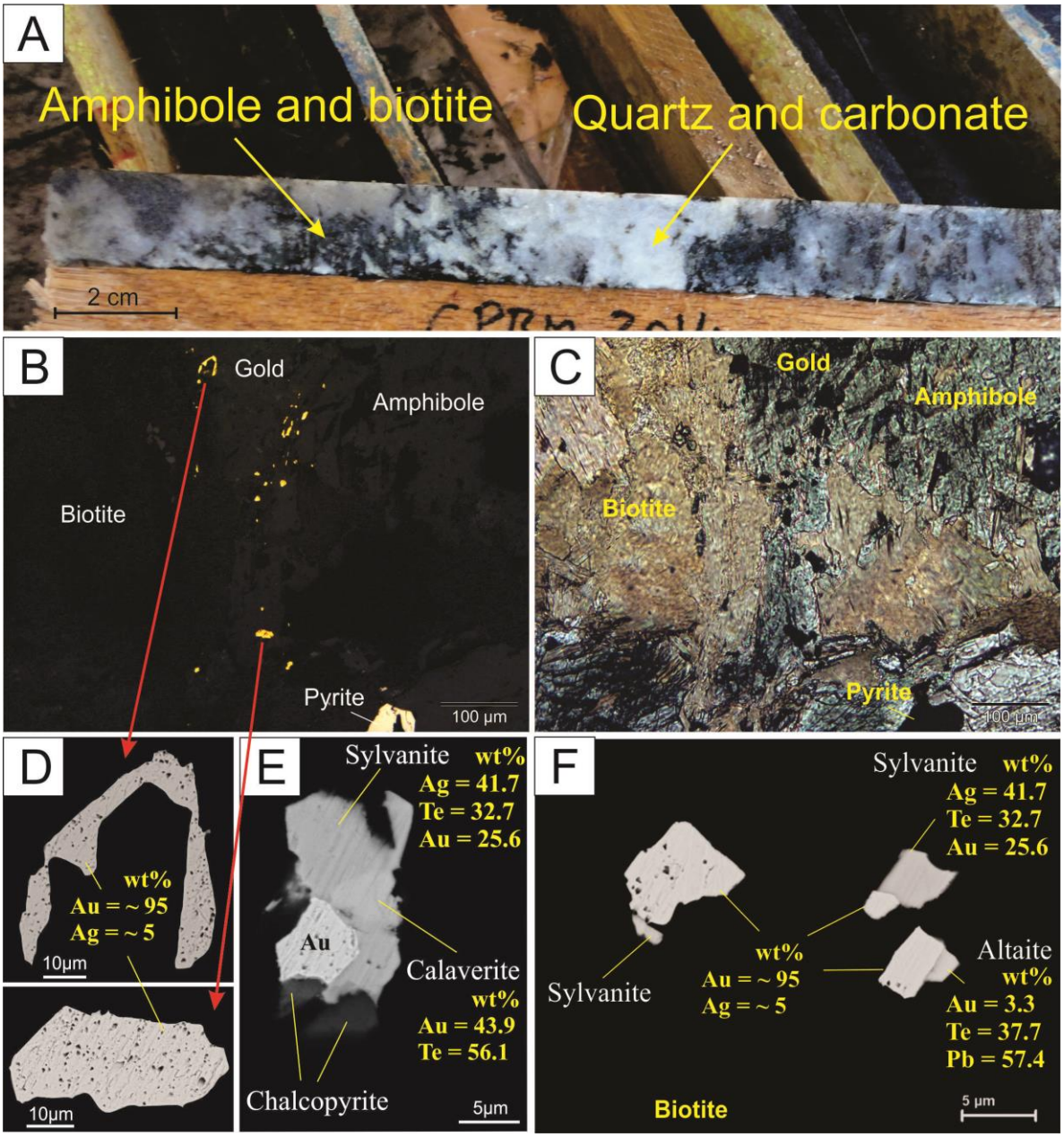

Fig. 3.4*. Mirador area. (A) Mineralized quartz–carbonate vein (sample FQ–06) with hydrothermal biotite and amphibole (hornblende). (B) Photomicrography under reflected light, showing gold associated with amphibole and biotite. (C) Photo of the same view, with transmitted light (uncrossed nicols). (D) BSD images and EDS analyses of gold/silver alloy particles. (E) Gold–silver alloy associated to calaverite, sylvanite and chalcopyrite. (F) Gold–silver alloy associated to sylvanite and altaite.*

3.3.2.2. Albite alteration

One of the main mineralized zones of the Queimadas area is mainly hosted by metatonalites (sheets) and/or intermediate subvolcanic rocks, herein referred to as "hydrothermal albitites" or just “albitites”. In these rocks, besides to the opaque minerals and the hydrothermal albite, which is a pseudomorph of the original (igneous) plagioclase, no other hydrothermal minerals are found in the hand samples (**Fig. 3.5A, B, C** and **D**). Albite

reaches about 80% of the total rock (albitites). In semi–quantitative analyzes by EDS in SEM, little or no calcium (Ca) occurs in the plagioclase, and therefore these can be classified as pure albite, associated with hydrothermal alteration (albitization). The contacts of these rocks with the metavolcano–sedimentary unit are generally abrupt, suggesting an intrusive character in the sequence (**Fig. 3.5B**), and are commonly associated to calc–silicate alteration and quartz veins (**Fig. 3.5C**). Sulfides (mainly pyrite) are visible in drill core samples, generally disseminated and associated with magnetite (**Fig. 3.5A**). Locally, discordant quartz–carbonate veinlets in the albitized metatonalite also present pyrite crystals (**Fig. 3.5D**).

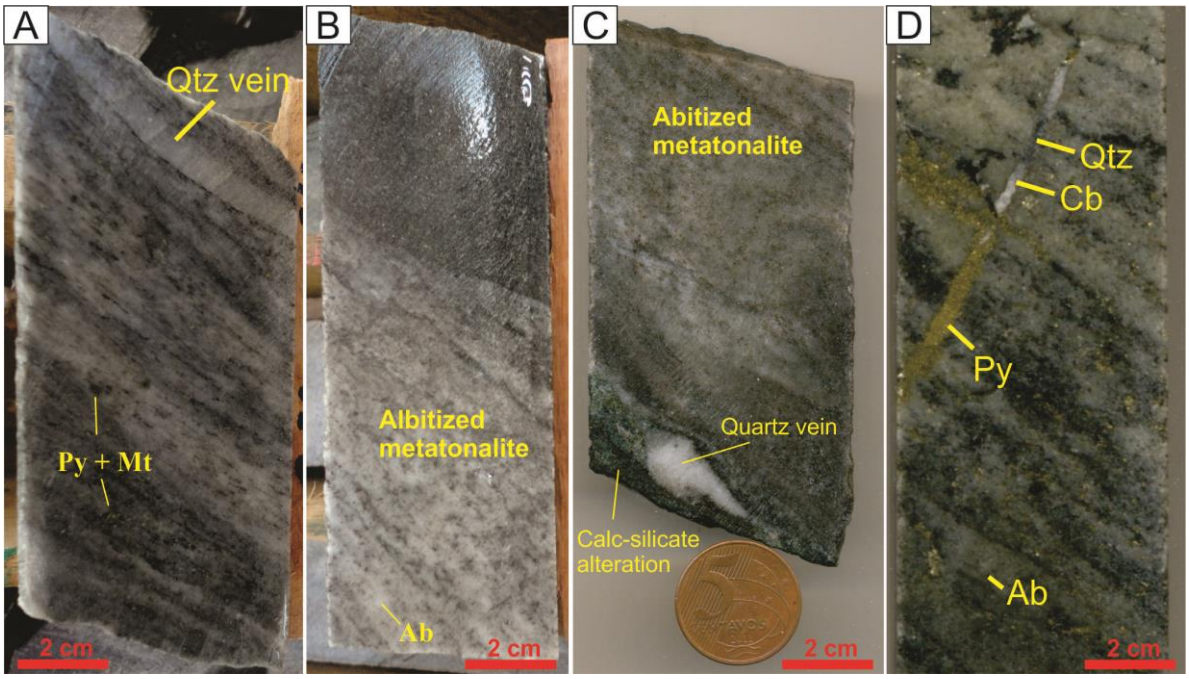

***Fig. 3.5**. (A) Albitized felsic/intermediate intrusive (albitites) with disseminated pyrite (Py) and magnetite (Mt), and locally concordant quartz (Qtz) vein (Sample Fi-09). (B) Albitite (albite = Ab) (igneous/hydrothermal) showing abrupt (intrusive) contact with amphibolite of the metavolcano–sedimentary sequence (enclave?) (Sample FJ-06). (C) Albitized felsic/intermediate intrusive in contact with quartz vein and calc–silicate alteration (Sample FL-19). (D) Albitized felsic/intermediate intrusive with disseminated pyrite, and pyrite, quartz and carbonate (Cb) fracture fills (Sample FK-08).*

In the albitites, pyrite occurs associated with albite, pyrrhotite, magnetite, biotite and carbonate (**Fig. 3.6A**). Biotite is generally in contact with the pyrite, suggesting that biotite is also of hydrothermal origin (**Fig. 3.6A** and **B**). Magnetite always occurs at the borders of pyrite, and it can be seen in both hand–samples (**Fig. 3.6C**) and microscope petrography (**Fig. 6B, D** and **E**). It is texturally evident that magnetite replaces pyrite crystals, as pyrite

commonly occurs as inclusions in the late magnetite (**Fig. 3.6B**). Pyrrhotite occurs always as inclusions in pyrite crystals, suggesting its precipitation prior to pyrite (**Fig. 6D** and **E**).

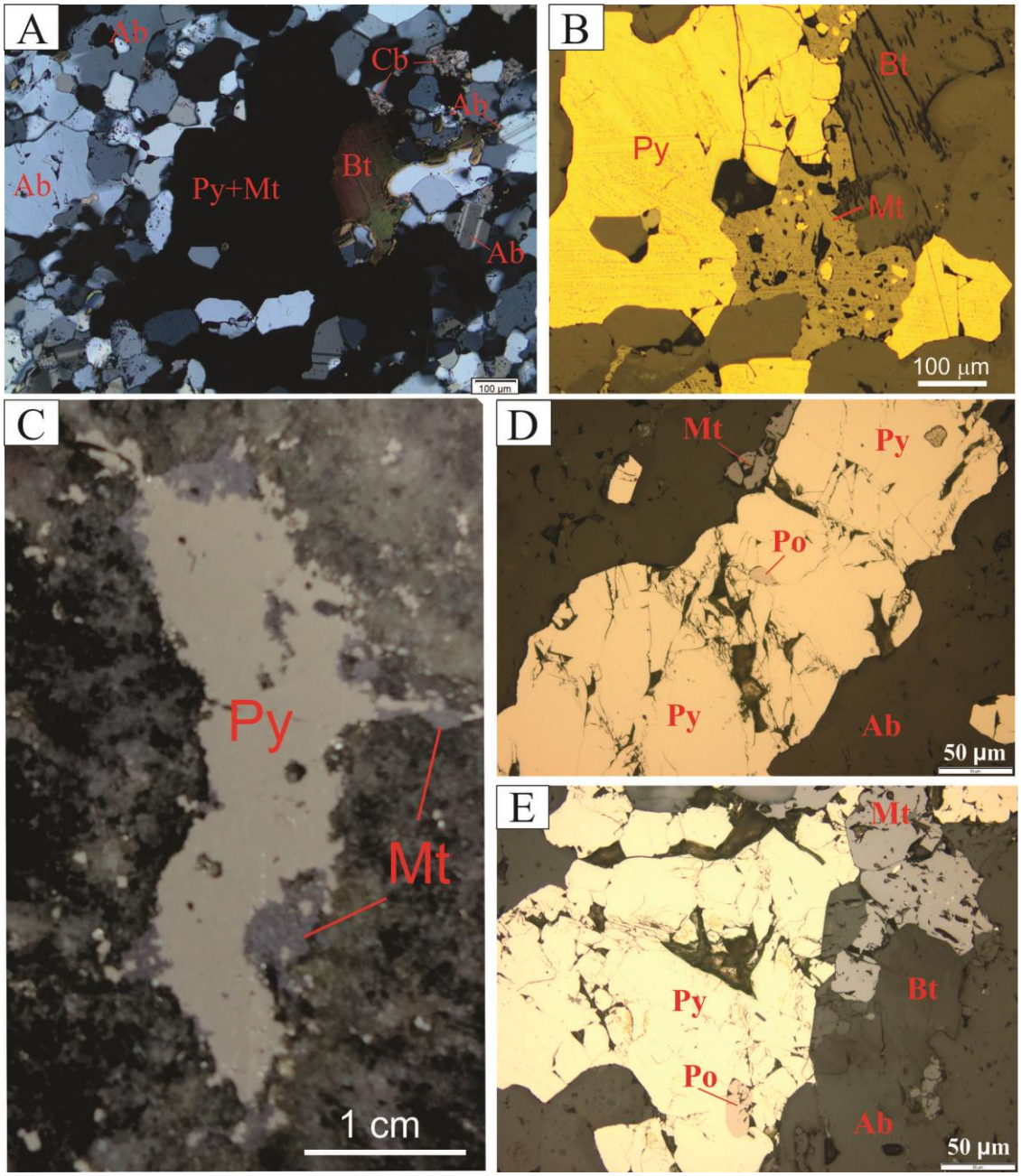

Fig. 3.6*. (A) Photomicrographic image for albitite under transmited light (crossed nicols) showing albite (Ab) and pyrite (Py) + magnetite (Mt) (opaque minerals) in contact with biotite (Bt) and carbonate (Cb). (B) Photomicrographic image on reflected light showing pyrite crystals substituted by magnetite. (C) Drill core sample with pyrite crystal replaced by magnetite at the edges. (D) and (E) Photomicrographic image on reflected light showing pyrrhotite (Po) crystals as inclusion in pyrite and late magnetite on the edges of pyrite. Locally, magnetite has inclusions of pyrite.*

Therefore, evolution of the opaque minerals from pyrrhotite to pyrite, and later magnetite, is in concordance with the observed features of the calc–silicate alteration (e.g. late

magnetites), which suggest that both hydrothermal alteration (calc–silicate and albitization) occurred together at similar physicochemical conditions. Pyrrhotite crystals being replaced by pyrite, and pyrite being replaced by late magnetite, suggest a progressive oxidation of the hydrothermal fluid (**Fig. 3.7**).

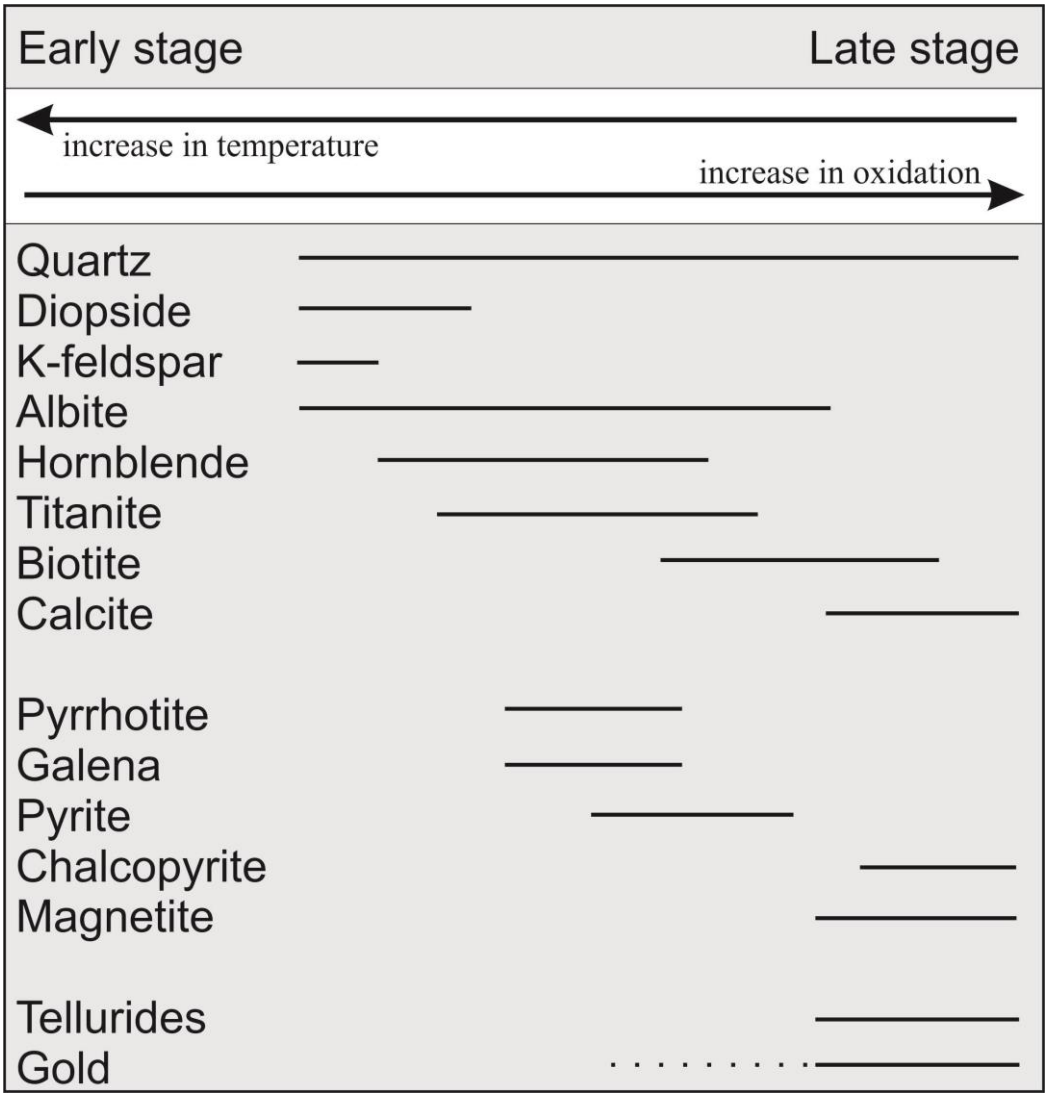

Fig. 3.7*. Paragenetic sequence of the hydrothermal alteration in the Pedra Branca gold deposit interpreted from ore petrography. The figure is effective for both albitization and calc–silicate alteration.*

Mineralogic and textural observations indicate that gold generally occurs at the late stage of alteration, associated with precipitation of magnetite and tellurides (in both calc–silicate alteration and albitization) (**Fig. 3.7**). In the hydrothermal albitites, disseminated free–milling gold can be seen in spatial association with albite and magnetite crystals (**Fig. 3.8A, B, C** and **D**). Gold particles are also located in a fracture parallel to the twinning planes

of plagioclase (albite) (**Fig. 8C** and **D**). Carbonates occur close to the gold particles, also at the grain boundaries and in the cleavage planes of the albite, suggesting alteration in plagioclase by carbonatization (**Fig. 8D**). In the BSE images and EDS analyses of the free–milling gold particles, a percentage (~5–15%) of silver (Ag) is always present, characterizing them as electrum (**Fig. 9A, B** and **C**). Locally bismuth and lead tellurides occur as tellurobismuthite (Bi_2Te_3) and altaite (PbTe), respectively, enveloping gold–silver alloy (electrum) (**Fig. 9C**). In addition, in EDS analyzes, galena (PbS) and a possible Pb–Ag–Au alloy were identified associated to early stage pyrrhotite crystal (**Fig. 9D**). This suggests that some gold could also had precipitated at early (more reduced) stages of the hydrothermal evolution, without being associated to magnetite and tellurides (**Fig. 7**).

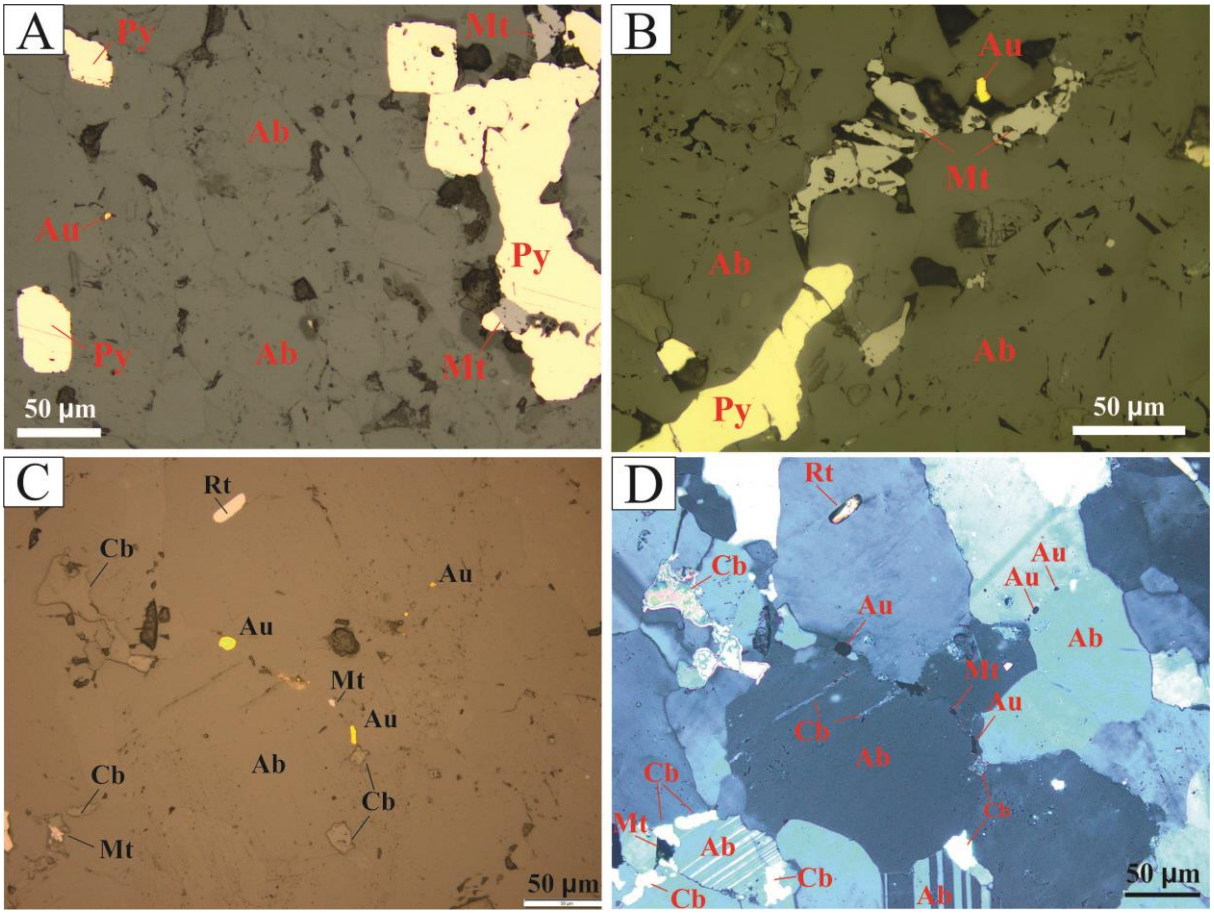

***Fig. 3.8**. (A) Photomicrographic image on reflected light showing disseminated free–milling gold (Au) within albite (Ab) crystals. (B) Photomicrographic image on reflected light showing pyrite (Py) and free–milling gold in spatial association with the magnetite (Mt). (C) Photomicrographic image on reflected light showing free–milling gold particles in the contact of albite grains next to carbonate (Cb) and magnetite. (D) Photomicrographic image on transmitted light (crossed nicols) of the prior view, highlighting carbonates (Cb) at the edges and planes of albite cleavage. Gold occurs at the grain boundaries and is locally included parallel to the twinning planes of the albite.*

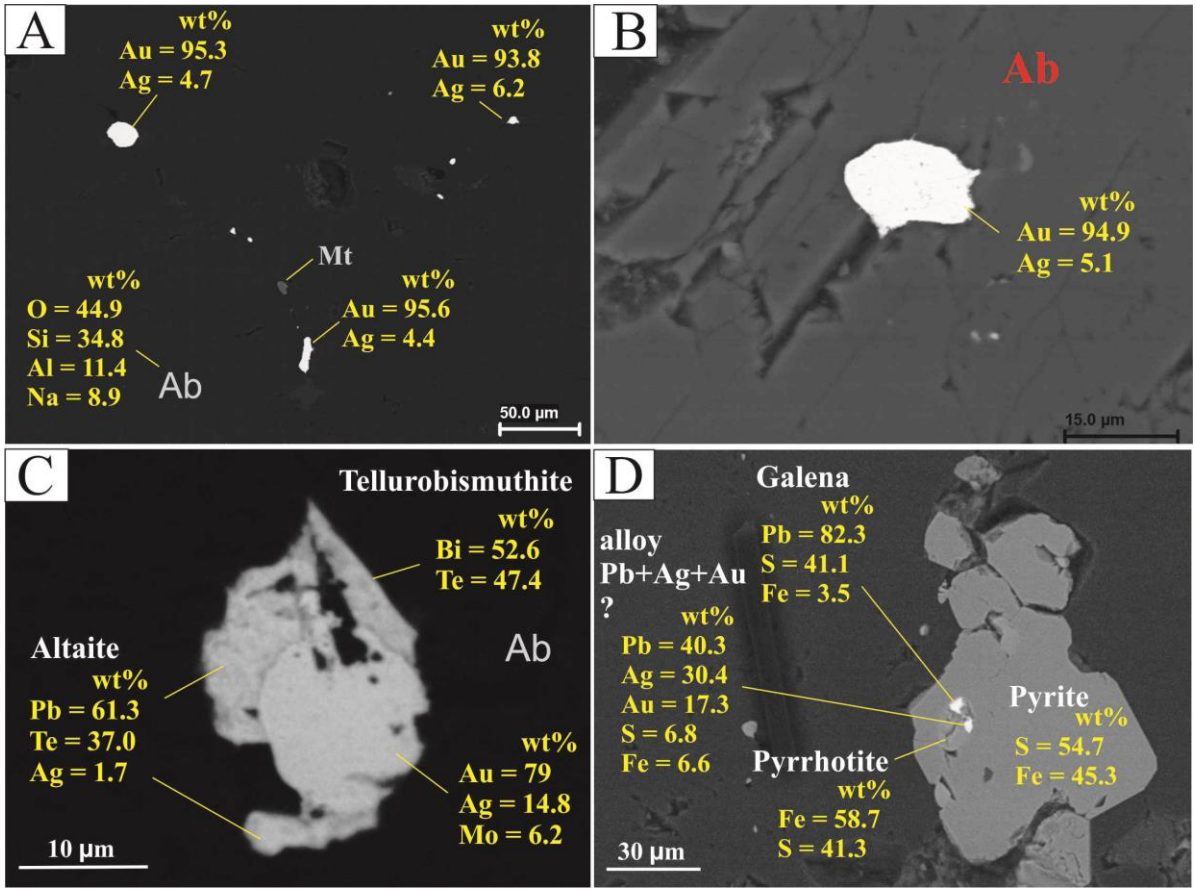

Fig. 3.9*. BSE images and EDS analyzes by SEM in samples of the hydrothermal albitite. (A) BSE image and EDS analysis of free–milling gold (Au) particles (± silver (Ag) contents) arranged in contact between albite (Ab) grains, and in close association with magnetite (Mt). (B) BSE image and EDS analysis of free–milling gold (Au) particles (± silver (Ag) contents) arranged in fracture plane of albite crystal. (C) BSE image and EDS analysis of gold–silver particle with ±molybdenum (Mo) content, surrounded by altaite and tellurobismuthite crystals. (D) BSE image and EDS analysis of pyrite encompassing pyrrhotite crystal associated with galena and probable gold/silver/lead alloy (?).*

3.4. Analytical procedures

3.4.1. Fluid inclusions

For the microthermometric study of fluid inclusions in mineralized quartz veins, doubly polished thick–sections (< 0.3 mm thick) were prepared at the Federal University of Pará – UFPA, Belém, Brazil. The microthermometric measurements were carried out at the Geological Survey of Brazil, Belém, Brazil, using a Linkam THMSG 600 heating–freezing stage, following procedures described elsewhere (Roedder, 1984; Shepherd et al., 1985; Wilkinson, 2001). The equipment was previously calibrated with synthetic samples of fluid inclusions. The data are reproducible to ±0.5 °C for the freezing which lowers to -180 °C and ±5 °C for the heating that rises to the appropriate temperature of total homogenization. The

salinities of the NaCl–H_2O aqueous inclusions were calculated according to the ice melting temperature (Tm,ice) and using the equation provided by Bodnar (1993). Salinities of CO_2–NaCl–H_2O inclusions were calculated using the final melting temperatures of CO_2–clathrate (Tm,cla) (Collins, 1979). The Package FLUID 1 software from Bakker (2003) was used to calculate bulk–fluid densities of CO_2 and NaCl–H_2O inclusions to define isochores and trapping conditions.

3.4.2. Stable isotopes

All stable isotope (oxygen, hydrogen and carbon) data presented in this study were produced at the University of Cape Town (UCT), South Africa. Sample preparation and isotope extraction were carried out in the Stable Isotope Laboratory of the Department of Geological Sciences, and isotope ratios were measured off-line using a Finnigan Delta XP mass spectrometer in dual inlet mode, hosted in the Department of Archaeology. Data are reported in δ notation, where $\delta = (R_{sample}/R_{standard} -1)*1000$, and R = the measured ratio (i.e. $^{18}O/^{16}O$, $^{13}C/^{12}C$ or D/H). The $^{13}C/^{12}C$, $^{18}O/^{16}O$, and D/H ratios are normalized to the standard PDB (carbon) and SMOW (oxygen and hydrogen) scales.

For oxygen isotopes, both conventional and laser fluorination methods were used. The mineral separates (except two samples of hornblende; A-15-2 and Fi-01-2) were analyzed by the laser fluorination method described by Harris and Vogeli (2010). Each sample (2 to 4 mg of single/multiple mineral pieces) were reacted in the presence of ~10 kPa BrF_5, and the purified O_2 was collected onto a 5 Å molecular sieve contained in a glass storage bottle. An internal standard (Monastery garnet – MONGT, $\delta^{18}O$ = +5.55‰) was analyzed to calibrate the data to the SMOW scale, and duplicates gave agreement within 0.2 per mil. For oxygen, powdered whole–rock samples and two hornblende separates were analyzed using a conventional silicate line following methods described by Harris and Ashwal (2002). Approximately 10 mg of sample was reacted with ClF_3, and the liberated O_2 converted to CO_2 using a hot platinized carbon rod. An internal standard (Murch Quartz – MQ, $\delta^{18}O$ = +10.1‰) was analyzed to calibrate the data to the SMOW scale. The mean values obtained from repeated analyses of MQ gave a difference of 0.3 per mil from the accepted value.

Hydrogen isotopes were measured on biotite, muscovite and amphibole on the hydrogen silicate line, extracted from 100 mg of amphibole and 50 mg of biotite and muscovite using the method of Vennemann and O'Neil (1993) with reduction by "Low-blank Indiana Zinc" (Schimmelmann and DeNiro, 1993). For D/H determination, the inhouse Serina Kaolinite standard (Serina bulk kaolinite, D= -57‰, H_2O=12.4 wt.%) (Harris et al., 1999

sample SB8) was analyzed in triplicate with the silicates, and internal water standards CTMP2010 (Cape Town Millipore Water 2010, D= -7.4‰) and RMW (Rocky Mountain Water, D= -131.4‰) were used to convert raw data to the Standard Mean Ocean water (SMOW) scale and correct for scale compression. Water concentrations (H_2O+) were determined from the voltage measured on the mass 2 collector of the mass spectrometer, using identical sample inlet volume (Vennemann and O'Neil, 1993). The expected voltage per milligram of water was determined from accurately measured amounts of the 5 standard waters analyzed with the samples. The precision for δD for the internal kaolinite standard were ±2‰ (1 σ, n=3). The typical precision for water amounts based on many measurements of water and kaolinite standards is ±0.1 wt.%. The average standard kaolinite gave a δD value of -63‰, after all the corrections to the raw data were applied. All data were adjusted to the accepted kaolinite value of -57‰. Hydrogen isotopes were also measured on quartz vein samples, by extraction (thermal decrepitation at >800°C) of the fluids inclusions from ~3.5 g of quartz samples. The quartz vein fragments were degassed under vacuum at 200°C using a hot air gun to eliminate any moisture before heating it to about 800°C. The obtained water was trapped cryogenically and transferred to pyrex tubes containing Zn. The hydrogen isotope composition of the H_2O was determined using the closed tube Zn reduction method of Vennemann and O'Neil (1993). For hydrogen isotopes from fluid inclusion water, internal water standard CTMP2010 and RMW were used to calibrate the data to the SMOW scale. The amount of CO_2 pressure liberated from the fluid inclusions was insufficient to collect for carbon isotope analysis.

Carbon and oxygen isotopes from calcite were measured by the method of McCrea (1950), using 100% phosphoric acid as the reagent. Samples were reacted at 50°C and a CO_2-calcite fractionation factor of 1.009 was used to correct the raw data. Most carbonate samples contain some dolomite and the $\delta^{18}O$ value obtained is, therefore, a mixture derived from both calcite and dolomite. The total carbonate content was estimated by comparing the pressure of gas produced for weighed aliquots of samples and standards during the extraction procedure. For carbon isotope analysis on graphite from graphitic-schists, samples were cleaned by ultrasound in various media and combusted in a Thermo 1112 Elemental Analyzer interfaced via a Conflo II device to the Thermo Delta XP Plus mass spectrometer. The quartz oxidizing tube used chromium oxide at 1020°C, the reducing tube used reduced copper wires at 650°C and the calibration to the PDB scale was made using a variety of standards, as descripted in Kramers et al. (2013).

3.5. Fluid inclusions

3.5.1. Types and distribution

The petrographic study of fluid inclusions was performed in quartz veins associated with the calc–silicate hydrothermal alteration. The selected quartz samples show clear association with pyrite, magnetite, titanite, amphibole and biotite. In the petrographic description, fluid inclusions were carefully observed to identify their genetic and compositional types, vapor–liquid ratios, and spatial clustering. According to their spatial occurrence and clustering, the observed fluid inclusions were classified as distinct Fluid Inclusion Assemblages (FIA), according to the proposed classification method of Goldstein and Reynolds (1994). For the observed samples, the presence of two main FIA was evidenced; (FIA 1) Pseudo–secondary trails composed of CO_2–rich inclusions (Type–I) together with CO_2–NaCl–H_2O (Type–II) and NaCl–H_2O (Type–III) inclusions (**Fig. 3.10A, B** and **C**), and (FIA 2) Secondary (transgranular) trails of late NaCl–H_2O inclusions (Type–IV) (**Fig. 3.10D** and **E**).

The pseudo–secondary trails of the FIA 1 are mainly composed of Type–I and Type–III inclusions, followed by less abundant Type–II inclusions (**Fig. 3.10A, B** and **C**). The CO_2 inclusions (Type–I) of the FIA 1 are shown as biphasic (liquid CO_2 + vapor CO_2) and monophasic (vapor CO_2) at room temperature (**Fig. 3.10B, C** and **D**). In the biphasic varieties, the vapor phase occupies between 60–80% of the cavity (**Fig. 3.10C**). They have negative crystal and ellipsoidal shapes, with sizes ranging from 8 to 12 μm (**Fig. 3.10B, C** and **D**). The CO_2–NaCl–H_2O inclusions (Type–II) of the FIA 1 occur with three–phases at room temperature (vapor CO_2 + liquid CO_2 + liquid H_2O) with variable proportions of CO_2 and H_2O phases (**Fig. 3.10C**). Their CO_2 (vapor CO_2 + liquid CO_2) volumetric proportion ranges from 35 to 80%. They are ellipsoidal and irregular in shape, 10 to 15 μm in size, coexisting with Type–I and Type–III inclusions. The NaCl–H_2O inclusions (Type–III) of the FIA 1 are two–phase aqueous inclusions carrying vapor and liquid water at room temperature, with bubbles usually accounting for 20–35% in volume (**Fig. 3.10B** and **C**). They are generally ellipsoidal and irregular in shape, with 5–10 μm in size (**Fig. 3.10B** and **C**). The fluid inclusions of FIA 2 generally occur in trails of secondary inclusions showing intersection features with FIA 1 trails (**Fig. 3.10D**). Only NaCl–H_2O inclusions were found in the FIA 2, showing homogeneous two–phase (vapor H_2O + liquid H_2O) characteristics at room temperature, with bubbles usually accounting for 10 to 15% in volume (**Fig. 3.10D** and **E**).

They are ellipsoidal and irregular in shape, ranging from 10 to 20 μm in size (**Fig. 3.10D** and **E**).

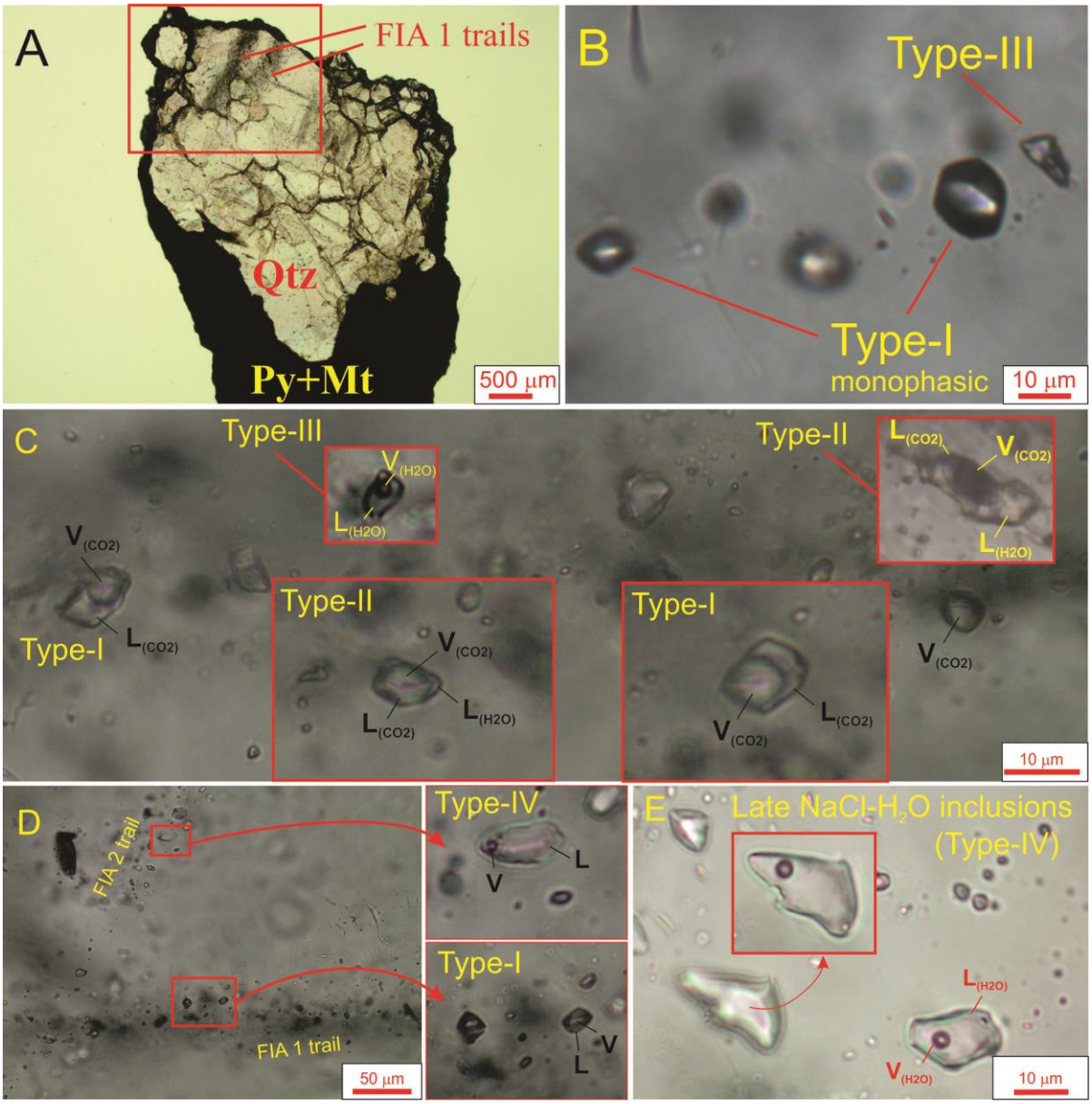

Fig. 3.10*. Fluid inclusion types. (A) Microscopic view on transmitted light of doubly polished sections of quartz associated with opaque mineral (Py= pyrite and Mt= magnetite). This photo also shows the detail of pseudosecondary trails of fluid inclusions from FIA 1 (predominantly CO_2–rich, Type–I). (B) Detail for coeval NaCl+H_2O aqueous inclusion (Type–III) and monophasic CO_2–rich inclusions (Type–I) of the FIA 1. (C) Inclusion trail of FIA 1 (details at different levels of focus) showing predominance of CO_2–rich inclusions (Type–I) associated with CO_2–NaCl–H_2O (Type–II) NaCl–H_2O and aqueous (Type–III) inclusions. Emphasis was given to the carbonic inclusions (Type–I and II), with variable percentage of filling of the vapor and liquid phases. (E) Trail of late NaCl–H_2O aqueous inclusions (Type–IV) of the FIA 2 intersecting trail of FIA 1. Zoom detail of representative inclusions are shown. (D) Detail for late NaCl–H_2O aqueous (Type–IV) inclusions of FIA 2.*

3.5.2. Microthermometry

Microthermometric data collected for the fluid inclusions are summarized in **Table 3.1**, and **Fig. 3.11**.

Table 3.1. Summary of the microthermometric data for fluid inclusions

Type	N	FIA	Size (μm)	Vapor (vol.%)	$TmCO_2$ (°C)	Tm,ice (°C)	Tm,cla (°C)	$ThCO_2$ (°C)	Th (°C)	wt.% NaCl	ρ (g/cm^3)
Type–I	30	FIA 1	8–12	60–80	–57.6 to –56.9			7.5–31			0.594–0.879
Type–II	9	FIA 1	10–15	50–85 (CO_2)	–58.1 to –56.8		7.3–8.5	8.5–31	240–400	3.0–5.2	0.872–0.880
Type–III	55	FIA 1	5–10	20–35		–8.9 to –0.2			200–430	0.5–7.3	0.537–0.938
Type–IV	12	FIA 2	10–15	10–15		–3.2 to –0.2			125–179	0.3–5.3	0.659–1.016

Notation: $TmCO_2$ = CO_2 melting temperature; Tm,ice = final ice melting temperature; Tm,cla = melting temperature of the CO_2 clathrate; $ThCO_2$ = CO_2 partial homogenization temperature; Th = homogenization temperature.

The CO_2 melting temperatures ($TmCO_2$) for CO_2–rich inclusions (Type-I) range from -57.6 to -56.9°C, suggesting a fluid composition near pure CO_2 with minor presence of other volatile components (e.g. N_2 and/or CH_4) (**Fig. 3.11A** and **C**). For Type–I inclusions, the calculated densities range from 0.594 to 0.879 g/cm^3 (**Table 3.1**) and given by partial homogenization temperatures ($ThCO_2$) ranging from 7.5 to 31°C (**Fig. 3.11B** and **C**). For the CO_2–NaCl–H_2O (Type–II) inclusions, the melting temperatures of solid CO_2 ($TmCO_2$) ranges from -58.1 to -56.8°C (**Fig. 3.11A** and **C**), also suggesting minor presence of other gaseous components (e.g. N_2 and/or CH_4) (Roedder, 1984). The clathrate melting temperature (Tm,cla) between 7.3 and 8.5°C is indicative of salinities between 3.0 and 5.2 wt.% NaCl equiv. (**Fig. 3.11E, Table 3.1**). The Type–II fluid inclusions, with the calculated densities ranging from 0.872 to 0.880 g/cm^3 (**Table 3.1**), have partial ($ThCO_2$) and total homogenization (Th) at 8.5 to 31°C and 240 to 400°C, respectively (**Fig. 3.11B, C** and **D**). Partial homogenization temperatures ($ThCO_2$) for Type-I and Type-II inclusions, and total homogenization for Type-II inclusions, occur both to liquid and vapor state.

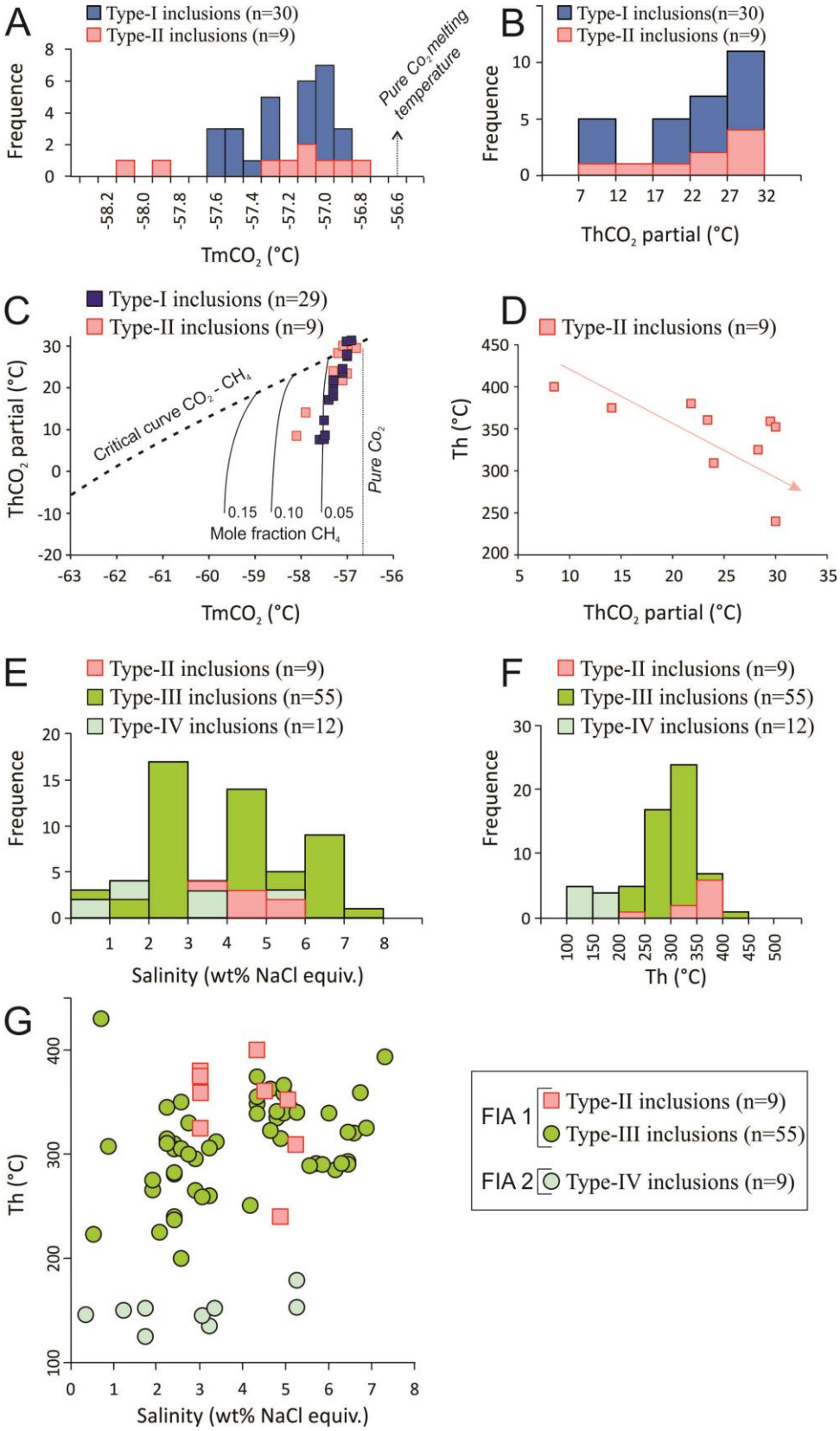

Fig. 3.11. *(A) Histogram for CO_2 melting temperature ($TmCO_2$) for CO_2 (Type–I) and CO_2–NaCl–H_2O (Type–III) inclusions. (B) Histogram for CO_2 partial homogenization temperature ($ThCO_2$) of Type–I and Type-II inclusions. (C) Diagram for CO_2 melting temperature ($TmCO_2$) vs. CO_2 partial homogenization temperature ($ThCO_2$) of Type-I and Type-II inclusions. Mole fractions of CH_4 are from Van der Kerkhof and Thiéry (2001). (D) Diagram for CO_2 partial homogenization temperature*

($ThCO_2$) vs. homogenization temperature (Th) of Type-II inclusions. (E) Histogram for salinity (wt% NaCl equivalent) of Type–II, Type–III and Type–IV inclusions. (F) Histogram for homogenization temperature (Th) of Type–II, Type–III and Type–IV inclusions. (G) Salinity (wt% NaCl equivalent) vs. Homogenization Temperature (Th) of Type–II, Type–III and Type–IV inclusions.

For the aqueous NaCl–H_2O (Type–III) inclusions of FIA 1, the ice-melting temperature (Tm,ice) ranges from -8.9 to -0.2°C, which defines salinities between 0.5 and 7.3 wt.% NaCl equiv. (**Fig. 11E** and **G**). Their homogenization temperatures (Th) vary from 200° to 430°C (**Fig. 3.11F** and **G**), with densities of 0.61–0.92 g/cm^3. The late aqueous NaCl–H_2O (Type–IV) inclusions of the FIA 2 have ice-melting temperatures (Tm,ice) ranging from -3.2 to -0.2°C, salinities between 0.3 and 5.3 wt.% NaCl equiv. (**Fig. 3.11E** and **G**), homogenization temperatures (Th) varying from 125° to 179°C (**Fig. 3.11F** and **G**) and densities of 0.659–1.016 g/cm^3 (**Table 3.1**).

3.6. Stable isotopes (Oxygen, hydrogen and carbon)

3.6.1. Calc–silicate and albite alteration

The $\delta^{18}O$, δD and $\delta^{13}C$ values for minerals from the hydrothermal assemblages of the Pedra Branca gold deposit and associated country rocks are presented in **Table 3.2**.

The fractionation factor for fluid–mineral equilibrium for biotite, hornblende and muscovite are from Suzouki and Epstein (1976) for hydrogen and from Zheng et al (1993a) for oxygen. Oxygen fractionation factor for quartz, magnetite and calcite are those from Clayton et al. (1972), Cole et al. (2004) and Hu and Clayton et al. (2003), respectively. Most of the temperatures used to calculate the fluid $\delta^{18}O$ and δD composition are those obtained from the oxygen isotope thermometry (**Table 3.2,** and item **3.6.2**). The temperature of 500°C was used to calculate $\delta^{18}O$ of the fluid in equilibrium for some of the quartz samples, based on the mean value of Qz–Mt isotopic thermometer. To calculate the $\delta^{18}O$ and δD values of the fluid in equilibrium with muscovite of S–type granite, a temperature of 850°C was assumed (average temperature for S–type granites; Clemens, 2006) and for hornblende of garnet–amphibolite country rocks, a temperature of 600°C (average amphibolite facies temperature). To estimate $\delta^{18}O$ values of fluid composition for the analyzed whole–rock albitites and monzogranite, the mineral–water fractionation factors for fluid–albite (albitite) and fluid–(alkali feldspar) (monzogranite) from Zheng et al. (1993b) were used, with temperatures of 850°C (estimated for magmatic–hydrothermal fluid) and 600°C (albitization process, Hovelmann et al., 2010).

***Table 3.2**. The results of oxygen, hydrogen and carbon isotopes*

Sample	Rock/Alteration	Mineral	$\delta^{18}O$ (‰)	δD (‰)	$\delta^{13}C$ (‰)	Pair	$\Delta^{18}O$	T	± (°C)	$\delta^{18}O_{fluid}$ (‰)	δD_{fluid} (‰)
Ore-related samples											
Fi-12	calc-silicate alteration	quartz vein	11.2	-37 (f.i.)				500		9.0	-37
		quartz vein	11.1					500		8.9	
		hornblende	7.5	-63		Qz–Hb	3.7	629	± 36	9.8	-42
		hornblende	7.5	-61		Qz–Hb	3.8	622	± 36	9.8	-39
		hornblende	6.7			Qz–Hb	4.5	545	± 27	8.9	
		hornblende	8.9			Qz–Hb	2.3	870	± 75	11.0	
		biotite	7.7	-88		Qz–Bt	3.4	521	± 35	10.2	-51
		biotite	8.1	-98		Qz–Bt	3.1	557	± 40	10.6	-64
FL-12	calc-silicate alteration	whole rock	9.4					600		8.8	
	and associated albitite	quartz vein	11.5			Qz–Mt	9.9	515	± 12	9.3	
		magnetite	1.6							9.4	
		hornblende	8.0	-65		Qz–Hb	3.5	654	± 40	10.3	-45
		hornblende	7.8	-62		Qz–Hb	3.7	627	± 36	10.1	-40
		hornblende	7.6			Qz–Hb	3.9	611	± 34	9.9	
		hornblende	8.3			Qz–Hb	3.2	693	± 45	10.6	
		biotite	7.3	-83		Qz–Bt	4.2	448	± 26	9.6	-39
		biotite	7.3	-73		Qz–Bt	4.2	448	± 26	9.6	-29
		calcite	10.7		-9.4	Cc–Mt	9.0	524	± 13	10.8	
		calcite	10.1		-9.3	Cc–Mt	8.5	551	± 15	10.5	
						Cc–Qz	-0.8	404	± 125		
FQ-06	calc-silicate alteration	quartz vein	11.5	-32 (f.i.)				500		9.3	-32
		hornblende	7.5	-86		Qz–Hb	4.0	590	± 32	9.8	-62
		hornblende	7.1	-84		Qz–Hb	4.5	549	± 28	9.3	-57
		hornblende	6.7			Qz–Hb	4.9	515	± 24	8.9	
		hornblende	6.9			Qz–Hb	4.6	538	± 27	9.1	
		biotite	6.9	-93		Qz–Bt	4.6	412	± 22	9.0	-45
		biotite	6.6	-85		Qz–Bt	4.9	390	± 20	8.6	-33
		biotite	6.4			Qz–Bt	5.1	377	± 19	8.4	
		biotite	6.5			Qz–Bt	5.0	387	± 20	8.5	
		calcite	10.7		-6.3	Cc–Qz	-0.9	394	± 119	9.0	
FL-19	calc-silicate alteration	quartz vein	11.3							9.1	
		biotite	7.4	-72		Qz–Bt	3.9	471	± 29	9.8	-30
		biotite	7.2	-77		Qz–Bt	4.0	458	± 27	9.5	-34
FK-08	albitite	whole rock	9.9					600		9.3	
		magnetite	2.4					500		10.2	
FJ-06	albitite	whole rock	10.4					600		9.8	
		magnetite	1.3							9.1	
FK-09	albitite	quartz	11.5			Qz–Mt	10.4	493	± 11	9.3	
		magnetite	1.0							8.8	
FK-10	albitite	whole rock	9.7					600		9.1	
		quartz	11.8			Qz–Mt	10.0	508	± 12	9.6	
		quartz	11.5			Qz–Mt	9.7	522	± 12	9.3	
		magnetite	1.8							9.6	
FJ-09	albitite	whole rock	9.2					600		8.6	
		quartz	11.5	-32 (f.i.)		Qz–Mt	9.6	526	± 12	9.3	-32
		magnetite	1.9							9.7	
Fi-09	albitite	whole rock	10.4					600		9.8	
		magnetite	1.3					500		9.1	
Fi-10	albitite	whole rock	9.7					600		9.1	
		quartz	12.4			Qz–Mt	11.2	467	± 10	10.2	
		quartz	11.7			Qz–Mt	10.5	492	± 11	9.5	
		magnetite	1.3							9.1	
FQ-10	quartz vein	quartz	11.5	-93 (f.i.)				500		9.3	-93
FN-04	quartz vein	quartz	11.8	-72 (f.i.)				500		9.6	-72
FJ-18	quartz vein	quartz	11.3	-59 (f.i.)				500		9.1	-59
FK-02	quartz vein	quartz	10.5	-74 (f.i.)				500		8.3	-74
FL-02	quartz vein	quartz	11.0	-46 (f.i.)				500		8.8	-46
FJ-13	quartz vein	quartz	11.2	-59 (f.i.)				500		9.0	-59
FJ-14	quartz vein	quartz	11.5	-72 (f.i.)				500		9.3	-72
FL-10	quartz vein	quartz	11.5					500		9.3	
Greenstone belt - barren country rocks											
FC-278	c. 2068 Ma mozogranite	whole rock	8.6					850		8.8	
FC-143	S-type granite	muscovite	10.4	-62				850		11.7	-60
		muscovite	10.4	-78				850		11.7	-76
A-15-2	garnet–amphibolite	hornblende	7.7	-73				600		10.0	-58
Fi-01-2	garnet–amphibolite	hornblende	8.1	-68				600		10.4	-54
FC-03	graphitic-schist (metapelite)	graphite			-22.7						
FC-04	graphitic-schist (metapelite)	graphite			-27.1						

Notes: Abbreviations are f.i.= fluid inclusions; Qz= quartz, Hb= hornblende, Bt= biotite, Cc= calcite, Mt= magnetite. The temperatures for coexisting minerals were calculated by the equation $\Delta = A \times 10^6/T^2$, where T is temperature (K) and A is an

experimentally or empirically determined coefficient. The A coefficients used for oxygen isotope thermometry are the following: Qz–Mt= 6.12, Cc–Mt= 5.74 and Qz–Cc= -0.38 (Clayton and Kieffer, 1991); Qz–Bt= 2.16 (Chacko et al., 2001); Qz–Hb= 3.01 (Lackey et al., 2008). Errors on the temperatures are calculated assuming a 0.15 per mil error on all delta values. The equation $1000ln\alpha = (D.10^6)/T^2 + (E.10^3)/T + F$ *was used to calculate the fractionation factor for fluid–mineral equilibrium for quartz, magnetite, calcite, biotite, hornblende and muscovite. The D, E and F coefficients used for oxygen isotope are from Zheng et al. (1993a) for biotite (D= 3.84, E= -8.76 and F= 2.46); for hornblende (D= 3.89, E= -856 and F= 2.43) and for muscovite (D= 4.10, E= -7.61 and F= 2.25). The D, E and F coefficients used for hydrogen isotope are from Suzouki and Epstein (1976) for biotite (D= -21.3, E= 0 and F= -2.8); for hornblende (D= -23.9, E= 0 and F= 7.9); and for muscovite (D= -22.1, E= 0 and F= 19.1). For calcite coefficients used for oxygen isotope are from Hu and Clayton et al. (2003) (D= 2.01, E= 0 and F= -1.77), and coefficients for quartz are from Clayton et al. (1972) (D= 2.51, E= 0 and F= -1.96). Fractionation factor for fluid–magnetite was calculated by the equation* $1000ln\alpha = (B.10^2)/T^4 + (D.10^3)/T^2$*, with B= 2.181 and D= -8.284, according to Cole et al. (2004).*

The $\delta^{18}O$ values for ore–related hydrothermal minerals range from +10.5 to +12.4‰ for quartz (n=19), +1.0 to +2.4‰ for magnetite (n=8), +6.4 to +8.1‰ for biotite (n=10), +6.7 to +8.9‰ for hornblende (n=12) and +10.1 to +10.7‰ for calcite (n=3), corresponding to fluid $\delta^{18}O$ values of +8.3 to +10.2‰, +8.8 to +10.2‰, +8.4 to +10.6‰, +8.9 to +11.0‰ and +9.1 to +10.8‰, respectively (**Table 3.2**). The δD values range from -93 to -32‰ for fluid inclusions in quartz (n=10), -98 to -72‰ for biotite (n=8) and -86 to -61‰ for hornblende (n=6), corresponding to fluid δD values of -93 to -32‰, -64 to -29‰ and -39 to -62‰, respectively (**Table 3.2**). For the associated country rocks of the Pedra Branca gold deposit, metamorphic hornblende from garnet–amphibolite samples have $\delta^{18}O$ values of +7.7 and +8.1‰, and δD values of -73 and -68‰, corresponding to fluid $\delta^{18}O$ values of +10.0 and +10.4‰, and fluid δD values of -58 and -54‰, respectively (**Table 3.2**). Muscovite from spatially–related S–type granite have $\delta^{18}O$ values of +10.4‰ and δD of -78 and -62‰, corresponding to fluid $\delta^{18}O$ values of +11.7‰ and fluid δD values of -76 and -60‰, respectively (**Table 3.2**). The $\delta^{13}C$ values for ore–related hydrothermal calcite range from -9.4 to -6.3‰ (n=3), whereas the analyzed graphite from metasedimentary country rocks yield $\delta^{13}C$ values of -27.1 and -22.7‰ (**Table 3.2**).

3.6.2. Isotope thermometry

Oxygen isotope thermometry for the mineral pairs from the hydrothermal assemblages of the Pedra Branca gold deposit is presented in Table 2 and Fig. 12. Temperature for coexisting minerals was calculated by the equation $\Delta = A \times 10^6/T^2$, where T is temperature (K) and A is an experimentally or empirically determined coefficient. The A coefficients used for oxygen isotope thermometry are the following: Qz–Mt= 6.12, Cc–Mt= 5.74 and Qz–Cc= -0.38 (Clayton and Kieffer, 1991); Qz–Bt= 2.16 (Chacko et al., 2001); Qz–Hb= 3.01 (Lackey

et al., 2008). Seven quartz–magnetite pairs indicate isotopic temperatures from 467 to 526°C (average 503°C), (**Table 3.2, Fig. 3.12A**). The approximate concordance of the calculated temperature for all the O–isotope data from different samples suggests that oxygen isotopic equilibrium was approached (**Table 3.2, Fig. 3.12A**). Also, on the plot of $\delta^{18}O_{mineral}$ versus $\Delta^{18}O_{Qz\text{-}Mt}$, the data define positive and negative slopes (**Fig. 3.13**), which is consistent with isotopic equilibration under closed-system conditions of originally hydrothermal mineral pairs (e.g. Gregory and Criss, 1986). The calculated temperatures of quartz–magnetite pairs are also similar to those calculated for two calcite–magnetite pairs (524 and 551°C) (sample FL-12, **Table 3.2, Fig. 3.12B**). Two calculated temperatures for a quartz–calcite pair gave much lower values of 404 and 394°C, but with much larger errors (**Table 3.2**).

Calculated temperatures for the quartz–hornblende and quartz–biotite pairs are presented for the calc-silicate alteration of the Pedra Branca gold deposit (**Table 3.2**). For these, separates of quartz vein and spatially associated hydrothermal hornblende and biotite were extracted from samples Fi–12, FQ–06, FL–12 and FL–19, which can be seen in **Fig. 3.3B, 3.4A** and **3.5C** (FL–12 has no photo). For each sample, the analyzed quartz separates are from the quartz vein, in spatial association with the hydrothermal hornblendes and biotites (**Fig. 3.3B, 3.4A** and **3.5C**). Therefore, the obtained $\delta^{18}O$ value of the quartz vein was used for temperature calculation with the associated hornblendes and biotites (**Table 3.2**). To test the degree of internal oxygen isotope equilibrium among these pairs, the $\delta^{18}O$ values of hornblende and biotite are plotted against the $\delta^{18}O$ value of the coexisting quartz veins (**Fig. 3.12C** and **D**). For sample Fi–12, the $\delta^{18}O$ values for separates of hornblende and the coexisting quartz, apparently exhibit a pattern in disequilibrium, wildly varying from 545 to 870°C and crossing the isotherm lines (**Fig. 3.12C**). Temperatures for quartz–hornblende pairs from samples FL–12 and FQ–06 yield less–variable temperatures, ranging from 611 to 693°C (average 646°C) and 515 to 590°C (average 548°C), respectively (**Table 3.2, Fig. 3.12C**). Temperatures calculated for all quartz–biotite pairs yield values from 377 to 557°C, which are systematically lower than the calculated ones from quartz–hornblende pairs of the same sample (**Table 3.2, Fig. 3.12 C** and **D**).

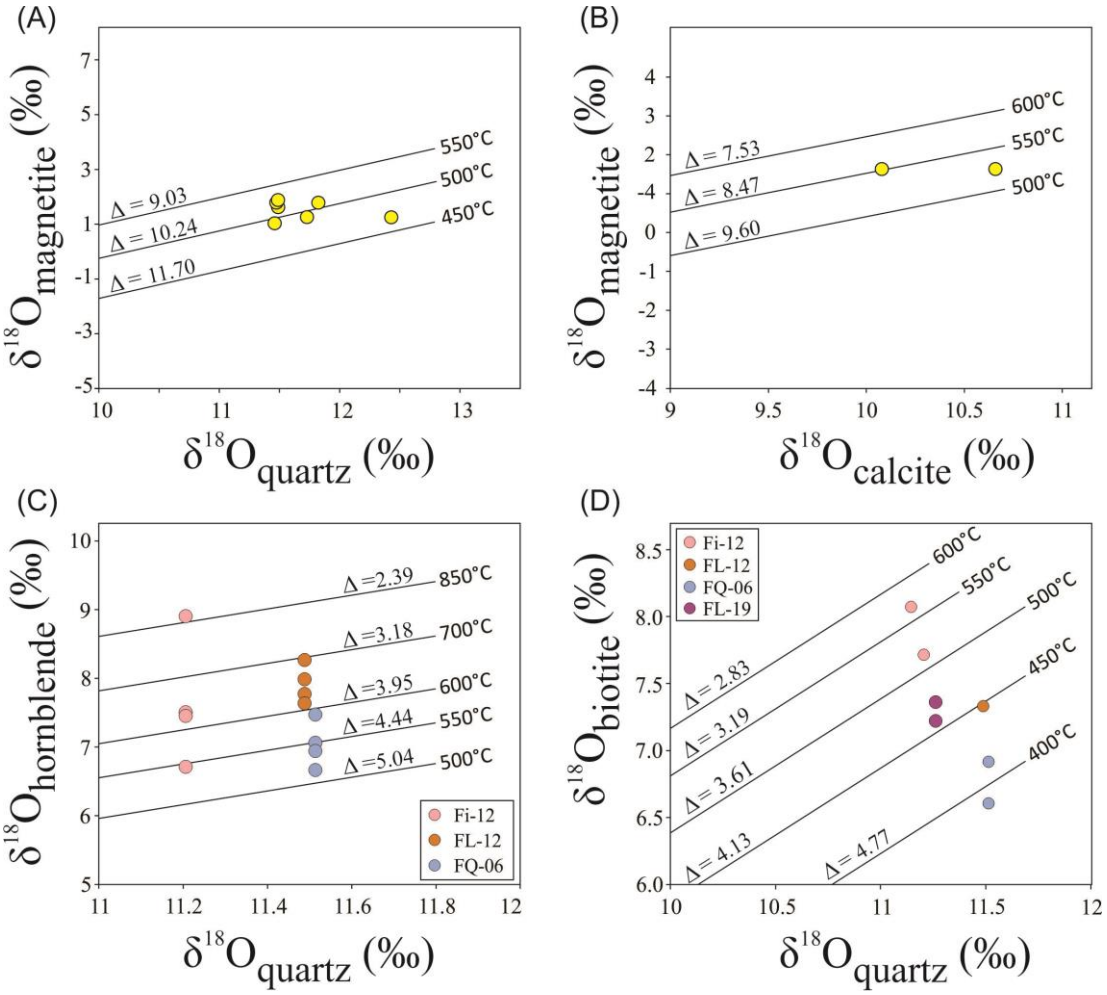

Fig. 3.12. *$\delta^{18}O$ for (A) quartz vs. magnetite, (B) calcite vs. magnetite, (C) quartz vs. hornblende and (D) quartz vs. biotite. Lines of constant per mil difference (Δ) are shown for each mineral pair.*

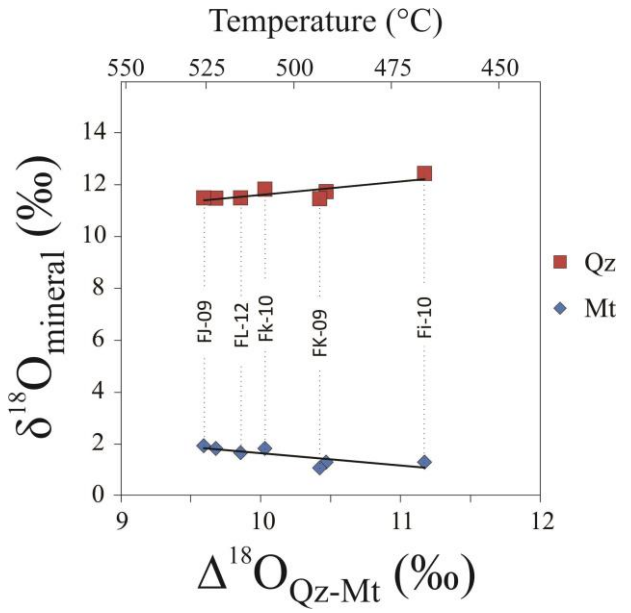

Fig. 3.13. *Plot for quartz and magnetite in the diagram of $\delta^{18}O_{mineral}$ vs. $\Delta^{18}O_{Qz\text{-}Mt}$ ($\Delta^{18}O_{Qz\text{-}Mt} = \delta^{18}O_{quartz} - \delta^{18}O_{magnetite}$). The data define positive and negative slopes consistent with isotopic equilibration under closed–system conditions.*

3.7. Discussion

3.7.1. Relating fluid inclusions to mineralization

In this study, whether the coexisting types of fluid inclusions of the FIA 1 are truly related to gold mineralization of the Pedra Branca deposit is difficult to prove, but there are some evidence to support this possibility: (1) These analyzed fluid inclusions come from a mineralized quartz vein; (2) The Type–II and Type–III inclusions of the FIA 1 have a much higher total homogenization temperature than the secondary Type–IV aqueous inclusions of the FIA 2 (**Table 3.1**), which makes the FIA 1 inclusions much more reliable to represent hydrothermal fluids associated with the gold–related high–temperature mineral assemblage (e.g. diopside, amphiboles, biotite, titanite, pyrite, magnetite) of the Pedra Branca gold deposit; (3) There is no need to link ore–forming fluids to primary fluid inclusions in the Pedra Branca gold deposit because this deposit is associated with shear zone and structural–controlled quartz veins (orogenic gold), so the pseudo–secondary nature of the FIA 1 could be ore–related, as early quartz in shear zones is repeatedly refractured, and much of the gold endowment may be sited in fractures in already–formed quartz veins (e.g. Wilson et al., 2013); (4) Fluid inclusion characteristics of the FIA 1 are consistent with a low–salinity H_2O–NaCl–CO_2 ± CH_4 hydrothermal fluid, which has been frequently reported as the most common ore–related fluid for orogenic gold deposits (e.g. Ridley and Diamond, 2000; Garofalo et al., 2014).

3.7.2. Fluid immiscibility

Fluid immiscibility has been proposed by several authors to interpret the coexistence of carbon–rich, aqueous–carbonic and aqueous–rich inclusions from many orogenic gold deposits, generally associating this phenomenon (phase separation, fluid immiscibility) as a trigger for gold deposition (e.g. Klein et al. 2000; 2001; 2006; 2015; Coulibaly et al., 2008; Zhang et al., 2012; Lawrence et al. 2013; Wang et al., 2015; Lambert–Smith et al., 2016).

The three types of fluid inclusions, CO_2–rich (Type–I), CO_2–NaCl–H_2O (Type–II) and NaCl–H_2O (Type–III), coexisting in the same fluid inclusion assemblage (FIA 1) are suggestive of phase separation (fluid immiscibility) (Fig. 7.1 B and C). Nevertheless, both mixing of different fluids (Anderson et al., 1992; Xavier and Foster, 1999) and necking down (Bakker and Jansen, 1994; Roedder, 1979) could also lead to the occurrence of CO_2–rich, CO_2–NaCl–H_2O and NaCl–H_2O inclusions in the same fluid inclusion assemblage. Therefore, it is firstly important to determine which process is related to the formation of the inclusions

identified in this study, which bears implications on the interpretation of PT conditions of fluid trapping. Mixing of two different fluids would result in distinct inclusion populations showing widely variable temperatures of total homogenization and salinities (e.g. Xavier and Foster, 1999). However, CO_2–NaCl–H_2O (Type–II) and NaCl–H_2O (Type–III) inclusions in this study show relatively uniform low salinity (0 to 7 wt% NaCl equiv.), but variable homogenization temperatures (**Table 3.1**) (**Fig. 3.11 G**). This lack of covariation indicates that the mixing of two separate fluids was not a relevant process for the formation of the coexisting Type–II and Type–III inclusions. This phenomenon of having a similar salinity alongside variable homogenized temperatures can also be due to necking down of the inclusions (Roedder, 1979). However, quartz hosting the analyzed fluid inclusions exhibits only weak deformation, and few necking down features were observed for fluid inclusions of the FIA 1, suggesting that these inclusions were unaffected (or least affected) by post-entrapment deformation.

The similar $TmCO_2$ and $ThCO_2$ of Type–I and Type–II fluid inclusions (**Fig. 3.11A** and **B**) from FIA 1 indicate that these inclusions trapped the same fluid during the evolution of the hydrothermal event. Furthermore, at room temperature, the variable proportions of CO_2 and H_2O phases of the Type–II inclusions (**Fig. 3.10C**) also indicate that liquid and vapour coexisted during entrapment (e.g. Diamond, 2001). Therefore, the following evidence favours fluid immiscibility (phase separation) having taken place for the observed FIA 1 in this study.

The Type–I and Type–II fluid inclusions show a positive correlation between $ThCO_2$ and $TmCO_2$ (**Fig. 3.11C**), and two mechanisms may explain this behavior (e.g. Klein et al. 2000): (1) oxidation of an early fluid at low oxidation-state, following the reaction $CH_4 + 2O_2 = CO_2 + H_2O$; or (2) reduction of an initially more oxidized fluid exemplified by the hydration reaction $CO_2 + 4H_2 = CH_4 + 2H_2O$. The predominance of inclusions with high $ThCO_2$ and $TmCO_2$ strongly indicates that the first mechanism has occurred. The oxidation might be related to fluid immiscibility. During phase separation of a CO_2–CH_4–H_2O–salt fluid, the CH_4 content of the fluid decreases toward the end of the process in response to the higher gas distribution coefficient of the CH_4 in relation to CO_2 (Drummond and Ohmoto, 1985).

3.7.3. PT conditions of alteration and mineralization

The isochore calculations were performed in software from Bakker et al. (2003), using the equation from Belonoshko and Saxena (1991) (pure CO_2) for CO_2–rich inclusions (Type–I) and the equations from Bakker (1999) and Bowers and Helgeson (1983) for NaCl–H_2O aqueous inclusions (Type–III). The possible range of PT conditions for the gold

mineralization was obtained from the intersection of the maximum and minimum density isochores of Type–III inclusions with the temperature range of 467–525°C from quartz–magnetite isotopic geothermometer ($\Delta^{18}O_{(Qz–Mt)}$) (**Fig. 3.14**). The gray area represents the possible range of PT conditions for the gold mineralization, from 467 °C and 1.93 kbar (c. 7 km) to 526 °C and 3.48 kbar (c. 13 km). Related lithostatic depth was calculated using a density of 2.8 g/cm^3. The intersection of the isochores of Type–III inclusions with the quartz–magnetite isotopic geothermometer provide very consistent PT conditions, compared to hydrothermal alteration (e.g. diopside, hornblende, biotite) and results our from isotope geothermometry (**Fig. 3.13**) (**Table 3.2**). The fluctuation in the range of density of the calculated isochores (**Fig. 3.14**) correlates well with an alternating lithostatic fluid system, associated to the fault-valve model, which is common in orogenic gold deposits (e.g. Sibson et al., 1988; Kerrich et al., 2000; Deng et al., 2014).

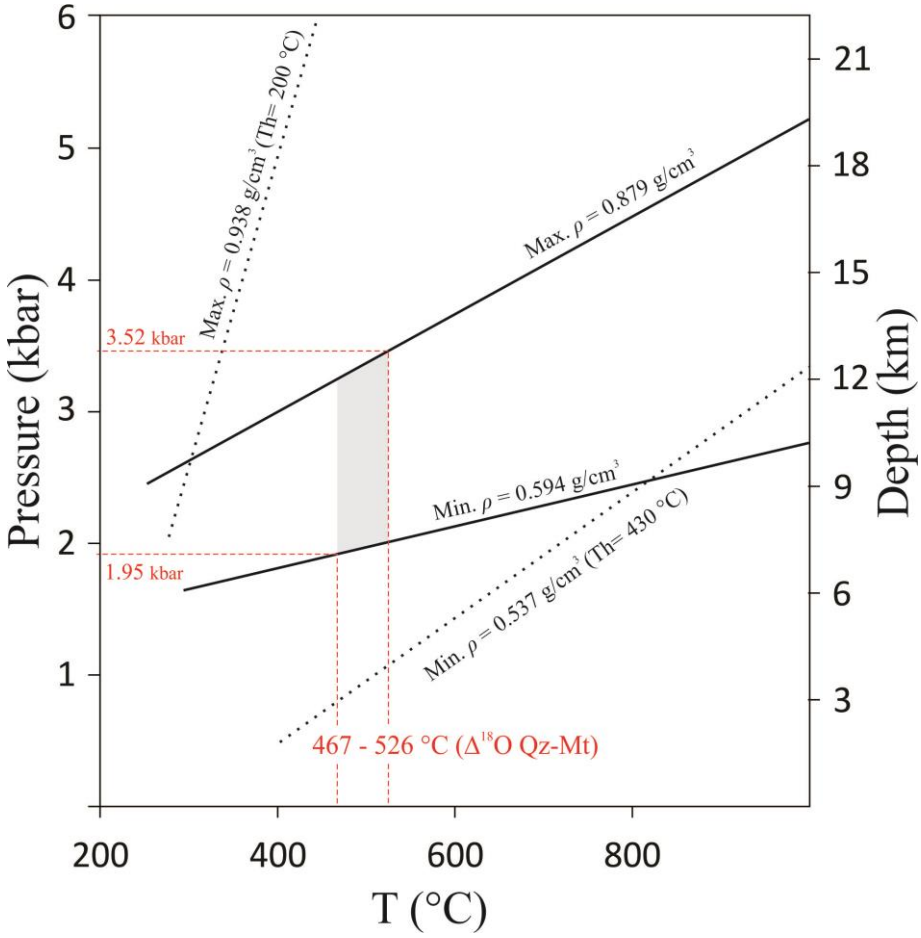

***Fig. 3.14**. Isochores for coexisting Type–I and Type–III inclusions of the FIA 1. Dashed lines are for CO_2–rich (Type–I) inclusions and solid lines for NaCl–H_2O aqueous (Type–III) inclusions. The temperature range of 467–525 °C was obtained from calculation of the quartz–magnetite isotopic geothermometer ($\Delta^{18}O_{(Qz–Mt)}$). The gray area represents the possible range of PT conditions for the gold mineralization, from 467 °C and 1.93 kbar (c. 7 km) to 526 °C and 3.48 kbar (c. 13 km).*

The high temperatures obtained for quartz–hornblende pairs (515 to 870°C, n=12) from ore–related hydrothermal assemblage of the Pedra Branca gold deposit, suggest that fluid evolution underwent high temperatures during its early stages, compatible with hydrothermal "skarn–type" calc–silicate alteration and albitization (**Fig. 3.7**). The presence of diopside replaced by hornblende (**Fig. 3.3**), and the decreasing calculated temperature from quartz–hornblende (average 620°C, n=12) to quartz–biotite (average 442°C, n=8) isotopic thermometers (**Table 3.2** and **Fig. 3.12C** and **D**), reflect strong temperature variation of the hydrothermal system, which can also trigger gold deposition (e.g. Orde and Hobbs et al. 2018). For sample FQ-06 (Mirador area) (**Fig. 3.4A**), oxygen isotope thermometry for the quartz–hornblende and quartz–biotite pairs yield temperatures from 515 to 590°C (average 548°C, n=4) and 377 to 412°C (average 392°C, n=4), respectively (**Table 3.2, Fig. 3.12C** and **D**). The average temperature (392°C) for the quartz–biotite thermometer is also very similar to the obtained temperature of 394°C from the calcite–quartz pair of the same sample (FQ-06) (**Table 3.2**).

Free–milling gold has been found in spatial association with late magnetite that replaces pyrite crystals (**Fig. 3.6** and **3.8**). This implies that major gold deposition probably occurred by oxidation of the fluid during its evolution (**Fig. 3.7**). Therefore, as magnetite appears to be genetically linked to gold mineralization, the best estimated temperature for gold precipitation is given by the quartz–magnetite isotope geothermometer (**Table 3.2, Fig. 3.12A**). The relative large oxygen isotope fractionation between quartz and magnetite make this mineral pair one of the most sensitive isotope geothermometers on nature (Bottinga and Javoy, 1973; Chiba et al., 1989; Clayton and Kieffer, 1991). For the analyzed samples, quartz and magnetite occurs in well isotopic equilibrium (**Fig. 3.13**), and the temperature for the quartz–magnetite pairs reported for albitites and calc–silicate alteration yield values from 467 to 526°C (n=7, average 503°C) (**Table 3.2** and **Fig. 3.12A**). This is also consistent with the temperature obtained by the fluid inclusion isochore method (**Fig. 3.14**).

3.7.4. Origin of gold–associated magnetite

The $\delta^{18}O$ value of magnetite is commonly used to interpret if magnetite crystallizes from low–temperature hydrothermal fluids or magmatic processes (e.g. Taylor, 1967; Nystrom et al., 2008; Jonsson et al., 2013). According to Taylor (1967), igneous magnetite is very uniform in $^{18}O/^{16}O$ ratio ($\delta^{18}O$= +1 to +4 ‰), and any magnetite with $\delta^{18}O$ values substantially outside this range must have a different derivation or have been recrystallized and altered later to its formation. To distinguish magmatic and/or magmatic–hydrothermal

magnetite from low–temperature (≤ 400°C) hydrothermal magnetite, samples with $\delta^{18}O$ values ≥ +0.9‰ satisfy equilibrium conditions with high–temperature magmatic waters (Nystrom et al., 2008; Jonsson et al., 2013) (**Fig. 3.15**). However, it is not possible to distinguish between magmatic (igneous magnetite) and magmatic–hydrothermal magnetites using O–isotopes alone, and according to Jonsson et al. (2013), they can just be termed as "ortho–magmatic", to distinguish it from low–temperature (≤ 400°C) hydrothermal magnetites (**Fig. 3.15**).

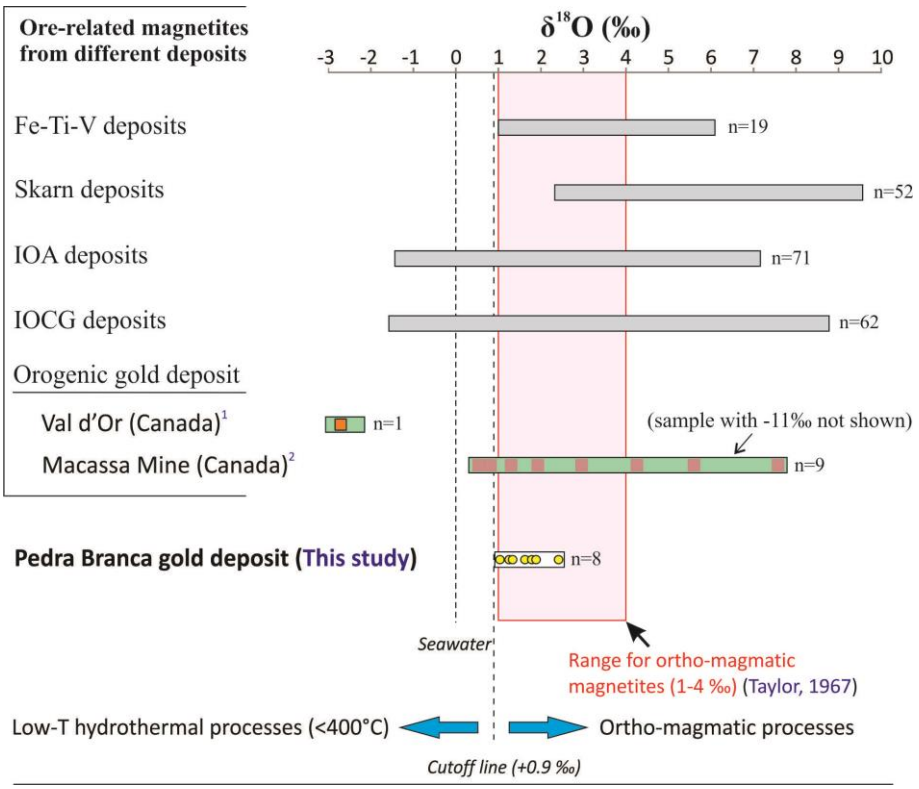

***Fig. 3.15**. Magnetite $\delta^{18}O$ values from the Pedra Branca gold deposit compared to other ore–related magnetites from different deposit types (modified after Jonsson et al., 2013). Range for typical ortho–magmatic magnetites (+1 to +4‰) is according to Taylor (1967) (pink field). The Pedra Branca gold–related magnetites range between +1.04‰ and +2.42‰ and thus plot entirely in the field of ortho–magmatic magnetites, suggesting that they must have been in equilibrium with high–temperature (>400 °C) magmatic fluids. The cut–off point between ortho–magmatic and low–T hydrothermal magnetites is +0.9‰ (Jonsson et al., 2013). Magnetites with $\delta^{18}O$ values lower than +0.9‰ are believed to have been in equilibrium with a high negative $\delta^{18}O$ fluid at temperatures of <400 °C. References for ore–related magnetites from different deposit types are: Orogenic gold deposits (1- Beaudoin and Pitre, 2005; 2- Kerrich and Watson, 1984), Fe–Ti–V deposits (Yu et al., 2015; Ganino et al., 2013; Rose et al., 1985; Singoyi, 1995; Zürcher et al., 2001; Zheng et al., 2017; Xie et al., 2017), IOA deposits (Nystrom et al., 2008; Jonsson et al., 2013; Childress et al., 2016) and IOCG deposits (Chen et al., 2011; Dreher et al., 2008; Acosta-Góngora et al., 2015; Bastrakov et al., 2007; Monteiro et al., 2008; Silva et al., 2015; Rotherham et al., 1998; Oreskes and Einaudi, 1992).*

The compiled $\delta^{18}O$ values for ore–related magnetite from different deposit types, such as Iron–Oxide–Apatite (IOA), Iron–Oxide–Cooper–Gold (IOCG), Fe–Ti–V and orogenic gold deposits are shown in **Fig. 3.15**. In this diagram, the less–variable and high $\delta^{18}O$ values are found for skarn–type magnetite (**Fig. 3.15**). Magnetite in the skarn iron ores are generally interpreted as precipitation from a reaction between ^{18}O–rich carbonate–dominated country rocks and magmatic–hydrothermal fluids (e.g. Zürcher et al., 2001; Zheng et al., 2017; Xie et al., 2017). The $\delta^{18}O$ values of magnetite from IOA deposits usually plot in the range of ortho–magmatic magnetite, indicating magnetite derivation from magma and/or high–temperature magmatic–hydrothermal fluid (**Fig. 3.15**) (Nystrom et al., 2008; Jonsson et al., 2013; and references therein). However, for the low $\delta^{18}O$ values (< +0.9‰) of some IOA magnetites, the influence (e.g. mixing) of low–temperature hydrothermal fluids (e.g. meteoric water) is generally assumed to be involved (**Fig. 3.15**) (Nystrom et al., 2008; Jonsson et al., 2013; and references therein). In IOCG deposits, wild variation on $\delta^{18}O$ values of magnetite is observed (**Fig. 3.15**), suggesting distinct processes to its genesis. In general, magnetite associated to IOCG deposits are interpreted to precipitate from early high–temperature magmatic–hydrothermal fluids, but gold/copper mineralization is usually interpreted to precipitate by the interaction (e.g. mixing) with late low–temperature fluids (e.g. meteoric water) (e.g., Oreskes and Einaudi, 1992; Bastrakov et al., 2007; Monteiro et al., 2008; Dreher et al., 2008; Chen et al., 2011; Silva et al., 2015).

For those deposits interpreted as orogenic gold, only a few $\delta^{18}O$ values of hydrothermal magnetite are found in literature (Kerrich and Watson, 1984; Beaudoin and Pitre, 2005) (**Fig. 3.15**), since magnetite is not a common mineral within hydrothermal alteration of orogenic gold deposits (e.g. Eilu et al., 1991; Eilu and Mikucki, 1998). According to Beaudoin and Pitre (2005), one sample of hydrothermal magnetite of the Val-d'Or vein field, Abitibi greenstone belt, yielded a $\delta^{18}O$ of -2.8‰, evidencing a low–temperature (>400°C) derivation (**Fig. 3.15**). This is consistent with the calculated temperature of 384°C obtained by Beaudoin and Pitre (2005) for a quartz–magnetite pair of the Val-d'Or vein field. In other example, the lode–gold Macassa Mine, also in Abitibi, the $\delta^{18}O$ values of magnetite presented by Kerrich and Watson (1984) are generally higher than the +0.9‰ cutoff for low–temperature (>400°C) magnetite (**Fig. 3.15**). This is also consistent with the calculated temperature for quartz–magnetite pairs of the Macassa Mine, ranging from 400 to 420°C (Kerrich and Watson, 1984). According to these authors, gold mineralization and associated magnetite of the Macassa Mine originated from metamorphic hydrothermal solution, with a possible contribution from magmatic–hydrothermal fluids.

The $\delta^{18}O$ values of magnetites from the Pedra Branca gold deposit range between +1.0 to +2.4‰ (n=8) (**Table 3.2**), and therefore, they fit entirely within the range of "ortho–magmatic" magnetite (**Fig. 3.15**). This indicates a high–temperature (>400°C), and probably magmatic–hydrothermal genesis for the Pedra Branca gold–related magnetites (**Fig. 3.15**). This is also consistent with the calculated temperature for quartz-magnetite pairs, ranging from 467 to 526°C (**Table 3.2**) (**Fig. 3.12A**).

3.7.5. Nature and source of the hydrothermal fluid

3.7.5.1. Oxygen and Hydrogen

The oxygen stable isotope data presented for the Pedra Branca deposit have fluid $\delta^{18}O$ values ranging from +8.3 to +11.0‰ (n=59) (**Table 3.2**), which indicate an average fluid $\delta^{18}O$ value of +9.4‰ for fluids circulating through mineralized rocks. The narrow range in fluid $\delta^{18}O$ values for the analyzed ore–related hydrothermal minerals, indicate a common fluid source for all hydrothermal minerals (**Table 3.2**) (**Fig. 3.16**). The uniformity of oxygen isotope values for mineralizing fluids is common in orogenic gold deposits (e.g. Kerrich 1987; McCuaig and Kerrich, 1998; Kontak et al., 2011; Goldfarb and Groves, 2015), and the fluid $\delta^{18}O$ values for Precambrian orogenic gold deposits generally range from +6 to +11‰ (McCuaig and Kerrich, 1998). However, there is no consensus if hydrothermal fluids in orogenic gold deposits originated from a magmatic and/or metamorphic source (e.g. Goldfarb and Groves, 2015 and references therein). According to McCuaig and Kerrich (1998), fluid $\delta^{18}O$ values greater than +8‰ cannot be magmatic fluids alone, and some ^{18}O–rich crustal contribution (e.g. fluid mixing and/or exchange) is needed for the genesis of orogenic gold deposits. Some authors have interpreted that the high $\delta^{18}O$ values in original derived magmatic fluid is the result of fluid–rock interaction in the metavolcano–sedimentary sequence (e.g. ^{18}O–enriched metasedimentary rocks) (e.g. Roger et al., 2013; Bhattacharya et al., 2014).

The calculated δD and $\delta^{18}O$ composition of the fluid taken for ore–related hydrothermal minerals of the Pedra Branca gold deposit, and δD values measured in inclusion fluids, plot in the overlapping fields of magmatic and metamorphic fluids, after Sheppard (1986), or are slightly displaced from the magmatic water box (**Fig. 3.16**). This suggests that the hydrothermal fluid originated from a magmatic and/or deep–seated metamorphic source, which is also consistent with fluid composition of those related to Precambrian orogenic gold deposits (**Fig. 3.16**).

The calculated fluid $\delta^{18}O$ value of +8.8‰ for the c. 2068 Ma monzogranite (**Table 3.2**) located in the northern part of the Serra das Pipocas greenstone belt (**Fig. 3.2**), suggest that it could be a possible candidate for the source of ore–forming fluids (magmatic–hydrothermal fluid). However, the fluid $\delta^{18}O$ = +8.8‰ value of the monzogranite is slightly lower than the average fluid $\delta^{18}O$ = +9.4‰ value of the analyzed samples ranging from +8.3 to +11.0‰ (n=59) (**Table 3.2**). The calculated fluid $\delta^{18}O$ values for muscovites from S–type granite, which is intruded in the Serra das Pipocas greenstone belt (**Fig. 3.2**), yields two similar values of 11.7‰, which are higher than the range of fluid $\delta^{18}O$ values in equilibrium with the hydrothermal minerals (**Table 3.2**) (**Fig. 3.16**). The S–type granite perhaps represents partial melting of the greenstone metasedimentary rocks at greater depth, inheriting the high $\delta^{18}O$ value from the metasedimentary source. This also implicates that none of the ^{18}O–rich S–type granite and/or metasedimentary rocks of the greenstone pile may solely represent the source of the ore–forming fluid (**Fig. 3.16**). More likely, the calculated fluid $\delta^{18}O$ values for metamorphic hornblende from two garnet–amphibolite samples of the Serra das Pipocas greenstone belt yielded values of +10.0 and +10.4‰, which is in the range of calculated fluid $\delta^{18}O$ values related to the Pedra Branca gold deposit (**Table 3.2**) (**Fig. 3.16**). This could suggest that the amphibolites (after mafic metavolcanic rocks) may represent a potential source of the ore–forming fluid, as some of it went through a devolatization process at greater depths in the greenstone pile (e.g. Phillips and Powell, 2010). However, fluid $\delta^{18}O$ values of +10.0 and +10.4‰ for hornblende of the metamorphic amphibolites cannot alone explain some low fluid $\delta^{18}O$ values (down to +8.3‰) of the calculated ore–related hydrothermal minerals (**Table 3.2**) (**Fig. 3.16**).

Calculated δD values of the hydrothermal ore–forming fluid vary more than the calculated fluid $\delta^{18}O$ values, especially the fluid δD values from the analyzed fluid inclusions from quartz veins (e.g. down to -93‰) (**Table 3.2**) (**Fig. 3.16**). However, bulk extraction of fluid inclusions from quartz veins has to be carefully interpreted (e.g. Goldfarb and Groves, 2015). According to these authors, several low fluid δD values obtained by analyzing bulk extraction of fluid inclusions are due to late generations of secondary inclusions, trapping meteoric water unrelated to gold deposition. Thus, the lowest fluid δD value of -93‰ obtained for sample FQ-10 (quartz vein) of this study (**Table 3.2**) (**Fig. 3.16**), may be due to late secondary aqueous inclusions in this sample. However, large δD variations can also be produced during fluid immiscibility (Kerrich 1987; Taylor 1997), by changes in the oxygen fugacity of the fluid at the depositional site (Colvine et al. 1988) and/or postentrapment

modification in fluid inclusions (selective water leakage), causing H_2 difusion (Klein et al., 2006).

Therefore, based only on oxygen and hydrogen isotopes, we suggest that the most likely evolution of the ore–forming fluid in the Pedra Branca gold deposit, may be related to a magmatic–hydrothermal fluid (e.g. ~2068 Ma granite magmatism with fluid $\delta^{18}O$ = +8.8‰), that interacted with ^{18}O–rich metavolcano–sedimentary rocks of the greenstone pile (e.g. fluid $\delta^{18}O$ from amphibolites = +10.0 and +10.4‰). In addition, preliminary constraints on the age of gold mineralization in 2029 ± 28 Ma (U-Pb titanite age) (Costa et al., submitted), also corroborate with the link to the ~2090–2030 Ma post–collisional granite magmatism, associating gold mineralization to the end of Paleoproterozoic crustal evolution of the Troia Massif (e.g. Costa et al., 2018).

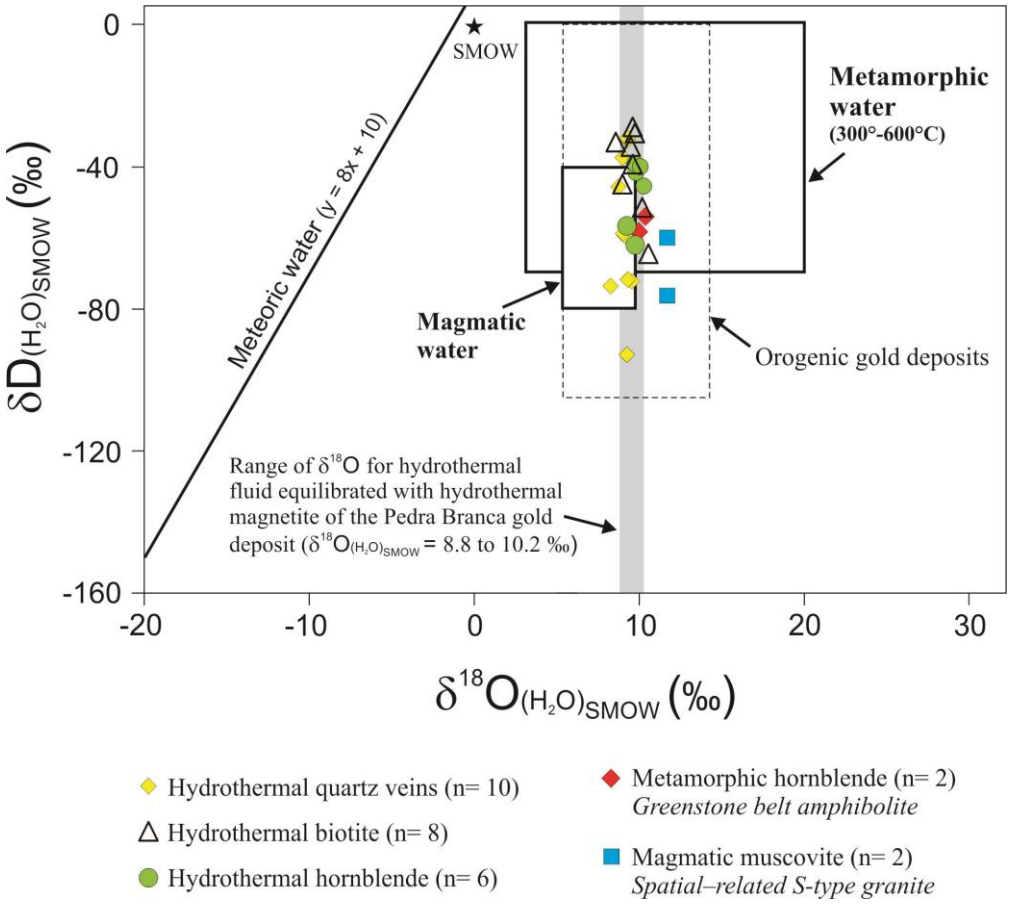

Fig. 3.16*. Oxygen and hydrogen isotopic compositions for fluid in equilibrium with ore–related hydrothermal minerals, metamorphic hornblende (amphibolite) and muscovite from S–type granite. Fields for metamorphic and magmatic water are from Sheppard (1986), and the field for Precambrian orogenic gold deposits is from Goldfarb et al. (2005). The meteoric water line is from Craig (1961).*

3.7.5.2. Carbonate and graphite isotopic signature

Since CO_2–rich fluid is a common characteristic of hydrothermal gold deposits (e.g. orogenic gold), several studies on stable carbon and/or oxygen isotopes have been presented for hydrothermal carbonates and/or fluid inclusions to infer the possible sources for CO_2 in hydrothermal fluids (e.g. Kerrich and Fyfe, 1981; Burrows et al. 1986; Groves and Phillips, 1987; Groves et al., 1988; Santosh et al., 1995; McCuaig and Kerrich, 1998; Knight et al., 2000; Klein et al. 2006; Sun et al., 2009; Sarangi et al., 2012; Lüders et al., 2015; Swain et al., 2015; 2018). Among these authors, interpretations are generally in favor of a mantle and/or magmatic origin for CO_2 (Burrows et al. 1986; Groves et al., 1988; Santosh et al., 1995; Sun et al., 2009; Sarangi et al., 2012; Swain et al., 2015; 2018), or in favor of the metamorphic model, in which CO_2 derives from dehydration of mafic metavolcanic rocks and/or decarbonation of metasedimentary carbonaceous rocks (Kerrich and Fyfe, 1981; Groves and Phillips, 1987; Lüders et al., 2015). However, the interaction of mantle and/or magmatic–derived fluids with supracrustal rocks and/or metamorphic fluids has also been proposed for the origin of CO_2 in orogenic gold deposits (McCuaig and Kerrich 1998; Kinght et al., 2000; Klein et al., 2006).

The hydrothermal carbonates (calcite) of the Pedra Branca gold have $\delta^{13}C$ values from -6.3 to -9.4‰ and $\delta^{18}O$ values from +10.1 to +10.7‰ (**Table 3.2**). This indicates composition near the carbonatite field of Taylor et al. (1967) (**Fig. 3.17**), and, is therefore, compatible with a magmatic fluid and/or mantle–derived fluid signature (e.g., Burrows et al., 1986; Groves et al., 1988). The calculated $\delta^{18}O$ composition of the fluid in equilibrium with the analyzed carbonates range from 9.1 to 10.8‰, which are in the range of the calculated fluid $\delta^{18}O$ values for other hydrothermal minerals of the Pedra Branca gold deposit (**Table 3.2**). Thus, similar interpretation for the increase of $\delta^{18}O$ values in an originally derived magmatic fluid by fluid–rock interaction in the greenstone pile (e.g. ^{18}O–enriched metasedimentary rocks), may also be applied for the oxygen isotope composition of the analyzed carbonates. Similarly, the $\delta^{13}C$ values (-6.3 to -9.4‰) from the analyzed carbonates may also represent an originally derived magmatic fluid ($\delta^{13}C$ ~ -5.0‰; Burrows et al., 1986), that underwent fluid–rock interaction in the greenstone pile (e.g. ^{13}C–depleted metasedimentary rocks). In addition, graphite separates from metasedimentary rocks (graphitic–schist) of the Serra das Pipocas greenstone sequence yields $\delta^{13}C$ values of -22.7 and -27.1‰ (**Table 3.2**), which is consistent with an organic carbon source (Hoefs, 2009).

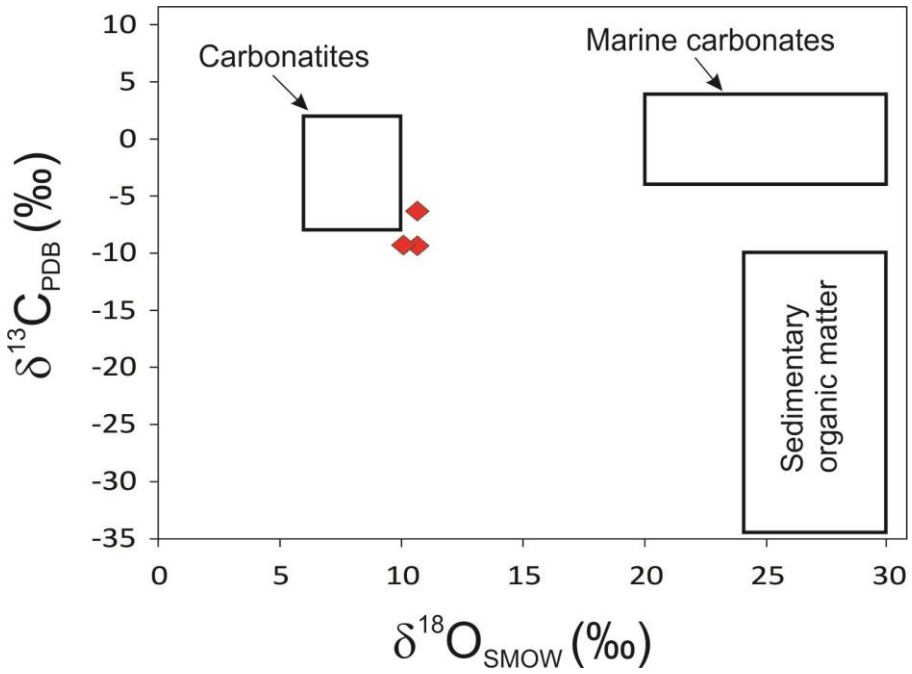

Fig. 3.17*. Carbon and oxygen isotope composition for hydrothermal calcites from the Pedra Branca gold deposit. Fields for igneous carbonatites from Taylor et al. (1967) Marine carbonates from Veizer and Hoefs (1976) and sedimentary organic matter from Hoefs (2009).*

So far, a magmatic–hydrothermal fluid that interacted with ^{13}C–depleted metasedimentary rocks of the greenstone pile may be a plausible interpretation for the observed $\delta^{13}C$ values of the analyzed carbonates from the Pedra Branca gold deposit, as similarly interpreted for other hydrothermal gold deposits (e.g. Klein et al., 2006; Marshall et al., 2006). For example, according to Klein et al. (2006), in the Serrinha gold deposit of the Gurupi Belt, Brazil, the $\delta^{13}C$ values in vein carbonates vary from -14.2 to -15.7‰, and is -23.6‰ in graphite of the host rocks, suggesting a contribution of organic carbon to fluids that were originally rich in ^{13}C (e.g. magmatic fluid and/or mantle–derived).

3.7.6. Hypozonal orogenic gold deposits and commonly associated fluids

The calculated values for pressure and temperature taken from fluid inclusion density and isotopic thermometry for the Pedra Branca gold mineralization give a possible range of PT conditions for the gold mineralization from 467 °C and 1.93 kbar (c. 7 km) to 526 °C and 3.48 kbar (c. 13 km) (**Fig. 3.14**). This is fairly compatible with the compiled PT data for hypozonal orogenic gold deposits, mainly between c. 500–700ºC and 2–7 kbar, while the mesozonal orogenic gold deposits exhibits temperatures and pressures lower than 400°C and 2.5 kbar, respectively (e.g. Kolb et al., 2015 and references therein).

However, many gold deposits in high–grade metamorphic rocks can be explained by mineralization at greenschist facies conditions, wich is subsequently metamorphosed to mid–amphibolite (e.g., Hemlo, Tomkins et al., 2004; Big Bell, Phillips and Powell, 2009) or granulite facies (Challenger, Tomkins and Mavrogenes, 2002; Griffins Find, Tomkins and Grundy, 2009). Therefore, the recognition of texture diagnostics of ore mineral assemblage melting and deformation of the studied deposit is crucial for interpreting it as a hypozonal type, or an overprinted mesozonal deposit (e.g. Tomkins and Mavrogenes, 2002; Tomkins et al., 2004). For example, inclusion of gold or gold-bearing sulfide minerals in peak metamorphic minerals (particularly K-feldspar and garnet) may be diagnostic of a mesozonal gold mineralization overprinted by high–grade regional metamorphism (e.g. Tomkins and Mavrogenes, 2002; Tomkins et al., 2004). In the Pedra Branca gold deposit, none of these features have been recognized, and the documented albitization and calc–silicate alteration are more likely to represent processes of the hypozonal hydrothermal gold mineralization.

The "skarn–type", diopside–bearing calc–silicate hydrothermal alteration (**Fig. 3.3**), is developed in many examples of hypozonal orogenic gold deposits, and commonly associated with the emplacement of granites, late in the regional metamorphic evolution (Mueller and Groves, 1991; Bucci et al., 2002; Wulff et al., 2010; Mueller et al., 2004; Doublier et al., 2014). Because of the deep crustal origin of hypozonal gold mineralization, anatectic melts are coeval and spatially related to many of these high–temperature mineralizations, and form an integral part of the terrane deformation, metamorphism and mineralization (e.g. Bucci et al., 2002; Ootes et al., 2011; Biczok et al., 2012; Doublier et al., 2014; Kolb et al., 2015). So far, the magmatic fluid source of some hypozonal gold deposits is commonly associated to crustal–derived granites (e.g. Knight et al., 2000; Krienitz et al., 2008; Biczok et al., 2012; Rogers et al., 2013; Doublier et al., 2014; Sahoo et al., 2018). For example, in the Hutti and Hira–Buddini orogenic gold deposits of southern India, gold precipitation at c. 530°C and 3 to 4 kbar is interpreted to be related to magmatic fluid derived from the Yellagatti and Kavital granites, that later underwent fluid–rock interaction in the greenstone pile (Krienitz et al., 2008; Rogers et al., 2013; Sahoo et al., 2018).

Therefore, as discussed in the above examples, and as highlighted by Kolb et al. (2015), the formation of hypozonal gold deposits occur in dynamic settings involving a complex tectono–metamorphic and magmatic evolution in a given orogeny, where fluids may derive from both metamorphism and contemporaneous magmatism. The wide spread of granitic melts present late in the orogeny evolution (e.g. "late granite bloom") release fluids that mix with the metamorphic fluids, as generally interpreted for many hypozonal orogenic

gold mineralizations (Mueller et al., 2004; Krienitz et al., 2008; Mueller et al., 2008; Rogers et al., 2013; Doublier et al., 2014; Kolb et al., 2015; Sahoo et al., 2018).

3.7.7. Orogenic oxidized intrusion–related systems

Magnetite–bearing calc–silicate hydrothermal alteration and/or albitization, as reported here for the Pedra Branca gold deposit, has been recognized in other hydrothermal gold deposits within Precambrian greenstone belts, such those of the Eastern Goldfields, Yilgarn Craton, Western Australia (e.g. Bucci et al., 2002; Salier et al., 2004; Mueller et al., 2008; Neumayr et al., 2008; Evans, 2010; Mueller et al., 2012; Jowett et al. 2014; Witt et al., 2015; 2018). However, this magnetite–bearing alteration is mineralogically unusual for a typical orogenic gold deposit (e.g. Eilu et al., 1991; Eilu and Mikucki, 1998). Many authors interpret that magnetite within these lode–gold deposits derives from oxidized magmatic–hydrothermal fluids (e.g. Bucci et al., 2002; Salier et al., 2004; Mueller et al., 2008; Neumayr et al., 2008; Mueller et al., 2012; Jowett et al. 2014; Witt et al., 2015; 2018). However, Evans (2010) interpreted that strong oxidation by fluid–rock interaction may generate abundant magnetite in the deposit site, without any need for an external oxidizing fluid. For these magnetite–bearing deposit types, Witt et al. (2015) placed them within the "proximal intrusion–related" subclass of orogenic gold deposits, which is characterized by proximal biotite and/or amphibole alteration associated with hydrothermal magnetite. These gold deposits have generally a close temporal–spatial association with mantle–derived syenitic intrusions (Mueller et al., 2008; Witt et al., 2018) or crustal–derived granites (Jowett et al. 2014). Many of these deposits contain proximal albite–rich alteration, in which gold is associated with disseminated pyrite/magnetite in albite–rich host rocks (Witt et al., 2015; 2018). This is very similar to the features found in the gold–mineralized albitites of the Queimadas area (**Fig. 3.8**), in association with gold–bearing amphibole–biotite–pyrite–magnetite calc–silicate (or "skarn–type") alteration (**Fig. 3.3** and **3.4**).

In the Pedra Branca gold deposit, free–milling gold is generally associated to magnetite (**Fig. 3.8**) and tellurides (**Fig. 3, 4, 8** and **9**). The main tellurides found in the Pedra Branca gold deposit are hessite (Ag_2Te), altaite (PbTe), sylvanite $(AgAu)Te_2$), calaverite ($AuTe_2$) and tellurobismuthite (Bi_2Te_3) (**Fig. 3, 4, 8** and **9**). The association of gold with telluride minerals in hydrothermal gold deposits is generally interpreted as derivation from an oxidized fluid source of magmatic–hydrothermal origin (e.g. Bucci et al., 2002; Grundler et al., 2013; Jowett et al. 2014; Xu and Campbell, 2015; Zhou et al., 2018; Spence–Jones et al., 2018). Several hydrothermal gold deposits have been genetically linked to oxidized magmatic

intrusions, such as those examples described in the Archean Abitibi greenstone belts in Canada (e.g. Robert et al., 2001; Beakhouse, 2007; 2011; Helt et al., 2014; Bigot and Jébrak, 2015; Fayol and Jébrak, 2017) and the aforementioned Eastern Goldfields in Western Australia (e.g. Mueller et al., 2008; 2012; Witt et al., 2015; 2018). As highlighted by Witt et al. (2015; 2018), it is important to recognize that these intrusion–related deposits discussed here, are associated with oxidized, alkali–rich intrusions, and are therefore distinct from intrusion–related gold systems associated with reduced intrusions (e.g. Lang and Baker, 2001; Hart, 2007). In addition, as also commented by Witt et al. (2015), these oxidized intrusion–related gold deposits are mostly connected with late orogenic granitoids, so they may be termed as "orogenic oxidized intrusion–related gold systems".

3.7.8. Gold mineralization and post–collisional magmatism

The 2029 ± 27 Ma U-Pb titanite age of gold mineralization in the Pedra Branca deposit (Costa et al., submitted), places it in the final setting of Paleoproterozoic crustal evolution of the country rocks. The age of gold mineralization is very close (within error) to the ages of 2068 ± 5 and 2079 ± 4 Ma potassic magmatism of the Bananeira suite (Costa et al., 2018), to the c. 2100 Ma Boa Viagem mafic–ultramafic intrusion (Almeida, 2014), the 2100–2070 Ma S–type granitoids (Pessoa et al., 1986; Garcia et al., 2014), the c. 2040 Ma for metamorphic zircon overgrowth in detrital zircons from high–grade paragneiss of the Jaguaretama complex (Calado et al., 2018), the 2046 ± 12 Ma leucosome age from migmatite (Gomes, 2013) and the 2036 ± 28 Ma PGE–bearing chromitite of the Troia Massif (Costa et al., 2014b). This clearly relates the gold mineralization to the late tectonic evolution of the Rhyacian granite–greenstone terranes of the Troia Massif, similarly as proposed for many Paleoproterozoic greenstone belts of the surrounding cratonic domains, such as the São Francisco craton (e.g. Rio Itapicuru greenstone belt, gold mineralization at c. 2080–2050 Ma, Mello et al., 2006), Guiana shield (Omai area, gold mineralization at c. 2002–2094 Ma, Norcross et al., 2000), São Luís craton (Caxias and Piaba deposit, gold mineralization at c. 2009–1990 Ma, Klein et al., 2014) and West Africa craton (e.g. Wassa deposit at 2055 ± 18 Ma and Obuasi at 2045 ± 40 Ma, Mignot et al., 2017).

The evidence for high–grade metamorphism and the contemporaneity of crustal– and mantle–derived magmas during the Paleoproterozoic evolution of the Troia Massif is typical of post–collisional setting (e.g. Liégeois et al., 1998; Bonin, 2004). Mantle– and crust–derived magmatism in a post–collisional setting is generally attributed to slab breakoff (Liégeois and Black, 1987; Davies and von Blanckenburg, 1995; Atherton and Ghani, 2002) or large scale

continental lithospheric delamination (e.g. Kay and Mahlburg Kay, 1993; Rey et al., 2001; Liégeois et al., 2003, 2013). For both of these geodynamic processes, asthenosphere upwelling is thought to be an important mechanism for heat transfer to continental crust, resulting in partial melting of the lower and middle crustal sources (e.g. Liégeois, 1998; Atherton and Ghani, 2002). In addition, this mantle–crust lithospheric interaction has been proposed to be the first–order parameter controlling the formation of orogenic gold deposits (Bierlein et al., 2006; 2009). For example, according to Eglinger et al. (2017), at the western subprovince of the Baoulé–Mossi, West–Africa craton, the late potassic magmatism bloom that occurs between c. 2.10 and 2.08 Ga is interpreted as a critical magmatic event, even driving large–scale fluid and metal migration to the crust. Therefore, a genetic link with post–collisional magmatism may be inferred for the Pedra Branca gold deposit, as similarly interpreted to many 2.10 to 2.07 Ga orogenic gold deposits in the West–Africa craton (e.g. Eglinger et al., 2017), in the Archean greenstone belts of the Eastern Goldfields (e.g. Blewett et al., 2010; Davis et al., 2010), in the Abitibi greenstone belts (e.g. Lin and Beakhouse, 2013) and also Phanerozoic orogenic gold deposits elsewhere (e.g. Zhang et al., 2017; Spence–Jones et al., 2018).

3.7.9. Genetic model

Several factors indicate that the Pedra Branca gold deposit fits into the proposed classification of Groves et al. (1998) for orogenic gold deposits. These factors include: (1) gold mineralization occurs associated with structurally controlled quartz veins; (2) it is associated with regional Archean–Paleoproterozoic terrane boundary (trans–crustal shear zone), and locally associated to second order shear zones in the greenstone pile (**Fig. 3.1B** and **2**); (3) it is an epigenetic greenstone–hosted gold mineralization; (4) the c. 2029 ± 27 Ma U-Pb titanite age of gold mineralization places it in the final setting of the Rhyacian orogeny, slightly later than metamorphic peak and syn– to post–collisional magmatism (Costa et al., submitted); (5) the mineralizing fluid is characterized as low–salinity (0 to 8 wt% NaCl equiv.) and H_2O–CO_2±CH_4 in composition; and (6) the hydrothermal mineral assemblages are in equilibrium (pressure and temperature) with the host mid–amphibolite facies metamorphic rocks.

However, within the crustal continuum of orogenic gold classification (Groves et al., 1993), the PT conditions performed by isochore intersection with calculated temperatures from the quartz–magnetite isotope pair (**Fig. 3.14**), evidence that the Pedra Branca gold deposit may be classified as an hypozonal orogenic gold deposit. As discussed here, in these

type of orogenic gold deposits, a contribution of deep–seated magmatic–hydrothermal fluid is commonly ascribed to their ore genesis (e.g. Knight et al., 2000; Krienitz et al., 2008; Biczok et al., 2012; Rogers et al., 2013; Doublier et al., 2014). In addition, the occurrence of magnetite–bearing hydrothermal assemblage and the association of free–milling gold with telluride minerals, also suggests a connection of the Pedra Branca gold deposit with magmatic–hydrothermal fluid, such as interpreted for those "orogenic oxidized intrusion–related gold systems", existent at the Abitibi (e.g. Helt et al., 2014) and Eastern Goldfield (e.g. Witt et al., 2018) greenstone belts.

Based on the stable isotopes (O, H, C) presented in this work (**Table 3.2**), a plausible interpretation, is that the hydrothermal minerals associated with gold mineralization in the Pedra Branca gold deposit, derived from a magmatic–hydrothermal fluid that interacted with the metavolcano–sedimentary rocks of the Serra das Pipocas greenstone belt. This might explain some high $\delta^{18}O$ values (e.g. quartz $\delta^{18}O$ values ranging from +10.5 to +12.4‰, n=18) (**Table 3.2**), in which an ore–forming fluid of magmatic–hydrothermal origin (e.g. ~2068 Ma granite magmatism with fluid $\delta^{18}O$ = +8.8‰, **Table 3.2**), interacted with ^{18}O–rich metavolcano–sedimentary rocks of the greenstone pile (e.g. fluid $\delta^{18}O$ from amphibolites = +10.0 and +10.4‰, **Table 3.2**). In addition, $\delta^{18}O$ values of gold–associated magnetite from the Pedra Branca gold deposit range between +1.0 to +2.4‰ (n=8) (**Table 3.2**), which are typical of "ortho–magmatic" magnetite (**Fig. 3.15**), and the hydrothermal carbonates yields a $\delta^{13}C$ and $\delta^{18}O$ composition that plots near the carbonatite field of Taylor et al. (1967) (**Fig. 3.17**), and, therefore, is compatible with a magmatic fluid and/or mantle–derived fluid signature.

3.8. Conclusions

Based on the petrographic relationships, fluid inclusion and stable isotopes (O, C, H) presented here for the Pedra Branca gold deposit, we summarize below the main conclusions.

(1) The main gold mineralization is found in association with quartz veins, calc–silicate alteration (e.g. diopside, hornblende, biotite, and titanite) and abitization.

(2) Pyrrhotite is commonly found as inclusions in pyrite, and late magnetite substitutes pyrite, suggesting progressive oxidation of the ore–forming fluid.

(3) Free–milling gold commonly precipitates at the late stages of alteration, in close association with magnetite and tellurides.

(4) Two fluid inclusion assemblages were identified from quartz veins. Assemblage 1 is characterized by the coexistence of CO_2–rich (Type–I) and low salinity (0 to 8 wt%

NaCl equiv.) CO_2–H_2O–NaCl (Type–II) and H_2O–NaCl (Type–III) inclusions, suggesting formation during phase separation. Assemblage 2 is represented by late secondary low–temperature (Th<200°C) H_2O–NaCl inclusions (Type–IV), probably unrelated to gold mineralization.

(5) Oxygen isotope thermometry for quartz–magnetite pairs gave temperatures from 467 to 526°C, which probably represents the approximated temperature of gold deposition, as gold is generally associated to magnetite in the ore mineral assemblage. However, higher temperatures were obtained from quartz–hornblende thermometer, suggesting that fluid evolution underwent high temperatures during its early stages.

(6) The possible range of PT conditions for the gold mineralization from 467 °C and 1.93 kbar (c. 7 km) to 526 °C and 3.48 kbar (c. 13 km) was obtained from the intersection of the isochores of Type–III inclusions with the temperature range from quartz–magnetite isotopic geothermometer. This range of PT conditions is akin to hypozonal orogenic gold deposits.

(7) The $\delta^{18}O$, δD and $\delta^{13}C$ values of hydrothermal minerals (quartz, calcite, biotite, hornblende and magnetite) and fluid inclusions are compatible with a magmatic–hydrothermal ore–forming fluid that underwent fluid–rock interaction with the greenstone pile.

(8) The association of gold with magnetite and tellurides strongly suggests an ore–forming fluid sourced by oxidized magmas, similar to those interpreted as “orogenic oxidized intrusion–related gold deposits” in other Precambrian greenstone belts (e.g. Abitibi and Eastern Goldfields).

Acknowledgements

This is a contribution to the Conselho Nacional de Desenvolvimento Científico e Tecnológico (CNPq), project (306798/2016-6) “Evolução crustal, modelos geodinâmicos e metalogênese: exemplos do Maciço de Troia (CE) e do Cinturão Gurupi (PA-MA)”. FGC thanks CNPq for a scholarship (203250/2017-6) to pursue a joint PhD fellowship program with the University of Cape Town, South Africa. The authors acknowledge Jaguar Mining Inc. for the kind provision and access to drill cores that are central to this paper.

References

Acosta-Góngora, P., Gleeson, S.A., Samson, I.M., Corriveau, L., Ootes, L., Taylor, B.E., Creaser, R.A., Muehlenbachs, K., 2015. The Paleoproterozoic NICO iron-oxide-cobalt-gold-bismuth

deposit, Northwest Territories, Canada: evidence from isotope geochemistry and fluid inclusions. Precambrian Res., 268, 168–193.

Almeida, F.F.M., Hasui, Y., Brito Neves, B.B., Fuck, R.A., 1981. Brazilian structural provinces: an introduction. Earth-Sciences Reviews, 17, 1–21.

Almeida, R.S., 2014. Geologia, geoquímica e geocronologia da suíte intrusiva máfica–ultramáfica de Boa Viagem, Ceará, Brasil. Master Dissertation, Federal University of Ceará (UFC), 103 p.

Anderson, M.R., Rankin, A.H., Spiro, B., 1992. Fluid mixing in the generation of isothermal gold mineralization in the Transvaal Sequence, Transvaal, South Africa. Eur. J. Mineral., 4, 933–948.

Angeli, N., Bevenutti, C.F., Antunes, L.A., Campos, M.C., Mamani, R., 2009. Cromititos do Complexo de Pedra Branca: química mineral e platinóides associados, Ceará, Brasil. In: Simpósio de Geologia do Nordeste, Fortaleza, 23, cd rom.

Arthaud, M.H., Caby, R., Fuck, R.A., Dantas, E.L., Parente, C.V., 2008. Geology of the northern Borborema Province, NE Brazil and its correlation with Nigeria, NW Africa. In: Pankhurst, R.J., Trouw, R.A.J., Brito Neves, B.B., de Wit, M.J. (Eds.), West Gondwana: Pre–Cenozoic Correlations Across the South Atlantic Region, vol. 294. Geological Society of London, pp. 49–67. Special Publications.

Atherton, M.P., Ghani, A.A., 2002. Slab breakoff: a model for Caledonian, late granite syn–collisional magmatism in the orthotectonic (metamorphic) zone of Scotland and Donegal, Ireland. Lithos 62, 65–85.

Bakker, R.J., 2003. Package FLUIDS 1. Computer programs for analysis of fluid inclusion data and modelling bulk fluid properties: Chemical Geology, 194, 3–23.

Bakker, R.J., Jansen, J.B.H., 1994. A mechanism for preferential H2O leakage from fluid inclusions in quartz, based on TEM observations. Contrib. Mineral. Petrol., 116, 7–20.

Barrueto, H.R., Hunt, W., 2010. Main features of the Pt-Pd chromitite-type ore deposit, Tróia Unit, Cruzeta Complex, Northeast Brazil: Insights provided by microscopic and chemical approaches. In: 11th International Platinum Symposium, Sudbury, Canada.

Bastrakov, E.N., Skirrow, R.G., Davidson, G.J., 2007. Fluid evolution and origins of iron oxide Cu–Au prospects in the Olympic Dam District, Gawler Craton, South Australia. Econ. Geol., 102, 1415–1440.

Beakhouse, G.P., 2007. Structurally controlled, magmatic hydrothermal model for Archean lode gold deposits: a working hypothesis; Ontario Geological Survey, Open File Report 6193, 133p.

Beakhouse, G.P., 2011. The Abitibi Subprovince plutonic record: Tectonic and metallogenic implications; Ontario Geological Survey, Open File Report 6268, 161p.

Beaudoin, G., Pitre, D., 2005. Stable isotope geochemistry of the Archean Val-d'Or (Canada) orogenic gold vein field. Mineralium Deposita, 40, 59–75.

Belonoshko, A., Saxena, S.K., 1991. A molecular dynamics study of the pressure-volume-temperature properties of super-critical fluids: 1. H20, Geochim. Cosmochim. Acta, 55, 381-387.

Bhattacharya, S., Panigrahi, M.K., Sachan, H.K., Kharya, A., 2014. Oxygen isotope ratio of quartz veins from the auriferous Ramagiri–Penakacherla schist belt and surrounding granitoids in the Eastern Dharwar craton: a case for a possible link between gold mineralization and granite magmatism. Ore Geology Reviews, 63, 201–208.

Biczok, J., Hollings, P., Klipfel, P., Heaman, L., Maas, R., Hamilton, M., Kamo, S., Friedman, R., 2012. Geochronology of the North Caribou greenstone belt, Superior Province Canada: implications for tectonic history and gold mineralization at the Musselwhite mine. Precambrian Res., 192–195, 209–230.

Bierlein, F.P. Groves, D.I. Goldfarb, R.J. Dubé, B. 2006. Lithospheric controls on the formation of provinces hosting giant orogenic gold deposits. Miner. Deposita, 40, 874–886.

Bierlein, F.P., Groves, D.I., Cawood, P.A., 2009. Metallogeny of accretionary orogens – The connection between lithospheric processes and metal endowment. Ore Geol. Rev., 36, 282–292.

Bierlein, F.P., Pisarevsky, S., 2008. Plume-related oceanic plateaus as a potential source of gold mineralisation. Econ Geol 103, 425–430.

Bigot, L., Jébrak, M., 2015. Gold Mineralization at the Syenite-Hosted Beattie Gold Deposit, Duparquet, Neoarchean Abitibi Belt, Canada. Economic Geology, 110, 315–335.

Blewett, R.S., Henson, P.A., Roy, I.G., Champion, D.C., Cassidy, K.F., 2010. Scale-integrated architecture of the world-class gold mineral systems of the Eastern Yilgarn Craton. Precambrian Research, 183, 230–250.

Block, S., Baratoux, L., Zeh, A., Laurent, O., Bruguier, O., Jessell, M., Ailleres, L., Sagna, R., Parra–Avila, L.A., Bosch, D., 2016. Paleoproterozoic juvenile crust formation and stabilisation in the south–eastern West African Craton (Ghana); New insights from U–Pb–Hf zircon data and geochemistry. Precambrian Research, 287, 1–30.

Bodnar, R.J., 1993. Revised equation and table for determining the freezing point depression of H2O–NaCl solutions. Geochim. Cosmochim. Acta 57, 683–684.

Bonin, B., 2004. Do coeval mafic and felsic magmas in post–collisional to within–plate regimes necessarily imply two contrasting, mantle and crustal, sources? A review. Lithos, 78 (1–2), 1–24.

Bottinga, Y., Javoy, M., 1973. Comments on oxygen isotope geothermometry: Earth and Planetary Science Letters, 20, 250–265.

Bowers, T.S., Helgeson, H.C., 1983. Calculations of the thermodynamic and geochemical consequences of non-ideal mixing in the system H2O-CO2-NaCl on phase relations in geological systems: Equation of state for H2O-CO2-NaCl fluids at high pressures and temperatures: Geochimica et Cosmochimica Acta, 47, 1247–1275.

Brito Neves, B.B., 1975. Regionalização geotectônica do Pré–Cambriano Nordestino. PhD Thesis. Universidade de São Paulo, São Paulo–SP, p. 198.

Bucci, L.A., Hagemann, S.G., Groves, I.D., Standing, J.G., 2002. The Archean Chalice gold deposit: a record of complex, multistage, high-temperature hydrothermal activity and gold mineralisation associated with granitic rocks in the Yilgarn Craton, Western Australia. Ore geology Reviews, 19, 23–67.

Burrows, D.R., Wood, P.C., Spooner, E.T.C., 1986. Carbon isotope evidence for a magmatic origin for Archaean gold quartz vein ore deposits. Nature, 321, 851–854.

Calado, B.O., Costa, F.G., Gomes, I.P., Rodrigues, J.B., 2018. U–Pb (LA–ICP–MS) Detrital zircon ages from the Jaguaretama complex: Implications for Rhyacian – Sthaterian geological evolution. 49º Congresso Brasileiro de Geologia, Rio de Janeiro.

Cavalcante, J.C., Vasconcelos, A.M., Medeiros, M.F., Paiva, I.P., Gomes, F.E.M., Cavalcante, S.N., Cavalcante, J.E., Melo, A.C.R., Duarte Neto, V.C., Benevides, H.C., 2003. Mapa Geológico do Estado do Ceará. Escale 1:500.000. Serviço Geológico do Brasil, Fortaleza. CPRM.

Chacko, T., Cole, D.R., Horita, J., Valley, J.W., Cole, D.R., 2001. Equilibrium oxygen, hydrogen, and carbon isotope fractionation factors applicable to geological systems, Stable Isotope Geochemistry. Mineralogical Society of America/Geochemical Society, Reviews in Mineralogy and Geochemistry, 2001, 43, 1–81.

Chen, H.Y., Kyser, T.K., Clark, A.H., 2011. Contrasting fluids and reservoirs in the contiguous Marcona and Mina Justa iron oxide-Cu (-Ag-Au) deposits, south-central Peru. Miner. Deposita, 46, 677–706.

Chiba, H., Chacko, T., Clayton, R.N., Goldsmith, J.R., 1989. Oxygen isotope fractionations involving diopside, forsterite and calcite: applications to geothermometry. Geochim. Cosmochim. Acta, 53, 2985–2995.

Childress, T.M., Simon, A.C., Day, W.C., Lundstrom, C.C., Bindeman, I.N., 2016. Iron and Oxygen Isotope Signatures of the Pea Ridge and Pilot Knob Magnetite-Apatite Deposits, Southeast Missouri, USA. Economic Geology, 111, 2033–2044.

Clayton, R.N., Kieffer, S.W., 1991. Oxygen isotope thermometer calibrations. In Taylor, H.P.Jr., O'Neil, J.R., Kaplan, I.R., eds., Stable isotope geochemistry: A tribute to Samuel Epstein: The Geogemical Society, Special Publication No. 3, p. 3–10.

Clayton, R.N., O'Neil, J.R., Mayeda, T.K., 1972. Oxygen isotope exchange between quartz and water. J. Geophys. Res., 77, 3057-3067.

Clemens, J.D., 2006, Melting of the continental crust: Fluid regimes, melting reactions, and source-rock fertility, in Brown, M., and Rushmer, T., eds., Evolution and Differentiation of the Continental Crust: Cambridge, UK, Cambridge University Press, p. 297–331.

Cole, D.R., Horita, J., Eniamin, V., Polyakov, V.B., Valley, J.W., Spicuzza, M.J., Coffey, D.W., 2004. An experimental and theoretical determination of oxygen isotope fractionation in the system magnetite-H2O from 300 to 800°C. Geochimica et Cosmochimica Acta, 68, 3569–3585.

Collins, P.L.F., 1979. Gas hydrates in CO2–bearing fluid inclusions and the use of freezing data for estimation of salinity. Econ. Geol. 74, 1435–1444.

Colvine, A.C., Fyon, J.A., Heather, K.B., Marmont, S., Smith, P.M., Troop, D.G., 1988. Archean lode gold deposits in Ontario. Ont. Geol. Surv. Misc. Pap., p. 139–136.

Costa, F.G., Klein, E.L., Corrêa-Lima, R.G., Naleto, J.L.C., 2016. Geology, geochronology and gold metallogenesis of the Serra das Pipocas granite-greenstone terrane. 48° Congresso Brasileiro de Geologia, Porto Alegre – RS, p. 9278. (on line)

Costa, F.G., Klein, E.L., Galarza, M.A., Pinéo, T.R.G., (submitted). Structural control and age of gold mineralization in the Troia Massif, Borborema Province, NE Brazil: A Paleoproterozoic (~2029 Ma) hypozonal orogenic gold deposit overprinted by the late Neoproterozoic Brasiliano/Pan–African orogeny. (Submitted to J. South Am. Earth Sc.).

Costa, F.G., Klein, E.L., Lafon, J.M., Milhoman, J.M., Galarza, M.A., Rodrigues, J.B., Naleto, J.L.C., Corrêa-Lima, R.G., 2018. Geochemistry and U-Pb-Hf zircon data for plutonic rocks at the Troia Massif, Borborema Province, NE Brazil: Evidence for reworking of Archean and juvenile Paleoproterozoic crust during Rhyacian accretionary and collisional tectonics. Precambrian Research, 311, 167–194.

Costa, F.G., Oliveira, E.P., McNaughton, N., 2011. The Fazenda Gavião granodiorite and associated potassic plutons as evidence for Palaeoproterozoic arc–continent collision in the Rio Itapicuru greenstone belt, Brazil. J. South Am. Earth Sci., 32 (2), 127–141.

Costa, F.G., Palheta, E.S.M., Rodrigues, J.B., Gomes, I.P., Vasconcelos, A.M., 2015. Geochemistry and U–Pb zircon ages of plutonic rocks from the Algodões granite–greenstone terrane, Troia Massif, northern Borborema Province, Brazil: Implications for Paleoproterozoic subduction–accretion processes. Journal of South American Earth Sciences, 59, 45–68.

Costa, F.G., Rodrigues, J.B., Cavalcanti, J.A.D., Palheta, E.S.M., Vasconcelos, A.M., 2014a. U–Pb LA–ICPMS ages of detrital zircons from the Paleoproterozoic Algodões and Serra das Pipocas greenstone–like sequences, Ceará Central Domain. In: 9th South American Symposium on Isotope Geology, São Paulo, Brazil, p. 110.

Costa, F.G., Rodrigues, J.B., Naleto, J.L.C., Vasconcelos, A.M., Barrueto, H.R., 2014b. 2036 Ma SHRIMP U–Pb zircon age for PGE–bearing chromitites of the Troia mafic–ultramafic complex, Ceará Central Domain. In: 9th South American Symposium on Isotope Geology, São Paulo, Brazil, p. 164.

Coulibaly, Y., Boiron, M.C., Cathelineau, M., and Kouamelan, A.N., 2008. Fluid immiscibility and gold deposition in the Birimian quartz veins of the Angovia deposit (Yaoure, Ivory Coast). J. Afr. Earth Sci., 50, 234–254.

Craig, H., 1961. Isotopic variations in meteoric waters. Science, 133, 1702–1703.

Dantas, E.L., Van Schmus, W.R., Hackspacher, P.C., Fetter, A.H., Brito Neves, B.B., Cordani, U., Nutman, A.P., Williams, I.S., 2004. The 3.4–3.5 São José de Campestre massif, NE Brazil: remnants of the oldest crust in South America. Precambrian Res. 130, 113–137.

Davis, B.K., Blewett, R.S., Squire, R., Champion, D.C., Henson, P.A., 2010. The special role of granite-cored domes to gold mineralisation: Architectural and geodynamic controls around the Archaean Scotia–Kanowna Dome, Kalgoorlie Terrane, Western Australia. Precambrian Research, 183, 316–337.

Davis, J.H., von Blanckenburg, F., 1995. Slab breakoff: A model of lithosphere detachment and its test in the magmatism and deformation of collisional orogens. Earth and Planetary Science Letters, 129 (1–4), 85–102.

Delor, C., Lahondère, D., Egal, E., Lafon, J.M., Cocherie, A., Guerrot, C., Rossi, P., Trufert, C., Theveniaut, H., Phillips, D., Avelar, V.G., 2003. Transamazonian crustal growth and reworking as revealed by the 1:500,000-scale geological map of French Guiana (2nd edition). Geologie de la France, 2-3-4, 5–57.

Deng, X.H., Yao, J.M., Santosh, M., Chen, Y.J., 2014. Geological, fluid inclusion and sulphides isotope of the Zhifang Mo deposit in Qinling Orogen, central China: a case study of orogenic–type Mo systems. Geol. J., 49, 515-533.

Diamond, L.W., 2001. Review of systematic of CO2–H2O fluid inclusions Lithos, 55 (1–4), 69–99.

Doublier, M.P., Thébaud, N., Wingate, M.T.D., Romano, S.S., Kirkland, C.L., Gessner, K., Mole, D.R., Evans, N., 2014. Structure and timing of Neoarchean gold mineralization in the Southern Cross district (Yilgarn Craton, Western Australia) suggest leading role of late Low-Ca I-type granite intrusions. Journal of Structural Geology, 67, 205–221.

Dreher, A.M., Xavier, R.P., Taylor, B.E., Martini, S., 2008. New geologic, fluid inclusion and stable isotope studies on the controversial Igarapé Bahia Cu–Au deposit, Carajás Province, Brazil. Miner Dep., 43, 161–184.

Drummond, S.E., Ohmoto, H., 1985. Chemical evolution and mineral deposition in boiling hydrothermal systems. Economic Geology, 80, 126–147.

Duuring, P., Cassidy, K.F., Hagemann, S.G., 2007. Granitoid-associated orogenic, intrusion-related, and porphyry style metal deposits in the Archean Yilgarn Craton, Western Australia. Ore Geology Review, 32, 157–186.

Eglinger, A., Thébaud, N., Zeh, A., Davis, J., Miller, J., Parra–Avila, L.A., Loucks, R., McCuaig, C., Belousova, E., 2017. New insights into the crustal growth of the Paleoproterozoic margin of the Archean Kéména–Man domain, West African craton (Guinea): Implications for gold mineral system. Precambrian Research, 292, 258–289.

Eilu, P., Mathison, C.I., Groves, D.I., Allardyce, W., 1998. Atlas of Alteration Assemblages, Styles and Zoning in Orogenic Lode-Gold Deposits in a Variety of Host Rock and Metamorphic Settings. Geology Department & University Extension, The University of Western Australia, Publ. 30.

Eilu, P., Mikucki, E.J., 1998. Alteration and primary geochemical dispersion associated with the Bulletin lode-gold deposit, Wiluna, Western Australia. Journal of Geochemical Exploration 63, 73–103.

Elmer, F.L., White, R.W., Powell, R., 2006. Devolatilization of metabasic rocks during green schist–amphibolite facies metamorphism. J. Metamorph. Geol. 9, 497–513.

Evans, K.A., 2010. A test of the viability of fluid-wall rock interaction mechanisms for changes in opaque phase assemblage in metasedimentary rocks in the Kambalda-St. Ives goldfield, Western Australia. Miner. Deposita, 45, 207–213.

Fayol, N., Jébrak, M., 2017. Archean Sanukitoid Gold Porphyry Deposits: A New Understanding and Genetic Model from the Lac Bachelor Gold Deposit, Abitibi, Canada. Economic Geology, 112, 1913–1936.

Fetter, A.H., 1999. U/Pb and Sm/Nd Geocronological Constraints on the Crustal Framework and Geologic History of Ceará State, NW Borborema Province, NE Brazil: Implications for the Assembly of Gondwana. Tese de PhD. Departament of Geology, Kansas University, Lawrence, p. 164.

Fetter, A.H., Van Schmus, W.R., Santos, T.J.S., Nogueira Neto, J.A., Arthaud, M.H., 2000. U-Pb and Sm-Nd geochronological constraints on the crustal evolution and basement architecture of Ceará State, NW Borborema Province, NE Brazil: implications for the existence of the Paleoproterozoic Supercontinent “Atlantica”. Revista Brasileira de Geociências, 30 (1), 102–106.

Feybesse, J.L., Billa, M., Guerrot, C., Duguey, J.L.L., Milesi, J.P., Bouchot, V., 2006. The Palaeoproterozoic Ghanaian province: geodynamic model and ore controls, including regional stress modeling. Precambrian Research, 149, 149–196.

Freimann, M.A., 2014. Geocronologia e Petrotrama de quartzo milonitos do duplex transcorrente de Lavras da Mangabeira. Master Dissertation, Universidade de São Paulo, São Paulo–SP, 84 p.

Fu, B., Touret, J.L.R., 2014. From granulite fluids to quartz-carbonate megashear zones: The gold rush. Geoscience Frontier, 5, 747–758.

Ganade, C.E., Basei, M.A.S., Grandjean, F.C., Armstrong, R., Brito, R.S., 2017. Contrasting Archaean (2.85–2.68 Ga) TTGs from the Tróia Massif (NE-Brazil) and their geodynamic implications for flat to steep subduction transition. Precambrian Research, 297, 1–18.

Ganino, C., Harris, C., Arndt, N.T., Prevec, S.A., Howarth, G.H., 2013. Assimilation of carbonate country rock by the parent magma of the Panzhihua Fe-Ti-V deposit (SW China): evidence from stable isotopes. Geosci. Front., 4, 547–554.

Garcia, M.G.M., Santos, T.J.S., Amaral, W.S., 2014. Provenance and tectonic setting of neoproterozoic supracrustal rocks from the Ceara Central Domain, Borborema Province (NE Brazil): constraints from geochemistry and detrital zircon ages. Int. Geol. Rev. 56 (4), 1–20.

Garofalo, P.S., Fricker, P.S., Gunther, M.B., Bersani, D., Lotticci, P.P., 2014. Physical–chemical properties and metal budget of gold-transporting hydrothermal fluids in orogenic deposits. In: Garofalo, P.S., Ridley, J.R. (Eds.), Gold-transporting Hydrothermal Fluids in the Earth's Crust. Geological Society Special Publication (402), 71–102.

Goldfarb, R.J., Baker, T., Dubé, B., Groves, D.I.., Hart, C.J.R., Gosselin, P., 2005. Distribution, character, and genesis of gold deposits in metamorphic terranes. Economic Geology, 100th Anniversary Volume, 407–450.

Goldfarb, R.J., Groves, D.I., 2015. Orogenic gold: Common or evolving fluid and metal sources through time. Lithos, 233, 2–26.

Goldstein, R.H., Reynolds, T.J., 1994. Systematics of fluid inclusions in diagenetic minerals. Society for Sedimentary Geology, Short Course 31, SEPM, Tulsa, OK, 199 pp.

Gomes, E.N., 2013. Protominérios e minérios de manganês de Juá–CE. Master Dissertation, Universidade Federal do Ceará (UFC), Ceará–CE, p. 102.

Gregory, R.T., Criss, R.E., 1986. Isotopic exchange in open and closed systems: Reviews in Mineralogy, 16, 91–127.

Griffin, W.L., Begg, G.C., O'Reilley, S.Y., 2013. Continental root control on the genesis of magmatic ore deposits. Nature Geoscience 6, 905–910.

Groves, D.I., 1993. The crustal continuum model for late-Archaean lode gold deposits of the Yilgarn block, Western Australia. Mineralium Deposita 28, 366–374.

Groves, D.I., Goldfarb, R.J., Gebre-Mariam, M., Hagemann, S.G., Robert, F., 1998. Orogenic gold deposits—a proposed classification in the context of their crustal distribution and relationship to other gold deposit types. Ore Geology Reviews 13, 7–27.

Groves, D.I., Golding, S.D., Rock, N.M.S., Barley, M.E., McNaughton, N.J., 1988. Archaean carbon reservoirs and their relevance to the fluid source for gold deposits. Nature, 321, 254–257.

Groves, D.I., Phillips, G.N., 1987. The genesis and tectonic controls on Archaean lode gold deposits of the Western Australian shield: a metamorphic-replacement model. Ore Geol. Rev. 2, 287–322.

Groves, D.I., Santosh, M., 2016. The giant Jiaodong gold province: The key to a unified model for orogenic gold deposits? Geoscience Frontier, 7 (3), 409–417.

Grundler, P.V., Brugger, J., Etschmann, B.E., Helm, L., Liu, W.H., Spry, P.G., Tian, Y., Testemale, D., Pring, A., 2013. Speciation of aqueous tellurium (IV) in hydrothermal solutions and vapors, and the role of oxidized tellurium species in Te transport and gold deposition. Geochim. Cosmochim. Acta, 120, 298–325.

Harris, C., Ashwal, L.D., 2002. The origin of low δ18O granites and related rocks from the Seychelles Contrib. Mineral. Petrol., 143, 366–376.

Harris, C., Compton, J.S., Bevington, S.A., 1999. Oxygen and hydrogen isotope composition of kaolinite deposits, Cape Peninsula, South Africa: low-temperature, meteoric origin. Economic Geology, 94, 1353–1366.

Harris, C., Vogeli, J., 2010. Oxygen isotope composition of garnet in the Peninsula Granite, Cape Granite Suite, South Africa: constraints on melting and emplacement mechanisms. South African Journal of Geology, 113, 401–412.

Helt, K.M., Williams-Jones, A.E., Clark, J.R., Wing, B.A., Wares, R.P., 2014. Constraints on the genesis of the Archean oxidized, intrusions-related Canadian Malartic gold deposit, Quebec, Canada. Economic Geology, 109, 713–73.

Hoefs, J., 2009. Stable Isotope Geochemistry (6th ed.), Springer, pp. 227.

Hoffmann, I.B., Philipp, R.P., Borghetti, C., 2018. Geochemistry and origin of the Rhyacian tholeiitic metabasalts and meta-andesites from the Vila Nova Greenstone Belt, Guyana Shield, Amapá, Brazil. J. South Am. Earth Sc., 88, 29–49.

Hollanda, M.H.B.M., Archanjo, C.J., Souza, L.C., Dunyi, L., Armstrong, R., 2011. Long–lived Paleoproterozoic granitic magmatism in the Seridó-Jaguaribe domain, Borborema Province - NE Brazil. J. South Am. Earth Sci. 32 (4), 287–300.

Hovelmann, J., Putnis, A., Geisler, T., Schmidt, B.C., Golla-Schindler, U., 2010. The replacement of plagioclase feldspars by albite: observations from hydrothermal experiments. Contrib. Mineral Petrol., 159, 43–59.

Hronsky, J.M.A., Groves, D.I., Loucks, R.R., Begg, G.C., 2012. A unified model for gold mineralisation in accretionary orogens and implications for regional-scale exploration targeting methods. Mineralium Deposita 47, 339–358.

Hu, G.X., Clayton, R.N., 2003. Oxygen isotope salt effects at high pressure and high temperature and the calibration of oxygen isotope geothermometers. Geochimica Et Cosmochimica Acta, 67, 3227–3246.

Isaac, C., 2008. Stable isotope (N, O, H) geochemistry, petrology and compositions of biotite of the Musselwhite Mine, Ontario: implications for mineralisation. Unpublished M.Sc. thesis, Lakehead University, 104 pp.

Jonsson, E., Troll, V.R., Högdahl, K., Harris, C., Weis, F., Nilsson, K.P., and Skelton, A., 2013. Magmatic origin of giant 'Kiruna-type' apatite-iron oxide ores in central Sweden: Scientific Reports, 3, 1644.

Jowett, S.M., Cooper, K., Squire, R.J., Thebaud, N., Fisher, L.A., Cas, R.A.F., Pegg, I., 2014. Geology, mineralogy and geochemistry of magnetite-associated gold mineralization of the ultramafic-basalt greenstone hosted Crusader Complex, Agnew gold camp, eastern Yilgarn craton, Western Australia: a late-Archean, intrusion-related gold deposit? Ore Geol. Rev. 56, 53–72.

Kay, R.W., Mahlburg Kay, S., 1993. Delamination and delamination magmatism. Tectonophysics, 219, 177–189.

Kendrick, M.A., Honda, M., Walshe, J., Peteresen, K., 2011. Fluid sources and the role of abiogenic-CH4 in Archean gold mineralization: Constraints from noble gases and halogens. Precambrian Research, 189, 331–327.

Kerrich, R., 1987. The stable isotope geochemistry of Au–Ag vein deposits inmetamorphic rocks. In: Kyser, T.K. (Ed.), Stable Isotope Geochemistry of Low Temperature Fluids 13. Mineralogical Association of Canada Short Course, pp. 287–336.

Kerrich, R., Fyfe, W.S., 1981. The gold-carbonate association: source of CO2 and CO2 fixation reactions in Archaean lode deposits. Chem. Geol., 33, 265–293.

Kerrich, R., Goldfarb, R., Groves, D., Garwin, S., Jia, Y., 2000. The characteristics, origins, and geodynamic settings of supergiant gold metallogenic provinces. Sci. China Ser. D Earth Sci., 43, 1-68.

Kerrich, R., Watson, G.P., 1984. The Macassa Mine Archean Lode Gold Deposit, Kirkland Lake, Ontario: Geology, Patterns of Alteration, and Hydrothermal Regimes. Economic Geology, 79, 1104–1130.

Klein, E.L., Fuzikawa, K., Koppe, J.C., 2000. Fluid inclusion studies on Caxias and Areal gold mineralizations, São Luís Craton, northern Brazil. Journal of Geochemical Exploration, 71, 51–72.

Klein, E.L., Harris, C., Renac, C., Giret, A., Moura, C.A.V., Fuzikawa, K., 2006. Fluid inclusion and stable isotope (O, H, C, and S) constraints on the genesis of the Serrinha gold deposit, Gurupi Belt, northern Brazil. Mineralium Deposita, 41, 160–178.

Klein, E.L., Lucas, F.R.A., Queiroz, J.D.S., Freitas, S.C.F., Renac, C., Galarza, M.A., Jourdan, F., Armstrong, R., 2015. Metallogenesis of the Paleoproterozoic Piaba orogenic gold deposit, São Luís cratonic fragment, Brazil. Ore Geology Reviews, 65, 1–25.

Klein, E.L., Luzardo, R., Moura, C.A.V., Armstrong, R., 2008. Geochemistry and zircon geochronology of paleoproterozoic granitoids: further evidence on the magmatic and rustal evolution of the São Luís cratonic fragment, Brazil. Precambrian Research, 165, 221–242.

Klein, E.L., Rodrigues, J.B., Lopes, E.C.S., Soledade, G.L., 2012. Diversity of Rhyacian granitoids in the basement of the Neoproterozoic–Early Cambrian Gurupi Belt, northern Brazil: geochemistry, U–Pb zircon geochronology, and Nd isotope constraints on the Paleoproterozoic magmatic and crustal evolution. Precambrian Research, 220-221, 192–216.

Klein, E.L., Santos, R.A., Fuzikawa, K., Angélica, R.S., 2001. Hydrothermal fluid evolution and structural control of the Guarim gold mineralisation, Tapajós Province, Amazon Craton, Brazil. Mineralium Deposita, 36, 149–164.

Klein, E.L., Tassinari, C.C.G., Vasconcelos, P., 2014. U-Pb SHRIMP and 40Ar/ 39Ar constraints on the timing of mineralization in the Paleoproterozoic Caxias orogenic gold deposit, São Luís cratonic fragment, Brazil. Brazilian Journal of Geology, 44, 277–288.

Knight, J., Ridley, J.R., Groves, D.I., 2000. The Archean Amphibolite Facies Coolgardie Goldfield, Yilgarn, Western Australia: Nature, Controls, and Gold Field-Scale Patterns of Hydrothermal Wall-Rock Alteration. Economiv Geology, 95, 49–84.

Kolb, J., Dziggel, A., Bagas, L., 2015. Hypozonal lode gold deposits: a genetic concept based on a review of the New Consort, Hutti, Hira Buddini, Navachab, Nevoria, and the Granites deposits. Precambrian Research 262, 20–44.

Kontak, D.J., Horne, R.J., Kyser, K., 2011. An oxygen isotope study of two contrasting orogenic vein gold systems in the Meguma Terrane, Nova Scotia, Canada, with implications for fluid sources and genetic models. Mineralium Deposita, 46, 289–304.

Kramers, J.D., Andreoli, M.A.G., Atanasova, M., Belyanin, G.A., Block, D.L., Franklyn, C., Harris, C., Lekgoathi, M., Montross, C.S., Ntsoane, T., Pischedda, V., Segonyane, P., Viljoen, K.S.F., Westraadt, J.E., 2013. Unique chemistry of a diamond bearing pebble from the Libyan Desert Glass strewnfield, SW Egypt: evidence for a shocked comet fragment. Earth Planet. Sci. Lett. 382, 21–31.

Krienitz, M.S., Trumbull, R.B., Hellmann, A., Kolb, J., Meyer, F.M., Wiedenbeck, M., 2008. Hydrothermal gold mineralization at the Hira Buddini gold mine, India: constraints on fluid evolution and fluid sources from boron isotopic compositions of tourmaline. Miner. Depos., 43, 421–434.

Lackey, J.S., Valley, J.W., Chen, J.H., Stockli, D.F., 2008. Dynamic magma systems, crustal recycling, and alteration in the central Sierra Nevada Batholith: the oxygen isotope record, Journal of Petrology , 49, 1397–1426.

Lambert–Smith, J.S., Lawrence, D.M., Vargas, C.A., Boyce, A.J., Treloar, P.J., 2016. The Gounkoto Au deposit, West Africa: constraints on ore genesis and volatile sources from petrological, fluid inclusion and stable isotope data. Ore Geol. Rev., 78, 606-622.

Large, R., Thomas, H., Craw, D., Henne, A., Henderson, S., 2012. Diagenetic pyrite as a source for metals in orogenic gold deposits, Otago Schist, New Zealand. New Zealand Journal of Geology and Geophysics, 55, 137–149.

Lawrence, D.M., Treloar, P.J., Rankin, A.H., Boyce, A., Harbidge, P., 2013. A Fluid Inclusion and Stable Isotope Study at the Loulo Mining District, Mali, West Africa: Implications for Multifluid Sources in the Generation of Orogenic Gold Deposits. Economic Geology, 108 (2), 229–-257.

Liégeois, J.P., Abdelsalam, M.G., Ennih, N., Ouabadi, A., 2013. Metacraton: Nature, genesis and behavior. Gondwana Research, 23, 220–237.

Liégeois, J.P., Black, R., 1987. Alkaline magmatism subsequent to collision in the Pan-African belt of the Adrar des Iforas (Mali). Geological Society, London, Special Publications, 30 (1), 381–401.

Liégeois, J.P., Claessens, W., Camara, D., Klerkx, J., 1991. Short-lived Eburnean orogeny in southern Mali. Geology, tectonics, U–Pb and Rb–Sr geochronology. Precambrian Research, 50, 111–136.

Liégeois, J.P., Latouche, L., Boughrara, M., Navez, J., Guiraud, M., 2003. The LATEA metacraton (Central Hoggar, Tuareg shield, Algeria): behaviour of an old passive margin during the Pan-African orogeny. Journal of African Earth Sciences 37, 161–190.

Liégeois, J.P., Navez, J., Hertogen, J., Black, R., 1998. Contrasting origin of post–collisional high–K calc–alkaline and shoshonitic versus alkaline and peralkaline granitoids. The use of sliding normalization. Lithos, 45, 1–28.

Lin, S., Beakhouse, G.P., 2013. Synchronous vertical and horizontal tectonism at late stages of Archean cratonization and genesis of Helmo gold deposit, Superior Craton, Ontario, Canada. Geology, 41, 359–362.

Lopez, J.M., 2012. Programa de exploração mineral do grupo Jaguar Mining Inc. http://www.adimb.com.br/simexmin2012/wp-content/themes/simexmin/palestras/02%20-%20Programas%20Empresariais/III_5_Marc%20Lopez.pdf (accessed 17 setember 2018).

Lüders, V., Klemd, R., Oberthür, T., Plessen, B., 2015. Different carbon reservoirs of auriferous fluids in African Archean and Proterozoic gold deposits? Constraints from stable carbon isotopic compositions of quartz-hosted CO2-rich fluid inclusions. Miner. Deposita, 50, 449–454.

Mao, J., Wang, Y., Li, H., Pirajano, F., Zhang, C., Wang, R., 2008. The relationship of mantle-derived fluids to gold metallogenesis in the Jiaodong Peninsula: Evidence from D–O–C–S isotope systematics. Re Geology Reviews, 33, 361–381.

Marshall, L.J., Oliver, N.H.S., Davidson, G.J., 2006. Carbon and oxygen isotope constraints on fluid sources and fluid-wallrock interaction in regional alteration and iron-oxide-copper-gold mineralisation, eastern Mt Isa Block, Australia. Mineralium Deposita, 41, 429–452.

Martins, G., 2000. Litogeoquímica e Controles Geocronológicos da Suíte Metamórfica Algodões–Choró. Phd Thesis. Universidade Estadual de Campinas, Campinas–SP, p. 220.

Martins, G., Oliveira, E.P., Lafon, J.M., 2009. The Algodões amphibolite-tonalite gneiss sequence, Borborema Province, NE Brazil: geochemical and geochronological evidence for Paleoproterozoic accretion of oceanic plateu/back–arc basalts and adakitic plutons. Gondwana Res. 15, 71–85.

McCrea, J.M., 1950. On the isotopic chemistry of carbonates and a paleotemperature scale. J. Chem. Phys., 18 (6), 849–857.

McCuaig, T.C., Kerrich, R., 1998. P-T-t-deformation-fluid characteristics of lode gold deposits: evidence from alteration systematics. Ore Geology Reviews, 12, 381–453.

McReath, I., Faraco, M.T.L., 2006. Paleoproterozoic greenstone–granite belts in Northern Brazil and the former Guyana Shield – West African Craton province. Geol. USP Série Científica, 5 (2), 49–63.

Mello, E.F., Xavier, R.P., McNaughton, N.J., Hagemann, S.G., Fletcher, I., Snee, L., 2006. Age constraints on felsic intrusions, metamorphism and gold mineralization in the Palaeoproterozoic Rio Itapicuru greenstone belt, NE Bahia State, Brazil. Miner. Deposita 40, 849–866.

Mignot, E.L., Reisberg, L., André–Mayer, A.S., Bourassa, Y., Fointaine, A., Miller, J., 2017. Re–Os Geochronological Evidence for Multiple Paleoproterozoic Gold Events at the Scale of the West African Craton. Economic Geology, 112, 145–168.

Monteiro, L.V.S., Xavier, R.P., Carvalho, E.R., Hitzman, M.W., Johnson, C.A.,Souza Filho, C.R., Torresi, I., 2008. Spatial and temporal zoning of hydrothermal alteration and mineralization in the Sossego iron oxide–copper–gold deposit, Carajás Mineral Province, Brazil: parageneses and stable isotope constraints. Miner. Dep., 43, 129–159.

Mueller, A.G., 1992. Petrogenesis of amphibole-biotite-calcite-plagioclase alteration and laminated gold-silver quartz veins in four Archean shear zones of the Norseman district, Western Australia. Canadian Journal of Earth Science, 29, 388–417.

Mueller, A.G., Groves, D.I., 1991. The classification of Western Australian greenstone-hosted gold deposits according to wallrock-alteration mineral assemblages. Ore Geol. Rev., 6, 291–331.

Mueller, A.G., Hall, G.C., Nemchin, A.A., Stein, H.J., Creaser, R.A., Mason, D.R., 2008. Archean high-Mg monzodiorite-syenite, epidote skarn, and biotite-sericite gold lodes in the Granny Smith-Wallaby district, Australia: U-Pb and Re-Os chronology of two intrusion-related systems. Mineralium Deposita, 43, 337–362.

Mueller, A.G., Lawrence, L.M., Muhling, J., Pooley, G.D., 2012. Mineralogy and PTX relationships of the Archaean Hanna South Au-Cu (Bi-Co) deposit, Kalgooorlie, Western Australia: Thermodynamic constraints on the formation of a zoned intrusion-related skarn. Economic Geology, 107, 1–24.

Mueller, A.G., Nemchin, A.A., Frei, R., 2004. The Nevoria gold skarn deposit, Southern Cross Greenstone Belt. Western Australia: II. Pressure–temperature–time path and relationship to post–orogenic granites. Econ. Geol., 99, 453–478.

Neumayr, P., Walshe, J., Hagemann, S., Petersen, K., Roache, A., Frikken, P., Horn, L., Halley, S., 2008. Oxidized and reduced mineral assemblages in greenstone belt rocks of the St. Ives gold camp, Western Australia: vectors to high-grade ore bodies in Archaean gold deposits? Mineralium Deposita, 43, 363-371.

Nogueira, J.F., 2004. Estrutura, geocronologia e alojamento dos batólitos de Quixadá, Quixeramobim e Senador Pompeu e Ceará Central. PhD Thesis. Universidade Estadual Paulista (UNESP), Rio Claro–SP, p. 123.

Norcross, C., Davis, D.W., Spooner, T.C., Rust, A., 2000. U-Pb and Pb-Pb age constraints on Paleoproterozoic magmatism, deformation and gold mineralization in the Omai area, Guiana Shield. Precambrian Research. 102, 69–86.

Nyström, J.O., Billström, K., Henríquez, F., Fallick, A.E., Naslund, H.R., 2008. Oxygen isotope composition of magnetite in iron ores of the Kiruna type in Chile and Sweden. GFF 130, 177–188.

Oberthür, T., Vetter, U., Davis, D.W., Amanor, J.A., 1998. Age constraints on gold mineralization and Paleoproterozoic crustal evolution in the Ashanti belt of southern Ghana. Precambr. Res., 89 (3–4), 129–143.

Oliveira, E.P., Souza, Z.S., McNaughton, N., Lafon, J.M., Costa, F.G., Figueiredo, A.M., 2011. The Rio Capim volcanic–plutonic–sedimentary belt, São Francisco Craton, Brazil: geological, geochemical and isotopic evidence for oceanic arc accretion during Palaeoproterozoic continental collision. Gondwana Research, 19 (3), 735–750.

Oliveira, J.F., Cavalcante, J.C., 1993. Folha Mombaça. Folha SB-24-V-D-V. Escala: 1:100.000. Geologia e Metalogênese. In: Programa Levantamentos Geológicos Básicos do Brasil. Fortaleza: Serviço Geológico do Brasil, CPRM.

Ootes, L., Morelli, R.M., Creaser, R.A., Lentz, D.R., Falck, H., Davis, W.J., 2011. The timing of Yellowknife gold mineralization: a temporal relationship with crustal anatexis? Economic Geology 106, 713–720.

Ord, A., Hobbs, B.E., 2018. Episodic modes of operation in hydrothermal gold systems: Part I. Deformation, ineral reactions and chaos. In: Gessner, K., Blenkinsop, T.G. & Sorjonen-Ward, P. (eds) Characterization of Ore-Forming Systems from Geological, Geochemical and Geophysical Studies. Geological Society, London, Special Publications, 453.

Oreskes, N., Einaudi, M.T., 1992. Origin of Hydrothermal Fluids at Olympic Dam: Preliminary Results from Fluid Inclusionsa nd StableI sotopes. Economic Geology, 87,64–90.

Pessoa, R.R., Archanjo, C.J., 1984. Tectônica de empurrões na região de Tróia–CE. In: Congresso Brasileiro de Geologia, 33, Rio de Janeiro: SGB, pp. 1721–1728.

Pessoa, R.R., Brito Neves, B.B., Kawashita, K., Pessoa, D.R., Fuck, R.A., 1986. Contribuição ao estudo de evolução geocronológica do Maciço de Troia–CE. In: 12 Simpósio de Geologia do Nordeste, João Pessoa, pp. 1721–1728.

Petersson, A., Scherstén, A., Gerdes, A., 2017. Extensive reworking of Archaean crust within the Birimian terrane in Ghana as revealed by combined zircon U–Pb and Lu–Hf isotopes. Geoscience Frontier, 9 (1), 173–189.

Petersson, A., Scherstén, A., Kemp, A.I.S., Kristinsdóttir, B., Kalvig, P., Anum, S., 2016. Zircon U–Pb–Hf evidence for subduction related crustal growth and reworking of Archaean crust within the Palaeoproterozoic Birimian terrane, West African Craton, SE Ghana. Precambrian Research, 275, 286–309.

Phillips, G.N., Powell, R., 2009. Formation of gold deposits: review and evaluation of the continuum model. Earth-Sci. Rev., 94, 1–21.

Phillips, G.N., Powell, R., 2010. Formation of gold deposits: A metamorphic devolatilization model: Journal of Metamorphic Geology, 28, 689–718.

Pinéo, T.R.G., Costa, F.G., 2013. Dados aerogamaespectrométricos aplicados na delimitação do Complexo Cruzeta (Maciço arqueano de Tróia), Domínio Ceará Central da Província Borborema. In: 13th International Congress of the Brazilian Geophysical Society, Rio de Janeiro, Brazil, p. 5.

Pitcairn, I.K., Craw, D., Teagle, A.H., 2015. Metabasalts as sources of metals in orogenic gold deposits. Mineralium Deposita, 50 (3), 373–390.

Pitcairn, I.K., Teagle, D.A.H., Craw, D., Olivo, G.R., Kerrich, R., Brewer, T.S., 2006. Sources of metals and fluids in orogenic gold deposits: Insights from the Otago and Alpine Schists, New Zealand: Economic Geology and the Bulletin of the Society of Economic Geologists, 101, 1525–1546.

Pope, E.C., Rosing, M.T., Bird, D.K., 2011. Geochemical evidence for subduction in the early Archaean from quartz-carbonate-fuchsite mineralization, Isua Supracrustal Belt, West Greenland. Eos Trans. AGU, Fall Meeting Supplement 92, Abstract U13A-0036.

Rey, P., Vanderhaeghe, O., Teyssier, C., 2001. Gravitational collapse of the continental crust: definition, regimes and modes. Tectonophysics 342, 435–449.

Ridley, J.R., Diamond, L.W., 2000. Fluid chemistry of orogenic lode gold deposits and implications for genetic models. In: Hagemann, S.G., Brown, P.E. (Eds.), Gold in 2000: Reviews in Economic Geology. Vol. 13, pp. 141–162.

Robert, F., 2001. Syenite-associated disseminated gold deposits in the Abitibi greenstone belt, Canada: Mineralium Deposita, 36, 503–516.

Rock, N.M.S., Groves, D.I., Perring, C.S., Golding, S.D., 1989. Gold, lamprophyres, and porphyries: what does their association mean? In: Keays, R.R., Ramsay, W.R.H., Groves, D.I. (Eds.), The Geology of Gold Deposits, the Perspective in 1988. Economic Geology Monograph, vol. 6. Economic Geology Publishing, New Haven, Connecticut, pp. 609–625.

Roedder, E., 1979. Fluid Inclusions as Samples of Ore Fluids. Geochemistry of Hydrothermal Ore Deposits (2nd ed.), Wiley, New York, pp. 684–737.

Roedder, E., 1984. Fluid inclusions. Reviews in Mineralogy 12, 644 pp.

Rogers, A.J., Kolb, J., Meyer, F.M., Vennemann, T., 2013. Two stages of gold mineralization at Hutti mine, India Mineralium Deposita, 48, 99–114.

Rosa–Costa, L.T., Lafon, J.M., Delor, C., 2006. Zircon geochronology and Sm–Nd isotopic study: further constraints for the Archean and Paleoproterozoic geodynamical evolution of the southeastern Guiana Shield, north of Amazonian Craton, Brazil. Gondwana Research, 10 (3–4), 277–300.

Rose, A.W., Herrick, D.C., Deines, P., 1985. An oxygen and sulfur isotope study of skarn-type magnetite deposits of the Cornwall type, Southeastern Pennsylvania. Econ. Geol. 80, 418–443.

Rotherham, J.F., Blake, K.L., Cartwright, I., Williams, P.J., 1998. Stable Isotope Evidence for the Origin of the Mesoproterozo Starra Au-Cu Deposit, Cloncurry District, Northwest Queensland. Economic Geology, 9 (3), 1435–1449.

Sahoo, A.K., Krishnamurthi, R., Sangurmath, P., 2018. Nature of ore forming fluids, wallrock alteration and P-T conditions of gold mineralization at Hira-Buddini, Hutti-Maski Greenstone Belt, Dharwar Craton, India. Ore Geology Review, 99, 195–216.

Salier, B.P., Groves, D.I., McNaughton, N.J., Fletcher, I.R., 2005. Geochronological and Stable Isotope Evidence for Widespread Orogenic Gold Mineralization from a Deep-Seated Fluid Source at ca 2.65 Ga in the Laverton Gold Province, Western Australia. Economic Geology, 100 (7), 1366–1388.

Santosh, M., Nadeau, S., Javoy, M., 1995. Stable isotopic evidence for the involvement of mantle-derived fluids in Wynad gold mineralization, South India. Journal of Geology, 103, 718–728.

Sarangi, S., Sarkar, A., Srinivasan, R., Patel, S.C., 2012. Carbon isotope studies of auriferous QCVs from two orogenic gold deposits from the Neoarchean Chitradurga schist belt, Dharwar craton, India: evidence for mantle/magmatic source of auriferous fluid. J. Asian Earth Sci., 52, 1–11.

Schimmelmann, A., DeNiro, M.J., 1993. Preparation of organic and water hydrogen for stable isotope analysis: effects due to reaction vessels and zinc, Analytical Chemistry, 65, 789–792.

Shepherd, T.J., Rankin, A.H., Alderton, D.H., 1985. A practical guide for fluid inclusion studies. Blackie & Son, Glasgow, 239 pp.

Sheppard, S.M.F., 1986. Characterization and isotopic variations in natural waters, in Valley, J.W., Taylor, H.P., and O'Neil, J.R., eds., Stable isotopes in high temperature geological processe: Mineralogical Society of America, Reviews in Mineralogy, 16, 165–183.

Sibson, R.H., Robert, F., Poulsen, K.H., 1988. High–angle reverse faults, fluid–pressure cycling, and mesothermal gold–quartz deposits. Geology, 16, 551–555.

Silva, A.R.C., Villas, R.N.N., Lafon, J.M., Craveiro, G.S., Ferreira, V.P., 2015. Stable isotope systematics and fluid inclusion studies in the Cu–Au Visconde deposit, Carajás Mineral Province, Brazil: implications for fluid source generation. Miner. Deposita, 50, 547–569.

Silva, L.C., MacNaughton, N.J., Vasconcelos, A.M., Gomes, J.R.C., Fletcher, I.R., 1997. U–Pb SHRIMP ages in southern State of Ceará, Borborema Province, NE Brazil: Archean TTG

accretion and Proterozoic crustal reworking. In: Second International Symposium on Granites and Associated Mineralizations, Salvador, p. 280.

Silva, M.G., Coelho, C.E.S., Teixeira, J.B.G., Alves da Silva, F.C., Silva, R.A., Souza, J.A.B., 2001. The Rio Itapicuru greenstone belt, Bahia, Brazil: geologic evolution and review of gold mineralization. Miner. Deposita, 36, 345–357.

Singoyi, B., 1995. Mineral paragenesis, geochemistry and fluid characteristics of the Kara scheelite-magnetite skarn deposit, northwestern Tasmania. Master degree thesis, University of Tasmania, 182 p.

Sousa, H.P., 2016. Caracterização das unidades máfica–ultramáficas e potencial metalogenético da sequência metavulcanossedimentar Serra das Pipocas (Ceará): um provável greenstone belt. Master Dissertation, Universidade Federal do Ceará, Ceará–CE, 203 p.

Spence–Jones, C., Jenkin, G.R.T., Boyce, A.J., Hill, N.J., Sangster, C.J.S., 2018. Tellurium, magmatic fluids and orogenic gold: An early magmatic fluid pulse at Cononish gold deposit? Ore Geology Review, in press.

Sun, X., Zhang, Y., Xiong, D., Sun, W., Shi, G., Zhai, W., Wang. S., 2009. Crust and mantle contributions to gold forming processes at Daping deposit, Ailaoshan gold belt, Yunnan, China. Ore Geology Reviews, 36, 235–249.

Suzuoki, T., Epstein, S., 1976. Hydrogen isotope fractionation between OH-bearing minerals and water. Geochim. Cosmochim. Acta, 40, 1229–1240.

Swain, S.K., Sarangi, S., Srinivasan, R., Sarkar, A., Bhattacaharya, S., Patel., S.C., Pasayat, R.M., Sawkar, R.H., 2015. Isotope (C and O) composition of auriferous Quartz Carbonate Veins, Central Lode System, Gadag Gold Field, Dharwar Craton, India: Implications to source of ore fluids. Ore Geology Reviews, 70, 305–320.

Swain, S.K., Sarangi, S., Srinivasan, R., Sarkar, A., Kesarwani, M., Mazumdar, A., Satyanarayanan, M., 2018. Stable isotope (C-O-S) and geochemical studies of auriferous quartz carbonate veins, Neoarchaean orogenic Ajjanahalli and Gadag Gold Field, Chitradurga schist belt, Dharwar Craton, southern India: Implication for the source of gold mineralizing fluids. Ore Geology Reviews, 95, 456–479.

Taylor, H.P., Frechen, J., Degens, E.T., 1967. Oxygen carbon isotope studies of carbonatites from the Laachersee district West Germany and Alno district, Sweden. Geochim. Cosmochim. Acta 31, 407–430.

Tomkins, A.G., 2010. Windows of metamorphic sulfur liberation in the crust: Implications for gold deposit genesis: Geochimica et Cosmochimica Acta, 74, 3246–3259.

Tomkins, A.G., 2013. On the source of orogenic gold. Geology, 41 (12), 1255–1256.

Tomkins, A.G., and Grundy, C., 2009. Upper Temperature Limits of Orogenic Gold Deposit Formation: Constraints from the Granulite-Hosted Griffi n's Find Deposit, Yilgarn Craton: Economic Geology and the Bulletin of the Society of Economic Geologists, 104, 669–685.

Tomkins, A.G., Mavrogenes, J.A., 2002. Mobilization of gold as a polymetallic melt during pelite anatexis at the Challenger deposit, South Australia: a metamorphosed Archean gold deposit. Econ. Geol., 97, 1249–1271.

Tomkins, A.G., Pattison, D.R.M., Zaleski, E., 2004. The Hemlo gold deposit, Ontario: an example of melting and mobilization of a precious metal-sulfosalt assemblage during amphibolite facies metamorphism and deformation. Econ. Geol., 99, 1063–1084.

Treloar, P.J., Lawrence, D.M., Senghor, D., Boyce, A. Harbidge P., 2015. The Massawa gold deposit, Eastern Senegal, West Africa: an orogenic gold deposit sourced from magmatically derived fluids? In: Jenkin, G.R.T., Lusty, P.A.J., McDonald, I., Smith, M.P., Boyce, A.J., Wilkinson, J.J. (eds), 2015. Ore Deposits in an Evolving Earth. Geol. Soc. Lond. Spec. Publ., 393, 135–160.

Van der Kerkhof, A., Thiéry, R., 2001. Carbonic inclusions. Lithos, 55, 49–68.

Vanderhaeghe, O., Ledru, P., Thiéblemont, D., Egal, E., Cocherie, A., Tegyey, M., Milési, J.P., 1998. Contrasting mechanism of crustal growth: geodynamic evolution of the Paleoproterozoic granite–greenstone belts of French Guiana. Precambrian Research, 92 (2), 165–193.

Vauchez, A., Neves, S.P., Caby, R., Corsini, M.E.S., Arthaud, M.H., Amaro, V., 1995. The Borborema shear zone system, NE Brazil. J. South Am. Earth Sci. 8, 247–266.

Veizer, J., Hoefs, J., 1976. The nature of 18O/16O and 13C/12C secular trends in sedimentary carbonate rocks. Geochim. Cosmochim. Acta, 40, 1387–1395.

Vennemann, T.W., O'Neil, J.R., 1993. A simple and inexpensive method of hydrogen isotope and water analyses of minerals and rocks based on zinc reagent. Chemical Geology (Isotope Geosciences Section), 103, 227–234.

Vielreicher, N.M., Groves, D.I., Snee, L.W., Fletcher, I.R., McNaughton N.J., 2010. Broad synchroneity of three gold mineralization styles in the Kalgoorlie gold field: SHRIMP, U-Pb, and 40Ar/39Ar geochronological evidence. Economic Geology, 105, 187–227.

Wang, Z.L., Yang, L.Q., Guo, L.N., Marsh, E., Wang, J.P., Liu, Y., Zhang, C., Li, R.H., Zhang, L., Zheng, X.L., Zhao, R.X., 2015. Fluid immiscibility and gold deposition in the Xincheng deposit, Jiaodong Peninsula, China: a fluid inclusion study. Ore Geology Reviews, 65, (3), 701–717.

Wilkinson, J.J., 2001. Fluid inclusions in hydrothermal ore deposits. Lithos 55, 229–172.

Wilson, C.J.L., Schaubs, P.M., Leader, L.D., 2013. Mineral precipitation in the quartz reefs of the Bendigo gold deposit, Victoria, Australia. Economic Geology (108), 259–278.

Witt, W.K., Cassidy, K.F., Lu, Y.J., Hagemann, S.G., 2018. Syenitic Group intrusions of the Archean Kurnalpi terrane, Yilgarn craton: Hosts to ancient alkali porphyry gold deposits? Ore Geol Rev., 96, 262–268.

Witt, W.K., Hagemann, S.G., Cassidy, K.F., 2015. A proposed division of the orogenic gold class, based on multiple fluid compositions inferred from proximal alteration. In: 13th SGA Biennial Conference, Nancy, France. Abstracts Volume, p. 241–244.

Wulff, K., Dziggel, A., Kolb, J., Vennemann, T.W., Böttcher, M.E., Meyer, F.M., 2010. Origin of mineralizing fluids of the sediment-hosted Navachab gold mine, Namibia: constraints from stable (O, H, C, S) isotopes. Econ. Geol., 105, 285–302.

Xavier, R.P., Foster, R.P., 1999. Fluid evolution and chemical controls in the Fazenda Maria Preta (FMP) gold deposit, Rio Itapicuru greenstone belt, Bahia, Brazil. Chem. Geol., 154, 133–154.

Xie, Q., Zhang, Z., Hou, T., Jin, Z., Santosh, M., 2017. Geochemistry and oxygen isotope composition of magnetite from the Zhangmatun deposit, North China Craton: Implications for the magmatic-hydrothermal evolution of Cornwall-type iron mineralization. Ore Geology Reviews, 88, 57–70.

Xue, Y., Campbell, I., 2015. The mineralogy of the Bellerophon–Nelson telluride-bearing gold deposit, St Ives Camp, Yilgarn Craton, Western Australia. Can. Mineral., 52, 981–1006.

Xue, Y., Campbell, I., Ireland, T.R., Holden, P., Armstrong, R., 2013. No mass-independent sulfur isotope fractionation in auriferous fluids supports amagmatic origin for Archean gold deposits. Geology 41, 791–794.

Yu, S.Y., Song, X.Y., Ripley, E.M., Li, C., Chen, L.M., She, Y.W., Luan, Y., 2015. Integrated O-Sr–Nd isotope constraints on the evolution of four important Fe–Ti oxide ore-bearing mafic–ultramafic intrusions in the Emeishan large igneous province, SW China. Chem. Geol. 401, 28–42.

Zhang, J.Y., Ma, C.Q., Li, J.W., Pan, Y.M., 2017. A possible genetic relationship between orogenic gold mineralization and post-collisional magmatism in the eastern Kunlun Orogen, western China. Ore Geol. Rev., 81, 342–357.

Zhang, L., Chen, H., Chen, Y., Qin, Y., Liu, C., Zheng, Y., Jansen, N.H., 2012. Geology and fluid evolution of the Wangfeng orogenictype gold deposit, Western Tian Shan, China. Ore Geol. Rev., 49, 85–95.

Zhao, H., Wang, Q., Groves, D.I., Deng, J., 2018. A rare Phanerozoic amphibolite-hosted gold deposit at Danba, Yangtze Craton, China: significance to fluid and metal sources for orogenic gold systems. Mineralium Deposita. https://doi.org/10.1007/s00126-018-0845-x.

Zheng, J., Ma, J., Yang, F., Chai, F., Zhu, Y., 2017. Mineralogy, fluid inclusions, and isotopes of the Cihai iron deposit, eastern Tianshan, NW China: Implication for hydrothermal evolution and genesis of subvolcanic rocks-hosted skarn-type deposits. Ore Geology Reviews, 86, 404–425.

Zheng, Y.F., 1993a. Calculation of oxygen isotope fractionation in hydroxyl–bearing silicates. Earth Planet. Sci. Lett., 120, 247–263.

Zheng, Y.F., 1993b. Calculation of oxygen isotope fractionation in anhydrous silicate minerals. Geochim. Cosmochim. Acta, 57, 1079–1091.

Zürcher, L., Ruiz, J., Barton, M.D., 2001. Paragenesis, elemental distribution, and stable isotopes at the Peña Colorada Iron Skarn, Colima, Mexico. Econ. Geol. 96(3), 535–557.

4. (3º ARTIGO): STRUCTURAL CONTROL AND AGE OF GOLD MINERALIZATION IN THE TROIA MASSIF, BORBOREMA PROVINCE, NE BRAZIL: A PALEOPROTEROZOIC (~2029 Ma) HYPOZONAL OROGENIC GOLD DEPOSIT OVERPRINTED BY THE LATE NEOPROTEROZOIC BRASILIANO/PAN–AFRICAN OROGENY (Artigo submetido – *Journal of South American Earth Sciences*)

Artigo submetido para revista **Journal of South American Earth Sciences**

Submetido em 02 de novembro de 2018

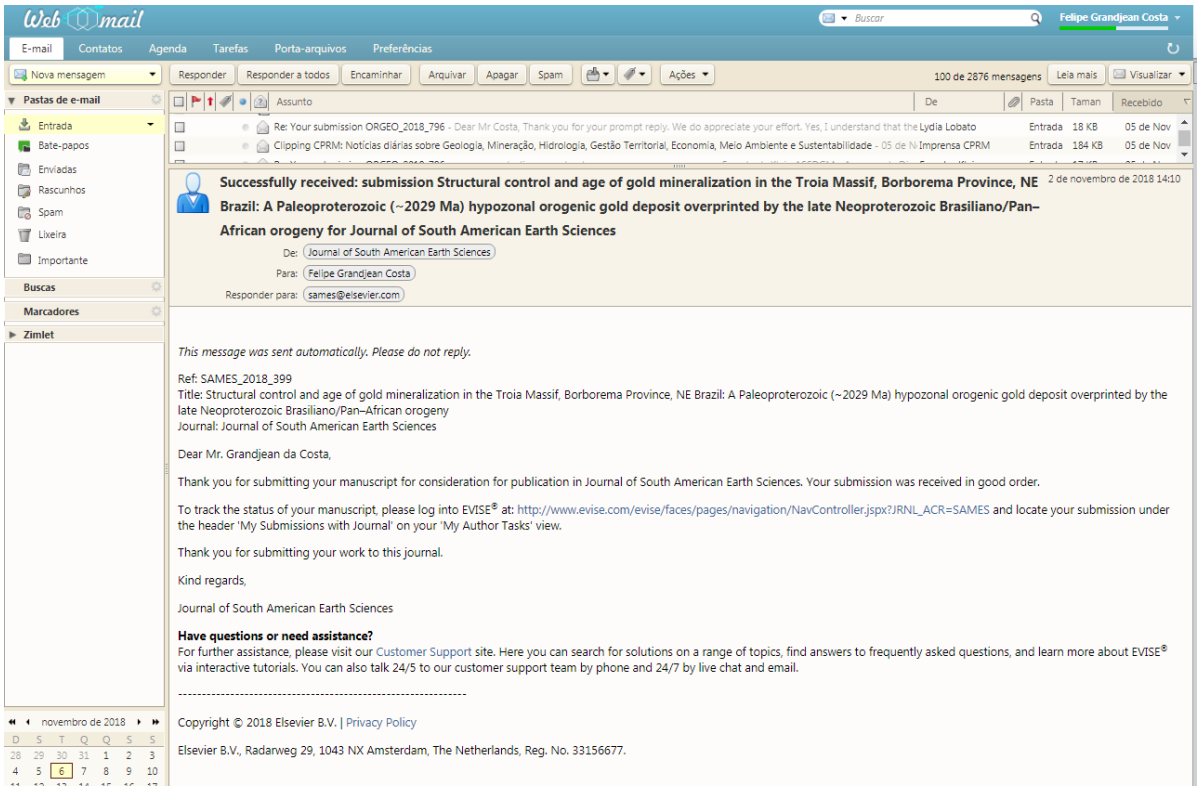

Structural control and age of gold mineralization in the Troia Massif, Borborema Province, NE Brazil: A Paleoproterozoic (~2029 Ma) hypozonal orogenic gold deposit overprinted by the late Neoproterozoic Brasiliano/Pan–African orogeny

Felipe Grandjean da Costa[a,b,c], Evandro Luiz Klein[d,b,c], Marco A. Galarza[c,e], Tércyo R. G. Pineo[a]

[a] *Geological Survey of Brazil, Fortaleza, CE, Brazil*
[b] *GPGE – Grupo de Pesquisas em Geologia Econômica, Federal University of Pará, Belém, PA, Brazil*
[c] *PPGG – Programa de Pós–Graduação em Geologia e Geoquímica, Federal University of Pará, Belém, PA, Brazil*
[d] *Geological Survey of Brazil, Brasília, DF, Brazil*
[e] *Isotope Geology Laboratory (Pará–iso), Institute of Geosciences, Federal University of Pará, Belém, PA, Brazil*

Abstract

The hypozonal orogenic Pedra Branca gold deposit is located in the Troia Massif, an Archean/Paleoproterozoic inlier within the Neoproterozoic Borborema Province, NE Brazil, and hosted by the amphibolite facies Paleoproterozoic Serra das Pipocas greenstone belt. Ore bodies are located near parallel to the stratigraphy, siting on shear zones established at metavolcanic and metasedimentary boundary. Four deformation events are recognized: (1) Dn was responsible for the early Sn foliation, parallel to the greenstone bedding (So). (2) Dn+1 is characterized by a pervasive, southeasterly–dipping Sn+1 foliation that is axial–planar to a number of asymmetric, tight to isoclinal and recumbent folds. (3) Dn+2 represents a strike–slip deformation phase, and (4) the late Dn+3 event is characterized by ductile–brittle deformation. The main stage of gold mineralization comprises deformed quartz veins and associated high–temperature calc–silicate alteration (diopside, amphibole, titanite) and albitization of the host rocks, and is associated to Dn. Lower temperature gold (± Te, Ag) occurs along late stage brittle structures (Dn+3). The U–Pb titanite age of 2029 ± 28 Ma for the calc–silicate alteration (and gold mineralization) of the Pedra Branca gold deposit is similar to the age of many Transamazonian/Eburnean gold mineralizations elsewhere. However, the strong Pb loss of titanite grains defines a 574 ± 7 Ma lower intercept age, indicating that early gold mineralization was affected (remobilization?) by Neoproterozoic deformational events and metamorphism (Brasiliano/Pan–African orogeny). This is in line with the U–Pb zircon age of 575 ± 3 Ma obtained for the syn–tectonic Guaribas diques, which bracketed the age of Dn+3. Dn+1, Dn+2 and Dn+3 are of Neoproterozoic age, with the maximum compressive stress in the WNW–ESE direction. Locally, the Paleoproterozoic Dn is still preserved. The two–stage gold mineralization at Pedra Branca is here interpreted as product of crustal exhumation, with (1) early hypozonal orogenic gold mineralization occurring shortly after the high–grade Paleoproterozoic metamorphism and first exhumation processes of the greenstone pile; and (2) late gold mineralization occurring at shallow levels (second exhumation process), associated to the Neoproterozoic Brasiliano/Pan–African orogeny.

Keywords

Hypozonal, Orogenic, Gold, Structural, Rework, Remobilization

4.1. Introduction

Craton margins are one of the most dynamic geological settings on the planet, and also the site of major lithospheric discontinuities, which can become mineralizing corridors that transfer elements (by fluid/melt) from mantle depths to shallow crustal levels (Hronsky et al., 2012, Groves and Santosh, 2015; Tassara et al., 2017; Li and Santosh, 2017; Groves et al., 2018). Also, in cratonic margins, many Archean to early Paleoproterozoic granite–greenstone terranes hosting orogenic gold mineralizations have been reworked by younger orogenies, which brought new complexities to unravel the structural control and timing of gold mineralization at these locations (Perring and McNaughton, 1990; McMillan, 1996; Fortes et al., 1997; Queiroz et al., 2000; Vielreicher et al., 2002; Jost et al., 2010; Morelli et al., 2010; Gazley, 2011; Duclaux et al., 2012; Larionova et al., 2013; Molnár et al., 2016; Gazley et al., 2016; Martins et al., 2016; Zhang et al., 2018).

Surrounding the Borborema Province, in northeastern Brazil, Rhyacian granite–greenstone terranes are a very conspicuous feature of many cratonic domains (**Fig. 4.1**), including the Birimian/Transamazonian granite-greenstone terranes of São Luís-West African craton (Liégeois et al., 1991; Feybesse et al. 2006; Klein and Moura, 2008; Klein et al., 2012; Block et al., 2016; Petersson et al., 2016, 2017) and correlated terranes of the Guyana Shield (Amazon craton) (Vanderhaeghe et al., 1998; Delor et al., 2003; Rosa-Costa et al., 2006; McReath and Faraco, 2006) and northern São Francisco craton (Silva et al., 2001; Costa et al., 2011; Oliveira et al., 2011) (**Fig. 4.1**). In addition, orogenic gold mineralizations are also a very common characteristic for all of the above mentioned Rhyacian metavolcano–sedimentary sequences, and related to the late episodes of the 2.2–2.0 Ga Transamazonian/Eburnean orogeny (Mello et al., 2006; Silva et al., 2001; Voicu et al., 2001; McReath and Faraco, 2006; Daoust et al., 2011; Béziat et al., 2008; Hammond et al., 2011; Klein, 2014; Klein et al., 2014; 2015; Mignot et al., 2017).

However, at the craton margins, some of these Transamazonian/Eburnean orogenic gold deposits and associated Paleoproterozoic granite–greenstone terranes were tectonically reworked during the 620–580 Ma Brasiliano/Pan–African orogeny, such as the Goiás Massif in the Brasília belt (Queiroz et al., 2000; Fortes et al., 1997; 2003; Jost et al., 2010), and the Gurupi belt (Klein et al., 2005; 2006) (**Fig. 4.1**). Similarly, Paleoproterozoic greenstone belts hosting gold mineralization have been recognized in the Troia Massif, an Archean/Paleoproterozoic basement inlier of the Neoproterozoic Borborema Province (**Fig. 4.1**). However, besides private company reports, only a few literature information is available about this newly discovered gold mineralization (Lopez, 2012; Costa et al., 2016; Naleto et

al., 2016; 2018; Costa et al., submitted). Gold mineralization in the Serra das Pipocas greenstone belt (Pedra Branca gold deposit) is associated to structurally–controlled quartz veins and high–temperature hydrothermal assemblage (diopside, hornblende, titanite, and biotite), suggesting that the Pedra Branca is probably a hypozonal orogenic gold deposit (Costa et al., 2016).

In this work, we present the stratigraphic and structural framework of the Serra das Pipocas greenstone belt, which hosts the Pedra Branca deposit, based on field and airborne geophysical data, along with U–Pb titanite and zircon ages constraints on the timing of gold mineralization, deformation and metamorphism. The results suggests that early hypozonal orogenic gold mineralization is of Paleoproterozoic age, but underwent later overprint by the Neoproterozoic Brasiliano/Pan–African orogeny, and provide an ideal opportunity to study the effects of subsequent orogenies and hydrothermal activity on a pre–existing orogenic gold deposit hosted by amphibolite facies greenstone belt.

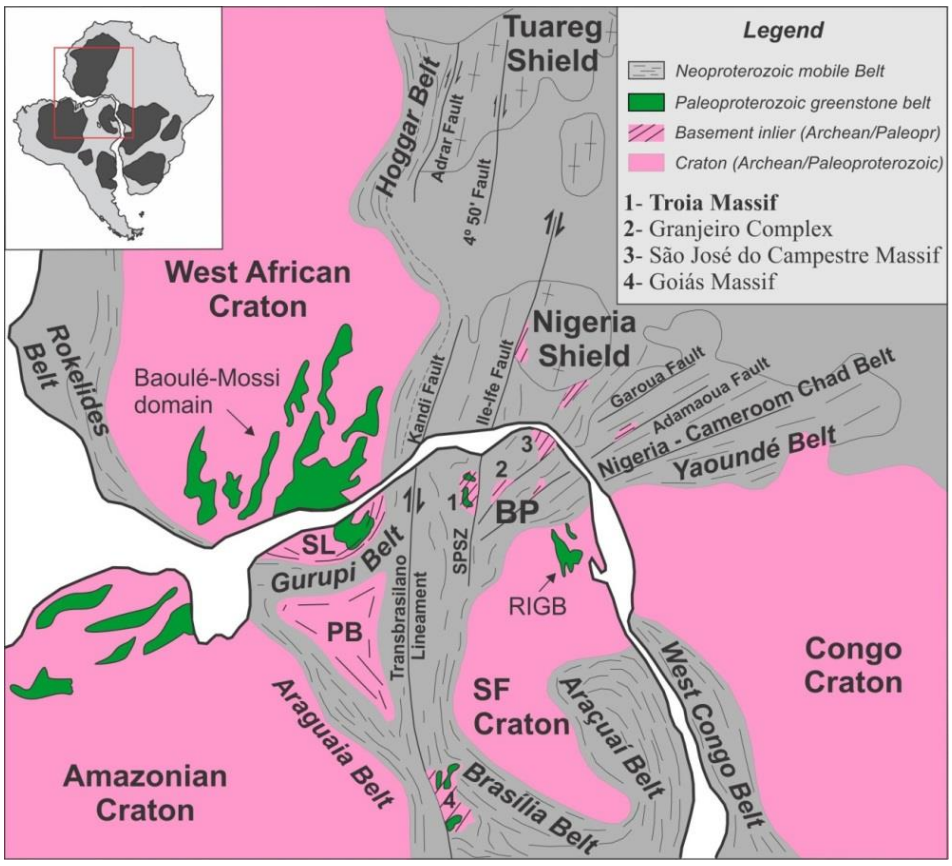

Fig. 4.1. *Schematic cartoon (not to scale) of pre–Mesozoic drift reconstruction of parts of Africa and South America showing the major cratonic domains, Paleoproterozoic greenstone belts and Pan–African/Brasiliano provinces (modified from Trompette, 1994). (BP= Borborema Province; PB= Parnaíba block; SF= São Francisco, SL= São Luis craton, RIGB= Rio Itapicuru greenstone belt and SPSZ= Senador Pompeu shear zone).*

4.2. Regional geology

4.2.1. Northern Borborema Province and its basement inliers

The Borborema Province represents a Neoproterozoic mobile belt related to the agglutination between the São Luis–West African and São Francisco–Congo cratons around 600 Ma, during the Pan–African/Brasiliano orogenic event, related to the amalgamation of the West–Gondwana supercontinent (Almeida et al., 1981) (**Fig. 4.2A**). This geotectonic unit has as its main structural features an extensive transcurrent shear zone network, associated with several intrusion of 590–530 Ma–old, syn– to late–tectonic plutonism (Caby and Arthaud, 1986; Vauchez et al., 1995; Monié et al., 1997; Fetter, 1999; Nogueira, 2004; Arthaud et al., 2008; Araújo et al., 2012; Costa et al., 2013; Amaral et al., 2012; Garcia et al., 2014; Santos et al., 2015). The northern Borborema Province, bounded to the south by the Patos shear zone (or lineament), has been divided into three main crustal blocks: Médio Coreaú, Ceará Central, and Rio Grande do Norte (Van Schmus et al., 2008) (**Fig. 4.2B**). The Médio Coreaú and Ceará Central domains are divided by the Sobral–Pedro II shear zone (or Transbrasiliano Lineament) and the limit between the Ceará Central and Rio Grande do Norte (and/or Jaguaribe) domains is marked to the east by the Senador Pompeu shear zone (Brito Neves et al., 2000; Oliveira, 2008; Padilha et al., 2017; Oliveira and Mederios, 2018). According to Padilha et al., (2017), magnetotelluric data collected along the northern Borborema Province revealed that the limits of these blocks are compatible with high conductivity anomalies in the crust and upper mantle, interpreted as suture zones correlated to their Neoproterozoic collage. However, according to Neves (2003; 2015), these regional–scale structures are mostly reactivations of older Paleoproterozoic shear zones, and the lack of evidence for vast Neoproterozoic oceans suggests that the Neoproterozoic metamorphism and deformation in the whole Borborema Province may be the product of an intra–continental orogeny.

For the northern Borborema Province, basement rocks are mostly of Paleoproterozoic ages (Fetter et al., 2000; Hollanda et al., 2011; Souza et al., 2016), but located Archean crustal domains have also been indentified (**Fig. 4.1** and **4.2B**). Three main Archean nuclei have been identified in northern Borborema Province, corresponding to: (1) Neoarchean (2.8–2.7 Ga) TTG gneisses of Troia Massif in the Ceará Central Domain (Fetter, 1999; Silva et al., 2002; Ganade et al., 2017); (2) the 3.2 to 2.5 Ga Granjeiro complex (Silva et al., 1997; Freimann, 2014; Hollanda et al., 2015); and (3) the 3.4 to 2.7 Ga São José do Campestre Massif, cropping out in the northeastern portion of the Rio Grande do Norte Domain (Dantas et al.,

2004, 2013). More recently, Archean rocks have also been identified in the Central Borborema Province (2.6 Ga Riacho das Lages suite) (Santos et al., 2017). Mostly, these Archean fragments are enveloped by Rhyacian granite–gneissic domains and associated metavolcano–sedimentary sequences (Fetter et al., 2000; Dantas et al., 2004; Souza et al., 2007; Hollanda et al., 2011; Costa et al., 2015; Souza et al., 2016). For more details of the northern Borborema Province geology and its correlation with the African counterpart, see Arthaud et al. (2008) and Santos et al. (2008).

4.2.2. Troia Massif and its Paleoproterozoic greenstone belts

The Archean–Paleoproterozoic basement rocks in the Ceará Central Domain were originally named Troia Massif (Brito Neves, 1975), and as Cruzeta complex by Oliveira and Cavalcante (1993) (**Fig. 4.2B** and **C**). U–Pb TIMS zircon ages obtained by Fetter (1999) confirmed its 2.8–2.7Ga Archean age. The southeastern limit of this Archean domain is sharply defined by the Senador Pompeu shear zone (**Fig. 4.2B** and **C**), whereas the northern and western limits are less clear, and have been inferred on the basis of geochronological data and airborne gamma–spectrometry (Pinéo and Costa, 2013). According to Fetter (1999), the Troia Massif can be divided into two distinct crustal blocks: (i) Pedra Branca and (ii) Mombaça block, both with Neoarchean 2.8–2.7 Ga U–Pb TIMS zircon ages, but differing in their Sm–Nd isotopic signature. The Mombaça block has ƐNd(t) values ranging from -0.79 to +2.73, and the Pedra Branca block yielded slightly more radiogenic values (juvenile) (-0.02 to +2.48) (Fetter, 1999). According to Ganade et al. (2017), new SHRIMP U–Pb geochronological data demonstrate that the Mombaça block (2793 ± 6 Ma) is older than the grey gneisses of the Pedra Branca block (2698 ± 8 Ma), as also suggested by Fetter (1999). However, in the simplified regional–scale map of the Troia Massif, all the Neoarchean rocks of the Troia Massif are represented by the Cruzeta complex (**Fig. 4.2C**). These Archean rocks are mostly TTG orthogneisses and migmatites. The migmatites are mainly composed of stromatic metatexites with main protolith represented by biotite gneiss of granodioritic composition (Mombaça unit), and tonalitic to dioritic compositions (Pedra Branca unit) (Ganade et al., 2017). The U–Pb (SHRIMP) age of 3270 ± 5 Ma was determined by Silva et al. (2002) for a metatonalite of the Cruzeta complex. This age provides evidence that the emplacement of the Mombaça and Pedra Branca TTGs occurred over pre–existing crust with ages similar to those reported in the São José do Campestre Massif (Dantas et al., 2004, 2013; Souza et al., 2016).

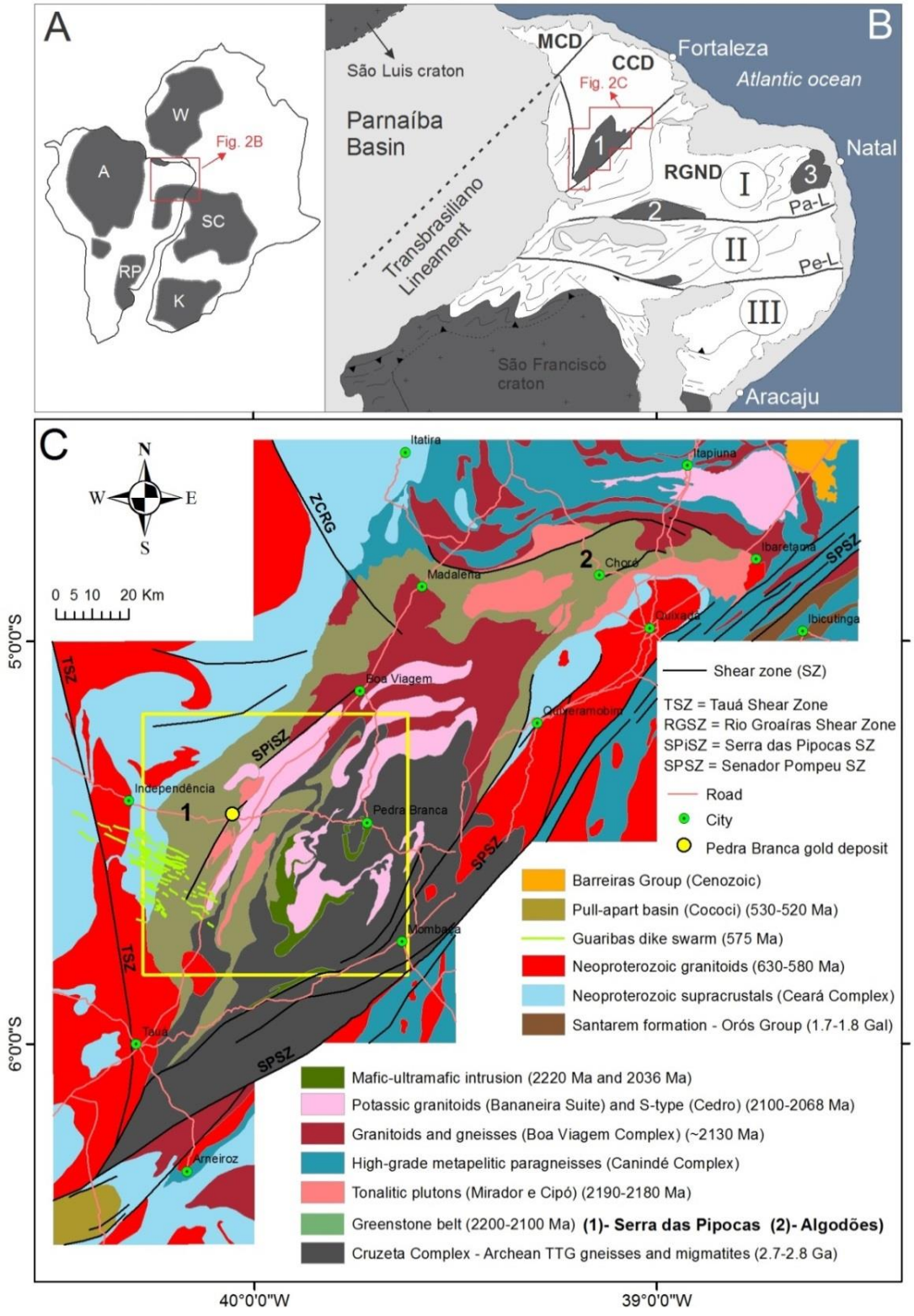

Fig. 4.2. *(A) Pre–drift reconstruction for Africa and South America (WA = West Africa craton; AC = Amazonian craton; SC = São Francisco–Congo craton; RP = Rio de la Plata craton; K = Kalahari craton. (B) Schematic structural map of NE Brazil (modified from Trompette, 1994) showing the three major subdivisions of the Borborema Province delimited by the Patos Lineament (Pa–L) and the Pernambuco Lineament (Pe–L); (I)– Northern Borborema Province, (II)– Transversal zone, (III)– Southern frontal zone; and three major tectonic domains of northern Borborema: MCD = Médio Coreaú Domain, CCD = Ceará Central Domain, RGND = Rio Grande do Norte Domain. Archean*

blocks are (1) Troia Massif, (2) Granjeiro Complex and (3) São Jose do Campestre Massif. (C) Geological map of the Troia Massif (Modified from Costa et al., 2015).

Paleoproterozoic granitoids of the Troia Massif occur as intrusions into both Archean rocks of the Cruzeta Complex and Paleoproterozoic greenstone belts (**Fig. 4.2C**). For example, the Boa Viagem Complex is represented by tonalitic to granodioritic orthogneisses with U–Pb (SHRIMP) zircon ages of 2150 ± 29 Ma and 2124 ± 35 Ma, and may probably represent continental arc plutonism at the northern portion of the Cruzeta complex (Silva et al., 2014) (**Fig. 4.2C**). The São José da Macaoca Complex, defined by Torres et al. (2007) to the north of the Troia Massif, also represents a large portion of tonalitic to granodioritic orthogneisses with similar U–Pb TIMS zircon ages of 2139 ± 12 Ma (Castro, 2004) and 2130 ± 3 Ma (Fetter, 1999) (**Fig. 4.2C**). According to Costa et al. (2015), the 2139–2130 Ma Macaoca orthogneisses have low–silica adakitic signature (mantle–related magmas), and were probably associated to the accretion of the Algodões greenstone terrane to the north margin of the Troia Massif. In this massif, two major metavolcano–sedimentary sequences have been recognized as Paleoproterozoic greenstone belts, named Algodões greenstone belt to the north (Martins et al., 2009; Costa et al., 2015), and Troia greenstone belt (or Serra das Pipocas greenstone belt) to the south (Pessoa and Archanjo, 1984; Pessoa et al., 1986; Costa et al., 2014a, 2015; Sousa, 2016; Costa et al., 2018) (**Fig. 4.2C**).

4.2.2.1. Algodões greenstone belt

The Algodões greenstone belt occurs at the northern portion of the Troia Massif (**Fig. 4.2C**). This sequence comprises mainly amphibolites derived from metabasalts, fine–grained leucocratic paragneisses, metagreywackes, meta–arkoses, rare metapelites, quartzites, meta–andesites, meta–conglomerates, and calc–silicate rocks (Martins, 2000; Martins et al., 2009; Costa, 2013). Amphibolites were dated at 2236 ± 55 Ma (whole–rock Sm–Nd isochron; four samples) (Martins et al., 2009) and share geochemical features akin to oceanic plateau and/or back–arc basalts (Martins et al., 2009; Verma and Oliveira, 2014). They record upper greenschist to lower amphibolite metamorphic conditions and lack migmatization (Martins, 2000; Costa, 2013). Structurally, the Algodões greenstone belt shows penetrative regional northeastward trending foliation dipping to SE (Martins, 2000; Costa, 2013). A LA–ICPMS U–Pb zircon age of 2046 ± 12 Ma obtained by Gomes (2013) for the leucosome of a migmatitic (Macaoca) orthogneiss found close to the Algodões sequence shows that regional metamorphism is probably of Paleoproterozoic age. Based on Pb–Pb zircon ages, Sm–Nd

isotopes, and whole–rock geochemistry, the 2190 to 2160 Ma Cipó tonalites, which intrude the Algodões greenstone belt, are thought to represent TTG–like (trondhjemite or high–silica adakite) plutonic rocks that probably evolved in an intra–oceanic arc, to account for their juvenile Nd signature (TDM model ages = 2.24 to 2.29 Ga and ℇNd(t) values = +0.29 to +1.9) (Martins et al. 2009). For these plutonic rocks (Cipó tonalites), Costa et al. (2015) reported LA–ICPMS U–Pb zircon ages of 2189 ± 14 Ma and 2180 ± 15 Ma, and also suggested a pre–collisional (arc–related) setting to these tonalites.

4.2.2.2. Serra das Pipocas greenstone belt

The first structural and lithological mapping in the central–west part of the Troia Massif was presented by Pessoa and Archanjo (1984). According to these authors, thrust tectonics was responsible for the allochthonous character of the metavolcano–sedimentary sequences and related mafic–ultramafic metaplutonic rocks, overlying the gneiss–migmatitic basement of the Troia Massif. Additional work, with Rb–Sr and K–Ar geochronological data, evidenced that the Troia Massif exhibits a polycyclic character, with Archean and Paleoproterozoic rocks, mostly presenting K–Ar and Rb–Sr isotopic rejuvenating during the Neoproterozoic (Brasiliano) orogenic cycle (Pessoa et al., 1986). These authors also suggested that the thrust tectonics in the Troia Massif is Paleoproterozoic in age. However, because of the lack of reliable isotopic results for the supracrustal sequences of the Serra das Pipocas region, Pessoa et al. (1986) interpreted it as an Archean greenstone belt. Later on, Fetter (1999) provided 2151 ± 9 Ma a U–Pb zircon age for a metadacite layer close to the Serra das Pipocas region, suggesting a minimum depositional (Paleoproterozoic) age for the Serra das Pipocas granite–greenstone sequence, whilst the metamafic–ultramafic plutons and associated greenstone belts of the central portion of the massif were still interpreted as of Archean age. However, new U–Pb (in situ) zircon ages in metasedimentary and intrusive rocks confirmed the Rhyacian age for the Serra das Pipocas metavolcano–sedimentary sequence and related metamafic–ultramafic rocks in the Troia Massif (Costa et al., 2014a, 2014b; Sousa, 2016).

The Serra das Pipocas greenstone belt, in the central–west portion of the Troia Massif (**Fig. 4.2C**) is composed of metabasalts (amphibolites), felsic to intermediate metavolcanic rocks, metasedimentary rocks, metacherts, marbles, serpentinites, and associated S–type leucogranite (i.e., Cedro suite), tonalitic (TTG–like) intrusions and mafic–ultramafic metaplutonic rocks (Pessoa and Archanjo, 1984; Pessoa et al., 1986; Cavalcante et al., 2003; Costa et al., 2014a; Sousa, 2016; Costa et al., 2018). According to Pessoa and Archanjo

(1984), metabasalt with pillow–like structures was locally identified. Geochemistry of mafic metavolcanic rocks shows transitional tholeiitic to calc–alkaline affinity and arc–related signature, suggesting an arc/back–arc tectonic setting to this volcanism (Sousa, 2016). U–Pb detrital zircon dating of a metagreywacke of the metavolcano–sedimentary sequence yielded a younger age population around 2200 Ma and older ($^{207}Pb/^{206}Pb$) ages of 3096 ± 53 Ma, 3074 ± 55 Ma, 2608 ± 54 and 2546 ± 55 Ma, which indicates a mixture of Archean and Rhyacian sources and a maximum depositional age of 2.2 Ga (Costa et al., 2014a). The presence of Archean detrital zircon grains suggests an ensialic (or continental proximity) setting for part of this granite–greenstone terrane (Costa et al., 2014a). The mafic and ultramafic metaplutonic rocks are more abundant in the central Troia region (**Fig. 4.2C**), and are mainly interpreted as fragmented layered bodies, well–known because of the platinum and palladium mineralization in metachromitites (Pessoa and Archanjo, 1984; Angeli et al., 2009; Barrueto and Hunt, 2010). A Sm–Nd isochron of 2060 Ma was obtained for this mafic–ultramafic magmatism (Liégeois, unpublished data; cited by Fetter, 1999), recently attested by a U–Pb (SHRIMP) zircon age of 2036 ± 28 Ma obtained for a PGE–bearing metachromitite sample (Costa et al., 2014b).

4.3. Methodology

U–Pb titanite dating was carried out at the isotope/geochemistry laboratory of the Department of Geology, Federal University of Ouro Preto, Brazil. Gold–related titanites were hand–piked from the calc–silicate alteration, after crushing a mineralized drill core sample. Titanites were analyzed for U–Pb isotopes by Laser Ablation Inductively Coupled Plasma Mass Spectrometry (LA–ICPMS). The LA–ICPMS analyzes were performed using a Thermo Scientific Element II and a 213 nm CETAC laser. The analyzes were performed on a conventional polished epoxy mount, 100% free of common Pb. Acquisitions consisted of 20 seconds measurement of the gas blank, followed by 20 seconds measurement of U, Th, and Pb signals during ablation, and 20 seconds washout. Laser conditions were 20 µm beam at 10 Hz and 0.02 J energy, giving a fluency of 8 J/mm. Common Pb corrected isotopic ratios were reduced using an Excel spreadsheet (Gerdes and Zeh 2006). Apparent age calculations and Concordia diagrams were produced using Isoplot 3.7 (Ludwig, 2012). Two standards were used during runs: the primary standard BLR (1049.9 ± 1.3 Ma; Aleinikoff et al. 2007) and the secondary standard Khan titanite (522.2 ± 2.2 Ma, Heaman 2009).

U–Pb zircon dating was carried at the Isotope Geology Laboratory of the Federal University of Pará, in Belém, Brazil. The U–Pb analyses were performed on zircon using a

high–resolution Neptune Thermo Finnigan Multi–collector ICP–MS, equipped with a Nd:YAG 213 nm LSX–213 G2 CETAC laser microprobe. The analytical procedures followed, in general, the work of Chemale et al. (2012). Acquisitions consisted of measurement of the gas blank, followed by 40 seconds measurement of U, Th, and Pb signals during ablation. Laser conditions were 25 μm beam at frequency rate of 10 Hz, energy of 45–50 mJ/cm^2. The instrumental mass discrimination was corrected by the analyses of zircon reference material GJ–1 (Jackson et al., 2004) and 91500 (Wiedenbeck et al., 1995), which ages are 608.5 ± 1.5 Ma and 1065.4 ± 0.3 Ma, respectively. Common lead (^{204}Pb) interference and background correction is normally carried out monitoring the ^{202}Hg and ^{204}(Hg + Pb) masses during analytical sessions and using a model Pb composition (Stacey and Kramers, 1975). Age calculations and U–Pb plots in Concordia diagrams were performed using the software Isoplot 3.7 (Ludwig, 2012).

Magnetic and gamaspectrometric data from airborne geophysical survey was acquired by the Geological Survey of Brazil. Survey parameters are: N–S line spacing of 500 m, E–W tie–line spacing of 1000 m and an elevation of 100 m. Data processing was performed using Oasis Montaj software developed by GEOSOFT. After cutting the area of interest and quality analysis, the data were then interpolated using the Bi-Directional Gridding method, resulting in regular grids of 125 x 125 m. A series of maps were produced by digital processing methods of the geophysical grids, which include the generation of a total-field magnetic anomaly, analytic signal, first vertical derivative and ternary composition (eU in blue, eTh in green, K in red) of airborne gamma–ray spectrometric image. The total-field magnetic anomaly map was processed according to Medeiros et al. (2011) and Spector and Grant (1970) to quantify the depth of the top of different magnetics fonts. The topographic data was obtained from the Shuttle Radar Topography Mission (SRTM), designed by NASA. Shaded–relief image was generated from SRTM image of 30 meters in resolution, and using a 35° solar illumination angle at azimuth angle of 0°. The data was processed using ArcMap™ software, in order to generate shaded relief images by changing the azimuth angle of the light source. Landsat–8 image (217/64) (RGB–5, 6, 7 band composition) was also used in this work.

4.4. Tectono–stratigraphy of the Serra das Pipocas greenstone belt

According to our recent mapping and reappraisal to this work, the Serra das Pipocas greenstone belt represents the major metavolcano–sedimentary sequence in the central–west portion of the Troia Massif (**Fig. 2C** and **3**). This sequence is flanked on the east by granitoids

of the Bananeria suite and basement rocks of the Archean Cruzeta complex. Neoproterozoic micaschists of the Ceará complex flank the west boundary of the sequence. All metavolcano–sedimentary sequences in the Troia Massif are found with similar lithologies of the Serra das Pipocas greenstone belt (Algodões greenstone belt, **Fig. 4.2C**). However, the effects of deformation, such as folding and thrusting in the original stratigraphy of these sequences, have probably caused local repetition and thickening of the greenstone sequence. In a simplified way, we propose here, that the Serra das Pipocas greenstone belt may be divided into two main tectono–stratigraphic units: **(1) Lower unit**, with predominance of mafic metavolcanic and associated gabbroic rocks and **(2) Upper unit**, which consist mainly of metasedimentary rocks. Latter, these units have been intruded by distinct pulses of plutonic rocks and dikes (**Fig. 4.3** and **4.4**).

4.4.1. Lower unit (mafic/intermediate metavolcanic rocks)

Mafic metavolcanic rocks are the predominant rock type in the Lower unit of the Serra das Pipocas sequence (**Fig. 4.3** and **4.4**) and are mainly represented by layers of amphibolites and/or garnet–amphibolites associated with schists (metapelites) and metagraywackes. Amphibolites occur parallel to the bedding of their host metasedimentary rocks, suggesting that these volcanic rocks represent lava flows that extruded during sedimentation (**Fig. 4.5A**). Locally, layers of meta–ultramafic rocks represented by talc–schists and actinolite–tremolite–schists (metapicrites and/or metakomatiites) are also found in this sequence, as well as intermediate (andesitic/dacitic) metatuffs, metacherts and banded iron formation alternated with the amphibolites and metapelites. The U–Pb zircon ages presented by Sousa (2016) for felsic metavolcanic rocks (metadacites) in the Serra das Pipocas greenstone belt vary from 2234 ± 13 to 2156 ± 45 Ma. According to Sousa (2016), the older age of 2234 ± 13 Ma is for a metadacite of the west part of the sequence, related to the mafic and ultramafic metavolcanic rocks, while the younger ages were found at the Upper metasedimentary unit (**Fig. 4.3** and **4.4**). Therefore, the metadacite age of 2234 ± 13 Ma may bracket the minimum age for the Lower unit (Sousa, 2016). Many gabbroic plutons are found within the Lower unit, and may probably represent plutonic (or subvolcanic sill) equivalent of the mafic metavolcanic rocks.

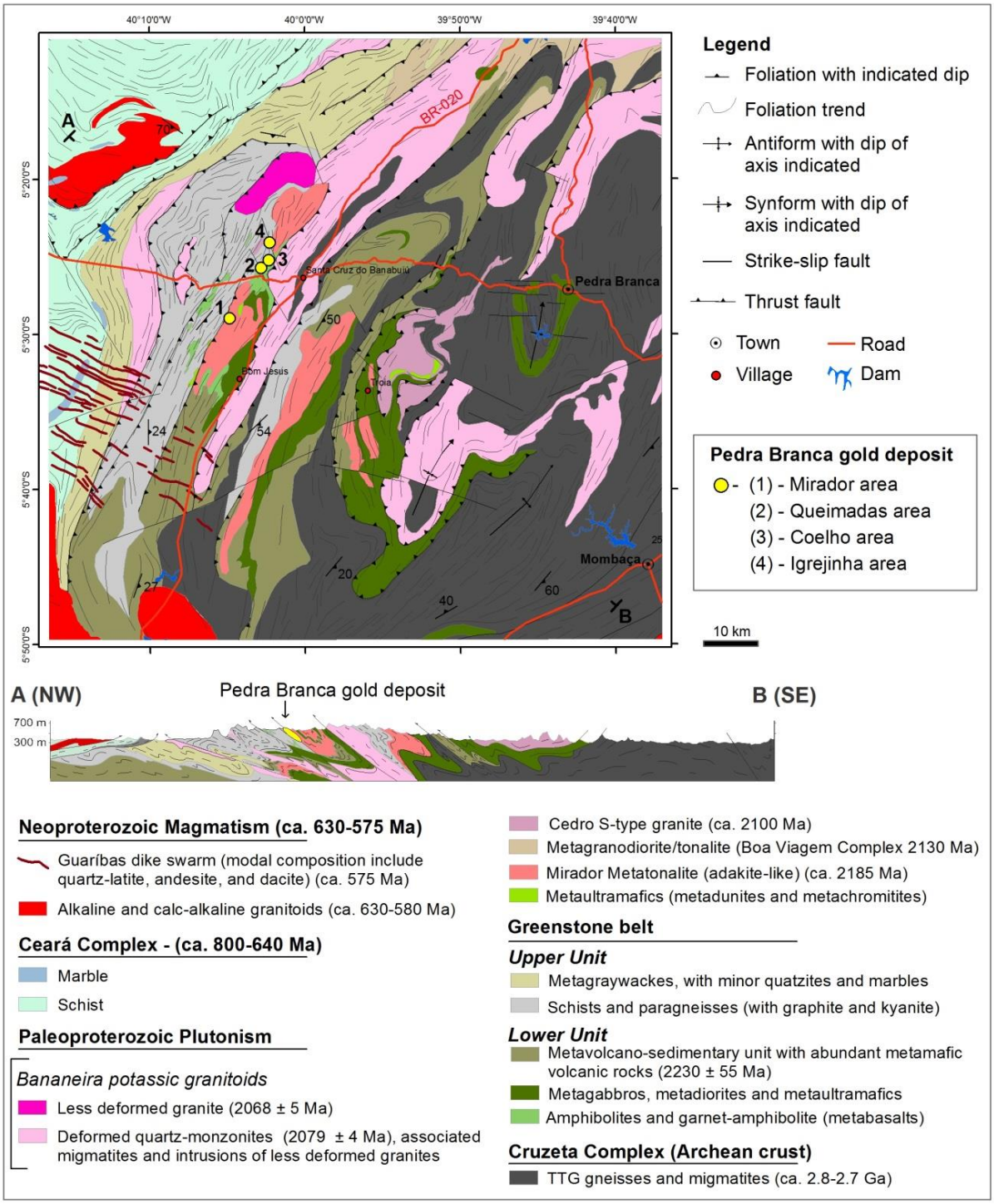

Fig. 4.3*. Geological map and schematic cross section of the study area with the location of the mineralized areas from the Pedra Branca gold deposit (After Costa et al., 2018).*

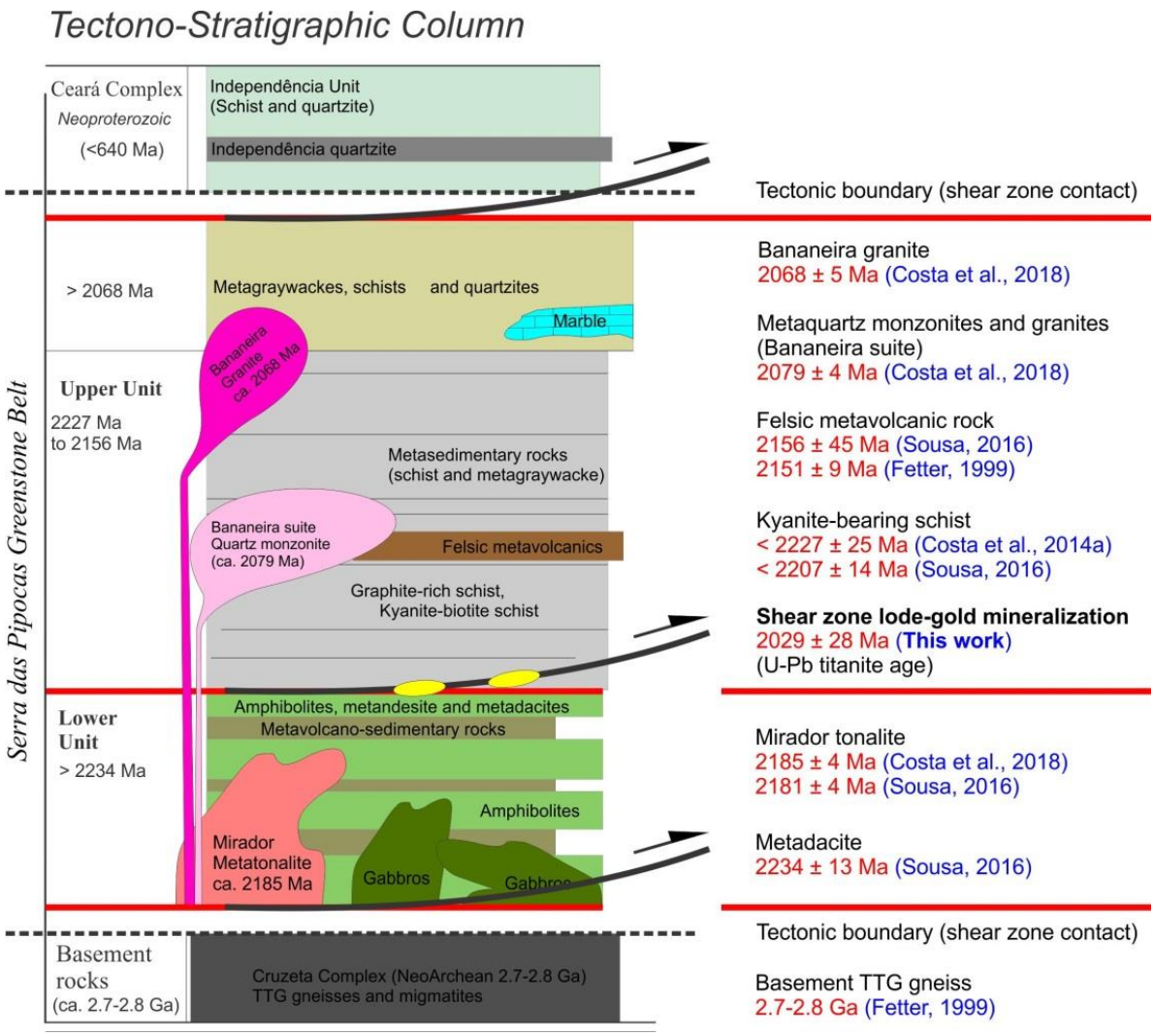

***Fig. 4.4**. Simplified tectono–stratigraphic column of the Serra das Pipocas greenstone belt.*

4.4.2. Upper unit (metasedimentary rocks)

The Upper unit of the Serra das Pipocas greenstone belt is mainly composed of intercalated metagraywacke and mica schist (metapelites) layers. Mica schists comprise biotite–muscovite schists (**Fig. 4.5B**), but higher metamorphic conditions are locally indicated by the presence of graphite, garnet and kyanite (**Fig. 4.5C, D, E** and **F**). Therefore, these rocks may have reached medium– to high–pressure upper amphibolite metamorphic condition. Kyanite crystals are generally aligned along the main foliation (**Fig. 4.5D**). Kyanite is commonly overgrown by muscovite, in association with biotite and sillimanite (**Fig. 4.5E** and **F**), suggesting decompression processes (exhumation), typical for clockwise PT trajectory of high–grade metamorphic rocks (Foster, 1991; Gervais and Hynes, 2013).

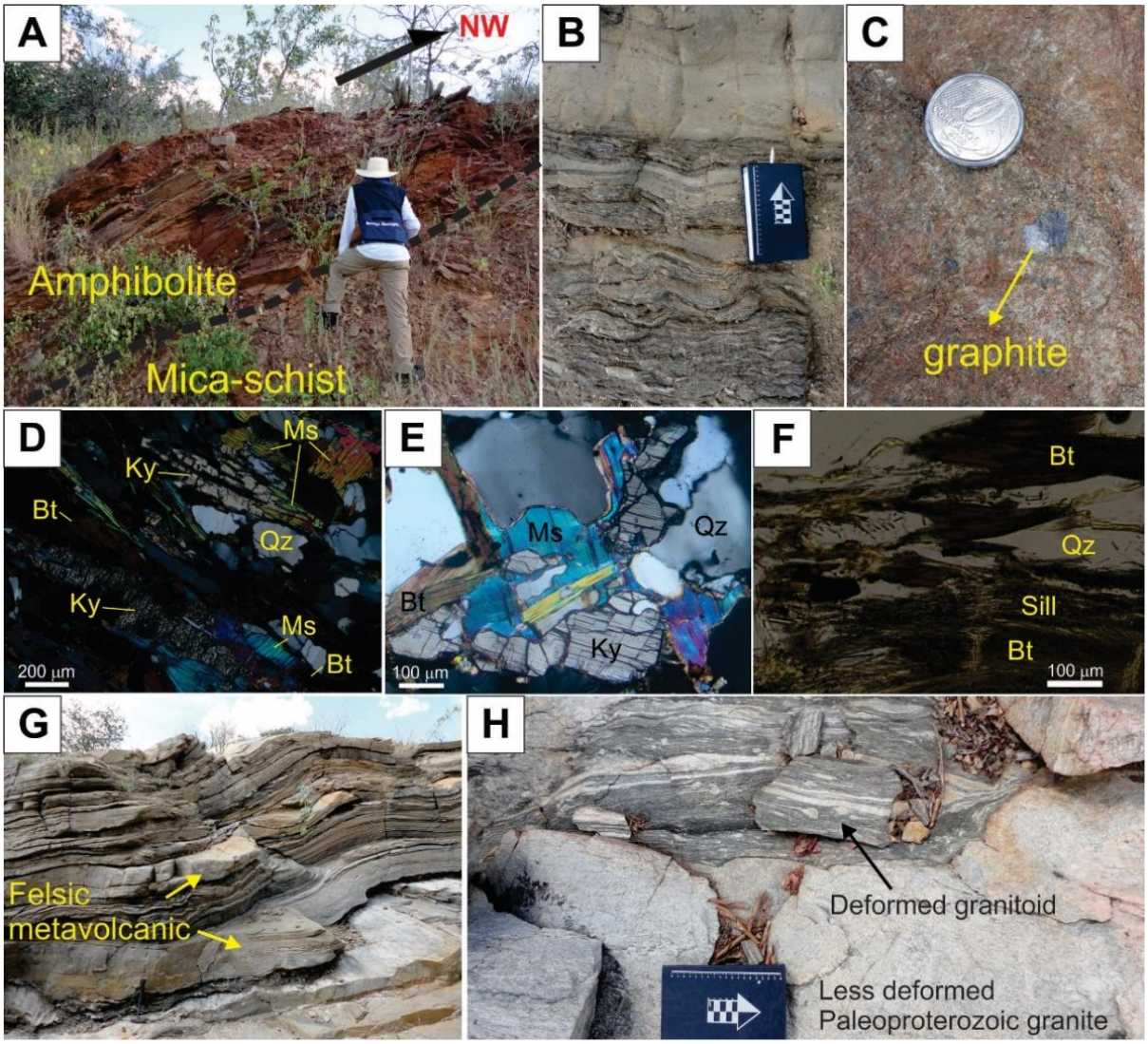

Fig. 4.5. *(A) Mafic metavolcanic rock in contact with muscovite–biotite schist of the Serra das Pipocas region, with metamorphic foliation parallel to bedding (So), plunging to SE. (B) Detail of the outcropping with alternating metagraywacke and mica schist layers. (C) Detail for graphite crystal in garnet–kyanite schist. (D) Thin section microphotography (on transmitted light, crossed nicols) showing aligned kyanite (Ky), biotite (Bt) crystals defining th metamorphic foliation. Muscovite overgrowths occur locally at the kyanite borders. (E) Thin section microphotography (on transmitted light, crossed nicols) showing kyanite (Ky) porphyroblast with muscovite and biotite overgrowth indicating decompression processes. (F) Thin section microphotography (unpollirezed light) for fibrolitic sillimanite (Sill) aligned with biotite (Bt) suggesting a retrograde phase from pseudomorphic pre-existing kyanite porphyroblasts. Fibrolitic sillimanite is sub-parallel to the foliation (probably Sn//Sn+1). (G) Alternating muscovite–biotite schist and metagraywacke layers with felsic metavolcanic rocks (metariodacite). (H) Deformed granitoid with mylonitic foliation croscutted by late–tectonic less–deformed granitic dike. Both deformed and less–deformed granitoid are Paleoproterozoic in age.*

The U–Pb detrital zircon ages available on the literature for these kyanite–bearing schists, evidence a younger zircon population at 2227 ± 25 Ma according to Costa et al. (2014a), and similarly, at 2207 ± 14 Ma according to Sousa (2016). This bracket the

maximum depositional age of these metassedimentary rocks (Upper unit) at 2227 Ma (**Fig. 4.4**). Locally, rhythmically compositional bedding of metagraywacke and mica schist alternate with felsic metavolcanic rocks (**Fig. 4.5G**). Fetter (1999) was the first one to recognize the age of felsic metavolcanic rocks in the Serra das Pipocas sequence by a U–Pb (TIMS) zircon age of 2151 ± 9 Ma, later reinforced by Sousa (2016) with U–Pb (LA–ICPMS) zircon age of 2156 ± 46 Ma. Thus, the age of 2150 ± 9 Ma of these felsic metavolcanic rocks may bracket the minimum age for the deposition of the Upper metasedimentary unit of the Serra das Pipocas greenstone belt (**Fig. 4.4**). Toward the top of the Upper unit, a subunit was also individualized, in which metasedimentary rocks are more psamitic, alternating thick layers of metagraywarcke, less metapelites, and several occurrence of quartzites, marbles and calc–silicate rocks (**Fig. 4.3** and **4.4**). This uppermost subunit is probably correlated to quartzites and meta–conglomerates of the Choró Unit, in the Algodões greenstone belt (Costa et al., 2015). No geochronological information have been presented to this late psamitic subunit, but because granitoids of the Bananeira unit intruded part of this rocks, the depositional age may be necessary older than 2068 ± 5 Ma (**Fig. 4.4**). Neoproterozoic mica schists of the Ceará complex flank the west boundary of the Paleoproterozoic Serra das Pipocas greenstone belt (**Fig. 4.3**).

4.4.3. Granitoids at the Serra das Pipocas granite–greenstone terrane

Two major Paleoproterozoic plutonic events are recognized at the Serra das Pipocas granite–greenstone terrain: (1) The 2180–2190 Ma sodium–rich (adakite–like) plutonism, represented by the Mirador tonalites, and (2) the 2068–2079 Ma potassium–rich plutonism represented by the Bananeira suite (Costa et al., 2018). The recognition of these two plutonic events is a powerful tool to interpret the tectono–stratigraphic evolution of the Serra das Pipocas greenstone belt, as the pluton ages and their geochemical signatures are suggestive for the record of arc–related (Mirador tonalites) and collisional (Bananeira suite) magmatism (Costa et al., 2018). The 2180–2190 Ma Mirador tonalites have intrusive contact with amphibolites and metasedimentary rocks of the Lower unit of Serra das Pipocas greenstone belt, and do not occur in the surrounding basement rocks (**Fig. 4.3** and **4.4**). These tonalitic intrusions are restricted to the Lower unit of the greenstone belt and are not intrusive in the Upper unit (**Fig. 4.3** and **4.4**). This suggests that most of the Upper unit must be younger than 2180–2190 Ma and probably deposited in a distinct tectonic setting when compared to the Lower unit of the greenstone sequence. The ages of the Mirador tonalites are also similar to those of the 2180–2190 Ma Cipó tonalites of the Algodões greenstone belt (**Fig. 4.2C**), in the

northern part of the Troia Massif (Martins et al., 2009; Costa et al., 2015), suggesting a regional tectono–stratigraphic correlation between these two greenstone belts.

The Bananeira suite represents a large plutonic manifestation in the study area, mainly represented by potassic granitoids that are intrusive both in the Paleoproterozoic greenstone sequences and Archean basement rocks of the Troia Massif (**Fig. 4.3**) (Oliveira and Cavalcante, 1993; Costa et a., 2018). According to Costa et al. (2018), a SHRIMP U–Pb zircon age of 2079 ± 4 Ma was obtained for the deformed quartz–monzonites and a LA–ICPMS U–Pb zircon age of 2068 ± 5 Ma for the less–deformed granites. In general, both Mirador and Bananeira plutons are affected by regional deformation, with development of sub–solid ductile foliation and late ductile–brittle structures. However, for the Bananeira suite, less–deformed and fine–grained granites are also found, occurring as late aplite dikes in the deformed porphyritic granitoids (**Fig. 4.5H**), or as isolated semi–circular granitic intrusions (**Fig. 4.3**).

4.4.4. Neoproterozoic Guaribas dike swarm

The Guaribas dike swarm occurs in the south portion of the Serra das Pipocas greenstone belt, represented by the intrusion of subparallel dikes oriented in the NW–SE direction (**Fig. 4.3**). These dikes are undeformed acid to intermediate subvolcanic rocks, raging in composition from latite, quartz latite, andesite and rhyolite (Almeida et al., 1984; Almeida, 1987). The dikes are metric to kilometric (up to 2 km) in thickness, with vertical to subvertical dipping, extending as long as 30 km (**Fig. 4.3**). These dikes are strictly connected to large syn–transcurrent Neoproterozoic (590–580 Ma) batholiths that emplaced along the Tauá and Senador Pompeu shear zones (Tauá and Quixadá–Quixeramobim batholiths) (**Fig. 4.2C**) (Almeida, 1987; Neves, 1991; Fetter, 1999; Nogueira, 2004).

4.5. Structural geology

4.5.1. Previous works

According to Pessoa and Archanjo (1984), three main deformational events (or phases) were identified in the granite–greenstone terranes of the Troia Massif. The first deformation event (D1) resulted in an intensive intrafolial folding, gneissic banding and down–dip mineral lineation, the second (D2) is associated to asymmetric folds of an imbricate thrust tectonic, with transport to NW, and (D3) the last deformation event, is related to the development of open folds (Pessoa and Archanjo, 1984). According to Oliveira and

Cavalcante (1993), five deformation events were characterized; Dn–1, Dn, Dn+1, Dn+2, Dn+3 and Dn+4. In brief, the Dn–1 and Dn events are recognized only by foliation planes and locally transposed intrafolial folds, the Dn+1 is related to the thrust tectonic, the Dn+2/Dn+3 are associated to transcurrent deformation, and the Dn+4 event associated to NW–direction brittle–ductile shear zones and open folds (Oliveira and Cavalcante, 1993). According to these two previously works on the study area, the most important deformation event, which developed the most pervasive foliation plane in the area, is the thrust tectonics, considered as the D2 event by Pessoa and Archanjo (1984) and Dn+1 by Oliveira and Cavalcante (1993). The deformation event associated with dextral trascurrent shear zones were only described by the regional (1:100.000 mapping) work of Cavalcante and Oliveira (1993), but not identified by local scale mapping of Pessoa and Archanjo (1984).

4.5.2. Field work results

Based on the above mentioned literature information, and on our field data, we interpret the structural data of the study area as the record of four deformation events (Dn, Dn+1, Dn+2 and Dn+3). The first deformation event is referred here as the Dn tectonic event, responsible for the generation of the early Sn foliation plane, which is parallel to the bedding (So) of the Serra das Pipocas greenstone belt rock units (**Fig. 4.5A, B, E,** and **4.6A**). However, no folding related to this Dn event has been recognized in the study area. Most of the observed folds on the compositional layering (So) of the rock units, and the parallelized Sn foliation, define a Dn+1 compressional event in the area. The Dn+1 tectonic event is characterized by a pervasive, southeasterly–dipping, NE–trending Sn+1 foliation that is axial–planar to a number of asymmetric, tight to isoclinal and recumbent folds (**Fig. 4.6A, B, C, D, E** and **F**). The parallelized foliation planes (Sn//Sn+1) define the main regional fabric of the area, which can be attributed to a maximum shortening axis oriented in a WNW–ESE direction. Most of the asymmetric folds evidence tectonic transport to W/NW, associated to thrust shear zones (**Fig. 4.6A, B, C, D**). Isoclinal to recumbent folds are also associated to this Dn+1 event (tangencial tectonic) (**Fig. 4.6E, F**). On the Sn+1 foliation planes, the development of a down–dip stretching lineation (Ln+1) are attributed to the Dn+1 thrusting and folding event.

Fig. 4.6. *(A), (B), (C) Asymmetric fold in metasedimentary rocks (Upper unit) of the Serra das Pipocas greenstone belt (road BR–226). Fold recording Dn+1 compressional event, with tectonic transport to west/northwest (W/NW). (D) Tight to isoclinal syn–thrust (intrafolial) folds (Transport to W/NW). (E) A recumbent fold in metagraywacke (Upper unit) and the interpreted Sn+1 axial–planar foliation. (F) Recumbent fold in metagabbro (Lower unit) and the interpreted Sn+1 axial–planar foliation.*

The Dn+2 event represents a transcurrent (strike–slip) deformation phase in the area, dominated by moderately to steeply–dipping dextral shear zones with NE–SW direction. At regional scale, the Senador Pompeu Shear Zone (SPSZ) is the most notable example of these NE–trending macro–structures associated to the Dn+2 trancurrent event (**Fig. 4.2C**). The

SPSZ delimit the southeast boundary of the Troia Massif and connect to the Ile–Ife Fault in the Nigeria shield (**Fig. 4.1**). The development of the Sn+2 foliations associated to Dn+2 transcurrent event concentrates on the proximity of the SPSZ, and also at the Serra das Pipocas Shear Zone (**Fig. 4.2C**). The Serra das Pipocas shear zone is hosted almost entirely by the granite–gneisses of the Bananeira suite and is characterised by a well–developed mylonitic foliation near the greenstone margin (**Fig. 4.7A**). At high strain domains, the Dn+2 deformation generates a zonal crenulation fabric, in which the Sn//Sn+1 foliation planes deflected into parallelism with spaced Sn+2 foliations, characterizing narrow zones of concentrated shear (**Fig. 4.7A**). The Sn+2 mylonitic foliations, commonly found in deformed granitoids of the Bananeira suite, locally developed eye-shaped feldspar augen textures (**Fig. 4.5H**).

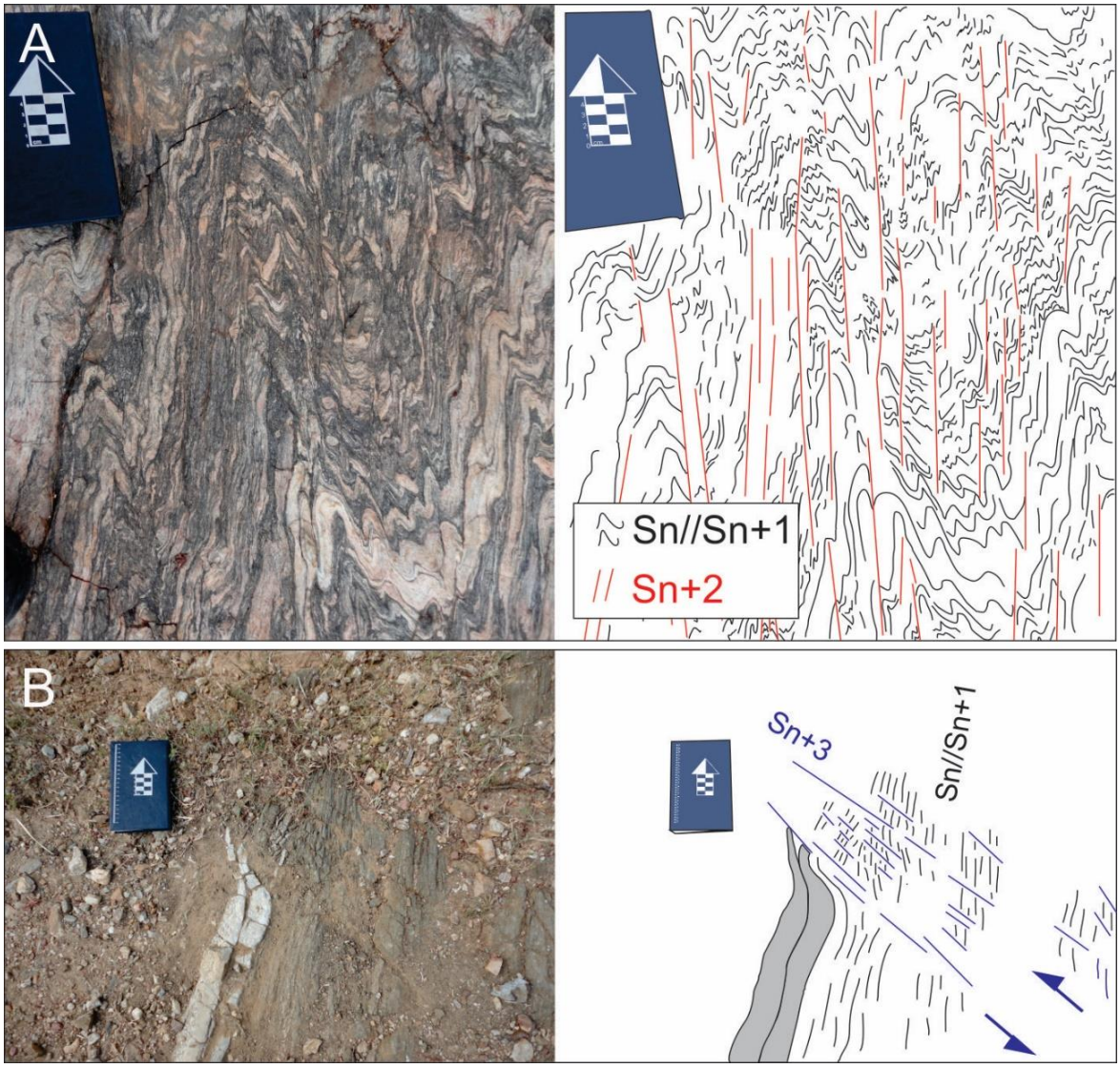

Fig. 4.7*. (A) Deformed migmatitic–orthogneiss (Bananeira suite) close to the greenstone–basement boundary, and sketch showing the geometric relationship of Sn//Sn+1 and Sn+2 foliation planes. The Sn//Sn+1 foliation planes are transposed by spaced Sn+2 milonitic foliation. Fold axis is dipping 20*

to 30º to N05E. (B) Drag fold in quartz vein showing sinistral kinematics of a Dn+3 ductile–brittle fault with NW–SE direction. A spaced Sn+3 ductile–brittle cleavage can also be observed. Notebook is pointing north.

Finally, the Dn+3 deformation event represents a late deformation characterized by the development of WNW–trending faults and fractures (**Fig. 4.7B**). Both sinistral and dextral movements occurred along these steeply–dipping planes. Most of the Dn+3 NW–trending faults have sinistral sense of shear, while the W–trending faults present dextral movements. The recorded of drag folds, and localized Sn+3 foliation planes is also observed along these WNW–trending faults (**Fig. 4.7B**). The Sn+3 ductile–brittle cleavage is the less pervasive foliation in the study area. The record of open folds with sub–horizontal NE–trending axis is also interpreted to develop during this late Dn+3 event.

The stereonet and rosette plots of our field data show that the overall foliation planes (Sn//Sn+1) have generally NE–SW strike direction and average dip of 40–60° to the SE (**Fig. 4.8A**). Field data of stretching lineation show two distinct generations: (1) a Ln+1 early down–dip stretching lineation related to Dn+1 thrust tectonics, and (2) a Ln+2 low–rake stretching lineation associated with transcurrent movements of the Dn+2 event (**Fig. 4.8B**).

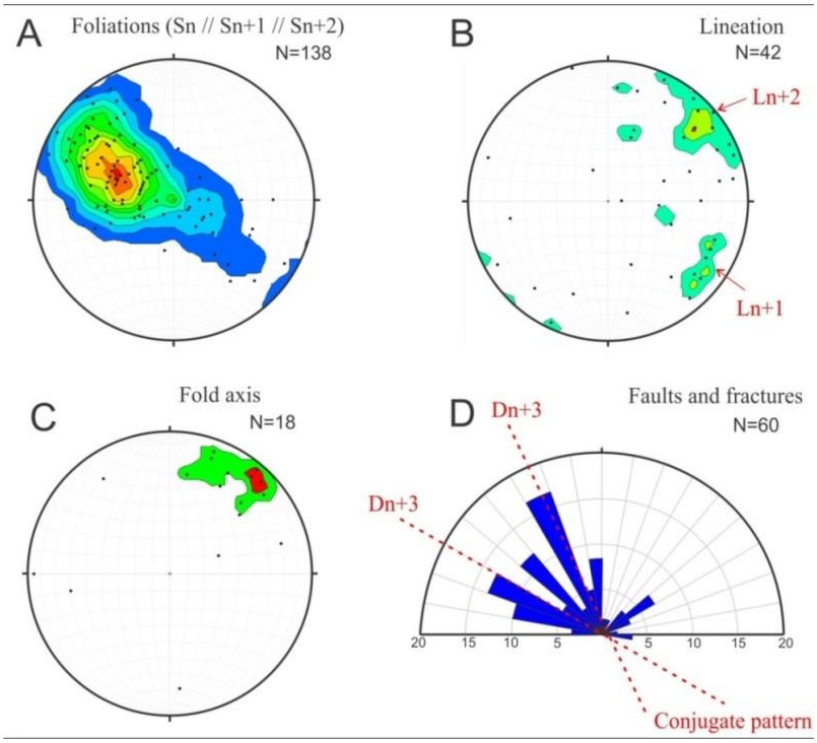

***Fig. 4.8**. Stereonet plots of structural measurements taken in field work: (A) Foliation poles and density contour plot; (B) Lineation measures with relative density contour plot; (C) Fold–axis plot with relative density contour; (D) Rosette diagram displaying similar orientation of conjugated structures.*

The plunge of the low–rake Ln+2 stretching lineation is sub–parallel to most of the fold axis measurements (**Fig. 4.8B** and **C**), evidencing a high–strain deformation associated to the Dn+2 event, in which mostly of the sub–horizontal Dn+1 fold axis were probably rotated during the Dn+2 strike–slip shearing. Most of fold axis generally dip 30–45° to NE (**Fig. 4.8C**). Finally, the field data for faults and fractures associated to the ductile–brittle Dn+3 deformation event show a visible NW–SE strike direction, displaying orientation of conjugated fractures of the Riedel shears patterns (**Fig. 4.8D**).

Based on these field observations, a simplified structural evolution of the area is proposed here, consisting of four deformational events: Dn, Dn+1, Dn+2 and Dn+3 (**Fig. 4.9**). After an early Dn event, the following Dn+1, Dn+2 and Dn+3 probably developed by progressive deformation (from ductile to brittle) with the maximum compressive stress (σ1) in the WNW–ESE direction (**Fig. 4.9**).

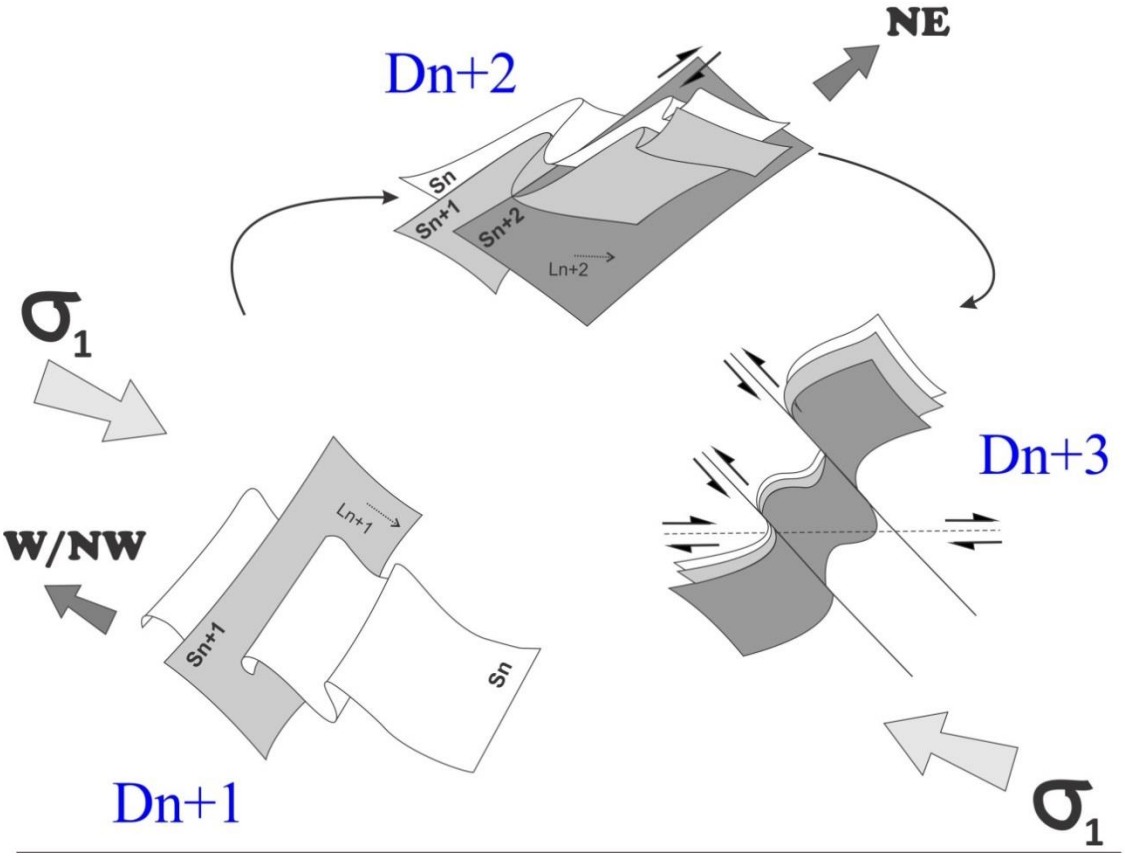

***Fig. 4.9**. Scheme of the main deformation events with the maximum compressive stress (σ1) in the WNW–ESE direction. A previous Sn foliation (Dn event) is folded by Dn+1 thrusting deformation with tectonic transport to W/NW. This evolves to Dn+2 deformation event, characterized by transcurrent movement and development of the Sn+2 (mylonitic) foliations. The later ductile–brittle deformation develops in response of the same compressive stress (σ1), described as typical conjugated fractures of the Riedel shears patterns.*

4.5.3. Structural control on gold mineralization

Gold mineralization in the Serra das Pipocas greenstone belt (Pedra Branca gold deposit) occurs associated with NE–SW regional shear zone (**Fig. 4.2C** and **4.3**), crosscutting metavolcano–sedimentary rocks that underwent amphibolite facies metamorphic conditions. The mineralization (Pedra Branca gold deposit) occurs in quartz veins associated to zones of hydrothermal alteration and the main mineralized areas are referred as Mirador, Queimadas, Coelho and Igrejinha (**Fig. 4.3**). The main host rocks of the gold mineralization are metatonalites (Mirador area), amphibolites (Coelho area), intermediate metavolcanic/subvolcanic rocks and metasedimentary rocks (Queimadas and Igrejinha areas) (**Fig. 4.3**). Gold mineralization has hundreds of meters along the strike, with 1 to 5 meters of thickness, containing ~1 g/t up to 7 g/t of gold (Lopez, 2012). However, no economic report has been released yet for the Pedra Branca gold deposit.

According to the cartography of the Serra das Pipocas greenstone belt, the stratigraphic layers that host gold mineralization are apparently overturned by tectonics (**Fig. 4.3** and **4.4**). Gold mineralization is controlled by local (second to third order) shear zones that is preferentially sited between contrasting layers of the sequence, occurring at the boundary of the Lower and Upper units (**Fig. 4.3** and **4.4**). The hydrothermal alteration associated to gold mineralization may be included in two main types: (1) calc–silicate alteration (diopside, K–feldspar, amphibole, biotite, titanite, pyrite, albite, magnetite ± carbonates) and (2) albitization (mainly albite, carbonates, pyrite, magnetite and gold) (Costa et al., 2016). The high–temperature hydrothermal assemblage evidences that the Pedra Branca gold deposit may be classified as a hypozonal orogenic gold deposit (Costa et al., 2016).

Deformation style at outcrop to hand specimen scale suggest that mineralized quartz veins and associated hydrothermal calc–silicate alteration occur intensively folded (**Fig. 4.10A, B, C** and **D**). The calc–silicate alteration occurs mainly as hydrothermal halos (1 to 3 cm) associated with deformed (folded and/or boudinaged) quartz veins, as observed from both outcrop and drill core samples (**Fig. 4.10A, B, C** and **D**). At the Queimadas area, the main host rocks are intermediate metavolcanic to subvolcanic rocks and associated metatonalites, which commonly show hydrothermal albite alteration and host the quartz veins with calc–silicate vein selvage alteration (**Fig. 4.10A, C, D**). Free–milling gold and gold–silver tellurides have been found in both calc–silicate alteration and albitized rocks (**Fig. 4.10E, F, G, H, I** and **J**). The main tellurides found are hessite, altaite, sylvanite, calaverite and tellurobismuthite (Costa et al., submitted). Most of the folds on quartz veins and calc–silicate alteration of the mineralized zones are asymmetric folds related to the Dn+1 and/or Dn+2

deformation event (**Fig. 4.10A, B, C** and **D**). Undeformed sulfide precipitation is also observed in zones of pressure–shadow related to quartz vein boudinage, suggesting that gold may have also been remobilized during the Dn+1 and/or Dn+2 event (**Fig. 4.10L**).

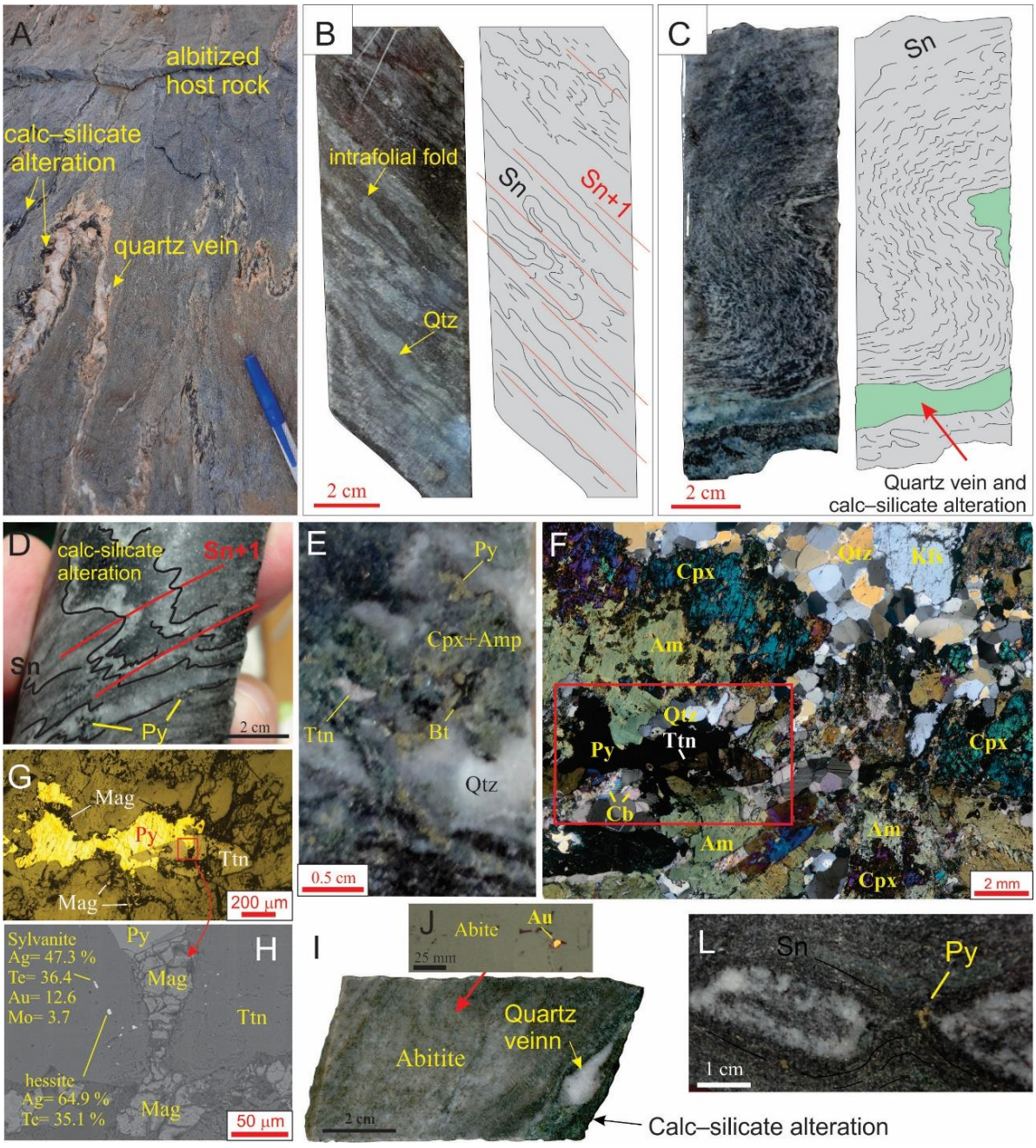

Fig. 4.10. *(A) Outcrop with folded quartz veins hosted by albitized intermediate metavolcanic/subvolcanic rock. Fold axis measurements record low–rake dipping (10–20º) to N25E, suggesting that sub–horizontal Fn+1 fold axis were probably rotated during the Dn+2 strike–slip shearing. Pencil in the photo is pointing north. (B) Mineralized drill core sample with transposed intrafolial folds on quartz (Qtz) veins and sketch showing the geometric relationship of Sn and Sn+1 foliation planes. (C) and (D) Folding of quartz veinlets and associated calc–silicate alteration that probably represents NW–verging structures of the Dn+1 compressional event (Py = pyrite). (E) Drill core sample (Fi–12) with detail of hydrothermal calc–silicate minerals associated with quartz vein*

(Amp = amphibole, Cpx= clinopyroxene, Py = pyrite, Ttn = titanite, Bt = biotite and Qtz = quartz). (F) Photomicrographic image on transmitted light (crossed nicoles) showing arrangement of the main minerals of the hydrothermal assembly, in which clinopyroxene (Cpx) are partially replaced by amphibole (Am). Red polygon locates next figure. (G) Photomicrographic image on reflected light showing intergrowth between pyrite (Py), magnetite (Mag) and titanite (Ttn). Red polygon locates next figure. (H) Back–scattered electron image and Energy Dispersive x–ray Spectrometer (EDS) analyzes by Scanning Electron Microscope in gold/silver and silver telluride (sylvanite and hessite) inclusions in titanite, in spatial association with the magnetite. (I) Mineralized drill core sample showing albitized metaigneous rock (intermediate metavolcanic rock) in association with quartz vein and calc–silicate alteration. (J) Photomicrographic image on reflected light showing free–milling gold (Au) from albitized igneous rock (Ab= albite). (L) Undeformed pyrite crystals in zones of pressure–shadow during quartz vein boudinage, evidencing the precipitation of sulfides during Dn+1 event.

Deformed pyrite crystals occur disseminated along foliation planes, but also, undeformed pyrite crystals filling late–tectonic Dn+3 fractures are also observed (**Fig. 4.11A** and **B**). Most of the observed sulfides are pyrite, with minor relicts of early pyrrhotite crystals (**Fig. 4.11B** and **C**). Locally, some tracks of gold/silver tellurires have been identified in association with late–tectonic Dn+3 undeformed sulfides (**Fig. 4.11D**). Most of these undeformed sulfides occur in association with quartz–carbonate veins filling the Dn+3 fractures, but no calc–silicate alteration and albitization are associated to this (low–temperature) Dn+3 deformation event (**Fig. 4.11E, F** and **G**).

4.5.4. Structural lineaments from airborne geophysical data

Linear interpretations on magnetometric image (1st vertical derivative) (**Fig. 4.12A** and **B**) demonstrate that the main magnetic trend occurs in the NE–SW direction. This can probably correspond to the imprint of the last tectono–thermal event (metamorphism) in the area (Dn+2), in which, many iron– and magnesium–bearing minerals were magnetic oriented (Curie temperature for magnetite, 580ºC). The abrupt terminations of these magnetic lineaments are interpreted as ductile–brittle structures, represented by faults and fractures mostly with NW–SE strike direction (Dn+3). These ductile–brittle structures are not magnetic, and generally occur displacing the magnetic lineaments (**Fig. 4.12A** and **B**). In the rosette diagram, the direction of the magnetic (ductile) lineaments is predominantly NE–SW, with an average value in N50E, while the ductile–brittle lineament (Dn+3) shows two well–defined NW–SE striking structures (**Fig. 4.12C** and **D**). These automatic azimuth plots in the rosette diagrams are compatible with the structural field data of the study area (**Fig. 4.8**).

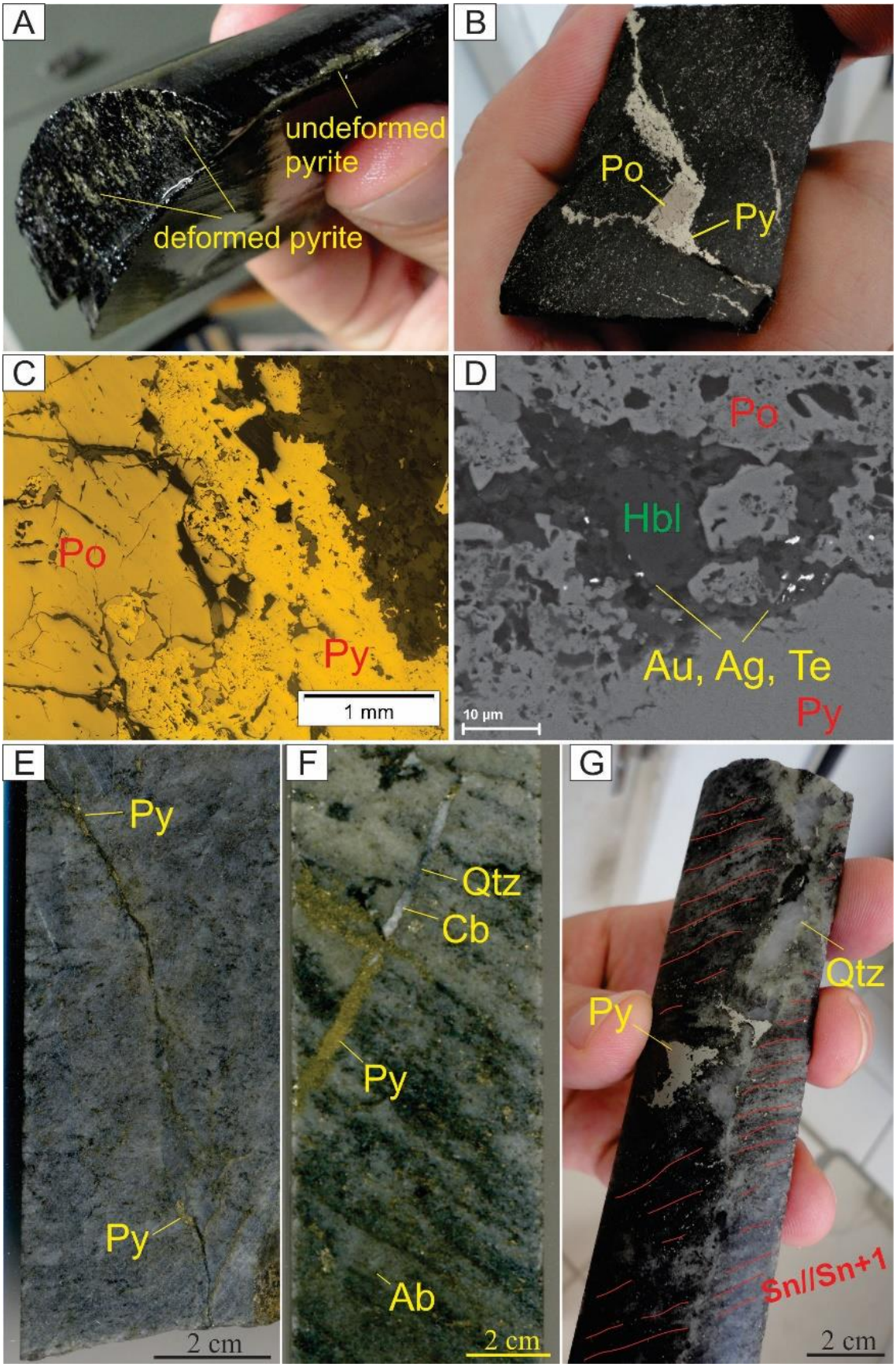

Fig. 4.11. *(A) Drill core sample of mineralized amphibolite with deformed pyrite along foliation planes and undeformed pyrite along a Dn+3 fracture. (B) Detail of amphibolite sample with deformed sulfides along foliation planes and undeformed sulfides in late Dn+3 fractures. Pyrrhotite (Po)*

crystals are replaced by pyrite (Py). (C) Petrographic microscopy (reflected light) of pyrrhotite crystal (Po) replaced by pyrite (Py). (D) Back–scattered electron (BSE) image and Energy Dispersive x–ray Spectrometer (EDS) analyzes by Scanning Electron Microscope (SEM) showing gold and silver telluride precipitation between pyrite and pyrrhotite crystals. (E) and (F) Albitized intermediate metavolcanic/subvolcanic rock with Dn+3 fractures filled by pyrite–bearing quartz/carbonate vein. (F) Undeformed pyrite (Py) crystal associated to late–tectonic Dn+3 quartz (Qtz) vein crosscutting Sn//Sn+1 foliation.

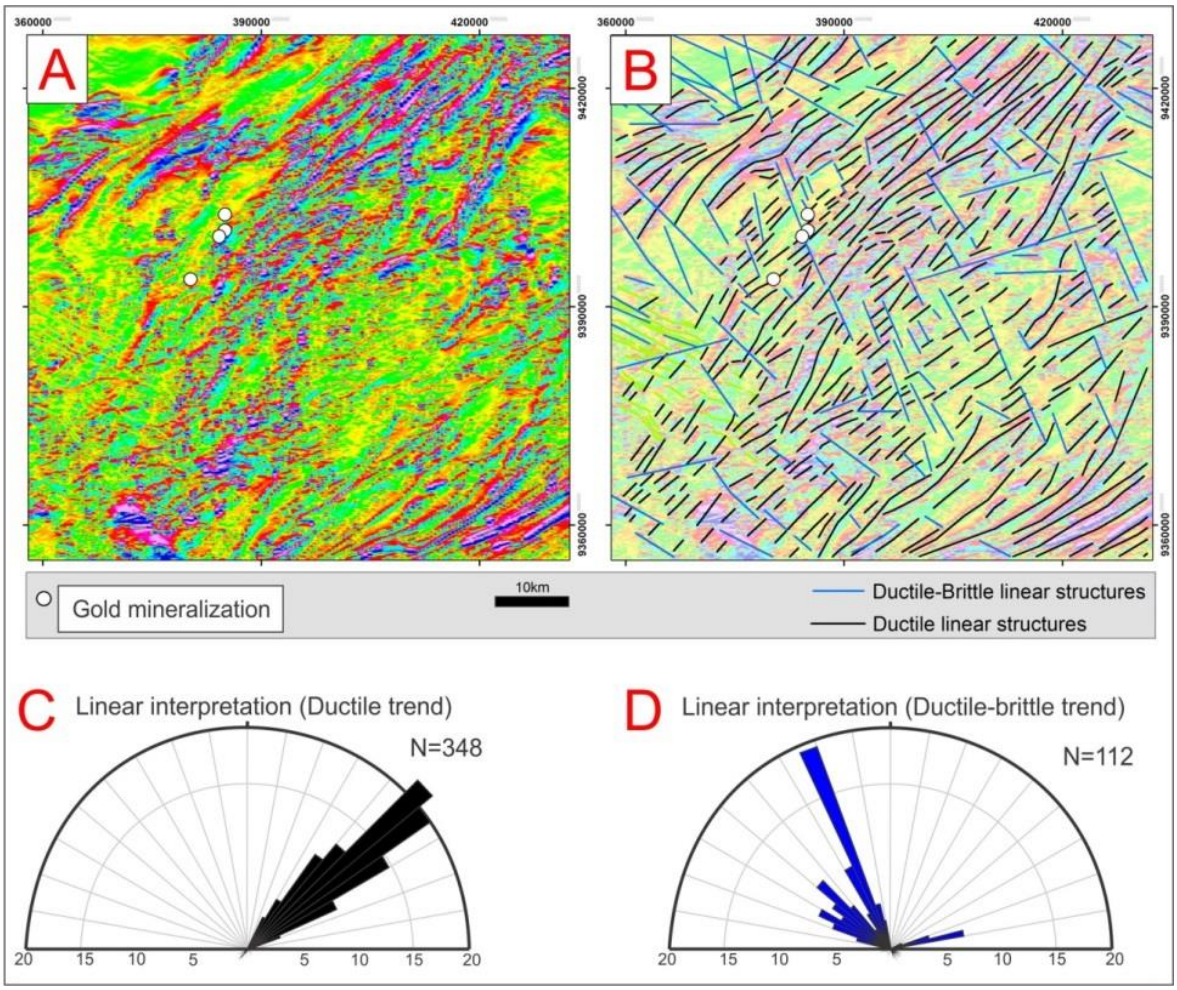

Fig. 4.12. *(A) Magnetometric (1st vertical derivative) image. (B) Magnetometric image with linear interpretation. (C) Rosette diagram with direction of magnetic lineaments interpreted as ductile structures. (D) Rosette diagrams with direction of magnetic lineaments interpreted as ductile–brittle structures. (Azimuth extracted automatically by the ArcGis program). The area of the **Fig. 4.12A** and **B** correspond to the area of the geological map in **Fig. 4.3**.*

Using the airborne gamma–ray ternary image to interpret the main foliation trend in the area, a strongly folded pattern can be envisaged (**Fig. 4.13A** and **B**). The plot of the liner interpretation extracted from the 1st vertical derivative magnetometric image together with foliation trend extracted from the gama–ray image, suggests that the magnetic lineaments represent the projection of planar structures that are plane–axial to the folded Sn//Sn+1

foliations (**Fig. 4.13C** and **D**). The Sn//Sn+1 and Sn+2 foliations are parallel to each other at fold limbs (fold transposition) (**Fig. 4.13C** and **D**). The older Sn//Sn+1 foliations are both folded by the Dn+2 strike–slip deformation event (**Fig. 4.13C** and **D**). This regional scale framework is a similar structural pattern observed in some local scale outcrop description of the Sn+2 mylonitic foliations (**Fig. 4.7A**).

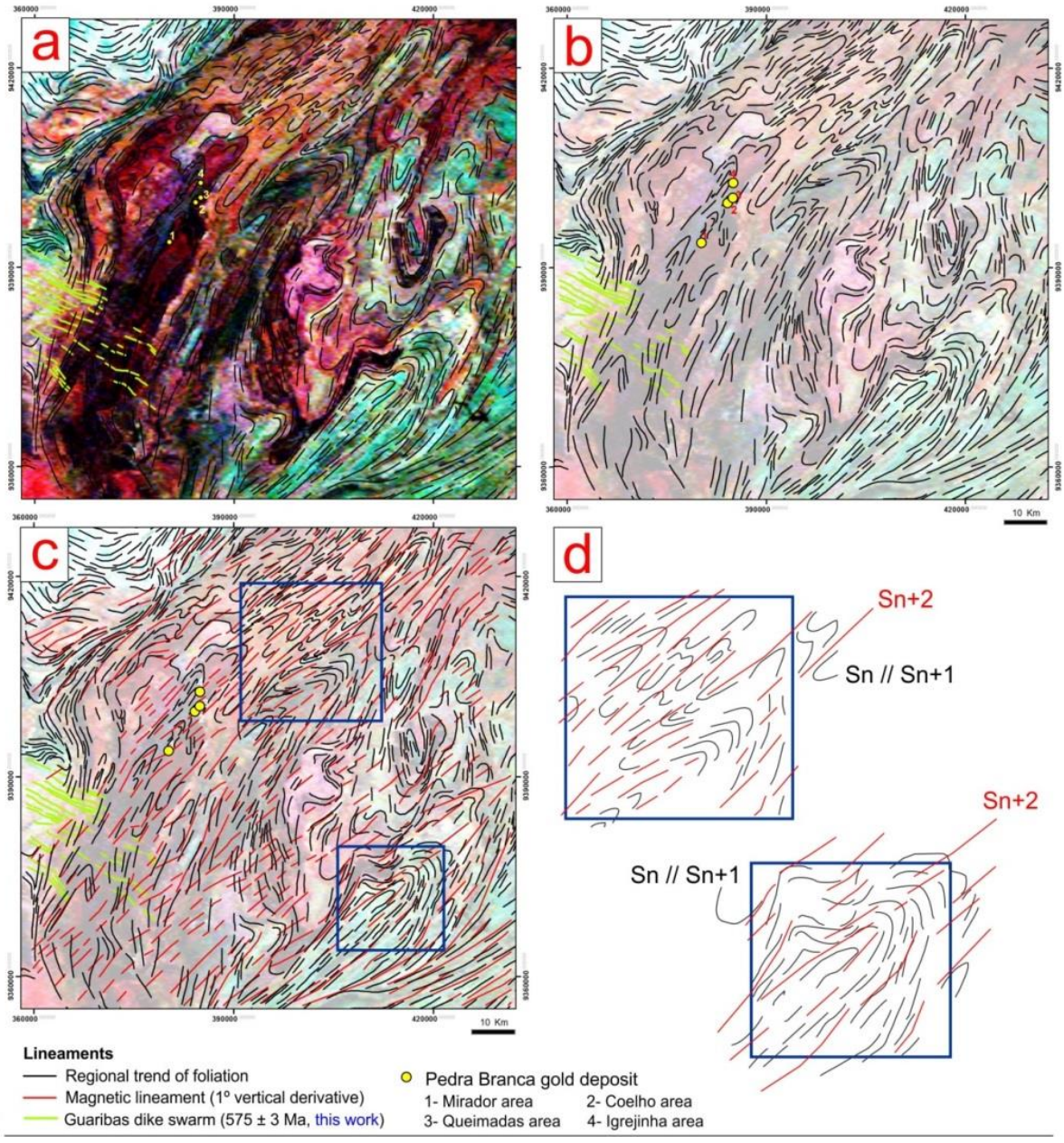

***Fig. 4.13**. (A) Ternary composition (U in blue, Th in green, K in red) of airborne gamma–ray spectrometric image and liner interpretation of the fold patterns in the area. (B) Ternary image with transparency to highlight the interpreted foliation trend. (C) Ternary image with foliation trend (in black) together with magnetic lineaments (in red). (D) Detail of the foliation trend showing the plane–axial arranging of the magnetic lineaments in folded Sn//Sn+1 foliations. The area of the **Fig. 4.13A, B** and **C** corresponds to the area of the geological map in **Fig. 4.3**.*

In the interpretation of the reduced to pole (RTP) magnetic image, main linear magnetic structures are easily delineated. As such, the main mineralized areas of the Pedra Branca gold deposit are clearly bounded by a well–marked NE–trending magnetic anomaly. This large magnetic signal delineates the greenstone–basement boundary in the study area, which we interpret as the Serra das Pipocas shear zone (**Fig. 4.14**).

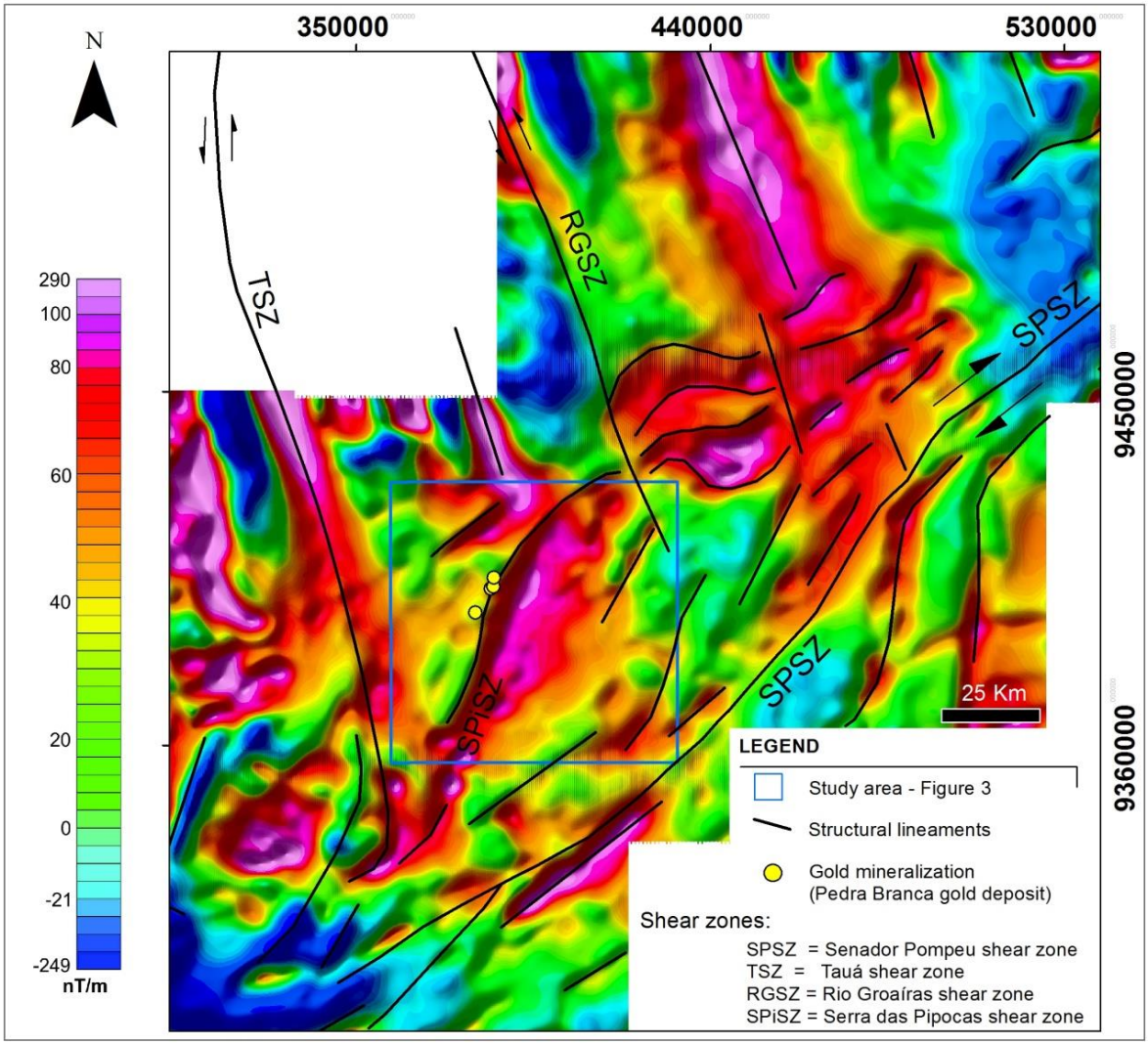

***Fig. 4.14**. Linear interpretation on reduced to pole image derived from total magnetic field data.*

Along the greenstone–basement boundary, granitoids of the Bananeira suite are largely intrusive, represented by Paleoproterozoic (2079–2068 Ma) deformed and less–deformed potassic granitoids (**Fig. 4.3**). Magnetite crystals can be often found in many of these plutonic rocks, so the observed magnetic signal may be reflecting large amount of magnetite–bearing plutonic rocks along this regional structure (**Fig. 4.3** and **4.14**). Reducing

the magnetic data to the pole, the angle of magnetic inclination has been removed, thus, without the effect of asymmetry caused by the magnetic inclination, the anomalies are better located relative to the orientation of the causative bodies. The approximated dip direction of the structures seen in the RTP image may be interpreted by the asymmetry of the magnetic signal (**Fig. 4.14**). Structures with high–angle dips (80–90°) tend to be symmetrical in the magnetic signal, while structures with low– to medium dipping angles (10–45°) show clearly asymmetric pattern. Therefore, the dip direction of the greenstone–basement boundary, Serra das Pipocas shear zone and related magnetite–bearing granitoids are clearly seen in RTP image, evidenced by the asymmetric magnetic signature, gradually lowering intensity toward the southeast direction. In the other hand, the Tauá shear zone, for example, and other NW–SE trending steeply–dipping Dn+3 structures, show symmetric signals in RTP image, evidencing the high–angle dip (close to vertical) of these regional structures (**Fig. 4.14**).

4.5.5. Structural lineaments from remote sense image

Shaded–relief image was also used for interpreting structural elements in the study area (**Fig. 4.15A**). On this image, we omitted the NE–SW linear structures because it is mainly related to ductile structures, and we focused on the linear interpretation of the WNW–ESE direction ductile–brittle structures. The rosette diagram (**Fig. 4.15B**) is similar to those obtained from airborne geophysical data (**Fig. 4.12D**) and field data (**Fig. 4.8D**). The interpreted lineaments on the shaded–relief image evidence many WNW–ESE trending structures which configures a conjugated R and R' faults Riedel pattern. This indicates a maximum compressive stress (σ_1) in the NW–SE direction, compatible with a regional dextral strike–slip shear system (**Fig. 4.15C**). In this context, the Guaribas dike swarm, which represents a late–collisional Neoproterozoic felsic/intermediate magmatism in the area, probably intruded along the tension (T) fractures of the Riedel system, parallel to the maximum compressive stress (σ_1) (**Fig. 4.15A** and **C**).

The Guaribas dike swarm, close to the Pedra Branca gold deposit, is characterized by several NW–SE trending hills, clearly seen on the Landsat–8 image (**Fig. 4.16A**). Structural interpretation on this Landsat–8 image show that the Guaribas dikes are influenced by two conjugated faults, parallel to the R and R' structures, that probably controlled the development of tension (T) fractures of the Riedel system (**Fig. 4.16B** and **C**). However, the principal mineralization of gold in this area are oriented in the NE–SW direction, suggesting that gold mineralization is not related to regional late Dn+3 brittle–ductile NW–SE trending

structures (**Fig. 4.16B**). The Guaribas dikes are not affected by ductile deformation, and only fractures have been seen on these rocks (**Fig. 4.16D**).

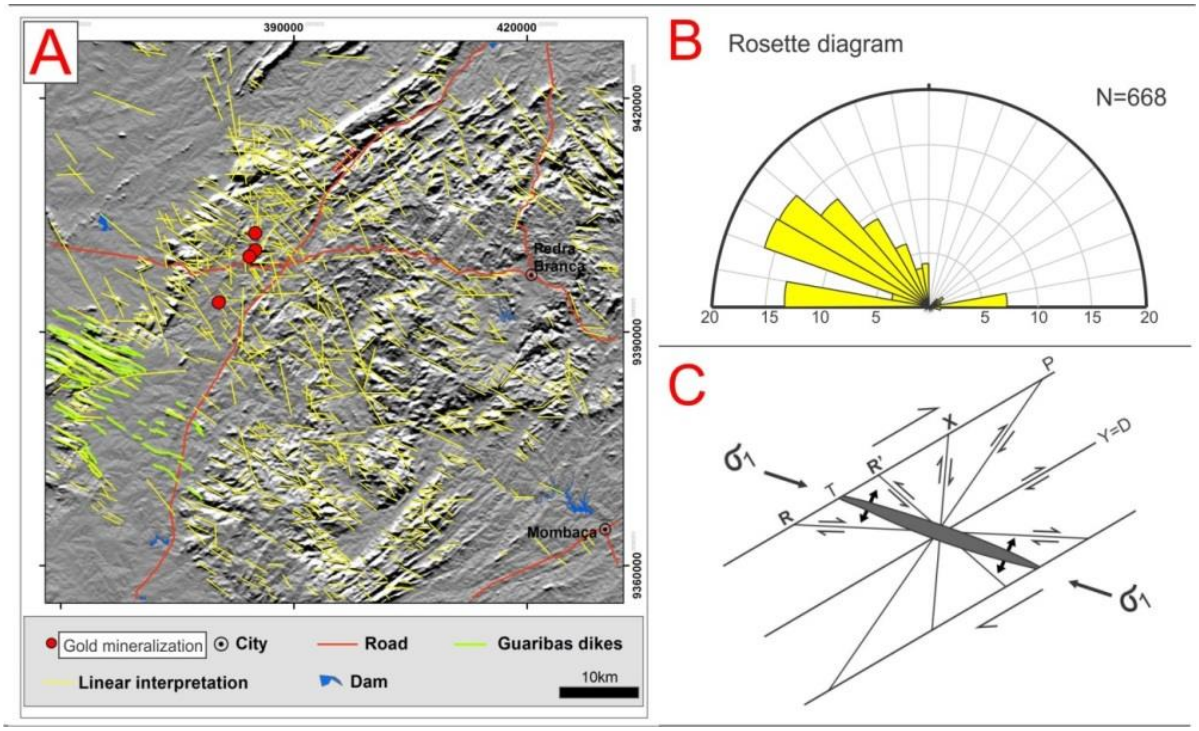

Fig. 4.15*. (A) Shaded–relief image from Shuttle radar topographic mission (30m resolution) using a 35° solar illumination angle at azimuth angle of 0°. Red dots refer to the mineralized areas of the Pedra Branca gold deposit. The yellow lineaments are interpreted as ductile–brittle lineaments. (B) Rosette diagram with azimuth direction extracted automatically by the ArcGis program. (C) Riedel structural system for a regional dextral shear. The* σ_1 *is positioned parallel to the Guaribas dikes. The area of* ***Fig. 4.13A*** *corresponds to the same area of the geological map in* ***Fig. 4.3****.*

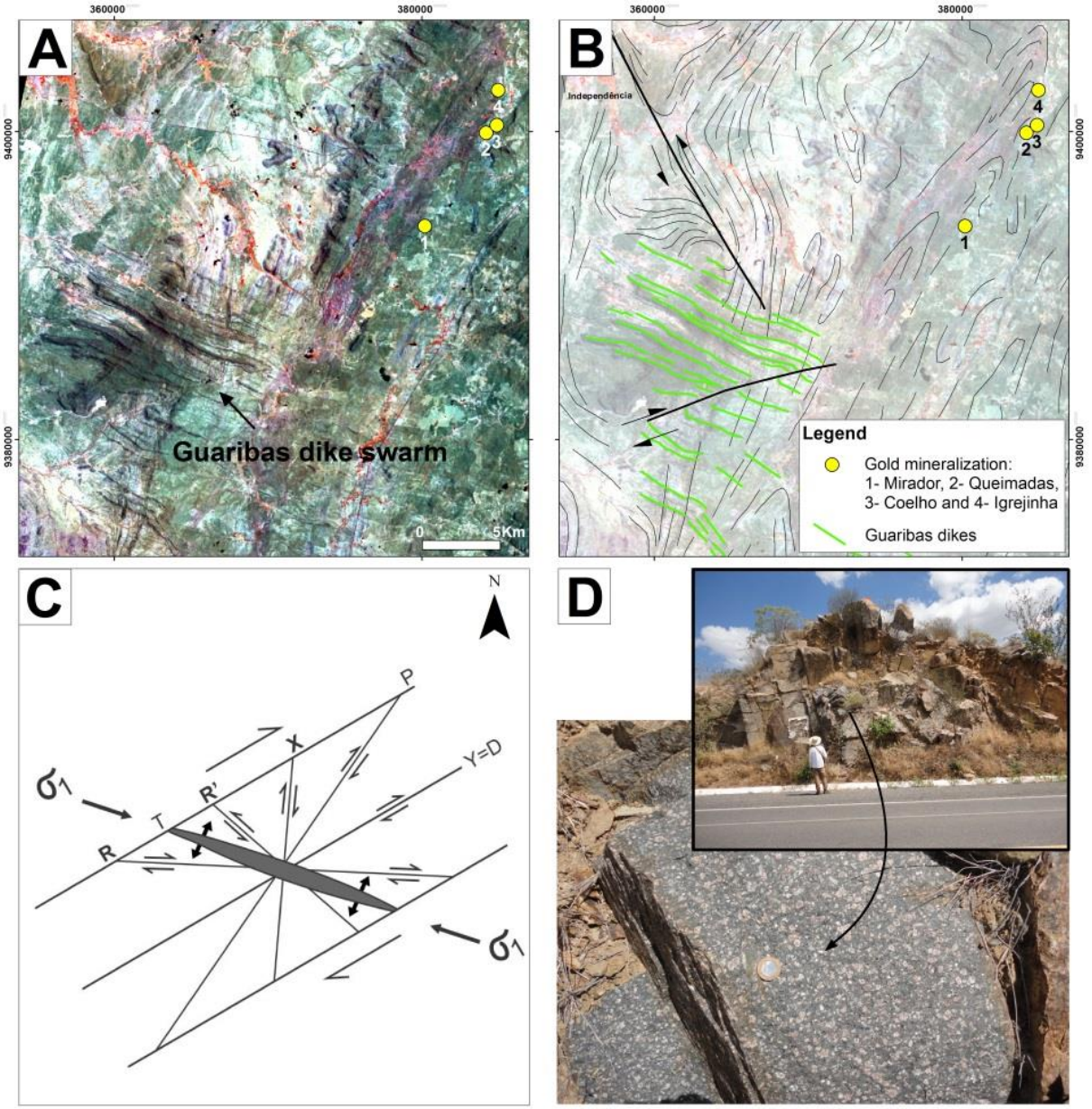

Fig. 4.16*. (A) Location of the Guaribas dike swarm and the main mineralized areas on the Landsat–8 image (RGB–567). (B) Landsat image (60% of transparence) with structural interpretation of the foliation trend. (C) Riedel shear system for dextral kinematics. (D) Outcrop of the undeformed Guaribas dike, represented by a porphyritic quartz latite (equivalent of a quartz monzonite in composition) (sample FC–207).*

4.6. U–Pb titanite and zircon ages

Hydrothermal titanite is a common mineral in the calc–silicate alteration associated to gold mineralization in the study area (**Fig. 4.10E** and **F**). We analyzed titanite grains from a drill core (FCQ–01, UTM 385075; 9400584). These are brown, euhedral to subhedral, up to 0.5 cm long (**Fig. 4.10E**), and locally present gold and gold–silver telluride inclusions (**Fig. 4.10F**). A total of 52 laser spots by LA–ICPMS technics were carried out (**Table 4.1**).

Table 4.1. U–Pb LA–ICPMS titanite data.

(*spot*)	U (ppm)	Pb (ppm)	Th/U	%^{206}Pb_c	^{206}Pb/^{238}U	±2s (%)	^{207}Pb/^{235}U	±2s (%)	^{207}Pb/^{206}Pb	±2s (%)	rhoe	^{206}Pb/^{238}U	±2s (Ma)	^{207}Pb/^{235}U	±2s (Ma)	^{207}Pb/^{206}Pb	±2s (Ma)	conc. (%)
14	4	2	0.0212	9.74	0.328	2.08	5.511	4.65	0.122	4.16	0.448	1828	33	1902	41	1984	74	92
67	3	1	0.0127	13.58	0.244	1.84	3.851	5.18	0.115	4.84	0.355	1406	23	1604	43	1873	87	75
21	8	1	0.0059	5.10	0.110	0.72	0.993	3.82	0.065	3.75	0.187	675	5	700	20	781	79	86
34	6	1	0.0278	15.42	0.102	1.64	0.992	6.28	0.070	6.06	0.261	627	10	700	32	941	124	67
70	7	1	0.0214	14.10	0.098	1.82	0.978	5.79	0.072	5.50	0.314	605	11	693	29	989	112	61
56	6	1	0.0147	13.21	0.100	1.53	0.969	5.43	0.070	5.21	0.281	617	9	688	28	929	107	66
11	4	1	0.0275	10.54	0.103	1.38	0.969	5.25	0.068	5.06	0.263	635	8	688	27	867	105	73
58	7	1	0.0140	7.20	0.106	1.38	0.965	4.48	0.066	4.27	0.308	649	9	686	23	809	89	80
79	6	1	0.0092	6.81	0.106	1.17	0.963	4.37	0.066	4.21	0.268	650	7	685	22	801	88	81
78	8	1	0.0089	6.41	0.106	1.11	0.960	4.30	0.065	4.16	0.257	652	7	683	22	788	87	83
27	11	2	0.0119	8.01	0.104	1.06	0.954	4.63	0.066	4.50	0.230	640	6	680	23	817	94	78
32	12	2	0.0204	12.65	0.101	1.39	0.951	5.69	0.069	5.52	0.243	618	8	678	29	886	114	70
80	7	1	0.0112	8.18	0.104	1.55	0.948	4.76	0.066	4.50	0.327	638	9	677	24	807	94	79
12	7	1	0.0131	12.63	0.100	1.48	0.940	6.11	0.068	5.93	0.243	615	9	673	31	871	123	71
41	8	1	0.0257	8.90	0.101	2.26	0.922	5.55	0.066	5.07	0.406	619	13	663	27	819	106	76
76	5	1	0.0264	10.37	0.103	1.36	0.918	5.20	0.065	5.02	0.262	631	8	661	26	765	106	83
54	8	1	0.0150	6.65	0.101	1.25	0.912	3.98	0.066	3.78	0.314	619	7	658	19	795	79	78
77	7	1	0.0143	7.06	0.101	1.15	0.905	4.35	0.065	4.19	0.264	618	7	655	21	782	88	79
30	7	1	0.0101	6.30	0.101	0.98	0.902	4.06	0.065	3.94	0.242	619	6	653	20	770	83	80
64	10	1	0.0189	5.85	0.102	1.04	0.901	4.07	0.064	3.94	0.256	623	6	652	20	754	83	83
28	18	2	0.0074	4.27	0.103	0.91	0.901	3.60	0.063	3.48	0.254	634	6	652	17	717	74	88
40	5	1	0.0228	9.43	0.098	1.29	0.898	4.87	0.067	4.69	0.265	602	7	651	24	823	98	73
37	8	1	0.0156	7.74	0.099	0.98	0.897	4.58	0.065	4.47	0.214	611	6	650	22	790	94	77
65	10	1	0.0179	8.23	0.099	1.10	0.897	4.73	0.066	4.60	0.233	610	6	650	23	793	97	77
48	7	1	0.0118	7.89	0.099	1.26	0.893	4.65	0.065	4.47	0.272	609	7	648	23	788	94	77
44	7	1	0.0158	7.20	0.100	0.94	0.893	4.44	0.065	4.34	0.211	612	5	648	21	775	91	79
45	12	2	0.0180	7.21	0.100	1.04	0.891	5.19	0.065	5.08	0.201	614	6	647	25	764	107	80
36	9	1	0.0288	7.29	0.099	0.87	0.890	4.46	0.065	4.38	0.194	611	5	647	22	773	92	79
57	8	1	0.0142	7.02	0.099	0.96	0.888	4.24	0.065	4.13	0.226	608	6	645	20	776	87	78
35	9	1	0.0130	5.57	0.100	0.75	0.886	3.79	0.064	3.71	0.198	615	4	644	18	749	78	82
15	11	1	0.0030	5.80	0.100	0.94	0.883	4.14	0.064	4.04	0.227	616	6	643	20	737	85	84
63	11	1	0.0211	5.85	0.100	0.80	0.883	4.06	0.064	3.98	0.196	614	5	643	20	744	84	83
46	7	1	0.0124	7.83	0.098	1.07	0.881	4.70	0.065	4.58	0.227	603	6	641	23	777	96	78
18	9	1	0.0032	6.37	0.099	0.81	0.877	4.23	0.064	4.15	0.191	609	5	640	20	748	88	81
60	12	1	0.0055	4.78	0.100	0.70	0.875	3.66	0.063	3.59	0.192	615	4	638	18	720	76	85
61	18	2	0.0014	4.61	0.100	0.66	0.874	3.55	0.063	3.49	0.187	616	4	638	17	717	74	86
43	8	1	0.0139	6.79	0.098	0.96	0.874	4.20	0.065	4.08	0.230	602	6	638	20	766	86	79
7	11	1	0.0053	4.04	0.101	0.70	0.873	3.45	0.063	3.38	0.202	619	4	637	16	705	72	88
59	18	2	0.0082	4.02	0.101	0.66	0.873	3.27	0.063	3.20	0.203	618	4	637	16	708	68	87
81	12	1	0.0055	4.64	0.100	0.75	0.870	3.59	0.063	3.51	0.210	613	4	635	17	715	75	86
62	16	2	0.0015	4.96	0.099	0.69	0.869	3.67	0.063	3.60	0.187	611	4	635	17	721	76	85
33	11	1	0.0072	8.83	0.096	1.06	0.868	4.78	0.066	4.66	0.221	591	6	634	23	791	98	75
19	10	1	0.0052	5.55	0.099	0.78	0.867	4.13	0.063	4.05	0.190	611	5	634	20	718	86	85
31	12	2	0.0198	5.54	0.099	0.95	0.867	3.98	0.064	3.86	0.238	608	5	634	19	728	82	84
17	7	1	0.0159	6.78	0.097	0.96	0.862	4.25	0.064	4.14	0.226	597	5	631	20	755	87	79
47	10	1	0.0030	6.41	0.097	0.89	0.860	4.10	0.064	4.00	0.217	596	5	630	19	757	84	79
10	7	1	0.0137	7.01	0.097	0.90	0.858	4.36	0.064	4.27	0.206	595	5	629	21	753	90	79
9	7	1	0.0127	7.71	0.096	1.01	0.857	4.57	0.065	4.46	0.221	591	6	628	22	764	94	77
42	8	1	0.0127	7.09	0.095	0.88	0.855	4.30	0.065	4.21	0.206	586	5	628	20	782	88	75
8	18	2	0.0071	4.71	0.098	0.79	0.847	3.99	0.063	3.91	0.198	601	5	623	19	703	83	85
16	7	1	0.0122	8.69	0.093	1.15	0.832	4.82	0.065	4.68	0.239	573	6	615	22	774	98	74
29	10	1	0.0056	5.36	0.095	0.78	0.828	3.84	0.063	3.76	0.203	587	4	613	18	707	80	83

Table 4.2. U–Pb LA–ICPMS zircon data.

Samples	U (ppm)	Pb (ppm)	Th/U[b]	^{207}Pb/^{235}U	2σ (%)	^{206}Pb/^{238}U	2σ (%)	Rho[d]	^{207}Pb/^{206}Pb [e]	2σ (%)	^{206}Pb/^{238}U	2σ	^{207}Pb/^{235}U	2σ	^{207}Pb/^{206}Pb	2σ	Conc[f]	f_{206} [a]
FC207 01	132.4	13.0	0.68	0.74766	2.43	0.09382	0.96	0.39	0.05780	2.24	578.1	5.5	566.9	13.8	522.0	11.7	90.3	0.00003
FC207 02	110.1	12.2	0.64	0.76685	2.26	0.09471	0.93	0.41	0.05873	2.06	583.3	5.5	578.0	13.1	556.9	11.5	95.5	0.00033
FC207 03	68.1	7.1	0.45	0.74884	3.06	0.09278	1.81	0.59	0.05854	2.47	571.9	10.4	567.6	17.4	550.0	13.6	96.2	0.00011
FC207 04	76.0	8.0	0.59	0.76025	2.84	0.09367	1.32	0.46	0.05887	2.51	577.2	7.6	574.2	16.3	562.1	14.1	97.4	0.00021
FC207 05	46.7	4.5	0.38	0.73752	4.61	0.09149	2.91	0.63	0.05847	3.58	564.3	16.4	561.0	25.8	547.2	19.6	97.0	0.00007
FC207 07	42.6	5.0	0.40	0.77210	6.25	0.09386	2.77	0.44	0.05966	5.60	578.3	16.0	581.0	36.3	591.3	33.1	102.2	0.00000
FC207 08	94.2	9.9	0.64	0.75475	3.17	0.09290	1.22	0.38	0.05892	2.93	572.7	7.0	571.0	18.1	564.3	16.5	98.5	0.00012
FC207 10	55.0	4.9	0.32	0.74747	5.22	0.09071	2.29	0.44	0.05976	4.69	559.8	12.8	566.8	29.6	594.9	27.9	106.3	0.00010
FC207 12	88.5	7.6	0.42	0.72539	4.21	0.09349	2.31	0.55	0.05628	3.51	576.1	13.3	553.8	23.3	463.3	16.3	80.4	0.00009
FC207 14	132.4	14.2	0.61	0.75451	2.40	0.09226	1.21	0.50	0.05931	2.07	568.9	6.9	570.8	13.7	578.6	12.0	101.7	0.00026
FC207 15	697.1	58.3	0.36	0.77279	2.07	0.09524	1.06	0.52	0.05885	1.77	586.4	6.2	581.4	12.0	561.6	9.9	95.8	0.00021
FC207 16	255.0	26.6	0.47	0.76799	2.02	0.09348	0.94	0.47	0.05958	1.79	576.1	5.4	578.6	11.7	588.5	10.5	102.2	0.00027
FC207 17	104.6	10.6	0.56	0.76210	2.49	0.09152	1.21	0.49	0.06039	2.17	564.5	6.8	575.2	14.3	617.7	13.4	109.4	0.00027
FC207 18	312.7	25.8	0.54	0.74882	1.82	0.09256	0.82	0.45	0.05868	1.62	570.7	4.7	567.5	10.3	555.1	9.0	97.3	0.00028
FC207 20	97.9	9.9	0.38	0.76742	3.86	0.09167	1.78	0.46	0.06072	3.43	565.4	10.0	578.3	22.3	629.3	21.6	111.3	0.00011
FC207 22	209.3	18.2	0.39	0.75519	1.87	0.09184	0.89	0.48	0.05964	1.64	566.4	5.1	571.2	10.7	590.4	9.7	104.2	0.00003
FC207 23	130.2	14.9	0.54	0.72644	3.28	0.09386	1.58	0.48	0.05613	2.87	578.3	9.1	554.5	18.2	457.6	13.2	79.1	0.00026
FC207 27	111.9	14.7	0.84	0.75960	2.48	0.09383	1.36	0.55	0.05872	2.08	578.1	7.9	573.8	14.2	556.6	11.6	96.3	0.00000
FC207 28	93.4	9.1	0.51	0.72204	2.98	0.09140	1.51	0.51	0.05729	2.57	563.8	8.5	551.9	16.4	502.9	12.9	89.2	0.00013
FC207 29	139.6	11.8	0.30	0.74609	2.37	0.09152	1.40	0.59	0.05912	1.91	564.5	7.9	566.0	13.4	571.6	10.9	101.3	0.00028
FC207 30	52.8	6.7	0.48	0.74737	4.82	0.09284	1.89	0.39	0.05839	4.43	572.3	10.8	566.7	27.3	544.3	24.1	95.1	0.00009

[a] Fraction of the non-radiogenic ^{206}Pb in the analyzed zircon spot, where f_{206} = [^{206}Pb/^{204}Pb]c / [^{206}Pb/^{204}Pb]s (c=common; s=sample)

[b] Th/U ratios and amount of Pb, Th and U (in ppm) are calculated relative to **GJ-1** reference zircon

[c] Corrected for background and within-run Pb/U fractionation and normalised to reference zircon **GJ-1** (ID-TIMS values/measured value); ^{207}Pb/^{235}U calculated using (^{207}Pb/^{206}Pb) / (^{238}U/^{206}Pb * 1/137.88)

[d] Rho is the error correlation defined as the quotient of the propagated errors of the ^{206}Pb/^{238}U and the ^{207}/^{235}U ratio

[e] Corrected for mass-bias by normalising to **GJ-1** reference zircon and common Pb using the model Pb composition of Stacey and Kramers (1975)

[f] Degree of concordance = (^{206}Pb/^{238}U age * 100/^{207}Pb/^{206}U age)

Individual ^{206}Pb/^{238}U ages range from 613 Ma to 1828 Ma and define a Pb–loss discordia with an upper intercept at 2029 ± 28 Ma and a lower intercept at 574 ± 7 Ma (MSWD = 3.4) (**Fig. 4.17A**). The age of 2029 ± 28 Ma is interpreted as the crystallization age of the titanite grains and associated gold mineralization, while the age of 574 ± 7 Ma is

interpreted as the timing of thermal metamorphism (**Fig. 4.17A**). Most of the grains are close to the lower intercept of the discordia line, suggesting expressive loss of radiogenic lead during the Neoproterozoic thermal metamorphism (**Fig. 4.17A**).

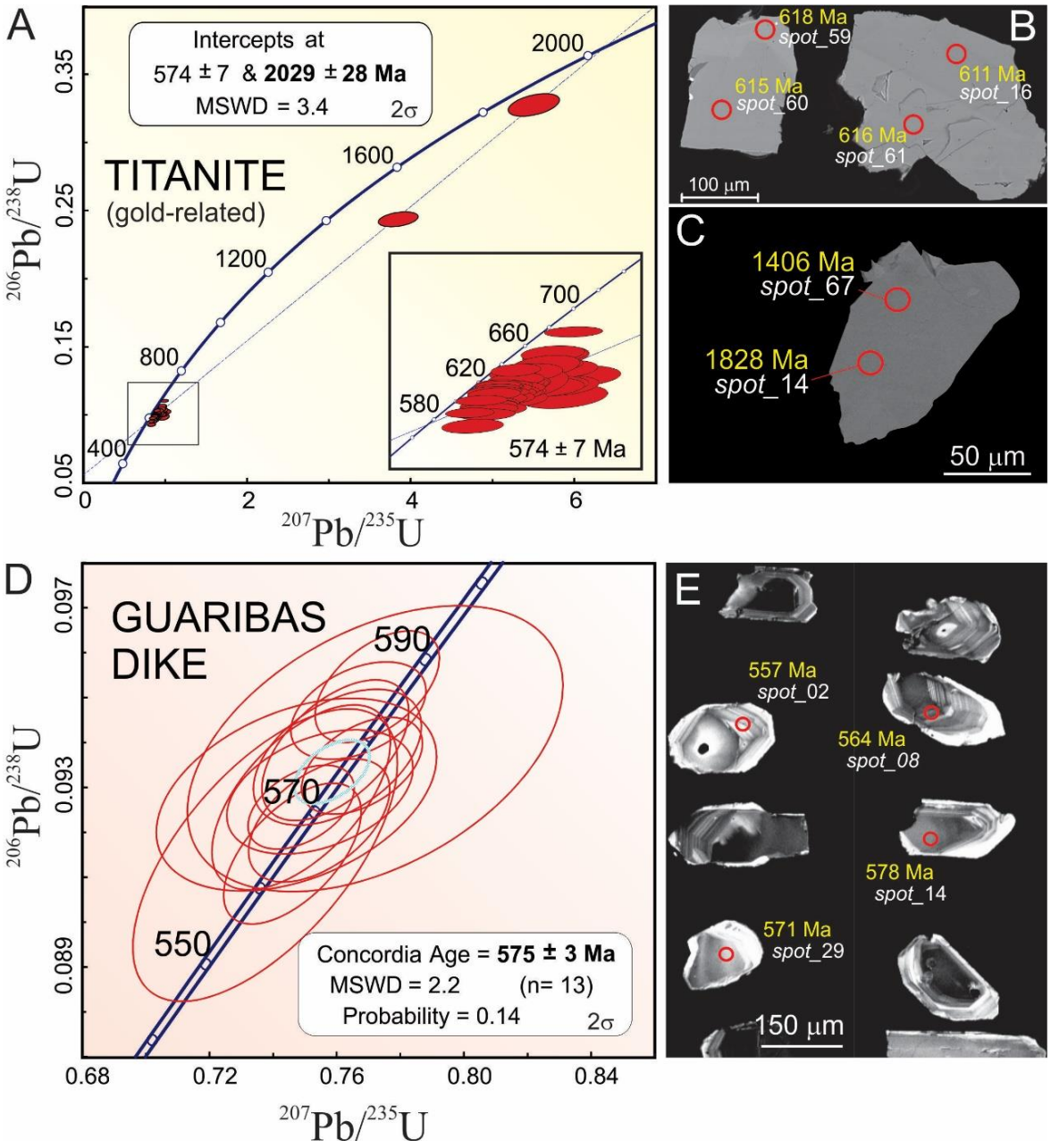

Fig. 4.17. *(A) Concordia diagram ($^{207}Pb/^{235}U$ vs. $^{206}Pb/^{238}U$) for titanites from gold–related cal–silicate alteration (sample Fi–12). All ellipses are plotted with 2σ. (B) Selected $^{206}Pb/^{238}U$ ages shown on BSE images of "zoned" titanite. (C) Selected $^{206}Pb/^{238}U$ ages shown on BSE image of titanite without zoning. (D) Concordia diagram ($^{207}Pb/^{235}U$ vs. $^{206}Pb/^{238}U$) for zircon analyzes of the Guaribas dike (sample FC–207). All ellipses are plotted with 2σ. (E) Selected $^{206}Pb/^{207}Pb$ ages shown on CL image of zircon grains of the Guaribas dike.*

Some of the titanite grains present zoning pattern in the Back–Scattered Electron image, and the ages obtained in both domains are always Neoproterozoic, suggesting that the zoning was produced by recrystallization (**Fig. 4.17B**). In one unzoned grain, two discordant Paleoproterozoic ages were obtained (**Fig. 4.17C**), which plot near the upper intercept of the discordia line (**Fig. 4.15A**). This less–discordant Paleoproterozoic grain, bracketing the upper intercept in the position of 2029 ± 28 Ma, probably represents a domain (core?) of a titanite grain that was less affected by the Neoproterozoic thermal metamorphism (**Fig. 4.17A** and **C**).

For a representative sample (FC–207, UTM 377143; 9391204) of the Guaribas dike swarm (**Fig. 4.17D**), *in situ* U–Pb ages were performed on twenty one zircon grains by the LA–ICPMS technique (**Table 4.2**). The thirteen most concordant (95 to 102%) zircon grains gave a precise Concordia age of 575 ± 3 Ma (MWSD = 2.2) (**Fig. 4.17C**). The analyzed zircon grains are generally euhedral, 150 µm long and mostly show oscillatory zoning on cathodoluminescence images (**Fig. 4.15D**). This textural pattern is typical of magmatic zircons, and the age of 575 ± 3 Ma is interpreted as the crystallization age for the Guaribas dike swarm.

4.7. Discussion

4.7.1. Main structural controls on gold mineralization

Structural studies on orogenic gold deposits in granite–greenstone terranes demonstrate that the distribution of the deposits is generally linked with kilometer-long ductile shear zones, which represent large transcrustal discontinuities, such as terrane boundaries (O'Driscoll, 1986; Groves et al., 1987, 2000; 2016, 2018; Eisenlohr et al., 1989; Robert et al., 1990; Cox, 1999; Kolb et al., 2004; Weinberg et al., 2004; de Boorder et al., 2006; Bierlein et al., 2006; Blewett et al., 2010).

Interpreting the regional structures from the geological map and cross sections of the study area (**Fig. 4.3**), it is suggestive that the Serra das Pipocas shear zone is part of a large fault system of a transcrustal character, representing the tectonic boundary between the Archean (Cruzeta complex) and the Paleoproterozoic granite–greenstone terrane (**Fig. 4.18**). This shear zone probably played an important role in gold mineralization of the study area, representing a deep (transcrustal) first–order structure, in which large amounts of fluids and magmas may have circulated (**Fig. 4.18**). Syn– to late–tectonic plutons intruded along this shear zone and are mainly represented by the granitoids of the Bananeira suite (**Fig. 4.2C, 4.3** and **4.5H**). According to Costa et al. (2018), the 2068 Ma old less–deformed monzogranites

occur as late–tectonic intrusions and locally as fine–grained aplitic granitic dikes crosscutting early 2079 Ma deformed granitoids of the Bananeira suite, evidencing that Paleoproterozoic deformation fabrics are still preserved in the Troia Massif (**Fig. 4.5H**).

So far, it is possible that the Serra das Pipocas shear zone configures a Paleoproterozoic cryptic suture in the Troia Massif, delimiting contrasting crustal domains (**Fig. 4.18**). It does probable established during the Transamazonian/Eburnean orogeny (2.2–2.0 Ga), when then, gold mineralizing fluids first percolated through. This is also supported by the crystallization age of 2029 ± 28 Ma for the hydrothermal titanite grains of the gold–related calc–silicate hydrothermal alteration of the Pedra Branca gold deposit (**Fig. 4.17A**). However, such deep structures, considered as first–order shear zones, are generally not economically mineralized, whereas economic mineralizations are commonly found on second– or third–order faults that splay off these first–order structures (Groves et al. 1987, 2018; Eisenlohr et al. 1989; Robert et al. 1990; Cox, 1999; Bierlein and Crowe, 2000; Morey et al., 2007; Zhou et al., 2016). The second– to third–order faults within the granite–greenstone terranes transect a diversity of lithologies which are chemically reactive to the auriferous fluid, such as mafic volcanic rocks, graphitic schist, carbonaceous phyllite, and banded iron formations (Cox et al., 1995; Witt et al., 1993; Bierlein et al., 2001; Henne and Craw, 2012; Sahoo and Venkatesh, 2014; Zhou et al., 2016; Hu et al., 2017). Similarly, in the Serra das Pipocas greenstone belt, the main mineralized areas of the Pedra Branca gold deposit occur exactly on the tectonic contact (shear/fault) of the Lower unit (predominantly mafic metavolcanic rocks) with the Upper unit (metassedimentary rocks) of the sequence (**Fig. 4.3, 4.4** and **4.18**). Many of orogenic gold deposits worldwide are located near–parallel to the stratigraphy, generally between metavolcanic and metasedimentary unit boundaries, acting as shear planes, and as a relatively impermeable and/or reactive cap on the hydrothermal systems (Cox et al., 2001; Morey et al., 2007; Gazley, 2011; Oliver et al., 2012; Duclaux et al., 2012; Zhou et al., 2016; Lawley et al., 2016). For example, in the Neoarchean Plutonic Well greenstone belt, Australia, orogenic gold mineralization tends to be found near–parallel to the stratigraphy and preferentially focussed between metasedimentary and mafic unit boundaries. This near–parallelism of the lode–gold mineralization in the Plutonic Well greentone belt, suggests that the original stratigraphy may have been a primary control on the localization of gold–bearing fluids (Gazley, 2011; Duclaux et al., 2012). Historically, this apparent lithostratigraphic control, similar to the stratabound nature of BIF–hosted deposits, led to proliferation of syn–sedimentary models for greenstone–hosted gold deposits

(Hutchinson, 1987). However, later in the 1990s, researchers clearly demonstrated an epigenetic origin for this type of orogenic deposits (Groves et al., 1998).

So far, interpreting all these elements together, gold mineralization in the Serra das Pipocas greenstone belt displays the typical stratigraphic and structural characteristics of other greenstone–hosted orogenic gold deposits (Morey et al., 2007; Oliver et al., 2012; Zhou et al., 2016; Lawley et al., 2016; Groves et al., 2018), such as the connection with a first–order structure and the apparent lithological control of gold deposition, and therefore, supporting its classification as an orogenic gold deposit.

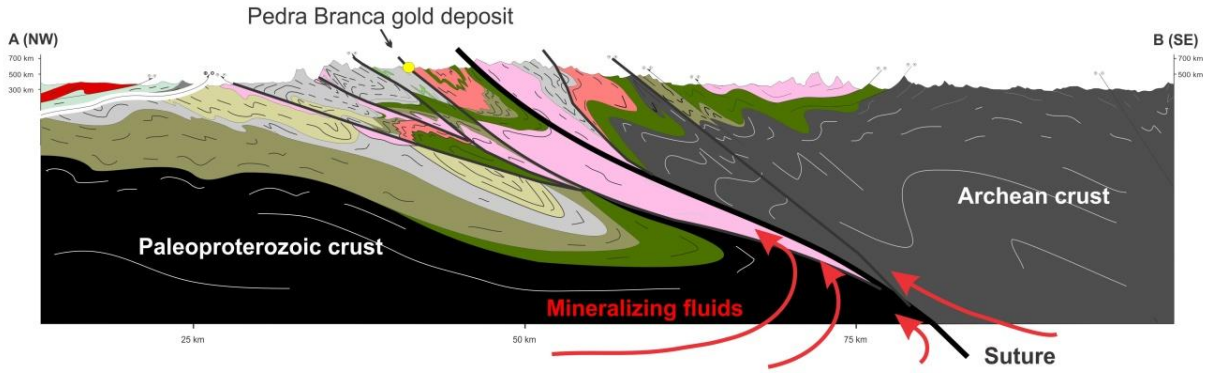

***Fig. 4.18**. Interpretation of the Archean–Paleoproterozoic terrane boundary of the Troia Massif and the interplay of first–order (crustal–scale) structures, higher–order structures and hydrothermal fluids. Location of the cross section in **Fig. 4.3**.*

4.7.2. Timing of metamorphism, deformation and gold mineralization

The ages of the different deformation events in the Troia Massif are still not well established. For example, in the case of the tangential tectonics Dn+1, some authors interpret it as the record of the Brasiliano/Pan–African orogeny (620–580 Ma), characterized by the development of Hymalayan–type nappe tectonics, associated to agglutination of the Supercontinent Gondwana (Arthaud and Hartmann, 1986; Caby and Arthaud, 1986). According to these authors, the concordance of the basement structures (folds) with those of the Neoproterozoic metasedimentary rocks suggests that the Neoproterozoic deformation was pervasive in both basement inliers and surrounding Neoproterozoic rocks (thick–skinned deformation). However, other authors advocate that the tangential tectonics in the region of the Troia Massif is a record of a Paleoproterozoic deformation, associated with the Eburnean/Transamazonian cycle (Pessoa et al., 1986; Oliveira and Cavalcante, 1993). These authors interpreted the S-type leucogranites of the Cedro suite (**Fig. 4.3**) as synchronic intrusions with respect to the tangential tectonics. According to Pessoa et al. (1986), the

available Rb–Sr (whole rock) isochronic ages between 1700 and 2100 Ma for these syn–tectonic leucogranites, suggest that the thrust tectonics recorded on the Troia Massif is of Paleoproterozoic age. These Rb–Sr ages suggest that the Cedro leucogranites formed during the Eburnean/Transamazonian orogenic cycle, and also indicate that there was no complete resetting of the Rb–Sr system in the Troia Massif due to the Neoproterozoic Brasiliano/Pan–African orogeny. However, the loss of radiogenic Sr during the Neoproterozoic metamorphism may be reflected by some "rejuvenated" (apparent) ages (1700 Ma) of the leucogranites (Pessoa et al., 1986). In addition, a Rb–Sr age of 2888 ± 96 Ma was obtained for a TTG orthogneiss of the Pedra Branca unit (Cruzeta complex), also supporting that the Rb–Sr system was not completely re–equilibrated by the Neoproterozoic metamorphism in the Troia Massif (Pessoa et al., 1986).

Gold mineralization at the Pedra Branca deposit has been found in the deformed quartz veins and associated calc–silicate and albite alteration (**Fig. 4.10**). In addition, quartz veins with associated calc–silicate alteration are deformed by the Dn+1, Dn+2 and Dn+3 tectonic events, suggesting that main quartz vein formation and gold mineralization probably took place during the early Dn event (**Fig. 4.10**). Most of the sulfides occur as deformed crystals along Sn//Sn+1 foliation planes, which also supports that the main stage of gold–sulfide deposition was during the Dn tectonic event (**Fig. 4.10D** and **4.11A**). However, the presence of undeformed pyrite crystals at pressure shadows of boudinage formation, indicates that precipitation of sulfides also occurred during Dn+1 (and/or Dn+2) event (**Fig. 4.10H**). In addition, gold (± Te–Ag) mineralization also occurs associated to undeformed sulfides filling fractures and late quartz/carbonate veins of the ductile–brittle tectonic event (Dn+3) (**Fig. 4.11**). The occurrence of gold–silver tellurides also in sulfides filling fractures, suggests that gold mineralization occurred continually (remobilization?) from early (Dn, Dn+1 and Dn+2) ductile high–temperature events to late stage (Dn+3 event) brittle structures (**Fig. 4.10 and 4.11**). However, the main stage of gold mineralization is thought to be related to the (deformed) quartz veins and associated high–temperature calc–silicate alteration and albitization (early Dn), when gold was firstly introduced by hydrothermal fluids in the greenstone sequence.

According to our structural and geochronological data for the Pedra Branca gold deposit, in Troia Massif, early gold mineralization (Dn) is Paleoproterozoic in age (2029 ± 28 Ma), while the late remobilization of this gold (or new gold influx) along late stage brittle structures (Dn+3) occurred during the Neoproterozoic (574 ± 7 Ma) (**Fig. 4.17A**). The U–Pb ages of titanite grains extracted from gold–related calc–silicate alteration of the Pedra Branca

gold deposit recorded powerful information for both gold mineralization and later tectono–thermal reworking (**Fig. 4.17A**).

The 2029 ± 28 Ma U-Pb titanite crystallization age places this gold mineralization at the end of the Paleoproterozoic crustal evolution of the Troia Massif (**Table 4.3**). This age of gold mineralization is slightly younger (within the error) than the ages of 2088 ± 41 Ma obtained in metamorphic zircon overgrowths from high–grade paragneisses (Calado et al., 2018), younger than the 2068 and 2079 Ma potassic magmatism of the Bananeira suite (Costa et al., 2018), the 2100 Ma Boa Viagem mafic–ultramafic intrusion (Almeida, 2014), the 2070 Ma S–type granitoids of the Canindé complex (Garcia et al., 2014), the 2046 Ma leucosome age from the Macaoca migmatitic–orthogneiss (Gomes, 2013) and the 2036 Ma PGE–bearing chromitites of the Troia Massif (Costa et al., 2014b) (**Table 4.3**).

Table 4.3. Geochronological data for Archean/Paleoproterozic rocks of the Troia Massif.

	Complex / unit	Rock type	Analytical technique	Age (Ma)	Refer.
	ARCHEAN RECORD				
Basement rocks	Cruzeta complex	Metatonalite	(U-Pb SHRIMP in zircon)	3270 ± 5	Silva et al. (2002)
	Cruzeta complex	Metatonalite	(U-Pb isotopic dilution in zircon)	2857 ± 42	Fetter (1999)
	Cruzeta complex	Metatonalite	(U-Pb isotopic dilution in zircon)	2794 ± 77	Fetter (1999)
	Cruzeta complex	Metatonalite	(U-Pb SHRIMP in zircon)	2793 ± 6.3	Ganade et al. (2017)
	Cruzeta complex	Metarhyolite	(U-Pb isotopic dilution in zircon)	2776 ± 65	Fetter (1999)
	Cruzeta complex	Metatonalite	(U-Pb isotopic dilution in zircon)	2773 ± 60	Fetter (1999)
	Cruzeta complex	Metatonalite	(U-Pb SHRIMP in zircon)	2698 ± 8	Ganade et al. (2017)
	Cruzeta complex	Metatonalite	(U-Pb isotopic dilution in zircon)	2675 ± 64	Fetter (1999)
	PALEOPROTEROZOIC RECORD				
Accretionary event (pre–collisional)	Algodões unit	Amphibolite (metabasalt)	(Sm-Nd whole rock isochron)	2236 ± 55	Martins et al. (2009)
	Serra das Pipocas	Matadacito	(U-Pb LA-ICPMS in zircon)	2234 ± 13	Sousa (2016)
	Cipó tonalites	Metatonalite	(U-Pb LA-ICPMS in zircon)	2190 ± 6	Costa et al. (2015)
	Mirador tonalites	Metatonalite/granodiorite	(U-Pb SHRIMP in zircon)	2185 ± 4	Costa et al. (2018)
	Mirador tonalites	Metatonalite/granodiorite	(U-Pb LA-ICPMS in zircon)	2181 ± 4	Sousa, (2016)
	Cipó tonalites	Metatonalite	(U-Pb LA-ICPMS in zircon)	2180 ± 15	Costa et al. (2015)
	Cipó tonalites	Metatonalite	(Pb-Pb evaporation in zircon)	2172 ± 7	Martins et al. (2009)
	Cipó tonalites	Metatonalite	(Pb-Pb evaporation in zircon)	2160 ± 9	Martins et al. (2009)
	Madalena orthogneiss	Metaquartz diorite	(U-Pb isotopic dilution in zircon)	2156 ± 8	Castro (2004)
	Serra das Pipocas	Felsic metavolcanic	(U-Pb isotopic dilution in zircon)	2151 ± 9	Fetter (1999)
	Serra das Pipocas	Felsic metavolcanic	(U-Pb LA-ICPMS in zircon)	2156 ± 45	Sousa (2016)
	Serra da Palha ortho.	Granitic orthogneiss	(U-Pb LA-ICPMS in zircon)	2150 ± 16	Costa et al. (2015)
	Boa Viagem complex	Bt-Hb-Orthogneiss	(U-Pb SHRIMP in zircon)	2150 ± 29	Silva et al. (2014)
	Madalena orthogneiss	Bt-Hb-Orthogneiss	(U-Pb isotopic dilution in zircon)	2142 ± 20	Castro (2004)
	Algodões unit	Metaquartz diorite	(U-Pb isotopic dilution in zircon)	2140 ± 6	Fetter (1999)
	Madalena orthogneiss	Metatonalite	(Pb-Pb evaporation in zircon)	2140 ± 6	Martins et al. (2009)
	Macaoca orthogneiss	Bt-Hb-Orthogneiss	(U-Pb isotopic dilution in zircon)	2139 ± 12	Castro (2004)
	Boa Viagem complex	Bt-Hb-Orthogneiss	(U-Pb SHRIMP in zircon)	2124 ± 35	Silva et al. (2014)
	Algodões unit	Metarhyolite	(U-Pb SHRIMP in zircon)	2130 ± 17	Castro (2004)
	Macaoca orthogneiss	Metatonalite	(U-Pb isotopic dilution in zircon)	2130 ± 3	Fetter (1999)
	Madalena orthogneiss	Metaquartz diorite	(U-Pb isotopic dilution in zircon)	2130 ± 3	Martins et al. (2009)
Collisional event	Boa Viagem mafic	Metagabbro	(U-Pb LA-ICPMS in zircon)	2103 ± 3	Almeida (2014)
	Jaguaretama complex	Grt-Sill paragneiss	(U-Pb LA-ICPMS zircon overgrowth)	2088 ± 41	Calado et al. (2018)
	Bananeira suite	Qtz-monzonite	(U-Pb SHRIMP in zircon)	2079 ± 4	Costa et al. (2018)
	Canindé unit (?)	Leucogranite	(U-Pb LA-ICPMS in zircon)	2070 ± 19	Garcia et al. (2014)
	Bananeira suite	Granite	(U-Pb LA-ICPMS in zircon)	2068 ± 5	Costa et al. (2018)
	Macaoca orthogneiss	Leucosome	(U-Pb LA-ICPMS in zircon)	2046 ± 12	Gomes (2013)
	Troia mafic/ultramafics	Chromitite	(U-Pb SHRIMP in zircon)	2036 ± 28	Costa et al. (2014b)
	Gold mineralization	Calc-silicate alteration	(U-Pb LA-ICPMS in titanite)	**2029 ± 27**	**This work**

Bt = biotite, Hb = hornblende, Qtz = quartz, SHRIMP = Sensitive High Resolution Ion Microprobe, LA-ICMS = Laser Ablation Inductively Coupled Plasma Mass Spectrometry
Error for the ages are 1σ for the SHRIMP technique and 2 σ for the others.

This clearly relates the timing of gold mineralization to the late tectonic evolution of the Rhyacian granite–greenstone terranes of the Troia Massif, similar to the reported ages for

gold mineralization in many Paleoproterozoic greenstone belts of the surrounding cratonic domains (**Fig. 4.1**), such as the São Francisco craton (Rio Itapicuru greenstone belt, 2080–2050 Ma, Mello et al., 2006), Guiana shield (Omai area, 2002–2094 Ma, Norcross et al., 2000), São Luís craton (Caxias and Piaba deposits, 2009–1990 Ma, Klein et al., 2014, 2015) and West Africa craton (Wassa deposit at 2055 ± 18 Ma and Obuasi at 2045 ± 40 Ma, Mignot et al., 2017).

The late mineralization age is typical of orogenic gold deposits worldwide, that consistently formed slightly late in the tectonic evolution of their host terranes (Groves et al., 1998). Few geochronological records of high–grade metamorphism at the Troia Massif suggest that it may occurred between 2088 to 2046 Ma, bracketed by the age of metamorphic zircon overgrowth from garnet–sillimanite paragneiss and the lecossome age (partial melting) in the north part of the Troia Massif (Canindé and Jaguretama complexes) (**Table 4.3**) (**Fig. 4.2C**). Therefore, early gold mineralization was firstly introduced (by fluid flow in shear zone) in the Serra das Pipocas greenstone belt at 2029 ± 28 Ma, probably in the late stages of the Paleoproterozoic upper amphibolite to granulite facies metamorphism. However, the late quartz–carbonate veins, with euhedral sulfides and associated gold–silver tellurides found in the late stage brittle structures of the Dn+3 event, are intrinsic related to the Neoproterozoic Brasiliano/Pan–African orogeny (**Fig. 4.11**), as suggested by the 575 ± 3 Ma U–Pb zircon age of the syn–tectonic Guaribas dikes (**Fig. 4.16** and **4.17D**), similar to the discordance pattern of large amount of titanite grains in the 574 ± 7 Ma lower intercept age (**Fig. 4.17A**).

4.7.3. Neoproterozoic reworking of the Troia Massif

At a province–scale overview, the Troia Massif represents an Archean/Paleoproterozoic basement inlier within the Neoproterozoic regional framework of the Borborema Province (**Fig. 4.1**), established during the 620–580 Ma Brasiliano/Pan–African tectono–thermal event of West Gondwana Supercontinent agglutination (Almeida et al., 1981; Trompette, 1994; Arthaud et al., 2008; Santos et al., 2015). In this context, most of the Neoproterozoic supracrustal rocks and surrounding basement inlier (including the Troia Massif) were deformed, metamorphosed and intruded by syn– to late–tectonic granitoids during the Brasiliano/Pan–African orogeny. The structural pattern at this regional–scale framework clearly evidence a structural configuration driven by large NE–SW strike–slip shear zones with dextral kinematics (**Fig. 4.19**). These regional structures are mainly represented by the NE–trending Senador Pompeu and the Sobral–Pedro–II shear zones, while the Tauá and Rio Groaíras NW–trending shear zones delineate subsidiary antithetic structures

(**Fig. 4.19**). The Sobral–Pedro–II shear zone is also known as Transbrasiliano Lineament, which connects with the Kandi fault at the African counterpart (**Fig. 4.1**) (Trompette, 1994; Cordani et al., 2013).

In the Ceará Central domain (**Fig. 4.2B** and **4.19**), the structural patterns of low–angle foliation and associated asymmetric folds were imprinted by crustal shortening and related Neoproterozoic nappe tectonics of the Brasiliano/Pan–African orogeny (Caby and Arthaud, 1986). According to these authors, this early tangencial (nappe) tectonics affected both the Archean/Paleoproterozic rocks of the Troia Massif and surrounding Neoproterozoic rocks (thick–skinned deformation). The time of the nappe (tangencial) tectonics probably took place at 640 Ma, as suggested by the exhumation age of the retrograde eclogites found in the Ceará Central domain (Castro, 2004; Araújo, 2014; Santos et al., 2015). According to Santos et al. (2015), the presence of coesite–bearing retrograde eclogites in the Ceará Central domain indicates that these rocks have been subducted to depths exceeding 90 km and were exhumed as fast extrusive slices, pushed up by low–angle thrust tectonics. This regional Neoproterozoic nappe tectonics may possible be responsible for the overprinted Dn+1 structures observed in the study area (Troia Massif). The Neoproterozoic magmatism associated to this early 640–610 Ma nappe tectonics is mainly represented by the Tamboril–Santa Quitéria arc/collisional igneous–migmatite complex (Fetter et al., 2003; Costa et al., 2010; Araújo et al., 2012; Costa et al., 2013; Padilha et al., 2014). According to Costa et al. (2013), most of the 640–610 Ma Tamboril–Santa Quitéria plutonic magmatism is syn–tectonic to the regional low–angle foliation (Sn+1), and may represent the record of collisional magmatism associated to slab breakoff processes, following the Neoproterozoic high–pressure metamorphic peak at 640 Ma (Santos et al., 2015).

Several U–Pb analyses of zircon and monazite from deformed rocks of the Ceará Central domain indicate that the transition from tangential collision (nappe) to transcurrent tectonic processes occurred 600 Ma (Castro, 2004; Nogueira, 2004; Santos et al., 2008, 2015; Arthaud et al., 2008; Araújo et al., 2012; Garcia et al., 2014). The late transcurrent tectonic processes culminated on the development of large NNE–SSW transcurrent shear zones at 590–530 Ma (Vauchez et al., 1995; Monié et al., 1997). Mica and amphibole cooling ages ($^{40}Ar/^{39}Ar$) obtained by Monié et al. (1997) suggest that the transcurrent movements continued up to 540 Ma. During this transcurrent tectonic regime, several granite plutons were emplaced along transtractive zones, at 597 to 532 Ma (**Fig. 4.19**).

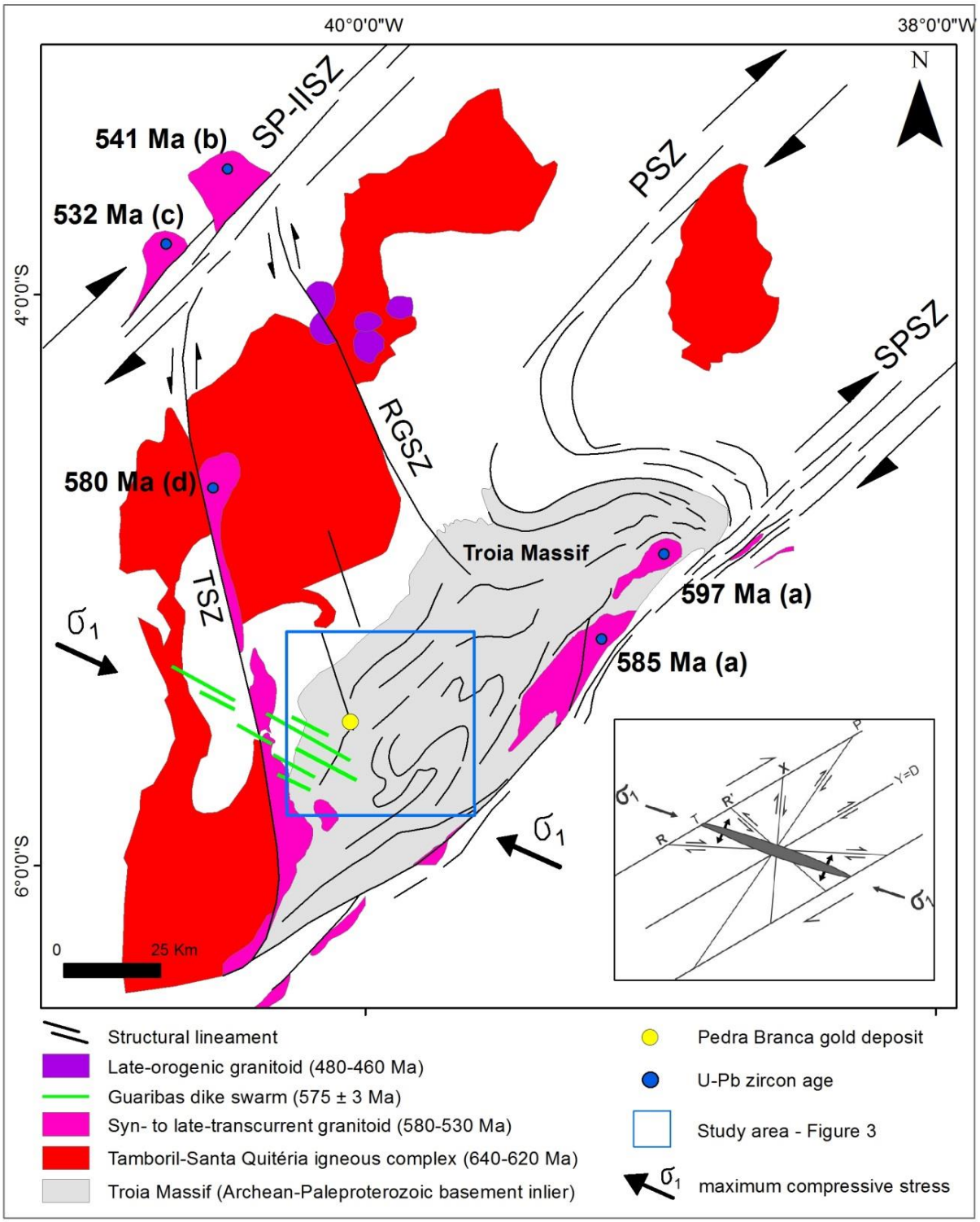

Fig. 4.19*. Structural view of the main regional shear zones and Neoproterozoic syn–tectonic granites surrounding the Troia Massif. (SP–IISZ= Sobral–Pedro–II shear zone, PSZ= Paramoti shear zone, SPSZ= Senador Pompeu shear zone; TSZ= Tauá shear zone, RGSZ= Rio Groaíras shear zone). U–Pb ages for syn– to late–tectonic granitoids are: (a) Quixadá and Quixeramobim plutons – Nogueira (2004), (b) Meruoca pluton – Santos et al. (2013), (c) Mucambo pluton – Fetter (1999) and (d) Nova Russas pluton– Archanjo and Hollanda (2013).*

The framework imprinted by these large transcurrent shear zones, with dextral kinematics, strongly control the observed structural features related to Dn+2, observed in the study area (**Fig. 4.13C** and **D**). In this regional overview, the Troia Massif is dragged over the Senador Pompeu shear zone, toward northeast direction (**Fig. 4.19**). Many of the local–scale Dn+2 structures, such as the Sn+2 foliation planes, Ln+2 lineations and folds with NE–plunging axis (**Fig. 4.7A, 4.8B** and **C**), is in structural concordance with this large regional drag fold outlined in the central part of the Troia Massif (**Fig. 4.19**). The coaxial relationship between fold hinges and Ln+2 stretching lineations oriented in the NE–SW direction, is also a common feature observed in the study area (**Fig. 4.8B** and **C**). This geometry may be indicative of constrictional deformation and folding under transtension (Dewey, et al., 1998; Krabbendam and Dewey, 1998; Fossen, et al., 2013), clearly developed in association with NE–SW striking Shear Zones within the Ceará Central domain (**Fig. 4.19**). This thermo–mechanical behavior is commonly observed extensional collapse of orogens, in association with exhumation of high– and ultra–high pressure rocks (Dewey, 1988; Dewey, et al., 1998; Krabbendam and Dewey, 1998). This could also suggest, that the Archean/Paleoproterozoic rocks of the Troia Massif have also been exhumed during this Neoproterozoic period of extensional tectonics (orogenic collapse), and thus, exposing some deep crustal (hypozonal) orogenic gold mineralization of the Paleoproterozoic granite–greenstone terranes.

4.7.4. Reworked orogenic gold mineralizations at craton margins

At craton margins, some examples of Archean granite–greenstone terranes hosting orogenic gold mineralization that have been later reworked by younger orogenies are presented in the literature, such as the ones found at the margins of the Karelian craton (Larionova et al., 2013; Molnár et al., 2016), northern Yilgarn craton (Perring and McNaughton, 1990; McMillan, 1996; Vielreicher et al., 2002; Gazley, 2011; Duclaux et al., 2012; Gazley et al., 2016) and the North China craton (Zhang et al., 2018). However, in many others instances, the presence of the older primary ores is not evaluated, and the recognized gold mineralizations are not only associated to greenstone belts, but also to high grade gneisses, and to new fluid flow events imprinted by the new orogeny (Carpenter et al., 2005; Davies et al., 2010; Lawley et al., 2014; Blenkinsop and Doyle, 2014; Zhang et al., 2014; Lawley et al., 2015; Doyle et al., 2015; Kirkland et al., 2015; Fielding et al., 2017; 2018).

The best studied example of greentone–hosted orogenic gold mineralization that has been overprinted by a new orogenic cycle is found in the Marymia Inlier, a reworked margin of the Yilgarn Craton, Australia (McMillan, 1996; Vielreicher et al., 2002; Gazley, 2011;

Duclaux et al., 2012; Gazley et al., 2016). In the Marymia Inlier, 2.65 Ga amphibolite facies orogenic gold deposits are hosted by NeoArchean greenstone belts that were tectonically reworked by the 1.8–1.7 Ga Capricorn orogeny (McMillan, 1996; Vielreicher et al., 2002; Gazley, 2011; Duclaux et al., 2012; Gazley et al., 2016). The Neoarchean greenstone sequences of the Marymia Inlier (Plutonic Well greenstone belt) are stratigraphically and geochemically similar to greenstone sequences in the Yilgarn craton (Eastern Goldfields Superterrane), but were subjected to further deformation and metamorphism in the Palaeoproterozoic 1.8–1.7 Ga Capricorn orogeny (Vielreicher et al., 2002; Gazley, 2011). In this scenery, multiple gold mineralization events occurred in the Marymia Inlier, with major gold mineralization dated at 2.65 Ga, and later mineralizing events at 1.8–1.7 Ga during the Capricorn Orogeny (McMillan, 1996; Vielreicher et al., 2002; Gazley, 2011; Duclaux et al., 2012; Gazley et al., 2016). The Pb isotope composition derived from sulfides support that it crystallized in two different events (2650 and 1720 Ma) with a common source of Pb for both, suggesting that the later Proterozoic event may represent remobilization of the early Archean orogenic gold deposit (Vielreicher et al., 2002; Gazley et al., 2016). However, according to Vielreicher et al. (2002), in the 1.8–1.7 Ga Paleoproterozoic hydrothermal activity and greenschist facies regional metamorphism, only limited gold was remobilized from the Archean lode–gold mineralization of the Marymia deposit.

Similarly, in the North China craton, Archean and Paleoproterozoic orogenic gold mineralization are identified in the Wutai greenstone belt. The first mineralizing event at 2.5 Ga is associated to late tectonic evolution and metamorphism of the Neoarchean greenstone sequence, while the late 1.9–1.8 Ga mineralizing event is due to regional metamorphism associated with Paleoproterozoic collision of the Western and Eastern Archean blocks of the North China craton (Zhang et al., 2018). In addition, at the margins of the Archean Karelian craton, orogenic gold mineralization is associated to the overprint of the 2.0–1.7 Ga Paleoproterozoic Svecofennian and Lapland–Kola orogenies (Larionova et al., 2013; Molnár et al., 2016).

As we already discussed, the Archean/Paleoproterozoic rocks of the Troia Massif represent a basement inlier within the Neoproterozoic lithostructural framework of the Borborema Province (**Fig. 4.1**). This tectonic scenario is very similar to the previously mentioned examples, such as the Marymia Inlier. Therefore, similar tectonic interpretations may be taken to discuss the tectono–metamorphic evolution of the Troia Massif. For example, the Archean rocks of the Marymia Inlier are interpreted to remained “buried” during a long time, until it has been exhumed by tectonic processes of the 1.8–1.7 Ga Paleoproterozoic

Capricorn orogeny (Muhling, 1988; 1990; Bagas, 1999). According to Gazley et al., (2014), the calculated PT conditions up to 7.3–8.2 kbar and 580–590°C from the garnet–bearing rocks of the Plutonic gold mine, in the Marymia Inlier, evidence that these rocks underwent to high–pressure amphibolite facies metamorphism, most probably during the late Archean (2.65 Ga). In addition, these high–pressure conditions for amphibolite facies greenstone belts in the Marymia Inlier are anomalous in the context of the Yilgarn Craton, in which greenschist facies greenstone belts and mesozonal orogenic gold mineralization predominate (Bagas, 1999; Gazley et al., 2014). This suggests that the Marymia Inlier may represents an exhumed lower crustal segment exposed along the northern margin of the Yilgarn Craton, and that the Neoarchean amphibolite facies (hypozonal) orogenic gold deposits of the Marymia Inlier may represent deep crustal equivalents of the widespread greenschist facies (mesozonal) orogenic gold deposits of the Yilgarn craton (Vielreicher et al., 2002; Gazley, 2011).

Similarly, the Paleoproterozoic granite–greenstone terranes of the Troia Massif are stratigraphically and geochemically similar to those in the surrounding cratonic domains (Martins et al., 2009; Costa et al., 2015; 2018) (**Fig. 4.1**), and also with similar age (2029 Ma) of gold mineralization. However, most of the Paleoproterozoic orogenic gold mineralizations at the surrounding cratons were formed at mesozonal depths (Leube et al., 1990; Eisenlohr and Hirdes, 1992; Vanderhaeghe et al., 1998; Klein et al., 2015; Silva et al., 2001; Mello et al., 2006; Goldfarb et al., 2017). Therefore, the record of Paleoproterozoic hypozonal orogenic gold mineralization in the amphibolite–facies Serra das Pipocas greenstone belt may represent an exhumed deep crustal equivalent of the widespread mesozonal gold mineralizations found at the surrounding craton domains (West Africa and São Francisco–Congo cratons) (**Fig. 4.1**). This is also in agreement with the crustal continuum model for orogenic gold deposits from Groves (1993), in which orogenic gold deposits may continually form under a variety of crustal levels, at PT conditions ranging from 700°C at 5 kbar (20 km depth) to 180°C at <1 kbar (near surface). However, some authors disagree with the crustal continuum model, because at greater depths, metamorphic fluid generation cannot be easily explained (Tomkins and Grundy, 2009; Phillips and Powell, 2009), and thus, for many hypozonal orogenic gold deposits, a contribution of mantle– and/or magmatic– derived hydrothermal fluids are commonly advocated (Mueller et al., 2004; Krienitz et al., 2008; Muller et al., 2008; Rogers et al., 2013; Doublier et al., 2014; Kolb et al., 2015; Sahoo et al., 2018).

4.7.5. Tectonic model: Two stages of exhumation–driven gold mineralization

Exhumation–driven gold mineralization is commonly reported for many hypozonal orogenic gold deposits, as the gold–related hydrothermal assemblages replace the metamorphic mineral assemblages of the host rocks and follow the same retrograde PT path (Blenkinsop et al., 2004; Kolb et al., 2015). This indicates that the mineralization forms an integral part of the terrane evolution during exhumation, from syn– to post–peak regional metamorphism (Kolb et al., 2015). For example, the host rocks of the hypozonal Renco gold deposit, southern Zimbabwe, experienced retrograde metamorphism associated to terrane exhumation from 830ºC and 8 kbar to a late stage of retrogression (and gold mineralization) of 600ºC and 4 kbar, at 2556 Ma. In this case, mineralization is associated to high–temperature hydrothermal minerals, such as garnet, biotite, K–feldspar, quartz and amphibole, overlapping with the regional conditions of amphibolite facies retrogression of the host rocks (Kolb and Meyer, 2002; Kolb et al., 2000). In the New Consort gold mine, in the Barberton greenstone belt, South Africa, host rocks underwent near isothermal decompression from 700ºC and 5 kbar to 550ºC and 3 kbar. This progressive exhumation of the host rocks led to the formation of the 3030 Ma old gold mineralization, in equilibrium with the late regional conditions of amphibolite facies retrogression (550ºC and 3 kbar) and with high–temperature hydrothermal assemblage of garnet, diopside, hornblende, K–feldspar, quartz, calcite and biotite (Otto et al., 2007; Dziggel et al., 2010). According to Dziggel et al. (2010), U-Pb ages of zircon and titanite, and hornblende Ar-Ar dating of regional metamorphism, exhumation and the gold mineralization, indicate that the extensional exhumation and gold mineralization were more or less contemporaneous.

According to our results and available literature information on the Troia Massif, we suggest that during the 2088 to 2046 Ma Transamazonian/Eburnean metamorphism (**Table 4.3**), post–collisional tectonics may have driven the Serra das Pipocas greenstone belt to its first exhumation event, probably from 9 kbar to 3 kbar pressure conditions (30 to 10 km depth), as evidenced by mineral chemical composition from the greenstone lithologies (Sousa, 2016). According to Sousa (2016), the garnet–kyanite schist of the Serra das Pipocas greenstone belt may had experienced PT conditions up to 9.4 kbar and 772°C, reveled by mineral chemistry and thermobarometric calculations. However, for garnet–amphibolites of the same area, by the aluminum content in amphibole, much lower PT conditions of 2.97 kbar and 547°C were calculated, which can be interpreted as the record of regional amphibolite facies retrogression, following decompression (exhumation) of the greenstone pile (Sousa, 2016). These PT conditions (547°C and 2.97 kbar) for the regional amphibolite facies

retrogression of the greenstone pile are very similar to the PT conditions of gold mineralization in the Pedra Branca deposit, calculated by fluid inclusions data (Costa et al., submitted). Whilst, it is also typical of hypozonal orogenic gold deposits, in which gold mineralization and associated high–temperature hydrothermal assemblage overlap with the retrograde PT path of regional metamorphism (Kolb et al., 2015).

First exhumation processes imprinted in the greenstone piles of Troia Massif is thus interpreted as the recorded of Paleoproterozoic post–collisional setting (2088 to 2046 Ma), responsible for the regional amphibolite facies retrograde metamorphism. The high–temperature hydrothermal assemblage and gold mineralization of the Pedra Branca deposit occurred in close equilibrium with PT retrograde path of this first exhumation processes. The relationship between kyanite and muscovite overgrowths, together with coexisting biotite and sillimanite, found in the metasedimentary rocks of the Serra das Pipocas greenstone belt (**Fig. 4.5D, E** and **F**), may be interpreted as the decompression product of closed–system sillimanite forming, by the reaction: Ky + Bt + Qz → Ms + Sil + Bt +Qz (Foster, 1991; Gervais and Hynes, 2013). In this context, the evidence of diopside being replaced by hornblende in the gold–related calc–silicate hydrothermal alteration, suggest that mineralization took place in PT equilibrium with the regional amphibolite facies retrogression (**Fig. 4.10F**). Therefore, during this first exhumation process, fluid migration along shear zones were responsible for early quartz vein formation, calc–silicate alteration, albitization and the main phase gold mineralization at 2029 Ma. In addition, during this Paleoproterozoic post–collisional setting, several crustal– and mantle–derived plutonic magmatism occurred coeval to this regional decompression (exhumation, orogenic collapse) (**Table 4.3**), and may have contributed to gold mineralization with magmatic–sourced hydrothermal fluids.

However, the age of the titanite grains from the Paleoproterozoic calc–silicate alteration evidences that the Neoproterozoic metamorphic overprint may have reached amphibolite facies temperatures at 574 ± 7 Ma (lower intercept age), indicated by the large amount of Pb loss for most of the analyzed titanite grains (**Fig. 4.17A**). Titanite is a common accessory mineral in a wide range of amphibolite facies metamorphic rocks, and its closure temperature may vary from 650 to 800°C, depending mainly on the grains sizes and the cooling rate of the given terrane (Cherniak, 1993; Scott and St-Onge, 1995; Spencer et al., 2013; Stearns et al., 2015; Kirkland et al., 2016). Therefore, gold mineralization in the Pedra Branca deposit was broadly affected by this late Neoproterozoic metamorphism, from deep metamorphism–related deformation events (Dn+1 to Dn+2) (**Fig. 4.10**), through auriferous (±

Ag, Te) late stage fissure sulfides and quartz/carbonate veins at shallower levels (Dn+3 event) (**Fig. 4.11**).

The evidence of a two–stage gold mineralization at Pedra Branca is also suggested by Naleto et. al. (2018). Using spectroscopic data, X–ray powder diffraction and petrographic analyses, these authors identified that hydrothermal minerals from "type–I" veins are mainly diopside, hornblende, titanite and biotite, consistent with the high–temperature calc–silicate alteration assemblage developed in amphibolite facies orogenic gold deposits. However, epidote, chlorite and white micas were identified as the main hydrothermal minerals associated to the late "type–II" veins that fill some ductile–brittle faults and fractures (Naleto et al., 2018). This indicates that the late "type–II' veins and associated hydrothermal alteration developed under equivalent conditions of greenschist facies metamorphism. Epidote and chlorite were also identified in the "type–I" veins, but, occurring as products of retrogressive alteration of the high–temperature assemblage (Naleto et al., 2018). Also, for the "type–II" veins, using spectroscopic data, some zeolite crystals were found occurring as fracture filling mineral, evidencing that low temperature (< 300ºC) hydrothermal alteration also occurred along late brittle structures (Naleto et al., 2018). Therefore, Neoproterozoic metamorphic overprint in the Pedra Branca gold deposit, may suggests a second stage of exhumation and gold mineralization, recorded by retrogression from amphibolite facies (650ºC) (titanite Pb loss), to late greenschist (400ºC) and zeolite (< 300ºC) facies metamorphism and/or hydrothermal alteration along ductile–brittle structures. Therefore, in brief, gold mineralization of the Pedra Branca deposit can be roughly described as a two–stage exhumation–drive mineralization, once in the Paleoproterozoic (2029 Ma), in association with regional conditions of amphibolite facies retrogression, and later in the Neoproterozoic (580 Ma), associated to greenschist facies metamorphism retrogression.

We suggested that after the early 2029 Ma hypozonal orogenic gold mineralization, the Archean/Paleoproterozoic rocks of the Troia Massif remained in middle crustal levels for a prolonged period of time, and was exhumed only much later, during the 620–580 Ma Brasiliano/Pan-African tectonic event. So far, the time interval between early high–temperature to late (brittle) stages of gold mineralization in the Pedra Branca deposit, span 1.4 Ga (from 2029 to 580 Ma). Similarly, 1.0 Ga separates the early high–temperature orogenic gold mineralization and late stages of gold mineralization (remobilization?) in the Plutonic gold mine, Marymia inlier (Vielreicher et al., 2002; Duclaux et al., 2012; Gazley et al., 2016). According to these authors, in the Plutonic gold mine, the main gold mineralization is associated to quartz–biotite–amphibole–titanite high–temperature alteration (up to 600ºC) and

interpreted as Neoarchean in age (2.65 Ga). However, late marginally economic gold grades that are associated with the late stage (400ºC) quartz–carbonate veins that infill some ductile–brittle faults are of 1.8–1.7 Ga, related to tectonic exhumation of the Archean granite–greenstone terrane during the Paleoproterozoic Capricorn orogeny (Vielreicher et al., 2002; Duclaux et al., 2012; Gazley et al., 2014; 2016).

4.8. Conclusions

The Serra das Pipocas greenstone belt shares similar ages and lithostratigraphic characteristic to other Rhyacian granite–greenstone terranes of the surrounding cratons and also hosts similar–aged (2029 ± 28 Ma, U–Pb titanite) Transamazonian/Eburnean orogenic gold mineralization. The Serra das Pipocas shear zone (at the basement–greenstone belt boundary) probably plays an important role on orogenic gold mineralization of the study area, representing a deep (trans–crustal) first–order structure. However, the main mineralized areas are sited on higher–order shear zones, located near–parallel to the stratigraphy, between metavolcanic and metasedimentary unit boundaries.

Constraints from the titanite Pb loss, yielding a 574 ± 7 Ma lower intercept age, and the 575 ± 3 Ma U–Pb zircon age of the syn–tectonic Guaribas diques, suggest that the Archean/Paleoproterozoic rocks of the Troia Massif and gold mineralization were broadly affected by the late Neoproterozoic regional–scale deformation and metamorphism, related to the 620-580 Ma Brasiliano/Pan–African orogeny. The main deformation recorded (Dn+1, Dn+2 and Dn+3) in the Troia Massif is probably of Neoproterozoic age, with the maximum compressive stress (σ1) in the WNW–ESE direction. However, at local scale, Paleoproterozoic deformation record (Dn) still preserved.

Hypozonal orogenic gold mineralization was introduced (by fluid flow in shear zone) in the Serra das Pipocas greenstone belt at 2029 ± 28 Ma, shortly after high–grade regional metamorphism of the Paleoproterozoic Transamazonian/Eburnean orogeny, following the first regional exhumation of the greenstone pile. However, later on, during the 620–580 Ma Brasiliano/Pan–African orogeny, this early Paleoproterozoic hypozonal gold mineralization has been deformed by Neoproterozoic nappe tectonics (Dn+1) and transcurrent (shear–related) deformation (Dn+2), which has imprinted a new stage of exhumation and gold mineralization. Along the late stage brittle structures (Dn+3 event), some gold/silver tellurides were found in the late undeformed quartz–carbonate veins and sulfides filling fractures, suggesting that during the Neoproterozoic deformation of early Paleoproterozoic gold mineralization, introduction of new influx of mineralizing fluids (or only remobilization?)

may have occurred. Therefore, gold mineralization in the Troia Massif reflects this poly–cyclic deformation scenery, with a two–stage gold mineralization, associated to both Paleoproterozoic and Neoproterozoic tectono–thermal evolution. However, whether if the Neoproterozoic event led only to gold remobilizations and/or also to new (fluid influx) mineralizing event is remain uncertain, and call for further investigation.

Acknowledgment

The work reported here formed part of the first author's Ph.D. thesis project and was supported by mapping program of the Geological Survey of Brazil (CPRM). This is also a contribution to the Conselho Nacional de Desenvolvimento Científico e Tecnológico (CNPq), project (306798/2016-6) "Evolução crustal, modelos geodinâmicos e metalogênese: exemplos do Maciço de Troia (CE) e do Cinturão Gurupi (PA-MA)". FGC and ELK also thank the Jaguar Mining In, as this paper would not be possible without the access to drill cores, kindly provided by this company.

References

Aleinikoff, J.N., Wintsch, R.P., Tollo, R.P., Unruh, D.M., Fanning, C.M., Schmitz, M.D. 2007. Ages and origins of rocks of Killingworth dome, South–Central Connecticut: Implications for the tectonic evolution of southern New England. American Journal of Sciences, 307, 63–118.

Almeida, A.R., 1987. Petrologia da província subvulcânica de Tauá e Independência–CE. Master Dissertation, Universidade Federal de Pernambuco–UFPE. Recife. 130p.

Almeida, A.R., Sial, A.N., Ferreira, V.P., 1984. Petrologia e geoquímica de enxames de diques cambrianos no Nordeste do Brasil. In: 9º Simpósio de Geologia do Nordeste, Natal.

Almeida, F.F.M., Hasui, Y., Brito Neves, B.B., Fuck, R.A., 1981. Brazilian structural provinces: an introduction. Earth Science Reviews, 17, 1–29.

Almeida, R.S., 2014. Geologia, geoquímica e geocronologia da suíte intrusiva máfica–ultramáfica de Boa Viagem, Ceará, Brasil. Master Dissertation, Federal University of Ceará (UFC), 103 p.

Amaral, W.S., Santos, T.J.S., Wernick, E., Nogueira Neto, J.A., Dantas, E.L., Matteini, M., 2012. High–pressure granulites from Cariré, Borborema Province, NE Brazil: tectonic setting, metamorphic conditions and U–Pb, Lu–Hf and Sm–Nd geochronology. Gondwana Research, 22, 883–909.

Angeli, N., Bevenutti, C.F., Antunes, L.A., Campos, M.C., Mamani, R., 2009. Cromititos do Complexo de Pedra Branca: química mineral e platinóides associados, Ceará, Brasil. In: Simpósio de Geologia do Nordeste, Fortaleza, 23, cd rom.

Araújo, C.E.G., 2014. Evolução tectônica da margem ativa Neoproterozóica do Orógeno Gondwana Oeste na Província Borborema (NE–Brasil) PhD thesis Universidade de São Paulo, 243 p.

Araujo, C.E.G., Costa, F.G., Pinéo, T.R.G., Cavalcante, J.C., Moura, C.A.V., 2012. Geochemistry and $^{207}Pb/^{206}Pb$ zircon ages of granitoids from the southern portion of the Tamboril–Santa Quitéria granitic–migmatitic complex, Ceará Central Domain, Borborema Province (NE Brazil). J. South Am. Earth Sci., 33, 21–33.

Archanjo, C.J., Hollanda, M.H.B.M., 2013. Deformação e magmatismo na zona de cisalhamento Tauá (Ceará Central). 25º Simpósio de Geologia do Nordeste, Gravatá, Pernambuco, p. 481-482.

Arthaud, M.H., Caby, R., Fuck, R.A., Dantas, E.L., Parente, C.V., 2008. Geology of the northern Borborema Province, NE Brazil and its correlation with Nigeria, NW Africa. In: West Gondwana: Pre–Cenozoic Correlations Across the South Atlantic Region, Pankhurst, R.J.,

Trouw, R.A.J., Brito Neves, B.B., de Wit, M.J., (eds). Geological Society of London, Special Publications, 294, 49–67.

Arthaud, M.H., Hartmann, M.B., 1986. A geologia da região de Independência (CE): um exemplo de tectônica de nappes no Ceará. In: Congresso Brasileiro de Geologia, 34. Goiânia, SBG. 3, 1160–1169.

Bagas, L, 1999. Early tectonic history of the Marymia Inlier and correlation with the Archaean Yilgarn Craton, Western Australia, Australian Journal of Earth Sciences, 46, 115–125.

Barrueto, H.R., Hunt, W., 2010. Main features of the Pt–Pd chromitite–type ore deposit, Tróia Unit, Cruzeta Complex, Northeast Brazil: Insights provided by microscopic and chemical approaches. In: 11th International Platinum Symposium, Sudbury, Canada.

Béziat, D., Dubois, M., Debat, P., Nikiéma, S., Salvi, S., Tollon, F., 2008. Gold metallogeny in the Birrimian craton of Burkina Faso (West Africa). J. Afr. Earth Sci., 50, 215–233.

Bierlein, F.P., Cartwright, I., Mcknight, S., 2001. The role of carbonaceous "indicator" slates in the genesis of lode gold mineralization in the western Lachlan Orogen, Victoria, southestern Australia. Economic Geology, 96, 431–451.

Bierlein, F.P., Crowe, D.E., 2000. Phanerozoic orogenic lode gold deposits. In: Hagemann SG, Brown PE (eds) Gold in 2000. Reviews in Economic Geology 13, 103–139.

Bierlein, F.P., Murphy, F.C., Weinberg, R.F., Lees, T., 2006. Distribution of orogenic gold deposits in relation to fault zones and gravity gradients: targeting tools applied to the Eastern Goldfields, Yilgarn Craton, Western Australia. Mineralium Deposita, 41, 107–126.

Blenkinsop, T.G., Doyle, M.G., 2014. Structural controls on gold mineralization on the margin of the Yilgarn craton, Albany–Fraser orogen: The Tropicana deposit, Western Australia. Journal of Structural Geology, 67 (B), 189–204.

Blenkinsop, T.G., Kröner, A., Chiwara, V., 2004. Single stage, late Archaean exhumation of granulites in the Northern Marginal Zone, Limpopo Belt, Zimbabwe, and relevance to gold mineralization at Renco mine: South African, Journal of Geology, 107, 377–396.

Blewett, R.S., Henson, P.A. Roy, I.G., Champion, D.C., Cassidy, K.F., 2010. Scale–integrated architecture of a world–class gold mineral system: The Archaean eastern Yilgarn Craton, Western Australia. Precambrian Research, 183, 230–250.

Block, S., Baratoux, L., Zeh, A., Laurent, O., Bruguier, O., Jessell, M., Ailleres, L., Sagna, R., Parra–Avila, L.A., Bosch, D., 2016. Paleoproterozoic juvenile crust formation and stabilisation in the south–eastern West African Craton (Ghana); New insights from U–Pb–Hf zircon data and geochemistry. Precambrian Research, 287, 1–30.

Brito Neves, B.B., 1975. Regionalização geotectônica do Pré–Cambriano Nordestino. PhD Thesis, Universidade de São Paulo, São Paulo–SP, 198p.

Brito Neves, B.B., Santos, E.J., Van Schmus, W.R., 2000. Tectonic history of the Borborema province, in: Cordani, U.G., Milani, E.J., Thomaz Filho, A., Campos, D.A., (Eds.). Tectonic Evolution of South America, 31° International Geological Congress, Rio de Janeiro, 151–182.

Caby, R., Arthaud, M.H., 1986. Major Precambrian nappes of the Brazilian belt, Ceará, northeast Brazil. Geology, 14, 871–874p.

Calado, B.O., Costa, F.G., Gomes, I.P., Rodrigues, J.B., 2018. U–Pb (LA–ICP–MS) Detrital zircon ages from the Jaguaretama complex: Implications for Rhyacian – Sthaterian geological evolution. 49º Congresso Brasileiro de Geologia, Rio de Janeiro.

Carpenter, R., Duke, N.A., Sandeman, H.A., Stern, R., 2005. Relative and absolute timing of gold mineralization along the Meliadine trend, Nunavut, Canada: Evidence for Paleoproterozoic gold hosted in an Archean greenstone belt. Economic Geology, 100, 567–576.

Castro, N.A., 2004. Evolução Geológica Proterozóica da Região entre Madalena e Taperuaba, Domínio Tectônico Ceará Central (Província Borborema). PhD Thesis. Universidade de São Paulo, São Paulo–SP, p. 221.

Cavalcante, J.C., Vasconcelos, A.M., Medeiros, M.F., Paiva, I.P., Gomes, F.E.M., Cavalcante, S.N., Cavalcante, J.E., Melo, A.C.R., Duarte Neto, V.C., Benevides, H.C., 2003. Mapa Geológico do Estado do Ceará. Escale 1:500.000. Serviço Geológico do Brasil, Fortaleza. CPRM.

Chemale, F.J., Kawashita, K., Dussin, I.V., Ávila, J.N., Justino, D., Bertotti, A., 2012. U–Pb zircon in situ dating with LA–MC–ICP–MS using a mixed detector configuration. An. Acad. Bras. Ciências, 84, 275–295.

Cherniak, D.J., 1993. Lead diffusion in titanite and preliminary results on the effects of radiation damage on Pb transport. Chem. Geol., 110 (1), 177–194.

Cordani, U.G., Pimentel, M.M., Araújo, C.E.G., Fuck, R.A., 2013. The significance of the Transbrasiliano–Kandi tectonic corridor for the amalgamation of West Gondwana. Brazilian Journal of Geology, 43, 583–597.

Costa, F.G. Araújo, C.E.G., Amaral, W.S., Vasconcelos, A.M., Rodrigues, J.B., 2013. U–Pb (LA–ICPMS) zircon ages and Nd isotopes for granitoids of the Tamboril–Santa Quitéria Complex, Ceará Central Domain: implication for neoproterozoic syncollisional magmatism in north Borborema Province. Geologia USP Série Científica, 13, 159–174.

Costa, F.G., 2013. Geologia e Recursos Minerais da Folha Quixadá (SB–24–V–B–VI). Escala: 1:100.000. Programa Levantamentos Geologicos Basicos do Brasil. Serviço Geológico do Brasil, Fortaleza. CPRM.

Costa, F.G., Klein, E.L., Corrêa–Lima, R.G., Naleto, J.L.C., 2016. Geology, geochronology and gold metallogenesis of the Serra das Pipocas granite–greenstone terrane. 48° Congresso Brasileiro de Geologia, Porto Alegre – RS, p. 9278.

Costa, F.G., Klein, E.L., Harris, C., Roopnarain, S., Corrêa–Lima, R., Radu, B., (submitted). Fluid inclusion and stable isotope (O, H, C) constraints on the genesis of the Pedra Branca gold deposit, Troia Massif, NE Brazil: A hypozonal orogenic gold mineralization sourced by magmatic–hydrothermal fluid. Ore Geology Rewiew.

Costa, F.G., Klein, E.L., Lafon, J.M., Milhomen Neto, J.M., Galarza, M.A., Rodrigues, J.B., Naleto, J.L.C., Corrêa–Lima, R.G., 2018. Geochemistry and U–Pb–Hf zircon data for plutonic rocks of the Troia Massif, Borborema Province, NE Brazil: Evidence for reworking of Archean and juvenile Paleoproterozoic crust during Rhyacian accretionary and collisional tectonics. Precambrian Research, 311, 167–194.

Costa, F.G., Oliveira, E.P., McNaughton, N., 2011. The Fazenda Gavião granodiorite and associated potassic plutons as evidence for Palaeoproterozoic arc–continent collision in the Rio Itapicuru greenstone belt, Brazil. J. South Am. Earth Sci., 32 (2), 127–141.

Costa, F.G., Palheta, E.S.M., Rodrigues, J.B., Gomes, I.P., Vasconcelos, A.M., 2015. Geochemistry and U–Pb zircon ages of plutonic rocks from the Algodões granite–greenstone terrane, Troia Massif, northern Borborema Province, Brazil: Implications for Paleoproterozoic subduction–accretion processes. J. South Am. Earth Sci., 59, 45–68.

Costa, F.G., Rodrigues, J.B., Cavalcanti, J.A.D., Palheta, E.S.M., Vasconcelos, A.M., 2014a. U–Pb LA–ICPMS ages of detrital zircons from the Paleoproterozoic Algodões and Serra das Pipocas greenstone–like sequences, Ceará Central Domain. In: 9th South American Symposium on Isotope Geology, São Paulo, Brazil, p. 110.

Costa, F.G., Rodrigues, J.B., Naleto, J.L.C., Vasconcelos, A.M., Barrueto, H.R., 2014b. 2036 Ma SHRIMP U–Pb zircon age for PGE–bearing chromitites of the Troia mafic–ultramafic complex, Ceará Central Domain. In: 9th South American Symposium on Isotope Geology, São Paulo, Brazil, p. 164.

Cox, S.F., 1999. Deformational controls on the dynamics of fluid flow in mesothermal gold systems. In: McCaffrey KJW, Lonergan L, Wilkinson JJ (eds) Fractures, Fluid Flow and Mineralization. Geological Society of London Special Publications, 155, 123–140.

Cox, S.F., Knackstedt, M.A., Braun, J., 2001. Principles of structural control on permeability and fluid flow in hydrothermal systems. In: Richards, J.P., Tosdal, R.M. (Eds.), Structural Controls on Ore Genesis. Reviews in Economic Geology, 14. Society of Economic Geologists, Boulder, Colorado, pp. 1–25.

Cox, S.F., Sun, S.S., Etheridge, M.A., Wall, V.J., Potter, T.F., 1995. Structural and geochemical controls on the development of turbidite–hosted gold quartz vein deposits, Wattle Gully mine, central Victoria, Australia. Economic Geology, 90, 1722–1746.

Dantas, E.L., Souza, Z.S., Wernick, E., Hackspacher, P.C., Xiaodong, D., Li, J.W., 2013. Crustal growth in the 3.4–2.7 Ga São Jose de Campestre Massif, Borborema Province, NE Brazil. Precambr. Res. 227, 120–156.

Dantas, E.L., Van Schmus, W.R., Hackspacher, P.C., Fetter, A.H., Brito Neves, B.B., Cordani, U., Nutman, A.P., Williams, I.S., 2004. The 3.4–3.5 São José de Campestre massif, NE Brazil: remnants of the oldest crust in South America. Precambrian Res. 130, 113–137.

Daoust, C., Voicu, G., Brisson, H., Gauthier, M., 2011. Geological setting ofthe Paleoproterozoic Rosebel gold district, Guiana Shield, Suriname. J. South Am. Earth Sci., 32, 222–245.

Davies, T., Richards, J.P., Creaser, R.A., Heaman, L.M., Chacko, T., Simonetti, A., Williamson, J., McDonald, D.W., 2010. Paleoproterozoic Age Relationships in the Three Bluffs Archean Iron Formation–Hosted Gold Deposit, Committee Bay Greenstone Belt, Nunavut, Canada. Exploration and Mining Geology, 19 (3–4), 55–80.

de Boorder, H., van Emmichoven, M.J.Z., Privalov, V.A 2006. Distribution of Precambrian iron and gold deposits on the southwestern East European Platform reflected in underlying transcrustal structure and current river systems. Ore Geology Reviews, 29 (3–4), 242–259.

Delor, C., Lahondère, D., Egal, E., Lafon, J.M., Cocherie, A., Guerrot, C., Rossi, P., Trufert, C., Theveniaut, H., Phillips, D., Avelar, V.G., 2003. Transamazonian crustal growth and reworking as revealed by the 1:500,000–scale geological map of French Guiana (2nd edition). Geologie de la France, 2–3–4, 5–57.

Dewey, J.F., 1988. Extensional collapse of orogens. Tectonics, 7(6), 1123–1139.

Dewey, J.F., Holdsworth, R.E., Strachan, R.A., 1998. Transpression and transtension zones. Geological Society, London, Special Publications, 135 (1), 1–14.

Doublier, M.P., Thébaud, N., Wingate, M.T.D., Romano, S.S., Kirkland, L.C., Gessner, K., Mole, D.R., Evans, N., 2014. Structure and timing of Neoarchean gold mineralization in the Southern Cross district (Yilgarn Craton, Western Australia) suggest leading role of late Low–Ca I–type granite intrusions. Journal of Structural Geology, 67, 205–221.

Doyle, M.G., Fletcher, I.R., Foster, J., Large, R.R., Mathur, R., McNaughton, N.J., Meffre, S., Muhling, J.R., Phillips, D., Rasmussen, B., 2015. Geochronological Constraints on the Tropicana Gold Deposit and Albany–Fraser Orogen, Western Australia. Economic Geology, 110, 355–386.

Duclaux, G., Hough, R., Gazley, M. F., 2012. Late tectonic evolution of Plutonic Gold Mine and controls on gold mineralisation. Structural Geology and Resources. Australian Institute of Geoscientists Bulletin, 56, 75–78.

Dziggel, A., Knipfer, S., Kisters, A.F.M., Meyer, F.M., 2006. P–T and structural evolu–tion during exhumation of high–T, medium–P basement rocks in the Barberton Mountain Land, South Africa. J. Metamorph. Geol. 24, 535–551.

Dziggel, A., Poujol, M., Otto, A., Kisters, A.F.M., Trieloff, M., Schwarz, W., Meyer, F.M., 2010. New U–Pb and $^{40}Ar/^{39}Ar$ ages from the northern part of the Barbertongreenstone belt, South Africa: implications for the formation of Mesoarchaean gold deposits. Precambrian Research, 179, 206–220.

Eisenlohr, B.N., Groves, D., Partington, G.A., 1989. Crustal–scale shear zones and their significance to Archaean gold mineralization in Western Australia. Mineralium Deposita, 24, 1–8.

Eisenlohr, B.N., Hirdes, W., 1992. The structural development of the early Proterozoic Birimian and Tarkwaian rocks of southwest Ghana, West Africa. Journal of African Earth Sciences, 14, 313–325.

Fetter, A. H., Santos, T.J.S., Van Schumus, W.R.,Hackspacher, P.C., Brito Neves, B.B., Arthaud, M.H., Nogueira Neto, J.A., Wernick, E. 2003. Evidence for Neoproterozoic continental arc magmatism in the Santa Quitéria Batholith of Ceará State, NW Borborema Province, NE Brazil: implications for the assembly of west Gondwana. Gondwana Research, 6(2): 265–273.

Fetter, A.H., 1999. U/Pb and Sm/Nd Geocronological Constraints on the Crustal Framework and Geologic History of Ceará State, NW Borborema Province, NE Brazil: Implications for the Assembly of Gondwana. PhD Thesis, Departament of Geology, Kansas University, Lawrence, 164p.

Fetter, A.H., Van Schmus, W.R., Santos, T.J.S., Nogueira Neto, J.A., Arthaud, M.H., 2000. U–Pb and Sm–Nd geochronological constraints on the crustal evolution and basement architecture of Ceará State, NW Borborema Province, NE Brazil: implications for the existence of the Paleoproterozoic Supercontinent “Atlantica”. Revista Brasileira de Geociências, 30 (1), 102–106.

Feybesse, J.L., Billa, M., Guerrot, C., Duguey, J.L.L., Milesi, J.P., Bouchot, V., 2006. The Palaeoproterozoic Ghanaian province: geodynamic model and ore controls, including regional stress modeling. Precambrian Research, 149, 149–196.

Fielding, I.O.H., Johnson, S.P., Zi, J.W., Rasmussen, B., Muhling, J.R., Dunkley, D.J., Sheppard, S., Wingate, M.T.D., Rogers, J.R., 2017. Using in situ SHRIMP U–Pb monazite and xenotime geochronology to determine the age of orogenic gold mineralization: an example from the paulsens mine, southern Pilbara craton. Economic Geology, 112, 1205–1230.

Fielding, I.O.H., Johnson, S.P., Zi, J.W., Sheppard, S., Rasmussen, B., 2018. Neighbouring orogenic gold deposits may be the products of unrelated mineralizing events. Ore Geology Reviews, 95, 593–603.

Fortes, P.T.F.O., Cheilletz, A., Giuliani, G., Féraud, G., 1997. A Brasiliano age (500±5 Ma) for the Mina III gold deposit, Crixás greenstone belt, central Brazil. International Geology Reviews, 39, 449–460.

Fortes, P.T.F.O., Pimentel, M.M., Santos, R.V., Junges, S.L., 2003. Sm–Nd studies at Mina III gold deposit, Crixás greenstone belt, Central Brazil: implications for the depositional age of the upper metasedimentary rocks and associated Au mineralization. J. South Am. Earth Sci. 16, 503–512.

Fossen, H., Teyssier, C., Whitney, D.L., 2013. Transtensional folding. Journal of Structural Geology, 56, 89–102.

Foster, C.T., 1991. The role of biotite as a catalyst in reaction mechanisms that form sillimanite. The Canadian Mineralogist, 29 (4), 943–963.

Freimann, M.A., 2014. Geocronologia e Petrotrama de quartzo milonitos do duplex transcorrente de Lavras da Mangabeira. Master Dissertation, Universidade de São Paulo, São Paulo–SP, 84 p.

Ganade, C.E.G., Basei, M.A.S., Grandjean, F.C., Armstrong, R., Brito, R.S., 2017. Contrasting Archaean (2.85–2.68 Ga) TTGs from the Tróia Massif (NE–Brazil) and their geodynamic implications for flat to steep subduction transition. Precambrian Research, 297, 1–18.

Garcia, M.G.M., Santos, T.J.S., Amaral, W.S., 2014. Provenance and tectonic setting of neoproterozoic supracrustal rocks from the Ceará Central Domain, Borborema Province (NE Brazil): constraints from geochemistry and detrital zircon ages. International Geology Review, 56 (4), 1–20.

Gazley, M F, 2011. Metamorphism, geochronology and stratigraphy of an amphibolite–facies greenstone–hosted gold deposit: Plutonic Gold Mine, Marymia Inlier, Western Australia. PhD thesis, Victoria University of Wellington, New Zealand.

Gazley, M.F., Vry, J.K., Millet, M.A., Handler, Plessis, E.D., Baker, J.A., 2016. New age constraints on metamorphism, metasomatism and gold mineralisation at Plutonic Gold Mine, Marymia Inlier, Western Australia. Australian Journal of Earth Sciences, 63 (4), 413–426.

Gazley, M.F., Vry, J.K., Pearce, M.A., 2014. Further evidence for ~8 kbar amphibolite facies metamorphism in the Marymia Inlier, Western Australia. Australian Journal of Earth Science, 61, 919–926.

Gerdes, A., Zeh, A., 2006. Combined U–Pb and Hf isotope LA–(MC)–ICP–MS analyses of detrital zircons: comparison with SHRIMP and new constraints for the provenance and age of an Armorican metasediment in Central Germany. Earth and Planetary Science Letters, 249 (1–2), 47–61.

Gervais, F., Hynes, A., 2013. Linking metamorphic textures to U–Pb monazite in–situ geochronology to determine the age and nature of aluminosilicate–forming reactions in the northern Monashee Mountains, British Columbia. Lithos, 160, 250–267.

Goldfarb, R.J., André–Mayer, A.–S., Jowitt, S.M., Mudd, G.M., 2017. West Africa: the world's premier paleoproterozoic Gold Province. Econ. Geol. 112, 123–143.

Gomes, E.N., 2013. Protominérios e minérios de manganês de Juá–CE. Master Dissertation, Universidade Federal do Ceará (UFC), Ceará–CE, p. 102.

Groves, D.I, Goldfarb, R.J., Santosh, M., 2016. The conjunction of factors that lead to formation of giant gold provinces and deposits in non–arc settings. Geoscience Frontiers, 7 (3), 303–314.

Groves, D.I., 1993. The crustal continuum model for late–Archaean lode gold deposits of the Yilgarn block, Western Australia. Mineralium Deposita 28, 366–374.

Groves, D.I., Goldfarb, R.J., Gebre–Mariam, M., Hagemann, S.G., Robert, F., 1998. Orogenic gold deposits: A proposed classification in the context of their crustal distribution and relationship to other gold deposit types. Ore Geology Reviews 13, 7–27.

Groves, D.I., Goldfarb, R.J., Knox–Robinson, C.M., Ojala, J., Gardoll, S., Yun, G.Y., Holyland, P., 2000. Late–kinematic timing of orogenic gold deposits and significance for computer based exploration techniques with emphasis on the Yilgarn block, Western Australia: Ore Geology Reviews, 17, 1–38.

Groves, D.I., Phillips, G.N., Ho, S.E., Houston, S.M., Standing, C.A., 1987. Craton–scale distribution of Archean greenstone gold deposits: predictive capacity of the Metamophic Model. Economic Geology, 82, 2045–2058.

Groves, D.I., Santosh, M., 2015. Province–scale commonalities of some world–class gold deposits: Implications for mineral exploration. Geoscience Frontiers, 6 (3), 389–399.

Groves, D.I., Santosh, M., Goldfarb, R.J., Zhang, L., 2018. Structural geometry of orogenic gold deposits: Implications for exploration of world–class and giant deposits. Geoscience Frontier, 9, 1163–1177.

Hammond, N.Q., Robb, L.J., Foya, S., Ishiyama, D., 2011. Mineralogical, fluid inclusions and stable isotope characteristics of Birimian orogenic gold mineralization at the Morila mine, Mali, West Africa: Ore Geology Reviews, 39, 218–229.

Heaman, L.M. 2009. The application of U–Pb geochronology to mafic, ultramafic and alkaline rocks: an evaluation of three mineral standards. Chemical Geology, 261, 42–51.

Henne, A., Craw, D., 2012. Synmetamorphic carbon mobility and graphite enrichment in metaturbidites as a precursor to orogenic gold mineralisation, Otago Schist, New Zealand. Mineralium Deposita, 47, 781–797.

Hollanda, M.H.B.M., Archanjo, C.J., Bautista, J.R., Souza, L.C., 2015. Detrital zircon ages and Nd isotope compositions of the Seridó andLavras da Mangabeira basins (Borborema Province, NE Brazil): Evidence for exhumation and recycling associated with a major shift in sedimentary provenance. Precambrian Research, 258, 186–207.

Hollanda, M.H.B.M., Archanjo, C.J., Souza, C.L., Dunyi, L., Armstrong, R., 2011. Long–lived Paleoproterozoic granitic magmatism in the Seridó–Jaguaribe domain, Borborema Province – NE Brazil. J. South Am. Earth Sci., 32 (4), 287–300.

Hronsky, J.M.A., Groves, D.I., Loucks, R.R., Begg, G.C., 2012. A unified model for gold mineralisation in accretionary orogens and implications for regional scale targeting methods. Mineraliun Deposita, 47, 339–358.

Hu, S.Y., Evans, K., Craw, D., Rempel, K., Grice, K., 2017. Resolving the role of carbonaceous material in gold precipitation in metasediment–hosted orogenic gold deposits. Geology, 45 (2), 167–170.

Hutchinson, R.W., 1987. Metallogeny of Precambrian gold deposits: space and time relationships. Economic Geology, 90, 1918–1933.

Jackson, S.E., Pearson, N.J., Griffin, W.L., Belousova, E.A., 2004. The application of laser ablation–inductively coupled plasma–mass spectrometry to in situ U–Pb zircon geochronology. Chem. Geol., 211, 47–69.

Jost, H., Chemale, F., Dussin, I.A., Martins, R.A., 2010. U–Pb zircon Paleoproterozoic age for the metasedimentary host rocks and gold mineralization of the Crixás greenstone belt, Goiás, Central Brazil. Ore Geology Reviews , 37, 127–139.

Kirkland, C.L., Spaggiari, C., Johnson, T., Smithies, R., Danišík, M., Evans, N., Wingate, M., Clark, C., Spencer, C., Mikucki, E., McDonald, B.J., 2016. Grain size matters: Implications for element and isotopic mobility in titanite. Precambrian Research, 278, 283–302.

Kirkland, C.L., Spaggiari, C., Smithies, R.H., Wingate, M.T.D., Belousova, E.A., Gréau, Y., Sweetapple, M.T., Watkins, R., Tessalina, S., Creaser, R., 2015. The affinity of Archean crust on the Yilgarn—Albany–Fraser Orogen boundary: implications for gold mineralisation in the Tropicana Zone. Precambrian Research, 266, 260–281.

Klein, E.L., 2014. Ore fluids of orogenic gold deposits of the Gurupi Belt, Brazil: a review of the physico–chemical properties, sources, and mechanisms of Au transport and deposition. In: Garofalo, P. S., Ridley, J. R. (eds). Gold–Transporting Hydrothermal Fluids in the Earth's Crust. Geological Society, London, Special Publications, 402, 121–145.

Klein, E.L., Harris, C., Giret, A., Moura, C.A.V., Angélica, R.S., 2005. Geology and stable isotope (O, H, C, S) constraints on the genesis of the Cachoeira gold deposit, Gurupi Belt, northern Brazil. Chemical Geology, 221, 188–206.

Klein, E.L., Harris, C., Renac, C., Giret, A., Moura, A.V., Fuzikawa, K., 2006. Fluid inclusion and stable isotope (O, H, C, and S) constraints on the genesis of the Serrinha gold deposit, Gurupi Belt, northern Brazil. Mineralium Deposita, 41, 160–178.

Klein, E.L., Lucas, F.R.A., Queiroz, J.D.S., Freitas, S.C.F., Renac, C., Galarza, M.A., Jourdan, F., Armstrong, R., 2015. Metallogenesis of the Paleoproterozoic Piaba orogenic gold deposit, São Luís cratonic fragment, Brazil. Ore Geology Reviews, 65 (1), 1–25.

Klein, E.L., Moura, C.A.V., 2008. São Luís craton and Gurupi belt (Brazil): possible links with the West African craton and surrounding Pan–African belts. In: Pankhurst, R.J., Trouw, R.A.J., Brito Neves, B.B., de Wit, M.J. (Eds.), West Gondwana: Pre–Cenozoic Correlations across the South Atlantic Region. Geological Society, London, Special Publications, 294, 137–151.

Klein, E.L., Rodrigues, J.B., Lopes, E.C.S., Soledade, G.L., 2012. Diversity of Rhyacian granitoids in the basement of the Neoproterozoic–Early Cambrian Gurupi Belt, northern Brazil: geochemistry, U–Pb zircon geochronology, and Nd isotope constraints on the Paleoproterozoic magmatic and crustal evolution. Precambrian Research, 220–221, 192–216.

Klein, E.L., Tassinari, C.G., Vasconcelos, P.M., 2014. U–Pb SHRIMP and $^{40}Ar/^{39}Ar$ constraints on the timing of mineralization in the Paleoproterozoic Caxias orogenic gold deposit, São Luís cratonic fragment, Brazil. Brazilian Journal of Geology, 44 (2), 277–288.

Kolb, J., Dziggel, A., Bagas, L., 2015. Hypozonal lode gold deposits: a genetic concept based on a review of the New Consort, Hutti, Hira Buddini, Navachab, Nevoria, and the Granites deposits. Precambrian Research, 262, 20–44.

Kolb, J., Hellmann, A., Rogers, A., Sindern, S., Vennemann, T.W., Bottcher, M.E., Meyer, F.M., 2004. The role of a transcrustal shear zone in orogenic gold mineralization at the Ajjanahalli Mine, Dharwar Craton, south India. Economic Geology, 99, 743–759.

Kolb, J., Kisters, A.F.M., Hoernes, S., Meyer, F.M., 2000. The origin of fluids and nature of fluid–rock interaction in auriferous mylonites of the Renco Mine, southern Zimbabwe. Miner. Depos. 35 (1), 109–125.

Kolb, J., Meyer, F.M., 2002. Fluid inclusion record of the hypozonal orogenic Rencogold deposit (Zimbabwe) during the retrograde P–T evolution. Contrib. Mineral.Petrol. 143, 495–509.

Krabbendam, M., Dewey, J. F., 1998. Exhumation of UHP rocks by transtension in the Western Gneiss Region, Scandinavian Caledonides. Geological Society, London, Special Publications, 135(1), 159–181.

Krienitz, M.S., Trumbull, R.B., Hellmann, A., Kolb, J., Meyer, F.M., Wiedenbeck, M., 2008. Hydrothermal gold mineralization at the Hira Buddini gold mine, India: constraints on fluid evolution and fluid sources from boron isotopic compositions of tourmaline. Miner. Depos., 43, 421–434.

Larionova, Y.O., Samsonov, K.N., Shatagin, K.N., Nosova, A.A., 2013. Isotopic Geochronological Evidence for the Paleoproterozoic Age of Gold Mineralization in Archean Greenstone Belts of Karelia, the Baltic Shield. Geology of Ore Deposits, 55, 320–340.

Lawley, C.J.M., Creaser, R., Jackson, S., Yang, Z., Davis, B., Pehrsson, S., Dubé, B., Mercier–Langevin, P., Vaillancourt, D., 2015. Unravelling the Western Churchill Province Paleoproterozoic gold metallotect: constraints from Re–Os arsenopyrite and U–Pb xenotime geochronology and LA–ICP–MS arsenopyrite geochemistry at the BIF–Hosted Meliadine Gold District, Nunavut, Canada. Economic Geology, 110, 1425–1454.

Lawley, C.J.M., McNicoll, V., Sandeman, H., Pehrsson, S., Simard, M., Castonguay, S., Mercier–Langevin, P., Dubé, B., 2016. Age and geological setting of the Rankin Inlet greenstone belt and its relationships to the gold endowment of the Meliadine gold district, Nunavut, Canada. Precambrian Research, 275, 471–495.

Lawley, C.J.M., Selby, D., Condon, D., Imber, J., 2014. Palaeoproterozoic orogenic gold style mineralization at the Southwestern Archaean Tanzanian cratonic margin, Lupa Goldfield, SW Tanzania: Implications from U–Pb titanite geochronology. Gondwana Research, 26 (3–4), 1141–1158.

Leube, A., Hirdes, W., Mauer, R., Kesse, G., 1990. The early Proterozoic Birimian Supergroup of Ghana and some aspects of its associated mineralization: Precambrian Research, 46, 139–165.

Li, S.R., Santosh, M., 2017. Geodynamics of heterogeneous gold mineralization in the North China Craton and its relationship to lithospheric destruction. Gondwana Research 50, 267–292.

Liégeois, J.P., Claessens, W., Camara, D., Klerkx, J., 1991. Short–lived Eburnean orogeny in southern Mali. Geology, tectonics, U–Pb and Rb–Sr geochronology. Precambrian Research, 50, 111–136.

Lopez, J.M., 2012. Programa de exploração mineral do grupo Jaguar Mining Inc. Simpósio de Exploração Mineral – SIMEXMIN, Ouro Preto, Minas Gerais.

Ludwig, K.R. 2012. Isoplot/Ex Version 3.75: A Geochronological toolkit for Microsoft Excel. Berkeley, CA, Berkeley Geochronology Center Special Publication, 5, 72 p.

Martins, G., 2000. Litogeoquímica e Controles Geocronológicos da Suíte Metamórfica Algodões–Choró. Phd Thesis. Universidade Estadual de Campinas, Campinas–SP, p. 220.

Martins, B.S., Lobato, L.M, Rosière, C.A., Hagemann, S.G., Santos, J.O., Villanova, F.L., Silva, R.C., Lemos, L.H., 2016. The Archean BIF-hosted Lamego gold deposit, Rio das Velhas greenstone belt, Quadrilátero Ferrífero: Evidence for Cambrian structural modification of an Archean orogenic gold deposit. Ore Geology Reviews, 72, 963–988.

Martins, G., Oliveira, E.P., Lafon, J.M., 2009. The Algodões amphibolite–tonalite gneiss sequence, Borborema Province, NE Brazil: geochemical and geochronological evidence for Paleoproterozoic accretion of oceanic plateu/back–arc basalts and adakitic plutons. Gondwana Res. 15, 71–85.

McMillan, N.M., 1996. Late–Archaean, syn–amphibolite facies, lode–gold deposits overprinted by Palaeoproterozoic deformation, metasomatism and hydrothermal activity at Marymia, Western Australia. PhD Dissertation. Perth WA: University of Western Australia. Perth, Western Australia.

McReath, I., Faraco, M.T.L., 2006. Paleoproterozoic greenstone–granite belts in northern Brazil and the former Guyana Shield–West African craton province. Geologia USP. Série Científica, 5 (2), 49–63.

Medeiros, V.C., Medeiros, W.E., Jardim de Sá, E.F., 2011. Utilização de imagens aerogamaespestrométricas, Landsat 7 ETM+ e aeromagnéticas no estudo do arcabouço crustal da porção central do domínio da Zona Transversal, Província Borborema, NE do Brasil. Revista Brasileira de Geofísica. 29 (1). 83-97.

Mello, E.F., Xavier, R.P., McNaughton, N.J., Hagemann, S.G., Fletcher, I., Snee, L., 2006. Age constraints on felsic intrusions, metamorphism and gold mineralization in the Palaeoproterozoic Rio Itapicuru greenstone belt, NE Bahia State, Brazil. Miner. Deposita 40, 849–866.

Mignot, E.L., Reisberg, L., André–Mayer, A.S., Bourassa, Y., Fointaine, A., Miller, J., 2017. Re–Os Geochronological Evidence for Multiple Paleoproterozoic Gold Events at the Scale of the West African Craton. Economic Geology, 112, 145–168.

Molnár, F, O'Brien, H., Lahaye, Y., Käpyaho, A., Sorjonen–Ward, P., Hyodo, H., Sakellaris, G., 2016. Signatures of Multiple Mineralization Processes in the Archean Orogenic Gold Deposit of the Pampalo Mine, Hattu Schist Belt, Eastern Finland. Economic Geology, 111, 1659–1703.

Monié, P., Caby, R., Arthaud, M.H., 1997. The Neoproterozoic Brasiliano Orogeny in Northeast Brazil: $^{40}Ar/^{39}Ar$ and petrostructural data from Ceará. Precambrian Research, 81, 241–264.

Morelli, R.M., Bell, C.C., Creaser, R.A., 2010. Constraints on the genesis of gold mineralization at the Homestake Gold Deposit, Black Hills, South Dakota from rhenium–osmium sulfide geochronology. Mineralium Deposita, 45, 461–480.

Morey, A.A., Weinberg, R.F., Bierlein, F.P., 2007. The structural controls of gold mineralization within the Bardoc Tectonic Zone, Eastern Goldfields Province, Western Australia: implications for gold endowment in shear systems. Mineralium Deposita, 42 (6), 583–600.

Mueller, A.G., Hall, G.C., Nemchin, A.A., Stein, H.J., Creaser, R.A., Mason, D.R., 2008. Archean high–Mg monzodiorite–syenite, epidote skarn, and biotite–sericite gold lodes in the Granny Smith–Wallaby district, Australia: U–Pb and Re–Os chronology of two intrusion–related systems. Mineralium Deposita, 43, 337–362.

Mueller, A.G., Nemchin, A.A., Frei, R., 2004. The Nevoria gold skarn deposit, Southern Cross Greenstone Belt. Western Australia: II. Pressure–temperature–time path and relationship to post–orogenic granites. Econ. Geol., 99, 453–478.

Muhling, J.R., 1988. The Early to Middle Proterozoic of Australia. The nature of Proterozoic reworking of early Archaean gneisses, Mukalo Creek Area, Southern Gascoyne Province, Western Australia. Precambrian Research. 40, 341–362.

Muhling, J.R., 1990. The Narryer Gneiss Complex of the Yilgarn Block, Western Australia: A segment of Archaean lower crust uplifted during Proterozoic orogeny. Journal of Metamorphic Geology, 8, 47–64.

Naleto, J.L.C., Perrota, M.M., Corrêa Costa, M.A., Mendes, D., 2018. Espectroscopia mineral e mineralização aurífera. In: Costa, F.G., Naleto, J.L.C., Calado, B.O., 2018. Geologia e mineralização aurífera da sequência metavulcanossedimentar da Serra das Pipocas, Maciço de Troia, Ceará. Áreas de Relevante Interesse Mineral – ARIM, Serviço Geológico do Brasil (CPRM), 106p.

Naleto, J.L.C., Perrotta, M.M., Souza Filho, C.R., Costa, F.G., 2016. Caracterização Espectro–Mineralógica da Assembleia Hidrotermal Associada à Mineralização de Ouro na Serra das Pipocas, Sequência Metavulcanossedimentar de Troia, Ceará. In: 48º Congresso Brasileiro de Geologia, 2016, Porto Alegre–RS.

Neves, S.P., 1991. A zona de cisalhamento Tauá, Ceará: Sentido e estimativa do deslocamento, evolução estrutural e granitogênese associada. Revista Brasileira de Geociências, 21 (2), 161–173.

Neves, S.P., 2003. Proterozoic history of the Borborema province (NE Brazil): Correlations with neighboring cratons and Pan–African belts and implications for the evolution of western Gondwana. Tectonics, 22 (4), p. 1031.

Neves, S.P., 2015. Constraints from zircon geochronology on the tectonic evolution of the Borborema Province (NE Brazil): Widespread intracontinental Neoproterozoic reworking of a Paleoproterozoic accretionary orogeny. J. South Am. Earth Sci., 58, 150–164.

Nogueira, J.F., 2004. Estrutura, geocronologia e alojamento dos batólitos de Quixadá, Quixeramobim e Senador Pompeu – Ceará Central. PhD Thesis, Universidade Estadual Paulista (UNESP), Rio Claro–SP. 123p.

Norcross, C., Davis, D.W., Spooner, E.T.C., Rust, A., 2000. U–Pb and Pb– Pb age constraints on Paleoproterozoic magmatism, deformation and gold mineralization in the Omai area, Guyana Shield. Precambrian Research, 102, 69–86.

O'Driscoll, E.S.T., 1986. Observations of the lineament–ore relation. Phil. Trans. Roy. Soc. Lond. A., 317, 195–218.

Oliveira, E.P., Souza, Z.S., McNaughton, N., Lafon, J.M., Costa, F.G., Figueiredo, A.M., 2011. The Rio Capim volcanic–plutonic–sedimentary belt, São Francisco Craton, Brazil: geological, geochemical and isotopic evidence for oceanic arc accretion during Palaeoproterozoic continental collision. Gondwana Research, 19 (3), 735–750.

Oliveira, J.F., Cavalcante, J.C., 1993. Programa Levantamentos Geológicos Básicos do Brasil; Mombaça, Folha SB.24–V–D–V, Estado do Ceará, Escala 1:100.000, Texto Explicativo. Brasília, DNPM/CPRM, 195p.

Oliveira, R.G., 2008. Arcabouço Geofísico, Isostasia e Causas do Magmatismo Cenozóico da Província Borborema e de Sua Margem Continental (Nordeste do Brasil). Ph.D. Thesis. Universidade Federal do Rio Grande do, Norte, Natal, pp. 411.

Oliveira, R.G., Medeiros, W.E., 2018. Deep crustal framework of the Borborema Province, NE Brazil, derived from gravity and magnetic data. Precambrian Research, 315, 45–65.

Oliver, J., Ayer, J., Dubé, B., Aubertin, R., Burson, M., Panneton, G., Friedman, R., Hamilton, M., 2012. Structure, Stratigraphy, U–Pb Geochronology and Alteration Characteristics of Gold Mineralization at the Detour Lake Gold Deposit, Ontario, Canada. Exploration and Mining Geology, 20, 1–30.

Otto, A., Dziggel, A., Kisters, A.F.M., Meyer, F.M., 2007. The New Consort gold mine, Barberton greenstone belt, South Africa: orogenic gold mineralization in a con–densed metamorphic profile. Miner. Depos. 42, 715–735.

Padilha, A.L., Vitorello, Í., Pádua, M.B., Bologna, M.S., 2014. Electromagnetic constraints for subduction zones beneath the northwest Borborema province: Evidence for Neoproterozoic island arc–continent collision in northeast Brazil. Geology 42, 91–94.

Padilha, A.L., Vitorello, I., Pádua, M.B., Fuck, R., 2017. Cryptic signatures of Neoproterozoic accretionary events in northeast Brazil imaged by magnetotellurics: Implications for the assembly of West Gondwana. Tectonophysics, 699, 164–177.

Perring, C.S., McNaughton, N.J., 1990. Geological note: Proterozoic remobilization of ore metals within Archaean gold deposits: Lead isotope evidence from Norseman, Western Australia: Australian Journal of Earth Sciences, 37, 369–372.

Pessoa, R.R., Archanjo, C.J., 1984. Tectônica de empurrões na região de Tróia–CE. Congresso Brasileiro de Geologia, 33, Rio de Janeiro: SGB, 1721–1728.

Pessoa, R.R., Brito Neves, B.B., Kawashita, K., Pessoa, D.R., Fuck, R.A., 1986. Contribuição ao estudo de evolução geocronológica do Maciço de Troia – CE. 12 Simpósio de Geologia do Nordeste, João Pessoa, p.1721–1728.

Petersson, A., Scherstén, A., Gerdes, A., 2017. Extensive reworking of Archaean crust within the Birimian terrane in Ghana as revealed by combined zircon U–Pb and Lu–Hf isotopes. Geoscience Frontier, (in press).

Petersson, A., Scherstén, A., Kemp, A.I.S., Kristinsdóttir, B., Kalvig, P., Anum, S., 2016. Zircon U–Pb–Hf evidence for subduction related crustal growth and reworking of Archaean crust within the Palaeoproterozoic Birimian terrane, West African Craton, SE Ghana. Precambrian Research, 275, 286–309.

Phillips, G.N., Powell, R., 2010. Formation of gold deposits: A metamorphic devolatilization model: Journal of Metamorphic Geology, 28, 689–718.

Pinéo, T.R.G., Costa, F.G., 2013. Dados aerogamaespectrométricos aplicados na delimitação do Complexo Cruzeta (Maciço arqueano de Tróia), Domínio Ceará Central da Província Borborema. In: 13th International Congress of the Brazilian Geophysical Society, Rio de Janeiro, Brazil, p. 5.

Queiroz, C.L., McNaughton, N., Fletcher, I., Jost, H., Barley, M.E., 2000. Polymetamorphic History of the Crixás–Açu Gneiss, Central Brazil: SHRIMP U–Pb Evidence from Titanite and Zircon. Revista Brasileira de Geociências, 30 (1), 40–44.

Robert, F., 1990. The internal structure of the Cadillac tectonic zone southeast of Val d'Or, Abitibi Belt, Quebec. Can. J. Earth Sc., 26, 2661–2675.

Rogers, A.J., Kolb, J., Meyer, F.M., Vennemann, T., 2013. Two stages of gold mineralization at Hutti mine, India Mineralium Deposita, 48, 99–114.

Rosa–Costa, L.T., Lafon, J.M., Delor, C., 2006. Zircon geochronology and Sm–Nd isotopic study: further constraints for the Archean and Paleoproterozoic geodynamical evolution of the southeastern Guiana Shield, north of Amazonian Craton, Brazil. Gondwana Research, 10 (3–4), 277–300.

Sahoo, A.K., Krishnamurthi, R., Sangurmath, P., 2018. Nature of ore forming fluids, wallrock alteration and P–T conditions of gold mineralization at Hira–Buddini, Hutti–Maski Greenstone Belt, Dharwar Craton, India. Ore Geology Review, 99, 195–216.

Sahoo, P.R., Venkatesh, A.S., 2014. 'Indicator' carbonaceous phyllite/graphitic schist in the Archean Kundarkocha gold deposit, Singhbhum orogenic belt, eastern India: Implications for gold mineralization vis–a–vis organic matter. Journal of Earth System Science, 123 (7), 1693–1703.

Santos, L.C.M.L., Dantas, E.L., Cawood, P.A., Santos, E.J., Fuck, R.A., 2017. Neoarchean crustal growth and Paleoproterozoic reworking in the Borborema Province, NE Brazil: Insights from geochemical and isotopic data of TTG and metagranitic rocks of the Alto Moxotó Terrane. Journal of South American Earth Science, 79, 342–363.

Santos, R.V., Oliveira, C.G., Parente, C.V. Garcia, M.G.M., Dantas, E.L., 2013. Hydrothermal alteration related to a deep mantle source controlled by a Cambrian intracontinental strike–slip fault: Evidence for the Meruoca felsic intrusion associated with the Transbraziliano Lineament, Northeastern Brazil. Journal of South American Earth Science, 43, 33–41.

Santos, T.J.S., Amaral, W.S., Ancelmi, M.F., Pitarello, M.Z., Fuck, R.A., Dantas, E.L., 2015. U–Pb age of the coesite–bearing eclogite from NW Borborema Province, NE Brazil: Implications for western Gondwana assembly. Gondwana Research, 28, 1183–1196.

Santos, T.J.S., Fetter, A.H., Nogueira Neto, J.A., 2008. Comparison between the northwestern Borborema Province, NE Brazil, and the southwestern Pharusian Dahomey Belt, SW Central Africa. In: Pankhurst, R.J., Trouw, R.A.J., Brito Neves, B.B., de Wit, M.J. (Eds.), West Gondwana: Pre–Cenozoic Correlations across the South Atlantic Region, vol. 294. Geological Society of London, pp. 101–119. Special Publications.

Scott, D.J., St–Onge, M.R., 1995. Constraints on Pb closure temperature in titanite based on rocks from the Ungava orogen, Canada: Implications for U–Pb geochronology and PTt path determinations. Geology, 23 (12), 1123–1126.

Silva, L.C., Armstrong, R., Pimentel, M.M., Scandolara, J., Ramgrab, G., Wildner, W., Angelim, L.A.A., Vasconcelos, A.M., Rizzoto, G., Quadros, M.L.E.S., Sander, A., Rosa, A.L.Z., 2002. Reavaliação da evolução geológica em terrenos Pré–Cambrianos brasileiros com base em novos dados U–Pb SHRIMP, Parte III: Província Borborema, Mantiqueira Meridional e Rio Negro–Juruena. Rev. Bras. Geociências 32, 529–544.

Silva, L.C., Costa, F.G., Armstrong, R., McNaugthon, N.J., 2014. U–Pb (SHRIMP) zircon dating and Nd isotopes at basement inliers from northern Borborema Province, Ceará State, NE Brazil: evidences for the Archean and Paleoproterozoic crustal evolution. In: 9th South American Symposium on Isotope Geology, São Paulo, Brazil, p. 175.

Silva, L.C., MacNaughton, N.J., Vasconcelos, A.M., Gomes, J.R.C., Fletcher, I.R., 1997. U–Pb SHRIMP ages in southern State of Ceará, Borborema Province, NE Brazil: Archean TTG accretion and Proterozoic crustal reworking. Second International Symposium on Granites and Associated Mineralizations, Salvador, 280p.

Silva, M.G., Coelho, C.E.S., Teixeira, J.B.G., Alves da Silva, F.C., Silva, R.A., Souza, J.A.B., 2001. The Rio Itapicuru greenstone belt, Bahia, Brazil: geologic evolution and review of gold mineralization. Miner. Deposita, 36, 345–357.

Sousa, H.P., 2016. Caracterização das unidades máfica–ultramáficas e potencial metalogenético da sequência metavulcanossedimentar Serra das Pipocas (Ceará): um provável greenstone belt. Master Dissertation, Universidade Federal do Ceará, Ceará–CE, 203 p.

Souza, Z.S., Kalsbeek, F., Deng, X.D., Frei, R., Kokfelt, T.F., Dantas, E.L., Li, J.W., Pimentel, M.M., Galindo, A.C., 2016. Generation of continental crust in the northern part of the Borborema Province, northeastern Brazil, from Archaean to Neoproterozoic. J. South Am. Earth Sci. 68, 68–96.

Souza, Z.S., Martin, H., Peucat, J.J., Jardim de Sá, E.F., Macedo, M.H.F., 2007. Calc–alkaline magmatism at the Archean–Proterozoic transition: the Caicó complex basement (NE Brazil). J. Petrol. 48, 2149–2185.

Spector, A., Grant, F.S., 1970. Statistical models for interpreting aeromagnetic data. Geophysics, 35, 293-302.

Spencer, K.J., Hacker, B.R., Kylander–Clark, A.R.C., Andersen, T.B., Cottle, J.M., Stearns, M.A., Poletti, J.E., Seward, G.G.E., 2013. Campaign–style titanite U–Pb dating by laserablation ICP: Implications for crustal flow, phase transformations and tita0nite closure. Chem. Geol., 341, 84–101.

Stacey, J.S., Kramers, J.D., 1975. Approximation of terrestrial lead isotope evolution by a two–stage model. Earth Planet. Sci. Lett., 26, 207–221.

Stearns, M.A., Hacker, B.R., Ratschbacher, L., Rutte, D., Kylander–Clark, A.R.C., 2015. Titanite petrochronology of the Pamir gneiss domes: Implications for mid–deep crust exhumation and titanite closure to Pb and Zr diffusion. Tectonics, 34, 1–19.

Tassara, S., González–Jiménez, J.M., Reich, M., Schilling, M.E., Morata, D., Begg, G., Saunders, E., Griffin, W.L., O'Reilly, S.Y., Grégoire, M., Barra, F., Corgne, A., 2017. Plume–subduction interaction forms large auriferous provinces. Nat. Comms. 8, 843.

Tomkins, A.G., Grundy, C., 2009. Upper Temperature Limits of Orogenic Gold Deposit Formation: Constraints from the Granulite–Hosted Griffi n's Find Deposit, Yilgarn Craton: Economic Geology and the Bulletin of the Society of Economic Geologists, 104, 669–685

Torres, P.F.M., Cavalcante, J.C., Palheta, E.S.M., Vasconcelos, A.M., Oliveira, F.V., 2007. Folha Quixadá. Folha SB–24–V–B, Escala 1:250.000. Geologia e Metalogênese. In: Programa Levantamentos Geológicos Básicos do Brasil. Fortaleza: Serviço Geológico do Brasil. CPRM.

Trompette, R. 1994. Geology of western gondwana, Pan–African–Brasiliano aggregation of South América. A.A. Balkema, Rotterdam, Brookfield, 350p.

Van Schumus, W.R., Oliveira, E.P., Da Silva Filho, A., Toteu, S.F., Penaye, J., Guimarães, I.P., 2008. Proterozoic links between the Borborema Province, NE Brazil, and Central African Fold Belt. In: West Gondwana: Pre–Cenozoic Correlations Across the South Atlantic Region, Pankhurst,

R.J., Trouw, R.A.J., Brito Neves, B.B., de Wit, M.J., (eds). Geological Society of London, Special Publications, 294: 69–99.

Vanderhaeghe, O., Ledru, P., Thiéblemont, D., Egal, E., Cocherie, A., Tegyey, M., Milési, J.P., 1998. Contrasting mechanism of crustal growth: geodynamic evolution of the Paleoproterozoic granite–greenstone belts of French Guiana. Precambrian Research, 92 (2), 165–193.

Vauchez, A., Neves, S.P., Caby, R., Corsini, M.E.S., Arthaud, M.H., Amaro, V., 1995. The Borborema shear zone system, NE Brazil. J. South Am. Earth Sci. 8, 247–266.

Verma, S.K., Oliveira, E.P., 2014. Tectonic setting of basic igneous and metaigneous rocks of Borborema Province, Brazil using multi–dimensional geochemical discrimination diagrams. J. South Am. Earth Sci., 58, 309–317.

Vielreicher, N.M., Ridley, J.R., Groves, D. I., 2002. Marymia: An Archean–amphibolite facies–hosted, orogenic lode–gold deposit overprinted by Palaeoproterozoic orogenesis and base metal mineralisation, Western Australia. Mineralium Deposita, 37, 737–764.

Voicu, G., Bardoux, M., Stevenson, R., 2001. Lithostratigraphy, geochronologyand gold metallogeny in the northern Guiana Shield, South America: a review. Ore Geology Reviews, 18, 211–236.

Weinberg, R.F., Hodkiewicz, P.F., Groves, D.I., 2004. What controls gold distribution in Archean terranes? Geology, 32 (7), 545–548.

Wiedenbeck, M., Alle, P., Corfu, F., Griffin, W.L., Meier, M., Oberli, F., Von Quadt, A., Roddick, J.C., Spiegel, W., 1995. Three natural zircon standards for U–Th–Pb, Lu–Hf, trace element and REE analyses. Geostand. Newsl., 19 (1), 1–23.

Witt, W.K., 1993. Lithological and structural controls on gold mineralization in the Archaean Menzies–Kambalda area, Western Australia. Aust. J. Earth. Sci., 40, 65–86.

Zhang, J., Linnen, R., Lin, S., Davis, D., Martin, R., 2014. Paleoproterozoic hydrothermal reactivation in a neoarchean orogenic lode–gold deposit of the southern Abitibi subprovince: U–Pb monazite geochronological evidence from the Young–Davidson mine, Ontario. Precambrian Research, 249, 263–272.

Zhang, J.Q., Li, S.R., Santosh, M., Lu, J., Wang, C.L., 2018. Metallogenesis of Precambrian gold deposits in the Wutai greenstone belt: Constrains on the tectonic evolution of the North China Craton. Geoscience Frontier, 9 (2), 317–333.

Zhou, X., Lin, S., Anderson, S.D., 2016. Stratigraphy, structure and lode gold system at the Central Manitoba mine trend, Rice Lake greenstone belt, Archean Superior Province, Manitoba, Canada. Precambrian Research, 281, 80–100.

5. CONCLUSÕES

Com base nas relações de campo, geocronologia U–Pb, isótopos de Hf, características geoquímicas e correlações regionais, as rochas plutônicas estudadas neste trabalho podem ser divididas em dois grupos principais; (i) tonalitos pré–colisionais (Suíte Mirador) com idade em cerca de 2185 Ma e (ii) granitoides colisionais da Suíte Bananeira, representados por quartzo–monzonitos e granitos (Suíte Bananeira) com idades em torno de 2068 e 2079 Ma, respectivamente. Os tonalitos Mirador são intrusivos apenas na Unidade Inferior do *greenstone belt* da Serra das Pipocas, evidenciando que possuem associação intrínseca com a evolução tectônica da sequência *greenstone*. Idade U–Pb (SHRIMP) em zircão de 2185 ± 4 Ma obtida para um destes plutons evidencia sua evolução precoce no registro riaciano do Maciço Troia. A assinatura geoquímica dos tonalitos Mirador é típica de rochas adakíticas, porem, daqueles derivados de fonte mantélica e com evolução controlada por cristalização fracionada, principalmente de anfibólio. A cristalização fracionada de anfibólio em magmas hidratados derivados do manto pode gerar assinatura similar (ex. alta razão Sr/Y e baixo HREE) à dos adakitos clássicos (derivados da fusão parcial de granada–anfibolitos/eclogitos), e por isso são denominados na literatura internacional como *adakite–like rocks*. As idades modelo (crustal) de Hf em zircão obtidas para estes tonalitos variam entre 2660 e 2800 Ma, evidenciando que componentes de crosta arqueana contribuíram para a gênese do magma, possivelmente por meio da subducção de sedimentos continentais em ambiênte de arco insular.

Os granitóides da Súite Bananeira são intrusivos tanto na sequência *greenstone* paleoproterozoica quanto nas rochas do embasamento arqueano do Maciço Troia. Esses plutons são representados principalmente por quartzo–monzonitos deformados e granitos menos deformados. Para os quartzo–monzonitos, uma idade U–Pb (SHRIMP) em zircão de 2079 ± 4 Ma foi obtida, e sua assinatura geoquímica sugere fusão parcial de uma crosta máfica rica em potássio (*K–rich mafic crust*). Para os granitos, pouco deformados, foi obtida uma idade U–Pb (LA-ICPMS) em zircão de 2068 ± 5 Ma. A assinatura cálcio–alcalina de alto–K e caráter levemente peraluminoso desses granitos sugere fusão parcial de fontes crustais de composição tonalíticas (ex. gnaisses TTG e/ou metagrauvacas). Uma expressiva população de zircões herdados de 2307 ± 14 Ma foi identificada na análise U–Pb (LA-ICPMS) do granito pouco deformado. As idades modelo de Hf nos zircões relacionados à cristalização do granito variam entre 2536 e 2713 Ma, enquanto que, dois grãos de zircão da população herdada de c. 2307 Ma mostraram valores de $\varepsilon_{Hf(t)}$ em torno de +4,8 e idades

modelo de Hf de 2.5 Ga, indicando que estes granitos representam uma combinação de retrabalhamento crustal de rochas arqueanas e fontes paleoproterozoicas menos radiogênicas.

Correlações dos resultados obtidos nesta Tese com o magmatismo plutônico paleoproterozoico na Província Borborema e nos domínios cratônicos circunvizinhos, sugerem que estas rochas plutônicas estão relacionadas ao ciclo orogênico Transamazônico/Eburneano, ativo em cerca de 2.2–2.0 Ga. Neste contexto, a idade de 2185 ± 4 Ma e isótopos de Hf para os tonalitos Mirador sugere que estes se desenvolveram no início deste ciclo, provavelmente em ambiente de arco continental ou em arcos insulares próximos de margem continental, para explicar a contaminação com componentes de crosta arqueana. Similarmente, na compilação dos dados de U–Pb em zircão e isótopos de Nd presentes na literatura para rochas plutônicas riacianas da Província Borborema (não há dados de Hf publicados), a grande maioria também apresenta evidência de retrabalhamento de crosta arqueana na sua gênese (ex. Complexo Caicó, Domínio Rio Grande do Norte). Este fato sugere que grande parte das rochas plutônicas com idades entre 2.22 e 2.15 Ga da Província Borborema se desenvolveram em ambiente de arco continental e/ou em arcos oceânicos instalados próximos de uma margem continental. Adicionalmente, recentes publicações de isótopos de Hf em zircão de granitoides do Domínio Baoulé–Mossi, no Cráton Oeste Africano, evidenciam que componentes de crosta arqueana encontram–se nos granitoides de *greenstone belts* próximos de rochas arqueanas do Domínio Kénéma–Man, ou na porção sul/sudeste do Domínio Baoulé–Mossi, próximo da Província Borborema e do Cráton São Francisco–Congo (**Fig. 2.10**). Nas porções interiores do Domínio Baoulé–Mossi, os dados isotópicos de Hf e Nd evidenciam terrenos com caráter exclusivamente juvenil, mas tonando–se progressivamente mais radiogênico à N/NW e S/SE deste domínio (**Fig. 2.10**). Este fato sugere uma configuração paleocontinental onde os terrenos granito–*greenstone* Birimianos evoluíram bordejados por duas grandes margens continentais ativas, provavelmente em um orógeno acrescionário, similar ao que se tem hoje no "Círculo de fogo do Oceano Pacífico". A evolução do orógeno acrescionário Transamazônico/Eburneano, embora diacrônico, teve seu ápice pré–colisional em torno de 2.22–2.15 Ga, com o consumo e fechamento desde "grande" paleoceano Birimiano, envolvendo arcos intra–oceânicos, arcos continentais e diversos fragmentos (terrenos) arqueanos dos crátons São Luis–Oeste Africano, São Francisco–Congo e Amazônico. A progressiva acresção de arcos e terrenos nas margens continentais finalizou–se com a colisão continental de paleocrátons arqueanos, metamorfismo regional e formação do supercontinente Columbia em torno de 2.0 Ga, acompanhado de um expressivo

magmatismo granítico sin– a pós–colisional, no qual se enquadram os granitoides potássicos da Suíte Bananeira apresentados nesta Tese.

O *greenstone belt* da Serra das Pipocas tem idades e características litoestratigráficas semelhantes a outros terrenos granito–*greenstone* riacianos dos crátons circunvizinhos e também hospeda mineralização aurífera em veios de quartzo, estruturalmente controlados, assim como em muitos dos terrenos correlatos. O limite da sequência *greenstone* com as rochas arqueanas do Maciço de Troia é marcado por zona de cisalhamento e intrusões graníticas alongadas (Suíte Bananeira). Provavelmente, este contato *greenstone*–embasamento, desempenha um papel importante na mineralização aurífera, representando uma estrutura profunda (transcrustal) de primeira ordem. No entanto, as principais áreas mineralizadas estão situadas em zonas de cisalhamento de ordem superior, localizadas paralelamente à estratigrafia da sequência *greenstone*, entre os limites das unidades metavulcânicas máficas e metassedimentares. A mineralização apresenta caráter claramente epigenético, associada a veios de quartzo concordantes e discordantes da foliação das rochas hospedeiras.

Com base nas relações petrográficas apresentadas nesta Tese para o depósito de ouro da Pedra Branca, o principal estágio da mineralização aurífera ocorre em associação com veios de quartzo, alteração de cálcio–silicática (ex. diopsídio, hornblenda, biotita e titanita) e abitização. Nos minerais de alteração, a pirrotita é comumente encontrada como inclusões na pirita, e magnetita tardia substitui a pirita, sugerindo oxidação progressiva do fluido formador de minério. O ouro livre, geralmente contendo 5% de prata, comumente precipita nos últimos estágios de alteração, em íntima associação espacial com magnetita e teluretos de prata e ouro.

Duas assembleias de inclusões fluidas foram identificadas em veios de quartzo associados à alteração cálcio–silicática. A assembléia 1 é caracterizada pela coexistência de inclusões de CO_2-H_2O-NaCl e H_2O-NaCl com baixa salinidade (0 a 8% de NaCl equiv.), e inclusões ricas em CO_2, sugerindo formação durante a separação de fases (imiscibilidade de fluidos). A possível faixa de condições de PT para mineralização de ouro entre 467°C e 1,93 kbar (7 km) e 526°C e 3,48 kbar (13 km) foi obtida pela interseção de isócoras com a faixa de temperatura do geotermômetro isotópico quartzo-magnetita. A assembleia 2 é representada por inclusões fluidas secundárias, aquosas e de baixa temperatura (Th < 200°C), provavelmente não relacionadas à mineralização aurífera.

Os valores de $\delta^{18}O$, δD e $\delta^{13}C$ dos minerais hidrotermais (quartzo, calcita, biotita, hornblenda e magnetita) evidenciam valores de $\delta^{18}O$ do fluido variando de +8,3 a +11,0 ‰

(n=59), δD do fluido de -98 a -32‰ (n=24) e valores de $\delta^{13}C$ de calcita de -6,35 a -9,40 ‰ (n=3). A geotermometria por isótopos de oxigênio em pares de quartzo–magnetita forneceu temperaturas de 467 a 526°C (n=7, média de 503°C), que provavelmente, representa a temperatura de deposição de ouro, em função da íntima associação espacial do ouro com magnetita. A associação de ouro com magnetita e teluretos sugere um fluido formador de minério proveniente de magmas oxidados, semelhante àqueles interpretados como "depósitos de ouro orogênico relacionado a intrusões oxidadas", comumente descrito em outros *greenstone belts* pré–cambrianos (ex., Abitibi e Eastern Goldfields).

A idade U–Pb (LA–ICPMS) em titanita da alteração cálcio–silicática sugere que o principal estágio da mineralização ocorreu em 2029 ± 28 Ma. No entanto, a expressiva perda de chumbo radiogênico, produz uma idade no intercepto inferior do diagrama concórdia de 574 ± 7 Ma, indicando que a mineralização de ouro foi afetada pelo metamorfismo regional neoproterozoico, relacionado à orogênese Brasiliana/Pan-Africana (620–580 Ma).

Quatro eventos de deformação (Dn, Dn+1, Dn+2 e Dn+3) são reconhecidos no *greenstone belt* da Serra das Pipocas. O evento Dn é responsável pela foliação Sn, paralela ao acamamento (So) da pilha metavulcanossedimentar. O evento Dn+1 é caracterizado pela foliação Sn+1, de mergulho principal para SE, sendo plano-axial a uma série de dobras assimétricas que evidenciam transporte tectônico para NW. O evento Dn+2 representa a fase de deformação transcorrente e o evento Dn+3 é caracterizado por deformação dúctil–rúptil. O estágio principal da mineralização de ouro é encontrado em veios de quartzo deformados, associados à alteração de alta temperatura (cálcio–silicática e albitização), no entanto, ocorrência de ouro (± Te, Ag) em estruturas Dn+3 (dúctil-rúptil) também foi observada. A principal deformação registrada (Dn+1, Dn+2 e Dn+3) no Maciço de Troia é provavelmente de idade neoproterozoica, no entanto, em escala local, o registro de deformação paleoproterozoica (Dn) ainda se encontra preservado. Assumindo uma deformação progressiva para Dn+1, Dn+2 e Dn+3, a idade U–Pb (LA–ICPMS) em zircão de 575 ± 3 Ma obtida para os diques Guaribas, sin-tectônicos a deformação Dn+3, indica idade neoproterozoica para deformação (ou pelo menos para o estágio rúptil–dúctil).

Como modelo genético para o depósito de ouro de Pedra Branca, é sugerido aqui, uma mineralização de ouro orogênico controlada por dois estágios de exumação tectônica; (1) inicialmente a mineralização de ouro orogênico hipozonal ocorreu em c. 2029 Ma, após pico do metamorfismo de alto grau e durante primeira exumação tectônica da sequência *greenstone*, e, posteriormente, em c. 575 Ma, (2) mineralização aurífera tardia

(remobilização?) ocorreu em nível crustal mais raso, durante o segundo estágio de exumação tectônica, associado à orogênese Brasiliana/Pan–Africana.

A presença desta mineralização de ouro orogênico hipozonal em *greenstone belt* de fácies anfibolito, sugere que o depósito de Pedra Branca, no Maciço de Troia, representa um equivalente profundo dos depósitos de ouro orogênico mesozonal encontrado nos domínios cratônicos circunvizinhos, frequentemente descrito em *greenstone belts* de fácies xisto verde.

REFERÊNCIAS

Almeida F.F.M., Hasui Y., Brito Neves B.B., Fuck R.A. 1981. Brazilian structural provinces: an introduction. *Earth–Sciences Reviews*, **17**: 1–21.

Amponsah P.O., Salvi S., Didier B., Baratoux L., Siebenaller L., Jessel M., Nude P.M., Gyawu E.A. 2016. Multistage gold mineralization in the Wa-Lawra greenstone belt, NW Ghana: The Bepkong deposit. *Journal of African Earth Sciences*, **120**: 220–237.

Ancelmi M.F. 2016. *Geocronologia e geoquímica das rochas arqueanas do complexo Granjeiro, Província Borborema*. Tese de Doutorado, Instituto de Geociências, Universidade Estadual de Campinas – UNICAMP, Campinas-SP, 159 p.

Angeli N., Bevenutti C.F., Antunes L.A., Campos M.C., Mamani R., 2009. Cromititos do Complexo de Pedra Branca: química mineral e platinóides associados, Ceará, Brasil. *In*: 23º SBG – Núcleo Nordeste, Fortaleza, *Resumos…* 1 CD-ROM.

Arthaud M.H., Caby R., Fuck R.A., Dantas E.L., Parente C.V. 2008. Geology of the northern Borborema Province, NE Brazil and its correlation with Nigeria, NW Africa. *In*: Pankhurst, R.J., Trouw, R.A.J., Brito Neves, B.B., de Wit, M.J. (Eds.), West Gondwana: Pre–Cenozoic Correlations Across the South Atlantic Region, Geological Society of London, vol. 294, p. 49–67. Special Publications.

Arthaud M.H., Fuck R.A., Dantas E.L., Santos T.J.S., Caby R., Armstrong R. 2015. The Neoproterozoic Ceará Group, Ceará Central domain, NE Brazil: Depositional age and provenance of detrital material. New insights from U–Pb and Sm–Nd geochronology. *Journal of South American Earth Sciences*, **58**: 223–237.

Arthaud M.H., Vasconcelos A.M., Nogueira Neto J.A., Oliveira F.V.C., Parente C. V., Monié P., Liégeois J.P., Caby R., Fetter A. 1998. Main Structural Features of Precambrian Domains fron Ceará (NE – Brazil). *In*: 14th International Conference on Basement Tectonics, Ouro Preto-MG, Brasil p. 84–85.

Augustin J., Gaboury D., Crevier M. 2017. Structural and gold mineralizing evolution of the world-class orogenic Mana district, Burkina Faso: Multiple mineralizing events over 150 million years. *Ore Geology Reviews*, **91**: 981–1012.

Barreto C.J.S., Lafon J.M., Rosa-Costa L.T., Dantas E.L. 2013. Paleoproterozoic granitoids from the northern limit of the Archean Amapá block (Brazil), southeastern Guyana Shield: Pb–Pb evaporation in zircons and Sm–Nd geochronology. *Journal of South American Earth Sciences*, **45**: 97–116.

Barrueto H.R. 2002. *Petrogenese das intrusões graniticas compostas de Teofilandia e Barrocas, Greenstone Belt do Rio Itapicuru, Bahia, Brasil*. Tese de doutorado, Universidade Estadual de Campinas, UNICAMP, Campinas–SP, 188 p.

Barrueto H.R. & Hunt W. 2010. Main features of the Pt–Pd chromitite–type ore deposit, Troia Unit, Cruzeta Complex, Northeast Brazil: insights provided by microscopic and chemical approaches. *In*: 11th International Platinum Symposium, Sudbury, Canada.

Beakhouse G.P. 2011. The Abitibi Subprovince plutonic record: Tectonic and metallogenic implications; Ontario Geological Survey, Open File Report 6268, 161p.

Beurlen H., Silva A.F., Guimarães I.P., Barreto S.B., 1992. Proterozoic C-type eclogites hosting unusual Ti-Fe-Cr-Cu mineralization in northeastern Brazil. *Precambrian Research*, **58**: 195–214.

Béziat D., Dubois M., Debat P., Nikiéma S., Salvi S., Tollon F. 2008. Gold metallogeny in the Birrimian craton of Burkina Faso (West Africa). *Journal of African Earth Sciences*, **50**: 215–233.

Bierlein F.P., Murphy F.C., Weinberg R.F., Lees T. 2006. Distribution of orogenic gold deposits in relation to fault zones and gravity gradients: targeting tools applied to the Eastern Goldfields, Yilgarn Craton, Western Australia. *Mineralium Deposita*, **41**: 107–126.

Bierlein F.P. & Pisarevsky S. 2008. Plume-related oceanic plateaus as a potential source of gold mineralisation. *Economic Geology*, **103**: 425–430.

Blenkinsop T.G. & Doyle M.G. 2014. Structural controls on gold mineralization on the margin of the Yilgarn craton, Albany–Fraser orogen: The Tropicana deposit, Western Australia. *Journal of Structural Geology*, **67**(B): 189-204.

Block S., Baratoux L., Zeh A., Laurent O., Bruguier O., Jessell M., Ailleres L., Sagna R., Parra–Avila L.A., Bosch D. 2016. Paleoproterozoic juvenile crust formation and stabilisation in the south–eastern West African Craton (Ghana); New insights from U–Pb–Hf zircon data and geochemistry. *Precambrian Research*, **287**: 1–30.

Brito Neves B.B. 1975. *Regionalização geotectônica do Pré–Cambriano Nordestino*. Tese de Doutorado, Universidade de São Paulo - USP, São Paulo–SP, p. 198.

Brito Neves B.B. & Cordani U.G. 1991. Tectonic evolution of South America during the late proterozoic. *Precambrian Research*, **53**: 23-40.

Brito Neves B.B., Santos E.J., Schmus W.R.Q. 2000. Tectonic history of the Borborema Province. *In*: Umberto Cordani; Edson José Milani; Antonio Thomaz Filho; Diogenes de Almeida Campos (Org.). *Tectonic Evolution of South America*. Rio de Janeiro: 31st International Geological Congress, pp. 151–182. Special Publication.

Bucci L.A., Hagemann S.G., Groves I.D., Standing J.G. 2002. The Archean Chalice gold deposit: a record of complex, multistage, high-temperature hydrothermal activity and gold mineralisation associated with granitic rocks in the Yilgarn Craton, Western Australia. *Ore geology Reviews*, **19**: 23–67.

Carpenter R., Duke N.A., Sandeman H.A., Stern R. 2005. Relative and absolute timing of gold mineralization along the Meliadine trend, Nunavut, Canada: Evidence for Paleoproterozoic gold hosted in an Archean greenstone belt. *Economic Geology*, **100**: 567–576.

Castro N.A. 2004. *Evolução Geológica Proterozóica da Região entre Madalena e Taperuaba, Domínio Tectônico Ceará Central (Província Borborema)*. Tese de Doutorado, Universidade de São Paulo - USP, São Paulo–SP, p. 221.

Cavalcante J.C. 1999. *Limites e evolução geodinâmica do Sistema Jaguaribeano, Província Borborema, Nordeste do Brasil CE*. Dissertação de Mestrado, Pós-Graduação em Geofísica e Geodinâmica, Universide Federal do Rio Grande do Norte - UFRN, Natal, 125p.

Cawood P.A., Kroner A., Collins W.J., Kusky T.M., Mooney W.D., Windley B.F., 2009. Accretionary orogens through earth history. *Geol. Soc. London Spec. Publ.*, **318**: 1–36.

Cawood P.A., Kroner A., Pisarevsky S. 2006. Precambrian plate tectonics: criteria and evidence. *GSA Today*, **16**: 4–11.

Caxito F.A., Ulhein A., Dantas E.L. 2014. The Afeição augen–gneiss Suite and the record of the Cariris Velhos Orogeny (1000–960 Ma) within the Riacho do Pontal fold belt, NE Brazil. *Journal of South American Earth Sciences*, **51**: 12–27.

Coney P.J. 1989. Structural aspects of suspect terranes and accretionary tectonics in western North America. *Journal of South American Earth Science*, **11(1–2)**: 107–125.

Coney, P.J., Jones, D.L., Monger, J.W.H., 1980. Cordilleran suspect terranes. Nature 288, 329–333.

Cordeiro P.F.O. & Oliveira C.G. 2017. The Goiás Massif: Implications for a pre–Columbia 2.2–2.0 Ga continent–wide amalgamation cycle in central Brazil. *Precambrian Research*, **298**: 403–420.

Cordeiro P.F.O., Oliveira C.G., Giustina M.E.S.D., Dantas E.L., Santos R.V. 2014. The Paleoproterozoic Campinorte Arc: Tectonic evolution of a Central Brazil pre–Columbia orogeny. *Precambrian Research*, **251**: 49–61.

Correa R.T., Vidotti R.M., Oksum E. 2016. Curie surface of Borborema Province, Brazil. *Tectonophysics*, **679**: 73–87.

Costa F.G. 2013. *Geologia e Recursos Minerais da Folha Quixadá (SB-24-V-B-VI)*. Programa Levantamentos Geologicos Basicos do Brasil. Serviço Geológico do Brasil, Fortaleza. CPRM. 1 mapa. Escala: 1:100,000.

Costa F.G., Araújo C.E.G., Amaral W.S., Vasconcelos A.M., Rodrigues J.B. 2013. U-Pb (LA-ICPMS) zircon ages and Nd isotopes for granitoids of the Tamboril-Santa Quitéria Complex, Ceará Central domain: implication for Neoproterozoic syncollisional magmatism in north Borborema Province. *Geologia USP – Série Científica*, **13**: 159–174.

Costa F.G., De Araújo C.E.G., Vasconcelos A.M., Palheta E.S.M., Justo A.P. 2010. O complexo Tamboril–Santa Quitéria: Evidências de slab breakoff durante colisão continental neoproterozóica, norte da província Borborema. In: 45º Congresso Brasileiro de Geologia, Belém–PA, Brazil, *Resumos*… p. 165.

Costa F.G., Oliveira E.P., McNaughton N. 2011. The Fazenda Gavião granodiorite and associated potassic plutons as evidence for Palaeoproterozoic arc–continent collision in the Rio Itapicuru greenstone belt, Brazil. *J. South Am. Earth Sci.*, **32**(2): 127–141.

Costa F.G., Palheta E.S.M., Rodrigues J.B., Gomes I.P., Vasconcelos A.M. 2015. Geochemistry and U-Pb zircon ages of plutonic rocks from the Algodões granite–greenstone terrane, Troia Massif, northern Borborema Province, Brazil: implications for Paleoproterozoic subduction–accretion processes. *J. South Am. Earth Sci*. **59**: 45–68.

Costa F.G., Rodrigues J.B., Cavalcanti J.A.D., Palheta E.S.M., Vasconcelos A.M. 2014a. U–Pb LA-ICPMS ages of detrital zircons from the Paleoproterozoic Algodões and Serra das Pipocas greenstone-like sequences, Ceará Central Domain. *In*: 9th South American Symposium on Isotope Geology, São Paulo, Brazil, p. 110. 1 CD–ROM.

Costa F.G., Rodrigues J.B., Naleto J.L.C., Vasconcelos A.M., Barrueto H.R. 2014b. 2036 Ma SHRIMP U–Pb zircon age for PGE-bearing chromitites of the Troia maficultramafic complex, Ceará Central Domain. *In*: 9th South American Symposium on Isotope Geology, São Paulo, Brazil, pp. 164. 1 CD–ROM.

Craw D., Upton P., Yu B.S., Horton T., Chen Y.G. 2010. Young orogenic gold mineralisation in active collisional mountains, Taiwan. *Mineralium Deposita*, **45**: 631–646.

Cutts K., Lana C., Alkmim F., Peres G.G. 2018. Metamorphic imprints on units of the southern Araçuaí belt, SE Brazil: The history of superimposed Transamazonian and Brasiliano orogenesis. *Gondwana Research*, **58**: 211–234.

Dantas E.L., Souza Z.S., Wernick E., Hackspacher P.C., Xiaodong D., Li J.W. 2013. Crustal growth in the 3.4–2.7 Ga São Jose de Campestre Massif, Borborema Province, NE Brazil. *Precambrian Research,* **227**: 120–156.

Dantas E.L., Van Schmus W.R., Hackspacher P.C., Fetter A.H., Brito Neves B.B., Cordani U., Nutman A.P., Williams I.S. 2004. The 3.4–3.5 São José de Campestre massif, NE Brazil: remnants of the oldest crust in South America. *Precambrian Research,* **130**: 113–137.

Daoust C., Voicu G., Brisson H., Gauthier M. 2011. Geological setting ofthe Paleoproterozoic Rosebel gold district, Guiana Shield, Suriname. *J. South Am. Earth Sci*., **32**: 222–245.

Davies T., Richards J.P., Creaser R.A., Heaman L.M., Chacko T., Simonetti A., Williamson J., McDonald D.W. 2010. Paleoproterozoic Age Relationships in the Three Bluffs Archean Iron Formation-Hosted Gold Deposit, Committee Bay Greenstone Belt, Nunavut, Canada. *Exploration and Mining Geology*, **19**(3-4): 55–80.

Delgado I.M, Souza J.D., Silva L.C., Silveira-Filho N.C., Santos R.A., Pedreira A.J., Guimarães J.T., Angelin L.A.A., Vasconcelos A.M., Gomes I.P, Lacerda Filho, J.V., Valente C.R., Perrota M.M., Heineck C.R. 2003. Geotectônica do Escudo Atlântico. *In*: L.A., Bizzi, C., Schobbenhaus, R.M., Vidotti, J.H., Gonçalves (Ed.). *Geologia, Tectônica e Recursos Minerais do Brasil*. Rio de Janeiro: CPRM, p. 227–334. 1 CD–ROM.

Delor, C., Lahondère, D., Egal, E., Lafon, J.M., Cocherie, A., Guerrot, C., Rossi, P., Trufert, C., Theveniaut, H., Phillips, D., Avelar, V.G., 2003. Transamazonian crustal growth and reworking as revealed by the 1:500,000–scale geological map of French Guiana (2nd edition). Geologie de la France, 2–3–4, 5–57.

Doublier M.P., Thébaud N., Wingate M.T.D., Romano S.S., Kirkland C.L., Gessner K., Mole D.R., Evans N. 2014. Structure and timing of Neoarchean gold mineralization in the Southern Cross district (Yilgarn Craton, Western Australia) suggest leading role of late Low-Ca I-type granite intrusions. *Journal of Structural Geology*, **67**: 205–221.

Doyle M.G., Fletcher I.R., Foster J., Large R.R., Mathur R., McNaughton N.J., Meffre S., Muhling J.R., Phillips D., Rasmussen B., 2015. Geochronological Constraints on the Tropicana Gold Deposit and Albany-Fraser Orogen, Western Australia. *Economic Geology*, **110**: 355-386.

Duarte B.P., Valente S.C., Heilbron M., Campos Neto M.C. 2004. Petrogenesis of the Orthogneisses of the Mantiqueira Complex, Central Ribeira Belt, SE Brazil: An Archaean to Palaeoproterozoic Basement Unit Reworked During the Pan–African Orogeny. *Gondwana Research*, **7**(2): 437–450.

Dubé B. & Mercier–Langevin P. 2015. Targeted Geoscience Initiative 4: Contributions to the Understanding of Precambrian Lode Gold Deposits and Implications for Exploration; Geological Survey of Canada, Open File 7852, 297 p. doi:10.4095/296624.

Duclaux G., Hough R., Gazley M.F. 2012. Late tectonic evolution of Plutonic Gold Mine and controls on gold mineralisation. Structural Geology and Resources. *Australian Institute of Geoscientists Bulletin*, **56**: 75–78.

Duuring P., Cassidy K.F. Hagemann, S.G. 2007. Granitoid-associated orogenic, intrusion-related, and porphyry style metal deposits in the Archean Yilgarn Craton, Western Australia. *Ore Geology Review*, **32**: 157–186.

Dziggel A., Knipfer S., Kisters A.F.M., Meyer F.M. 2006. P–T and structural evolu–tion during exhumation of high–T, medium–P basement rocks in the Barberton Mountain Land, South Africa. *J. Metamorph. Geol.*, **24**: 535–551.

Dziggel A., Poujol M., Otto A., Kisters A.F.M., Trieloff M., Schwarz W., Meyer F.M. 2010. New U–Pb and 40Ar/39Ar ages from the northern part of the Barbertongreenstone belt, South Africa: implications for the formation of Mesoarchaean gold deposits. *Precambrian Research*, **179**: 206–220.

Elmer F.L., White R.W., Powell R. 2006. Devolatilization of metabasic rocks during green schist–amphibolite facies metamorphism. *J. Metamorph. Geol*., **9**: 497–513.

Farina F., Albert C., Lana C. 2015. The Neoarchean transition between medium- and high-K granitoids: Clues from the Southern São Francisco Craton (Brazil). *Precambrian Research*, **266**: 375–394.

Fetter A.H. 1999. *U/Pb and Sm/Nd Geocronological Constraints on the Crustal Framework and Geologic History of Ceará State, NW Borborema Province, NE Brazil: Implications for the Assembly of Gondwana*. Tese de Doutorado, Departament of Geology, Kansas University, Lawrence, USA, 164p.

Fetter A.H., Santos T.J.S., Van Schumus W.R., Hackspacher P.C., Brito Neves B.B., Arthaud M.H., Nogueira Neto J.A., Wernick E., 2003. Evidence for Neoproterozoic continental arc magmatism in the Santa Quitéria Batholith of Ceará State, NW Borborema Province, NE Brazil: implications for the assembly of west Gondwana. *Gondwana Research*, **6**(2): 265–273.

Fetter A.H., Van Schmus W.R., Santos T.J.S., Nogueira Neto J.A., Arthaud M.H. 2000. U-Pb and Sm-Nd geochronological constraints on the crustal evolution and basement architecture of Ceará State, NW Borborema Province, NE Brazil: implications for the existence of the Paleoproterozoic Supercontinent "Atlantica". *Revista Brasileira de Geociências*, **30**(1): 102–106.

Feybesse J.L., Billa M., Guerrot C., Duguey J.L.L., Milesi J.P., Bouchot V. 2006. The Palaeoproterozoic Ghanaian province: geodynamic model and ore controls, including regional stress modeling. *Precambrian Research*, **149**: 149–196.

Fielding I.O.H., Johnson S.P., Zi J.W., Sheppard S., Rasmussen B. 2018. Neighbouring orogenic gold deposits may be the products of unrelated mineralizing events. *Ore Geology Reviews*, **95**: 593–603.

Fortes P.T.F.O., Cheilletz A., Giuliani G., Féraud G. 1997. A Brasiliano age (500±5 Ma) for the Mina III gold deposit, Crixás greenstone belt, central Brazil. *International Geology Reviews*, **39**: 449–460.

Fortes P.T.F.O., Pimentel M.M., Santos R.V., Junges S.L. 2003. Sm–Nd studies at Mina III gold deposit, Crixás greenstone belt, Central Brazil: implications for the depositional age of the upper metasedimentary rocks and associated Au mineralization. *J. South Am. Earth Sci*., **16**: 503–512.

Foster R.P. 1993. *Gold metallogeny and exploration*. Chapman and Hall, London, 448 pp.

Fourgerouse D., Micklethwaite S., Ulrich S., Miller J., Godel B., Adams D., McCuaig T.C. 2017. Evidence for two stages of mineralization in West Africa's largest gold deposit: Obuasi, Ghana. *Economic Geology*, **112**: 3–2.

Freimann M.A. 2014. *Geocronologia e petrotrama de quartzo milonitos do duplex transcorrente de Lavras da Mangabeira*. Dissertação de Mestrado, Universidade de São Paulo - USP, São Paulo, Brasil, 83 p.

Frimmel H.E. 2008. Earth's continental crustal gold endowment. *Earth Plan. Sc. Letters*, **267**(1–2): 45–55.

Frimmel H.E. 2018. Episodic concentration of gold to ore grade through Earth's history. *Earth–Science Reviews*, **180**: 148–158.

Fu B. & Touret J.L.R. 2014. From granulite fluids to quartz-carbonate megashear zones: The gold rush. *Geoscience Frontier*, **5**: 747–758.

Furnes H., Dilek Y., Wit M. 2015. Precambrian greenstone sequences represent different ophiolite types. *Gondwana Research*, **27**(2): 649–685.

Ganade C.E., Basei M.A.S., Grandjean F.C., Armstrong R., Brito R.S. 2017. Contrasting Archaean (2.85–2.68 Ga) TTGs from the Troia Massif (NE-Brazil) and their geodynamic implications for flat to steep subduction transition. Precambr. Res. 297, 1–18.

Ganade, C.E., Cordani, G.U., Weinberg, R.F., Basei, M.A.S., Armstrong, R., Sato, K., 2014. Tracing Neoproterozoic subduction in the Borborema Province (NE-Brazil): Clues from U-Pb geochronology and Sr-Nd-Hf-O isotopes on granitoids and migmatites. *Lithos*, **202**: 167-189.

Ganne J., De Andrade V., Weinberg R.F., Vidal O., Dubacq B., Kagambenga N., Naba S., Baratoux L., Jessell M., Allibon J. 2011. Modern-style plate subduction preserved in the PalaeoproterozoicWest African craton. *Nature Geoscience*, **5**: 60–65.

Gazley, M F, 2011. Metamorphism, geochronology and stratigraphy of an amphibolite–facies greenstone–hosted gold deposit: Plutonic Gold Mine, Marymia Inlier, Western Australia. PhD thesis, Victoria University of Wellington, New Zealand.

Gazley M.F., Vry J.K., Boorman J.C. 2011. P-T evolution in greenstone-belt mafic amphibolites: an example from Plutonic Gold Mine, Marymia Inlier, Western Australia, *Journal of Metamorphic Geology*, **29**: 685–698.

Gazley M.F., Vry J.K., Millet M.A., Plessis, E.D., Baker J.A. 2016. New age constraints on metamorphism, metasomatism and gold mineralisation at Plutonic Gold Mine, Marymia Inlier, Western Australia. *Australian Journal of Earth Sciences*, **63**(4): 413–426.

Giustina M.E.S.D., Oliveira C.G., Pimentel M.M., Melo L.V., Fuck R.A., Dantas E.L., Buhn B. 2009. U–Pb and Sm–Nd constraints on the nature of the Campinorte sequence and related Palaeoproterozoic juvenile orthogneisses, Tocantins Province, central Brazil. *Geological Society, London, Special Publications*, **323**: 255–269.

Goldfarb R.J., André–Mayer A.–S., Jowitt S.M., Mudd G.M. 2017. West Africa: the world‘s premier paleoproterozoic Gold Province. *Economic Geology*, **112**: 123–143.

Goldfarb R.J., Baker T., Dubé B., Groves D.I.., Hart C.J.R., Gosselin P. 2005. Distribution, character, and genesis of gold deposits in metamorphic terranes. *Economic Geology*, 100th Anniversary Volume, 407–450.

Goldfarb R.J. & Groves D.I. 2015. Orogenic gold: Common or evolving fluid and metal sources through time. *Lithos*, **233**: 2–26.

Goldfarb R.J. & Santosh M. 2014. The dilemma of the Jiaodong gold deposits: Are they unique? *Geoscience Frontiers*, **5**(2): 139–153.

Gomes E.N. 2013. *Protominérios e minérios de manganês de Juá-CE*. Dissertação de Mestrado, Universidade Federal do Ceará (UFC), Ceará-CE, p. 102.

Goodwin N.R.J., Burgess R., Craw D., Teagle D.A.H., Ballentine C.J. 2017. Noble gases fingerprint a metasedimentary fluid source in the Macraes orogenic gold deposit, New Zealand. *Mineralium Deposita*, **52**(2): 197-209.

Griffin W.L., Begg G.C., O'Reilley S.Y. 2013. Continental root control on the genesis of magmatic ore deposits. *Nature Geoscience*, **6**: 905–910.

Groves D.I. 1993. The crustal continuum model for late-Archaean lode gold deposits of the Yilgarn block, Western Australia. *Mineralium Deposita*, **28**: 366–374.

Groves D.I., Goldfarb R.J., Gebre–Mariam M., Hagemann S.G., Robert F. 1998. Orogenic gold deposits: A proposed classification in the context of their crustal distribution and relationship to other gold deposit types. *Ore Geology Reviews*, **13**: 7–27.

Groves D.I. & Santosh M. 2015. Province–scale commonalities of some world–class gold deposits: Implications for mineral exploration. *Geoscience Frontiers*, **6**(3): 389–399.

Groves D.I. & Santosh M. 2016. The giant Jiaodong gold province: The key to a unified model for orogenic gold deposits? *Geoscience Frontier*, **7**(3), 409–417.

Groves D.I., Santosh M., Goldfarb R.J., Zhang L. 2018. Structural geometry of orogenic gold deposits: Implications for exploration of world–class and giant deposits. *Geoscience Frontier*, **9**: 1163–1177.

Hammond N.Q., Robb L.J., Foya S., Ishiyama D. 2011. Mineralogical, fluid inclusions and stable isotope characteristics of Birimian orogenic gold mineralization at the Morila mine, Mali, West Africa: *Ore Geology Reviews*, **39**: 218–229.

Hanski E. & Huhma H. 2005. Central Lapland greenstone belt. *In*: Lehtinen M., Nurmi P.A., Rämö O.T. (Eds.). *Precambrian Geology of Finland – Key to the Evolution of the Fennoscandian Shield*. Elsevier, Amsterdam, pp. 139-194.

Hanski E.J., Huhma H., Melezhik V.A. 2016. New isotopic and geochemical data from the Palaeoproterozoic Pechenga Greenstone Belt, NW Russia: Implication for basin development and duration of the volcanism. *Precambrian Research*, **245**: 51–65.

Harris C. & Vogeli J. 2010. Oxygen isotope composition of garnet in the Peninsula Granite, Cape Granite Suite, South Africa: constraints on melting and emplacement mechanisms. *South African Journal of Geology*, **113**: 401–412.

Heilbron M., Duarte B.P., Valeriano C.M., Simonetti A., Machado N., Nogueira J.R. 2010. Evolution of reworked Paleoproterozoic basement rocks within the Ribeira belt (Neoproterozoic), SE–Brazil, based on U–Pb geochronology: Implications for paleogeographic reconstructions of the São Francisco–Congo paleocontinent. *Precambrian Research*, **178**(1–4): 136–148.

Hollanda M.H.B.M., Archanjo C.J., Souza L.C., Dunyi L., Armstrong R. 2011. Longlived Paleoproterozoic granitic magmatism in the Seridó-Jaguaribe domain, Borborema Province – NE Brazil. *Journal South American Earth Sciences*, **32**(4): 287–300.

Hronsky J.M.A., Groves D.I., Loucks R.R., Begg G.C. 2012. A unified model for gold mineralisation in accretionary orogens and implications for regional-scale exploration targeting methods. *Mineralium Deposita*, **47**: 339–358.

Hutchinson, R.W., 1987. Metallogeny of Precambrian gold deposits: space and time relationships. Economic Geology, 90, 1918–1933.

Janoušek V., Farrow, G., Erban, V., 2006. Interpretation of whole-rock geochemical data in igneous geochemistry: introducing Geochemical Data Toolkit (GCDkit). J. Petrol. 47, 1255–1259.

Jost, H., Chemale F., Dussin I.A., Martins R.A. 2010. U–Pb zircon Paleoproterozoic age for the metasedimentary host rocks and gold mineralization of the Crixás greenstone belt, Goiás, Central Brazil. *Ore Geology Reviews*, 37: 127–139.

Kendrick M.A., Honda M., Walshe J., Peteresen K. 2011. Fluid sources and the role of abiogenic-CH4 in Archean gold mineralization: Constraints from noble gases and halogens. *Precambrian Research*, **189**: 331–327.

Kerrich R. & Fyfe W.S. 1981. The gold-carbonate association: source of CO2 and CO2 fixation reactions in Archaean lode deposits. *Chemical Geology*, **33**: 265–293.

Kirkland C.L., Spaggiari C., Smithies R.H., Wingate M.T.D., Belousova E.A., Gréau Y., Sweetapple M.T., Watkins R., Tessalina S., Creaser R. 2015. The affinity of Archean crust on the Yilgarn—Albany–Fraser Orogen boundary: implications for gold mineralisation in the Tropicana Zone. *Precambrian Research*, **266**: 260–281.

Klein E.L. 2014. Ore fluids of orogenic gold deposits of the Gurupi Belt, Brazil: a review of the physico–chemical properties, sources, and mechanisms of Au transport and deposition. *In*: Garofalo, P. S., Ridley, J. R. (eds). *Gold–Transporting Hydrothermal Fluids in the Earth's Crust*. Geological Society, London, Special Publications, **402**: 121–145.

Klein E.L., Harris C., Giret A., Moura C.A.V., Angélica R.S. 2005. Geology and stable isotope (O, H, C, S) constraints on the genesis of the Cachoeira gold deposit, Gurupi Belt, northern Brazil. *Chemical Geology*, **221**: 188–206.

Klein E.L., Harris C., Renac C., Giret A., Moura C.A.V., Fuzikawa K. 2006. Fluid inclusion and stable isotope (O, H, C, and S) constraints on the genesis of the Serrinha gold deposit, Gurupi Belt, northern Brazil. *Mineralium Deposita*, **41**: 160–178.

Klein E.L., Lucas F.R.A., Queiroz J.D.S., Freitas S.C.F., Renac C., Galarza M.A., Jourdan F., Armstrong R. 2015. Metallogenesis of the Paleoproterozoic Piaba orogenic gold deposit, São Luís cratonic fragment, Brazil. *Ore Geology Reviews*, **65**(1): 1–25.

Klein E.L. & Moura C.A.V. 2008. São Luís craton and Gurupi belt (Brazil): possible links with the West African craton and surrounding Pan–African belts. *In*: Pankhurst R.J., Trouw R.A.J., Brito Neves B.B., de Wit M.J. (Eds.). *West Gondwana: Pre–Cenozoic Correlations across the South Atlantic Region*. Geological Society, London, Special Publications, **294**: 137–151.

Klein E.L., Rodrigues J.B., Lopes E.C.S., Soledade G.L. 2012. Diversity of Rhyacian granitoids in the basement of the Neoproterozoic–Early Cambrian Gurupi Belt, northern Brazil: geochemistry, U–Pb zircon geochronology, and Nd isotope constraints on the Paleoproterozoic magmatic and crustal evolution. *Precambrian Research*, **220**: 192–216.

Klein E.L., Tassinari C.G., Vasconcelos P.M. 2014. U–Pb SHRIMP and $^{40}Ar/^{39}Ar$ constraints on the timing of mineralization in the Paleoproterozoic Caxias orogenic gold deposit, São Luís cratonic fragment, Brazil. *Brazilian Journal of Geology*, **44**(2): 277–288.

Kolb J., Dziggel A., Bagas L. 2015. Hypozonal lode gold deposits: a genetic concept based on a review of the New Consort, Hutti, Hira Buddini, Navachab, Nevoria, and the Granites deposits. *Precambrian Research*, **262**: 20–44.

Kolb J., Kisters A.F.M., Hoernes S., Meyer F.M. 2000. The origin of fluids and nature of fluid–rock interaction in auriferous mylonites of the Renco Mine, southern Zimbabwe. Mineralium Deposita, **35**(1): 109–125.

Kolb J. & Meyer F.M. 2002. Fluid inclusion record of the hypozonal orogenic Rencogold deposit (Zimbabwe) during the retrograde P–T evolution. *Contrib. Mineral.Petrol*., **143**: 495–509.

Korja A., Lahtinen R., Nironen M. 2006. The Svecofennian orogen: a collage of microcontinents and island arcs. *In*: Gee D.G. & Stephenson R.A. (Eds.). *European Lithosphere Dynamics*. Geological Society, London, Memoirs, pp. 561-578.

Kozuch M. 2003. *Isotopic and trace element geochemistry of Early Neoproterozoic gneissic and metavolcanic rocks in the Cariris Velhos Orogen of the Borborema Province, Brazil, and their bearing tectonic setting*. Tese de Doutorado, Kansas University, Lawrence, USA, p.199.

Kramers J.D., Andreoli M.A.G., Atanasova M., Belyanin, G.A., Block D.L., Franklyn C., Harris C., Lekgoathi M., Montross C.S., Ntsoane T., Pischedda V., Segonyane P., Viljoen K.S.F., Westraadt J.E. 2013. Unique chemistry of a diamond bearing pebble from the Libyan Desert Glass strewnfield, SW Egypt: evidence for a shocked comet fragment. *Earth Planet. Sci. Lett*., **382**: 21–31.

Lahtinen R., Huhma H., Lahaye Y., Lode S., Heinonen S., Sayab M., Whitehouse M.J. 2016. Paleoproterozoic magmatism across the Archean-Proterozoic boundary in central Fennoscandia: Geochronology, geochemistry and isotopic data (Sm–Nd, Lu–Hf, O). *Lithos*, 262: 507–525.

Large R., Thomas H., Craw D., Henne A., Henderson S. 2012. Diagenetic pyrite as a source for metals in orogenic gold deposits, Otago Schist, New Zealand. *New Zealand Journal of Geology and Geophysics*, **55**: 137–149.

Larionova Y.O., Samsonov K.N., Shatagin K.N., Nosova A.A. 2013. Isotopic Geochronological Evidence for the Paleoproterozoic Age of Gold Mineralization in Archean Greenstone Belts of Karelia, the Baltic Shield. *Geology of Ore Deposits*, **55**: 320–340.

Lawley C.J.M., Creaser R., Jackson S., Yang Z., Davis B., Pehrsson S., Dubé B., Mercier-Langevin P., Vaillancourt D. 2015. Unravelling the Western Churchill Province Paleoproterozoic gold metallotect: constraints from Re-Os arsenopyrite and U–Pb xenotime geochronology and LA-ICP-MS arsenopyrite geochemistry at the BIF-Hosted Meliadine Gold District, Nunavut, Canada. *Economic Geology*, **110**: 1425–1454.

Lawley C.J.M., Selby D., Condon D., Imber J. 2014. Palaeoproterozoic orogenic gold style mineralization at the Southwestern Archaean Tanzanian cratonic margin, Lupa Goldfield, SW Tanzania: Implications from U–Pb titanite geochronology. *Gondwana Research*, **26**(3-4): 1141–1158.

Li S.R. & Santosh M. 2017. Geodynamics of heterogeneous gold mineralization in the North China Craton and its relationship to lithospheric destruction. *Gondwana Research*, **50**: 267–292.

Li Z.X., Bogdanova S.V., Collins A.S., Davidson A., De Waele B., Ernst R.E., Fitzsimons I.C.W., Fuck R.A., Gladkochub D.P., Jacobs J., Karlstrom K.E., Lu S., Natapov L.M., Pease V., Pisarevsky S.A., Thrane K., Vernikovsky V. 2008. Assembly, configuration, and break–up history of Rodinia: a synthesis. *Precambrian Research*, **160**: 171–210.

Liégeois J.P., Claessens W., Camara D., Klerkx J. 1991. Short–lived Eburnean orogeny in southern Mali. Geology, tectonics, U–Pb and Rb–Sr geochronology. *Precambrian Research*, **50**: 111–136.

Lima M.V.A.G., Berrocal J., Soares E.P., Fuck R.A. 2015. Deep seismic refraction experiment in northeast Brazil: new constraints for Borborema province evolution. *Journal of South American Earth Sciences*, **58**: 335–349.

Lopez J.M. 2012. Programa de exploração mineral do grupo Jaguar Mining Inc. *In*: Simpósio de Exploração Mineral – SIMEXMIN, Ouro Preto, Minas Gerais.

Mao J., Wang Y., Li H., Pirajano F., Zhang C., Wang R. 2008. The relationship of mantle-derived fluids to gold metallogenesis in the Jiaodong Peninsula: Evidence from D–O–C–S isotope systematics. *Ore Geology Reviews*, **33**: 361–381.

Martins B.S., Lobato L.M, Rosière C.A., Hagemann S.G., Santos J.O., Villanova F.L., Silva R.C., Lemos L.H. 2016. The Archean BIF-hosted Lamego gold deposit, Rio das Velhas greenstone belt, Quadrilátero Ferrífero: Evidence for Cambrian structural modification of an Archean orogenic gold deposit. *Ore Geology Reviews*, **72**: 963–988.

Martins G. 2000. *Litogeoquímica e Controles Geocronológicos da Suíte Metamórfica Algodões-Choró*. Tese de Doutorado. Universidade Estadual de Campinas - UNICAMP, Campinas-SP, 220 p.

Martins G., Oliveira E.P., Lafon J.M. 2009. The Algodões amphibolite-tonalite gneiss sequence, Borborema Province, NE Brazil: geochemical and geochronological evidence for Paleoproterozoic accretion of oceanic plateu/back-arc basalts and adakitic plutons. *Gondwana Research*, **15**: 71–85.

McCrea J.M. 1950. On the isotopic chemistry of carbonates and a paleotemperature scale. *J. Chem. Phys*., **18**(6): 849–857.

Mcfarlane H. 2018. *The geodynamic and tectonic evolution of the Palaeoproterozoic Sefwi Greenstone Belt, West African Craton (Ghana)*. Tese de Doutorado. Université Toulouse (France) e Monash University (Australia), 326 p.

McMillan N.M. 1996. *Late-Archaean, syn-amphibolite facies, lode-gold deposits overprinted by Palaeoproterozoic deformation, metasomatism and hydrothermal activity at Marymia, Western Australia*. Tese de Doutorado. University of Western Australia. Perth, Western Australia, 244p.

McReath I. & Faraco M.T.L. 2006. Paleoproterozoic greenstone–granite belts in northern Brazil and the former Guyana Shield–West African craton province. *Geologia USP – Série Científica*, **5**(2): 49–63.

Mello E.F., Xavier R.P., McNaughton N.J., Hagemann S.G., Fletcher I., Snee L. 2006. Age constraints on felsic intrusions, metamorphism and gold mineralization in the Palaeoproterozoic Rio Itapicuru greenstone belt, NE Bahia State, Brazil. *Mineralium Deposita*, **40**: 849–866.

Mignot E.L., Reisberg L., André–Mayer A.S., Bourassa Y., Fointaine A., Miller J. 2017. Re–Os Geochronological Evidence for Multiple Paleoproterozoic Gold Events at the Scale of the West African Craton. *Economic Geology*, **112**: 145–168.

Milhomem Neto, J.M., Lafon J.M., Galarza M.A. 2016. First LA-MC-ICP-MS Lu–Hf zircon results for a Rhyacian granitoid and Mesoarchean orthogneiss of the Southeastern Guyana

Shield, north of Brazil. *In*: 10th South American Symposium on Isotope Geology (SSAGI), Puerto Vallarta. vol. 10.

Milhomem Neto J.M., Lafon J.M., Galarza M.A. 2015. Lu–Hf em zircão por LA–MC–ICP–MS no laboratório Pará–Iso/UFPA: Metodologia e exemplo de aplicação. *In*: 14º SBG–Norte, Simpósio de Geologia da Amazônia. Marabá. *Anais...*1 CD–ROM.

Molnár F, O'Brien H., Lahaye Y., Käpyaho A., Sorjonen–Ward P., Hyodo H., Sakellaris G., 2016. Signatures of Multiple Mineralization Processes in the Archean Orogenic Gold Deposit of the Pampalo Mine, Hattu Schist Belt, Eastern Finland. *Economic Geology,* **111**: 1659–1703.

Molnár F., Middleton A., Stein H., Brien H.O., Lahaye Y., Huhma H., Pakkanen L., Johanson B., 2018. Repeated syn- and post-orogenic gold mineralization events between 1.92 and 1.76 Ga along the Kiistala Shear Zone in the Central Lapland Greenstone Belt, northern Finland. *Precambrian Research,* **101**: 936–959.

Morelli R.M., Bell C.C., Creaser R.A. 2010. Constraints on the genesis of gold mineralization at the Homestake Gold Deposit, Black Hills, South Dakota from rhenium–osmium sulfide geochronology. *Mineralium Deposita*, **45**: 461–480.

Mueller A.G. 1992. Petrogenesis of amphibole-biotite-calcite-plagioclase alteration and laminated gold-silver quartz veins in four Archean shear zones of the Norseman district, Western Australia. *Canadian Journal of Earth Science,* **29**: 388–417.

Neves S.P. 2003. Proterozoic history of the Borborema province (NE Brazil): correlations with neighboring cratons and Pan-African belts and implications for the evolution of western Gondwana. *Tectonics*, **22**(4): 1031.

Neves, S.P., 2015. Constraints from zircon geochronology on the tectonic evolution of the Borborema Province (NE Brazil): widespread intracontinental Neoproterozoic reworking of a Paleoproterozoic accretionary orogeny. *Journal South American Earth Science,* **58**: 150–164.

Noce, C.M., Pedrasa–Soares, A.C., Silva, L.C., Armstrang, R., Piuzana, D., 2007. Evolution of polycyclic basement complexes in the Araçuaí Orogen, based on U–Pb SHRIMP data: Implications for Brazil–Africa links in Paleoproterozoic time. *Precambrian Research*, **159**(1–2): 60–78.

Nogueira J.F. 2004. *Estrutura, geocronologia e alojamento dos batólitos de Quixadá, Quixeramobim e Senador Pompeu e Ceará Central*. Tese de Doutorado. Universidade Estadual Paulista (UNESP), Rio Claro-SP, 123p.

Oliveira E.P., Souza Z.S., McNaughton N., Lafon J.M., Costa F.G., Figueiredo A.M. 2011. The Rio Capim volcanic–plutonic–sedimentary belt, São Francisco Craton, Brazil: geological, geochemical and isotopic evidence for oceanic arc accretion during Palaeoproterozoic continental collision. *Gondwana Research*, **19**(3), 735–750.

Oliveira E.P., Toteu S.F., Araújo M.N.C., Carvalho M.J., Nascimento R.S., Bueno J.F., McNaughton N., Basilici G. 2006. Geologic correlation between the Neoproterozoic Sergipano belt (NE Brazil) and the Yaoundé belt (Cameroon, Africa). *Journal of South American Earth Sciences*, **44**(4–5): 470–478.

Oliveira E.P., Windley B.F., Araújo M.N.C. 2010. The Neoproterozoic Sergipano orogenic belt, NE Brazil: A complete plate tectonic cycle in western Gondwana. *Precambrian Research*, **181**(1–4): 64–84.

Oliveira J.F. & Cavalcante J.C. 1993. *Folha Mombaça. Folha SB-24-V-D-V. Escala: 1:100.000. Geologia e Metalogênese*. In: Programa Levantamentos Geológicos Básicos do Brasil. Fortaleza: Serviço Geológico do Brasil, CPRM.

Oliveira R.G. 2008. *Arcabouço Geofísico, Isostasia e Causas do Magmatismo Cenozóico da Província Borborema e de Sua Margem Continental (Nordeste do Brasil)*. Tese de Doutorado, Universidade Federal do Rio Grande do Norte, Natal-RN, 345p.

Oliveira R.G. & Medeiros W.E. 2018. Deep crustal framework of the Borborema Province, NE Brazil, derived from gravity and magnetic data. *Precambrian Research*, **315**: 45–65.

Otto A., Dziggel A., Kisters A.F.M., Meyer F.M. 2007. The New Consort gold mine,Barberton greenstone belt, South Africa: orogenic gold mineralization in a con–densed metamorphic profile. Mineralium Deposita, **42**: 715–735.

Padilha A.L., Vitorello I., Pádua M.B., Bologna M.S. 2013. Electromagnetic constraints for subduction zones beneath the northwest Borborema province: evidence for Neoproterozoic island arc-continent collision in northeast Brazil. *Geology*, **42**: 91–94.

Padilha A.L., Vitorello I., Pádua M.B., Fuck R. 2017. Cryptic signatures of Neoproterozoic accretionary events in northeast Brazil imaged by magnetotellurics: implications for the assembly of West Gondwana. *Tectonophysics*, **699**: 164–177.

Padilha A.L., Vitorello I., Pádua M.B., Fuck R.A. 2016. Deep magnetotelluric signatures of the early Neoproterozoic Cariris Velhos tectonic event within the Transversal sub-province of the Borborema Province, NE Brazil. *Precambrian Research*, **275**: 70–83.

Parra-Avila L., Belousova E., Fiorentini M.L., Eglinger A., Block S., Miller J. 2018. Zircon Hf and O-isotope constraints on the evolution of the Paleoproterozoic Baoulé-Mossi domain of the southern West African Craton. *Precambrian Research*, **306**: 174–188.

Parra-Avila L.A., Belousova E., Fiorentini M.L., Baratoux L., Davis J., Miller J., McCuaig T.C., 2016. Crustal evolution of the Paleoproterozoic Birimian terranes of the Baoulé-Mossi domain, southern West African Craton: U-Pb and Hf–isotope studies of detrital zircons. *Precambrian Research*, **274**: 25–60.

Parra-Avila L.A., Kemp A.I.S., Fiorentini M.L., Belousova E., Baratoux L., Block S., Jessell M., Bruguier O., Begg G.C., Miller J., Davis J., McCuaig T.C. 2017. The geochronological

evolution of the Paleoproterozoic Baoulé-Mossi domain of the Southern West African Craton. Precambrian Research, **300**: 1–27.

Perring C.S. & McNaughton N.J. 1990. Geological note: Proterozoic remobilization of ore metals within Archaean gold deposits: Lead isotope evidence from Norseman, Western Australia: *Australian Journal of Earth Sciences*, **37**: 369–372.

Perrouty S., Jessel M.W., Bourassa Y., Miller J., Apau D., Parra-Avila L.A., Mignot E.L., Velásquez G., Ganne J., Siebenaller L., Baratoux L., Aillères L., André-Mayer A.S., Béziat D., Salvi S. 2016. Geological setting of the Wassa gold deposit, SW Ghana. *Ore Geology Reviews*, 78: 687–691.

Pessoa R.R. & Archanjo C.J. 1984. Tectônica de empurrões na região de Troia–CE. *In*: Congresso Brasileiro de Geologia. SGB, Rio de Janeiro, pp. 1721–1728.

Pessoa R.R., Brito Neves B.B., Kawashita K., Pessoa D.R., Fuck R.A. 1986. Contribuição ao estudo de evolução geocronológica do Maciço de Troia – CE. 12º Simpósio de Geologia do Nordeste, João Pessoa, p.1721–1728.

Petersson A., Scherstén A., Gerdes A. 2017. Extensive reworking of Archaean crust within the Birimian terrane in Ghana as revealed by combined zircon U–Pb and Lu–Hf isotopes. *Geoscience Frontier*, **9**(1): 173–189.

Petersson A., Scherstén A., Kemp A.I.S., Kristinsdóttir B., Kalvig P., Anum S. 2016. Zircon U–Pb–Hf evidence for subduction related crustal growth and reworking of Archaean crust within the Palaeoproterozoic Birimian terrane, West African Craton, SE Ghana. *Precambrian Research*, **275**: 286–309.

Petersson A., Scherstén A., Kristinsdóttir B., Kemp A., Whitehouse M. 2018. Birimian crustal growth in the West African Craton: U–Pb, O and Lu–Hf isotope constraints from detrital zircon in major rivers. *Chemical Geology*, **479**(20): 259–271.

Phillips G.N. & Powell R. 2009. Formation of gold deposits: review and evaluation of the continuum model. *Earth-Science Reviews*, **94**: 1–21.

Phillips G.N. & Powell R. 2010. Formation of gold deposits: A metamorphic devolatilization model: Journal of Metamorphic Geology, **28**: 689–718.

Pinéo T.R.G. & Costa F.G. 2013. Dados aerogamaespectrométricos aplicados na delimitação do Complexo Cruzeta (Maciço arqueano de Troia), Domínio Ceará Central da Província Borborema. *In*: 13th International Congress of the Brazilian Geophysical Society, Rio de Janeiro, Brazil, p.5.

Pitcairn I.K., Craw D., Teagle A.H. 2015. Metabasalts as sources of metals in orogenic gold deposits. Mineralium Deposita, **50**(3), 373–390.

Pitcairn I.K., Teagle D.A.H., Craw D., Olivo G.R., Kerrich R., Brewer T.S. 2006. Sources of metals and fluids in orogenic gold deposits: Insights from the Otago and Alpine Schists, New

Zealand: *Economic Geology and the Bulletin of the Society of Economic Geologists*, **101**: 1525–1546.

Pope E.C., Rosing M.T., Bird D.K. 2011. Geochemical evidence for subduction in the early Archaean from quartz-carbonate-fuchsite mineralization, Isua Supracrustal Belt, West Greenland. *Eos Trans. AGU*, Fall Meeting Supplement 92, Abstract U13A-0036.

Queiroz C.L., McNaughton N., Fletcher I., Jost H., Barley M.E. 2000. Polymetamorphic History of the Crixás–Açu Gneiss, Central Brazil: SHRIMP U–Pb Evidence from Titanite and Zircon. Revista Brasileira de Geociências, **30**(1), 40–44.

Rock N.M.S., Groves D.I., Perring C.S., Golding S.D. 1989. Gold, lamprophyres, and porphyries: what does their association mean? *In*: Keays R.R., Ramsay W.R.H., Groves D.I. (Eds.). *The Geology of Gold Deposits, the Perspective in 1988*. Economic Geology Monograph, vol. 6. Economic Geology Publishing, New Haven, Connecticut, pp. 609–625.

Roedder E. 1984. *Fluid inclusions*. Reviews in Mineralogy, 12: 644 pp.

Rosa–Costa L.T., Lafon J.M., Delor C. 2006. Zircon geochronology and Sm–Nd isotopic study: further constraints for the Archean and Paleoproterozoic geodynamical evolution of the southeastern Guiana Shield, north of Amazonian Craton, Brazil. *Gondwana Research*, **10**(3–4), 277–300.

Salier B.P., Groves D.I., McNaughton N.J., Fletcher I.R. 2005. Geochronological and Stable Isotope Evidence for Widespread Orogenic Gold Mineralization from a Deep-Seated Fluid Source at ca 2.65 Ga in the Laverton Gold Province, Western Australia. *Economic Geology*, **100**(7), 1366–1388.

Santos E.J. 1996. Ensaio preliminar sobre terrenos e tectônica acrescionária na Província Borborema. 39º Congresso Brasileiro de Geologia. Sociedade Brasileira de Geologia, Salvador, Brasil.

Santos E.J., Brito Neves B.B., Van Schmus W.R., Oliveira R.G., Medeiros V.C. 2000. An overall view on the displaced terrane arrangement of the Borborema Province, NE Brazil. *In*: 31th International Geological CongressRio de Janeiro, Brazil, General Symposia, Tectonic Evolution of South American Platform, 9–5.

Santos E.J., Van Schmus W.R., Kozuch M., Brito Neves B.B. 2010. The Cariris Velhos tectonic event in northeast Brazil. *Journal South American Earth Sciences*, **29**: 61–76.

Santos L.C.M., Dantas E.L., Cawood P.A., Lages G.A., Lima H.M., Santos E.J., 2018. Accretion tectonics in Western Gondwana deduced from Sm-Nd isotope mapping of terranes in the Borborema Province, NE Brazil. Tectonics, **37**(8): 2727–2743.

Santos L.C.M.L., Dantas E.L., Cawood P.A., Santos E.J., Fuck R.A. 2017. Neoarchean crustal growth and Paleoproterozoic reworking in the Borborema Province, NE Brazil: insights from geochemical and isotopic data of TTG and metagranitic rocks of the Alto Moxotó Terrane. *Journal South American Earth Sciences*, **79**: 342–363.

Santos T.J.S., Amaral W.S., Ancelmi M.F., Pitarello M.Z., Fuck R.A., Dantas E.L. 2015. U–Pb age of the coesite–bearing eclogite from NW Borborema Province, NE Brazil: Implications for western Gondwana assembly. *Gondwana Research*, **28**: 1183–1196.

Santos T.J.S., Fetter A.H., Nogueira Neto J.A. 2008. Comparison between the northwestern Borborema Province, NE Brazil, and the southwestern Pharusian Dahomey Belt, SW Central Africa. *In*: Pankhurst R.J., Trouw R.A.J., Brito Neves B.B., de Wit M.J. (Eds.). *West Gondwana: Pre-Cenozoic Correlations across the South Atlantic Region*. Geological Society of London, pp. 101–119 Special Publications.

Sato K., Basei M.A.S., Siga O.J. 2008. New techniques applied to U-Pb method at CPGeo – Igc/USP: advances in chemical digestion, mass spectrometry (TIMS) and examples of application integrated with SHRIMP. Geologia USP – Série Científica, **8**: 77–99.

Schimmelmann A., DeNiro M.J. 1993. Preparation of organic and water hydrogen for stable isotope analysis: effects due to reaction vessels and zinc. *Analytical Chemistry*, **65**: 789–792.

Shepherd T.J., Rankin A.H., Alderton D.H. 1985. *A practical guide for fluid inclusion studies*. Blackie & Son, Glasgow, 239 pp.

Silva L.C., Armstrong R., Pimentel M.M., Scandolara J., Ramgrab G., Wildner W., Angelim L.A.A., Vasconcelos A.M., Rizzoto G., Quadros M.L.E.S., Sander A., Rosa A.L.Z. 2002. Reavaliação da evolução geológica em terrenos Pré-Cambrianos brasileiros com base em novos dados U-Pb SHRIMP, Parte III: Província Borborema, Mantiqueira Meridional e Rio Negro-Juruena. *Revista Brasileira de Geociências*, **32**: 529–544.

Silva L.C., Costa F.G., Armstrong R., McNaugthon N.J. 2014. U–Pb (SHRIMP) zircon dating and Nd isotopes at basement inliers from northern Borborema Province, Ceará State, NE Brazil: evidences for the Archean and Paleoproterozoic crustal evolution. *In*: 9th South American Symposium on Isotope Geology, São Paulo, Brazil, p. 175.

Silva L.C., MacNaughton N.J., Vasconcelos A.M., Gomes J.R.C., Fletcher I.R. 1997. U–Pb SHRIMP ages in southern State of Ceará, Borborema Province, NE Brazil: Archean TTG accretion and Proterozoic crustal reworking. *In*: Second International Symposium on Granites and Associated Mineralizations, Salvador, p.280.

Silva L.C., Pedrasa–Soares A.C., Armstrong R., Pinto C.P., Magalhães J.T.R., Pinheiro M.A.P., Santos G.G., 2016. Disclosing the Paleoarchean to Ediacaran history of the São Francisco craton basement: The Porteirinha domain (northern Araçuaí orogen, Brazil). *Journal of South American Earth Sciences*, **68**: 50–67.

Silva M.G., Coelho C.E.S., Teixeira J.B.G., Alves da Silva F.C., Silva R.A., Souza J.A.B. 2001. The Rio Itapicuru greenstone belt, Bahia, Brazil: geologic evolution and review of gold mineralization. Mineralium Deposita, **36**: 345–357.

Simões S.J.C. 1993. *Análise da Deformação Regional e Mineral do Complexo Pedra Branca (CE) e de Seus Depósitos Cromitíferos*. Dissertação de Mestrado. Campinas – SP, IG–UNICAMP, 175p.

Sousa H.P. 2016. *Caracterização das unidades máfica–ultramáficas e potencial metalogenético da sequência metavulcanossedimentar Serra das Pipocas (Ceará): um provável greenstone belt*. Dissertação de Mestrado, Universidade Federal do Ceará, Ceará–CE, p. 203.

Souza Z.S., Kalsbeek F., Deng X.D., Frei R., Kokfelt T.F., Dantas E.L., Li J.W., Pimentel M.M., Galindo A.C. 2016. Generation of continental crust in the northern part of the Borborema Province, northeastern Brazil, from Archaean to Neoproterozoic. *Journal of South American Earth Sciences*, **68**: 68–96.

Spence–Jones C., Jenkin G.R.T., Boyce A.J., Hill N.J., Sangster C.J.S. 2018. Tellurium, magmatic fluids and orogenic gold: An early magmatic fluid pulse at Cononish gold deposit? *Ore Geology Review*, (in press).

Staude S., Bons P.D., Marki G. 2009. Hydrothermal vein formation by extension-driven dewatering of the middle crust: An example from SW Germany. *Earth and Planetary Science Letters*, **286**(3–4): 387–395.

Tassara S., González–Jiménez J.M., Reich M., Schilling M.E., Morata D., Begg G., Saunders E., Griffin W.L., O'Reilly S.Y., Grégoire M., Barra F., Corgne A. 2017. Plume–subduction interaction forms large auriferous provinces. *Nature Comunications*, **8**: 843.

Thurston P.C. 2015. Igneous Rock Associations 19. Greenstone belts and granite-greenstone terranes: constraints on the nature of the Archean world. *Geoscience Canada*, **42**: 437–484.

Tomkins A.G. 2010. Windows of metamorphic sulfur liberation in the crust: Implications for gold deposit genesis: *Geochimica et Cosmochimica Acta*, **74**: 3246–3259.

Tomkins A.G. 2013. On the source of orogenic gold. *Geology*, **41**(12), 1255–1256.

Tomkins A.G. & Grundy C. 2009. Upper Temperature Limits of Orogenic Gold Deposit Formation: Constraints from the Granulite-Hosted Griffi n‘s Find Deposit, Yilgarn Craton. *Economic Geology and the Bulletin of the Society of Economic Geologists*, **104**: 669–685.

Torres P.F.M., Cavalcante J.C., Palheta E.S.M., Vasconcelos A.M., Oliveira F.V. 2007. Folha Quixadá. Folha SB-24-V-B, Escala 1:250.000. Geologia e Metalogênese. *In*: Programa Levantamentos Geológicos Básicos do Brasil. Fortaleza: Serviço Geológico do Brasil. CPRM.

Treloar P.J., Lawrence D.M., Senghor D., Boyce A., Harbidge P. 2015. The Massawa gold deposit, Eastern Senegal, West Africa: an orogenic gold deposit sourced from magmatically derived fluids? *In*: Jenkin G.R.T., Lusty P.A.J., McDonald I., Smith M.P., Boyce A.J., Wilkinson J.J. (eds). *Ore Deposits in an Evolving Earth*. Geol. Soc. Lond. Spec. Publ., 393, 135–160.

Trompette R. 1994. *Geology of Western Gondwana. Pan-African-Brasiliano aggregation of South América and Africa*. A.A. Balkema, Rotterdam, Brookfield, 350p.

Valladares C.S., Duarte B.P., Machado H.T., Viana S.M., Figueiredo P.L.C. 2017. Genesis and evolution of a Paleoproterozoic basement inlier within West Gondwana addressed by Sm–Nd isotopic geochemistry and Zr saturation thermometry. *Journal of South American Earth Sciences*, **80**: 95–106.

Van Schmus W.R., Oliveira E.P., Silva Filho A.F., Toteu S.F., Penaye J., Guimarães I.P. 2008. Proterozoic links between the Borborema Province, NE Brazil, and the Central African Fold Belt. *Geological Society, London, Special Publications*, **294**: 69–99.

Vanderhaeghe O., Ledru P., Thiéblemont D., Egal E., Cocherie A., Tegyey M., Milési J.P. 1998. Contrasting mechanism of crustal growth: geodynamic evolution of the Paleoproterozoic granite–greenstone belts of French Guiana. *Precambrian Research*, **92**(2), 165–193.

Vauchez A., Neves S.P., Caby R., Corsini M.E.S., Arthaud M.H., Amaro V. 1995. The Borborema shear zone system, NE Brazil. *Journal of South American Earth Sciences*, **8**: 247–266.

Vennemann T.W. & O'Neil J.R. 1993. A simple and inexpensive method of hydrogen isotope and water analyses of minerals and rocks based on zinc reagent. *Chemical Geology*, **103**: 227–234.

Verma S.K. & Oliveira E.P. 2014. Tectonic setting of basic igneous and metaigneous rocks of Borborema Province, Brazil using multi-dimensional geochemical discrimination diagrams. Journal of South American Earth Sciences, **58**: 309–317.

Vielreicher N.M., Groves D.I., Snee L.W., Fletcher I.R., McNaughton N.J. 2010. Broad synchroneity of three gold mineralization styles in the Kalgoorlie gold field: SHRIMP, U-Pb, and 40Ar/39Ar geochronological evidence. *Economic Geology*, **105**: 187–227.

Vielreicher N.M. & McNaughton N.J. 2002. SHRIMP U–Pb geochronology of magnetism and thermal events in the Archaean Marymia Inlier, central Western Australia. *International Journal of Earth Science*, **91**: 406–432.

Voicu G., Bardoux M., Stevenson R. 2001. Lithostratigraphy, geochronologyand gold metallogeny in the northern Guiana Shield, South America: a review. *Ore Geology Reviews*, **18**: 211–236.

Vry J., Powell R., Golden K., Petersen K. 2010. The role of exhumation in metamorphic dehydration and fluid production. *Nature Geoscience*, **3**: 31–35.

Wannamaker P.E. 2010. Water from stone. *Nature Geoscience*, **3**: 10–11.

White A.J.R., Burgess R., Charnley N., Selby D., Whitehouse M., Robb L.J., Waters D.J. 2014. Constraints on the timing of late-Eburnean metamorphism, gold mineralisation and regional exhumation at Damang mine, Ghana. *Precambrian Research*, **243**: 18–38.

White A.J.R., Waters D.J., Robb L.J. 2013. The application of P-TX(CO_2) modeling in constraining metamorphism and hydrothermal alteration at the Damang gold deposit, Ghana: *Journal of Metamorphic Geology*, **31**: 937–961.

White A.J.R., Waters D.J., Roob L.J. 2015. Exhumation-Driven Devolatilization as a Fluid Source for Orogenic Gold Mineralization at the Damang Deposit, Ghana. *Economic Geology*, **110**(4): 1009–1025.

Wilkinson J.J. 2001. Fluid inclusions in hydrothermal ore deposits. *Lithos*, **55**: 229–172.

Xue Y., Campbell I., Ireland T.R., Holden P., Armstrong R. 2013. No mass-independent sulfur isotope fractionation in auriferous fluids supports amagmatic origin for Archean gold deposits. *Geology*, **41**: 791–794.

Zhang J., Linnen R., Lin S., Davis D., Martin R. 2014. Paleoproterozoic hydrothermal reactivation in a Neoarchean orogenic lode–gold deposit of the southern Abitibi subprovince: U–Pb monazite geochronological evidence from the Young–Davidson mine, Ontario. *Precambrian Research*, **249**: 263–272.

Zhang J.Q., Li S.R., Santosh M., Lu J., Wang C.L. 2018. Metallogenesis of Precambrian gold deposits in the Wutai greenstone belt: Constrains on the tectonic evolution of the North China Craton. *Geoscience Frontier*, **9**(2), 317–333.

Zhang J.Y., Ma C.Q., Li J.W., Pan Y.M. 2017. A possible genetic relationship between orogenic gold mineralization and post-collisional magmatism in the eastern Kunlun Orogen, western China. *Ore Geology Reviews*, **81**: 342–357.

UNIVERSIDADE FEDERAL DO PARÁ
INSTITUTO DE GEOCIÊNCIAS
PROGRAMA DE PÓS-GRADUAÇÃO EM GEOLOGIA E GEOQUÍMICA

PARECER

Sobre a Defesa Pública da Tese de Doutorado de

FELIPE GRANDJEAN DA COSTA

A banca examinadora da Tese de Doutorado de **FELIPE GRANDJEAN DA COSTA** orientando do Prof. Dr. Evandro Luiz Klein (UFPA/CPRM), composta pelos professores doutores Lydia Maria Lobato (UFMG), Roberto Perez Xavier (UNICAMP), Paulo Sergio de Sousa Gorayeb (UFPA), e Raimundo Netuno Nobre Villas (UFPA) após apresentação do projeto de tese intitulado **"GEOLOGIA E METALOGÊNESE DO OURO DO *GREENSTONE BELT* DA SERRA DAS PIPOCAS, MACIÇO DE TROIA, PROVÍNCIA BORBOREMA, NE-BRASIL",** emite o seguinte parecer:

O candidato realizou sua apresentação de forma clara, bem organizada e segura no tempo estipulado. Na arguição mostrou domínio da temática abordada e respondeu às perguntas formuladas pela banca. O trabalho escrito foi apresentado na forma de agregação de artigos científicos, um já publicado, e atende as exigências básicas para uma tese de doutorado.

Considerando a qualidade da tese e os critérios adotados pelo PPGG, a banca a aprova com distinção, outorgando o título de Doutor. Pelo exposto a banca aprova a tese de doutorado candidato **FELIPE GRANDJEAN DA COSTA**.

Belém, 13 de dezembro de 2018.

Prof. Dr. Evandro Luiz Klein (UFPA/**CPRM**)

Profa. Dra. Lydia Maria Lobato (UFMG)

Prof. Dr. Roberto Perez Xavier (UNICAMP)

Prof. Dr. Paulo Sérgio de Sousa Gorayeb (UFPA)

Prof. Dr. Raimundo Netuno Nobre Villas (UFPA)